

Mössbauer Spectroscopy and Its Chemical Applications

Mössbauer Spectroscopy and Its Chemical Applications

John G. Stevens, EDITOR

University of North Carolina at Asheville

Gopal K. Shenoy, EDITOR

Argonne National Laboratory

Based on a symposium jointly
sponsored by the Divisions of
Nuclear Chemistry and Technology
and Inorganic Chemistry at the
179th Meeting of the
American Chemical Society,
Houston, Texas,
March 24–26, 1980.

ADVANCES IN CHEMISTRY SERIES

194

AMERICAN CHEMICAL SOCIETY

WASHINGTON, D. C. 1981



Library of Congress CIP Data

Mössbauer spectroscopy and its chemical applications.
(Advances in chemistry series, ISSN 0065-2393;
194)

"Based on a symposium jointly sponsored by the Divisions of Nuclear Chemistry and Technology and Inorganic Chemistry at the 179th meeting of the American Chemical Society, Houston, Texas, March 24-26, 1980."

Includes bibliographies and index.

1. Mössbauer spectroscopy—Congresses.

I. Stevens, John Gehret, 1941- . II. Shenoy, G.K.,
III. American Chemical Society. Division of Nuclear
Chemistry and Technology. IV. American Chemical
Society. Division of Inorganic Chemistry. V. Series.
QD1.A355 no.194 [QD96.M6] 540s [543'.08586]
81-17540

ISBN 0-8412-0593-0 ADCSAJ 194 1-642 AACR2
1981

Copyright © 1981

American Chemical Society

All Rights Reserved. The appearance of the code at the bottom of the first page of each article in this volume indicates the copyright owner's consent that reprographic copies of the article may be made for personal or internal use or for the personal or internal use of specific clients. This consent is given on the condition, however, that the copier pay the stated per copy fee through the Copyright Clearance Center, Inc. for copying beyond that permitted by Sections 107 or 108 of the U.S. Copyright Law. This consent does not extend to copying or transmission by any means—graphic or electronic—for any other purpose, such as for general distribution, for advertising or promotional purposes, for creating new collective work, for resale, or for information storage and retrieval systems.

The citation of trade names and/or names of manufacturers in this publication is not to be construed as an endorsement or as approval by ACS of the commercial products or services referenced herein; nor should the mere reference herein to any drawing, specification, chemical process, or other data be regarded as a license or as a conveyance of any right or permission, to the holder, reader, or any other person or corporation, to manufacture, reproduce, use, or sell any patented invention or copyrighted work that may in any way be related thereto.

PRINTED IN THE UNITED STATES OF AMERICA

Advances in Chemistry Series

M. Joan Comstock, *Series Editor*

Advisory Board

David L. Allara	James P. Lodge
Kenneth B. Bischoff	Marvin Margoshes
Donald D. Dollberg	Leon Petrakis
Robert E. Feeney	Theodore Provder
Jack Halpern	F. Sherwood Rowland
Brian M. Harney	Dennis Schuetzle
W. Jeffrey Howe	Davis L. Temple, Jr.
James D. Idol, Jr.	Gunter Zweig

FOREWORD

ADVANCES IN CHEMISTRY SERIES was founded in 1949 by the American Chemical Society as an outlet for symposia and collections of data in special areas of topical interest that could not be accommodated in the Society's journals. It provides a medium for symposia that would otherwise be fragmented, their papers distributed among several journals or not published at all. Papers are reviewed critically according to ACS editorial standards and receive the careful attention and processing characteristic of ACS publications. Volumes in the **ADVANCES IN CHEMISTRY SERIES** maintain the integrity of the symposia on which they are based; however, verbatim reproductions of previously published papers are not accepted. Papers may include reports of research as well as reviews since symposia may embrace both types of presentation.

PREFACE

Mössbauer spectroscopy has matured to the point that the experimental parameters can be obtained and fairly well understood, so the usefulness of the technique to study problems in a number of areas is being explored vigorously. The great diversity of applications is evident immediately upon scanning the main category headings in this volume. Valuable information is being obtained, much of which is contained herein. Mössbauer spectroscopy has been used in conjunction with other forms of spectroscopy to maximize understanding of particular systems. Several chapters, most of them using ^{57}Fe , are demonstrations of ways in which very specific environments in materials such as catalysts, biological species, and surfaces can be investigated. The uses of the technique as an analytical tool for quantitative studies and in fast-time studies are also covered.

Specifically, the book is composed of seven extended papers and more than twenty short papers. These were selected from among those presented at the symposium upon which this book is based for expansion in order to give a good overview of the ways in which Mössbauer effect is being used in researching chemical problems. The seven longer papers contain reviews and/or useful detailed information on particular techniques. The topics include new uses, such as applications of resonance for isotopes other than ^{57}Fe and ^{119}Sn to important materials like coal, storage hydrides, steels, and catalysts, in modern technology, and to the studies of surfaces. Also included are use of internal conversion Mössbauer spectroscopy and the theoretical interpretation of Mössbauer spectroscopic measurements.

The short papers do not merely present new measurements or results, but provide, as well, introduction to the subject of the report, and generally give a critical evaluation of other relative studies. In many cases the experiments are quite novel. Collectively these papers show the breadth of new applications of the Mössbauer effect. Other isotopes reported in this volume besides ^{119}Sn and ^{57}Fe include ^{67}Zn , ^{99}Ru , ^{121}I , ^{151}Eu , ^{169}Tm , ^{197}Au , and ^{237}Np . The applications of molecular orbital calculations are surveyed and evaluated and, by correlation with the Mössbauer data, give new insights into chemical bonding. Conversion electron Mössbauer spectroscopy is finding more and more widespread use in surface analysis. Several chapters deal with the applications of

Mössbauer spectroscopy to the characterization of coal and its utilization. Examples of the many kinds of materials that can be studied are given: soils, iron-sulfur biological clusters, catalysts, battery materials, and hydrogen storage materials, among others.

Serving with us on the organizing committee were L. H. Bowen (North Carolina State University), M. L. Good (Louisiana State University), R. H. Herber (The Rutgers University), C. H. W. Jones (Simon Fraser University), G. L. Long (University of Missouri—Rolla), L. May (The Catholic University), and J. J. Zuckerman (University of Oklahoma).

Industrial sponsors that made the symposium and thus this volume possible include New England Nuclear, Spire Corporation, Amersham Corporation and The Radiochemical Centre, Harwell, Elscint, Inc., Ranger Engineering Corp., and WissEl. During every stage of the symposium and the preparation of the book, assistance was received from the staff of the Mössbauer Effect Data Center of the University of North Carolina at Asheville. Special appreciation is due to Virginia Stevens, who was involved in the interminable details and decisions from the beginning to the end.

Finally, we would like to dedicate this book to the memory of Jan Trooster, a scientist and friend extraordinaire, who was to have contributed specifically but, because of illness, was unable to do so. However, his spirit of adventure, dedication to careful research, and abounding good humor provided those around him with the inspiration and energy necessary to do the kind of work this book represents.

JOHN G. STEVENS
Mössbauer Effect Data Center
University of North Carolina at Asheville
Asheville, NC 28814

GOPAL K. SHENOY
Solid State Physics Division
Argonne National Laboratory
Argonne, IL 60439

June 27, 1981

INTRODUCTORY REMARKS

I am pleased to have the opportunity to review the breadth of applications of the Mössbauer effect which is represented by this book. My remarks reflect my two "hats" in that I represent the American Chemical Society through its Board of Directors and I am a member of that group of chemists who recognized early the potential utility of Mössbauer spectroscopy in solving chemical problems. First, I am pleased to see an interdisciplinary symposium such as this one attract such a diversified group of scientists for the extended exchange of basic science and technology in a specific area of interest. It illustrates the central place of chemistry in the discussion of major concepts in science and in the evaluation of current technological problems. The American Chemical Society, through its Divisions of Inorganic Chemistry and Nuclear Chemistry and Technology, is to be congratulated for providing a forum of this type.

A brief review of this volume reveals both the breadth and depth of the current state of the art of Mössbauer spectroscopy and its applications to current problems of interest. The chapters range from applications in theoretical chemistry to the analysis of the mineral content of coal. The overall symposium program, on which this book is based, proves that the early recognized potential of this technique for solving chemical problems has been realized. However, the obvious limitations are still with us. The overwhelming majority of the chapters focus on the Mössbauer effect in ^{57}Fe ; the extension to other isotopes is still not extensive. Perhaps what the symposium indicates best is our present ability to apply somewhat esoteric instrumental methods both to significant basic scientific questions and to applied research problems of technological interest. As our technological problems become more complex, this ability will become more and more important.

The organizers, particularly John Stevens, Virginia Stevens, and Gopal Shenoy, are to be congratulated for their efforts to bring this group together and for coaxing papers out of so many of the participants. Those who have helped organize meetings of this type know the work involved and can recognize the outstanding job that this small group has accomplished.

MARY L. GOOD

June 27, 1980

Application of Molecular Orbital Calculations to Mössbauer and NMR Spectroscopy of Halogen-Containing Compounds

MICHAEL GRODZICKI, SIEGFRIED LAUER, and
ALFRED X. TRAUTWEIN

Angewandte Physik, Universität der Saarlandes,
66 Saarbrücken 11, West Germany

ANNABELLA VERA

Universita degli Studi di Parma, 43100 Parma, Italy

Self-consistent field and charge molecular orbital (MO) calculations are applied to a series of fluorine-, chlorine-, bromine-, and iodine-containing molecules. Calculated orbital energies and dipole moments are used for testing and comparing the MO theories. The calculation procedures for deriving (1) electron charge densities $\rho(O)$, (2) electric field gradient tensors, and (3) internal magnetic fields are described in detail. In connection with calculated $\rho(O)$ values and measured isomer shifts δ , the relative change of nuclear charge radius, $\delta R/R$, is derived for iodine. Together with the various contributions to the electric field gradient, the quadrupole polarization of electronic cores $\gamma(r)$ and the nuclear quadrupole moments Q for chlorine, bromine, and iodine are discussed. For one specific compound, $N(C_2H_5)_4-FeI_4$, the internal magnetic fields at the iron and iodine nuclei are evaluated simultaneously from the magnetic MO structure of this compound. All calculated data are compared with experimental results.

Molecular orbital (MO) calculations provide us with electronic and magnetic structure properties of a molecule, from which suitable spectroscopic data can be derived for comparison with experimental Mössbauer and NMR work. Comparing experimental hyperfine data with

0065-2393/81/0194-0003\$08.75/0

© 1981 American Chemical Society

computed electronic data yields nuclear properties such as $\delta R/R$ (relative change of nuclear charge radius) and Q (nuclear quadrupole moments). Beyond this, the mutual feedback of theory and experiment helps the quantum chemist test the reliability of the various approximations involved in his calculations and helps the spectroscopist interpret his measured data.

In the present work, self-consistent field (SCF) and self-consistent charge (SCC) MO calculations are applied to a series of halogen-containing compounds. In the second section, some of the approximations inherent to these calculations are described, and experimental orbital energies and dipole moments are compared with calculated values derived from SCC- X_α -MO, SCC-IEH-MO (iterative extended Hückel), SCF-MO (close to the Hartree-Fock limit), and Gaussian 76-MO versions. The following sections deal with isomer shift and electron charge density at the Mössbauer nucleus, with electric field gradients, and with the interpretation of measured magnetic hyperfine fields at the iron and iodine nuclei.

Molecular Orbital Calculations

The one-electron equation that may describe the electronic structure of a many-particle system is (in a.u.)

$$(-\Delta + V(\vec{r})) \psi_k(\vec{r}) = \epsilon_k \psi_k(\vec{r}), \quad (1)$$

where $V(\vec{r})$ is a local pseudopotential, and $\psi_k(\vec{r})$ are molecular orbitals (MO)

$$\psi_k(\vec{r}) = \sum_{\nu j} \phi_j^{(\nu)}(\vec{r} - \vec{R}_\nu) c_{jk}^\nu \quad (2)$$

$\phi_j^{(\nu)}(\vec{r} - \vec{R}_\nu)$ is an atomic wave function characterizing the (n_j, l_j, m_j) -th atomic orbital of the ν -th atom; for the present work, Slater-type orbitals (STO) are used. Multiplication of Equation 1 from the left by $\phi_i^{(\nu)*}(\vec{r} - \vec{R}_\nu)$ and integration over the electronic coordinates yields the secular equation

$$\sum_{\nu j} (H_{ij}^{\nu\nu} - \epsilon_k S_{ij}^{\nu\nu}) c_{jk}^\nu = 0 \quad (3)$$

with the Hamiltonian matrix elements $H_{ij}^{\nu\nu}$ and the overlap matrix elements $S_{ij}^{\nu\nu}$

$$H_{ij}^{\nu\nu} = \int \phi_i^{(\nu)*}(\vec{r} - \vec{R}_\nu) [-\Delta + V(\vec{r})] \phi_j^{(\nu)}(\vec{r} - \vec{R}_\nu) d^3r \quad (4)$$

$$S_{ij}^{\nu\nu} = \int \phi_i^{(\nu)*}(\vec{r} - \vec{R}_{\nu'}) \phi_j^{(\nu)}(\vec{r} - \vec{R}_{\nu'}) d^3r \quad (5)$$

With the short notations

$$H_{\text{at}}^{(\nu)}(\vec{r}) = -\Delta + V_{\text{at}}^{(\nu)}(\vec{r} - \vec{R}_{\nu}) \quad (6)$$

$$V_{\text{nb}}(\vec{r}) = V(\vec{r}) - \frac{1}{2} [V_{\text{at}}^{(\nu)}(\vec{r} - \vec{R}_{\nu}) + V_{\text{at}}^{(\nu')}(\vec{r} - \vec{R}_{\nu'})] \quad (7)$$

the Hamiltonian matrix elements can be written as

$$\begin{aligned} H_{ij}^{\nu\nu} &= \int \phi_i^{(\nu)*}(\vec{r} - \vec{R}_{\nu'}) \left[\frac{1}{2} (H_{\text{at}}^{(\nu)} + H_{\text{at}}^{(\nu')}) + V_{\text{nb}} \right] \phi_j^{(\nu)}(\vec{r} - \vec{R}_{\nu'}) d^3r \\ &= \frac{1}{2} (\epsilon_i^{\nu'} + \epsilon_j^{\nu}) S_{ij}^{\nu\nu} + \frac{1}{2} (V_{ij}^{\nu\nu} + V_{ji}^{\nu\nu'}) \end{aligned} \quad (8)$$

$$V_{ij}^{\nu\nu} = \int \phi_i^{(\nu)*}(\vec{r} - \vec{R}_{\nu'}) [V(\vec{r}) - V_{\text{at}}^{(\nu)}(\vec{r} - \vec{R}_{\nu})] \phi_j^{(\nu)}(\vec{r} - \vec{R}_{\nu'}) d^3r \quad (9)$$

where ϵ^{ν} , is the valence orbital ionization potential of the ν -th atom or ion. From Equation 8 the extended Hückel type equations are obtained by the approximations

$$V_{ij}^{\nu\nu} = \frac{1}{2} (V_{ii}^{\nu\nu'} + V_{jj}^{\nu\nu}) S_{ij}^{\nu\nu} \quad ; \quad \epsilon_i^{\nu'} + V_{ii}^{\nu\nu'} = k H_{ii}^{\nu\nu'} \quad (10)$$

yielding

$$H_{ij}^{\nu\nu} = \frac{k}{2} (H_{ii}^{\nu\nu'} + H_{jj}^{\nu\nu}) S_{ij}^{\nu\nu}. \quad (11)$$

In the IEH calculations, the Cusachs approximation (1) is adapted for the proportionality constant k

$$k = 2 - |S_{ij}^{\nu\nu}| \quad (12)$$

and the diagonal Hamiltonian matrix elements are described in terms of valence orbital ionization potentials which depend on the effective charge Q_{ν} of the ν -th atom (2):

$$H_{ij}^{\nu\nu} = - (\epsilon_{j0}^{\nu} + \epsilon_{j1}^{\nu} Q_{\nu}) \quad (13)$$

So far we have successfully applied this method to the interpretation of electric and magnetic hyperfine parameters of ^{57}Fe -containing compounds (3).

In addition to the IEH method, a method was used that explicitly includes neighbor contributions to the Hamiltonian. Recently we have described this method in detail (4), and have applied it to a series of small molecules including second-row elements (5). The main feature of this method is that $V(\vec{r})$ is described in terms of an X_α -like model potential which depends on effective atomic charges, thus making the application of an SCC iteration procedure possible.

For one atom this potential is given by

$$V_{\text{at}}(r) = -\frac{2Z}{r} + 8\pi \left[\frac{1}{r} \int_0^r x^2 \rho_{\text{at}}(x) dx + \int_r^\infty x \rho_{\text{at}}(x) dx \right] - 6\alpha \left[\frac{3}{8\pi} \rho_{\text{at}}(r) \right]^{1/3} \quad (14)$$

Assuming that the atomic charge density $\rho_{\text{at}}(r)$ depends exponentially on r

$$\rho_{\text{at}}(r) = \frac{N\eta^3}{8\pi} e^{-\eta r}, \quad \eta = \eta(Q) \quad (15)$$

where N is the number of electrons, our atomic model potential has the form

$$V_{\text{at}}(r) = -\frac{2Q}{r} - N \left(\frac{2e^{-\eta r}}{r} + \eta e^{-\eta r} \right) - \alpha' \eta N^{1/3} e^{-\eta r/3}; \quad \alpha' = 1.5 \alpha \left(\frac{3}{\pi^2} \right)^{1/3} \quad (16)$$

$V_{\text{at}}(r)$ is a function of the effective atomic charge via Q , N , and η .

We represent the molecular potential $V_{\text{mol}}(\vec{r})$ by the superposition of atomic potentials (Equation 16)

$$V_{\text{mol}}(\vec{r}) = \sum_{\infty} V_{\text{at}}(|\vec{r} - \vec{R}_{\infty}|) \quad (17)$$

Equation 17 implies

$$V_{\text{ex, mol}}(\vec{r}) \sim \sum_{\infty} \rho_{\infty}^{1/3} (|\vec{r} - \vec{R}_{\infty}|) \quad (18)$$

which overestimates the exchange contribution because $V_{\text{ex, mol}}(\vec{r})$ should be replaced by

$$V_{\text{ex, mol}}(\vec{r}) \sim \rho_{\text{mol}}^{1/3}(\vec{r}) = \left(\sum_{\alpha} \rho_{\alpha} (|\vec{r} - \vec{R}_{\alpha}|)^{1/3} \right) \quad (19)$$

However, Equation 17 has considerable computational advantages over Equation 19.

It is well understood that the X_{α} exchange potential takes too large values for large distances r from the origin (6,7); therefore, we may account for this effect and for the approximation inherent in Equation 18 by replacing $\eta/3$ in the exchange part of Equation 16 by η , which also has obvious computational advantages.

Evaluating the potential matrix elements $V_{ij}^{\nu\nu}$, we expand the atomic potentials $V_{\text{at}}(|\vec{r} - \vec{R}_{\alpha}|)$, centered at \vec{R}_{α} , into spherical harmonics, centered at the origin of the molecular frame,

$$V_{\text{at}}(|\vec{r} - \vec{R}_{\alpha}|) = 4\pi \sum_{lm} V_{l, \text{at}}(r, R_{\alpha}) Y_{lm}^*(\hat{R}_{\alpha}) Y_{lm}(\hat{r}) \quad (20)$$

In this procedure, the first term in Equation 16, which is proportional to $1/r$, takes the form $(-2Q_{\alpha}/2l+1)(r_{\alpha}^l/r_{\alpha}^{l+1})$, while the remaining radial terms are evaluated using the Barnett-Coulson ζ -expansion technique (8). An analogous expansion is applied for the one-center expansion of the atomic wave functions (4). Then, the two-center integrals can be evaluated analytically in closed form. The three-center integrals are derived from

$$V_{ij,3}^{\nu\nu} = (4\pi)^{3/2} \sum_{\alpha \neq \nu\nu} \sum_{l=1}^{\infty} U_{ij,l}^{\nu\nu,\alpha}(r, R_{\alpha}) W_{ij,l}^{\nu\nu,\alpha}(\hat{R}_{\alpha}) \quad (21)$$

where the l -summation may be terminated for nonlinear molecules at $l = 1$ or 2, as has been shown previously (5).

The parameters of the SCC- X_{α} method are determined by

$$x_j^{\nu} = x_{j0}^{\nu} + x_{j1}^{\nu} Q_{\nu} + x_{j2}^{\nu} Q_{\nu}^2 \quad (22)$$

where x may be replaced by the ionization potential ϵ , the Slater exponent ζ , and the potential parameter η , respectively. To reduce the number of free parameters, $\epsilon_{j,1}$ and $\epsilon_{j,2}$ are taken from atomic data (9), while $\eta_{j,1}$, $\eta_{j,2}$, $\zeta_{j,0}$, $\zeta_{j,1}$, and $\zeta_{j,2}$ are determined from r expectation values (5) of atomic Hartree-Fock wave functions (10). Thus, the only free parameters are η_0 and ϵ_0 which have been determined by fitting experimental ionization potentials and dipole moments of the halogen hydrides (HF, HCl, HBr, and HI).

The parameters for the IEH calculations have been determined in a similar fashion. The resulting parameter sets are listed in Table I.

Table I. Final Parameter Set Used for SCC- X_α and IEH Calculations^a

Orbital		ϵ_0	ϵ_1	ϵ_2	ζ_0	ζ_1	η_0	η_1
F	2s	40.80 (34.0)	25.57 (18.0)	3.54	2.5 (2.6)	0.1	2.7	0.5
F	2p	16.84 (18.0)	20.54 (15.0)	3.54	2.3 (2.2)	0.3		
Cl	3s	27.20 (29.0)	15.78 (15.5)	1.63	2.15 (2.5)	0.1	2.5	0.4
Cl	3p	13.19 (13.0)	13.19 (10.0)	1.63	1.89 (2.1)	0.3		
Br	4s	24.75 (26.0)	14.14 (14.0)	1.36	2.45 (3.3)	0.1	2.4	0.4
Br	4p	11.83 (11.5)	11.69 (9.0)	1.36	1.95 (2.5)	0.3		
I	5s	19.72 (25.0)	12.24 (14.0)	1.09	2.50 (3.0)	0.1	2.3	0.4
I	5p	10.74 (10.5)	10.06 (8.0)	1.09	1.98 (2.4)	0.3		
C	2s	14.96 (25.0)	17.54 (11.0)	3.54	1.57 (1.61)	0.1	2.4	0.5
C	2p	9.52 (10.0)	14.69 (11.0)	3.54	1.46 (1.61)	0.3		
H	1s	10.34 (13.6)	20.67 (12.8)	10.34	1.2 (1.2)	0.4	2.4	0.8
N	2s	(30.0)	(12.0)		(1.95)			
N	2p	(11.5)	(12.0)		(1.95)			
O	2s	(33.0)	(15.0)		(2.27)			
O	2p	(15.2)	(15.0)		(2.0)			
S	3s	(22.0)	(9.6)		(1.82)			
S	3p	(11.5)	(9.6)		(1.82)			
Fe	3d	(7.0)	(8.0)		(2.87)			
Fe	4s	(7.5)	(8.0)		(1.4)			
Fe	4p	(6.5)	(8.0)		(1.4)			

^a Energies in eV; values in brackets correspond to IEH calculations, values without brackets to SCC- X_α calculations.

Besides the Mulliken population analysis, we use the population analysis which yields "dipole-corrected population numbers"

$$n_\nu = \sum_{\nu'} \sum_{ij} P_{ij}^{\nu'\nu} (S_{ij}^{\nu'\nu} - Z_{ij}^{\nu'\nu}) \quad (23)$$

with the bond order matrix

$$P_{ij}^{v'v} = \sum_k n_k (c_{ik}^{v'})^* c_{kj}^v \quad (24)$$

that is, the overlap density is partitioned in such a manner that its centroid is preserved (2,5). In Tables II and III we compare our calculated orbital energies and dipole moments with experimental values and with other calculated values that were reported in the literature. It is worth noting that the IEH results show the same level of agreement with experimental results as those obtained with more sophisticated MO methods (that is, SCC- X_α , Gaussian 76, SCF-MO).

Isomer Shift and Electron Charge Density at the Mössbauer Nucleus

The difference of the experimentally determined isomer shift of Compound A and Compound B, $\Delta\delta = \delta_A - \delta_B$, is related to the corresponding difference of electron densities at the Mössbauer nuclei, $\Delta\rho(0) = \rho_A(0) - \rho_B(0)$, by

$$\Delta\delta = \alpha\Delta\rho(0) \quad (25)$$

where α is the isomer shift calibration constant. The total charge density $\rho(0)$ consists of valence and core contributions

$$\begin{aligned} \rho(0) &= \rho_{\text{val}}(0) + \rho_{\text{c}}(0) \\ &= \sum_k n_k |\psi_k(0)|^2 + 2 \sum_n |\psi_n^{(\text{c})}(0)|^2 \end{aligned} \quad (26)$$

For the MO's $\psi_k(\vec{r})$ we are within the linear combination of atomic orbitals (LCAO) approximation, while the molecular core wave functions $\psi_n^{(\text{c})}(\vec{r})$ are derived from orthogonalization of the atomic core wave functions $\phi_n^{(\text{c})}(\vec{r})$ to all MO's $\psi_k(\vec{r})$:

$$\psi_n^{(\text{c})}(\vec{r}) = N_n \left\{ 1 - \sum_k |\psi_k\rangle \langle \psi_k| - \sum_{m=1}^{n-1} |\psi_m^{(\text{c})}\rangle \langle \psi_m^{(\text{c})}| \right\} |\phi_n^{(\text{c})}\rangle \quad (27)$$

(This procedure was first applied by Flygare and Hafemeister to iodine-containing compounds (11) and then was used for iron-containing compounds (3).

Neglecting all terms of third and higher order in the core-ligand overlap matrix

$$S_{in}^{\mu\text{c}} = \int \phi_i^{(\mu)}(\vec{r} - \vec{R}_\mu) \phi_n^{(\text{c})}(\vec{r}) d^3r \quad (28)$$

Table II. Experimental and Calculated Dipole Moments (in Debye) for Various Halogen-Containing Molecules

Molecule	Experimental	Calculated (Literature Values)	IEH	SCC- X _α	Gaus- sian 76
HI	0.4477 ^a , 0.445 ^d	0.654 ^f , 0.7135 ^g , 0.5812 ^o	1.350	0.44	
ClI	1.24 ^a , 0.65 ^{h, h}	1.6402 ^g , 0.7431 ^o	1.286	1.29	
BrI	0.737 ^b , 1.26 ^h	0.645 ^f , 1.2159 ^g , 1.3447 ^o	0.597	0.71	
FI	1.984 ^b	1.448 ^f , 2.1440 ^g , 2.3047 ^o	1.939	2.08	
H ₂ Cl ₂	1.08 ^d	1.2866 ^o	1.320		
ClC ₂ I	0.3 ^a	1.1851 ^o	1.139		
HIC ₂ IH	0.75 ^d	2.0995 ^o	1.360		
H ₃ Cl	1.647 ^c , 1.64 ^d	1.1771 ^g , 1.1830 ^o	0.996		
F ₃ Cl	1.0 ^c	1.1483 ^o	1.178		
FH	1.819 ^o	1.829 ^f	2.800	1.83	1.00
ClH	1.12 ^f , 1.12 ^h	1.114 ^f , -1.78 ^g	1.080	1.08	1.73
BrH	0.834 ^g	0.931 ^f , 1.7357 ^g	1.170	0.88	
BrCl	0.57 ^{h, i}	0.588 ^f , 0.3645 ^g	0.912	0.68	
BrF	1.29 ^f , 1.20 ^h	1.444 ^f , 1.2679 ^g	1.931	1.56	
ClF	0.8881 ^{m, i}	0.901 ^f , 0.8960 ^g , 1.099 ^o , 0.839 ^o , 2.0 ^o	0.952	0.93	0.49
H ₃ CF	1.885 ^r	1.66 ^f	2.444		
H ₃ CCl	1.94 ^h	2.0108 ^g	2.080		
H ₃ CBr	1.82 ^h	1.9203 ^g	1.176		
H ₂ CCl ₂	1.62 ^h	1.8525 ^g	2.103		
H ₂ CBr ₂	1.89 ^h	1.9563 ^g	1.425		
HC ₂ Cl	0.44 ^h	1.3183 ^g	0.344		
HC ₂ Br	0.0 ^h	1.2309 ^g	0.108		

^a Hellwege, K. H.; Hellwege, A.M., Eds. "Structure Data of Free Polyatomic Molecules"; Landolt-Börnstein, New Series II; Springer-Verlag: Berlin, 1976, Vol. 7.

^b Nair, K. P. R., et al. *Chem. Phys. Lett.* 1979, 60, 253.

^c Hellwege, K. H.; Hellwege, A. M., Eds. "Molecular Constants from Microwave Spectroscopy"; Landolt-Börnstein, New Series II; Springer-Verlag: Berlin, 1967, Vol. 4.

^d D'Aus-Lax "Taschenbuch für Chemiker und Physiker"; Springer: Berlin, 1970; Vol. 3.

^e Weiss, R. *Phys. Rev.* 1963, 131, 659.

^f Burrows, C. A. *J. Chem. Phys.* 1959, 31, 1270.

^g Robinette, W. H.; Sanderson, R. B. *Appl. Optics* 1969, 8, 711.

^h Cheesman, G. H., et al. *Theor. Chim. Acta* 1970, 15, 33.

ⁱ Sichel, J. M.; Whitehead, M. A. *Theor. Chim. Acta* 1968, 11, 254.

^j Straub, P. A.; McLean, A. D. *Theor. Chim. Acta* 1974, 32, 227.

^k Höjer, G.; Meza, S. *Acta Chem. Scand.* 1972, 26, 3723.

^l Hase, L. H.; Schweig, A. *Theor. Chim. Acta* 1973, 31, 215.

^m McGurk, I., et al. *J. Chem. Phys.* 1973, 58, 3118.

ⁿ Scharffenberg, P. *Theor. Chim. Acta* 1978, 49, 115.

^o Scharffenberg, P. *Chem Phys. Lett.* 1979, 65, 304.

^p Green, S. *Adv. Chem. Phys.* 1974, 25, 179.

^q Kenneth, C. J., et al. *J. Chem. Phys.* 1976, 64, 2698.

^r Larkin, M.; Gardy, W. *J. Chem. Phys.* 1963, 38, 2329.

^s Pople, T. A.; Beveridge, D. L. "Approximate Molecular Orbital Theory"; McGraw Hill: New York, 1970.

^t Davis, R. E.; Muentzer, J. S. *J. Chem. Phys.* 1972, 57, 2836.

we obtain

$$\psi_n^{(c)}(\vec{r}) = N_n \{ \phi_n^{(c)}(\vec{r}) + 2 \sum_{m=1}^{n-1} N_m^2 \phi_m^{(c)}(\vec{r}) \sum_{\mu\nu} \sum_k c_{ik}^{\mu} c_{jk}^{\nu} S_{im}^{\mu c} S_{jn}^{\nu c} - \sum_{\mu\nu} \sum_k c_{ik}^{\mu} c_{jk}^{\nu} S_{in}^{\mu c} S_{j}^{(\nu)}(\vec{r} - \vec{R}_\nu) \} \quad (29)$$

From Equation 29 the core contribution $\rho_c(0)$ is derived as

$$\rho_c(0) = 2 \sum_n |\psi_n^{(c)}(0)|^2 \quad (30)$$

The free ion contribution $|\phi_n^{(c)}(0)|^2$ is calculated for the actual orbital occupation n_s , n_p of the Mössbauer ion in the molecule from the interpolation formula

$$2|\phi_n^{(c)}(0)|^2 = a_0 + a_s n_s + a_p n_p + a_{ss} n_s^2 + a_{sp} n_s n_p + a_{pp} n_p^2 + a_{sss} n_s^3 + a_{ssp} n_s^2 n_p + a_{spp} n_s n_p^2 + a_{ppp} n_p^3 \quad (31)$$

The coefficients in Equations 31, listed in Table IV, are determined from relativistic Hartree-Fock-Slater calculations for electronic configurations $5s^0 5p^0, \dots, 5s^2 5p^5$. ($5s^2 5p^6$ has been omitted because the X_α method generally fails for negative ions.) With respect to differences in $\rho_c(0)$ as obtained from relativistic Hartree-Fock-Slater and Hartree-Fock-Dirac calculations, respectively, see footnote in Table IV.

As a preliminary result we present here electron densities $\rho(0)$ for five molecules: ICl, IBr, I_2 , IF_5 , and IF_7 . In Figure 1, our calculated relativistic $\rho(0)$ values (which have been derived on the basis of our SCC- X_α -MO calculations) are compared with experimental ^{129}I isomer shifts. The slope of the solid line in Figure 1 represents the isomer shift calibration constant α of Equation 25; α is related to the relative change of the nuclear charge radius of iodine $\delta R/R$ by

$$\frac{\delta R}{R} = \alpha C, \quad (32)$$

with R being the nuclear charge radius and δR the change in R when the nucleus is excited from its ground state to its first excited state. The constant C takes the value $1.9562 \cdot 10^{-3} a_0^{-3} \text{ mm}^{-1} \text{ s}$ for ^{129}I . Taking α from Figure 1 we derive a $\delta R/R$ value of $4.4 \cdot 10^{-4}$ which is in reasonable agreement with the value of $4 \cdot 10^{-4}$ reported by Spijkervet et al. (12) and Ladriere et al. (13).

Table III. Experimental and Calculated Orbital Energies

Molecule	Experimental			SCF-MO (Literature Values ^a)		
	ϵ_{π}	ϵ_{π}	ϵ_{σ}	ϵ_{π}	ϵ_{π}	ϵ_{σ}
ClF	12.66 ^b	16.39 ^b	17.80 ^b			
ClI	10.10 ^c	12.90 ^c	14.26 ^c	10.39	13.84	—
BrI	9.85 ^c	11.90 ^c	13.70 ^c	8.98	11.83	—
F ₂	15.63 ^d	17.35 ^d	18.46 ^d	17.68	22.47	21.23
Cl ₂	11.50 ^d	14.11 ^d	15.94 ^d	11.87	15.39	16.15
Br ₂	10.56 ^c	12.77 ^c	14.56 ^c	10.84	13.52	14.26
I ₂	9.35 ^c	11.00 ^c	12.95 ^c	8.43	10.75	11.57
H ₂	—	—	15.45 ^d	—	—	16.22
FH	16.27 ^d	—	19.86 ^d	17.33	—	20.60
ClH	12.80 ^d	—	16.27 ^d	12.77	—	16.93
BrH	11.87 ^d	—	15.31 ^d	11.54	—	15.59
IH	10.75 ^d	—	14.03 ^d	10.43	—	14.28

^a Straub, P. A.; McLean, A. D. *Theor. Chim. Acta* 1974, 32 227. (These calculations are close to the Hartree-Fock limit of self-consistent field-MO calculations; double-zeta wave functions have been used.)

Table IV. Coefficients (in a_0^{-3}) of the Interpolation from Relativistic Atomic

Shell	Coeff.			
	a_0	a_s	a_p	a_{ss}
4s	1121.677	-9.684	-2.851	9.710
3s	5142.395	-0.991	-1.070	-0.741
2s	25797.154	-4.200	-0.688	4.528
1s	214886.827	-6.094	-0.829	6.882
4p	31.709	-0.219	-0.112	0.162
3p	154.343	0.027	-0.040	-0.123
2p	711.829	-0.226	-0.036	0.251
5s	0.0	112.482	3.848	-21.761
5p	0.0	-4.136	0.661	14.944

^a It has been pointed out earlier (Mahanti, S. D.; Das, T. P.; Lee, T.; Ikenberry, D. *Phys. Rev.* 1974, A9, 2238.) that the relativistic Hartree-Fock-Slater (HFS) approximation is inadequate in obtaining reliable theoretical values of hyperfine constants. Therefore, we compared relativistic HFS results for $\rho(0)$ with those obtained from Hartree-Fock-Dirac (HFD) calculations (J. P. Desclaux, private communication). The absolute relativistic $\rho(0)$ values for free iodine ($5s^25p^5$) are

(in eV) for Various Halogen-Containing Molecules

IEH			SCC-X α			Gaussian 76		
$\epsilon\pi$	$\epsilon\pi$	$\epsilon\sigma$	$\epsilon\pi$	$\epsilon\pi$	$\epsilon\sigma$	$\epsilon\pi$	$\epsilon\pi$	$\epsilon\sigma$
13.48	16.42	16.36	13.46	16.04	18.09	11.23	16.64	15.14
10.76	12.37	12.80	11.02	12.65	14.04	—	—	—
10.35	11.54	12.23	10.34	12.38	14.00	—	—	—
16.29	19.41	19.50	16.04	18.36	21.08	—	—	—
11.88	13.94	14.18	11.83	14.14	16.05	11.07	14.36	14.50
10.93	12.01	12.83	10.88	12.92	15.09	—	—	—
9.82	11.09	11.68	9.93	11.70	13.33	—	—	—
—	—	15.38	—	—	15.48	—	—	—
15.46	—	17.01	15.64	—	20.00	12.61	—	12.89
12.68	—	14.46	12.64	—	16.59	11.51	—	15.35
11.84	—	13.80	11.69	—	15.50	—	—	—
11.11	—	13.04	10.74	—	13.87	—	—	—

^b Anderson, C. P., et al. *Chem. Phys. Lett.* 1971, 12, 137.

^c Hall, M. B. *Int. J. Quantum Chem., Symp.* 1975, 9, 237.

^d Frost, D. C., et al. *J. Chem. Phys.* 1967, 46, 2255.

Formula for $2|\phi_n^{(c)}(0)|^2$ of Equation 31, as Obtained Hartree-Fock-Slater Calculations^a

a_{sp}	a_{pp}	a_{sss}	a_{ssp}	a_{spp}	a_{ppp}
0.607	0.279	-3.117	-0.041	-0.026	-0.009
0.294	0.097	0.357	-0.049	-0.006	-0.003
0.132	0.030	-1.396	-0.046	0.013	0.0
0.123	0.090	-2.256	0.0	-0.001	-0.004
0.019	0.011	-0.052	0.0	-0.001	0.0
0.011	0.004	0.045	-0.002	0.0	0.0
0.006	0.002	-0.078	-0.002	0.001	0.0
-5.920	-1.021	5.998	-0.002	0.447	0.063
-1.374	-0.026	-5.874	0.446	0.005	0.002

on the order of 248,000 a_0^{-3} (HFS) and 255,000 a_0^{-3} (HFD), respectively, that is, the difference $\rho(0) \frac{\text{HFD}}{5s^25p^5} - \rho(0) \frac{\text{HFS}}{5s^25p^5}$ is on the order of 7000 a_0^{-3} . However, the difference $[\rho(0) 5s^25p^4 - \rho(0) 5s^25p^5]_{\text{HFD}} - [\rho(0) 5s^25p^4 - \rho(0) 5s^25p^5]_{\text{HFS}}$ is only on the order of 1 a_0^{-3} .

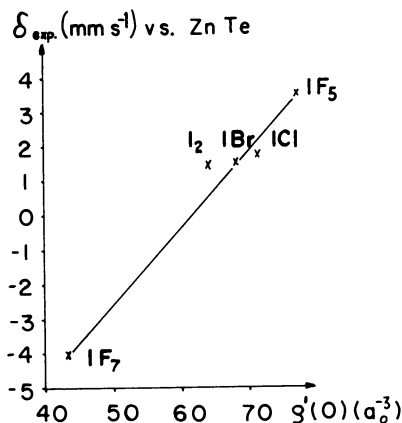


Figure 1. Calculated relativistic electron densities $\rho(0) = 247,900 + \rho'(0)$ in a_0^{-3} vs. experimental isomer shifts δ in mms^{-1} for ^{129}I -containing molecules. Experimental values are taken from Ref. 63. (δ_{exp} values for I_2 , IBr , and ICl correspond to rare gas matrix isolation measurements.)

Quadrupole Coupling Constant and Electric Field Gradient at the Halogen Nucleus

Electric Field Gradient Calculation. A rigorous treatment of the electric field gradient tensor V_{pq} consists of dividing the total charge of the molecule into the positive point-charges q_ν of the atomic cores and the charge distribution of all electrons (14),

$$\begin{aligned}
 V_{pq} &= V_{pq}^{\text{core}} + V_{pq}^{\text{el}} \\
 &= \sum_{\mathbf{R}_\nu \neq 0} q_\nu \hat{V}_{pq}(\vec{\mathbf{R}}_\nu) - e_0 \sum_{ij} P_{ij}^{\nu\nu} \int \phi_i^{(\nu)}(\vec{\mathbf{r}} - \vec{\mathbf{R}}_\nu) \hat{V}_{pq}(\vec{\mathbf{r}}) \phi_j^{(\nu)}(\vec{\mathbf{r}} - \vec{\mathbf{R}}_\nu) d^3r
 \end{aligned} \quad (33)$$

The e_0 is the (positive) elementary charge, and the tensor operator components $\hat{V}_{pq}(\vec{\mathbf{r}})$ are

$$\begin{aligned}
 \hat{V}_{pq}(\vec{\mathbf{r}}) &= [1 - \gamma(r)] \frac{3r_p r_q - r^2 \delta_{pq}}{r^5} \\
 &= \frac{1 - \gamma(r)}{r^3} \sum_{M=-2}^2 C_{pq}^{2M} Z_{2M}(\hat{\mathbf{r}})
 \end{aligned} \quad (34)$$

where $\gamma(r)$ is the Sternheimer shielding function, which will be discussed in the following section, $Z_{2M}(\hat{\mathbf{r}})$ are real spherical harmonics, and the numbers C_{pq}^{2M} are given in Ref. 14.

After calculating V_{pq} according to Equation 33, a matrix diagonalization is performed, and then the main axes elements are rearranged such that $|V_{zz}| \geq |V_{xx}| \geq |V_{yy}|$. With these new main axes elements, the asymmetry parameter η is defined as

$$\eta = \frac{|V_{xx} - V_{yy}|}{|V_{zz}|} \quad (35)$$

The nuclear quadrupole coupling constant e^2qQ , which is taken from experimental work (Mössbauer, NMR, and microwave measurements) for comparison, is related to V_{zz} by

$$e^2qQ = e^2V_{zz}Q \quad (36)$$

where Q is the nuclear quadrupole moment of the atom under consideration. The explicit evaluation of V_{pq} , Equation 33, includes integrals of the type

$$Q_{ij,M}^{v'v} = \int \phi_i^{(v')}(\vec{r} - \vec{R}_{v'}) \frac{Q(r)}{r^2} Z_{2M}(\hat{r}) \phi_j^{(v)}(\vec{r} - \vec{R}_v) d^3r \quad (37)$$

with $Q(r) = [1 - \gamma(r)]/r$. In Equation 37 we distinguish four cases (the superscript O stands for the Mössbauer atom and v, v' for its ligands):

$$Q_{ij,M}^{oo} = \int \phi_i^{(o)}(\vec{r}) \frac{Q(r)}{r^2} Z_{2M}(\hat{r}) \phi_j^{(o)}(\vec{r}) d^3r \quad (38)$$

$$Q_{ij,M}^{ov} = \int \phi_i^{(o)}(\vec{r}) \frac{Q(r)}{r^2} Z_{2M}(\hat{r}) \phi_j^{(v)}(\vec{r} - \vec{R}_v) d^3r \quad (v \neq 0) \quad (39)$$

$$Q_{ij,M}^{vv} = \int \phi_i^{(v)}(\vec{r} - \vec{R}_v) \frac{Q(r)}{r^2} Z_{2M}(\hat{r}) \phi_j^{(v)}(\vec{r} - \vec{R}_v) d^3r \quad (v \neq 0) \quad (40)$$

$$Q_{ij,M}^{v'v} = \int \phi_i^{(v')}(\vec{r} - \vec{R}_{v'}) \frac{Q(r)}{r^2} Z_{2M}(\hat{r}) \phi_j^{(v)}(\vec{r} - \vec{R}_v) d^3r \quad (v \neq v'; v, v' \neq 0). \quad (41)$$

The one-center contributions $Q_{ij,M}^{ov}$ are derived by substituting Equation 34 into Equation 38:

$$Q_{ij,M}^{oo} = G_{2M}(L_i L_j) (1 - R) \langle r^{-3} \rangle_{ij} \quad (42)$$

with $G_{2M}(L_i L_j)$ being a Gaunt number, $L = (lm)$, and $R = \langle \gamma(r)r^3 \rangle / \langle r^3 \rangle$. The $\langle r^{-3} \rangle_{ii}$ values have been derived from Hartree-Fock wave functions (10) taking into account the actual valence orbital population by an appropriate interpolation scheme (see caption of Figure 4). The two-center contributions (Equations 39 and 40) can be evaluated ana-

lytically, using STO's ϕ_i and ϕ_j , with the help of the one-center expansion of Equation 20. This procedure yields the following results for $Q_{ij,M}^{ov}$ and $Q_{ij,M}^{vv}$:

$$Q_{ij,M}^{ov} = \sqrt{4\pi} \sum_{l=|i-2|}^{i+2} \sum_{\mu=-l}^{l} U_{ij}^{ov}(l\mu) W_{ij,M}^{ov}(l\mu), \quad l_{<} = \min(l, l_j) \quad (43)$$

$$U_{ij}^{ov}(l\mu) = \sum_{\lambda=|\mu|}^{l_j} \Gamma_{l_j\mu}(\lambda) R_{\nu}^{lj-\lambda} \sum_{l'=|l-\lambda|} \sqrt{2l'+1} G_{l'}(\lambda\mu, l\mu) \int_0^{\infty} r^{\lambda} R_{i^{(o)}}(r) Q(r) \mu_{n_j l_j}^{(\nu)}(l'; r, R_{\nu}) dr \quad (44)$$

$$W_{ij,\mu}^{ov}(l\mu) = \sum_{m=-l}^l G_L(L_i, 2M) D_{\mu m}^{(l)}(\hat{R}_{\nu}) D_{\mu m, j}^{(l_j)}(\hat{R}_{\nu}) \quad (45)$$

$$Q_{ij,M}^{vv} = \sqrt{4\pi} \sum_{l=|i-l_j|}^{i+l_j} \sum_{\mu=-l}^{l} U_{ij}^{vv}(l\mu) W_{ij,M}^{vv}(l\mu), \quad l_{<} = \min(l, 2) \quad (46)$$

$$U_{ij}^{vv}(l\mu) = \sum_{\lambda=|\mu|}^l \Gamma_{l\mu}(\lambda) R_{\nu}^{l-\lambda} \sum_{l'=|\lambda-2|}^{\lambda+2} \sqrt{2l'+1} G_{l'}(\lambda\mu, 2\mu) \int_0^{\infty} r^{\lambda} Q(r) u_{n_j l_j}^{(\nu)}(l'; r, R_{\nu}) dr \quad (47)$$

$$W_{ij,M}^{vv}(l\mu) = \sum_{m=-l}^l G_L(L_i, l_j) D_{\mu m}^{(l)}(\hat{R}_{\nu}) D_{\mu m, M}^{(2)}(\hat{R}_{\nu}) \quad (48)$$

The notation in the second section has been adapted here. The three-center integrals, Equation 41, could be handled in an analogous manner. However, in view of the expected smallness of these contributions (see Table VIII), we use the following approximation:

$$Q_{ij,M}^{v'v} = Q_{s_i s_j, M}^{v'v} \frac{S_{ij}^{v'v}}{S_{s_i s_j}^{v'v}} \quad (49)$$

where $S_{ij}^{v'v}$ is the overlap matrix and $Q_{s_i s_j, M}^{v'v}$ is the matrix element between the two s functions of the (v', ν) -block of $Q_{ij,M}^{v'v}$ which is

$$Q_{s_i s_j, M}^{v'v} = 4\pi \sum_{l=0}^{l+2} \sum_{l'=|l-2|} U_{ij}^{v'v}(ll') W_{ij}^{v'v}(ll') \quad (50)$$

$$U_{ij}^{v'v}(ll') = \int_0^{\infty} u_{n_i 0}^{(v')}(l'; r, R_{\nu'}) Q(r) u_{n_j 0}^{(\nu)}(l; r, R_{\nu}) dr \quad (51)$$

$$W_{ij, \Delta l}^{v'v} (ll') = \sum_{m=-l}^l Z_L(\hat{R}_v) \sum_{m'=-l'}^{l'} Z_{L'}(\hat{R}_{v'}) G_{2M}(L'L) \quad (52)$$

The l -summation is truncated at $l = 2$, which is sufficient to get results to the third decimal place.

Shielding and Antishielding. The electric field gradient tensor operator components defined in Equation 34 contain the factor $(1 - \gamma(r))$. This factor arises from the polarization of core electrons of the Mössbauer atom by charges outside the core. Within the MO picture, core electrons are those that are excluded from the limited MO basis set. However, for the interpretation of atomic beam measurements the situation is slightly different: the hole in the p -valence electron shell of halides polarizes the inner core *and* the s - and p -valence electrons. In addition, the polarization depends on whether we are concerned with a p_0 - or a $p_{\pm 1}$ -hole.

The amount of polarization depends on $\gamma(r)$ and accounts for shielding ($\gamma(r) > 0$) or antishielding ($\gamma(r) < 0$) effects in deriving the electric field gradient. In the literature most of the work with respect to these shielding and antishielding corrections has been reported by Sternheimer (15–26). Therefore these corrections are also termed “Sternheimer corrections” and the method used by Sternheimer for calculating these terms as the “Sternheimer procedure.” Other methods used for deriving $\gamma(r)$ are the variational method (27–30), the many-body perturbation method (31–36), and the coupled Hartree–Fock method (37–39). Most of the publications report only factors R and γ_∞ or even only γ_∞ . Recently Lauer et al. (40) calculated self-consistent $\gamma(r)$ functions and R factors corresponding to electronic configurations that also exclude the valence orbitals, generally included in the MO calculations.

The polarization induces an electric field gradient in the electron core. The total electric field gradient ($q + q_{\text{ind}}$) interacts with the nuclear quadrupole moment. The total quadrupole coupling constant is then $e^2Q(q + q_{\text{ind}})$ which, including the proportionality factor $(1 - R^*)$, leads to

$$e^2(Qq)_{\text{total}} = e^2Q(q + q_{\text{ind}}) = e^2Qq(1 - R^*) \quad (53)$$

The quantity R^* depends on $\gamma(r)$ by the relation

$$R^* = \frac{\langle \gamma(r)r^{-3} \rangle}{\langle r^{-3} \rangle} \quad (54)$$

where r is the distance of the external charge from the nucleus. In case this external charge is a valence electron, the expectation values in Equation 54 are derived using the wave function of this valence electron;

then R^* is denoted by R . On the other hand, if the external charge is far away from the Mössbauer atoms, $\gamma(r)$ becomes constant and takes the value γ_∞ ; R^* then reduces to $R^* = \gamma_\infty$.

VALENCE ELECTRONS INCLUDED. Let us first consider the case where an outer electron polarizes the valence electrons and the core. For light atoms (lithium, sodium, fluorine) γ_∞ is relatively small (positive or negative) compared to the large and negative γ_∞ values obtained for heavier atoms (bromine, iodine). In a series of elements with similar electronic configurations, γ_∞ tends to become more negative with increasing atomic number (see Figure 2). In Figure 3, $\gamma(r)$ curves for Cl^- , Br^- , and I^- are shown; they vary significantly for r ranging from 1 to about 10 a.u., depending on the element. Therefore, to calculate the ligand (lattice) contributions to the electric field gradient within the point-charge model, it is important to take the appropriate value of $\gamma(r)$ instead of γ_∞ . Negative iodine reaches its saturation value only at about 10 a.u.

As an example for R , the various contributions to R for iodine are presented in Table V. The relatively strong and positive $5p \rightarrow p$ excitation corresponds to the situation of a $5p_0$ hole. On the other hand, when deriving the nuclear quadrupole moment from the interpretation of atomic beam experiments (see section on nuclear quadrupole moments), we are concerned with a $5p_{\pm 1}$ hole, yielding $R = -0.0118$ instead of -0.0114 for a $5p_0$ hole.

VALENCE ELECTRONS EXCLUDED. The same value, $R = -0.0118$, is required for the electric field gradient calculations on the basis of our MO results, since $5s$ and $5p$ valence electrons of iodine are already included in the MO basis set. In this context it is important to note that many Mössbauer spectroscopists still use the old and incorrect value of $R = 0.32$ for Fe^{2+} . The correct value is considerably smaller: 0.12 (22), 0.07 (35), 0.126 (40).

The $\gamma(r)$ and γ_∞ terms are more sensitive than R to the inclusion or exclusion of valence electrons. Table VI gives the γ_∞ values for neutral and negative halides with and without the contributions due to

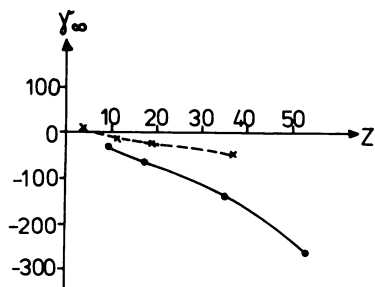
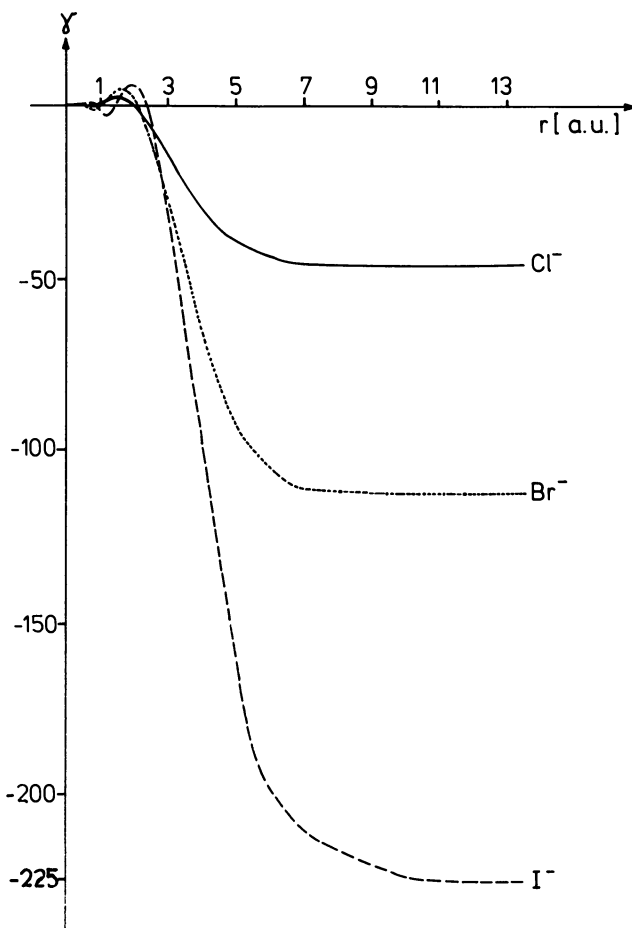


Figure 2. Self-consistent Sternheimer factors γ_∞ depending on the atomic number Z of the elements (\times) Li° , Na° , K° , Rb° , and (\bullet) F^- , Cl^- , Br^- , I^- (41).

S. Lauer (Diplomarbeit)



S. Lauer (Diplomarbeit)

Figure 3. Self-consistent Sternheimer functions $\gamma(r)$ for Cl^- , Br^- , and I^- (41).

ns , np valence orbitals (41). The γ_∞ value turns out to be much more negative when valence orbitals are included in the polarization calculations. In Figure 4, $\gamma(r)$ curves for Fe^{2+} and I^- with and without valence electrons are shown. From Table VI and Figure 4 it is obvious that the main contributions to $\gamma(r)$ come from np valence electrons.

For the explicit evaluation of the electric field gradient contributions according to the previous section, $\gamma(r)$ is required in analytical form. For this purpose we have fitted the numerical values which are given in Ref. 40 by

$$\gamma(r) = \gamma_\infty \left(\frac{1}{e^{-a(r-b)} + 1} - \frac{1}{e^{ab} + 1} \right) + d_1 e^{-\alpha_1(r-r_1)^2} + d_2 e^{-\alpha_2(r-r_2)^2} \quad (55)$$

Table V. Sternheimer Shielding Factor R for I° and Its Direct (R_D) and Exchange (R_E) Contributions (40)^a

<i>Excitations</i>	$10^2 R_D$	$10^2 R_E$	$10^2 R$
$1s \rightarrow d$	1.133	-0.616	0.517
$2s \rightarrow d$	0.211	-0.017	0.194
$3s \rightarrow d$	0.116	-0.005	0.111
$4s \rightarrow d$	0.082	-0.009	0.073
$5s \rightarrow d$	0.099	-0.111	-0.012
$2p \rightarrow f$	0.485	-0.147	0.338
$3p \rightarrow f$	0.256	-0.049	0.207
$4p \rightarrow f$	0.218	-0.028	0.190
$5p \rightarrow f$	0.049	-0.024	0.025
$3d \rightarrow g$	0.297	-0.034	0.264
$3d \rightarrow s$	-0.049	0.022	-0.027
$4d \rightarrow g$	0.270	-0.026	0.244
$4d \rightarrow s$	0.151	-0.055	0.096
$2p \rightarrow p$	-0.246	-2.441	-2.687
$3p \rightarrow p$	-1.761	-2.947	-4.708
$4p \rightarrow p$	-5.211	-6.539	-11.750
$5p \rightarrow p$	2.289	1.716	4.005
$3d \rightarrow d$	-0.460	0.012	-0.448
$4d \rightarrow d$	-1.751	0.893	-0.858
Total	-3.8	-10.4	-14.2

^aThe various contributions to R due to different angular and radial excitations are included.

Physical Review

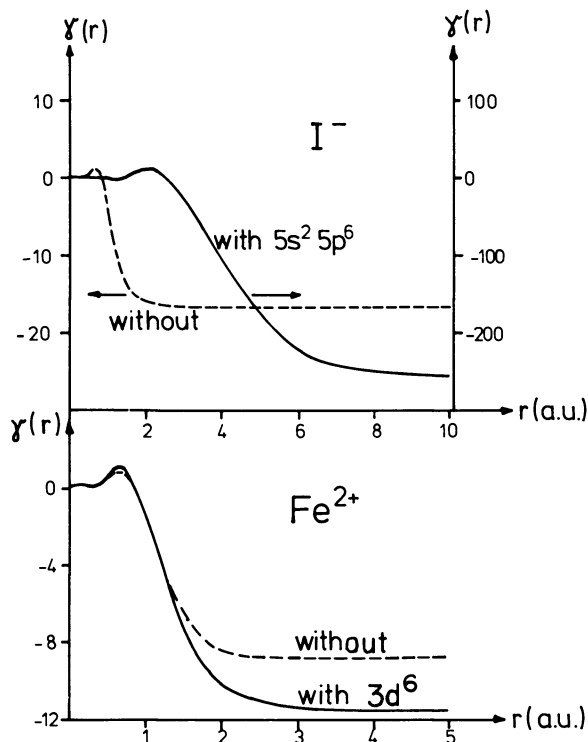
with parameters $a, b, c_1, d_1, r_1, c_2, d_2, r_2$ (Table VII) yielding an excellent agreement with the numerically computed $\gamma(r)$.

Comparison of Calculated V_{zz} and Measured e^2qQ . Along the lines described in the two previous sections, the electric field gradient V_{zz} at the ^{127}I , ^{79}Br , and ^{35}Cl nuclei for several molecules was calculated. The various contributions to this gradient at the ^{127}I nucleus are given together with the occupation numbers of the $5s, 5p$ valence orbitals

Table VI. Sternheimer Shielding Factors γ_∞ for Neutral and Negative Halides With and Without the ns, np Valence Orbitals (41)

<i>Element</i>	<i>Neutral Atom</i>		<i>Negative Ion</i>	
	<i>With Valence Orbitals</i>	<i>Without Valence Orbitals</i>	<i>With Valence Orbitals</i>	<i>Without Valence Orbitals</i>
F	-7.1	+0.08	-22.3	+0.08
Cl	-25.4	-1.2	-55.4	-1.2
Br	-66.0	-6.2	-133.0	-6.1
I	-136.0	-16.9	-254.0	-16.2

S. Lauer (Diplomarbeit)



S. Lauer (Diplomarbeit)

Figure 4. Self-consistent Sternheimer functions $\gamma(r)$ for I^- (top) with (—) and without (---) 5s and 5p electrons, and for Fe^{2+} (bottom) with (—) and without (---) 3d electrons (41).

n_s , n_{p_z} , n_{p_x} , and n_{p_y} in Table VIII. The general trend reflected in this table is that the valence contribution V_{zz}^{oo} (Equation 38) is the dominant contribution to the total electric field gradient, while the overlap contribution V_{zz}^{ov} (Equation 39) is relatively small and the three-center contribution $V_{zz}^{vv'}$ (Equation 41) is completely negligible. Another important feature is that the ligand contribution V_{zz}^{vv} (Equation 40) and the core contribution V_{zz}^{core} (Equation 33) nearly cancel each other in all cases. This finally results in a total V_{zz} that is nearly equal to the valence contribution V_{zz}^{oo} .

The calculated V_{zz} values for ^{127}I vs. the experimental nuclear quadrupole coupling constants (e^2qQ) are plotted in Figure 5. The slope of the solid line corresponds to the nuclear quadrupole moment $Q(^{127}I)$ which takes the value -0.62 barn. This value does not contain relativistic corrections of $\langle r^{-3} \rangle$ within the valence contribution V_{zz}^{oo} . The appropriate correction factor in $\langle r^{-3} \rangle_{rel} = R_{rel} \langle r^{-3} \rangle$ has been derived from comparing Hartree-Fock (10) and relativistic Hartree-Fock-Slater results

Table VII. Self-Consistent Sternheimer Factors γ_∞ and R (41)

Element	γ_∞	R	a	b
Fe ²⁺	-8.7	0.075	4.25	1.30
F ⁻	0.08	0.023	17.0	0.2
Cl ⁻	-1.2	-0.12	7.1	0.7
Br ⁻	-6.1	-0.16	6.0	0.9
I ⁻	-16.2	-0.18	5.0	1.2

* All values correspond to the situation that valence orbitals (Table I) are omitted from the self-consistent Sternheimer procedure.

for $\langle r^{-3} \rangle$. R_{rel} takes values of 1.05 for iodine, 1.025 for bromine, and 1.00 for chlorine. (The correction factors R_{rel} might be slightly larger when using relativistic HFD instead of HFS results for $\langle r^{-3} \rangle$.) The dashed line in Figure 5 takes care of the relativistic correction, resulting in $Q(^{127}\text{I}) = -0.59$ barn.

Using V_{zz}^{total} from Table VIII and the relativistic corrected nuclear quadrupole moment $Q(^{127}\text{I}) = -0.59$ barn, we derive e^2qQ values which are compared with experimental e^2qQ values (Table IX). In addition, e^2qQ values applying the semiempirical Townes Dailey theory (42, 43) on the basis of the U_p values of Table VIII are given in Table IX.

Since the largest contribution to V_{zz}^{total} comes from the valence contribution V_{zz}^{oo} , it is clear that the Townes Dailey values for e^2qQ show the same level of agreement with experimental e^2qQ values as the MO value for e^2qQ . However, it is important to note that the Townes Dailey approximation is only applicable in the electric field gradient main axes system.

Table VIII. Nonrelativistic Electric Field Gradient Populations for Iodine in Several

Molecule	V_{zz}^{total}	η	V_{zz}^{oo}	V_{zz}^{ov}	V_{zz}^{vv}
HI	15.6554	0	15.9586	-0.8922	-0.6402
FI	20.3708	0	20.6074	-0.6404	-4.7423
ClI	18.3931	0	18.5370	-0.5074	-2.5038
BrI	17.0166	0	17.1827	-0.4587	-2.0862
I ₂	16.6243	0	16.7201	-0.5079	-1.4796
OI	14.9915	0	15.1707	-0.8044	-4.0734
H ₃ CI	16.3198	0	16.2277	-0.6059	-1.9971
H ₂ CI ₂	16.0610	0.0285	—	—	—
IF ₇	1.4982	0	0.9643	0.0249	1.9015
IF ₅	-12.7196	0	-12.8691	0.6315	4.1359
FeI ₄ ⁻	7.0388	0.0213	—	—	—
HIO ₃	-7.4044	0.6241	—	—	—

* The separate identification of electric field gradient contributions to V_{zz}^{total} and the evaluation of U_p are only meaningful if the molecular coordinate system is identical to the main axes system of the electric field gradient. All values correspond to the IEH-MO approximation; electric field gradient values given in a_0^{-3} .

and Fit Parameters Describing $\gamma(r)$ (Equation 55)^a

c_1	c_2	d_1	d_2	r_1	r_2
102	14	0.14	1.05	0.19	0.71
0	0	0	0	0	0
28.0	0	0.26	0	0.34	0
40.0	50.0	0.90	0.11	0.47	0.14
52.0	42.0	0.40	1.50	0.265	0.670

In addition to the investigation of iodine-containing molecules, we also have studied bromine- and chlorine-containing compounds. Comparing calculated V_{zz}^{total} values and measured e^2qQ data in Figures 6 and 7 we derive nuclear quadrupole moments $Q(^{79}\text{Br}) = 0.25$ barn and $Q(^{35}\text{Cl}) = -0.065$ barn (these values include relativistic corrections of $\langle r^{-3} \rangle$). In Table X, the calculated V_{zz}^{total} values (derived in the IEH-MO approximation) are compared with V_{zz}^{total} values derived in the Hartree-Fock limit; both theoretical results show the same level of agreement with experimental values (last column of Table X).

Nuclear Quadrupole Moments. In the last section we derived nuclear quadrupole moments Q by comparing experimental quadrupole coupling constants e^2qQ and calculated electric field gradients V_{zz}^{total} from *molecular* clusters. An alternative procedure to obtain Q is to use the hyperfine structure of the *atomic* $^2P_{3/2}$ ground state of the stable isotopes of chlorine, bromine, and iodine. From the measured hyperfine structure intervals (for example, by the atomic beam magnetic-resonance

Contributions and (Dipole-Corrected) Orbital Iodine-Containing Molecules^a

$V_{zz}^{vv'}$	V_{zz}^{core}	$n_{\delta s}$	$n_{\delta pz}$	$n_{\delta px}$	$n_{\delta py}$	U_p^b
0.0	1.2292	1.9238	0.9826	2.0	2.0	1.0174
0.0	5.1461	1.9587	0.7681	2.0	2.0	1.2319
0.0	2.8673	1.9700	0.8993	2.0	2.0	1.1007
0.0	2.3788	1.9838	0.9628	2.0	2.0	1.0372
0.0	1.8917	1.9763	1.0237	2.0	2.0	0.9763
0.0	4.6986	1.9345	1.0245	1.8812	1.8812	0.8567
-0.0467	2.7418	1.9202	1.0399	1.9961	1.9961	0.9562
—	—	—	—	—	—	—
-0.0059	-1.3866	1.7995	1.1077	1.1656	1.1689	0.0596
0.0003	-4.6182	1.8480	1.6820	1.0822	1.0814	-0.6002
—	—	—	—	—	—	—
—	—	—	—	—	—	—

$$^b U_p = -n_{pz} + \frac{n_{px} + n_{py}}{2}$$

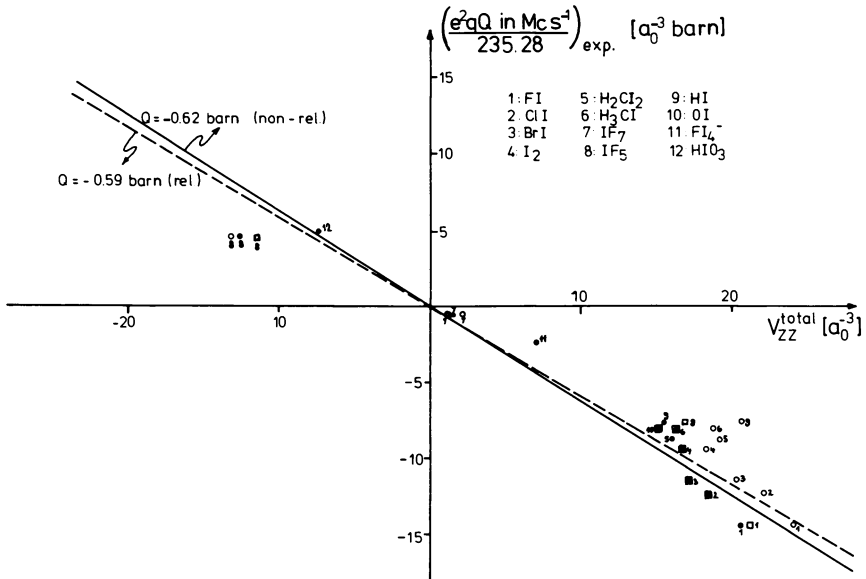


Figure 5. Plot of V_{zz}^{total} , derived according to the sections on electric field gradient calculation and shielding and antishielding, vs. experimental quadrupole coupling constants for ^{127}I .

(a) (●) The IEH-MO approximation with the following interpolation scheme for $\langle r^{-3} \rangle$ (in a_0^{-3}): $\langle r^{-3} \rangle_{HF} = 12.7274 + 2.0643 (6.0 - n_{5p})$, with n_{5p} being the total (dipole corrected) occupation of the $5p$ valence shell. (b) (○) The SCC- X_α -MO approximation; $\langle r^{-3} \rangle_{HF} = 32.1346 - 19.1546 n_s - 2.0475 n_p + 21.6858 n_s^2 + 0.3820 n_s n_p - 0.0670 n_p^2 - 6.9266 n_s^3 - 0.1601 n_s^2 n_p + 0.0068 n_s n_p^2 + 0.0053 n_p^3$. (c) (□) The Townes Dailey approximation: $V_{zz} = (e^2qQ)^{Townes\ Dailey} / Q^{rel} (= -0.59)$ in a_0^{-3} ; numerical values are given in Table IX.

method), the dipole magnetic a and the electric quadrupole b hyperfine constants can be deduced (44); a and b can be written as (45)

$$a_{l\pm 1/2} = \alpha_m 2\mu_B^2 \langle r^{-3} \rangle \frac{\mu_I m}{\mu_K m_P} \frac{l(l+1)}{j(j+1)} F_r (1-\delta)(1-\epsilon) \quad (56)$$

$$b_{3/2} = -\frac{1}{\alpha_e} e^2 Q \frac{2j-1}{2j+2} \langle r^{-3} \rangle R_r \quad (57)$$

The constants used in these equations are (45):

$$\begin{aligned} \alpha_e &= 4\pi\epsilon_0 = 1.1126 \cdot 10^{-10} \text{ As V}^{-1} \text{ m}^{-1} \\ \alpha_m &= \mu_0/4\pi = 1.0000 \cdot 10^{-7} \text{ Vs A}^{-1} \text{ m}^{-1} \\ \mu_B &= 1/2e\hbar/m = 0.9273 \cdot 10^{-23} \text{ A m}^2 \\ e &= 1.6021 \cdot 10^{-19} \text{ As} \end{aligned}$$

Table IX. Comparison of Calculated e^2qQ Values for ^{127}I with Experimental e^2qQ Values (in Mc s^{-1})

<i>Molecule</i>	$(e^2qQ)^a$	$(e^2qQ)^b$	$(e^2qQ)^{exp}$	η
HI	-2173.2	-2338	-1831.1 ^c	0
FI	-2828	-2914	-3438 ^d	0
ClI	-2553	-2558	-2944 ^e	0
BrI	-2362	-2389	-2731 ^e	0
I ₂	-2308	-2230	-2231 ^e	0
OI	-2081	-2022	-1907 ^d	0
H ₃ CI	-2265	-2182	-1934 ^d	—
H ₂ Cl ₂	-2230	—	-2092.6 ^f	—
IF ₇	-208	-166	-148 ^g	—
IF ₅	1766	1597	1073 ^g	—
FeI ₄ ⁻	-977	—	-565 ^h	—
HIO ₃	1028	—	1150 ⁱ	0.45 ^t 0.59 ^j

^a e^2qQ calculated with $V_{zz, \text{total}}$ from Table VIII (IEH-MO) using $Q(^{127}\text{I}) = -0.59$ barn.

^b e^2qQ values derived from the semiempirical Townes Dailey theory:

$$e^2qQ = U_p \frac{\langle r^{-3} \rangle_{\text{mol}}}{\langle r^{-3} \rangle_{\text{at}}} (e^2qQ)_{\text{at}}; U_p \text{ taken from Table VIII and } (e^2qQ)_{\text{at}} \text{ from Ref. 44.}$$

^c Lucken, E. A. "Nuclear Quadrupole Coupling Constants," Academic: London-New York; 1969.

^d Hellwege, K. H.; Hellwege, A. M., Eds. "Molecular Constants"; Landolt-Börnstein, New Series II; Springer-Verlag: Berlin, 1974, Vol. 6.

^e Buksphan, S.; Goldstein, C.; Sonnino, P. *J. Chem. Phys.* **1968**, *49*, 5477.

^f Friedt, J. M., private communication.

^g Ref. 62.

^h Friedt, J. M.; Petridis, D.; Sanchez, J. P.; Reschke, R.; Trautwein, A. *Phys. Rev.* **1979**, *B19*, 360.

ⁱ Du Pont de Nemours, private communication.

^j Calculated value.

$$\begin{aligned} \mu_k &= \mu_N m / m_p = 5.0504 \cdot 10^{-27} \text{ A m}^2 \\ \mu_I / \mu_K &= 2.7935 \text{ for } ^{127}\text{I} \\ I &= 5/2 \text{ for } ^{127}\text{I} \\ l &= 1 \\ j &= 3/2 \\ 1 - \delta &= \text{correction due to the finite nuclear volume, } \sim 0.98 \text{ for I} \\ 1 - \epsilon &= \text{correction due to deviations from magnetic point dipole, } \sim 0.96 \text{ for I} \\ \langle r^{-3} \rangle &= 14.8 a_0^{-3} \text{ for I } (5p^5), \text{ unrelativistic} \\ F_r, R_r &= \text{relativistic corrections for the HF value of } \langle r^{-3} \rangle; \\ &\sim 1.05 \text{ for I, } 1.025 \text{ for Br, } 1.00 \text{ for Cl} \\ a_{3/2} &= 827.265 \pm 0.003 \text{ Mc s}^{-1} \text{ for } ^{127}\text{I} \\ b_{3/2} &= 1146.356 \pm 0.010 \text{ Mc s}^{-1} \text{ for } ^{127}\text{I} \\ Q &= \text{nuclear quadrupole moment} \end{aligned}$$

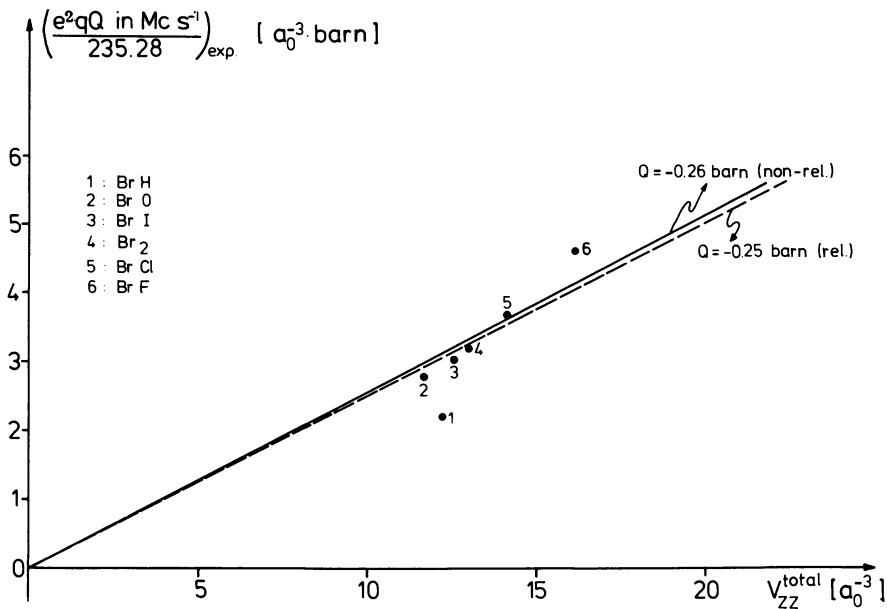


Figure 6. Plot of V_{zz}^{total} , derived according to the sections on electric field gradient calculations and shielding and antishielding vs. experimental quadrupole coupling constants for ^{79}Br .

Calculated values correspond to the IEH-MO approximation. The interpolation scheme for $\langle r^{-3} \rangle$ (in a_0^{-3}) is $\langle r^{-3} \rangle_{\text{HF}} = 10.2245 + 1.7535(6-n_{\text{lp}})$. Numerical values for V_{zz}^{total} and e^2qQ are given in Table X.

With these constants we derive for $Q(^{127}\text{I})$ the value -0.79 barn (^{79}Br : 0.33 barn, ^{35}Cl : -0.079 barn), which in several publications is defined as the "experimental value" (46, 47). The values derived in the last section are smaller by about 25%. In the following, we describe arguments that indicate why one has to be cautious with the experimental values: (1) The combination of Equations 56 and 57 eliminates the explicit evaluation of $\langle r^{-3} \rangle$. However, the $\langle r^{-3} \rangle$ values in these equations not only have to be corrected by different relativistic correction factors F_r and R_r , respectively, but also by different polarization factors (comparable to $1 - R$ in the section on shielding and antishielding). Bessis et al. (48) have evaluated both corrections for ^{79}Br and found significant changes in a and b . (2) An additional problem arises from the fact that the $^2P_{3/2}$ ground state may be perturbed by excited states. Such perturbations seem to have more influence on the a -factor than on the b -factor (see p. 143 of Ref. 45). Because the $^2P_{1/2}$ term remains practically unperturbed (45), $a(^2P_{1/2})$ values were used to recalibrate $a(^2P_{3/2})$

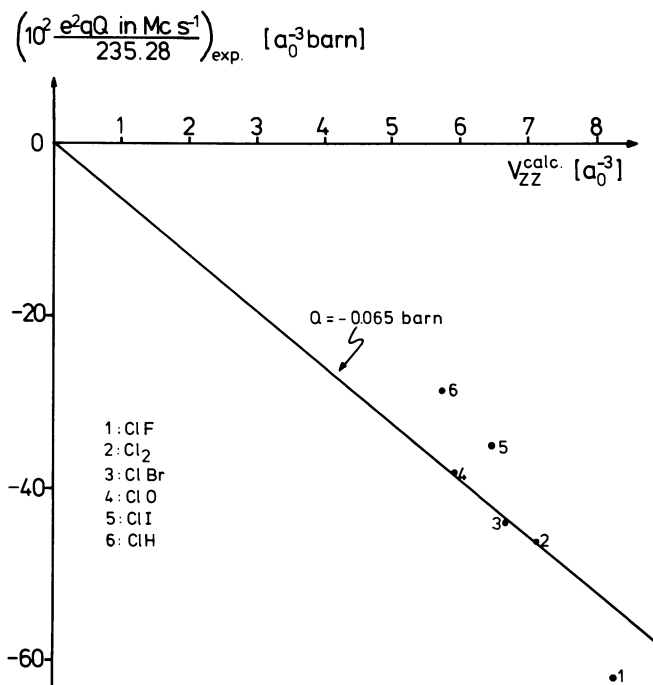


Figure 7. Plot of V_{zz}^{total} derived according to the sections on electric field gradient calculations and shielding and antishielding vs. experimental quadrupole coupling constants for ^{35}Cl .

Calculated values correspond to the IEH-MO approximation. The interpolation scheme for $\langle r^{-3} \rangle$ (in a_0^{-3}) is $\langle r^{-3} \rangle_{\text{HF}} = 5.74774 + 1.01463(6-n_{\text{sp}})$. Numerical values for V_{zz}^{total} and e^2qQ are given in Table X.

values. Such corrections lead to considerable reductions of Q , especially for heavier elements. In the case of chlorine this reduction is negligible, while for indium it is on the order of 30% (45).

Because of the probable difficulty with the $a(^2P_{3/2})$ value, we follow the procedure described by Bessis et al. (48) and derive Q from the electric quadrupole hyperfine constant b only. In Equation 57, $\langle r^{-3} \rangle$ is replaced by $\langle r^{-3} \rangle_{\text{rel}} (1 - R)p_{\pm 1}$, where $\langle r^{-3} \rangle_{\text{rel}}$ includes the relativistic correction to $\langle r^{-3} \rangle$ (see the previous section), and where $(1 - R)p_{\pm 1}$ describes the appropriate polarization due to a hole in a $p_{\pm 1}$ orbital (see section on shielding and antishielding). This procedure yields $Q(^{127}\text{I}) = -0.66$ barn, $Q(^{79}\text{Br}) = 0.29$ barn, and $Q(^{35}\text{Cl}) = -0.077$ barn, values which are in reasonable agreement with the values of -0.59 barn, 0.25 barn, and -0.065 barn derived in the last section.

In Table XI the nuclear quadrupole moments derived in this chapter are summarized and are compared with literature values. (The values

Table X. Comparison of Calculated and Measured V_{zz}^{total} and e^2qQ Values for ^{79}Br - and ^{35}Cl -Containing Molecules^a

Molecule	$V_{zz}^{\text{total}b}$	$V_{zz}^{\text{total}c}$	e^2qQ^d	$(e^2qQ)^{\text{exp}}$
^{79}BrH	12.2153	7.5842	718.5	535.4°
^{79}BrF	16.1035	15.2429	947.2	1089.0°
$^{79}\text{BrCl}$	14.1238	12.4162	830.8	876.8°
$^{79}\text{Br}_2$	13.0554	11.5026	767.9	765.9°
^{79}BrI	12.5021	—	735.4	722.0°
^{79}BrO	11.6175	—	683.3	654.0'
^{35}ClH	5.6768	3.6732	-86.8	-67.3'
^{35}ClF	8.2418	8.0187	-126.0	-146.0°
$^{35}\text{Cl}_2$	7.1385	6.1836	-109.2	-108.9°
$^{35}\text{ClBr}$	6.6480	5.6347	-101.7	-103.6°
^{35}ClI	6.3768	—	-97.5	-82.5°
^{35}ClO	5.9070	—	-90.3	-87.4'

^a Electric field gradient values in a.u.^{-3} and e^2qQ values in Mc s^{-1} .

^b V_{zz}^{total} calculated according to the sections on electric field gradient calculations and shielding and antishielding in the IEH-MO approximation.

^c V_{zz}^{total} derived from Hartree-Fock calculations: Straub, P. A.; McLean, A. D. *Theor. Chim. Acta* 1974, 32, 227.

^d e^2qQ calculated with the V_{zz}^{total} values from (b) using $Q = 0.25$ barn for ^{79}Br and $Q = -0.065$ barn for ^{35}Cl from Figures 6 and 7, respectively.

^e See Ref. c of Table IX.

^f See Ref. d of Table IX.

Table XI. Calculated and Experimental Quadrupole Moments Q (in barn) for ^{127}I , ^{79}Br , and ^{35}Cl

Q	Electric Field Gradient vs. e^2qQ^a	Atomic Beam Experiments					Microwave Experiments	
		De- rived from b	De- rived from b/a ^b	De- rived from b/a*	Two Inter-acting Nuclei: Cyano- gen Halides ^c	One Inter-acting Nucleus: Methyl Halides ^d		
^{127}I	-0.59 (-0.62)	-0.66	-0.79	—	-0.75	-0.59		
^{79}Br	0.25 (0.26)	0.29	0.33	—	0.28	0.24		
		0.30 ^e						
^{35}Cl	-0.065 (-0.065)	-0.077	-0.079	-0.079 ^f	-0.066	-0.06		

^a Values without (with) brackets include (exclude) relativistic corrections of $\langle r^{-3} \rangle$.

^b Derived from Equations 56 and 57 using experimental a and b values for Cl from Davis, L.; Field, B.; Zabel, W.; Zacharias, J. *Phys. Rev.* 1949, 76, 1076; for Br from King, J. G.; Jaccarino, V. *Phys. Rev.* 1954, 94, 1610; and, for I from Jaccarino, V.; King, J. G.; Satten, R. A.; Stroke, H.-H. *Phys. Rev.* 1954, 94, 1798.

^c Smith, A. G.; Ring, H.; Smith, W. V.; Gordy, W. *Phys. Rev.* 1948, 74, 370.

^d Gordy, W.; Simmons, J. W.; Smith, A. G. *Phys. Rev.* 1948, 74, 243.

^e Bessis, N.; Picart, J.; Desclaux, J. P. *Phys. Rev.* 1969, 187, 88.

^f $a(2P_{3/2})$ has been derived from $a(2P_{1/2})$: Kopfermann, H. In "Kernmomente"; Akad. Verlag GMBH: Frankfurt, West Germany; 1956.

obtained from microwave experiments of methyl halides seem to be more reliable than those of cyanogen halides because the resolution in the case of one interacting nucleus is better than that of two interacting nuclei (49).

Interpretation of Measured Magnetic Hyperfine Fields

Combined ^{57}Fe and ^{129}I Mössbauer Measurements. The tetraiodoferrate cluster FeI_4^- in $\text{N}(\text{C}_2\text{H}_5)_4\text{FeI}_4$ is an example of the useful combination of experimental ^{57}Fe and ^{129}I Mössbauer work and of theoretical electronic and magnetic structure work. Because of the tetrahedral point symmetry of iron in this compound, the measured quadrupole splitting is zero at the ^{57}Fe nucleus. The ^{129}I nuclei, however, "see" lower symmetry and therefore exhibit a nonzero quadrupole hyperfine structure, which is in reasonable agreement with our calculated electric field gradient result derived from the electronic structure of FeI_4^- (see Table IX and Figure 5).

In addition to the electric hyperfine structure, we study the magnetic hyperfine structure of FeI_4^- , which is paramagnetic ($S = 5/2$) above about 20 K and which shows magnetic ordering below 20 K (50). The spin is mainly concentrated at the iron site with a spin direction as shown in Figure 8, yielding an experimental hyperfine field of $H_{\text{hf}}(\text{Fe}) = -34.4 \pm 0.5 \text{ T}$. Part of the spin density is delocalized because of covalency, giving rise to hyperfine fields at the iodine nuclei also. The spin orientation in Figure 8 indicates that in $\text{N}(\text{C}_2\text{H}_5)_4\text{FeI}_4$ we are concerned with two magnetically nonequivalent *A* and *B* sites, with experimental hyperfine fields $|H_{\text{hf}}^A| = 10.7 \pm 0.3 \text{ T}$ and $|H_{\text{hf}}^B| = 8.4 \pm 0.4 \text{ T}$ (*A* = Sites 1, 4 and *B* = Sites 2, 3).

The open-shell MO electronic configuration derived for FeI_4^- is used in the following to calculate the hyperfine field contributions at the ^{57}Fe nucleus as well as at the ^{129}I nuclei I_A and I_B .

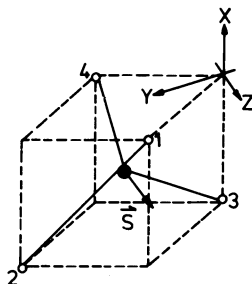
Hyperfine Field Calculation. The magnetic hyperfine splitting measured by Mössbauer spectroscopy is proportional to the effective magnetic field \vec{H}_{eff} produced at a Mössbauer nucleus (in the present case ^{57}Fe and ^{129}I). \vec{H}_{eff} is the vector sum of the externally applied magnetic field \vec{H}_{ext} and the internal magnetic field \vec{H}_{hf} :

$$\vec{H}_{\text{eff}} = \vec{H}_{\text{ext}} + \vec{H}_{\text{hf}} \quad (58)$$

The latter consists of four parts: the contact field \vec{H}^{C} , the orbital field \vec{H}^{L} , the spin dipolar field \vec{H}^{SD} , and the supertransferred field \vec{H}^{ST} ,

$$\vec{H}_{\text{hf}} = \vec{H}^{\text{C}} + \vec{H}^{\text{L}} + \vec{H}^{\text{SD}} + \vec{H}^{\text{ST}} \quad (59)$$

Figure 8. System of coordinate axes used in the MO calculation for FeI_4^- . The spin is along the z-axis. The two unequivalent iodine sites (A, B) are denoted by 1,4 and 2,3, respectively: (○) iodine, (●) iron.



In the following, the procedure of evaluating the various contributions to \vec{H}_{hf} from MO calculations is described.

The contact field \vec{H}^{C} is the contribution of the spin density at the nucleus (Fermi contact term) (51):

$$H^{\text{C}} = -\frac{16\pi}{3} \mu_{\text{B}} \sum_{ns} [|\phi_{ns}^{\uparrow}(0)|^2 - |\phi_{ns}^{\downarrow}(0)|^2] \quad (60)$$

In the case where the spin density originates from s electrons that have finite charge density $\rho(0)$ at the nucleus, Equation 60 can be represented by (52):

$$H^{\text{C}} = -\frac{16\pi}{3} \mu_{\text{B}} \rho(0) \langle S_s \rangle \quad (61)$$

where $\langle S_s \rangle$ is the effective spin produced by these s electrons. On the other hand, if the spin density originates from p or d electrons, the spin-paired core s electrons may become spin-polarized due to an exchange interaction with the p or d electrons; in this case Equation 60 is represented by (52):

$$H^{\text{C}} = 2H^{\text{core}} \langle S_{p,d} \rangle + 2H^{\text{val}} \langle S_{p,d} \rangle \quad (62)$$

where $\langle S_{p,d} \rangle$ is the effective spin produced by these p or d electrons, and H^{core} and H^{val} represent the spin polarization of core and valence s electrons, respectively. Collecting all terms and using the spin direction of the system under study as the z axis in the calculation, H^{C} takes the form

$$H^{\text{C}} = 2H^{\text{core}} \langle S_{p,d} \rangle_z + 2H^{\text{val}} \langle S_{p,d} \rangle_z - \frac{16\pi}{3} \mu_{\text{B}} \rho(0) \langle S_s \rangle_z \quad (63)$$

The core-polarization contribution to the hyperfine field at the iron nucleus (H^{core} in Equation 63) is approximated by interpolating the effect of the $3d$ orbital population q_{3d} between the $3d^5$ and $3d^6$ free-ion values as described by the relation (52)

$$H^{\text{core}}(\text{Fe}) = - [12.6 + 1.15 (q_{3d} - 5)] \text{ (in Tesla)} \quad (64)$$

The second term in Equation 64 accounts for the change of spin polarization of the inner s orbitals of iron ($1s$, $2s$, and $3s$) by adding iron $3d$ charge to a system with $3d^5$ configuration. Several models may be considered for evaluating q_{3d} : (1) q_{3d} is taken as equal to the sum over the iron $3d$ bond order matrix elements; (2) q_{3d} includes overlap charges that are estimated from a dipole correction procedure, and (3) q_{3d} includes overlap charges estimated from a Mulliken population analysis.

It turned out that the inclusion of overlap charges, either through (2) or (3), leads to a better description of the actual situation than neglecting them. The S expectation values in Equation 63 are derived from the AO coefficients of the singly populated MO's.

Combining Equations 63 and 64, the contact field for high-spin Fe^{3+} turns out to be -63 Tesla as derived from unrestricted Hartree-Fock calculations (52). Upon including correlation effects, the linked-cluster many-body perturbation-theory procedure (53) yields a contact field of -71 Tesla. We use -63 Tesla in our calculations.

Similar to Equation 64, the dependence of the valence contribution to the hyperfine field at the iron nucleus (H^{val} in Equation 63) on the $3d$ and $4s$ population is described by:

$$H^{\text{val}}(\text{Fe}) = \frac{1}{2} [15.3 - 3.06 (q_{3d} - 5)] q_{4s} \text{ (in Tesla)} \quad (65)$$

This relation assumes that the spin polarization of the iron $4s$ shell is proportional to the $4s$ orbital charge q_{4s} .

Compared to the first and second terms, the third term in Equation 63 is negligible in the case of iron because both $\rho_{4s}(0)$ and $\langle S_{4s} \rangle$ are relatively small due to the partial population of the iron $4s$ orbital.

Turning to iodine, the expression for H^{C} (Equation 63) becomes:

$$H^{\text{C}}(\text{I}) = 2H^{\text{ns}} \langle S_{5p} \rangle_z - \frac{16\pi}{3} \mu_B \rho_{5s}(0) \langle S_{5s} \rangle_z \quad (66)$$

In this equation the first and second terms of Equation 63 are lumped together, since the valence iodine $5s$ orbital is almost doubly occupied. The term $H^{\text{ns}}(\text{I})$ may be derived from the present study of the tetra-

Table XII. Calculated Iodine Parameters (Orbital Population q_{μ} and Spin Densities $\rho^{\delta_{\mu\nu}}$) for $N(C_2H_5)_4FeI_4$ Within the IEH-MO Approximation

	A Site		B Site	
q_{5s}	1.89 ^a	1.91 ^b	1.89 ^a	1.91 ^b
q_{5p_z}	1.53	1.68	1.87	1.90
q_{5p_y}	1.87	1.90	1.53	1.68
q_{5p_x}	1.70	1.79	1.70	1.79
	A Site		B Site	
$10^{-2}\rho^{\delta_{5s,5s}}$	0.0052 ^a	-0.00045 ^b	0.0052 ^a	-0.00045 ^b
$10^{-2}\rho^{\delta_{5p_z,5p_z}}$	6.45	6.02	5.73	5.26
$10^{-2}\rho^{\delta_{5p_y,5p_y}}$	5.73	5.26	6.45	6.02
$10^{-2}\rho^{\delta_{5p_x,5p_x}}$	6.09	5.68	6.09	5.68
$10^{-2}\rho^{\delta_{5p_y,5p_z}}$	0	—	0	—
$10^{-2}\rho^{\delta_{5p_x,5p_z}}$	0.51	—	0	—

^a Derived from bond-order matrix elements.

^b Values include overlap contributions as estimated in the Mulliken approximation.

iodoferrate (III) salt of tetraethylammonium; it takes the value -57 ± 2 Tesla. For $16\pi\mu_B\rho_{5s}(0)/3$ we have used 15,800 Tesla, including the relativistic HFS value for $\rho_{5s}(0)$. However, the corresponding HFD value is about 20% smaller, which is not of major significance for our results since $\langle S_{5s} \rangle_Z$ turns out to be very small (Table XII).

The orbital contribution (H^L) is expressed by

$$H_p^L = -2\mu_B \langle r^{-3} \rangle \langle \Psi | \hat{L}_p | \Psi \rangle \quad (67)$$

where $p = X, Y, Z$. The $\langle r^{-3} \rangle$ term represents a radial average over the non- s orbital; it vanishes to zero for both the ferric and iodine ions since the electronic structure of the $(FeI_4)^-$ clusters is represented by a single open-shell electronic configuration (Ψ) appropriate to describe the spin 5/2 system on the basis of one-electron MO functions.

The spin dipolar contribution (H^{SD}) is expressed as (54)

$$H_p^{SD} = -2\mu_B \sum_{q=X,Y,Z} \frac{3pq - r^2\delta_{pq}}{r^5} S_q \quad (68)$$

With the Z axis along the spin direction this term is rewritten as

$$H_p^{SD} = -2\mu_B r^{-3} W_{pZ} S_Z \quad (69)$$

and is evaluated with the many-electron wave function Ψ as

$$H_p^{SD} = -2\mu_B \sum_{\substack{\text{open shell} \\ \text{MO's } i}} \sum_{\mu\nu} c_{i\mu} c_{i\nu} \left\langle \mu \left| \frac{W_{pZ}}{r^3} \right| \nu \right\rangle \langle S_Z \rangle \quad (70)$$

The atomic values $\langle \mu | W_{pq} | \nu \rangle$ have been tabulated for p and d orbitals (55, 56). Depending on the atom on which the AO's $|\mu\rangle$ and $|\nu\rangle$ are centered, one distinguishes between a valence, an overlap, and a ligand contribution to H^{SD} at the Mössbauer probe nucleus (57, 58). The spin dipolar term (Equation 68) reflects the symmetry of the atom under investigation. Therefore, this contribution vanishes to zero for the Fe^{3+} ion in the $(\text{FeI}_4)^-$ clusters; on the other hand, it has a finite value for the iodine ions.

The supertransferred field (H^{ST}) which corresponds to the interaction between magnetic ions separated by a diamagnetic ligand is considered negligible for the present systems on the basis of the weakness of the magnetic exchange interactions. This is justified in view of the low ordering temperatures in the tetrahedral $(\text{FeX}_4)^-$ complexes in comparison to octahedral Fe^{3+} halides or oxides, where this contribution is already small (59, 60).

Summarizing the origin of the hyperfine field, for the Fe^{3+} ion, H_{hf} arises mainly from the contact term (Equation 63). For iodine, H_{hf} results from the sum of the contact and spin dipolar contribution, Equations 63 and 70; the unpaired spin density is transferred from the metal to the ligand by chemical bonding.

Comparison of Calculated and Measured Results. The two magnetically nonequivalent iodine sites A and B in $\text{N}(\text{C}_2\text{H}_5)_4\text{FeI}_4$ are due to the different spin-dipolar fields $H^{SD}(I_A)$ and $H^{SD}(I_B)$ because $H^C(I_A) = H^C(I_B) \neq 0$, and $H^L(I_A) = H^L(I_B) = H^{ST}(I_A) = H^{ST}(I_B) = 0$. The calculated orbital populations and spin densities are summarized in Table XII, and the components of the spin-dipolar field at the iodine nuclei in $\text{N}(\text{C}_2\text{H}_5)_4\text{FeI}_4$ are summarized in Table XIII for the two different Sites A and B . The experimental difference of $\pm 2.3 \pm 0.7$ Tesla between

Table XIII. Calculated Spin-Dipolar Fields (in Tesla) at the Iodine A and B Sites in $\text{N}(\text{C}_2\text{H}_5)_4\text{FeI}_4$ by Including Overlap Contributions Estimated in Mulliken Approximation

		Z-Axis	X-Axis
A Site	$H^{SD, \text{val} + \text{overlap}}$	-0.42	-0.30
	$H^{SD, \text{lig}}$	-0.25	-0.35
B Site	$H^{SD, \text{val} + \text{overlap}}$	+0.47	0
	$H^{SD, \text{lig}}$	+0.25	0

$H_{\text{hf}}(I_A)$ and $H_{\text{hf}}(I_B)$ at the two sites is well accounted for by the calculated spin-dipolar contributions when overlap and ligand effects are included. However, we want to point out the lack of agreement if the overlap and ligand contributions are neglected. It is interesting to note that $H^{\text{SD,lig}}$ is on the order of 0.2 Tesla. The H^{SD} components can be tested further with respect to the orientation Θ_A of $H_{\text{hf}}(I_A)$ and Θ_B of $H_{\text{hf}}(I_B)$, respectively, relative to the electric field gradient principal axis. The measurement yields $\Theta_A = 27^\circ \pm 5^\circ$ and $\Theta_B = 86^\circ \pm 5^\circ$. The deviation of Θ_A from the angle (35.3°) between the spin direction and the electric field gradient principal axis is due to the x -component H_x^{SD} (Table XIII). For the B site, H_x^{SD} is zero. Therefore, Θ_B is 90° (see Figure 8), which is in agreement with the experimental value. For the A site, however, H_x^{SD} takes the value -0.65 Tesla; this together with $H_{\text{hf}}(I_A) = -10.7 \pm 0.3$ Tesla results in an angle of $3.5^\circ \pm 0.1^\circ$ between the spin direction (z) and $H_{\text{hf}}(I_A)$. This leads finally to a calculated value $\Theta_A = 31.8^\circ \pm 0.1^\circ$, which is in reasonable agreement with the experimental value of $27^\circ \pm 5^\circ$.

From the experimental $H_{\text{hf}}(I)$ values and the calculated H^{SD} contribution, and with the help of Equation 66, the value -57 ± 2 Tesla is derived for $H^{\text{ns}}(I)$.

The calculated field $H_{\text{hf}}(\text{Fe})$ in $\text{N}(\text{C}_2\text{H}_5)_4\text{FeI}_4$ (depending on the model that is used to derive q_{3d} and q_{4s} in Equations 64 and 65, and the corresponding data for $\text{N}(\text{C}_2\text{H}_5)_4\text{FeBr}$ and $\text{N}(\text{C}_2\text{H}_5)_4\text{FeCl}$ are summarized in Table XIV together with experimental values (50).

The results from this section, derived on the basis of the overall consistent IEH-MO parameter set of Table I, are not very different from the values reported earlier for FeI_4^- (61) with a somewhat different parameter set. The main difference in the two calculations occurs only in the direct iodine $5s$ contribution to $H^{\text{C}}(I)$ (second term in Equation 66).

Table XIV. Calculated and Experimental Hyperfine Fields at the Nuclear Site of ^{57}Fe (in Tesla) for FeCl_4^- , FeBr_4^- , and FeI_4^- in $\text{N}(\text{C}_2\text{H}_5)_4\text{FeX}_4^a$

	FeCl_4^-	FeBr_4^-	FeI_4^-
$H_{\text{hf}}(\text{Fe})$	^b -50.78	-45.51	-44.33
	^c -45.05	-40.38	-33.93
	^d -44.40	-40.31	-33.30
	exp. ^e -47.0 ± 1	-42.0 ± 1	-34.4 ± 0.5

^a $X = \text{Cl, Br, I}$.

^b Derived from using bond-order matrix elements for iron $3d$ and $4s$ charges.

^c Includes overlap contributions as estimated from a dipole correction procedure.

^d Includes overlap contributions as estimated in the Mulliken approximation.

^e Friedt, J. M.; Petridis, D.; Sanchez, J. P.; Reschke, R.; Trautwein, A. *Phys. Rev.* 1979, B19, 360.

Summary

Self-consistent field and charge MO calculations were applied to a series of fluorine-, chlorine-, bromine-, and iodine-containing molecules. Orbital energies and dipole moments were used to find MO parameter sets for the SCC- X_α and SCC-IEH procedures. Comparing results obtained from SCF and SCC theories with experimental data indicates that the relatively simple SCC-MO methods can compete with the more sophisticated SCF-MO methods if a series of similar compounds is studied. The use of the SCC-MO methods described here is especially advantageous in cases when the application of SCF-MO methods becomes prohibitive because of limited memory space and computer time; such cases include all calculations where iodine is used.

When calculating hyperfine parameters such as electron densities $\rho(0)$, electric field gradients, and internal magnetic fields from a MO procedure with limited basis set, the strategy followed is to use the MO valence electron configuration (1) for directly evaluating valence contributions and (2) for deriving core contributions from shielding and polarizing the core. The calculational procedures, the results obtained, and their comparison with experimental data have been described in detail. Nuclear properties that were obtained from comparing $\rho(0)$ and δ , and V_{zz} and e^2qQ are the relative change of the nuclear charge radius for ^{129}I ($\delta R/R = 4.4 \cdot 10^{-4}$) and the nuclear quadrupole moments Q for ^{127}I , ^{79}Br , and ^{35}Cl ($Q_{\text{I}} = -0.59$ barn, $Q_{\text{Br}} = 0.25$ barn, $Q_{\text{Cl}} = -0.065$ barn). It must be emphasized that for the evaluation of both $\rho(0)$ and V_{zz} , relativistic effects were included and were found to be significant not only for $\rho(0)$.

The experimental ^{57}Fe and ^{129}I Mössbauer work on $\text{N}(\text{C}_2\text{H}_5)_4\text{FeI}_4$ provided us with Mössbauer parameters of both iron and iodine, enabling a double-check of our theoretical electronic and magnetic structure of this compound. This example was chosen to illuminate the interpretation of measured magnetic hyperfine fields on the basis of SCC-MO results.

Acknowledgments

We are grateful for the support of the Deutsche Forschungsgemeinschaft under Contract Tr 97/6 and of NATO under Contract 1605. We gratefully acknowledge the critical discussions with R. Bläs, J. Delhalle, J. M. Friedt, and F. E. Harris, and we thank J. P. Desclaux for supplying us with relativistic $\rho(0)$ values for iodine obtained from Hartree-Fock-Dirac calculations.

Literature Cited

1. Cusachs, L. C.; Reinolds, J. W. *J. Chem. Phys.* **1965**, *43*, S160.
2. Rein, J.; Fukuda, N.; Win, H.; Glarke, G. A.; Harris, F. E. *J. Chem. Phys.* **1966**, *45*, 4743.

3. Trautwein, A. *J. Phys. (Paris)* 1980, 1, C1–95.
4. Grodzicki, M. *J. Phys. B*, 1980, 13, 2683.
5. Bläs, R.; Grodzicki, M.; Marathe, V. R.; Trautwein, A. *J. Phys. B*, 1980, 13, 2693.
6. Kane, E. O. *Phys. Rev.* 1972, B5, 1493.
7. Robinson, J. E.; Bassani, F.; Knox, R. S.; Schieffer, J. R. *Phys. Rev. Lett.* 1962, 9, 215.
8. Barnett, M. P.; Coulson, C. A. *Philos. Trans. R. Soc. London* 1951, A243, 221.
9. Basch, H.; Viste, A.; Gray, H. B. *Theor. Chim. Acta* 1965, 3, 458.
10. Clementi, E.; Roetti, C. *At. Nucl. Data Tables* 1974, 14, 177.
11. Flygare, W. H.; Hafemeister, D. W. *J. Chem. Phys.* 1965, 43, 789.
12. Spijkervet, W. J. J.; Pleifer, I. *Hyperfine Interact.* 1979, 7, 285.
13. Ladrière, J.; Gogneau, M.; Meyheus, A. *J. Phys. (Paris)* 1980, 1, C1–131.
14. Reschke, R.; Trautwein, A. *Theor. Chim. Acta* 1978, 47, 85.
15. Sternheimer, R. M. *Phys. Rev.* 1950, 80, 102.
16. *Ibid.*, 1951, 84, 244.
17. *Ibid.*, 1952, 86, 316.
18. *Ibid.*, 1953, 92, 1460.
19. *Ibid.*, 1954, 95, 736.
20. *Ibid.*, 1957, 105, 158.
21. *Ibid.*, 1967, 164, 10.
22. *Ibid.*, 1966, 146, 140.
23. *Ibid.*, 1972, A6, 1702.
24. Foley, H. M.; Sternheimer, R. M.; Tycko, D. *Phys. Rev.* 1954, 93, 734.
25. Sternheimer, R. M.; Foley, H. M. *Phys. Rev.* 1956, 102, 731.
26. Sternheimer, R. M.; Peierls, R. F. *Phys. Rev.* 1971, A3, 837.
27. Das, T. P.; Bersohn, R. *Phys. Rev.* 1956, 102, 733.
28. Wikner, E. G.; Das, T. P. *Phys. Rev.* 1957, 107, 497.
29. *Ibid.*, 1958, 109, 360.
30. Ingalls, R. *Phys. Rev.* 1962, 128, 1155.
31. Chang, E. S.; Pu, R. T.; Das, T. P. *Phys. Rev.* 1968, 174, 16.
32. Ray, S. N.; Lee, T.; Das, T. P. *Phys. Rev.* 1974, A9, 93.
33. Ray, S. N.; Lee, T.; Das, T. P.; Sternheimer, R. M. *Phys. Rev.* 1974, A9, 1108.
34. *Ibid.*, 1975, A11, 1804.
35. Ray, S. N.; Das, T. P. *Phys. Rev.* 1977, B16, 4794.
36. Ahmad, S.; Newman, D. J. *J. Phys. C*, 1978, 11, L277.
37. Lahiri, J.; Mukherji, A. *Phys. Rev.* 1967, 153, 386.
38. *Ibid.*, 155, 24.
39. Mukherjee, P. K.; Roy, A. P.; Gupta, A. *Phys. Rev.* 1978, A17, 30.
40. Lauer, S.; Marathe, V. R.; Trautwein, A. *Phys. Rev.* 1979, A19, 1852.
41. Lauer, S., Diplomarbeit, Universität des Saarlandes, Saarbrücken, West Germany, 1979.
42. Townes, C. H.; Dailey, B. P. *J. Chem. Phys.* 1949, 17, 782.
43. Sanchez, J. P., Ph.D. Dissertation, Institut National de Physique Nucléaire et de Physique des Particules, Strasbourg, France, 1979.
44. Jaccarino, V.; King, J. G.; Satten, R. A.; Stroke, H.-H. *Phys. Rev.* 1954, 94, 1798.
45. Kopfermann, H. In "Kernmomente"; Akad.-Verlag GMBH: Frankfurt a.M., 1956.
46. Fuller, G.; Cohen, V. W. *Nucl. Data* 1969, A5, 433.
47. Straub, P. A.; McLean, A. D. *Theor. Chim. Acta* 1974, 32, 227.
48. Bessis, N.; Picart, J.; Desclaux, J. P. *Phys. Rev.* 1969, 187, 88.
49. Gordy, W. *Rev. Mod. Phys.* 1948, 20, 668.
50. Friedt, J. M.; Petridis, D.; Sanchez, J. P.; Reschke, R.; Trautwein, A. *Phys. Rev.* 1979, B19, 360.

51. Abragam, A.; Horowitz, J.; Pryce, M. H. L. *Proc. R. Soc. (London)* **1955**, *A230*, 169.
52. Watson, R. E.; Freeman, A. J. *Phys. Rev.* **1961**, *123*, 2027.
53. Ray, S. N.; Lee, T.; Das, T. P. *Phys. Rev.* **1977**, *B8*, 5291.
54. Trautwein, A.; Zimmermann, R. *Phys. Rev.* **1976**, *B13*, 2238.
55. Trautwein, A. In "Structure and Bonding"; Springer-Verlag: Berlin, 1974; Vol. 20, p. 101.
56. Reschke, R., Ph.D. Dissertation, Universität des Saarlandes, Saarbrücken, West Germany, 1976.
57. Zimmermann, R.; Trautwein, A.; Harris, F. E. *Phys. Rev.* **1975**, *B12*, 3902.
58. Reschke, R.; Trautwein, A.; Harris, F. E. *Phys. Rev.* **1977**, *B15*, 2708.
59. Boekema, C.; van der Woude, F.; Sawatzky, G. A. *Int. J. Magn.* **1972**, *3*, 341.
60. Sawatzky, G. A.; Geertsma, W.; Haas, C. *J. Magn. Mat.* **1976**, *3*, 37.
61. Sanchez, J. P.; Friedt, J. M.; Trautwein, A.; Reschke, R. *Phys. Rev.* **1979**, *B19*, 365.
62. DeWaard, H. In "Mössbauer Data Index", Stevens, J. G.; Stevens, V. E., Eds.; Plenum Press: New York, 1973.

RECEIVED June 27, 1980.

Application of Gold-197 Mössbauer Spectroscopy to Studies of Electronic Properties of Intermetallic, Inorganic, and Organometallic Compounds

T. K. SHAM, R. E. WATSON, and M. L. PERLMAN

Brookhaven National Laboratory, Upton, NY 11973

We present and discuss problems in the interpretation of ^{197}Au isomer shifts and quadrupole splittings, and treat the relationship of these parameters to the electronic properties of gold-containing systems. Emphasis is placed on the successful application of the relativistic Hartree-Fock method and a renormalized atom scheme to calculate $\langle r^{-3} \rangle$ values for the 6p and 5d orbitals of gold. This calculation enables us to visualize, perhaps for the first time, semiquantitative charge distributions in gold compounds. A unified picture of the electronic behavior of the gold valence electrons in various environments emerges.

In 1960, three years after Mössbauer's discovery of the low-energy nuclear gamma-ray resonance in ^{191}Ir , the first observation of the same phenomenon in the case of the 77-keV transition in ^{197}Au was reported (2). Since then, the ^{197}Au Mössbauer transition has become a very useful spectroscopic tool for applications ranging from the study of Friedel theory of conduction electron screening in dilute alloys (3-8) and charge transfer in intermetallic compounds and alloys (9-18) to the structure and bonding systematics in inorganic (19, 20) and organometallic (21-26) compounds, and in metal clusters (27, 28).

Despite the impressive research done with ^{197}Au over the past two decades, there remain important questions concerning the interpretation of the most important Mössbauer parameters, isomer shift and quadrupole

0065-2393/81/0194-0039\$05.50/0
© 1981 American Chemical Society

splitting. The problem is that very often only qualitative information about electronic (bonding) properties of the system has been derivable and that, more often than not, efforts to obtain quantitative results have not been satisfactory. One of the most striking observations deriving from isomer shift measurements is that pure gold metal has smaller contact electron density than gold in almost all gold compounds (11, 19). Although it may not be surprising to find that this is the case in metallic alloys or intermetallic compounds, because gold is often considered to be the most electronegative metallic element (29), it is indeed very surprising to discover that in inorganic compounds, where gold is formally +1 or +3, the contact density, as indicated by the isomer shift, is greater in most cases than in the pure metal. Only the very ionic gold(I) halides display slight negative shifts, of the order of 0.1 mms^{-1} , rather small compared with the entire isomer shift range, 8 mms^{-1} , observed in metallic systems.

The problem in interpreting the gold isomer shift is that one has to deal with the effects of volume, with gold $5d$ and non- $d(6s, 6p)$ interplay, and with definition of "6s" and "6p" valence electron character in a metallic or covalently bonded system. These considerations determine the conversion (3, 6, 7, 12, 16, 18) of isomer shift into change of $6s$ or conduction electron count as a result of charge transfer upon compound and, especially, alloy formation. The traditional view is that gold $5d$ character is only slightly involved in the alloying process and should not contribute greatly to the isomer shift through screening. However, our recent gold Mössbauer and x-ray photoemission measurements (12, 16, 17) indicate very strongly that the gold $5d$ bands are actively involved in compound formation and that the increase of valence s character at the gold site is effectively compensated by charge depletion to maintain electroneutrality locally.

There is a similar problem in interpreting quadrupole splitting; here one is concerned with the effective contribution of $6p$ and $5d$ electrons to the quadrupole field. The behavior of these electrons is crucial, especially to the chemistry and bonding properties of inorganic and organometallic compounds. In such systems, the gold atoms have much lower coordination than in the metal: two and four are common coordination numbers for the gold(I) and gold(III) compounds, respectively, and electric field gradients inevitably result from these geometries. The quadrupole fields arise from lattice terms and from the asymmetry in the $6p$ and, to a lesser extent, in the $5d$ bonding charges. However, until now, quadrupole splitting values have not been understood quantitatively because the free atom $\langle r^{-3} \rangle_{6p}$ values are too small to be consistent with the large quadrupole splittings observed in gold compounds.

In this chapter, we present and discuss these problems in interpreting isomer shift and quadrupole splitting. We then attempt to advance the

interpretation to at least a semiquantitative level. Emphasis is placed on the successful application of the relativistic Hartree–Fock method (30) and a renormalized atom scheme (31) to calculate $\langle r^{-3} \rangle_{6p}$ and $\langle r^{-3} \rangle_{5d}$. This procedure enables us to visualize, for the first time, valence charge distributions of gold compounds having very plausible bonding electron populations.

In the next section we discuss the ^{197}Au isomer shift in terms of contact densities associated with renormalized and free atoms. We also consider conduction electron screening in the pure metal. Of particular concern with respect to the gold isomer shifts in metallic systems are the effects of volume, s – d rehybridization and screening, and charge transfer. In a later section we discuss the large quadrupole splitting observed in $[\text{Au}(\text{CN})_2]^-$ in terms of a pseudoatomic model. We employ, in this model, $\langle r^{-3} \rangle$ values for $6p$ and $5d$ electrons calculated by the relativistic Hartree–Fock method and renormalized to the Wigner–Seitz volume of the gold site. Another section deals with the interpretation of Mössbauer parameters in gold(I) compounds. Using the $\langle r^{-3} \rangle$ values, we have estimated p charge distributions and clarified the question of σ vs. π bonding and s vs. p donation ability of ligands in gold(I) compounds. A new set of σ parameters is derived for the ligands on the basis of both quadrupole splitting and isomer shift considerations. These σ bonding parameters reflect quite accurately the ligand characteristics. Intermetallic and gold(III) systems are also discussed. In the final section we summarize the general behavior of gold valence electrons as interpreted from Mössbauer parameters, and present a unified picture of this behavior.

Isomer Shift, Contact Density, and Charge Transfer

Isomer Shifts in Metallic Systems and Coordination Complexes. For practical purposes, the experimental isomer shift (IS) (mms^{-1}) between an absorber and a source may be written (32)

$$\text{IS} = [0.00608 Z \delta \langle r^2 \rangle \Delta\rho(0)]/E\gamma \quad (1)$$

Here Z is the nuclear charge; $\delta \langle r^2 \rangle$ is the change in the square of the nuclear radius (10^{-3} fm^2) between the excited and the ground states and is known for ^{197}Au ; $E\gamma$ is the Mössbauer transition energy in keV; and $\Delta\rho(0) = [|\psi(0)|_a^2 - |\psi(0)|_s^2]$ is the difference between the contact densities (a_0^{-3}) of the source and the absorber. Equation 1 may be reduced to

$$\text{IS} = 0.0536 \Delta\rho \quad (2)$$

where the prefactor is a constant appropriate to the 77.3-keV transition, $Z = 79$, and $\delta \langle r^2 \rangle = 8.6 \times 10^{-3} \text{ fm}^2$ (32). The only parameter that concerns us is the change of contact density $\Delta\rho(0)$ between systems of interest.

Strictly speaking, $\Delta\rho(0)$ includes the effects of core electrons as well as valence electrons, but since deep core contributions to the contact density are almost unaffected by chemical differences, it is practical to consider $\Delta\rho(0)$ as arising primarily from redistribution of valence-like electrons that participate actively in bonding. However, the core 5s shell overlaps the valence 5d, and we do take into account changes in the 5s contact density. Two factors must be considered before isomer shift among compounds can be translated into differences of electron counts in the 6s and 5d gold site orbitals: the volume changes and *s*-*d* rehybridization effects associated with compound formation. These effects are particularly important in metallic systems, in which the gold sites are screened by charge density halos resulting from conduction electron displacement (33). If the conduction electron character n_c (basically *s* and *p*) at the gold site of a compound or alloy is increased relative to that of pure gold, the contact density is increased; an increase of *d* character, Δn_d , on the other hand, screens the conduction electrons and reduces $\rho(0)$. Calculations for free atoms as well as calculations renormalized to the Wigner-Seitz cell of gold show that the effect of the *d* screening can be quite important. Thus for metallic systems (14)

$$\Delta\rho(0) \propto \Delta n_c - R\Delta n_d \quad (3)$$

where *R* is as large as 1/2. Pauling (29) and Friedel (33) electroneutrality considerations apply in metallic systems and, as a result, a charge compensation is expected to take place, that is,

$$\Delta n_c + \Delta n_d \sim 0 \quad (4)$$

a relation that is borne out by core-level photoemission experiments. For coordination complexes, Equation 3 can be written in terms of the change of 6s electron count, Δn_s

$$\Delta\rho(0) \propto \Delta n_s - R \Delta n_d \quad (5)$$

Difficulties arise if one compares the isomer shift of linear two-coordinate gold(I) or square-planar gold(III) compounds with that of pure gold metal; in these low-coordinate complexes the screening of the gold site is achieved mainly by charge in the more localized molecular orbitals rather than by the diffuse conduction electrons of metallic systems. This is to say that one must estimate the effects on the isomer shift on going from a metal, for which n_c is applicable, to a covalent solid with its valence electron count n_s . In a comparison within a given system type, such as a series of gold(I) compounds, Equation 5 should reflect consistently the bonding behavior of the complexes. It is reasonable to

consider $R\Delta n_d$ to be negligible in gold(I) compounds, and small but not negligible in gold(III) compounds.

Conversion of Isomer Shifts to Electron Counts. To obtain quantitative bonding information from isomer shifts, one must evaluate the actual isomer shift, say in mms^{-1} , in terms of units of s or d charge transferred. Some investigators (6, 11, 17), assuming that d effects are negligible, have suggested that $\text{IS} \approx 8 \text{ mms}^{-1} \Delta n_s$ for most gold systems. We, however, (12, 16) believe that non- d , d compensation occurs in alloys (13). Based on experiments and Knight shift considerations (34, 35) we suggest (12, 16) that in metallic systems $\text{IS} \approx 12 \text{ mms}^{-1} \Delta n_c$. Here it is implied that $\Delta n_c/\Delta n_d \sim \text{constant}$ ($-R\Delta n_d \approx 0.5\Delta n_c$). Our study of a number of main-group metallic compounds and alloys indeed indicates that this ratio is roughly constant and that the overall charge flow ($\Delta n_c + \Delta n_d$) onto gold is on the order of 0.1 to 0.2 electrons. In gold(I) complexes, where Δn_d is negligible, $\text{IS} = 8 \text{ mms}^{-1} \Delta n_s$ is reasonable.

Not included in the foregoing considerations are effects in dilute alloys or metallic systems when there is a significant volume mismatch between the gold impurity and the host. In such cases, one normally takes into account the volume effect (14, 15) on the isomer shift by making use of Mössbauer data on pressure effects (9, 11, 14, 23). For most of the gold-nontransition metal compounds, this volume correction is small (16) and chemical effects dominate the isomer shift. However, in nonconducting gold complexes it is very difficult to assess the volume effects. Yet, it is reasonable to assume that within a series of similar inorganic and organometallic compounds the purely chemical effects are dominant.

Figure 1 shows the range of isomer shifts for the important classes of gold compounds: metallic compounds and alloys, gold(I) complexes, and gold(III) complexes. It is the alloys that display the largest variation in isomer shift. This indicates immediately that charge redistribution around the gold site is most flexible in metallic systems. It is also apparent that even in most gold(I) and gold(III) compounds the contact density is greater than it is in pure gold. These observations are best considered in the context of self-consistent field calculations of the contact density of $6s$ electrons at the gold site. Figure 2 illustrates the relative contact densities for the $6s$ electron of a free gold atom and for that $6s$ function renormalized to a Wigner-Seitz cell. In metallic systems, an increase of conduction electron count and the accompanying d compensation should always produce a positive isomer shift. Δn_c should be largest in the ionic limit; in the case of AuCs or of other alkali and alkaline earth systems, the electrons are relatively localized and their isomer shift effects should be correspondingly large. In gold(I) compounds, gold(I) formally has lost charge, yet covalency confines the $6s$ and $6p$ charge

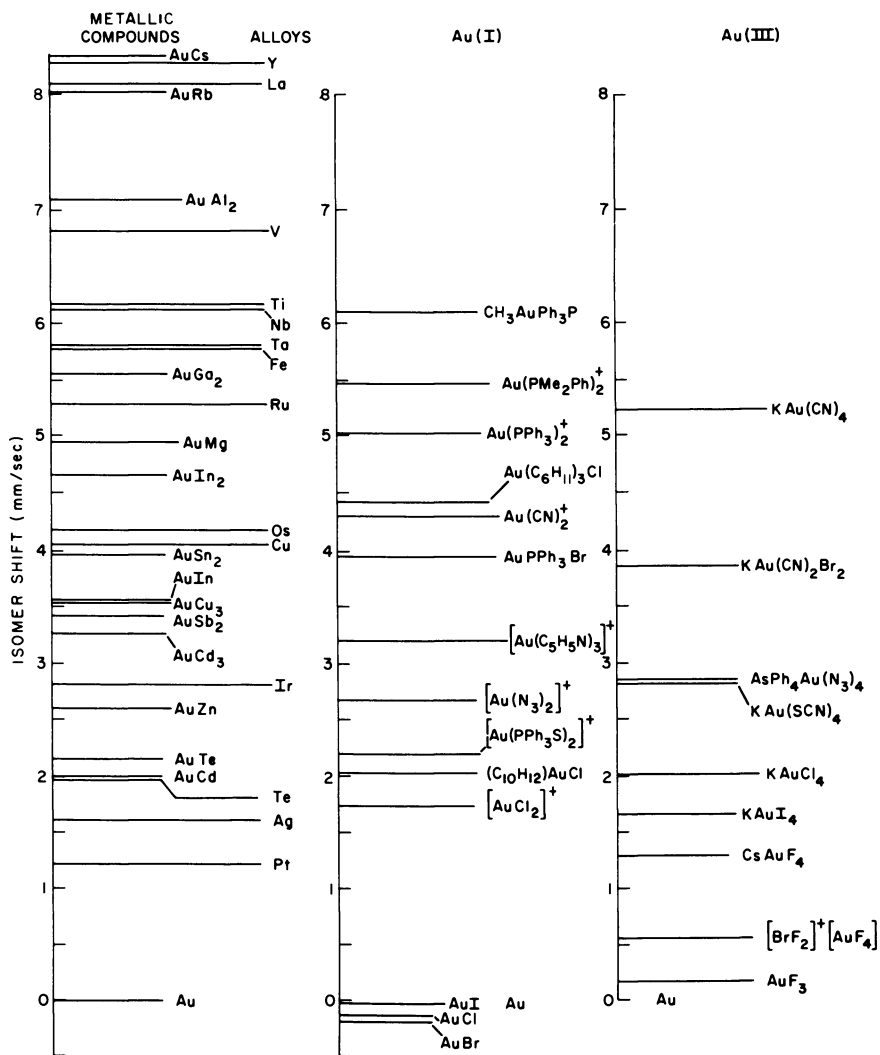


Figure 1. Representative isomer shifts in metallic and coordination gold complexes; metallic data are from Refs. 3, 7, 9, 10, 15, 16, 17; other data are selected from Refs. 19–25.

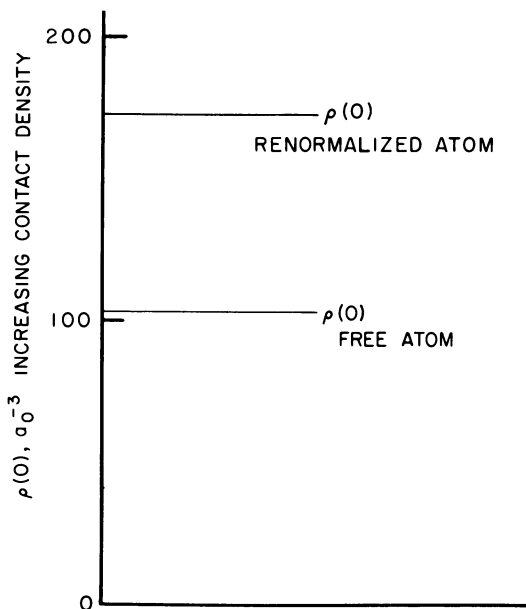


Figure 2. Contact densities at the gold nucleus corresponding to one 6s electron for the free $d^{10}s$ atom and the same 6s orbital renormalized to the metallic Wigner-Seitz cell. The results are based on a relativistic calculation with a finite nucleus.

character within the bonds. This seems to overcompensate the effect of the charge expected to be lost by gold when it forms compounds with more electronegative ligands. In the gold(III) system, the 5d hole has considerable effect on the isomer shift; this will be discussed together with quadrupole splitting in a later section.

The Pseudoatomic Model and the Interpretation of the Quadrupole Splitting in $K[Au(CN)_2]$

General Considerations. The local symmetry at the site of the Mössbauer atom determines whether or not an electric field gradient q is allowed. If it is, q involves valence electron and lattice contributions

$$q = q_{\text{val}}(1 - R_s) + q_{\text{latt}}(1 - \gamma_\infty). \quad (6)$$

Here R_s and γ_∞ , Sternheimer factors (37, 38), account for the fact that the closed-core electron shells, because they are distorted by the influences of q_{val} and q_{latt} , interact with the nucleus. One evaluates q_{latt} and q_{val} by integrating

$$\int \frac{Y_2^0(\cos\theta)}{r^3} \rho \, d\tau$$

over the charge distribution in the surrounding lattice and in the valence electrons at the atomic site, respectively. In the integrand, $Y_2^0(\cos \theta)$ is the spherical harmonic and ρ is the electron density. q_{val} and q_{latt} are commonly expressed as

$$q_{\text{val}} = - \sum \langle 3\cos^2\theta_i - 1 \rangle \langle r_i^{-3} \rangle \quad (7)$$

$$q_{\text{latt}} = \sum \frac{Z (3\cos^2\theta_i - 1)}{r_j^3} \quad (8)$$

where $\langle r_i^{-3} \rangle$ is the expectation value for the valence electron of interest and r_j is the distance of the external ligand charge from the nucleus. For the gold(I) and gold(III) compounds of concern, the q_{val} term is dominant. In metallic systems q is small because of conduction electron screening, so that in dilute alloys q_{latt} and q_{val} are comparable (39, 40). According to the Townes-Dailey theory (42), q_{val} in gold compounds of linear and square-planar symmetry with zero asymmetry parameter can be expressed

$$q = q_{\text{val}} = 4/5 [-p_z + (1/2)(p_x + p_y)] \langle r^{-3} \rangle_{6p} + 4/7 [-d_{z^2} + d_{x^2-y^2} + d_{xy} - (1/2)(d_{xz} + d_{yz})] \langle r^{-3} \rangle_{5d} \quad (9)$$

where p_z , d_{z^2} , etc. are orbital populations. Atomic $\langle r^{-3} \rangle$ parameters are commonly employed in deriving orbital population counts from Mössbauer quadrupole splittings. This pseudoatomic approach has been used by Faltens et al. (20) and Bartunik et al. (21) to study bonding systematics in gold compounds, and more specific applications of this approach, such as the additivity model of electric field gradients in organometallic compounds, have been developed (41).

If a pseudoatomic model is to be used generally, we need to know how well the atomic parameter $\langle r^{-3} \rangle$ represents the actual contributions of different valence charges resulting from charge redistribution. It has been common practice to calculate $\langle r^{-3} \rangle$ values for the valence orbitals of the free atom in appropriate configurations. Often, the variation in $\langle r^{-3} \rangle$ is modest and, for a reasonable range of configurations, it is sensible to assume that $\langle r^{-3} \rangle$ is constant for the set of similar structures, as was done for the Mössbauer study of tin(IV) compounds (41). Unfortunately, the free atom $\langle r^{-3} \rangle_{6p}$ values for gold not only vary drastically from one configuration to another, but they are also too small to account for the measured quadrupole splitting. For example, Faltens and Shirley (20) concluded that charge transfer, from the ligand to the $6p_z$ orbital of gold, is responsible for the large electric field gradients in gold(I) compounds, and that $5d$ participation is unimportant. However, they also pointed out that the calculated free atom $\langle r^{-3} \rangle_{6p}$ cannot

explain the large splittings observed. As a result of this observation, two different views of the electronic behavior in linear gold(I) compounds have evolved, in both of which the interplay of $5d$ and $6p$ bonding have been considered. For $\text{Au}(\text{CN})_2^-$, for instance, some researchers (20, 23, 24) have proposed that the donation of charge from the ligands to the $6s$ and $6p_z$ orbitals of gold via σ bonding accounts for the observed quadrupole splitting, and that $5d_\pi$ back-bonding is not important. This interpretation has been supported by systematic Mössbauer studies of a series of gold(I) compounds (24, 25), by the observation of negative electric field gradients in $\text{KAu}(\text{CN})_2$ (23), and by optical studies (44). Alternatively, other researchers consider that the involvement of the $5d$ orbitals via back-bonding is important. Esquivel et al. (45) have attempted, with the back-bonding argument and atomic self-consistent Hartree-Fock calculations of $\langle r^{-3} \rangle$ for gold in several electronic configurations, to rationalize the large field gradient observed in $\text{KAu}(\text{CN})_2$. They show that a large depletion of $5d$ character in the electronic configuration of gold causes a contraction of $6p$ orbitals and leads to comparatively large $\langle r^{-3} \rangle_{6p}$ values. They also predict the correct sign for the electric field gradient in gold(I) compounds and thus argue that $5d$ back-bonding must be important in the formation of gold(I) complexes. The problem with such approaches is that they involve troublesome large valence electron counts.

Yet another approach to this problem is to invoke detailed molecular orbital calculations. Although there are several reports available of these calculations (45, 46, 47) that yield information about the bonding in gold complexes, it is still a difficult problem and a high degree of accuracy has yet to be achieved (48). The most recent results (46) suggest, for example, the lack of d back-bonding.

Renormalized $\langle r^{-3} \rangle_{6p}$ and $\langle r^{-3} \rangle_{5d}$ Values. Relativistic calculations were performed for the gold $6p$ and $5d$ orbitals in the free atom and for the atom renormalized to the volume of the Wigner-Seitz cell in gold metal. We used this approach for two reasons. First, while $5d$ electrons are somewhat core-like, free-atom $6p$ orbitals, which have most of their charge at distances corresponding to neighboring atom sites in the crystal, are very diffuse. It is thus physically preferable, for compounds in the condensed phase, to discuss $6p$ electron charge and bonding in terms of relatively localized orbitals constrained to the vicinity of the gold atom. Such a model parallels the explanation for the large positive isomer shift observed in gold(I) compounds. Second, the Wigner-Seitz radius r_{WS} (49), that of a sphere enclosing the volume of gold site in the metal, has zero net charge in gold metal. As we will discuss later, this is a reasonable first-order estimate of the volume inside of which the pertinent $6p$ charge is localized and counted, even in linear covalent systems.

Table I. Gold $\langle r^{-3} \rangle$ Values (in a.u.) for the Free Atom and the Atom Renormalized to the Gold Wigner-Seitz Radius ($r_{\text{WS}} = 3.01$ a.u.) in Various Electronic Configurations

<i>Electronic Configuration</i>	<i>Free Atom</i>			<i>Renormalized Atom</i>		
	$5d_{3/2}$	$5d_{5/2}$	$6p_{3/2}$	$5d_{3/2}$	$5d_{5/2}$	$6p_{3/2}$
$5d^{10}6s$	15.8	12.0	—	16.1	12.4	—
$5d^{10}6p$	16.0	12.2	3.70	16.4	12.6	25.1
$5d^9 6s 6p$	16.7	12.9	5.98	17.0	13.2	26.4
$5d^9 6p$	17.1	13.2	9.66	17.3	13.4	27.1
$5d^8 6s 6p$	17.8	14.0	12.4	18.0	14.1	28.9
$5d^8 6p$	18.2	14.3	15.7	18.3	14.5	29.8

Values of $\langle r^{-3} \rangle$ calculated for the $6p$ and $5d$ orbitals of the free and renormalized gold atom (12, 31) according to Lindgren's Dirac-Fock scheme (30) are given in Table I. Some previously estimated values (20, 45, 50, 51) are given in Table II for comparison. Lindgren's scheme, which involves the renormalization of the wave functions to the Wigner-Seitz sphere, has been described elsewhere (30, 31) and will not be discussed here. Change in the radius r_{WS} does affect the $\langle r^{-3} \rangle_{6p}$ values somewhat, and the implications of this effect will be discussed briefly, later in the section.

It is important to note several interesting features in the data of Table I. (a) The free atom calculations show that $\langle r^{-3} \rangle_{6p}$ values increase with $5d$ electron depletion, whereas $\langle r^{-3} \rangle_{5d}$ values are relatively insensitive to changes of configuration; the latter result is expected in view of the almost core-like character of the gold $5d$ electrons. These results are consistent qualitatively with published results of nonrelativistic calculations (20, 45), but show larger effects. The $\langle r^{-3} \rangle_{6p}$ values increase by a factor of four from d^{10} to $d^8 p$, and s - d interplay is important. (b) While $\langle r^{-3} \rangle_{5d}$ values are insensitive to renormalization and to change of configuration after renormalization, the $\langle r^{-3} \rangle_{6p}$ values increase with renormalization so dramatically that they become much greater than the $\langle r^{-3} \rangle_{5d}$ values. This, the most rewarding result of these calculations, now enables us to explain readily the large field gradients in gold(I) compounds without needing significant $5d_{\pi}$ back-bonding, which often

Table II. The $\langle r^{-3} \rangle$ Values in a.u. Available in the Literature Prior to This Study

<i>Electronic Configuration</i>	$\langle r^{-3} \rangle_{5d}$	$\langle r^{-3} \rangle_{6p}$	<i>Reference</i>
$5d^9 6s^2$	12.3	—	50
$5d^{10} 6p$	—	14.6	51
$5d^9 6s 6p$	13.426	4.571	45
$5d^8 6s 6p$	14.359	9.599	45

has been introduced to account for the large field gradients observed. (c) The renormalized $\langle r^{-3} \rangle_{6p}$ values are only slightly sensitive to drastic change in configuration, that is, $\leq 20\%$ instead of $\sim 400\%$ in the free atom if one compares d^8p and $d^{10}p$.

So far, only electronic configurations of a local neutral "atomic" sphere of the gold atom in a compound have been considered. Several problems have to be examined so that the $\langle r^{-3} \rangle$ values can be applied more generally. These are: volume effects, polarization effects, and chemical bonding. It is obvious that the $d^{ms}x^p$ configuration enclosed by the Wigner-Seitz volume is only an approximation of the actual molecular system.

It is not entirely clear what radius should be chosen to maintain the atomic-like charges locally. Now, it is generally the $6p_\sigma$ electrons, pointing along the bond axis, that are primarily responsible for q_{val} . Normalizing the p_σ orbitals inside planes intersecting the bonds at the covalent radius can be equivalent to normalizing them to a sphere of slightly larger radius. The $\langle r^{-3} \rangle_{6p}$ increases as we shorten the interplanar distance or the sphere radius, and vice versa; a 10% change in volume from the Wigner-Seitz value results in a 10% order-of-magnitude effect on $\langle r^{-3} \rangle_{6p}$. A p_σ population, inferred from such an $\langle r^{-3} \rangle$ value, is then the p_σ electron count at the gold site. Note that in linear compounds, such as the gold(I) complexes, the p_π orbitals lie in the plane normal to the σ bonding axis, and one might argue that their functions are less affected by renormalization. Hence, little π bonding as well as smaller $\langle r^{-3} \rangle$ and q values are expected.

The Sternheimer factors (36,37), which account for the distortion of the core electrons and the resultant contributions to the observed quadrupole splitting, have been neglected because lattice effects in gold(I) covalent compounds are small and because the Sternheimer valence factor ($1-R$) should be only slightly less than unity.

Quite important, however, are chemical effects, which can result in different electronic configurations of the gold atomic sphere or polyhedron in the various compounds. As discussed previously, once an appropriate volume is chosen, various electronic configurations derived from $\langle r^{-3} \rangle$ and isomer shift analyses can be discussed in terms of such bonding characteristics as sp rehybridization and trans influence.

Quadrupole Splitting in $[\text{Au}(\text{CN})_2]$. With the pseudoatomic model, the relative charge populations in compounds can be estimated from the $\langle r^{-3} \rangle$ values and the known geometries of the complexes. For gold(I) compounds, we use the renormalized $\langle r^{-3} \rangle$ values calculated for the $d^{10}p$ configuration. This is an appropriate choice for these compounds, in which appreciable d charge depletion is not expected. Even with depletion, for example, in the case of d^9sp , the effect on

$\langle r^{-3} \rangle$ is only 5% (Table I). The quadrupole splitting (QS) for gold(I) linear or gold(III) square-planar compounds can be expressed using the theory of Townes and Dailey, Equation 9 (42, 52), as

$$\text{QS} = 1/2e^2Q\{(4/5) \left[\left(\frac{\alpha}{2} \right) (p_x + p_y) - p_z \right] \langle r^{-3} \rangle_{6p} + (4/7) [d_{x^2-y^2} - d_{z^2} + d_{xy} - (1/2)(d_{xz} + d_{yz})] \langle r^{-3} \rangle_{5d}\} \quad (10)$$

where $Q = 0.59$ b is the nuclear quadrupole moment and p_x , d_z^2 , etc. are orbital populations, with p_z and d_z^2 , of course, as the σ bonding orbitals. Here α is a factor which may be less than one to account for the possibility that the p_π orbitals are more diffuse than the p_σ orbitals and thus have a smaller $\langle r^{-3} \rangle$ value. For linear gold(I) compounds, which have nearly full d shells, Equation 10 can be written with Q evaluated,

$$\text{QS} = 1.116 \{(4/5) \left[\left(\frac{\alpha}{2} \right) (p_x + p_y) - p_z \right] \langle r^{-3} \rangle_{6p} + (4/7) [4 - d_z - (1/2)(d_{xz} + d_{yz})] \langle r^{-3} \rangle_{5d}\} \quad (11)$$

Equation 11 describes the quadrupole splitting in terms of the participating valence charge, and the orbital populations are a measure of the bonding properties of the ligands. This approach is in fact equivalent to a simple molecular orbital formalism (41, 52), according to which the relative contributions of the molecular orbitals to the atomic orbital character of the Mössbauer atom dominate the field gradient. The large quadrupole splitting observed for $[\text{Au}(\text{CN})_2]^-$ can now be understood. We first consider the p_σ -bonding model; Equation 11 becomes

$$\text{QS} = -1.116[(4/5) p_z \langle r^{-3} \rangle_{6p}] = -22.37 p_z \quad (12)$$

With the observed splitting -10.21 mms $^{-1}$ one obtains $p_z = 0.46$, a value consistent with the σ bonding picture in that the gold $6s$ and $6p$ orbitals are populated by ligand charge donation along the σ bond. That is, the approximate atomic configuration for gold in $[\text{Au}(\text{CN})_2]^-$ is such that there is an imbalance of p charge with an excess of 0.46 electrons along the bonding axis. Together with isomer shift considerations, this would indicate that the atomic sphere of gold enclosed by r_{WS} in this covalent structure is negatively charged, an observation that is not surprising since the Wigner-Seitz volume is greater than the volume enclosed by the covalent radius, and since gold is the most electronegative metallic element.

We consider the effect of a small π donation from the $d_{xz(yz)}$ orbital to the ligand. Equation 10 has the form

$$\begin{aligned} QS &= 1.116\{- (4/5) p_z \langle r^{-3} \rangle_{6p} + (4/7)[2 - (1/2) d_{xz} \\ &\quad - (1/2) d_{yz}] \langle r^{-3} \rangle_{5d}\} \\ &= -22.37 p_z + 8.985 (2 - d_{xz}/2 - d_{yz}/2) \quad (13) \end{aligned}$$

where a weighted-average $\langle r^{-3} \rangle_{5d}$ value for the $5d^{10} 6p$ configuration is used. Although the possibility of some $5d$ participation in chemical bonding cannot be totally eliminated on the basis of the result obtained with Equation 12, convincing evidence in the literature exists, such as the work reported by McAuliffe et al. (24) and Jones et al. (25), indicating that $p_z \gg (2 - d_{xz(yz)})$ in gold(I) compounds. Estimates of the extent of $5d$ back donation based on Equation 13 and isomer shift considerations show that $5d$ contribution to the observed splitting is small, even in the most favorable case; if one takes the $p_z/\Delta n_s$ ratio to be 0.90 in $[\text{Au}(\text{CN})_2]^-$ due to sp rehybridization, the value for $(2 - \frac{1}{2}d_{xz} - \frac{1}{2}d_{yz})$ becomes ~ 0.07 , as compared to $p_z \sim 0.5$.

Bonding Properties and Mössbauer Parameters in Linear Gold(I) and Related Compounds from Isomer Shift and Quadrupole Splitting

σ Parameter and Additivity Model. The previous section makes it appear that the renormalized $\langle r^{-3} \rangle_{6p}$ values yield reasonable $6p$ populations and that σ bonding dominates the field gradient in gold(I) compounds. We may now go on to estimate the σ bonding properties of the ligands in gold(I) chemistry from both isomer shift and quadrupole splitting measurements. We use $\Delta n_s = \text{IS}/8 \text{ mms}^{-1}$ and Equation 12 to evaluate a parameter σ , $2\sigma = (\Delta n_s + p_z)$. This parameter should represent, consistently among gold(I) compounds, the relative bonding ability of the ligands. A set of σ parameters derived from $[\text{AuL}_2]$ compounds is given in Table III.

It is interesting to note from the p_z and Δn_s values that Cl^- is a slightly better p than s donor; for the weak σ ligands s and p donation abilities are comparable, while for strong σ ligands there tends to be more s than p character in the metal-ligand bond. This trend is consistent with conventional wisdom and experience in coordination chemistry (25). The overall σ donation ability for these ligands can be arranged as: $\text{P}(\text{C}_6\text{H}_{11})_3 \sim \text{PMe}_2\text{Ph} \sim \text{PEt}_3 > \text{PPh}_3 \sim \text{PMePh}_2 \sim \text{CN}^- > \text{AsPh}_3 \sim \text{C}_5\text{H}_{10}\text{NH} > \text{SMe}_2 \sim \text{C}_5\text{H}_5\text{N} > \text{N}_3^- \sim \text{PPh}_3\text{S} > \text{Cl}^-$.

A test and application of these σ parameters is to examine their additivity (2σ of $\text{AuLL}' = \sigma_L + \sigma_{L'}$). It has been proposed in earlier Mössbauer work (41, 52) that the isomer shifts and the quadrupole

Table III. The σ Parameter Derived from Linear $[\text{AuL}_2]^+$ Complexes

Ligand ^a	IS	QS	Δn_s ^b	p_z ^b	2σ	σ
Cl ⁻	1.72	6.13	0.22	0.27	0.49	0.25
PPh ₃ S	2.46	6.82	0.31	0.31	0.61	0.31
[N ₃] ⁻	2.61	6.84	0.33	0.31	0.63	0.32
py	3.19	7.32	0.34	0.33	0.73	0.36
SMe ₂	3.43	7.56	0.34	0.43	0.77	0.38
AsPh ₃	3.98	8.45	0.50	0.38	0.88	0.44
C ₅ H ₁₀ NH	4.04	7.88	0.51	0.36	0.86	0.43
[CN] ⁻	4.30	10.12	0.54	0.45	0.99	0.50
PMePh ₂	4.75	9.69	0.43	0.59	1.03	0.51
PPh ₃	5.06	9.43	0.63	0.42	1.05	0.53
PEt ₃	5.40	10.18	0.68	0.46	1.13	0.57
P(C ₆ H ₁₁) ₃	5.44	10.37	0.68	0.46	1.14	0.57
PMe ₂ Ph	5.48	10.15	0.69	0.45	1.14	0.57

^a From Ref. 25 and references therein.

^b Reference to gold metal, $\Delta n_s = \text{IS}/8 \text{ mms}^{-1}$, $p_z = \text{QS}/22.37$ (Equation 12); it is assumed here that p_x, p_y are not populated.

splittings of low-spin iron(II) compounds and the quadrupole splittings of tin(IV) and antimony(V) compounds can be treated in an additive manner. Thus, on the basis of a set of parameters, such as partial isomer shift and partial quadrupole splittings derived from model compounds, the Mössbauer parameters of similar compounds should be predictable. This procedure, however, has not been successful for gold(I) compounds (24, 25), and the failure has been attributed to s - p rehybridization effects resulting from trans influence (25). Since rehybridization implies redistribution of s and p charge, σ should be less affected and remain additive. A plot of the predicted vs. the observed σ parameters (Figure 3) for a series of linear AuLCl and AuLPPH₃ compounds shows that this is indeed the case. It is also interesting to note that the σ parameters of individual ligands correlate well with the nuclear quadrupole resonance frequencies of chlorine (Figure 4) in a series of AuLCl compounds (53). This result, too, indicates that the σ parameters better represent the overall bonding properties of the ligands than do parameters based on either isomer shift or quadrupole splitting alone (20).

We can also use Equation 13 to estimate the effects of pressure on some of these compounds. For example, Prosser et al. (23) have made pressure-dependent Mössbauer measurements of AuCN and $[\text{Au}(\text{CN})_2]^-$. They found an increase in isomer shift and a decrease in quadrupole splitting with an increase of pressure in both compounds. Assuming that the increase in p_z is equal to the decrease in d_{xz}, d_{yz} population, attributable to donation and back donation, we estimate from the data (22) that the maximum additional d depletion is ~ 0.075 in AuCN and ~ 0.01

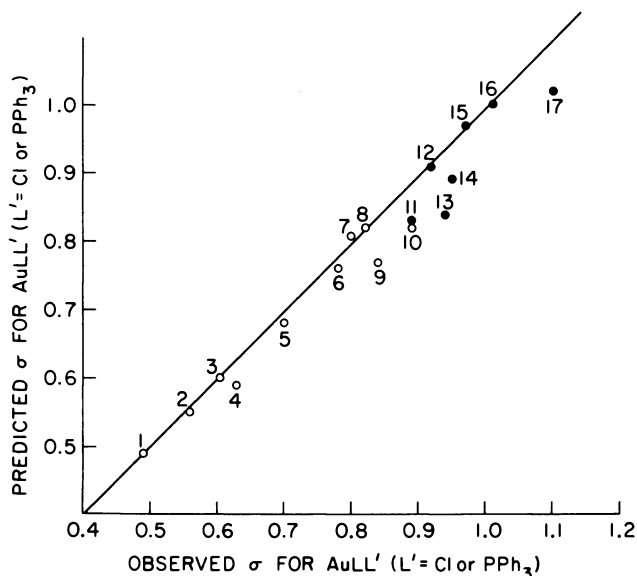


Figure 3. Plot of observed vs. predicted σ parameters for a series of $AuLCl$ (\circ), 1 to 10 and $AuLPPh_3$ (\bullet), 11 to 17 compounds. (L = (1) Cl^- ; (2) PPh_3S ; (3) *py*; (4) SMe_2 ; (5) $AsPh_3$; (6) $PMePh_2$; (7) PEt_3 ; (8) PMe_2Ph ; (9) PPh_3 ; (10) $P(C_{10}H_{11})_3$; (11) PPh_3S ; (12) SMe_2 ; (13) N_3^- ; (14) *py*; (15) $AsPh_3$; (16) PPh_3 ; (17) CN^- .)

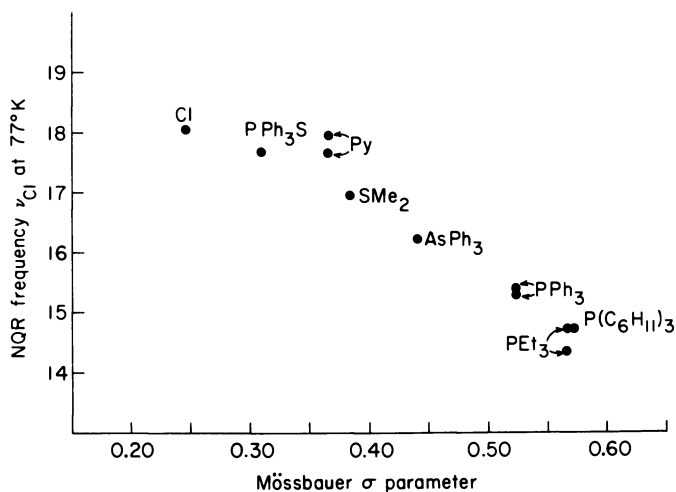


Figure 4. Plot of chlorine NQR frequency at 77 K vs. σ parameter of L in $AuLCl$ complexes. NQR data are from Ref. 53.

in $[\text{Au}(\text{CN})_2]^-$. Again, these are estimates; nevertheless they do allow us to have some feeling for π back-bonding effects on the gradients.

Quadrupole Splittings in AuTe_2 and Gold(III) Compounds. Recently it was found that the quadrupole splitting at the tetragonally distorted octahedral gold site in metallic AuTe_2 is -2.16 mms^{-1} , a relatively large value for an intermetallic compound (17). Using Equation 12 we calculate $6 p_z$ to be ~ 0.1 . This is consistent with the increase in overall conduction electron charge (basically of s and p character) of ~ 0.2 electron, estimated from isomer shift considerations.

It is also possible to extend the σ parameter consideration to gold(III) compounds, though less accurately because more bonding orbitals are involved. In square-planar gold(III) complexes, sp^2d hybridization involving $6s$, $6p_x$, and $5d_{x^2-y^2}$ is considered, rather than $5s$ and $6p$ appropriate to gold(I) complexes. We assume the p bonding character to be the same for a given ligand in both gold(I) and gold(III) compounds. Let us first consider the quadrupole splitting for $[\text{Au}(\text{CN})_4]^-$. If we focus on the occupancy of the least-bonding d_{z^2} and the σ bonding $d_{x^2-y^2}$, we see that for the square-planar $[\text{Au}(\text{CN})_4]^-$ complex, Equation 13 becomes

$$\text{QS} = 22.37 [(p_x + p_y)/2] - 8.98 (d_{z^2} - d_{x^2-y^2}) \quad (14)$$

The sign of QS is not given by experiment; if it is positive (20), meaning that the field is produced predominantly by charge along the bond directions, then $\text{QS} = +6.93 \text{ mms}^{-1}$, which from Equation 14 gives $d_{z^2} - d_{x^2-y^2} = 0.36$ under the assumption that $(p_x + p_y)/2$ in $[\text{Au}(\text{CN})_4]^- = p_z$ in $[\text{Au}(\text{CN})_2]^-$. Similarly, for $[\text{AuCl}_4]^-$, $d_{z^2} - d_{x^2-y^2} = 0.55$ when one accepts for its $(p_x + p_y)/2$ value that for p_z of $[\text{AuCl}_2]^-$ (25) and uses for the quadrupole splitting of $[\text{AuCl}_4]^-$ an average of values measured for three $[\text{AuCl}_4]^-$ complexes (21). These considerations show that Pauling's electroneutrality principle holds very well, even in gold(III) compounds.

Chemical Correlations Between Gold(I) and Gold(III). Let us consider the correlations between quadrupole splittings and isomer shifts for gold(I) and gold(III) complexes. A compilation of these data from Bartunik and Kaindl (19) appears in Figure 5.

In this figure, higher points in the plots correspond to increased electron charge along bond lines; increasing isomer shifts (points to the right) correspond to increased contact density at the gold nucleus. Faltens and Shirley (20) have indicated that the quadrupole splitting-isomer shift correlation can be explained qualitatively in terms of σ bonding to the sp and sp^2d hybrids in the cases of gold(I) and gold(III), respectively. They also observed that quadrupole splitting and isomer shift together can be used to distinguish between these two gold com-

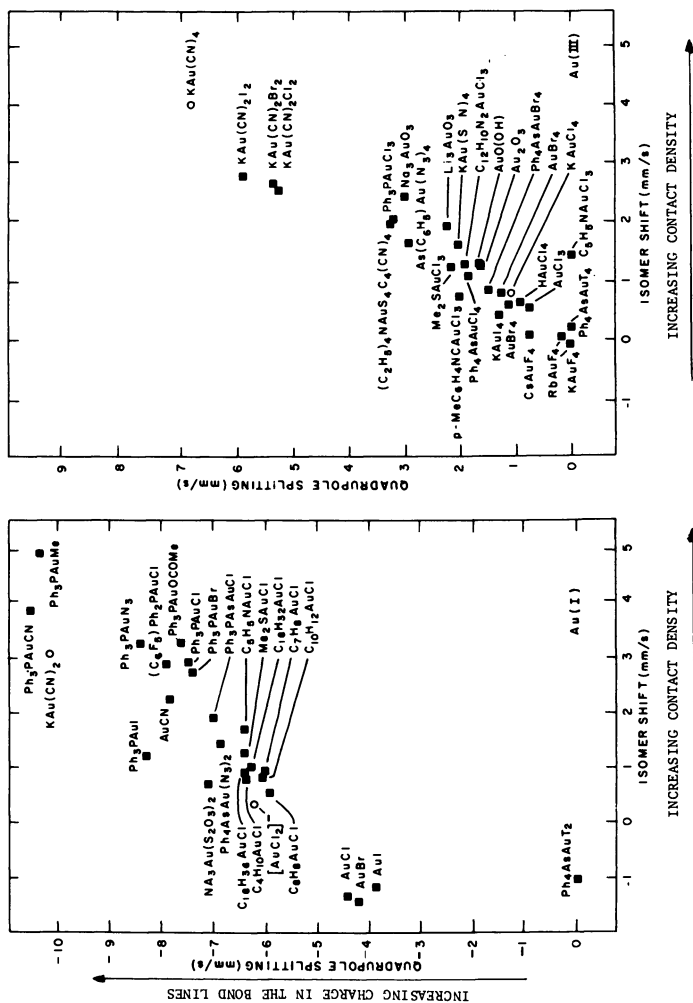


Figure 5. Plots of ^{197}Au Mössbauer quadrupole splittings vs. isomer shifts relative to $\text{Pt(Au)} (19)$; $[\text{AuCl}_2]^-$ is from Ref. 25.

North-Holland Publishing Company

plexes. Bartunik et al. (21) have arrived at similar conclusions on the basis of an LCAO-MO model in which both σ and π effects are considered, with σ dominant. Jones et al. (25) also have discussed the bonding questions in terms of s - p rehybridization. These several efforts, however, have not yielded a quantitative interpretation of the trends appearing in Figure 5. The slopes, intercepts, and curvatures (if present) of lines fitting the quadrupole splitting-isomer shift data are all of chemical relevance. In the following we discuss the implications of the differences in slopes and questions associated with the intercepts.

Consider the ratio of the slopes

$$R \equiv \frac{(\Delta QS/\Delta IS)_{\text{III}}}{(\Delta QS/\Delta IS)_{\text{I}}} \quad (15)$$

which from the plots is roughly equal to two. Neglecting d electron bonding for the moment, the ratio should be related to changes in $6s$ and $6p$ populations (Δn_s and Δn_p between compounds) and to the corresponding hyperfine parameters, that is,

$$R = \frac{[(\Delta n_p \langle r^{-3} \rangle_{6p}) / (\Delta n_s \rho(0))]_{\text{III}}}{[(\Delta n_p \langle r^{-3} \rangle_{6p}) / (\Delta n_s \rho(0))]_{\text{I}}} \quad (16)$$

If we consider the configurations of gold(III) and gold(I) to be d^8p and $d^{10}p$, respectively, for the purposes of estimating $\langle r^{-3} \rangle_{6p}$ values and to be d^8s and $d^{10}s$, respectively, for estimating the contact densities, we obtain for free-atom ions

$$\langle r^{-3} \rangle_{\text{III}} / \langle r^{-3} \rangle_{\text{I}} = 4.2$$

and

$$\rho(0)_{\text{III}} / \rho(0)_{\text{I}} = 1.5$$

but, for atoms renormalized to the Wigner-Seitz sphere,

$$\langle r^{-3} \rangle_{\text{III}} / \langle r^{-3} \rangle_{\text{I}} = 1.19$$

and

$$\rho(0)_{\text{III}} / \rho(0)_{\text{I}} = 1.18$$

Now from Equation 16, the ratio of ratios of covalent mixing parameters is

$$\frac{(\Delta n_p / \Delta n_s)_{\text{III}}}{(\Delta n_p / \Delta n_s)_{\text{I}}} = R \frac{[\langle r^{-3} \rangle_{6p} / \rho(0)]_{\text{I}}}{[\langle r^{-3} \rangle_{6p} / \rho(0)]_{\text{III}}}$$

~ 0.7 with free-ion parameters and ~ 2 with renormalized ion parameters. The value based on free-ion parameters indicates that there is less p bonding relative to s in the gold(III) complexes than in gold(I), contrary to chemical intuition and experience. In contrast, the renormalized atom model, which concentrates valence electron charge at radii corresponding to the centers of bonds, indicates that the variation of p bonding relative to that of s is twice as great in gold(III) complexes as in gold(I), a palatable result.

In the discussion of the slope ratio R , the role of d electron bonding has been neglected. For the ionic gold(III) configuration, the $d_{x^2-y^2}$ orbital in the square-planar crystal field is unoccupied. With the introduction of covalent mixing it becomes occupied and makes a positive contribution to the field gradient and hence to a steepening of the $(\Delta Q S / \Delta I S)_{III}$ slope. However, the ratio of $\langle r^{-3} \rangle_{5d}$ to $\langle r^{-3} \rangle_{6p}$ is small, but this effect is of secondary importance.

If one attempts to interpret the intercepts of lines through the data points of Figure 5 in terms of relative bonding of gold(I) and gold(III), one encounters difficulty. The problem is associated with defining a common reference "zero" for the coordinates. Consider that the atomic nonbonding limits correspond to gold(I) and gold(III) in $5d^9 6s^0 6p^0$ and $5d^8 6s^0 6p^0$ configurations, respectively. The s electron contact density of gold(III) will be slightly greater (to the right on the plots) because of reduced $5d$ screening in gold(III) in the core $5s$ shell, which $5d$ overlaps. Neglecting small lattice contributions, the field gradient of closed d shell gold(I) complexes is zero but, in the presence of an external crystal field, the gradient from the open shell of gold(III) is nonzero: the negatively charged ligands induce electrons to occupy d orbitals directed away from them. This leads to a negative field gradient, hence a negative intercept, for nonbonding gold(III). With this $5d^8 6s^0 6p^0$ description of gold(III), this intercept is calculated to be -20 mms^{-1} , and the resulting $\rho(0)_{III}$ origin would be to the left, rather than to the right, of $\rho(0)_I$. This is clearly unsatisfactory; the problem is that the local configurations appropriate to gold in these compounds deviate strongly from the assumed nonbonding limits. A competition of $5d_{xy}$, $5d_{xz}$, $5d_{yz}$, $5d_{z^2}$, $5d_{x^2-y^2}$, $6s$, $6p_x$, $6p_y$, and $6p_z$ occupancies is involved. While it is possible to compare the bonding of gold(I) and gold(III) with the same sets of ligands, as we have attempted in the preceding subsection, the results must be regarded as exploratory.

We should emphasize the principal result obtained with the renormalized atom hyperfine parameters: the variation in bonding from one ligand to another in gold(III) complexes involves changes of combined $6p$ and $5d$ bonding relative to the $6s$ differences which are larger than the analogous ratios for the gold(I) complexes.

Conclusion

We have presented and discussed some problems in the interpretation of ^{197}Au isomer shifts and quadrupole splittings. It has already been established that d and non- d charge compensation is important in gold intermetallics. For gold main-group systems, in view of the s - d compensation we propose a conversion $\text{IS} = 11.6 \text{ mms}^{-1} \Delta n_e$, and thus express the isomer shift in terms of change of conduction electron count. This conversion is probably valid for gold transition-metal systems, but it is not clear whether it applies to gold alloyed with alkalis and alkaline earths. From $\rho(0)$'s calculated for the $6s$ electron of the renormalized atom, of the free atom, and for conduction electrons in pure gold, it no longer appears surprising that pure gold has nearly the smallest isomer shift. Upon gold(I) compound formation from the metal, the localization of the $6s$ electrons, via the formation of more localized bonds, compensates the presumable loss of charge; increasing covalence further increases the isomer shift for gold(I) compounds. In gold(III) compounds, depletion of d charge has some effect on the isomer shift, but the actual charge at the gold site is far less than $+3$.

A new set of $\langle r^{-3} \rangle$ values for the $5d$ and $6p$ orbitals of gold is introduced. These values, calculated by the relativistic Hartree-Fock technique with renormalization to the Wigner-Seitz cell, are used to estimate the valence charge population from quadrupole splittings. It turns out that with these $\langle r^{-3} \rangle$ values, which are quantitatively different from the free-atom values, the observed large quadrupole splittings in gold(I) compounds are accounted for in the framework of a pseudo-atomic model on the basis of predominantly σ bonding. A set of σ parameters characteristic of the ligands is derived from the combined isomer shift and quadrupole splitting data for a number of gold(I) compounds. Unlike the result when free-atom $\langle r^{-3} \rangle$ values are employed, this set of bonding parameters is physically reasonable and displays a trend consistent with chemical intuition. Application of the model to gold(III) compounds is complicated by the participation of additional classes of bonding orbitals, but here too, chemically plausible trends emerge. In particular, the relative slopes for the gold(I) and gold(III) data in Figure 5 are satisfying.

Wave functions have been renormalized for a Wigner-Seitz sphere volume. One could equally well have utilized a polyhedron appropriate to a detailed choice of boundary conditions. Important to our considerations is the choice of a volume having a radius larger than the covalent radius, so that the bonding charge count is more closely characteristic of the σ electrons in the bond than of the charge solely within the gold site. Use of a smaller sphere would yield larger $\langle r^{-3} \rangle$ values and result in the lesser counts appropriate to the gold site alone.

Finally, we have presented here a somewhat interdisciplinary account based on Mössbauer isomer shift and quadrupole splitting of the general behavior of the valence electrons of gold. Perhaps for the first time, the bonding trends derived with renormalized $\langle r^{-3} \rangle$ values make chemical sense. We hope that these observations will facilitate and encourage further ^{197}Au Mössbauer research.

Glossary of Symbols

IS	Isomer shift
QS	Quadrupole splitting
q	Electric field gradient
Q	Nuclear quadrupole moment
PMe_2Ph	$\text{P}(\text{CH}_3)_2\text{C}_6\text{H}_5$
PEt_3	$\text{P}(\text{C}_2\text{H}_5)_3$
PPh_3	$\text{P}(\text{C}_6\text{H}_5)_3$
PMePh_2	$\text{PCH}_3(\text{C}_6\text{H}_5)_2$
AsPh_3	$\text{P}(\text{C}_6\text{H}_5)_3$
SMe_2	$\text{S}(\text{CH}_3)_2$
PPh_3S	$\text{SP}(\text{C}_6\text{H}_5)_3$
py	$\text{C}_5\text{H}_5\text{N}$

Acknowledgment

The research was performed at Brookhaven National Laboratory under contract with the U.S. Department of Energy.

Literature Cited

1. Mössbauer, R. L. *Z. Physik* **1958**, *151*, 124.
2. Nagle, D.; Craig, P. P.; Dash, J. G.; Reiswig, R. D. *Phys. Rev. Lett.* **1960**, *4*, 237.
3. Barrett, P. H.; Grant, R. W.; Kaplan, M.; Keller, D. A.; Shirley, D. A. *J. Chem. Phys.* **1963**, *39*, 1035.
4. Roberts, L. D.; Thomson, J. O.; Huray, P. G. *Phys. Rev.* **1963**, *129*, 664.
5. Roberts, L. D.; Becker, R. L.; Obenshain, F. E.; Thomson, J. O. *Phys. Rev.* **1965**, *137*, A895.
6. Roberts, L. D.; Patterson, D. O.; Thomson, J. O.; Levey, R. P. *Phys. Rev.* **1969**, *179*, 656.
7. Huray, P. G.; Roberts, L. D.; Thomson, J. O. *Phys. Rev. B* **1971**, *4*, 2147.
8. Charlton, J. S.; Harris, I. R. *Phys. Status Solidi* **1970**, *39*, K1.
9. Ingalls, R. *Solid State Commun.* **1974**, *14*, 11.
10. Wagner, F. E.; Wortmann, G.; Kalvis, G. M. *Phys. Lett.* **1973**, *42A*, 483.
11. Cohen, R. L. In "Mössbauer Isomer Shifts"; Shenoy, G. K., Ed.; North-Holland: Amsterdam, 1978; p. 541.
12. Friedman, R. M.; Hudis, J.; Perlman, M. L.; Watson, R. E. *Phys. Rev. B* **1973**, *8*, 2433.
13. Gütlich, P.; Odar, S.; Weiss, A. *J. Phys. Chem. Solids* **1976**, *37*, 1011.
14. Watson, R. E.; Bennett, L. H. *Phys. Rev. B* **1977**, *15*, 502.
15. Watson, R. E.; Bennett, L. H. *Phys. Rev. B* **1978**, *17*, 3714.
16. Sham, T. K.; Perlman, M. L.; Watson, R. E. *Phys. Rev. B* **1979**, *19*, 539.
17. Sham, T. K.; Watson, R.E.; Perlman, M. L. *Phys. Rev. B* **1979**, *20*, 3552.

18. Wertheim, G. K.; Cohen, R. L.; Crecelius, G.; West, K. W.; Wernick, J. H. *Phys. Rev. B* 1979, 20, 860.
19. Bartunik, H. D.; Kaindl, G. In "Mössbauer Isomer Shifts"; Shenoy, G. K., Ed.; North-Holland: Amsterdam, 1978; p. 516.
20. Faltens, M. O.; Shirley, D. A. *J. Chem. Phys.* 1970, 53, 4249.
21. Bartunik, H. D.; Potzel, W.; Mössbauer, R. L.; Kaindl, G. *Z. Physik* 1970, 240, 17.
22. Bartunik, H. D.; Holzapfel, W. H.; Mössbauer, R. L. *Phys. Lett.* 1970, 33A, 469.
23. Prosser, H.; Wortmann, G.; Syassen, K.; Holzapfel, W. B. *Z. Physik* 1976, B24, 7.
24. McAuliffe, C. A.; Parish, R. V.; Randall, P. D. *J. Chem. Soc. Dalton* 1977, 1426.
25. Jones, P. G.; Maddock, A. G.; Mays, M. J.; Muir, M. M.; Williams, A. F. *J. Chem. Soc. Dalton* 1977, 1434.
26. Johnson, A.; Puddephatt, R. J. *J. Chem. Soc. Dalton* 1978, 980.
27. Vollenbrock, F. A.; Bouten, P. C. P.; Trooster, J. M.; van den Berg, J. P.; Bour, J. J. *Inorg. Chem.* 1978, 17, 1345.
28. Vieggers, T. P. A.; Trooster, J. M.; Bouten, P.; Rit, T. P. *J. Chem. Soc. Dalton* 1977, 2074.
29. Pauling, L. "The Nature of the Chemical Bond", 3rd ed.; Cornell Univ. Press: Ithaca, NY, 1960.
30. Lindgren, I.; Rosen, A. *Case Stud. At. Phys.* 1974, 4, 93.
31. Hodges, L.; Watson, R. E.; Ehrenreich, H. *Phys. Rev. B* 1972, 5, 3953.
32. Kalvius, G. M.; Shenoy, G. K. *At. Data Nucl. Tables* 1974, 14, 639.
33. Freidel, J. *Philos. Mag.* 1952, 43, 153.
34. Watson, R. E., unpublished data.
35. Bennett, L. H.; Carter, G. C.; Watson, R. E. *J. Res. Natl. Bur. Stand. (U.S.)* 1970, A47, 569.
36. Goldanskii, V. I.; Herber, R. H., Eds. "Chemical Applications of Mössbauer Spectroscopy"; Academic: New York, London, 1968.
37. Sternheimer, R. M. *Phys. Rev.* 1951, 84, 244.
38. Sternheimer, R. M. *Phys. Rev.* 1963, 132, 1637.
39. Raghavan, P.; Kaufmann, E. N.; Raghavan, R. S.; Ansaldo, E.; Naumann, R. A. *Phys. Rev. B* 1976, 13, 2835.
40. Sham, T. K. *J. Chem. Phys.* 1979, 71, 3744.
41. Clark, M. G.; Maddock, A. G.; Platt, R. H. *J. Chem. Soc. Dalton* 1972, 281.
42. Townes, C. H.; Dailey, B. P. *J. Chem. Phys.* 1949, 17, 782.
43. Prosser, H.; Wagner, F. E.; Wortmann, G.; Kalvius, G. M. *Hyperfine Interact.* 1975, 1, 25.
44. Mason, W. R. *J. Amer. Chem. Soc.* 1976, 98, 5182.
45. Esquivel, D. M. S.; Guenzburger, D.; Danon, J. *Phys. Rev. B* 1979, 19, 1357.
46. Guenzburger, D.; Ellis, D. E., submitted for publication in *Phys. Rev.*
47. Hasselbach, K. M.; Wurtinger, W. *Proc. Workshop Chem. Appl. Mössbauer Spectrosc., West Germany*, 1978.
48. Ellis, D. E., to be published.
49. Kittel, C. "Introduction to Solid State Physics", 4th ed.; John Wiley and Sons: New York, 1971.
50. Childs, W. J.; Goodman, L. S. *Phys. Rev.* 1966, 141, 176.
51. Machmer, P. *Z. Naturforsch* 1966, 216, 1025.
52. Bancroft, G. M.; Platt, R. H. *Adv. Inorg. Chem. Radio. Chem.* 1972, 15, 59.
53. Jones, P. G.; Williams, A. F. *J. Chem. Soc. Dalton* 1977, 1430.

RECEIVED June 27, 1980.

Conversion Electron Mössbauer Spectroscopy and Its Recent Development

M. J. TRICKER¹

Department of Chemistry, Heriot-Watt University,
Riccarton, Currie, Edinburgh EH14 4AS

The principles and applications of conversion electron Mössbauer spectroscopy (CEMS) are reviewed in detail. Consideration is given to the surface selectivity and sensitivity of CEMS, and experimental and theoretical aspects of the method are discussed in depth. Applications of CEMS in areas such as the oxidation of iron and steels, surface treatment of steels, metallurgy, measurements of surface stress, ion-implantation, thin films, inorganic solids and minerals, and archeological materials are described.

The majority of Mössbauer spectroscopic experiments are performed in a transmission geometry and involve the detection of gamma radiation transmitted through thin absorbers. In this mode a wealth of data relating to the bulk properties of solids may be obtained. However, if information relating to the surface properties of solids is sought, the use of transmission methods is restricted to rather special absorbers. These may be microcrystallites, either freely supported or dispersed on high-area inert substrates, rather special solids with high internal surface areas such as zeolites or clay minerals, or simply stacks of very thin absorbers. To circumvent these restrictions and allow the study of the surface and near-surface regions of solids, there has been a significant increase in interest in the past few years in backscattering techniques based on the detection of conversion electrons emitted from the surface following the occurrence of a resonant event in the absorber. Because these electrons are attenuated rapidly in matter, only those electrons

¹Current address: The British Petroleum Company, Ltd., BP Research Centre, Chertsey Road, Sunbury-on-Thames, Middlesex TW16 7LN, England.

produced in regions close to the surface escape the surface, and the resulting Mössbauer spectrum is weighted towards the surface regions of the absorber. Although, in principle, many isotopes are amenable to study by conversion electron Mössbauer spectroscopy (CEMS), most studies to date have involved either ^{57}Fe or ^{119}Sn , and work with these isotopes forms the main content of this review.

Two basic types of CEMS experiments may be performed. The first of these involves the detection of the total flux of backscattered electrons without energy resolution. This approach will be referred to as integral CEMS. In the second type of experiment the flux of backscattered electrons is energy-resolved, and Mössbauer spectra are accumulated using selected bands of electron energies. It will emerge that this technique allows the surface regions of solids to be probed as a function of depth. Accordingly, this technique will be referred to as depth-resolved conversion electron Mössbauer spectroscopy (DCEMS). Since the area of CEMS has been reviewed in the past (1, 2, 3), emphasis here will be given to recent developments. However, the first section does outline the principles of the technique and give a broad overview of the developments in the area up to about mid-1976. Later sections will deal with recent developments in instrumentation, theoretical aspects and data reduction, and applications of CEMS.

Basic Principles and Overview of CEMS

Internal Conversion and Backscattering Experiments. For many Mössbauer nuclides the decay of the excited nuclear spin state is highly internally converted (4). The process of internal conversion is exemplified by reference to Table I, where the events that occur during the decay of the $I = 3/2$ excited spin state of ^{57}Fe are summarized. The internal conversion coefficient α for the $I = 3/2 \rightarrow I = \frac{1}{2}$ transition of iron is large, and only about 10% of the decay events occur by the emission of a 14.4-keV gamma photon. The predominant event is one of internal conversion which results in the ejection of a 7.3-keV K-conversion electron together with subsequent Auger electrons and x-ray photons. Internal conversion also occurs in the L- and M-shells, but with lower probability, and leads to the production of further conversion electrons, Auger electrons, and x-ray photons. A similar situation is found for the 23.8-keV transition of ^{119}Sn , although here the K-conversion process is energetically forbidden and the majority of electrons are 19.6-keV L-conversion electrons (Table I).

In view of this phenomenon, it is possible to record Mössbauer spectra in a backscatter geometry by detecting either the backscattered photons or electrons rather than by the more usual practice of detecting the

Table I. Summary of Major Events During the Decay of $I = 3/2$ Excited-Spin States of ^{57}Fe and $^{119}\text{Sn}^a$

^{57}Fe	Energy (keV)	Number (per 100) Absorption Events	Approximate Maximum Range
γ -photons	14.4	9	
K-x-rays	6.3	27	
K-conversion electrons	7.3	81	250 nm
L-conversion electrons	13.6	9	900 nm
M-conversion electrons	14.3	1	
KLL-Auger electrons	5.4	63	
LMM-Auger electrons	0.53		
^{119}Sn			
γ -photons	23.8	17	
X-rays	3.6	9	
L-conversion electrons	19.6	83	2.4 μm
LMM-Auger electrons	2.8	74	

^a The maximum electron ranges are calculated using the Bethe-Bloch expression and are taken from Ref. 29.

transmitted gamma radiation (Figure 1). In a backscatter geometry, the requirement of a thin absorber is removed and thick samples can be examined in a nondestructive fashion. If the backscattered photons are detected, information pertaining to the bulk of the solid or rather thick overlayers of a surface phase will be obtained, as the path lengths of the gamma- and x-radiation are at least on the order of magnitude of microns. However, because electrons are much more rapidly attenuated in matter, the backscattered CEM spectrum will be weighted towards the outermost

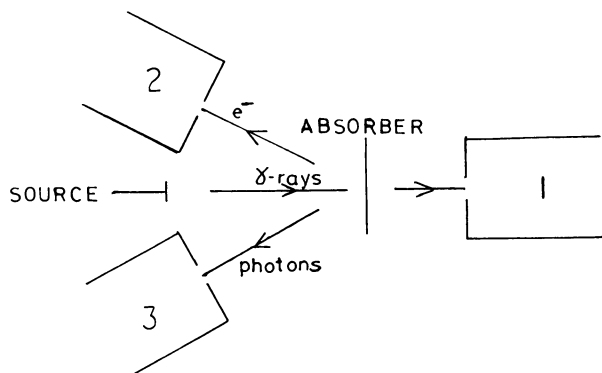


Figure 1. Schematic of possible geometries for Mössbauer experiments with detection of (1) transmitted gamma-rays, (2) backscattered electrons, and (3) backscattered photons, x-rays, and/or gamma-rays

surface regions of the sample, as only electrons produced close to the absorber surface will escape the surface. The depth selectivity of a given experiment will therefore depend on the energy spectrum of the electrons produced during the decay of the excited nuclear level of the isotope used, and on the energy of the electrons detected. An indication of the maximum ranges of the various electrons used is given in Table I.

Surface Selectivity and Sensitivity of CEMS. It follows from the previous section that CEMS opens up the possibility of studying the surface regions of low-area solids by Mössbauer spectroscopic techniques. In the simplest integral CEMS experiment, first performed by Swanson and Spijkerman (5), the backscattered electrons are detected efficiently with a 2π collection geometry by mounting the sample inside a He/CH₄ flow proportional counter. Here the electron count rates are usually significantly smaller than in transmission experiments per unit source strength. However, strong sources can be used without fear of causing saturation effects either in the detector or the counting electronics. For thick samples containing a natural abundance of ⁵⁷Fe, the signal-to-noise ratios are comparable to or less than those obtained in transmission experiments. The background arises largely from photoelectrons ejected from the absorber and walls of the detector. However, if samples enriched in ⁵⁷Fe are used, percentage effects on the order of hundreds of a percent may be obtained (6), and data accumulation times may be reduced to the order of minutes.

A qualitative indication of the surface selectivity of ⁵⁷Fe CEMS is shown in Figure 2 in which the integral CEM spectrum of an unenriched iron foil that had been exposed briefly to moist HCl vapor is shown (7). Apart from the signal resulting from the substrate, a doublet with parameters corresponding to a high-spin ferrous phase is clearly seen. This doublet was not observed in the transmission mode after a comparable counting time. This experiment demonstrated that ⁵⁷Fe CEMS is capable of revealing the presence of surface phases that would have gone undetected if transmission methods had been used alone. Apart from this observation, other studies unequivocally demonstrated the potential of CEMS as a surface tool in such areas as metallurgy (8), ion-implantation (9-16), corrosion and oxidation (7, 17-20), and geochemistry (21, 22).

Other experiments established that the probing depth of ⁵⁷Fe integral CEMS is approximately 300 nm, and that 66% of the electrons detected in a He/CH₄ counter arise from within 54 nm of natural iron foils (5, 19). The sensitivity of the method is such that about 10 nm of a new surface phase may be detected, and it has been demonstrated that it should be possible to detect a monolayer of ⁵⁷Fe present on a Mössbauer inert substrate (23). Anomalies concerning the measured mean-free path of

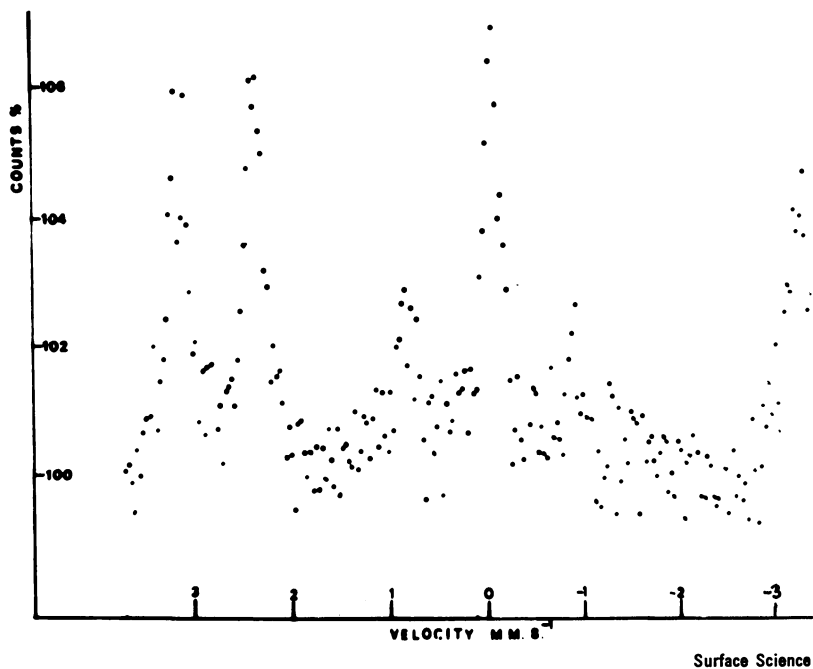


Figure 2. The ^{57}Fe CEM spectrum of an iron foil after brief exposure to HCl (7). The inner four peaks of the spectrum of the iron substrate are seen together with a new doublet arising from the surface species.

the ^{57}Fe conversion and Auger electrons were resolved with the discovery of an unexpected component in CEM spectra (24). It had been noted (1) that the measured probing depths of ^{57}Fe CEMS were larger than expected when compared to calculated values based on previously measured electron mass-absorption coefficients (25). The origin of this "electron tail" is caused by the production of so-called gamma- and x-ray correlated photoelectrons (XPEs and GPEs, respectively), produced in surface regions of the absorbers by the Mössbauer spectrum of gamma- and x-rays backscattered from deep within the sample. For ^{57}Fe , the XPEs and GPEs contribute about 10% to the total flux of backscattered electrons (26). The presence of a similar component in ^{119}Sn CEM spectra recently has been confirmed experimentally (27).

Depth Resolution by DCEMS. It was noted earlier that He/ CH_4 detectors do not permit the energy spectrum of the backscattered electrons to be resolved, and in this sense they can be regarded as integral detectors. However, if the electrons are energy-analyzed and spectra are accumulated with selected electron energies, each of the individual DCEM spectra will be weighted towards a particular depth in the sample, thus providing the possibility of depth profiling the immediate surface

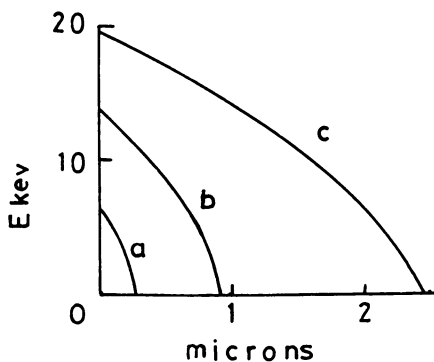


Figure 3. Relation between energy and range of electrons of initial energy ((a) 7.3 keV, (b) 13.6 eV, and (c) 19.6 keV) calculated using the Bethe-Bloch expression (adapted from Ref. 29)

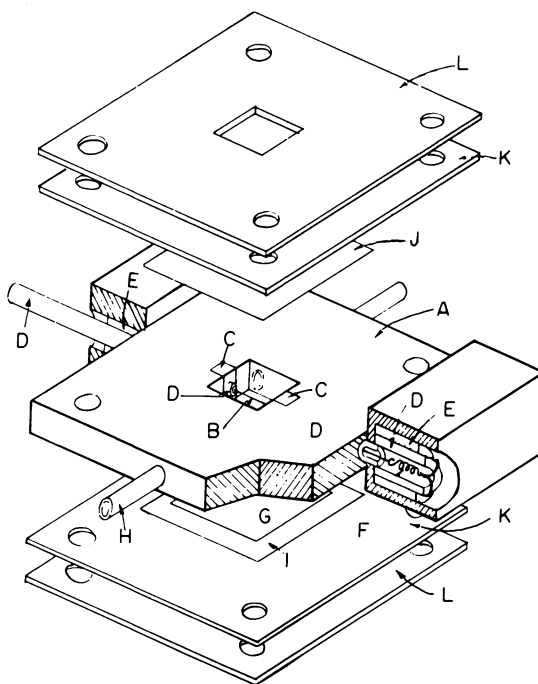
regions. This idea is illustrated in Figure 3 in which the mean energy loss is plotted against range for ^{57}Fe K - and L -conversion electrons and ^{119}Sn L -conversion electrons. It should be noted that such a figure can only be used as a very first approximation in the interpretation of CEM spectra, as no allowance for electron scattering or absorption is made. However, the figure does give an indication of the depths probed in ^{57}Fe and ^{119}Sn work if electrons of a particular energy are detected.

A degree of depth profiling may be achieved either with He/CH_4 detectors (6) or by evaporating inert overlayers onto the sample (28), but more accurate work requires the use of more sophisticated equipment. In a pioneering paper, Bonchev, Jordanov, and Minkova (29) described the design and use of a magnetic iron-free beta-ray spectrometer with intermediate image focusing for use in ^{119}Sn experiments. The spectrometer had an energy resolution of about 5% and a luminosity of about 8%. These workers were able to demonstrate that the ^{119}Sn CEM spectra of a brominated tin metal foil consisted of superpositions of peaks arising from α -Sn, SnO_2 , SnBr_2 , and SnBr_4 . More significantly, the area ratios of the spectral components changed with spectrometer settings (i.e., changing electron energy) in a manner that suggested that the overlayer consisted of SnBr_4 overlaying SnBr_2 . Other groups, notably Bäverstam and co-workers (30–33) at Stockholm, constructed similar spectrometers and demonstrated the feasibility of making depth-resolved measurements with ^{57}Fe . Developments in this area will be described in more detail in later sections.

Advances in Instrumentation

Integral Detectors. The majority of integral CEMS experiments performed to date have been carried out using the ubiquitous He/CH_4

flow proportional counters. Such detectors are simple to construct and a number of designs have appeared in the literature (5, 6, 34–37). The design of a typical detector is illustrated in Figure 4 (36). A particular feature of this detector is the small sensitive volume of $250 \text{ mm}^2 \times 3 \text{ mm}$, thus ensuring that the detector has virtually zero sensitivity for x-ray and gamma-ray photons. In fact, for the case of ^{57}Fe , a 3-mm layer of helium gas at one atmosphere has only a 0.01% efficiency for the 6.3-keV x-rays and less than 0.001% for the 14.4-keV gamma rays. In contrast, the backscattered electrons are detected with virtually 100% efficiency in a 2π -geometry. With such a device, 20% effects are obtainable with unenriched stainless-steel foils. The background largely arises from photo- and Auger electrons ejected from the sample and detector walls by 14.4-keV gamma rays and from the ≈ 100 -keV photo- and Compton electrons produced by the 122-keV gamma rays. Since these latter high-energy electrons deposit little energy in the gas, their contribution to the background may be suppressed by a correct choice of discriminator setting (36).



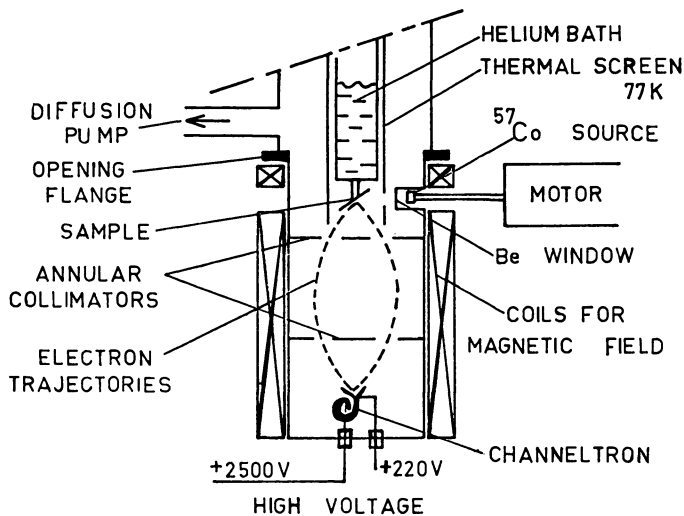
Bulletin of the Institute for Chemical Research

Figure 4. *The He/CH₄ flow proportional counter for CEMS studies (36). (A) Counter frame (Lucite); (B) anode wire (tungsten); (C) Teflon; (D) stainless-steel pipe; (E) Teflon pipe; (F) steel spring; (G) sample foil; (H) gas inlet; (I) aluminum foil; (J) aluminum-evaporated Mylar foil; (K) rubber sheet; (L) brass plate.*

A serious drawback of the simplest He/CH₄ detectors just referred to is that it is not possible to vary the sample temperature and thus explore the Mössbauer parameters of the sample as a function of temperature. Suitably modified He/CH₄ detectors have been described that operate satisfactorily at 80 K (38, 39). At 4.2 K the CH₄ quench gas has to be omitted, and this can lead to undesirable counting characteristics (40). Isozumi (41) recently has described a He/CH₄ detector that operates at temperatures up to 290°C. The detector is of conventional design but the body is of Teflon rather than the more commonly used Lucite. The entire detector is located in a furnace and is filled with He/CH₄ before use. The upper working temperature is limited by the production of spurious signals at 290°C caused by electric discharge at a Teflon pipe surrounding the anode lead. This author also discusses the high-temperature electrical characteristics of other materials in relation to their use in detector construction.

Weyer and others (42, 43) have described a parallel-plate avalanche counter. The construction is similar to a He/CH₄ detector except that the thin wire anodes are replaced by parallel plates between which the gas multiplication takes place. CEM spectra were obtained with ⁵⁷Fe, ¹¹⁹Sn, ¹⁸¹Ta, and ¹⁶¹Dy.

An alternative approach to gas detectors is to use other electron detectors such as channeltrons or open-ended photon-multiplier tubes. If this is done, the sample and detector must necessarily be mounted in a vacuum chamber, but under these conditions no difficulties are encountered in varying the sample temperature. Oswald and Ohring (44) have described a simple apparatus in which the electrons scattered from the sample surface are collected in the cone of a homemade channeltron that is carefully shielded from the incident gamma photons. A 40% effect (on Lines 1 and 6) was obtained using a 5000-Å thick enriched iron foil at a count rate of several hundreds per second with a 5-mCi source. Jones and co-workers (45) have described a similar apparatus based on a commercially available channeltron. This apparatus also included facilities to cool the absorber to 80 K. One disadvantage of arrangements of this type is that because of the small size of the channeltron cone (≈ 1 cm), only electrons scattered into a rather small solid angle are detected. This situation can be improved by focusing the scattered electrons into the cone of the channeltron using a uniform longitudinal magnetic field (46) (Figure 5). For the case of ⁵⁷Fe, the 7.3-keV *K*-conversion electrons are brought to focus in the channeltron cone which is located 245 mm from the absorber in a field of ≈ 60 G. It was further observed that application of a small positive potential, ≈ 200 V, to the channeltron cone increased the useful count rate by 100%. This effect arises from the collection of low-energy secondary electrons

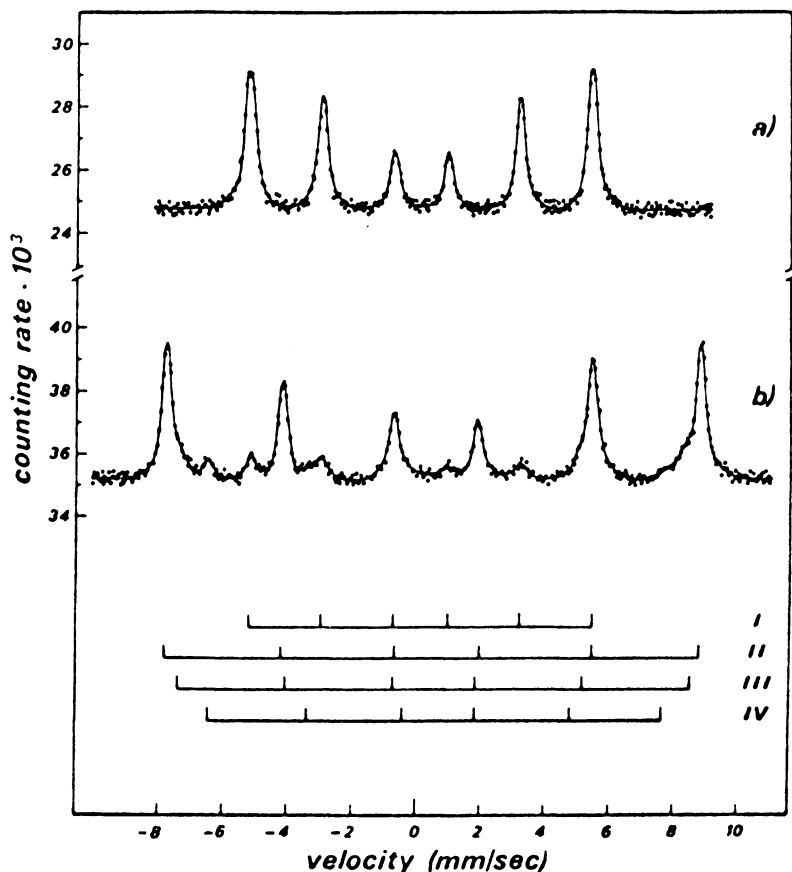


Journal of Physics

Figure 5. Schematic of low-temperature CEMS apparatus using a channeltron detector (46)

from the walls of the detector produced by conversion electrons that miss the detector. Count rates of 20,000 counts/min were obtained with a 100-mCi ^{57}Co source with 10% effects for natural iron foils. An additional and significant feature of the device is that the sample may be cooled to 4.2 K. A similar apparatus has been described by Tiby (47). An extremely versatile device for CEMS work has been described by Carbuccichio (48). The electrons are detected using an EMI 9643/2B open-ended photon-multiplier tube. The device incorporates facilities for electron detection as well as for in-situ treatment of the sample, controlling the sample temperature in the range 80 to 800 K and having an externally mounted detector to count backscattered photons. The capabilities of the apparatus are illustrated in Figure 6, where the CEMS and backscattered x-ray spectra of a lightly oxidized unenriched iron foil are shown. The CEM spectrum reveals the presence of a thin (≈ 100 nm) iron oxide overlayer. The counting times were 5 and 3 days for the CEM and x-ray spectra, respectively, using a 5-mCi ^{57}Co source.

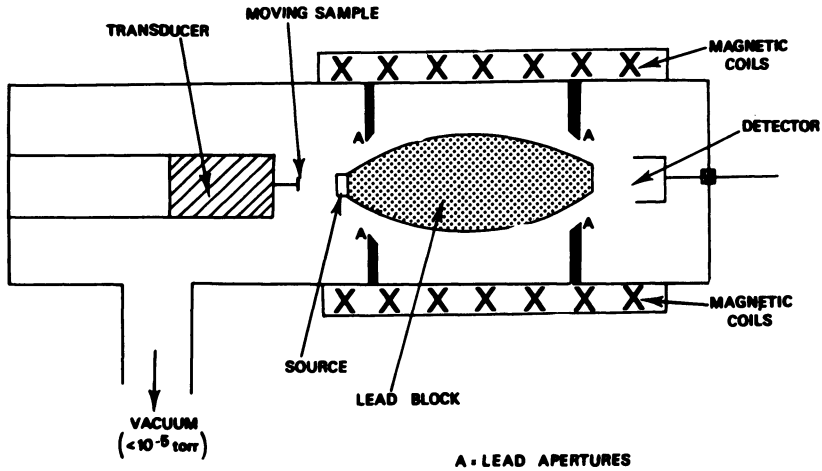
Beta-Ray Spectrometers for DCEMS Studies. To perform depth-selective measurements, a number of groups (30–33, 45, 49–52) have constructed magnetic beta-ray spectrometers similar to that described by Bonchev (29) (referred to earlier). Such spectrometers have energy resolutions of $\approx 5\%$ and transmission of $\approx 8\%$. Because the electron spectrum is now energy-resolved, the count rates are lower than those obtained with integral detectors, and the use of enriched samples is



Nuclear Instruments and Methods

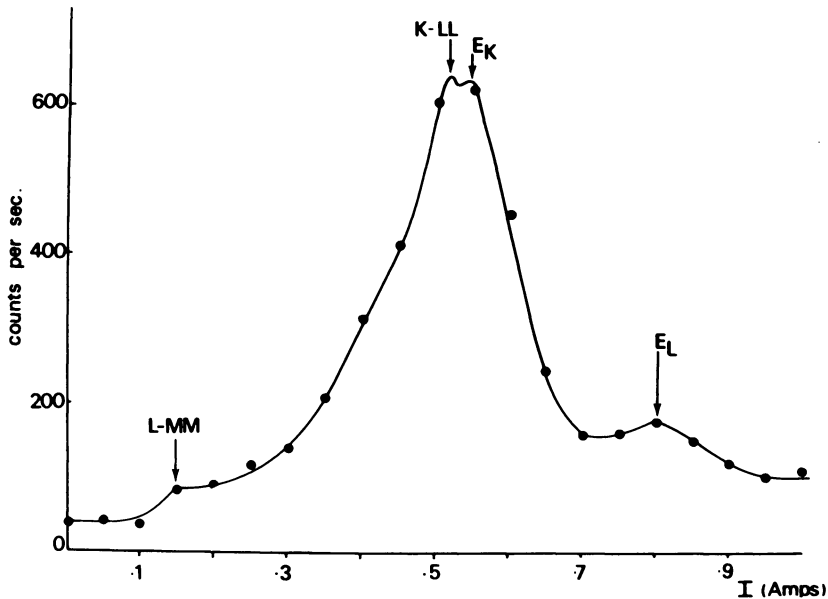
Figure 6. Room-temperature Mössbauer spectra of 6.3-keV x-rays (a) and electrons (b) for a natural iron sample previously heated for 10 min in air at 350°C, obtained using the apparatus of Carbuicchio (48). (I) Sextet due to metallic iron; (II) sextet due to Fe_2O_3 ; (III and IV) sextets due to Fe_3O_4 .

unavoidable if data acquisition times are to be realistic. A typical magnetic beta-ray spectrometer is shown schematically in Figure 7. In the device, the electrons of different energies emitted from the sample surface are brought to focus on the detector by changing the current flowing in the coils. The electron spectrum of an iron foil in the "in resonance" condition is shown in Figure 8 where it can be seen that the 13.6-keV *L*- and *K*-conversion electrons are clearly resolved from one another. CEM spectra of a fluorinated iron foil obtained with spectrometer settings ≈ 7 keV and ≈ 13.6 keV are shown in Figure 9. It can be seen that the doublet arising from the surface phase is relatively more



Applications of Surface Science

Figure 7. Essential features of a magnetic beta-ray spectrometer (45). The radius of the magnetic coils is 10 cm and the sample detector distance is 26 cm.



Applications of Surface Science

Figure 8. Electron energy spectrum obtained from a 90%-enriched ^{57}Fe foil illuminated by a moving ^{57}Co source using a magnetic beta-ray spectrometer (45)

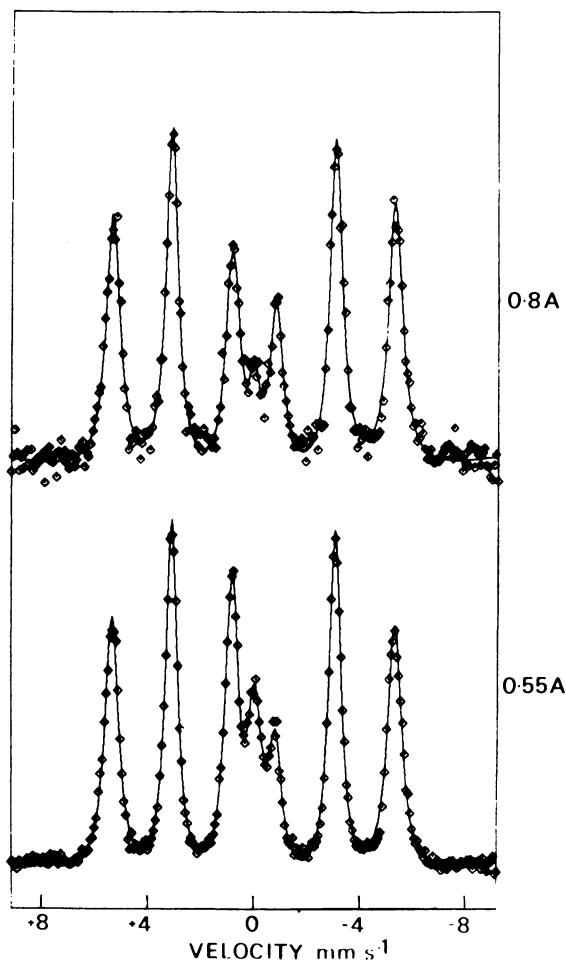


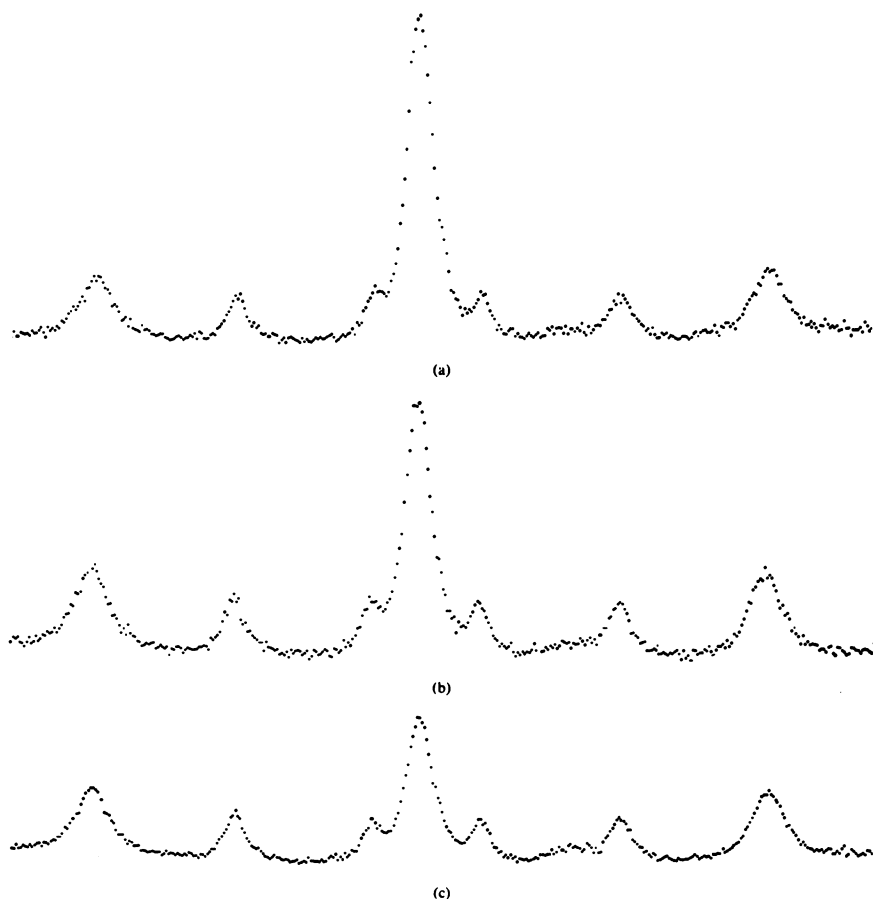
Figure 9. The ^{57}Fe DCEM spectra of a fluorinated iron foil using mainly (a) K-conversion electrons (lower) and (b) L-conversion electrons (upper) (45).

The surface phase is manifest as a doublet with one resolved peak at $\approx 0 \text{ mms}^{-1}$ and another obscured by Line 3 of the iron substrate spectrum. Note the enhanced intensity doublet in the spectrum obtained with the K-conversion electrons compared to the spectrum obtained with the L-conversion electrons.

intense in the K-conversion electron spectrum than in the L-conversion electron spectrum. It is of interest to note that the ratios of the area of the substrate-to-surface signal in the L-conversion electron spectrum is comparable to that obtained using a He/CH₄ detector, thus emphasizing the contribution of the L-conversion electrons, the XPEs, and the GPEs in the latter spectrum. Further degrees of depth resolution may

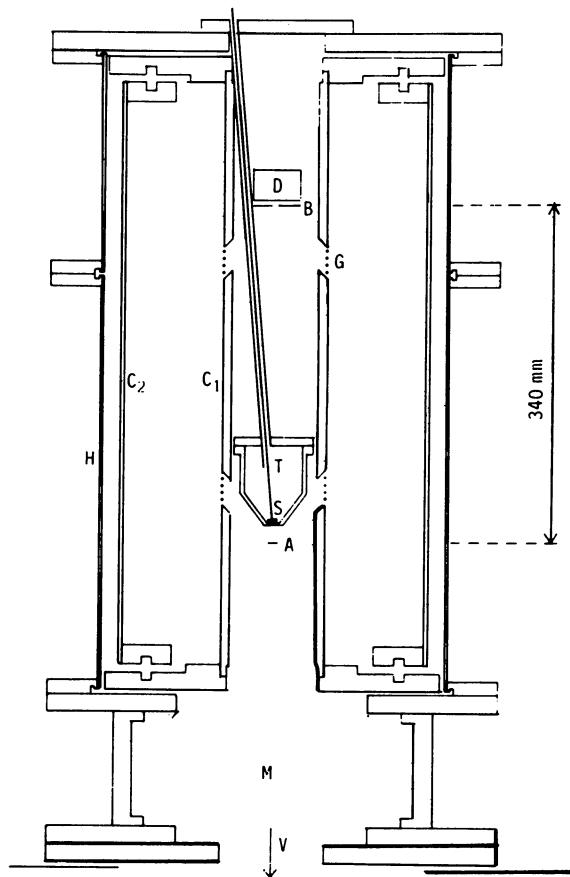
be obtained by recording spectra at spectrometer settings along the K-edge. As an example of this mode of operation, Figure 10 shows the spectra of a stainless-steel foil covered with 36 nm of iron recorded at various spectrometer settings by Bäverstam et al. (32). The change in surface-to-substrate signal is clearly seen to be a function of the spectrometer setting. The detailed analysis of spectra of this type will be described later.

Over the past few years, significant advances have been made in the design and construction of electrostatic beta-ray spectrometers, notably by the Stockholm group. They have described (53) the design and



Nuclear Instruments and Methods

Figure 10. The ^{57}Fe DCEM spectra of a 360-Å thick layer of iron on a stainless-steel substrate obtained at various electron energies along the K-edge (32). Note the relative enhancement of the iron signal relative to the stainless-steel signal as the electron energy is increased (bottom to top).



Nuclear Instruments and Methods

Figure 11. Drawing of the main parts of the electrostatic spectrometer (53): (C_1) inner cylinder (radius = 54 mm); (C_2) outer cylinder (radius = 158 mm); (G) thin grids; (A) absorber (i.e., electron source) (B) detector baffle; (D) detector

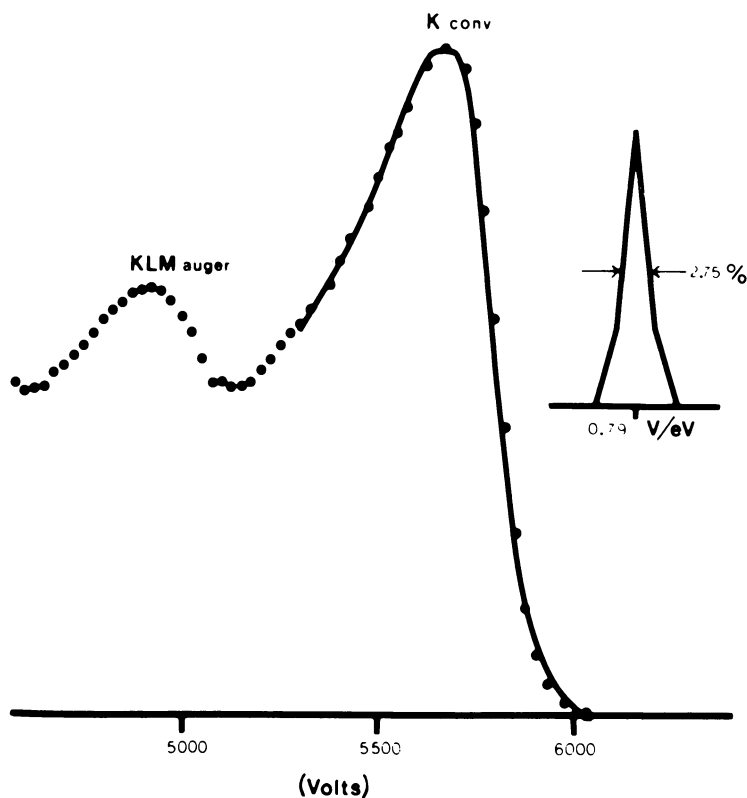
construction of an electrostatic cylindrical mirror spectrometer (Figure 11) operating at a 2.5% energy resolution, a 6% luminosity, and with a 5-mm diameter electron source. The design of the spectrometer was optimized using a computer program, and it is primarily intended for depth-resolution work with ^{57}Fe . The electron spectrum of an iron foil in the "in resonance" condition is shown in Figure 12, where it can be seen that the 5.6-eV Auger peak is clearly resolved from the 7.3-keV K -conversion electron peak. Experiments with this apparatus will be discussed in a later section.

Benczer-Koller and Kolk (54) have built a high transmission spherical electrostatic spectrometer with a transmission of 7% and an energy

resolution of 1.5% at 14.4 keV for a 1-cm diameter source. This spectrometer is primarily intended for the measurement of ^{57}Fe *L*- and *M*-internal conversion coefficients, where good resolution of the *M*- and *L*-conversion electron peaks is necessary. Toriyama and co-workers (55) have described a retarding-field electron spectrometer with an energy range 0–20 keV. Using a hot filament as a source of electrons, the resolution was 0.1% at 1% transmission. However, for conversion electrons the transmission was found to be an order of magnitude worse. The system incorporated a vacuum evaporator for sample preparation.

Advances in Theoretical Aspects and Data Reduction

A major objective in the field of CEMS is the extraction of information from the raw data concerning the way in which the Mössbauer param-



Nuclear Instruments and Methods

Figure 12. Experimental (\cdots) and computer-simulated (—) line profiles from a thin ^{57}Co source with radius = 5 mm, obtained using the spectrometer shown in Figure 11 (53).

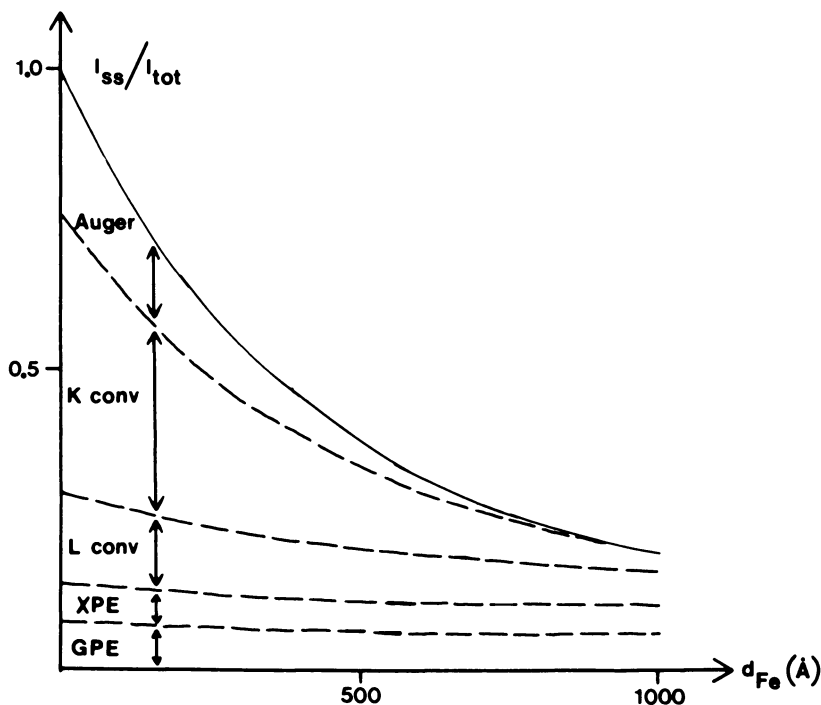
The inserted figure shows the spectrometer profile used for convolution with the simulated K-conversion-electron energy-loss distribution; it is constructed on the basis of the computed spectrometer profile. A source thickness of $47 \mu\text{g}/\text{cm}^2$ (corresponding to 600 Å of iron) was used in the electron scattering simulation.

eters vary as a function of depth. These parameters may then be related to the variations of the properties of the sample with depth and/or the nature and distribution of surface phases. The past few years have witnessed significant advances in this area and these advances have underpinned the essentially pragmatic and empirical approach to data reduction adopted by many workers. This section is again divided into two parts dealing with data obtained with integral detection and energy-resolved studies.

Integral CEMS Studies. Many of the practical problems amenable to study by CEMS involve the characterization of rather discrete overlayers of, for example, a corrosion product, on a thick substrate. It is clearly important to develop methods whereby the thickness of such substrates may be extracted from integral CEMS measurements. Much of the work in this area so far has assumed a simple exponential law for the attenuation of electrons in matter. Bainbridge (56) has extended the early work of Krakowski and Miller (57) and has derived expressions from which the thickness of individual layers within a multiplex film may be extracted from experimental spectra, providing the composition and order of these layers is known. He discusses the case of ^{57}Fe CEMS and only includes the *K*-conversion electrons in his analysis. Huffmann (58, 59) has derived similar expressions to extract quantities of interest from CEM spectra. Both ^{57}Fe and ^{119}Sn CEMS were considered, and the effects of conversion and Auger electrons were included in the theory. To use theories of this type, a knowledge of the appropriate mass absorption coefficients (μ) is necessary. Mass absorption coefficients should theoretically be derivable from first principles, but in practice are more often calculated from empirical laws such as those of Cosslett and Thomas (25). An alternative approach is to derive them from calibration experiments involving CEMS studies of substrates coated with known thicknesses of well-characterized overlayers. Such experiments have been performed by Thomas et al. (19) for the case of ^{57}Fe CEMS by the use of stainless-steel substrates coated with known thicknesses of iron using a He/CH_4 detector. The area ratio of the overlayer to total signal (substrate and overlayer) was measured as a function of overlayer thickness, and a value of $\mu = 1.3 \times 10^4 \text{ cm}^2\text{g}^{-1}$ was derived. This figure is roughly half that expected for the *K*-conversion electrons calculated from the formula of Cosslett and Thomas (25). Using this value, a curve relating the oxide overlayer thickness on an iron substrate to the spectral area ratios can be calculated provided that μ is insensitive to change in atomic number (19, 60). Graham, Mitchell, and Channing (61) have performed similar ^{57}Fe CEMS calibration experiments by growing magnetite films in the range 265–4250 Å on natural iron substrates. The oxide thicknesses were monitored during growth by measuring the oxygen

uptake of the foils and calculated by assuming smooth surfaces. The percentage (P) of the total CEM spectrum area contributed by the oxide was determined as a function of thickness (d) and found to follow a law of the form $d(\text{Å}) = -1.95 \times 10^3 \ln(1 - 0.01P)$. The experimental data were compared with the predictions of Huffmann (58, 59) and Bainbridge (56). Calculations of P based on μ -values calculated from the expression of Cosslett and Thomas (19) and the Huffmann treatment (58, 59) yielded values of P 30 to 40% higher than the experimental data. Better fits to the data were obtained with values of μ equal to $1.10 \times 10^4 \text{ cm}^2\text{g}^{-1}$ and $1.73 \times 10^4 \text{ cm}^2\text{g}^{-1}$ for the 7.3-keV and 5.4-keV electron, respectively. Huffmann and Podgurski (62) have performed similar experiments but invoked changes in surface roughness to explain the nonlinearity of plots of overlayer thickness derived from the CEMS data vs. the oxygen uptake measurements.

Subsequent to these studies, a comprehensive study of the intensity and energy distribution of initially monochromatic electrons emanating from an absorber surface was made using Monte Carlo methods by Liljequist et al. (26). The total transmission as well as the transmission into various angular and energy intervals of electrons from different depths in a ^{57}Fe absorber were calculated. The K -, L -, Auger, GPE, and XPE electrons were all included in the calculations. The scattering and energy loss of the electrons were computed for iron, Fe_2O_3 , and aluminum. It was found that the difference in the results was negligible and that the depth may be measured as mass/unit area. The results of their calculations were compared with the experimentally measured area ratios of the stainless-steel iron sandwich described earlier. The results are illustrated in Figures 13 and 14, where it can be seen that an excellent fit to the data was obtained. These figures emphasize the need to account for all the electrons contributing to the signal in any theory designed to extract information from integral ^{57}Fe CEMS data. In addition, these figures show that the use of any theory that neglects the contributions from L -conversion, GPE, and XPE electrons to the total flux, when combined with the μ values of Cosslett and Thomas (25) will lead to poor estimations of overlayer thickness, regardless of either the correctness of the μ -values or the appropriateness of the exponential law. The apparent discrepancies between the μ -values derived from the calibration experiments just described arise from the fact that the value measured by Thomas et al. (19) is simply an effective value for all electrons detected, whereas the values derived by Graham et al. (61) are effective values arising from the expressions used. However, there is a real discrepancy between the oxide thicknesses derived by the method of Thomas et al. (25) and those derived by Graham et al. (61). The origin of this discrepancy is not understood and warrants further investigation.



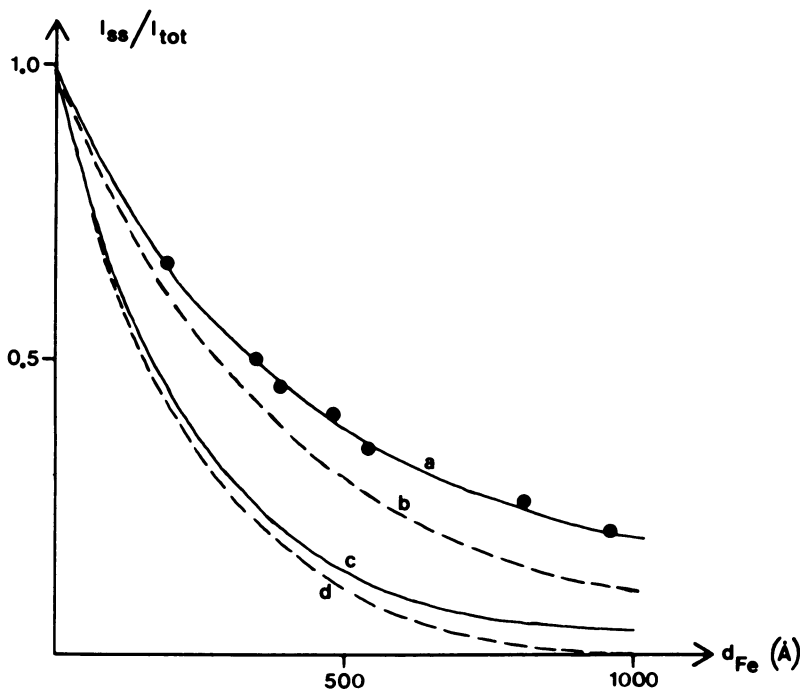
Nuclear Instruments and Methods

Figure 13. Relative contribution from various electrons in the integral CEM spectrum of an iron overlayer on a stainless-steel substrate as a function of overlayer thickness (d_{Fe} is the thickness of the iron overlayer) (26).

In relationship to Figure 13, it is of interest to note the enhanced depth selectivity gained by detecting the *K*-conversion electrons alone rather than with the integrated signals, as mentioned earlier in connection with the spectra of fluorinated iron foils.

The size of the resonant Mössbauer effects on β -Sn, CaSnO_3 , and SnO_2 have been measured using ^{119}Sn CEMS and compared with theoretical values (27). The measured percentage effects were 46%, 520%, and 510% for β -Sn, SnO_2 , and CaSnO_3 , respectively. Good agreement was obtained between experiment and theory, if the effects of nonisotropic scattering of photoelectrons are included in the theory. The anomalously large percentage effect of 950% for SnO_2 measured by Yagnik et al. (63) was shown to arise from an inadequate curve-fitting procedure caused by neglect of quadrupole line broadening of the resonance.

Depth-Resolved CEMS Studies. As pointed out earlier, the area ratios of the components of CEM spectra of inhomogeneous absorbers recorded at different spectrometer settings will vary and contain informa-



Nuclear Instruments and Methods

Figure 14. Relative stainless-steel signal in an iron-on-steel CEMS (integral) measurement (26).

Dots show experimental results from Thomas *et al.* Full curve (a) shows the result predicted by the present theory. Dashed curve (b) shows the predicted result if the XPE and GPE electrons are neglected. Full curve (c) shows the predicted result if the APK interval is selected in the detector (all angles). Dashed curve (d) shows the same result if the GPE and L-conversion electrons are neglected. d_r is the thickness of the iron layer.

tion relating to the depth distribution of the Mössbauer parameters. Bäverstam *et al.* (32) have shown that the number of counts recorded in the n th channel in a Mössbauer spectrum by means of scattered electrons at a spectrometer setting corresponding to an energy E may be written as

$$T(E)_n = \int_0^{\infty} w(E,x)P(x)_n dx$$

where $w(E,x)$ is a (weight) function giving the probability of an electron originating at depth x to be detected if the spectrometer setting is E . $P(x)_n$ is the emission probability for electrons at depth x when the gamma source velocity corresponds to the n th channel. The function $w(E,x)$ not only describes the intensity and energy distribution of electrons emanating from the surface, but also contains information relating to the response of the detection device. Using a magnetic

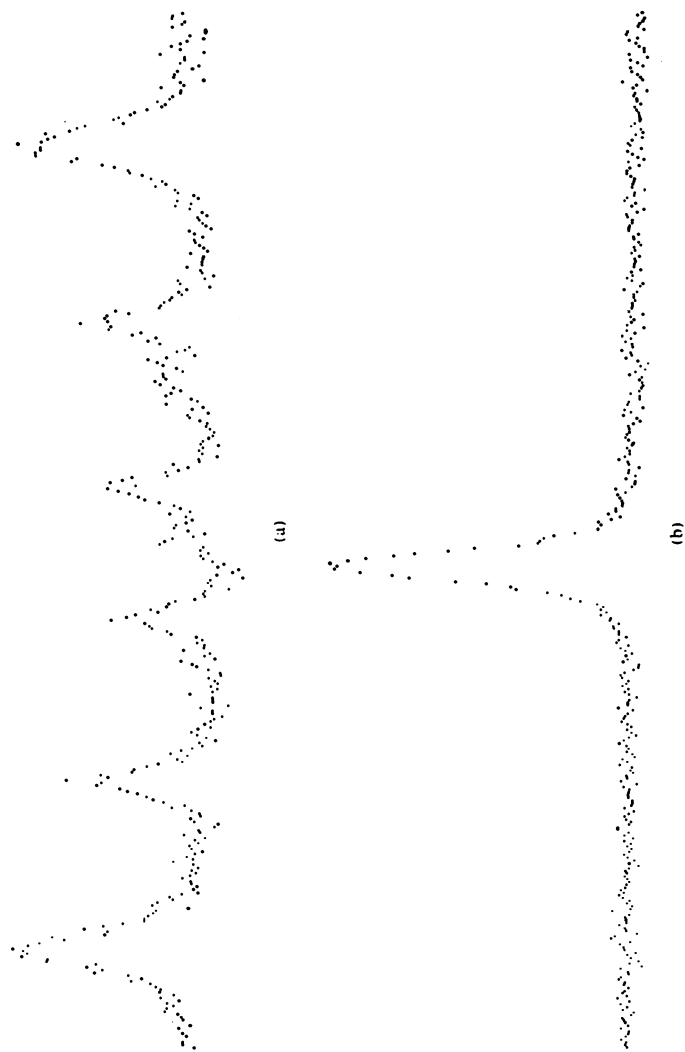
beta-ray spectrometer, Bäverstam et al. (33) carried out a series of experiments involving the scattering of electrons with energies close to 7.3 keV through thin iron films, in order to determine the function $w(E,x)$. Given $w(E,x)$, $P(x)_n$ can now, in principle, be extracted from a series of CEM spectra accumulated at different spectrometer settings E_j as

$$T(E_j)_n = \sum_{i=1}^I \left[\int_{l_i}^{l_{i+1}} w(E_j,x) dx \right] P_{in} \quad j = 1, 2, 3, \dots$$

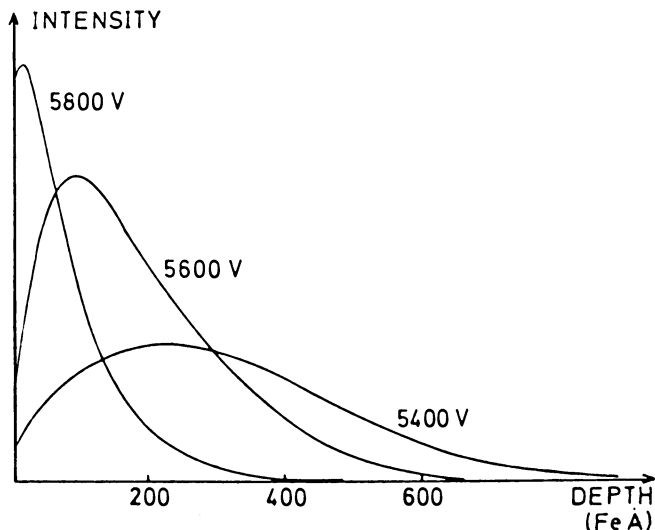
where P_{in} is unknown, j the number of spectra recorded, I the number of layers separated, and l_i the limits of these layers. A practical example of this technique is shown in Figure 15. Here the separate signals arising from the substrate and overlayer have been extracted from the series of spectra shown in Figure 10. The depth resolution of the method was estimated to be about 50 Å for their magnetic beta-ray spectrometer which had a 5% energy resolution.

More recently these workers (26) have calculated weight functions (Figure 16) using the Monte Carlo-type calculations described previously, in the energy interval 6.3–7.3 keV corresponding to almost pure K -conversion electrons. The solid line in Figure 13 is in fact computed on the basis of these functions convoluted with a suitable spectrometer line shape. The interpretation and practical analysis of depth-selective CEM spectra also have been discussed using a simplified theory (64). Expedient analysis in terms of absorber structure has demonstrated that DCEMS reveals more fundamental information than integral CEMS.

Bonchev and co-workers (64) have developed an empirical approach to the interpretation of ^{119}Sn data. The method was based on the experimental determination of the change in energy distribution of L -conversion electrons emitted from a source that was progressively covered with thin absorbing layers of copper in the range 0.02–0.25 mg cm⁻². Using these data the distribution of ^{119}Sn in unknown samples may be determined either by suitably constructed nomograms or by solving a series of linear equations with experimentally determined coefficients. In a later extension of this work, Bonchev and co-workers (66, 67) investigated the influence of atomic number, crystal structure, and applied electric field on the distribution of ^{119}Sn conversion electrons after passage through suitable layers. It was demonstrated that electron energy distribution was dependent on atomic number by performing experiments with overlayers of beryllium, copper, silver, and gold. Furthermore, it was noted (66, 67) that the results could not be explained in terms of present theories of the interactions of low-energy electrons with matter.



Nuclear Instruments and Methods
Figure 15. The "depth-selected" spectra corresponding to the layer (a) 0–375 Å and (b) from 350 Å and inward in the absorber extracted from the spectra shown in Figure 10 (32)



Journal of Vacuum Science and Technology

Figure 16. "Weight functions" corresponding to the settings, 5400, 5600, and 5800 V in the Stockholm group's electron spectrometer (104). These functions give the relative probabilities to detect electrons of initial energy 7.3 keV, ejected at different depths in iron and at different electron spectrometer settings.

Applications of ^{57}Fe CEMS

The potential of ^{57}Fe CEMS applications to the solution of real problems connected with the properties of surfaces has been realized over the past few years. The ability of the technique to probe the surface regions of low-area solids in situ and in a nondestructive manner has made the method particularly suitable for the examination of technical problems such as those encountered in metallurgical studies (68, 69). The majority of applications to date have used integral CEMS techniques, often combined with the x-ray scattering Mössbauer method, thus allowing the outer few microns of the surface to be probed and the distribution of the surface phases determined. Various applications of the techniques are now described in more detail.

Aqueous Oxidation Corrosion of Iron and Steels. Early work fully established the potential of CEMS as a powerful technique for the study of the initial stages of the corrosion of iron and steels. Simmons and co-workers (18) have studied the oxidation of enriched iron foils at 225°C, 350°C, and 450°C, and fully demonstrated the ability of the technique to identify new surface phases such as Fe_3O_4 and Fe_2O_3 formed at surfaces in the thickness range of five to several tens of

nanometers. Similar studies (19, 20) have been performed with natural iron substrates, and Fe_3O_4 , α - Fe_2O_3 , and wustite were all identified as oxidation products.

In addition to this phase identification aspect of CEMS, the data reduction methods described earlier have been used to derive kinetic parameters for oxidation processes from a knowledge of total oxide thicknesses derived from spectral area measurements (18, 20, 60). Information concerning the depth distribution (zoning) of oxide layers also can be gained. In cases where the oxide thickness is the order of the probing depth of CEMS, this may be done by either making use of the limited energy resolution of He/CH₄ detectors (6) or by the use of a beta-ray spectrometer (50, 52, 70). For thicker layers information may be drawn from a combination of CEMS and backscattered x-ray Mössbauer spectra. An interesting example of this latter approach is shown in Figure 17, which relates to a study (71) of the oxidation of a 9% chrome-steel in CO₂. Spectrum a is the integral CEM spectrum of the original steel. Here there are at least five different internal hyperfine fields at the iron sites arising from differing numbers of iron-chromium neighbors in the disordered alloys. Spectra b and c are CEM spectra of the corrosion product. This product consists of an outerlayer of magnetite and an inner layer of an iron-chromium spinel of composition $\text{Fe}_{1+x}\text{Cr}_{2-x}\text{O}_4$ ($1.4 < x < 1.8$). During the oxidation, iron diffuses out to the oxide/gas interface to give Fe_3O_4 and chromium remains behind to give the mixed spinel. Beneath the lower oxide layer is a region that is chromium depleted. This is clearly revealed in the backscattered x-ray spectrum d where the outmost 20 μm or so of the sample are probed. This spectrum is considerably sharper than that of the original steel, indicating a reduction in the variety of iron environments caused by the chromium depletion. The feasibility of depth-probing the outer 100 nm of oxide or oxyhydroxide overlayers on iron by DCEMS at a resolution on the order of 5 nm also has been demonstrated (50, 52, 70).

In the area of aqueous corrosion, Gütlich and co-workers (72) have studied the formation of protective oxide coatings on steam generator tubes in the presence of water at high temperatures and pressures. Magnetite was the only oxide phase detected at the surface of a martensitic iron-chromium steel and on an austenitic iron-chromium-nickel steel, whereas an iron-nickel ferrite was formed on an Incoloy 800 steel after treatment. The time dependence of the oxide growth was monitored and oxide thicknesses were derived using the method of Thomas et al. (19). An analysis of these data revealed that the oxidation process is most probably controlled by short-circuit diffusion. In a later paper (73) these workers extended this research to study the influence of the presence of P_2O_5 and SiO_2 in the water upon corrosion. Tiby (47) recently has made an

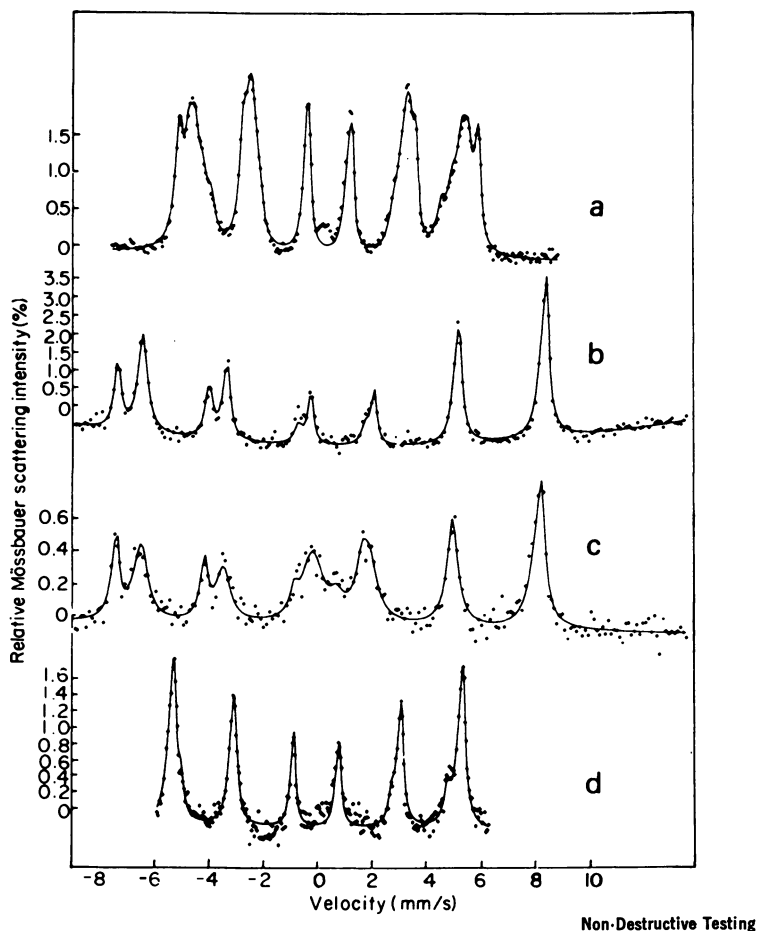


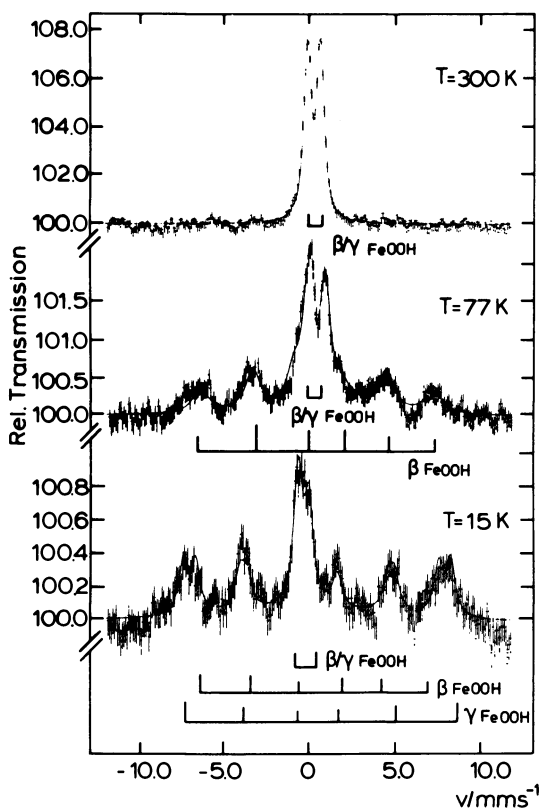
Figure 17. Mössbauer scattering spectra of 9% chromium-steel after oxidation in CO_2 (68): (a) original steel (CEM); (b) outer oxide layer (CEM); (c) inner oxide layer (CEM); (d) first 20 μm below inner oxide layer using the scattered x-rays

application of integral CEMS to the study of corrosion products formed during the aqueous corrosion of iron, at various pH and in the presence of dissolved salts, using the variable temperature device described in a previous section. The aqueous corrosion of iron may lead to a variety of products that include $\beta\text{-FeOOH}$, $\gamma\text{-FeOOH}$, $\alpha\text{-FeOOH}$, $\gamma\text{-Fe}_2\text{O}_3$, $\alpha\text{-Fe}_2\text{O}_3$, and Fe_3O_4 . If only room-temperature CEM spectra are recorded, difficulties may be encountered in the assignment of spectra that contain only quadrupole doublets, since these may arise from either β - or $\gamma\text{-FeOOH}$ or even superparamagnetic particles of either $\alpha\text{-FeOOH}$, $\gamma\text{-Fe}_2\text{O}_3$, $\alpha\text{-Fe}_2\text{O}_3$, or Fe_3O_4 . However, by making a variable temperature

study the occurrence of superparamagnetic behavior or the onset of magnetic ordering may be detected, thus providing a further insight into the nature and composition of the corrosion product. As an example of this approach, Figure 18 shows the variable temperature spectra of an iron foil corroded in concentrated HCl at 21°C for 60 h. It can be seen that both β - and γ -FeOOH are formed under these conditions.

Surface Treatments of Steels. Many surface treatments of steels involve chemical modification of the outermost surface regions of the steel in order to provide, for example, a hard wear-resistant surface or to afford protection against corrosion.

The phosphating of iron surfaces to provide corrosion protection has been examined by ^{57}Fe CEMS (74,75). Iron samples were treated with various phosphating solutions, and CEMS was used to establish the formation of iron(II) phosphate octahydrate at the iron surface. It was



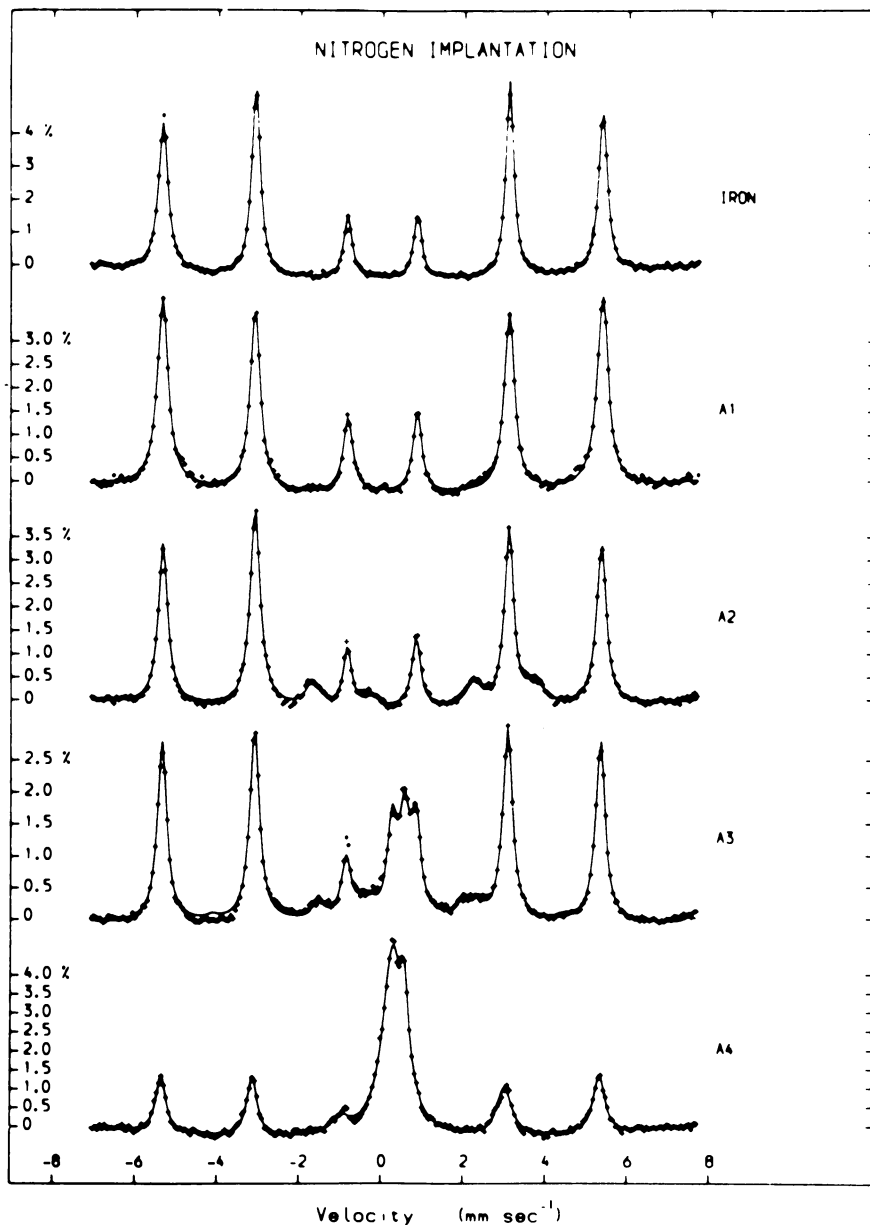
C. Tiby (PhD Thesis)

Figure 18. Temperature dependence of the ^{57}Fe CEM spectra of an iron foil after exposure to concentrated HCl for 60 h (47)

observed that heating in air dehydrates the surface phase without oxidizing iron(II) ions, whereas the bulk of the iron(II) phosphate octahydrate samples was readily oxidized to an iron(III) species as evidenced by transmission techniques. (This observation parallels a similar one made concerning the stability of the surface regions of the mineral vivianite, which is discussed in a later section). It was further observed that phosphating processes that produce heavier surface coatings lead to the inclusion of hydrolyzed iron(III) species in the iron(II) phosphate surface phase.

Ujihara and co-workers (76, 77) have used integral CEMS techniques to characterize the surface regions of nitrated steels. Polished surfaces of a carbon steel (0.56 at. % carbon) were nitrated by (a) heating the steel in a flow of ammonia for 30 h at 793 K; (b) dipping the steel in fused salt baths containing potassium cyanide and potassium cyanate for 7 h (tufftriding); and (c) placing the steel in flowing nitrogen and hydrogen subject to a glow discharge for 4 h at 793 K; under these conditions N^+ ions were formed. The chemical state of the outer few tens of microns of the surface was profiled by mechanical grinding of the surface using a fine SiC abrasive grit. It was found that a gas-nitrated steel surface is composed of an outer layer of $\epsilon\text{-Fe}_2\text{N}$ ($\approx 10\text{-}\mu\text{m}$ thick) followed by distorted Fe_{3+x}N , ($0 < x < 1$), $\gamma\text{'-Fe}_4\text{N}$, martensite, and then an α -iron layer slightly distorted by intruded nitrogen. Tufftrided steel surfaces consisted of $\epsilon\text{-Fe}_2\text{N}$, intermediate $\epsilon\text{-Fe}_3\text{N}$ and $\gamma\text{'-Fe}_4\text{N}$, $\gamma\text{'-Fe}_4\text{N}$, and a distorted α -iron layer. Ion-nitrated steel surfaces have an outermost layer of $\gamma_1\text{'-Fe}_4\text{N}$ ($2\text{-}3\ \mu\text{m}$ thick) then $\gamma_2\text{'-Fe}_4\text{N}$ overlying a distorted α -iron layer.

Longworth and Hartley (78) have made a ^{57}Fe CEMS study of nitrogen-implanted iron foils in relationship to their wear resistance. Pure-iron $125\text{-}\mu\text{m}$ foils were implanted with 100-keV N_2^+ molecular ions at doses of 1, 2, 3, and 6×10^{17} ions cm^{-2} . Clear evidence for the formation of iron nitrides was observed, as shown in Figure 19. In this figure the top spectrum is of the pure-iron foil whereas Spectra A1–A4 correspond to increasing doses of nitrogen implantation. The spectrum of Sample A2 contains an additional six-line component ($H_{\text{int}} \approx 220$ kOe), clearly seen in Sample A3, attributed to the presence of $\gamma\text{'-Fe}_4\text{N}$. The spectra of Samples A3 and A4 contain a quadruple doublet attributed to the formation of Fe_2N . There was no evidence for the formation of $\gamma\text{'-Fe}_4\text{N}$ in Sample A4. The formation of nitrides was linked to the maximum reduction in wear rate that occurs at these doses. The effects of annealing on the stability of the surface nitrides was examined also. In a related study (79), high-carbon martensite steel was implanted with N^+ ions. It was observed that the pre-existence of interstitial carbon atoms affects the sequence of formation of surface compounds attributable to



Thin Solid Films

Figure 19. The ^{57}Fe CEM spectra at room temperature of iron foil and iron foil implanted with doses of 1×10^{17} (Curve A1), 2×10^{17} (Curve A2), 4×10^{17} (Curve A3), and 6×10^{17} (Curve A4) nitrogen ions cm^{-2} . The full curves represent least-squares fits to the data points, and the zero on the velocity scale refers to the isomer shift of α -iron (78).

nitrogen implantation. In addition, some structural modifications of martensite were found at higher doses, and the formation of $\epsilon\text{-Fe}_{2+x}(\text{C},\text{N})$ was observed. Other workers (80) have described ^{57}Fe CEMS studies of the hardening of steels by various carburization processes. Evidence for carbide formation in the outermost surface regions was found.

Metallurgical Applications. An area of particular technological importance that has proved to be amenable to study by CEMS is the characterization of steel surfaces. Early work established that austenitic phases in steel surfaces could readily be distinguished from either ferritic or martensitic phases, and these studies have led to the more applied metallurgical applications described here. Swartzendruber (81) has carried out studies of the ferrite content of essentially austenitic steels (containing 15–20% chromium and $\approx 10\%$ nickel) in stainless-steel welds and castings. This group also discovered by the use of CEMS that appreciable amounts of austenite may be formed at the surface of carbon steels after light cutting, even in the presence of copious quantities of cutting oil (8). This work was later extended in a study (82) of the influence of cobalt on surface austenite formation. It was discovered that as cobalt raises the martensitic transformation temperature, the amount of surface austenite found decreased with increasing cobalt concentration. Iron-57 CEMS also has been used to explore the changes in lubricated (83) steel surfaces induced during sliding fatigue wear. Scoring was associated with the formation of a surface carbide arising from the breakdown of the oil-based lubricant, whereas scuffing was related to the formation of a deformed mixture of austenite and martensite with some evidence for the breakdown of the lubricant.

The effects of cold work on steel surfaces also has been examined (68). It has been demonstrated that an austenitic 18% chromium, 8% nickel steel will undergo a surface martensitic transformation when subjected to cold work. By using a combination of electron and x-ray backscattering techniques it was observed that the amount of martensite formed increased with increasing cold work and that the transformation was most pronounced in the outermost surface regions. Interestingly, when a sample was chemically thinned the new surface martensite concentration remained high. A similar effect has been observed in a 1095 stainless-steel which had been austenized at 930°C and oil quenched (84). Again it was demonstrated that exposure of a fresh surface by electropolishing led to further transformation of austenite to martensite in the surface. This study clearly demonstrates the important influence of surface energy on the transformation.

The effect of shot-blasting and shot-peening on steel surfaces also has been examined by CEMS (68).

The decarburization of iron foils in hydrogen atmospheres has been examined (85). The films were prepared by evaporation techniques and contained up to 8% carbon. The carbon was incorporated into the film during growth by interaction of the active growing surface with residual gas in the vacuum chamber. The decarburization process was studied in an apparatus that allowed the specimen to be passed from the decarburization area to the CH₄/He detector without exposure to the atmosphere. It was discovered that at 290°C decarburization was relatively fast in hydrogen since the carbon was contained in the form of iron ϵ -carbide. At temperatures greater than 300°C χ - and/or θ -carbides precipitated and caused a drastic reduction in the rate of decarburization. At 500°C the decarburization process was found to be essentially constant after a sharp decrease from the initially high carbon content. This sharp decrease was related to the segregation of carbon to the surface. The interplay of the decarburization reaction and the precipitation of iron carbides has been discussed elsewhere (85).

Measurement of Surface Stress. In principle it is possible to measure surface stress levels by examining the small pressure-induced changes in the Mössbauer parameters, but unfortunately these shifts are small. For example, a hydrostatic stress of 700 MN/m² will shift the centers of an iron spectrum by $\approx 6 \mu\text{m/s}$ (68). To measure such small shifts Yagnik and co-workers (86) have described a device in which the resonance is scanned by making use of the second-order Doppler shift brought about by changes in the source temperature. Such measurements have been used to determine isomer shift changes and hence surface stresses. For the case of ferrite, changes in the other hyperfine parameters will also contribute to the shift in the resonance line (87). In fact, these changes have been demonstrated experimentally by Mercader and Cranshaw (87), who measured the CEM spectra of an iron bar held both in tension and compression. The technique needs further development, but it is felt that surface stress eventually should be measured to within 35 MN/m² by CEMS, an accuracy comparable to existing x-ray diffraction techniques (68).

Ion-Implantation Studies. Iron-57 CEMS has proved to be a particularly valuable technique in the study of ion-implanted surfaces since the depth of implantation is usually on the order of a few tens to a few hundreds of nanometers—depths that are comparable to the probing depth of the ⁵⁷Fe CEMS. The experiments involve either the study of the environment of ⁵⁷Fe implanted into host matrices or the effect of foreign implants on iron-containing hosts as described earlier. In the field of ion-implantation studies, much of the early work was carried out by Sawicki and Sawicka (9–15, 88), who made wide-ranging studies of

the systematics of the Mössbauer parameters of iron implanted into a variety of host matrices. One system that has received particular attention is ^{57}Fe -implanted aluminum. Sawicki and co-workers (13) first observed that the CEM spectra of foils implanted with ^{57}Fe at room temperature consisted of a superposition of a doublet and a singlet. The ratio of these two sub-spectra varied as a function of doses, with the doublet increasing in intensity at the expense of the singlet at high doses. The doublet and singlet were assigned to the presence of iron dimers and monomers with the aluminum. More recently, other workers (89) have studied, in situ, the CEM spectra of aluminum foils implanted at 80 and 300 K. Similar spectra to those of Sawicki were observed for room-temperature implanted foils, but these workers assigned the doublet to an ordered Al_6Fe phase. Implantation at 80 K resulted in spectra similar to those of the 300-K implanted samples, but aging studies below 373 Å suggested that the doublet consisted of a superposition of several components. The gradual changes caused by low-temperature annealing were associated with the ordering of iron atoms, enhanced by the presence of supersaturated vacancies arising from collision-induced defects. A DCEMS study of ^{57}Fe aluminum foils implanted at high doses of 10^{17} ions cm^{-2} has been made (90). It was established that the quadrupole splitting of the doublet increased as the surface was approached, whereas the isomer shift remained constant. This behavior was thought to arise from either the enhanced electric field gradient near the surface attributable to the surface discontinuity itself, or by an increase in radiation damage in the surface regions.

Detailed studies (91–94) have been made of copper, silver, and gold alloys of iron produced by ion implantation as a function of dose and subsequent annealing temperature. The iron–copper alloys were produced by ^{57}Fe implantation at doses between 1×10^{15} and 5×10^{16} ions cm^{-2} (91). Effects attributable to defects on the hyperfine parameters of iron clusters were observed. At high dose rates the significantly different observed spectra were associated with both the effects of sputtering and with the presence of widespread damaged regions. In a related paper (92) it was demonstrated that the onset of diffusion of the iron implants during annealing experiments was related to the iron concentration and the nature of defects produced during implantation. For high dose rates (5×10^{16} ions cm^{-2}), an additional stage associated with the release of vacancies trapped at iron atoms was discovered. Similar studies (93) have been carried out for silver implanted with iron. An appreciable concentration of the iron implants resided at substitutional sites. Superparamagnetic α -iron precipitates were observed also. An analogous situation pertains to iron-implanted gold foils (94), although in this case

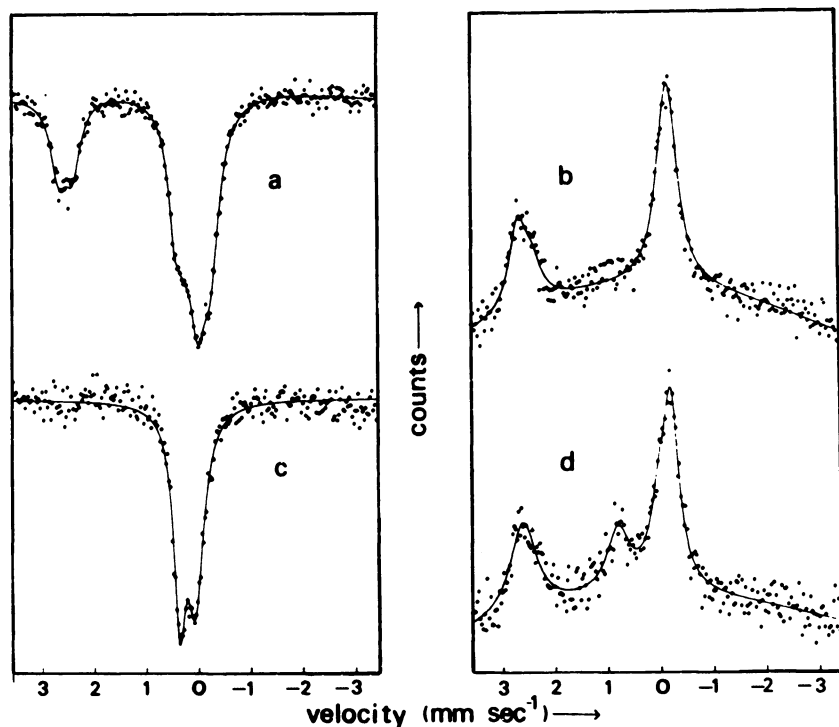
the degree of clustering of iron atoms was much less than in copper-iron or silver-iron alloys. This is understandable since the equilibrium solubilities of iron in copper and silver are much smaller than in gold.

Thin Films. In a comparison of transmission and CEMS techniques in the study of thin films, Oswald and Ohring (44) demonstrated that larger signal-to-background ratios are to be expected by the use of CEMS, thus allowing a significant decrease in counting times. These workers studied thin films of FeSi_2 and showed that the quadrupole splitting of the observed doublet increased with decreasing film thickness. Other studies (97) have been made of the annealing, thin, amorphous iron-silicon films prepared by vacuum evaporation techniques (95). Massenet and Davar (46, 96) have studied thin films of amorphous iron-germanium down to 4.2 K using the apparatus described in a previous section. Films of compositions of $\text{Fe}_x\text{Ge}_{1-x}$ ($x = 0.08$ to 0.53) were studied, and for $x > 0.4$, the films were found to be ferromagnetically ordered.

Inorganic Solids and Minerals and Archaeological Artifacts. Minikova and Schunck (49) demonstrated in a DCEMS study that the quadrupole splitting of $\gamma\text{-FeOOH}$ increases with decreasing film thickness. The quadrupole splittings were found to vary from $0.94 \pm 0.02 \text{ mm s}^{-1}$ for 10-Å films to $0.73 \pm 0.01 \text{ mm s}^{-1}$ for 50-Å films, values that are to be compared with the bulk value of $0.553 \pm 0.001 \text{ mm s}^{-1}$. Tominaga and Sato (97) recorded CEM and transmission spectra of photoirradiated potassium trisoxalatoferate(III). The CEM spectrum demonstrated that virtually complete photolytic reduction of the surface regions occurred after exposure of the compound to a 500-W superhigh-pressure mercury lamp (spectral range 300–600 nm) for 10 s, whereas the bulk material was only 20% converted. Similar differences between surface and bulk reactivity have been observed in studies of iron-phosphate glasses (98). The $\text{Fe}^{2+}/\text{Fe}^{3+}$ ratio of these glasses was found to be strongly reduced in surface regions compared to the bulk value after heat treatment in air. This process was partly reversed after heat treatment in vacuo. Iron-57 CEMS also has been used in a study of ion implantation phenomena in yttrium-iron garnets in relationship to hard-bubble suppression (99).

In the area of geochemistry, Forester (21) has used ^{57}Fe CEMS to characterize the surface regions of lunar materials, and has established the existence of fine superparamagnetic iron particles in these areas. The changes that occur in the surface region of biotites subjected to thermal treatment also have been monitored by ^{57}Fe CEMS (22). During the early stages of heat-treatment, changes in the CEM spectra were observed, whereas the transmission spectra of the bulk of the material remained unchanged. The spectra were discussed in terms of the mechanism of oxidation of biotites. The thermal decomposition of a naturally occurring

iron(II) phosphate octahydrate (vivianite) also has been studied by a combination of ^{57}Fe CEMS and transmission techniques (100). Freshly mined vivianite is colorless but rapidly attains a pale blue coloration after exposure to air. The blue coloration has been attributed to an intervalence charge transfer band caused by the partial oxidation of Fe^{2+} ions to Fe^{3+} ions. Thermal treatment at 120°C revealed that the surface regions of single crystals of vivianite are remarkably stable to oxidation, whereas the bulk of the mineral was rapidly converted to a Fe^{3+} -containing species (Figure 20). These results parallel the observations of Berry and Maddock (74, 75) on the phosphating of iron surfaces described earlier. The stability of the surface towards oxidation of $\text{Fe}_3(\text{PO}_4)_2 \cdot 8 \text{H}_2\text{O}$ is an intrinsic property of the compound. It is possible that the dehydration rate of the surface regions is faster than the oxidation rate, and that as a consequence, a layer of a lower hydrate is formed at the surface. In this



Journal of Inorganic and Nuclear Chemistry

Figure 20. (a) Transmission and (b) CEM spectra of a vivianite single crystal before heating (100). The spectrum after heating for 1 h at 120°C indicates conversion of the bulk ((c) is the transmission spectrum) to a mainly ferric-containing species, whereas the CEM spectrum (d) suggests that the surface is mainly ferrous in nature.

context it is known that certain lower iron(II) phosphate hydrates are resistant to oxidation (101).

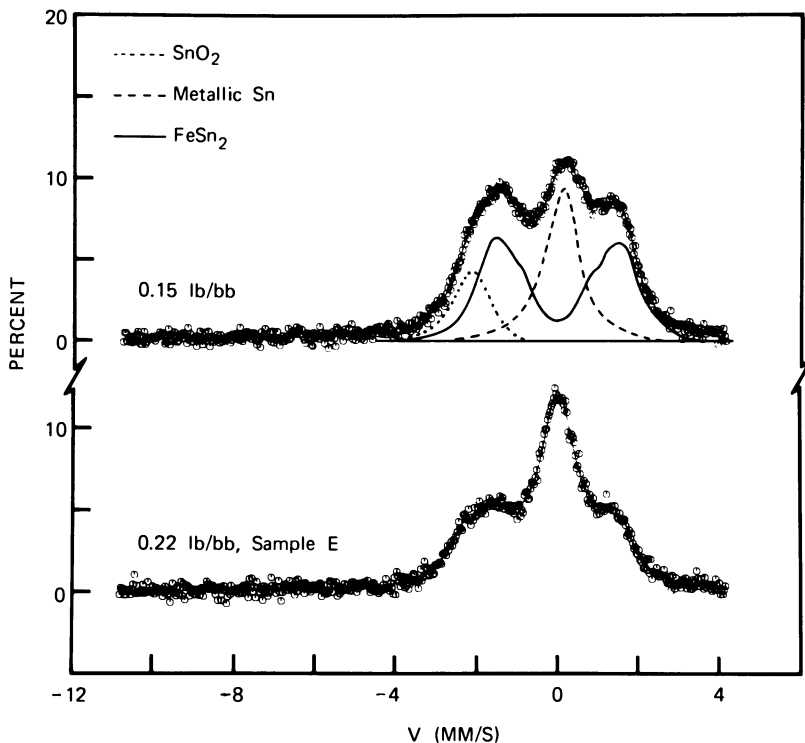
Iron-57 CEMS also has been used in combination with scanning electron microscopy and x-ray scattering Mössbauer spectroscopy to study the nature of red and black glazes on Greek- and Indian-painted ware (102). CEMS was shown to be particularly useful in the study of Indian pottery where the glazes are extremely thin.

Applications of DCEMS. Apart from its application to studies of γ -FeOOH (49), iron oxide and oxyhydroxide (50, 52, 70), and iron-implanted aluminum (90) just described, DCEMS has been used to measure the magnetic field near the surface of iron (103). It was demonstrated that the internal magnetic hyperfine field in the outermost 50 Å of the foil was 5% smaller than the bulk value. The Stockholm group has used the electrostatic beta-ray spectrometer described earlier to examine the surface condition of iron samples in an oil-diffusion-pumped vacuum system (104). After annealing at 750°C, the presence of FeCO₃ was detected in the surface regions of the sample. The data were analyzed using the weight functions computed according to the method described in an earlier section. It was found that the concentration of FeCO₃ decreased linearly from the surface down to 1100 Å, whereas a Mössbauer inert phase increased in concentration from the surface down to at least 1200 Å. In a cleaner turbo-pumped vacuum system, austenite was produced at the surface of an iron foil after repeated oxidation/reduction cycles over a period of one month. Analysis of these data showed that the austenite is confined to within 500 Å of the surface. It would appear that even in the clean vacuum system carbon contamination of samples can occur after long periods of time.

A DCEMS study (52) of the nature of the corrosion product formed on iron after exposure to a humid atmosphere also has been described. It was demonstrated that after 48 h a nonuniform layer of γ -FeOOH about 300 nm thick was formed. It also was shown that a layer of Fe₃(PO₄)₂ · 8 H₂O, ≈40 nm thick formed at an iron surface after immersion in 0.1M H₃PO₄ for 20 s.

Applications of ¹¹⁹Sn CEMS

In addition to the application of ¹¹⁹Sn DCEMS to the study of brominated tin foils described earlier, other applications of ¹¹⁹Sn CEMS have been made. Yagnik and co-workers (63) obtained very large effects for unenriched SnO₂ absorbers. Sano and co-workers (105) estimated the range of the ¹¹⁹Sn L-conversion electrons to be 1.17 ± 0.20 mg cm⁻² and also used the technique to study the aqueous corrosion of tin (106). In this latter study the corrosion products formed on tin metal immersed in



Journal of the Electrochemical Society

Figure 21. The ^{119}Sn CEM spectra of tinplate samples with coatings of 0.15 lb/bb (top) and 0.22 lb/bb (bottom) (106). The approximate contributions of the oxide, metal, and alloy (FeSn_2) layers are indicated separately in the top spectrum.

6.7M HNO_3 , 5.7M HCl , and 9.0M H_2SO_4 were determined to be $\text{SnO}_2 \cdot n\text{H}_2\text{O}$; $\text{Sn}_4(\text{OH})_2\text{Cl}_6$, and SnSO_4 , respectively. Huffmann and Dunmyre (106) have made detailed ^{119}Sn CEMS studies of tinplate. Typical spectra of tinplate on iron are shown in Figure 21 where the contributions from metallic Sn, SnO_2 , and FeSn_2 can be clearly seen. The overlayer thicknesses were determined and shown to be in good agreement with the results obtained from standard stripping techniques. A combined ESCA and ^{119}Sn CEMS study (108) was made of the oxidation of tin. Tin metal was exposed to dry oxygen at 1000°C , and it was demonstrated that under these conditions red SnO was formed at the tin surface. Schunk, Friedt, and Llabador (52) made a DCEMS study of a fluorinated tin foil; DCEM spectra recorded at various energy settings demonstrated that SnF_4 and SnF_2 were formed at the surface.

Conclusions

It is clear from the diversity of applications described here that CEMS, even in its simplest mode of operation, has begun to make a significant impact in many areas of pure and applied research. It is expected that the recent advances in data reduction, theory, and instrumentation, especially with regard to the control of sample temperature and depth selection, will be used advantageously in future studies of academic and technological problems.

Literature Cited

1. Tricker, M. J. "Surface and Defect Properties of Solids"; Chemical Society Specialist Periodical Report; London, 1977; Vol. 6, p. 106.
2. Berry, F. J. *Trans. Metall. Chem.* 1979, 4, 209.
3. Mahieu, B. *Rev. Quest. Sci.* 1979, 150, 187.
4. Greenwood, N. N.; Gibb, T. C. "Mössbauer Spectroscopy"; Chapman & Hall: London, 1971.
5. Swanson, K. R.; Spijkerman, J. J. *J. Appl. Phys.* 1970, 41, 3155.
6. Tricker, M. J.; Freeman, A. G.; Winterbottom, A. P.; Thomas, J. M. *Nucl. Instr. Methods* 1976, 135, 117.
7. Tricker, M. J.; Thomas, J. M.; Winterbottom, A. P. *Surf. Sci.* 1974, 45, 601.
8. Swartzendruber, L. J.; Bennett, L. H. *Scr. Metall.* 1972, 6, 737.
9. Stanek, J.; Sawicki, J. A.; Sawicka, B. D. *Nucl. Instr. Methods* 1975, 130, 613.
10. Sawicka, B. D.; Sawicki, J. A.; Stanek, J. *Nukleonika* 1966, 21, 949.
11. Sawicka, B. D.; Sawicki, J. A.; Stanek, J. *Phys. Lett.* 1976, 59A, 59.
12. Sawicki, J. A.; Sawicka, B. D.; Stanek, J.; Kowalsk, J. *Phys. Status Solidi B* 1976, 77, K1.
13. Sawicki, J. A.; Sawicka, B. G.; Lazarski, A.; Maydell, E.; Ondrusz, E. M. *Phys. Status Solidi B* 1973, 57, K143.
14. Sawicki, J. A.; Sawicka, B. D.; Lazarski, A.; Ondrusz, E. M. *Phys. Status Solidi B* 1973, 18, 85.
15. Sawicka, B. D.; Orwiega, M.; Sawicki, J. A. *Hyperfine Interact.* 1978, 5, 147.
16. Tricker, M. J.; Thorpe, R. K.; Freeman, J. H.; Gard, G. A. *Phys. Status Solidi A* 1976, 33, K97.
17. Onodera, H.; Yamamoto, H.; Watanabi, H.; Ebiko, H. *J. Appl. Phys., Jpn.* 1972, 11, 1380.
18. Simmons, G. W.; Kellerman, E.; Leidheiser, H. *Corrosion (Houston)* 1973, 29, 227.
19. Thomas, J. M.; Tricker, M. J.; Winterbottom, A. P. *J. Chem. Soc. Faraday* 2, 1975, 71, 1708.
20. Sette-Camara, A.; Keune, W. *Corros. Sci.* 1975, 15, 441.
21. Forester, D. W. *Proc. Lunar Sci. Conf., 4th* 1973, 3, 2697.
22. Petreva, M.; Gonser, U.; Hasmann, U.; Keune, W.; Lauer, J. *J. Phys. (Paris) Colloq.* 1976, C6, 295.
23. Tricker, M. J.; Ash, L. A.; Cranshaw, T. E. *Nucl. Instr. Methods* 1977, 143, 307.
24. Cosslett, V. E.; Thomas, R. N. *Br. J. Appl. Phys.* 1964, 15, 883.
25. Liljequist, D.; Ehdahl, T.; Bäverstam, U. *Nucl. Instr. Methods* 1978, 155, 529.

27. McCarthy, P. J.; Deeny, F. A. *Nucl. Instr. Methods* 1979, 159, 381.
28. Tricker, M. J.; Ash, L. A.; Jones, W. *Surf. Sci.* 1979, 79, L333.
29. Bonchev, Z. W.; Jordanov, A.; Minkova, A. *Nucl. Instr. Methods* 1969, 70, 36.
30. Bäverstam, U.; Bohm, C.; Ekdahl, T.; Liljequist, D.; Ringström, B. "Mössbauer Effect Methodology"; Plenum: New York, 1974; Vol. 9, p. 259.
31. Bäverstam, U.; Ekdahl, T.; Bohm, C.; Ringström, B.; Stefansson, V.; Liljequist, D. *Nucl. Instr. Methods* 1974, 115, 373.
32. Bäverstam, U.; Ekdahl, T.; Bohm, C.; Liljequist, D.; Ringström, B. *Nucl. Instr. Methods* 1974, 118, 313.
33. Bäverstam, U.; Bohm, C.; Ringström, B.; Ekdahl, T. *Nucl. Instr. Methods* 1973, 108, 439.
34. Fenger, J. *Nucl. Instr. Methods* 1973, 106, 203.
35. Spijkermann, J. J. "Mössbauer Effect Methodology"; Plenum: New York, 1971; Vol. 8, p. 85.
36. Takafuchi, M.; Isozumi, Y.; Katano, R. *Bull. Inst. Chem. Res., Kyoto Univ.* 1973, 51, 13.
37. Isozumi, Y.; Lee, D. I.; Kadar, I. *Nucl. Instr. Methods* 1974, 120, 23.
38. Sawicki, J. A.; Sawicka, B. D.; Stanek, J. *Nucl. Instr. Methods* 1976, 138, 565.
39. Isozumi, Y.; Takafuchi, M. *Bull. Inst. Chem. Res., Kyoto Univ.* 1975, 53, 63.
40. Sawicki, J. A.; Stanek, J.; Sawicki, B. D.; Kowalski, J., Internal Report No. 1009/PL, Inst. of Nuclear Physics, Cracow, Poland, 1978.
41. Isozumi, Y.; Kurahado, M.; Kabano, R. *Nucl. Instr. Methods* 1979, 166, 407.
42. Weyer, A. "Mössbauer Field Methodology"; Plenum: New York, 1976; Vol. 10, p. 301.
43. Salomon, D.; West, P. J.; Weyer, G. *Hyperfine Interact.* 1977, 5, 61.
44. Oswald, R.; Ohring, M. *J. Vac. Sci. Technol.* 1976, 13, 40.
45. Jones, W.; Thomas, J. M.; Thorpe, R. K.; Tricker, M. J. *Appl. Surf. Sci.* 1978, 1, 388.
46. Massenot, O. *J. Phys. (Paris) Colloq.* 1979, C1, 26.
47. Tiby, C., Diplomarbeit (Thesis), Johannes Gutenberg, Universität, Mainz, 1979.
48. Carbucicchio, M. *Nucl. Instr. Methods* 1977, 144, 225.
49. Minkova, A.; Schunck, J. P. *C. R. Acad. Bulg. Sci.* 1975, 28, 1171.
50. Toriyama, T.; Saneyashi, K.; Hisatake, K. *J. Phys. (Paris), Suppl. C2* 1979, 14.
51. Gruzin, P. L.; Petrikin, V.; Stukan, R. A. *Prib. Tekh. Eksp.* 1975, 48.
52. Schunk, J. P.; Friedt, J. M.; Llabador, Y. *Rev. Phys. Appl.* 1975, 10, 121.
53. Bäverstam, U.; Bodlund-Ringström, B.; Bohm, C.; Ekdahl, T.; Liljequist, D. *Nucl. Instr. Methods* 1978, 154, 401.
54. Benczer-Koller, N.; Kolk, B., *AIP Conf. Proc.* 1977, 38, 107; *Chem. Abstr.* 88.43634.
55. Toriyama, T.; Saneyashi, K.; Hisatake, K. *J. Phys. (Paris) Colloq.* 1979, 14.
56. Bainbridge, J. *Nucl. Instr. Methods* 1975, 128, 531.
57. Krakowski, R. A.; Miller, R. B. *Nucl. Instr. Methods* 1972, 100, 93.
58. Huffmann, G. P. *Nucl. Instr. Methods* 1976, 137, 267.
59. Huffmann, G. P. "Mössbauer Effect Methodology"; Plenum: New York, 1976; Vol. 10.
60. Tricker, M. J. *J. Mater. Sci.* 1979, 14, 995.
61. Graham, M. J.; Mitchell, D. F.; Channing, D. A. *Oxid. Met.* 1978, 12, 247.

62. Huffmann, G. P.; Podgurski, H. H. *Oxid. Met.* 1976, 10, 377.
63. Yagnik, C. H.; Mazak, R. A.; Collins, R. L. *Nucl. Instr. Methods* 1974, 114, 1.
64. Liljequist, D.; Bodlund-Ringström, B. *Nucl. Instr. Methods* 1979, 160, 131.
65. Bonchev, Ts.; Minkova, A.; Grozdanov, M. *Nucl. Instr. Methods* 1977, 147, 481.
66. Grozdanov, M.; Bonchev, Ts.; Likov, A. *Nucl. Instr. Methods* 1979, 165, 231.
67. Bonchev, Ts.; Grozdanov, M.; Shev, L. *Nucl. Instr. Methods* 1979, 165, 237.
68. Longworth, G., *Non-Destr. Test.* 1977, 242.
69. Rao, K. R. P. M. *Trans. Ind. Inst. Metall.* 1979, 32, 10.
70. Ekdahl, T.; Ringström, B.; Bäverstam, U. "Report No. 74," Univ. Stockholm Inst. Phys., 1974, p. 14.
71. Pritchard, A. M.; Truswell, A. E. "Corrosion of Steels in CO₂, International Conference, Reading, September 1974"; Holmes, D. R.; Hill, P. B.; Wyatt, L. M., Eds.; British Nuclear Energy Society, p. 234.
72. Ensling, J.; Fleisch, J.; Grimm, R.; Grüber, J.; Gütlich, P. *Corros. Sci.* 1978, 18, 797.
73. Ensling, J.; Gütlich, P.; Riess, R. *Werkst. Korros.* 1978, 29, 250.
74. Berry, F. J. *J. Chem. Soc. Dalton Trans.* 1979, 1736.
75. Berry, F. J.; Maddock, A. G. *J. Chem. Soc. Chem. Commun.* 1978, 308.
76. Ujihara, Y.; Handa, A.; Abe, Y.; Okabe, I. *Nippon Kagaku Kaishi* 1979, 234.
77. Ujihara, Y.; Handa, A. *J. Phys. (Paris) Colloq.* 1979, C1, 586.
78. Longworth, G.; Hartley, N. E. W. *Thin Solid Films* 1978, 48, 95.
79. Principi, G.; Mattaezzi, P.; Ramous, E.; Longworth, G. *J. Mater. Sci.*, in press.
80. Sedunov, V. K.; Men'shikova, T. Ya.; Mitrofanov, K. P.; Reiman, S. I.; Rokhlov, N. I. *Mater. Sci. Heat Treatment* 1977, 19, 742.
81. Swartzendruber, L. J.; Bennett, L. H.; Schoefer, E. A.; Delong, W. T.; Campbell, H. C. *Weld. J. (Miami), Suppl.* 1974, 53, 1.
82. Swartzendruber, L. J.; Siegal, E., *Magnetism and Magnetic Materials, AIP Conf. Proc. No. 18*, 1974, 735.
83. Cranshaw, T. E.; Campany, R. G. *J. Phys. (Paris), Colloq.* 1979, C2, 589.
84. Schwartz, L. H.; Kim, K. J. *Metall. Trans.* 1976, 1567.
85. Goodwin, J. G.; Parravano, G. *J. Phys. Chem.* 1978, 82, 1040.
86. Yagnik, C. M.; Collins, R. L.; Mazak, R. A.; Boer, W. H. *Proc. 10th Symp. on NDT, San Antonio, April 1975*, 194.
87. Mercader, R. C.; Cranshaw, T. E. *J. Phys. F.* 1975, 5, L124.
88. Sawicka, B. D.; Sawicki, J. A. *J. Phys. (Paris) Colloq.* 1979, C2, 576.
89. Sassa, K.; Ishida, Y.; Kaneko, K. *J. Phys. (Paris) Colloq.* 1979, C2, 556.
90. Jones, W.; Tricker, M. J.; Gard, G. A. *J. Mater. Sci.* 1979, 14, 751.
91. Longworth, G.; Jain, R. *J. Phys. F.* 1978, 8, 351.
92. Jain, R.; Longworth, G. *J. Phys. F.* 1978, 8, 363.
93. Longworth, G.; Jain, R. *J. Phys. F.* 1978, 8, 993.
94. Atkinson, R.; Longworth, G. *J. Phys. F.*, in press.
95. Yamakowa, K.; Fujita, F. E. *J. Phys. (Paris) Colloq.* 1979, C2, 101.
96. Massenot, O.; Daver, H. *Solid State Commun.* 1977, 21, 37.
97. Tominaga, T.; Sato, H. *Radiochem. Radioanal. Lett.* 1978, 33, 53.
98. Sawicki, J. A.; Sawicki, B. D.; Gzowski, O. *Phys. Status Solidi A*, in press.
99. Skrimshire, C. P.; Longworth, G.; Dearnaley, G. *J. Phys. D.* 1979, 12, 1951.
100. Tricker, M. J.; Ash, L. A.; Jones, W. *J. Inorg. Nucl. Chem.* 1979, 41, 891.
101. Mattievich, E.; Danon, J. *J. Inorg. Nucl. Chem.* 1977, 39, 569.

102. Longworth, G.; Tite, M. S. *J. Phys. (Paris) Colloq.* **1979**, 460.
103. Bäverstam, U.; Ekdahl, T.; Ringström, B. *J. Phys. (Paris) Colloq.* **1974**, C6, 685.
104. Bodlung-Ringström, B.; Bäverstam, U.; Bohm, C. *J. Vac. Sci. Technol.* **1979**, 16, 1013.
105. Endo, K.; Shilbuya, K.; Sano, H. *Radiochem. Radioanal. Lett.* **1977**, 28, 363.
106. Shibuya, M.; Endo, K.; Sano, H. *Bull. Chem. Soc. Jpn.* **1978**, 51, 1363.
107. Huffmann, G. P.; Dunmyre, G. R. *J. Electrochem. Soc.* **1978**, 125, 1652.
108. Lau, C. L.; Wertheim, G. K. *J. Vac. Sci. Technol.* **1978**, 622.

RECEIVED June 27, 1980.

The Use of Conversion Electron Mössbauer Spectroscopy to Study Ion-Implanted Alloys and Archaeological Materials

G. LONGWORTH and R. ATKINSON

Nuclear Physics Division, Atomic Energy Research Establishment,
Harwell, Oxfordshire, UK

Analysis of Mössbauer electron spectra for copper foils implanted with $1-5 \times 10^{16}$ ^{57}Fe ions cm^{-2} suggests that the iron atoms end up on substitutional sites, with a fraction being associated with nearby lattice defects. Similar spectra for iron foils implanted with up to 8×10^{17} carbon ions cm^{-2} contain a component attributable to Fe_5C_2 . On aging the foils, the carbon atoms migrate appreciably above 400°C . Finally, Mössbauer electron and x-ray backscattering are used to characterize the iron compounds in the glazes on examples of Attic Black, Samian, and Indian Northern Black Polished Wares.

The techniques of conversion electron Mössbauer spectroscopy (CEMS) and conversion x-ray Mössbauer spectroscopy (CXMS) have been used increasingly in recent years, mainly in the study of oxidation products at iron or steel surfaces (1, 2). This chapter illustrates the use of such techniques both in the study of surface alloys produced by ion implantation and as a tool in archaeology to characterize the iron compounds present in certain types of glaze on painted ceramic objects.

Experimental

CEMS or CXMS allows the near-surface layers of a sample to be characterized to a depth of either several tenths of a micron or about ten microns, respectively. Each type of radiation may be detected in a gas-filled proportional counter. In the former case, the energy resolution is poor and scattered

0065-2393/81/0194-0101\$05.00/0
© 1981 American Chemical Society

electrons are detected with energies from the *K* conversion electron energy (≈ 7 keV in iron) to essentially zero. Thus in the case of ^{57}Fe the *L* Auger electrons at approximately 5 keV are detected also.

Figure 1 shows a simple backscatter counter viewed from the back through which either helium/5% methane (electrons) or argon/10% methane (x-rays) is allowed to flow by means of pipes (C). The anode wire (A) is 25- μm stainless steel and is sufficiently long so that end effects are small. The gamma-ray beam passes into the counter through the front window, made of Perspex, and is incident on the sample which is mounted behind a hole in an aluminum backplate using sealing compound. Electrons backscattered into a solid angle of approximately 2π are detected. The counter thickness (2 cm) ensures a low efficiency for incident 14-keV gamma radiation while having a relatively high efficiency for scattered electrons.

To set a lower energy threshold in the pulse height spectrum so as to avoid unnecessary electronic noise, the spectrum measured with the source on resonance with a fluorescer foil for about 30 s is compared with that taken with the source moving so as to destroy resonance. The difference between the spectra indicates the energy dependence of the resonant electrons. A convenient fluorescer foil is *Rh* Fe 10 at. which is mounted on a movable arm B inside the counter so that it may be removed from the gamma-ray beam once the energy threshold has been set. The counter has a good energy resolution for iron *K* x-rays, and also has been used to measure conversion electrons from either ^{119}Sn or ^{151}Eu .

Since scattered electrons are detected over a range of energies, the amount of depth information in the spectrum is small. Even if electrons are detected over a narrow range of energies using a magnetic or electric spectrometer, the depth information is not directly available since all electrons detected at a given energy do not originate at the same scatterer depth. However, spectra measured at several electron energies may be used to produce depth-selective spectra (3, 4), although the technique requires the use of scatterers highly enriched in ^{57}Fe .

Nevertheless, when proportional counters are used for samples consisting of natural iron, it is possible to derive a limited amount of depth information. The probability that an electron emitted at a certain depth will escape and be detected has been determined approximately by measuring the areas of the

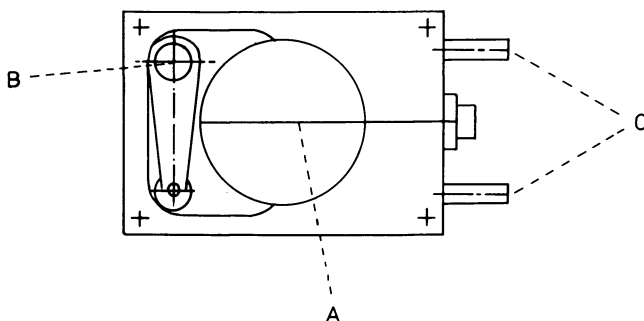


Figure 1. Simple backscattering counter for conversion electrons or x-rays. (A) anode; (B) fluorescer foil; (C) gas inlet and outlet pipes

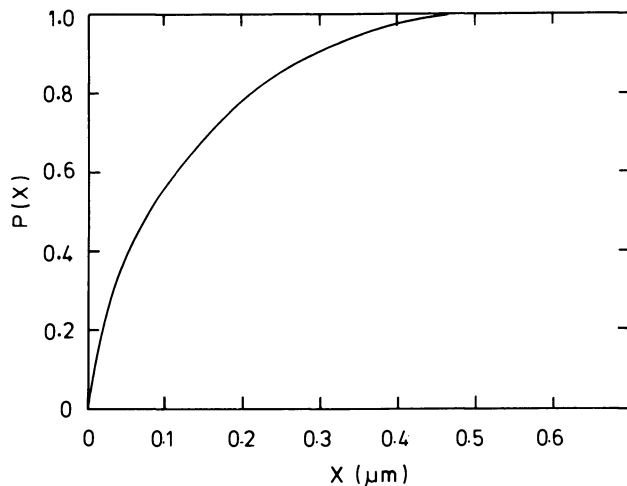


Figure 2. Relative area $P(x)$ in CEM spectrum attributable to iron atoms within a distance x of scatterer surface as a function of x

CEM spectra for natural iron foils on which layers of ^{57}Fe , varying from 0.02 to 0.3 μm , had been evaporated. The layer thicknesses were determined by weight. From the variation of area with layer thickness, a graph may be derived (Figure 2) for the relative area in the CEM spectrum $P(x)$ that is produced by electrons within a distance x from the surface. This suggests that about 50% of the spectrum results from iron atoms within the first 0.1 μm below the surface.

Ion Implantation

Ion implantation provides a means of introducing a controlled amount of a given atomic species into a target material. To do this, the atoms are first ionized and accelerated to 50–200 keV in vacuum before entering the target. The ions lose energy both by electronic excitation and by elastic collisions with the target atoms, and come to rest with an approximately Gaussian distribution about a mean range (Figure 3). The width of the distribution is caused by the statistical nature of the collision process. In polycrystalline materials the range and standard deviation of the implanted ions may be calculated approximately using the theory of Lindhard, Scharff, and Schiott (LSS) (5, 6). For the two systems discussed here, 85-keV ^{57}Fe ions on copper and 40-keV carbon ions on iron, the approximate mean ranges are 230 Å and 500 Å, with standard deviations of 90 Å and 250 Å, respectively.

In this way large amounts of impurity atoms may be introduced irrespective of the usual equilibrium solid solubilities. However, an upper limit for the impurity concentration is set by sputtering effects

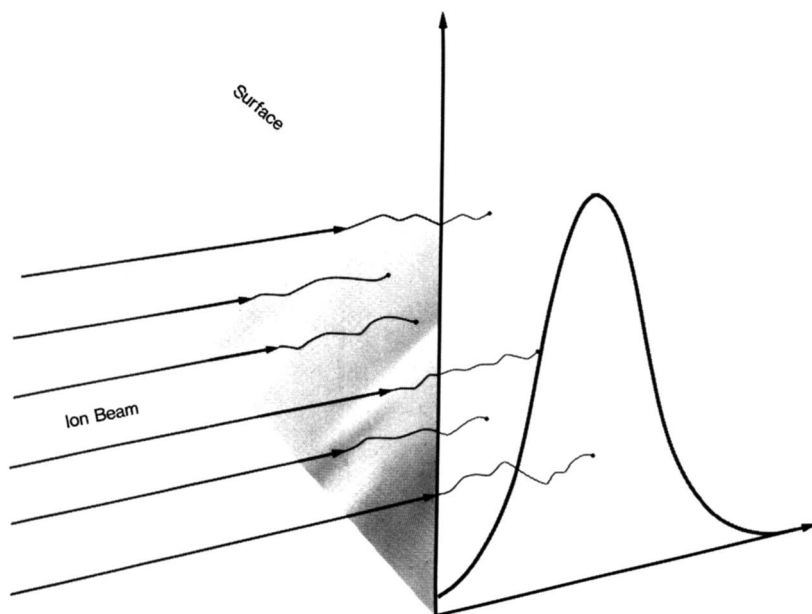


Figure 3. Schematic of ion-implantation process

where the incoming ions knock off atoms from the target surface. This leads to a maximum retained dose, and to a disturbance of the implantation profile at higher doses. The effect of increasing dose is to flatten the distribution and move it closer to the target surface. The degree of sputtering is usually expressed as a sputtering ratio, which is the ratio of target atoms removed per incident ion.

When the incident ions undergo elastic collisions with the host atoms, the latter are ejected from their lattice sites if the transferred energy exceeds about 25 eV, creating vacancies and interstitials (7). The recoil energy of the displaced atoms is often enough to produce secondary displacements, and a cascade of atomic displacements is formed. Towards the end of its path, the ion creates a large number of atomic displacements within a very small region and in a short amount of time ($\approx 10^{-13}$ s). Here the probability of an ion occupying a substitutional site is high. Implantation is always accompanied by radiation damage, which may lead to migration of the impurity atoms at temperatures below which thermal diffusion is operative. Thus, the final metallurgical state of an alloy will depend on the extent of this radiation-enhanced diffusion which is governed by the number of excess vacancies and interstitial atoms created during the implantation. For high incident dose rates it is also possible for the target temperature to become sufficiently high for thermal diffusion to occur.

Although the solubility limits for a given alloy may be exceeded in implantation, it must be emphasized that the solid solutions formed are metastable. Their decomposition either by solute precipitation or by the formation of intermetallic compounds will occur on thermal annealing.

Suitable alloys may be prepared either by implanting ^{57}Fe into any material or by implanting essentially any ion into iron. Here we give one example of each type of alloy. The spectra of the first type are easier to interpret since in the second case, part of the scattered spectrum comes from iron atoms outside the implantation profile.

Studies of Iron-Implanted Copper Alloys

In previous work (8, 9, 10) we have demonstrated how the normal solubilities of iron in copper or silver may be exceeded. CEM spectra were analyzed to determine the local atomic surroundings of the iron atoms, and the decomposition of the phases present was studied after the samples were aged.

Here we present similar measurements on copper foils ($12.5\ \mu\text{m}$) implanted with high doses (2, 3, 4, and 5×10^{16} ions cm^{-2}) of ^{57}Fe in order to study further an anomalous feature of the spectrum observed previously. The changes in the CEM spectrum occurring as a function of increasing ^{57}Fe dose are illustrated in Figure 4, where the spectrum for a dose of 1×10^{16} ions cm^{-2} is taken from previous work (8). The CEM spectra were fitted using a least-squares minimization program with the following Voigt profiles, resulting from a Gaussian distribution of Lorentzian lines, each having the natural linewidth:

1. a singlet (shift $S \simeq 0.2\ \text{mms}^{-1}$) resulting from iron atoms with all 12 copper nearest neighbors—isolated iron atoms;
2. a doublet (splitting $Q \simeq 0.6\ \text{mms}^{-1}$) resulting from iron atoms with one or more iron nearest neighbors;
3. a singlet ($S \simeq -0.09\ \text{mms}^{-1}$) resulting from iron atoms with all 12 iron nearest neighbors;
4. a singlet ($S \simeq 0.4\ \text{mms}^{-1}$) not observed in the spectra for conventional alloys produced by melting.

The values for the hyperfine parameters derived from the fits are shown in Table I.

The relative amplitudes of Lines 1, 2, and 3 are governed by the arrangement of iron atoms on substitutional sites. The approximate iron concentration was calculated, including the effects of sputtering, and it was shown (8) that there are more iron-iron pairs and hence fewer isolated iron atoms than expected for a random arrangement. Thus, the radiation-enhanced diffusion has promoted short-range ordering of the iron atoms. Eventually some iron atoms will be surrounded by all 12 iron nearest neighbors giving rise to Singlet 3, similar to the singlet observed

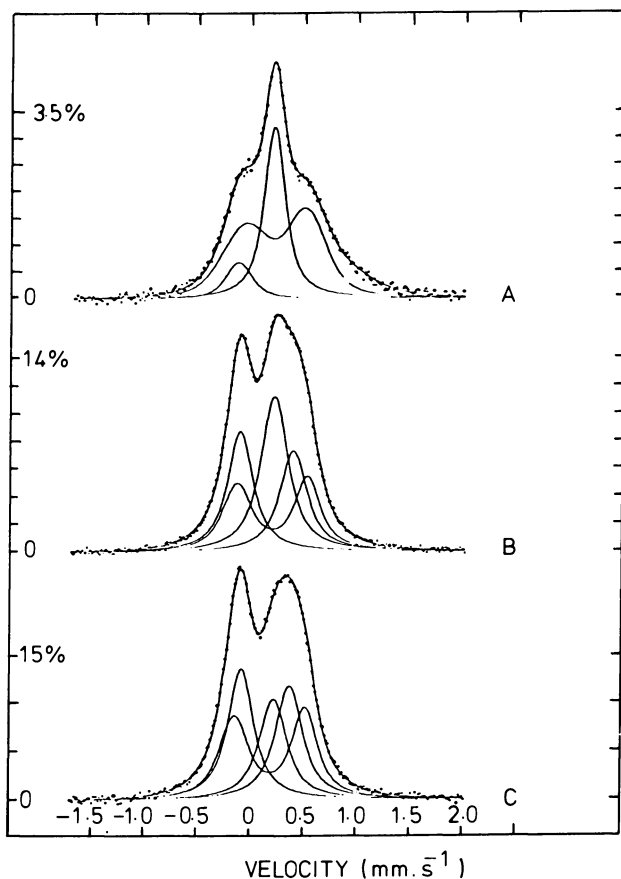


Figure 4. CEM spectra for iron-implanted copper alloys for doses of (A) 1×10^{16} ; (B) 3×10^{16} ; and (C) 5×10^{16} ^{57}Fe ions cm^{-2} . The full curves are derived from fits to the data and signify the total fit and component fits described. The zero of the velocity scale refers to the shift of α -iron.

Table I. Hyperfine Parameters Derived from Least-Squares Copper-Iron

Dose (ions cm^{-2})	Singlet (1)		Doublet (2)		
	S (mms^{-1})	Area (%)	S (mms^{-1})	Q (mms^{-1})	Area (%)
1×10^{16}	0.22	37	0.24	0.58	53
2×10^{16}	0.23	37	0.20	0.66	26
3×10^{16}	0.23	31	0.20	0.66	28
4×10^{16}	0.23	27	0.19	0.67	27
5×10^{16}	0.22	19	0.19	0.66	34

* S is the shift with respect to α -iron and Q is the quadrupole splitting.

for fcc γ -iron. The remaining iron atoms having both iron and copper neighbors will see a finite quadrupole interaction attributable to the distortion of their electronic screening charges (11) giving rise to the Doublet 2. The appearance of Singlet 4 at about 0.4 mms^{-1} is unexpected. In the spectrum for a previous sample ($5 \times 10^{16} \text{ ions cm}^{-2}$), Singlets 1 and 4 were fitted to a broad singlet ($S \simeq 0.3 \text{ mms}^{-1}$), and it was observed that the width decreased and its shift reverted to that for Singlet 1 after the sample was aged for 2 h at 245°C (8, 9). It was suggested that this singlet was attributable to iron atoms situated near vacancy clusters that produce a decreased S electron density. The vacancy clusters dispersed at a relatively low temperature. In a previous section it was mentioned that implanted atoms create vacancies as they come to rest in the lattice. However, as the damage is in a metastable state during implantation, subsequent implanted atoms may break up existing clusters of vacancies and trap these vacancies. The present work suggests that the anomalous line is present for doses above about $2 \times 10^{16} \text{ ions cm}^{-2}$, with the relative amount increasing with dose. Although the cause is still not entirely clear, it is being investigated further by careful aging of the present samples and by electron microscopy. It is interesting to note that the "defect-associated" line is not present in the spectra for carbon-implanted iron alloys (see next section), although the carbon doses were an order of magnitude higher. This illustrates the difference between the damage caused by light and heavy ions.

Studies of Carbon-Implanted Iron Foils

Ion implantation provides a means of improving the durability of metal surfaces (12). As an example, the wear resistance of steel surfaces may be increased by two orders of magnitude by implanting with light ions such as nitrogen, carbon, or boron (13). For these measurements a

Fits to Mössbauer Electron Scattering Spectra of Implanted Alloys^a

<i>Singlet (3)</i>		<i>Singlet (4)</i>	
S (mms^{-1})	Area (%)	S (mms^{-1})	Area (%)
-0.11	10	—	—
-0.09	20	0.42	17
-0.09	23	0.41	19
-0.08	26	0.41	21
-0.08	24	0.37	22

loaded pin wears against the rotating ion-implanted disc, and the wear rate of the couple is assessed mainly from the loss of material from the pin and from an analysis of the total wear debris. CEM spectra for iron foils implanted with nitrogen ions were used (14) to show that nitrides were formed above a dose of about 1×10^{17} ions cm^{-2} , which is comparable to the dose at which the maximum increase in wear resistance of steel surfaces had been observed (13). The principle of nitriding surfaces is not new and has been used previously to harden surfaces by introducing strong interatomic bonds. For implanted steel, although the original penetration depth of nitrogen ions is shallow, the increased wear resistance is long lasting and is maintained even when the wear track is several times the implantation depth (12). Annealing the nitrogen-implanted iron foils showed (14) changes in the CEM spectra above about 275°C associated with diffusion of the nitrogen atoms within the implanted layer. At higher temperatures ($\approx 500^\circ\text{C}$) the nitrogen atoms had diffused out of the implanted layer into the bulk of the iron foil. The relatively low temperature of 275°C could well be reached in the near-surface layers during wear, allowing the nitrogen ions to migrate to dislocations. This will impede the movement of the dislocations and give rise to hardening. As wear proceeds both the dislocations and nitrogen atoms are driven deeper, thus continuously recreating a hard surface (12).

CEM spectra have been measured also for iron foils implanted with 40-keV carbon ions (Figure 5). The spectra for incident doses of 5×10^{16} and 1×10^{17} ions cm^{-2} contain components from iron and Fe_3C ($H \approx 195$ kOe) (Table II). For the higher doses as well as the iron component there is an increasing contribution from Fe_5C_2 ($H \approx 220, 180,$ and 120 kOe). Also shown in Table II are the retained doses, peak carbon concentrations, and profile peak positions as a function of incident dose, assuming a sputtering ratio of 0.95 (15, 16). In the absence of sputtering the mean range is 500 \AA and σ is 250 \AA . The effect of sputtering on the implantation profile is marked above about 2×10^{17} ions cm^{-2} . For this dose the expected peak concentration, ≈ 27 at. %, is sufficient to allow the formation of Fe_5C_2 . Using Figure 2 and the parameters for the expected implantation profile we can calculate the expected relative area attributable to carbide in the CEM spectrum. If we approximate the Gaussian profile by a rectangular distribution centered at 400 \AA and of width 500 \AA (2σ), then the expected contribution from iron atoms within this distribution is about 28% of the total CEM spectrum. This is in good agreement with the observed value of 30% (Table II). However, for greater incident doses, since the peak carbon concentration is much higher than the carbon concentration in Fe_5C_2 , it is clear that some expansion of the implantation profiles must have taken place.

The effect of thermal annealing on one sample (4×10^{17} ions cm^{-2}) is shown in Figure 6. No change was observed below about 400°C when

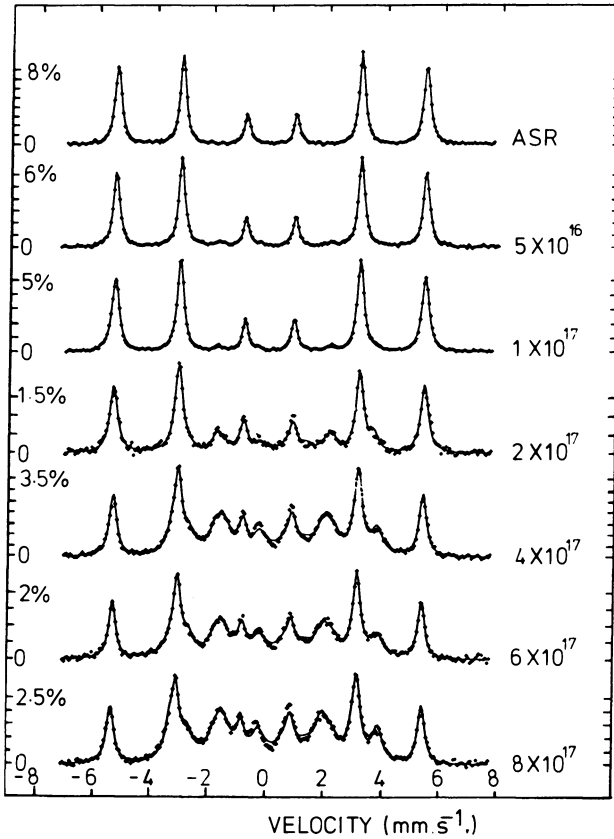


Figure 5. CEM spectra for iron foils in the received condition (ASR) or implanted with 5×10^{16} , and 1, 2, 4, 6, and 8×10^{17} carbon ions cm^{-2}

Table II. Variation of Retained Dose, Implantation Profile Parameters, and Relative Area Attributable to Carbide in CEM Spectrum, with Implanted Dose for 40-keV Carbon in Iron, Using a Sputtering Ratio of 0.95

Incident Dose (ions cm^{-2})	Retained Dose (ions cm^{-2})	Peak Position (\AA)	Carbon Concentration (at. %)	Carbide Area (%)
5×10^{16}	4.90×10^{16}	500	8.7	≈ 5
1×10^{17}	9.60×10^{16}	450	15.9	9
2×10^{17}	1.88×10^{17}	400	27	30
4×10^{17}	3.40×10^{17}	300	40	59
6×10^{17}	4.20×10^{17}	150	47	61
8×10^{17}	4.40×10^{17}	50	49	67

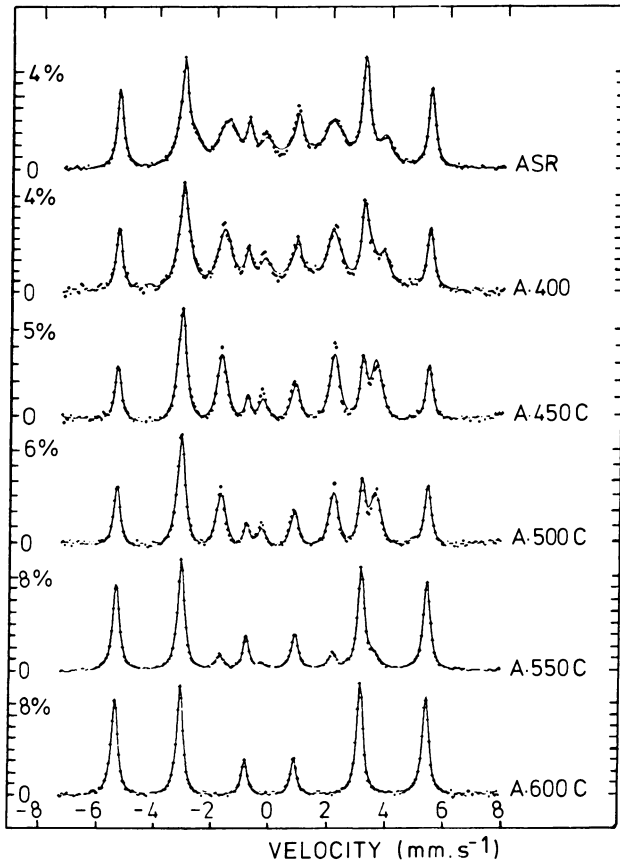


Figure 6. CEM spectra for a carbon-implanted iron foil for a dose of 4×10^{17} carbon ions cm^{-2} as a function of annealing for 1 h at various temperatures

the carbide contribution began to decrease, becoming zero at about 600°C. This suggests that above 400°C thermal diffusion of carbon atoms is sufficient to allow them to migrate away from the implanted layer. Such a relative low temperature might suggest that the carbide is present in the form of small precipitates surrounded by α -iron rather than as a uniform layer. It should be possible to check this using electron microscopy.

Carbides produced by ion implantation are more stable than nitrides, and therefore may show more promise for improvements in wear resistance. Such wear measurements for pure-iron foils implanted with either nitrogen or carbon currently are in progress in conjunction with Mössbauer measurements. In this way it should be possible to check whether in fact the nitrogen/carbon atoms are driven deeper in as wear proceeds.

Studies of Glazes on Painted Ceramic Objects

There have been several publications in which Mössbauer absorption spectra have been used to study the body fabric of potsherds (see, for example, Refs. 17, 18, 19). Here we are concerned with investigating the feasibility of using Mössbauer scattering to examine surface glazes.

The decoration on Attic pottery frequently was based on the use of black or red colors. These colors are associated with various forms of iron oxide derived from the iron in the original clay. The surface glazes typically are several tens of microns thick and thus are amenable to nondestructive examination by Mössbauer scattering. Ideally we may identify the particular oxide to gain information about the method of manufacture. The Greek or Attic Black Ware dating from around 500 BC consists of a shiny black gloss on a red body fabric (20). At about the same time on the Indian subcontinent, the Painted Grey Ware of India had reached its highest development in the Northern Black Polished Ware (21). Here the black gloss is somewhat duller and is based on a grey body fabric. In each case the colors were produced essentially using the same clay as in the body fabric, by control of the atmosphere during the firing, and it is interesting to identify and compare the iron-containing compound in each case. As an example of red-painted pottery we studied some samples of red Samian Ware dating from several centuries later. The thickness and degree of sintering or vitrification of the surface glazes were investigated using scanning electron microscopy (SEM) by M. S. Tite of the British Museum Research Laboratory. Preliminary results of this combined study have been published previously (22).

Attic Black Ware. SEM measurements indicate extensive vitrification of the gloss and body fabric, the gloss being 20–30 μm thick. In one sample, GA 2A, the gloss was found to consist of two layers of roughly equal thickness, with the outer layer showing more vitrification. The CXM spectra (Figure 7) contain magnetic components ($H \simeq 489$ and 465 kOe) that may be identified with an impure form of magnetite. There is an additional component ($H \simeq 503$ kOe) in the spectrum for GA 2A that is similar in field value to that in the absorption spectra (Figure 8) for the body fabric ($H \simeq 505$ kOe); this is attributable to ferric oxide (hematite). The appearance of two different oxides in the gloss for GA 2A is probably associated with the dual-layered nature. It must be remembered also that for this approximate gloss thickness, about 60% of the spectrum comes from the gloss material, with the remainder coming from the body fabric.

Samian Ware. Both CXM and absorption spectra (Figures 7 and 8) give a clear indication of hematite as expected ($H \simeq 505$ kOe), and again the gloss appears to be fully vitrified.

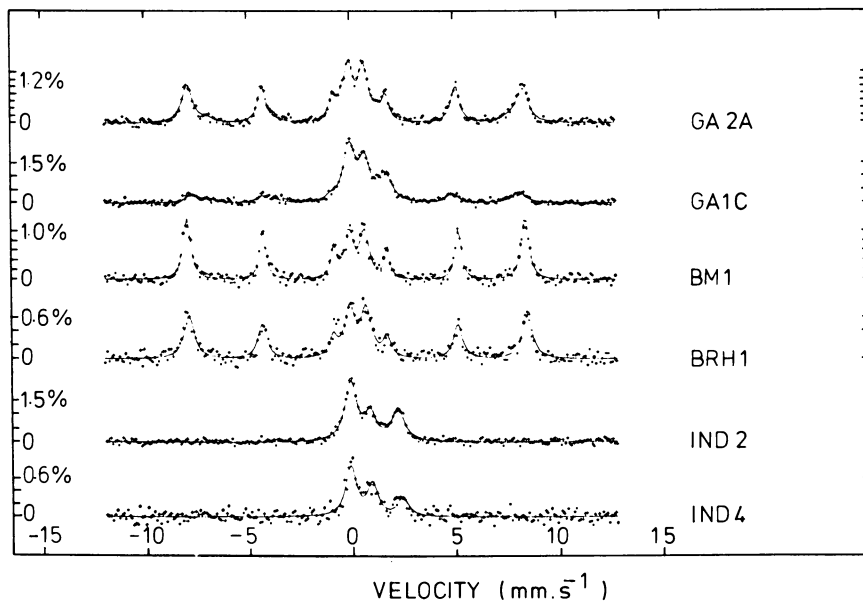


Figure 7. CXM spectra for surface gloss on samples of Greek Attic Black Ware (GA2A, GA1C), Samian Ware (BM1, BRH1), and Indian Northern Black Polished Ware (IND2, IND4)

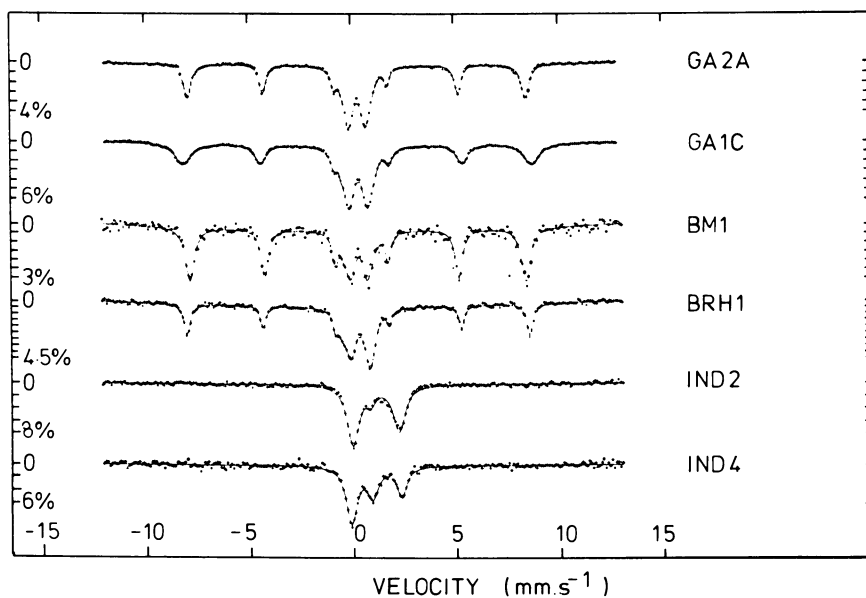


Figure 8. Mössbauer spectra for body fabric of Greek Attic Black Ware (GA2A, GA1A), Samian Ware (BM1, BRH1), and Indian Northern Black Polished Ware (IND2, IND4)

Northern Black Polished Ware. SEM measurements on two samples indicate a gloss thickness of only 10–15 μm , with neither gloss nor body fabric being vitrified. Because of this restricted thickness, it is not surprising that the CXM and absorption spectra on four samples are very similar (Figures 7 and 8). They consist of two doublets, one comprising about 60% of the total area attributable to ferrous ions (shift $S \simeq 1.07$ mms^{-1} , splitting $Q \simeq 2.35$ mms^{-1}) and the other, the remaining 40%, attributable to ferric ions ($S \simeq 0.48$ mms^{-1} , $Q \simeq 1.07$ mms^{-1}). For the measured gloss thickness the iron atoms in the gloss will contribute only about 20% of the CXM spectrum. In the CEM spectra for the same samples there is predominantly a doublet attributable to ferric ions ($S \simeq 0.41$ mms^{-1} , $Q \simeq 0.93$ mms^{-1}). This comprises the entire spectrum for the two samples IND 1 and IND 5, 70% of the spectrum for IND 4 (Figure 9), the remainder being a doublet attributable to ferrous ions, and 50% of the spectrum for IND 2, the remainder being a magnetic spectrum with $H \simeq 487$ kOe (Figure 9).

Thus, only in the spectrum for the gloss on one sample is there evidence for a component that reasonably may be associated with an impure form of magnetite. It is possible that for the remaining samples, any magnetite is in such a finely divided form that it is superparamagnetic at room temperature. Alternatively, the layer studied by CEMS ($\simeq 10^3$ Å) may not be characteristic of the main thickness of the gloss ($\simeq 10$

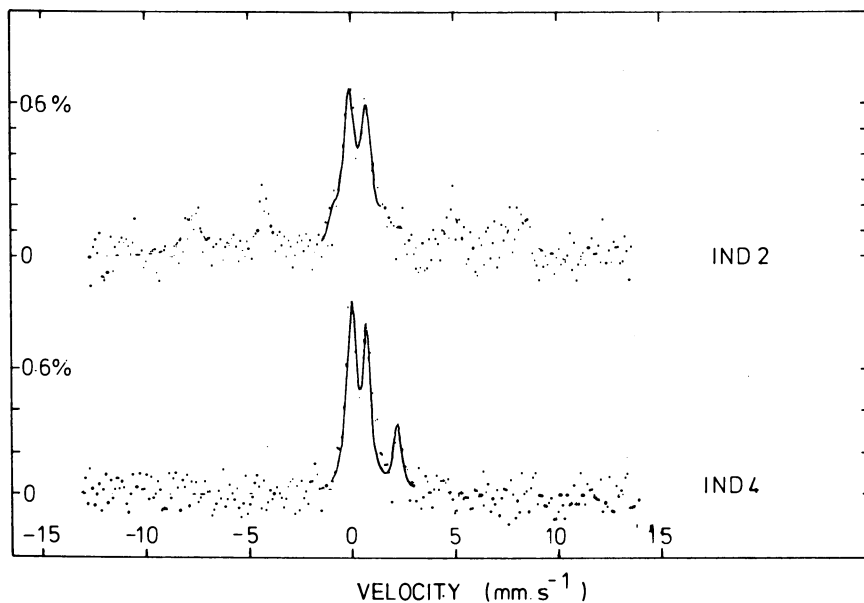


Figure 9. CEM spectra for surface gloss on samples of Indian Northern Black Polished Ware (IND2, IND4)

μm) because of the effects of weathering. If this were the case, then neither type of scattering spectrum would be representative of the gloss as a whole.

The differences in vitrification between the three types of pottery indicate a lower firing temperature for Northern Black Polished Ware ($\leq 800^\circ\text{C}$) and a somewhat higher temperature for Attic Black and Samian Wares ($850\text{--}1050^\circ\text{C}$). When samples of IND 1 and IND 2 were heated in air at 900°C , both gloss and body fabric became red in color, indicating oxidation. The Mössbauer absorption spectra showed no component attributable to ferrous ions, and in one case, IND 2 showed a component attributable to hematite ($H \simeq 514$ kOe, 40% of the total area). These results are in contrast to those obtained on refiring samples of Attic Black Ware in air, when the color of the gloss did not change. This is in agreement with the suggested lower original firing temperature for Northern Black Polished Ware, which leaves the gloss partially vitrified and thus able to be reoxidized.

It is difficult to identify the compounds responsible for the ferrous and ferric doublets in the spectra for Northern Black Polished body fabric on the basis of their hyperfine parameters because of the relative lack of sensitivity of these parameters to structural changes in silicate structures. Part of the ferric doublet in the spectrum for Sample IND 2, however, appears to result from finely divided iron oxide, since at 4.2 K the spectrum contains about 15% of a magnetic component ($H \simeq 480$ kOe).

Although the amount of information to be gained from Mössbauer scattering spectra is limited by their relatively poor quality, particularly the CEM spectra, the difference between the structures of the black gloss on Attic and Northern Black Polished Ware is quite apparent. Future work will depend upon improving the quality of these spectra by reducing the background scattering in the detector. Identification of the iron compounds would be facilitated by measuring the scattering spectra at 77 K. This would also allow a measurement of the superparamagnetic fraction, from which an idea of particle size may be gained.

Acknowledgments

The authors would like to thank T. E. Cranshaw and R. E. J. Watkins for several fruitful discussions. The collaboration of N. E. W. Hartley in the work on carbon-iron alloys and M. S. Tite in the work on painted ceramics is gratefully acknowledged.

Literature Cited

1. Sette C. A.; Keune, W. *Corros. Sci.* **1975**, *15*, 441.
2. Graham, M. J.; Mitchell, D. F.; Channing, D. A. *Oxid. Met.* **1978**, *12*, 247.

3. Bäverstam, U.; Ekdahl, T.; Bohm, C.; Liljequist, D.; Ringström, B. *Nucl. Instr. Meth.* 1974, 118, 313.
4. Bodlund-Ringström, B.; Bäverstam, U.; Bohm, C. *J. Vac. Sci. Technol.* 1979, 16, 1013.
5. Lindhard, J.; Scharff, M.; Schiott, H. E. *Mater. Fys. Medd. Dan. Vid. Selsk.* 1963, 33 (14).
6. Matthews, M. D. UKAEA Report, 1973, AERE-R7805.
7. Nelson, R. S. *Proc. Roy. Soc.* 1969, A311, 53.
8. Longworth, G.; Jain, R. *J. Phys. F.* 1978, 8, 351.
9. Jain, R.; Longworth, G. *J. Phys. F* 1978, 8, 363.
10. Longworth, G.; Jain, R. *J. Phys. F* 1978, 8, 993.
11. Window, B. *J. Phys. Chem. Solids* 1971, 32, 1059.
12. Dearnaley, G.; Hartley, N. E. W. *Thin Solid Film* 1978, 54, 215.
13. Hartley, N. E. W. *Wear* 1975, 34, 427.
14. Longworth, G.; Hartley, N.E.W. *Thin Solid Films* 1978, 48, 95.
15. Watkins, R. E. J., private communication, 1979.
16. Bett, R.; Charlesworth, J. P. UKAEA Report, 1973, AERE-R7052.
17. Kostikas, A.; Simopoulos, A.; Gangas, N. H. *J. Phys. (Paris)* 1974, 35, C6-537.
18. Bouchez, R.; Coey, J. M. D.; Coussement, R.; Schmidt, K. P.; van Rossum, M.; Aprahamian, J.; Deshayes, J. *J. Phys. (Paris)* 1974, 35, C6-541.
19. Riederer, J.; Wagner, U.; Wagner, F. E. *Radiochem. Radioanal. Lett.* 1979, 40(5), 319.
20. Bimson, M. *Antiquaries J.* 1956, 36, 200.
21. Hegde, K. T. M. *Antiquity*, 1975, XLIX, 187.
22. Longworth, G.; Tite, M. S. *J. Phys. (Paris)* 1979, 40, C2-460.

RECEIVED June 27, 1980.

Conversion Electron Mössbauer Spectroscopy of Europium-151 and Thulium-169

G. K. SHENOY, D. NIARCHOS, P. J. VICCARO, and B. D. DUNLAP

Argonne National Laboratory, Argonne, IL 60439

We demonstrate the feasibility of conversion electron Mössbauer spectroscopy of rare-earth systems using the 21.53-keV transition in ^{151}Eu and the 8.4-keV transition in ^{169}Tm . The resonance spectra of ^{151}Eu are measured using L conversion electrons with kinetic energy of about 13.5 keV. For ^{169}Tm the conversion process involves M electrons that have kinetic energy of approximately 6.1 keV. The comparison of the conversion electron spectra to transmission data for a number of europium-based compounds indicates that an enhancement of the resonant effect occurs in most cases using the conversion electron technique. For ^{169}Tm , a dilution of the effect occurs from photoelectrons of thulium.

In recent years, the use of ^{57}Fe and ^{119}Sn conversion electron Mössbauer spectroscopy (CEMS) has grown steadily (1). In this technique, the internal conversion and associated Auger electrons which result from the de-excitation of Mössbauer nuclei following resonant absorption of incident gamma rays are detected. The principal difference between this type of Mössbauer spectroscopy and the more usual one involving the detection of resonantly absorbed gamma rays in a transmission or scattering geometry is the much smaller range of the conversion electron in a given absorber compared to the gamma ray. As a result, CEMS is sensitive to those resonant nuclei contained in a thin layer (50–3000 Å) at the surface of the absorber. On the other hand, methods based on gamma ray detection probe depths on the order of tens of microns. This unique property of CEMS makes it suitable for studying surfaces.

In principle, CEMS could be used for any of the Mössbauer isotopes for which the nuclear de-excitation has a large enough probability of occurring through the internal conversion process. However, except for

0065-2393/81/0194-0117\$05.00/0
© 1981 American Chemical Society

^{57}Fe and ^{119}Sn , little is known concerning the application of the CEMS technique to other isotopes. Other candidates for which CEMS could prove useful are some of the Mössbauer isotopes from the rare-earth series. With this in mind, we have investigated CEMS applied to two of the rare-earth isotopes, ^{151}Eu and ^{169}Tm . Our results indicate that the 21.53-keV transition in ^{151}Eu is in fact very convenient for CEMS. The 8.4-keV transition in ^{169}Tm , on the other hand, does not appear to be as favorable.

For both isotopes, the conversion electron spectra are compared to simultaneously measured gamma-ray transmission spectra. An evaluation of the sensitivity of CEMS is made in each case, and in addition, the origin of nonresonant and resonant electrons is discussed.

Experimental

For the 8.4-keV $3/2^+ - 1/2^+$ transition in ^{169}Tm , an $^{169}\text{Er}:\text{Al}$ source at ambient temperature was used. The Tm_2O_3 oxide absorber was approximately 2 mg/cm^2 of compound. The 21.53-keV $7/2^+ - 5/2^+$ resonance in ^{151}Eu was investigated using a $^{151}\text{Sm}_2\text{O}_3$ source at ambient temperature. The absorbers consisted of approximately 5 mg/cm^2 of compound.

The transmission spectra and conversion electron spectra were collected simultaneously using the same absorber. The electron detector was of the backscatter type similar in design to that given in Ref. 2 in which the flow gas was He-10% CH_4 . The transmission spectra were collected by placing the appropriate proportional counter at the exit window of the conversion electron detector. The spectra were accumulated in a multichannel analyzer operated in the time mode and synchronized to the sinusoidal motion of the velocity transducer on which the source was mounted.

Results and Discussion

^{151}Eu 21.53-keV Resonance. The resonant absorption of the 21.53-keV gamma ray by ^{151}Eu results in the excitation from the $5/2^+$ nuclear ground state to the $7/2^+$ excited state. The subsequent de-excitation can occur through either the emission of a gamma ray or through the ejection of an electron from one of the inner shells. The probability for electron emission (internal conversion) is approximately 28.6 (3) times that for gamma-ray emission (internal conversion coefficient $\alpha = 28.6$).

The partial internal conversion coefficients for each of the electronic shells have been determined previously (3) for the 21.53-keV transition. As can be seen from Table I, L_I conversion is most probable (71%), producing electrons with a kinetic energy of approximately 13.5 keV. Higher-energy electrons from the M shells are also present. In addition, the filling of the vacancies primarily in the L shells results in either low-energy x-rays or secondary low-energy electrons.

Table I. Partial Internal Conversion Coefficients (3) for the 21.53-keV $7/2^+ \rightarrow 5/2^+$ Transition in $^{151}\text{Eu}^a$

Shell	Binding Energy (keV)	% Conversion	Electron Energy (keV)
K	48.5		
L_I	8.05	71	13.5
L_{II}	7.62	9	13.9
L_{III}	6.98	4	14.6
M_I-M_V	~ 1.40	16	~ 20

^a The total conversion coefficient is $\alpha_T = 28.6$.

All electrons produced in this manner that result from the resonant absorption process constitute the resonant effect in CEMS. All other sources of electrons such as photoelectric absorption of the source gamma rays or those gamma rays resulting from nonresonant re-emission processes in the absorber will contribute to the background. The efficiency or sensitivity of the technique is then determined by the number of resonant electrons that escape the surface of the absorber compared to those arising from nonresonant processes both in the absorber and detector.

An estimate of the thickness of the layer probed by the CEMS technique can be made by considering the range of the conversion electrons in a given compound. It has been shown experimentally (4) that for electrons with a kinetic energy between approximately 5 and 15 keV, the range follows an attenuation law of the form

$$I = I_0 e^{-\mu z}$$

where I_0 is the initial flux and I is the final flux after transversing a distance z in the material. The attenuation coefficient μ , in \AA^{-1} is given by

$$\mu = 4.43 \times 10^{-3} \rho / E^{3/2}$$

where ρ is the density in g/cc of the material and E is the initial kinetic energy of the electron in keV.

For L_I electrons with energy 13.5 keV in europium metal ($\rho = 5.26$ g/cc), the half-thickness is approximately 1500 \AA . The attenuation length for the 21.53-keV gamma ray of ^{151}Eu , on the other hand, is the order of 60 μ . Without considering secondary production of photoelectrons produced by resonantly scattered gamma rays deep inside the material (5), the relative range of gamma rays and conversion electrons indicates that CEMS is sensitive to a relatively thin surface layer of the material.

In Figure 1 we show the conversion electron spectra for three compounds of europium compared to corresponding spectra taken simultaneously in the transmission geometry. For the two trivalent compounds

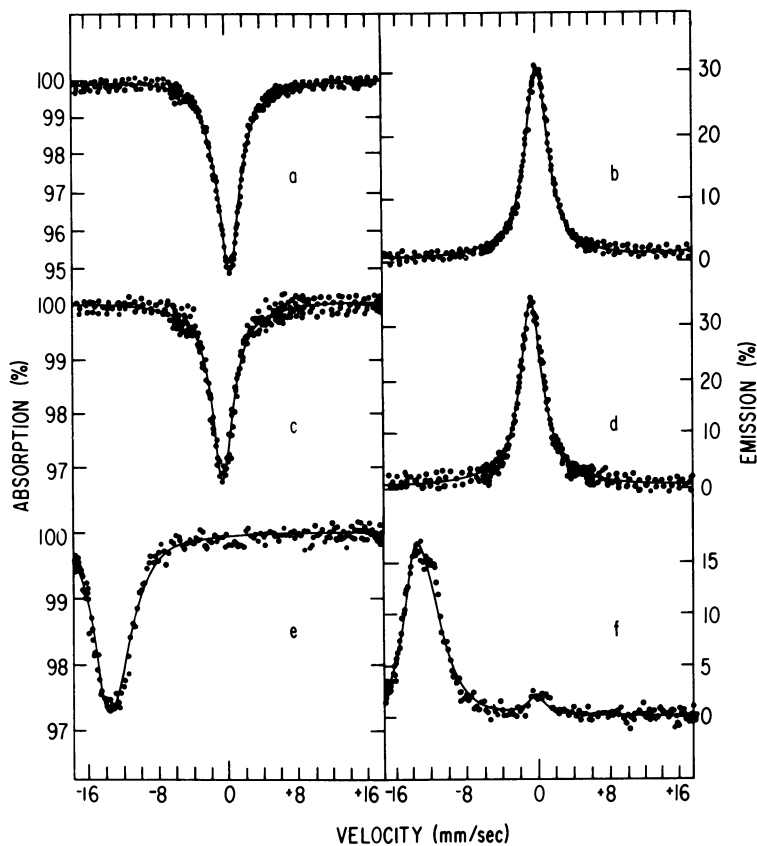


Figure 1. Transmission ^{151}Eu Mössbauer effect spectra at 300 K for (a) Eu_2O_3 , (c) EuF_3 , and (e) Eu_2SiO_4 . The conversion electron spectra also are shown for (b) Eu_2O_3 , (d) EuF_3 , and (f) Eu_2SiO_4 . A $^{151}\text{Sm}_2\text{O}_3$ source was used.

Eu_2O_3 (Figures 1a and b) and EuF_3 (Figures 1c and d) the most striking difference between the conversion electron and gamma-ray transmission spectra in each case is the 6- to 10-fold enhancement of the resonant effect achieved with the CEMS technique. For each compound the resonance widths for the conversion electron and transmission spectra are approximately equal. Consequently, the enhancement of the effect represents an increase in sensitivity without loss of resolution.

For the spectra of divalent compound Eu_2SiO_4 shown in Figures 1e and f, an enhancement of the resonant effect similar to that found for the trivalent compounds is found. In addition, two other differences between the conversion electron and gamma-ray transmission spectra are evident. First of all, a weak resonance at -0.33 ± 0.1 mm/s corresponding to a

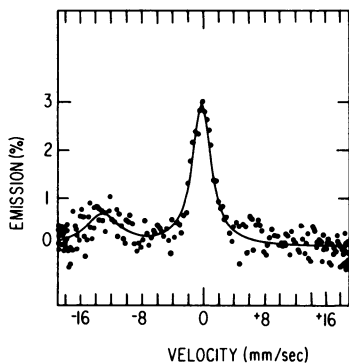


Figure 2. Conversion electron ^{151}Eu Mössbauer spectrum for 170 ppm europium in magnesium

Eu^{3+} species is present in the conversion electron spectrum (Figure 1f) and absent in the transmission one (Figure 1e). Since both spectra have approximately the same signal-to-noise ratio for the main Eu^{2+} resonance, it appears that the Eu^{3+} component arises primarily in the surface layer ($\sim 2000 \text{ \AA}$) probed by CEMS.

The second aspect of the CEMS data for Eu_2SiO_4 is the presence of some structure in the Eu^{2+} resonance which is not apparent in the transmission data. This structure appears to be associated with the presence of a small quadrupole interaction at the Eu^{2+} site. If an axial electric field gradient is assumed, the value of $e^2qQ = -12 \pm 1 \text{ mm/s}$ is obtained from a fit to the data. This value is the same as that determined (6) below the magnetic transition of 9 K for this compound in a transmission geometry. The presence of a quadrupole interaction of this order would account for the asymmetric broadening observed in our transmission data for Eu_2SiO_4 at 300 K. The increased resolution the CEMS data indicated by these results follows from the fact that thickness-broadening effects are minimal for this technique because of the thin layer probed.

A fourth example of ^{151}Eu CEMS that illustrates the sensitivity of the technique is europium-doped magnesium metal. Figure 2 shows the CEMS data at 300 K for 170 ppm europium in magnesium. As can be seen, both a Eu^{2+} species at $-13.0 \pm 0.3 \text{ mm/s}$ and a Eu^{3+} one at $-0.27 \pm 0.1 \text{ mm/s}$ are detected. The total resonant amplitude in the Eu^{3+} resonance is approximately 3%. The range of the L_I 13.5-keV conversion electrons in magnesium is characterized by a half thickness of about 4500 \AA . On the other hand, the half thickness for photoelectric absorption of the 21.53-keV gamma ray is approximately 1.6 mm, indicating a minimal contribution of photoelectrons resulting from the magnesium matrix. This, in turn, facilitates the detection of small quantities of europium in the material. This result demonstrates that under favorable conditions CEMS is capable of detecting small amounts of europium impurities in the surface, such as those realized in implantation experiments ($\sim 10^{18} \text{ atoms/cm}^3$).

^{169}Tm 8.4-keV Resonance. The resonant absorption of the 8.4-keV gamma ray by ^{169}Tm results in the transition from the $1/2^+$ ground to the $3/2^+$ nuclear excited state. The internal conversion coefficient for the decay is large with $\alpha_T = 291$ (7). Table II shows the binding energies for the *K*, *L*, and *M* shells of thulium, and as can be seen, only *M* conversion is possible. The theoretical estimate (8) of the partial conversion coefficients shows that M_I shell conversion is most probable. The kinetic energy of the resultant conversion electrons is approximately 6.1 keV. An estimate of the half thickness for electrons with this energy in thulium metal based on the same empirical relation given earlier results in $z_{1/2} \simeq 250 \text{ \AA}$.

Table II. Estimated Partial Internal Conversion Coefficients (8) for the 8.4-keV $3/2^+ \rightarrow 1/2^+$ Transition in ^{169}Tm ^a

Shell	Binding Energy (keV)	% Conversion	Electron Energy (keV)
<i>K</i>	69.4	—	—
L_I – L_{III}	8.6–10.1	—	—
M_I	2.3	95	6.1
M_{II} – M_V	1.5–2.1	5	~ 6

^a The total conversion coefficient is $\alpha_T = 291$ (7).

This value is nearly a factor of ten smaller than that for ^{151}Eu conversion electrons in europium metal and indicates that a much thinner surface layer is probed with ^{169}Tm CEMS.

One might expect that ^{169}Tm would be a more favorable candidate for CEMS than ^{151}Eu . Both the resonance fraction and the internal conversion coefficient are larger for the 8.4-keV transition in ^{169}Tm than in ^{151}Eu . However, Figure 3 shows that the resonant effect for Tm_2O_3 is smaller for the CEMS data than for the transmission data. This is just the opposite of what was observed for ^{151}Eu . The apparent decrease in resonant effect for ^{169}Tm CEMS is attributable to an increase in the background contribution, associated in part with a large increase in photoelectron production. For thulium metal, for example, the ratio of the resonant absorption cross section of the 8.4-keV gamma ray to that for photoelectric production is approximately six. While this is about four times smaller than that found for ^{151}Eu , it cannot fully account for the severe reduction in the observed intensity in ^{169}Tm CEMS data compared to the transmission data. In addition, the relation used for the half-thickness calculation is perhaps not valid in the 6-keV range, and as a consequence, we may be sampling considerably smaller numbers of resonant atoms. These results on ^{169}Tm CEMS suggest that the technique may be useful only under special circumstances.

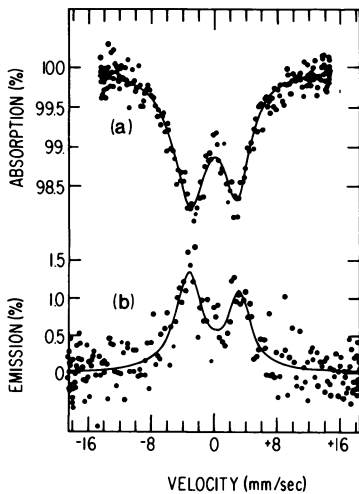


Figure 3. Transmission ^{169}Tm Mössbauer effect spectrum (a) at 300 K compared to the conversion electron spectrum (b) for Tm_2O_3 . An $^{169}\text{Er}:\text{Al}$ source was used.

Acknowledgment

This work was supported by the U.S. Department of Energy.

Literature Cited

1. Tricker, M. J., Chapter 3 in this book.
2. Spijkerman, J. J. "Mössbauer Effect Methodology"; Gruverman, I. J., Ed.; Plenum, 1971; Vol. 7, p. 85.
3. Antman, S.; Petterson, H.; Zehlev, V.; Adam, I., *Z. Physik* 1970, 237, 285.
4. Cosslett, V. G.; Thomas, R. N. *Brit. J. Appl. Phys.* 1964, 15, 883.
5. Tricker, M. J.; Ash, L. A.; Cranshaw, T. E. *Nucl. Inst. Meth.* 1977, 143, 307.
6. Kalvius, G. M.; Shenoy, G. K. *Z. Naturforsch.* 1971, 26a, 353.
7. Aratamonova, K. P.; Voronkov, A. A.; Grigor'ev, E. P.; Zolotavin, A. V. *Izv. Akad. Nauk SSSR, Ser. Fiz.* 1976, 40, 32.
8. Hager, R. S.; Seltzer, E. C. *Nucl. Data* 1968, A4, 1.

RECEIVED June 27, 1980.

Electron Spectrometer for Iron-57 Mössbauer Spectroscopy

T. SHIGEMATSU, H.-D. PFANNES, and W. KEUNE

Laboratorium für Angewandte Physik, Universität Duisburg,
D-4100 Duisburg, West Germany

A commercial electron energy analyzer (150° spherical sector analyzer) was used to detect energetically selected electrons that are emitted after the ^{57}Fe Mössbauer effect. The analyzer entrance aperture has a solid angle of 3.4×10^{-2} sterad, and the accepted sample area is approximately $10 \times 4 \text{ mm}^2$, resulting in a luminosity of about 0.1 mm^2 . For 2% energy resolution, 7.2-keV conversion electrons and KLM-, KLL-, and LXY-Auger electrons of iron have been identified in the electron spectrum of a ^{57}Co source. Detection of 6.6-keV and 7.2-keV electrons (with 2% energy resolution) from enriched α -Fe foils as Mössbauer absorbers resulted in typical α -Fe six-line spectra with up to 300% effect for the outer lines, accompanied, however, by extremely low count rates of the order of 1 count/h/channel. Clear evidence for depth-selective Mössbauer spectra was obtained for a composite sample of 250-Å iron evaporated on a stainless-steel foil.

Conversion electron Mössbauer spectroscopy (CEMS) is a useful technique for studying corrosion and surface metallurgy because of the small penetration depth of low-energy electrons in matter (1). In an extension of CEMS, known as "depth-selective" or energy-differential CEMS, one detects the emerging electrons energy-selectively by means of an electron spectrometer (2). Mössbauer scattering spectra thus are obtained at different electron energies, unlike conventional (integral) CEMS. This technique is especially useful for the investigation of surface properties of solids, since monochromatic electrons are emitted after the Mössbauer excitation, and their energy loss is related to the penetration depth below the surface of the material.

0065-2393/81/0194-0125\$05.00/0
© 1981 American Chemical Society

Krakowski and Miller (3) performed a theoretical analysis of the resonant line shape and the area under a Mössbauer spectrum, and estimated the depth probed by ^{57}Fe energy-differential CEMS. In this calculation, only 7.3-keV K-conversion electrons were considered, and an exponential attenuation law and Fermi age/diffusion theory were assumed. This analysis yielded the relative probability that an emerging electron of measured energy E_K originated from a particular depth below the surface (assuming 2% energy resolution). For conversion electron energies greater than about half of the initial energy of 7.3 keV, a spatial resolution exists that should permit the measurement of Mössbauer spectra from selected regions below the resonator surface. However, an exponential attenuation law for electrons of this energy range may not be valid. Liljequist et al. (4) and Proykova (5) used the Monte Carlo method to compute the total transmission as well as the transmission into various angles and energy intervals of electrons from different depths in a CEMS ^{57}Fe absorber. These results are useful for integral as well as energy-selective CEMS analysis. Bäverstam et al. (6) and Liljequist and Bodlund-Ringström (7) have obtained experimental evidence for depth-selectiveness of CEMS from surface layers on metals.

For the purpose of energy-differential CEMS, several types of electrostatic electron energy analyzers with sufficiently high resolution and luminosity have been constructed recently (8-11), but extensive experimental application of this technique is still lacking. In this investigation we tested a commercial electrostatic analyzer (which usually is used for ESCA or Auger studies) for its applicability to energy-differential ^{57}Fe CEMS.

Experimental

A schematic view of our apparatus is shown in Figure 1. The commercial electron energy analyzer (A) used is a 100-mm mean-radius-of-curvature, 150° spherical sector analyzer fitted with a channeltron electron multiplier detector (C) (manufacturer: Vacuum Generators, Ltd.; Model CLAM 100). Electrons emerging from the specimen (SP) are focused onto the analyzer entrance slit by an electrostatic inlet lens (L) that also acts as a (low-resolution) band pass filter. Electrons entering the analyzer slit are then deviated by the radial electric field within the analyzer, and only electrons with the "correct" pass energy reach the analyzer exit slit and the detector (C). External adjustment of entrance and exit slits (0.5-, 1-, 2-, or 4-mm slit width) allows discrete setting of the energy resolution $\Delta E/E$ (0.25, 0.5, 1.0, or 2.0%, respectively). For a chosen setting $\Delta E/E$ is constant over the entire energy range. Since the workable energy range usually is limited to 2.5 keV in ESCA or Auger experiments, modifications of the usual analyzer and inlet lens control electronics were necessary to allow for electron pass energies suitable for ^{57}Fe K-conversion electrons (7.3 keV), the analyzer itself being essentially unmodified. The maximum pass energy is 10 keV for our instrument. Though the solid angle from the center of the sample (SP) to the entrance aperture of the focusing

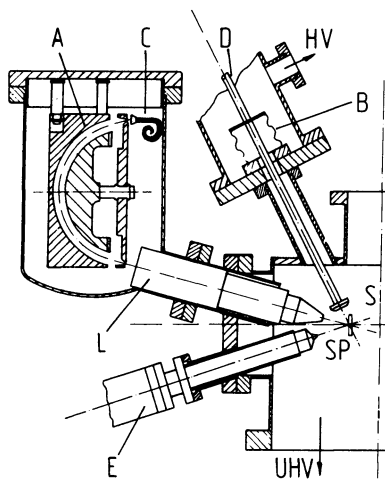


Figure 1. Schematic of the electron spectrometer for CEMS studies: (A) 150° spherical-sector electron analyzer; (C) channeltron detector; (SP) specimen (Mössbauer absorber); (L) electrostatic inlet lens; (S) ^{57}Co Mössbauer source; (B) flexible metal bellows; (E) Auger electron gun; (D) Mössbauer drive rod

lens (L) is only about 0.034 sterad (transmission $\sim 0.27\%$ of 4π), the accepted sample area is relatively large (about $10\text{ mm} \times 4\text{ mm}$). However, the low luminosity (accepted sample area \times transmission) of about 0.1 mm^2 results in very low count rates for CEMS experiments.

The whole assembly is located in a bakeable ultrahigh vacuum system with a base pressure in the 10^{-10} -Torr range or better. To avoid UHV-tight windows for the 14.4-keV Mössbauer radiation, our approximately 40-mCi ^{57}Co source (S) (Rh matrix) was put into the UHV chamber at a distance of 15–20 mm from the sample center and moved in the sine mode by an electromechanical Mössbauer drive system that was located outside of the UHV chamber and connected to the source-carrying drive rod (D) via UHV-tight flexible metal bellows (B). To release these bellows from air pressure, a high-vacuum, tightly closed cylinder surrounded the Mössbauer drive and bellows and was evacuated to approximately 10^{-2} Torr during Mössbauer measurements. The angle between the incident gamma-radiation and the sample normal was about 62° .

The arrangement also permits Auger sample analysis by the analyzer (A) and an Auger electron gun (E) as well as sample depth profiling and cleaning by argon sputtering.

For Mössbauer measurements we used conventional counting electronics consisting of a preamplifier, a main amplifier, and a 512-multichannel analyzer in multiscaling mode. (All Mössbauer spectra shown in the next section are direct (folded) printouts from the multichannel analyzer, and the velocity scale (channel number) is weakly nonlinear due to the sinusoidal velocity mode).

Results and Discussion

To measure the internal conversion and Auger electrons emitted during de-excitation of the 14.4-keV excited state, the ^{57}Co source was first set in place of the specimen. The electron spectrum taken with a constant analyzer resolution $\Delta E/E$ of 2% is shown in Figure 2. We can clearly identify the K-conversion electron peak at 7.2 keV, and KLM-,

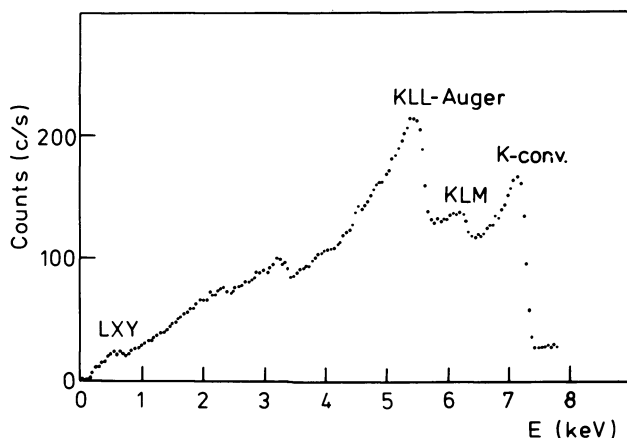


Figure 2. Electron spectrum of the ^{57}Co Mössbauer source (*Rh* matrix) taken with the present spectrometer at constant energy resolution $\Delta E/E = 2\%$

KLL-, and maybe LXY-Auger peaks of iron at 6.2, 5.4, and about 0.6 keV, respectively. The surface of the ^{57}Co containing rhodium foil was not cleaned by electron bombardment or argon sputtering prior to the measurement. Therefore, certainly surface contamination and/or a thin oxide layer existed on the source foil and possibly weakened the LXY-Auger signal by absorbing these low-energy electrons.

Figure 3 shows Mössbauer scattering spectra taken with a 95.2% ^{57}Fe -enriched α -Fe foil (1.9 mg $^{57}\text{Fe}/\text{cm}^2$) as specimen. The electron energy was set to 7.20 keV (*top*) and 6.60 keV (*bottom*), with 2% energy resolution. The 7.2-keV electrons have a much larger probability of originating from a region closer to the surface than 6.6-keV electrons (3). We observe typical six-line α -Fe spectra in each case. The signal-to-noise ratio in these spectra is very good because of the low photoelectron background of the electron spectrometer; for example, typically a 300% effect or more has been observed for the outer α -Fe lines. However, these large effects are compensated for by extremely low count rates of the order of 1 count/h/channel because of the low analyzer luminosity. Comparison of the theoretically estimated count rate for our spectrometer arrangement with the experimental count rate shows that both are of the same order of magnitude. The typical measuring time for a spectrum of Figure 3 was 4 days, using our 40-mCi ^{57}Co source.

The enriched α -Fe foil used for taking the spectra of Figure 3 was *not* surface cleaned by electron or argon ion bombardment prior to the Mössbauer measurements. Auger electron spectra (Figure 4) of this foil indicate iron Auger lines at about 600–700 eV and also oxygen and carbon peaks (at 510 and 272 eV, respectively). We conclude that a

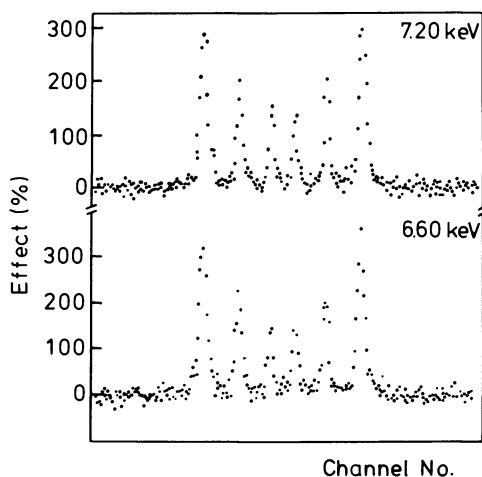


Figure 3. Conversion electron Mössbauer spectra of a 95.2%-enriched α -Fe foil ($1.9 \text{ mg } ^{57}\text{Fe}/\text{cm}^2$) measured with the present system. The energy of the detected electrons was 7.2 keV (top) and 6.6 keV (bottom) at 2% energy resolution (source: 40-mCi ^{57}Co in Rh matrix).

rather thin oxide layer covered our iron sample surface, and that additional contamination (perhaps by hydrocarbons) existed. Figure 3 indicates, however, that such an oxide layer or surface contamination was not detectable by CEMS since only the pure α -Fe pattern could be observed for the 7.2-keV or 6.6-keV energy setting. Obviously the mean free path of 7.3-keV electrons of roughly 100 Å (12) is too large and apparently does not permit a surface sensitivity for a few outermost atomic layers below the sample surface.

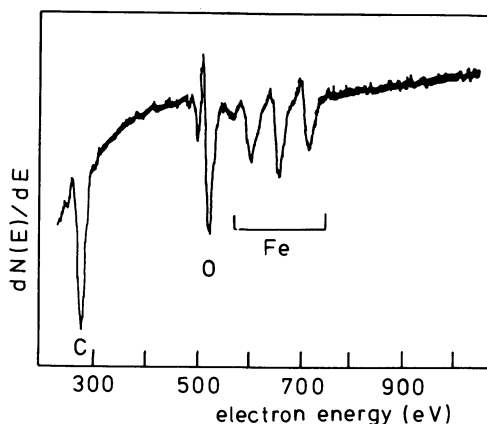


Figure 4. Auger electron spectrum of the surface-contaminated α -Fe foil that was used for taking the Mössbauer spectra of Figure 3

To test the depth-selectiveness of energy-differential CEMS, we made measurements on a layered sample consisting of a 250-Å thick ^{57}Fe film (95% enriched) that was vacuum deposited onto a 90.7%-enriched, 310 stainless-steel foil (1 mg $^{57}\text{Fe}/\text{cm}^2$). (This sample was exposed to air after preparation and prior to the CEMS experiments). Our first results of Mössbauer measurements with 7.2-, 6.9-, and 6.6-keV electron energy setting (at 2% energy resolution) are shown in Figure 5 (from *top* to *bottom*, respectively). Clear experimental evidence for depth selectiveness is found from these spectra. Thus the signal from the 250-Å α -Fe overlayer is clearly enhanced relative to the central stainless-steel peak of the substrate if electrons of higher energy (7.2 keV) are selected. Decreasing the electron energy reduces the α -Fe overlayer signal and enhances the stainless-steel peak; thus at the 6.6-keV electron energy setting the stainless-steel line is dominating and the α -Fe pattern is only barely detectable in Figure 5. No computer evaluation of the area ratios in these preliminary spectra has been performed yet, but an estimate of the relative spectral area for the α -Fe pattern gives roughly (80 ± 5)% at 7.2-keV, (30 ± 3)% at 6.9-keV, and (10 ± 10)% at 6.6-keV electron energy. These values appear to be somewhat lower than theory predicts (7).

In agreement with our former observation no oxide pattern could be found in any spectra in Figure 5, that is, the oxide phase (which certainly is present for our air-exposed sample) is too thin to be detectable even at 7.2-keV electron energy.

We have made an attempt to observe a thin oxide layer by our technique. For this purpose a 90.7% enriched α -Fe foil (1.9 mg $^{57}\text{Fe}/\text{cm}^2$) was annealed at 700°C in hydrogen atmosphere for several hours and subsequently oxidized at 250°C in air for 100 min. CEMS spectra with the oxidized foil at room temperature were recorded at 7.2-keV and 6.6-keV electron energy setting and 2% energy resolution (Figure 6 *top* and *bottom*, respectively). No trace of an oxide phase is detectable with 6.6-keV electrons, but a very weak contribution (roughly 20% effect) of an oxide layer (with a larger hyperfine field than α -Fe) can be found in the spectrum at 7.2-keV electron energy in the vicinity of the outer α -Fe lines (Figure 6, *top*). It is difficult to determine the oxide thickness of our sample exactly, but we can give a rough estimate by considering Figure 3 (*top*) and the magnitude of the 250-Å α -Fe signal ($\sim 200\%$ for the outer α -Fe lines). This leads to an oxide thickness of approximately 50 Å or less, if a homogeneous oxide layer is assumed. This small value is surprising in view of results by conventional CEMS on low-temperature-oxidized electroplated ^{57}Fe films (13). It seems as if a highest-purity (bulk) ^{57}Fe foil oxidizes more slowly at the same temperature than carbon- and defect-containing electroplated ^{57}Fe films.

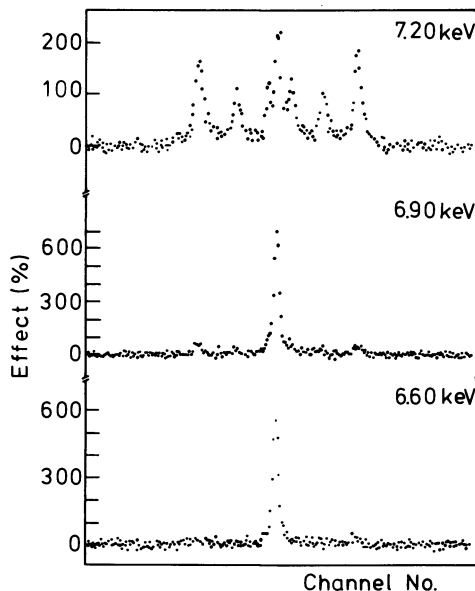


Figure 5. Conversion electron Mössbauer spectra of a 250-Å-thick α -Fe film (95% enriched) vacuum deposited onto a 90.7%-enriched 310 stainless-steel foil ($1.0 \text{ mg } ^{57}\text{Fe}/\text{cm}^2$). The energy of the detected electrons was 7.2 keV (top), 6.9 keV (middle), and 6.6 keV (bottom) at 2% energy resolution (source: 40-mCi ^{57}Co in Rh matrix).

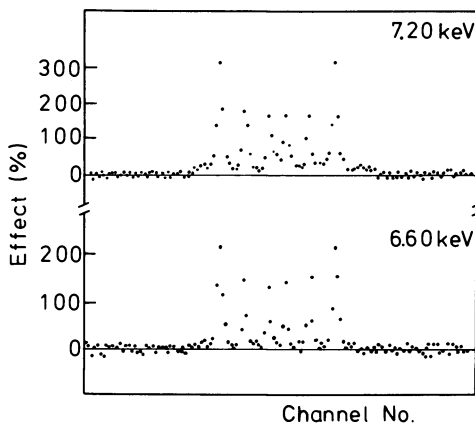


Figure 6. Conversion electron Mössbauer spectra of a 90.7%-enriched α -Fe foil ($1.9 \text{ mg } ^{57}\text{Fe}/\text{cm}^2$) oxidized at 250°C in air for 100 min. The energy of the detected electrons was 7.2 keV (top) and 6.6 keV (bottom) at 2% energy resolution (source: 40-mCi ^{57}Co in Rh matrix).

Conclusion

In this investigation a commercial electrostatic electron analyzer was tested for its applicability to energy-differential CEMS. The electron spectrometer was found to be suitable for such studies, although the relatively small luminosity of the analyzer resulted in low count rates. By using stronger ^{57}Co sources the count-rate problem can be reduced to some extent. Because of the low photoelectron background of the analyzer, large signal-to-noise ratios of several hundred percent have been measured in CEMS spectra of highly enriched iron and stainless-steel samples; therefore, it is possible to measure spectra with reasonable counting statistics within several days for such samples. In preliminary experiments we have obtained clear experimental evidence for depth-selectiveness of the technique. As was demonstrated in a few examples, detection of higher energy electrons (7.2 keV) with 2% energy resolution enhances the surface contribution in the Mössbauer spectra as compared to lower-energy electrons (6.6 keV). It is believed that important new information that is unattainable in conventional (integral) CEMS can be obtained by energy-differential CEMS in such fields as surface metallurgy, corrosion, and ion implantation.

Acknowledgments

The authors are grateful to J. Lauer for preparing the thin-film sample for this study. This work was supported financially by the Deutsche Forschungsgemeinschaft.

Literature Cited

1. Wagner, F. E. *J. Phys.* **1976**, *37*, C6–673.
2. Bonchev, Zw.; Jordanov, A.; Minkova, A. *Nucl. Instrum. Methods* **1969**, *70*, 36.
3. Krakowski, R. A.; Miller, R. B. *Nucl. Instrum. Methods* **1972**, *100*, 93.
4. Liljequist, D.; Ekdahl, T.; Bäverstam, U. *Nucl. Instrum. Methods* **1978**, *155*, 529.
5. Proykova, A. *Nucl. Instrum. Methods* **1979**, *160*, 321.
6. Bäverstam, U.; Ekdahl, T.; Bohm, C.; Liljequist, D.; Ringström, B. *Nucl. Instrum. Methods* **1974**, *118*, 313.
7. Liljequist, D.; Bodlund-Ringström, B. *Nucl. Instrum. Methods* **1979**, *160*, 131.
8. Bäverstam, U.; Bodlund-Ringström, B.; Bohm, C.; Ekdahl, T.; Liljequist, D. *Nucl. Instrum. Methods* **1978**, *154*, 401.
9. Polcari, M. R.; Parellada, J.; Burin, K.; Rothberg, G. M. *Am. Inst. Phys. Conf. Ser.* **1978**, *39*, 584.
10. Benczer-Koller, N.; Kolk, B. *Am. Inst. Phys. Conf. Proc.* **1977**, *38*, 107.
11. Toriyama, T.; Saneyoshi, K.; Hisatake, K. *J. Phys.* **1979**, *40*, C2–14.
12. Ibach, H., Ed. "Electron Spectroscopy for Surface Analysis"; Springer: Berlin–Heidelberg–New York, **1977**; p. 1.
13. Simmons, G. W.; Kellerman, E.; Leidheiser, Jr., H. *Corrosion* **1973**, *29*, 227.

RECEIVED June 27, 1980.

Application of Mössbauer Spectroscopy to Coal Characterization and Utilization

PEDRO A. MONTANO

Department of Physics, West Virginia University, Morgantown, WV 26506

To characterize a coal completely, a careful identification of its mineral matter is necessary. Due to the presence of iron in a large percentage of the minerals appearing in coal, the Mössbauer effect became a very powerful tool to identify iron-bearing minerals. In this chapter we review the applications of Mössbauer spectroscopy in coal research, and list the Mössbauer parameters of the major iron-bearing minerals in United States coals. The use of the Mössbauer effect as a quantitative analytical tool to determine pyritic sulfur is discussed initially, and we find the standard ASTM procedures to be as accurate as the Mössbauer results. We also have used the Mössbauer effect to determine the stoichiometry of the pyrrhotites present in liquefaction residues. There is considerable interest in the study of the transformation of the iron minerals in coal conversion processes, and several examples of such applications of the Mössbauer effect are included.

Existing and projected shortages of natural gas and petroleum products in the United States have created a stimulating environment for extensive research on the use of coal as a major source of electricity and synthetic fuels. Due to its importance as a source of energy and the environmental hazards involved in its use, considerable research has become necessary to understand fully the different compounds appearing in coal and how they transform during processing. The acceptance of a coal for a particular process depends critically on both the organic and inorganic components. A careful identification of the mineral matter is necessary for a complete characterization of a coal. Due to the presence of iron in a large percentage of the minerals appearing in coal, the Möss-

0065-2393/81/0194-0135\$10.25/0

© 1981 American Chemical Society

bauer effect became a useful, and to a certain degree, unique analytical tool in the identification of iron-bearing minerals in coal. Iron-sulfur compounds, although making up a relatively small portion of coal or coal mineral composition, are significant in that they may affect all phases of the coal industry including mining, processing, reclamation, and utilization. For the most part, the influence is deleterious and results in intolerable environmental impacts, namely water and air pollution. However, there are cases such as coal liquefaction where sulfur compounds actually may be beneficial (1, 2, 3). The importance of the iron-sulfur minerals in coal has increased interest in the use of the Mössbauer effect as a quantitative analytical tool to determine the amount of pyritic sulfur (4, 5, 6). We have carried out extensive studies in the classification of iron-bearing minerals in coal and have studied the transformation of the iron-bearing minerals during processing. In the following sections, we review the subject starting with a brief description of coal and a listing of the major iron-bearing minerals it contains.

The transformation of the iron-bearing minerals, especially pyrite, is discussed in the last sections of this chapter. A critical evaluation of the Mössbauer effect as a possible quantitative analytical tool is discussed, and favorable and unfavorable aspects of this technique are considered.

Coal: Organic and Inorganic Components

Coal has a vegetable origin (7, 8). The material from which it is created accumulated in marshes from the remains of plants, in lakes from algae and the remains of animal plankton, or in lagoons from shallow-water organic muds. Three major periods can be distinguished in the formation of coal: The first is the peat period, that is, when plant remains are decomposed and altered, mainly by biochemical processes taking place in the vegetable mass with the help of anaerobic bacteria. In the second period, after the bed is covered, a physicochemical alteration of the plant substance takes place during the diagenesis process; there is an increase in carbon content, a lowering of oxygen, dehydration, and transformation of the peat to lignite. In the last period lignite is converted into higher-rank coal and anthracite as the result of metamorphism.

The minerals that were present in the peat bog can act as catalysts, or can react chemically with the organic material, and their presence is reflected in the properties of the coal (7, 8). Coal is consequently a sedimentary rock consisting of an organic part with added minerals, diagenetic or syngenetic in origin. The composition and properties of a coal are controlled by the original material, the conditions of accumulation, and the method by which the material was converted into coal.

The coal is classified on the basis of fixed carbon and calorific values calculated on a mineral matter-free basis. The higher-rank coals, with a high degree of metamorphism, are classified according to fixed carbon on the dry basis; the lower-rank coals according to calorific value on the moist basis (9). The agglomerating character is used also to differentiate between groups. Table I gives a general classification of the coals (ASTM D388-66).

There are four major lithologic components of coal—vitrain, fusain, and attrital coal (clarain and durain) (10, 11)—and they are not equivalent in their genetic and practical relationships. Vitrain and fusain appear in the coal as lenses and inclusions of limited size; both seem to be homogeneous substances. Fusain resembles char coal and retains a distinctive plant structure. Vitrain appears in shiny black bands; it has a vitreous appearance and its plant origin is more concealed. The attrital coals, clarain and durain, are complex aggregates consisting of a ground mass and preserved portions of plants in any proportion.

The coal macerals are the organic components of coal that are distinguishable by microscopic inspection (10, 11). They are classified in three groups related to the aforementioned lithologic components, namely, vitrinite, exinite, and inertinite. Each of these groups include further subdivisions. The necessity for this petrographic classification is related to the heterogeneous character of coal (see Figures 1 and 2).

From the point of view of a solid-state chemist or physicist, coal is a composite material with organic and inorganic constituents. The carbon structure of coals can be viewed as consisting of hydroaromatic structures with aromaticity increasing from low-rank to high-rank coals (12, 13). The hetero atoms oxygen, nitrogen, and sulfur are associated with the coal in varying amounts. The organic sulfur is distributed throughout the entire coal mass and cannot be separated by concentration; sulfur in rings is the most difficult to remove. Nitrogen in the coal is found to be mainly in ring positions, and consequently, it is difficult to remove for cleaning processes. Oxygen is present in coal in phenolic hydroxyl, open ethers, and ring ethers. In general, lower-rank coals are rich in oxygen. The trace element content in coal is complicated, and many coals can have more than 60 trace elements in varying amounts.

From the point of view of the Mössbauer spectroscopist, the inorganic constituents of coal are of central importance. No evidence has been found of any detectable amount of iron associated with the organic part of coal. Consequently, in any Mössbauer study of coal only the mineral matter is analyzed. A certain amount of mineral grains and clay material is always present in coal (7, 8, 14, 15). The minerals are usually clays (kaolinite, illite, mixed layer clays, etc.), sulfides (pyrite, marcasite,

Table I. Classification

	<i>Fixed Carbon Limits (% DMf)</i>	
	<i>Equal or Greater Than</i>	<i>Less Than</i>
Anthracitic		
Meta-Anthracite	98	—
Anthracite	92	98
Semianthracite	86	92
Bituminous		
Low-volatile bituminous coal	78	86
Medium-volatile bituminous coal	69	78
High-volatile A bituminous coal	—	69
High-volatile B bituminous coal	—	—
High-volatile C bituminous coal	—	—
Subbituminous		
Subbituminous A coal	—	—
Subbituminous B coal	—	—
Subbituminous C coal	—	—
Lignite		
Lignite A	—	
Lignite B	—	



Figure 1. *Thin section of a coal. The majority of the sample is vitrinite; light spots are sphoronite and dark spots are attrital (courtesy of W. C. Grady Coal Research Bureau, West Virginia University).*

of Coals by Rank

<i>Volatile Matter Limits (%)</i>		<i>Caloric Value Limits BTU Per Pound (Moist Mineral-Matter-Free Basis)</i>	
<i>Greater Than</i>	<i>Equal or Less Than</i>	<i>Equal or Greater Than</i>	<i>Less Than</i>
—	2	—	—
2	8	—	—
8	14	—	—
14	22	—	—
22	31	—	—
31	—	14 000	—
—	—	13 000	14 000
—	—	11 500	13 000
—	—	10 500	11 500
—	—	10 500	11 500
—	—	9 500	10 500
—	—	8 300	9 500
—	—	6 300	8 300
—	—	—	6 300

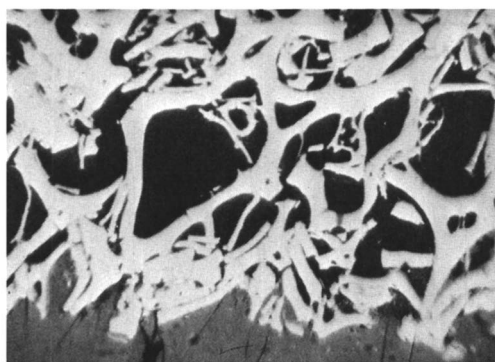


Figure 2. *Photomicrograph of fusinite. Most cell walls are broken and collapsed. (Courtesy of W. C. Grady Coal Research Bureau, West Virginia University.)*

sphalerite, galena, etc.), carbonates (like calcite, ankerite, siderite, dolomite), quartz, and other minerals in lesser amounts like rutile, hematite feldspar, etc. The amount, character, and distribution of the mineral matter in the coal greatly influence the physical properties. The clay minerals, pyrite, and calcite are the main mineral substances (15). They came into the coal seam by infiltration in the course of accumulation of the peat. The clay was brought to the swamp by running water, and the sulfides and calcite were formed in the coal joints and cavities. The origin of finely disseminated pyrite probably can be attributed to the activity of sulfur-forming bacteria. Large pyrite lenses in the coal are due to the deposition of iron sulfides when the hydrogen sulfide obtained from the decomposition of plant material interacts with iron compounds dissolved in the swamp water. Coal lying near the surface can contain clay, hydrated ferric oxide, and ferrous carbonates or sulfates brought by percolating surface waters and deposited in cracks of the coal seam. The presence of sulfates in the coal is almost a definite indication of weathering.

Iron-Bearing Minerals in Coal

Iron Sulfides. The major group of iron-sulfur compounds in coal is the disulfide group consisting of pyrite and marcasite. Of the two, pyrite is the most abundant. Pyrite and marcasite can be identified readily by x-ray diffraction (XRD), but because pyrite is usually dominant in any particular coal, the two dimorphs usually are considered collectively as pyrite.

A significant characteristic of pyrite in coal is the fact that it occurs in various morphological forms (16). Generally pyrite falls into two major classes. The first class consists of framboids, independent euhedral crystals and aggregates of euhedral crystals (syngenetic pyrite). The second class consists of the massive occurrences, dendritic, irregular, and cleat fillings, usually greater than 100 μ in mean diameter.

Of all the minerals in coal, pyrite is probably the most deleterious in the coal industry. It is the source of acid mine drainage (17), and the major source of SO₂ pollution in the combustion process. However, pyrite may have a beneficial effect as a potential catalyst in coal liquefaction processes (1, 2, 3, 18, 19).

Pyrite, FeS₂, is a cubic crystal that can be considered as an NaCl-like grouping of iron atoms and S₂ pairs. It has four molecules in a cell (20), with a lattice constant equal to 5.40667 Å and space group symmetry T_h. The iron in FeS₂ experiences a slightly distorted octahedral symmetry. In pyrite the iron ion is in the low-spin configuration iron(II). The six *d*-electrons are occupying the T_{2g} ground state and no magnetic moment

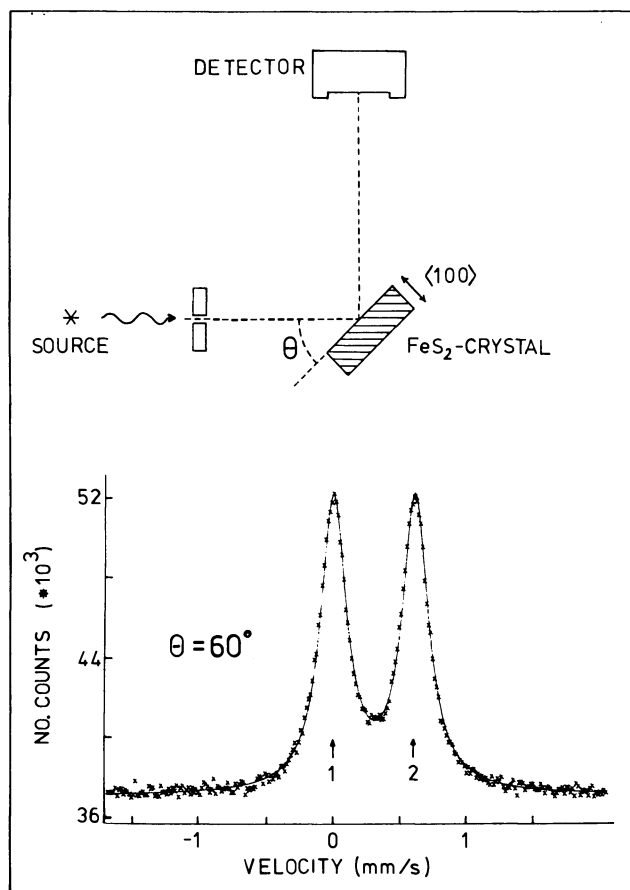


Figure 3. Scattering Mössbauer spectrum of a single crystal of pyrite. (Courtesy of Guettinger and Williamson.)

is present at the iron site (21). In Figure 3, the Mössbauer spectrum of a single crystal of pyrite is shown. Guettinger and Williamson (28) have found that the relative intensities of the two Mössbauer transitions in pyrite are equal and independent of the single-crystal orientation (Figure 3). The values of the Mössbauer parameters for FeS_2 are given in Table II. The temperature dependence of the center shift is probably due completely to the second-order Doppler shift.

The magnetic and electric properties of pyrite depend strongly on the presence of impurities in the crystals. Magnetic susceptibility measurements are sensitive to the presence of magnetic impurities on the sample; very small amounts, for example, of CoS_2 or NiS_2 will change appreciably the value of the susceptibility (23). Pyrite is a semiconductor with a zero-temperature band gap (24) of about 0.84 eV.

Table II. Iron Sulfides (Isomer Shifts with Respect to α -Iron)

	<i>IS (mm/s)</i>	<i>QS (mm/s)</i>	<i>MHF (kOe)</i>	<i>Ref.</i>
<i>Pyrite (FeS₂)</i>	0.31 ± 0.01	0.61 ± 0.01	0	
<i>Marcasite (FeS₂)</i>	0.25 ± 0.01	0.56 ± 0.01	—	
<i>Greigite (Fe₃S₄)</i>	0.70	0.3	322	(28)
	0.40 (<i>T</i> = 4.2 K)	0	486	
	0.45	0.4	465	
<i>Amorphous Fe₂S₃</i>	0.35 ± 0.06	0.82 ± 0.06	253 (4.2 K)	(102)
	0.51 ± 0.12	0.88 ± 0.12		
<i>Sphalerite (ZnFe)S</i>	0.66	0.80		
<i>(FeS) synthetic</i>	0.81	−0.32	315 (RT)	
<i>Troilite (FeS) natural</i>	0.86	−0.28	310 (RT)	(32)
<i>Fe₇S₈ (pyrrhotite monoclinic)</i>	0.69 ± 0.08	0.18 ± 0.15	307 ± 8	(32)
	0.64 ± 0.10	0.31 ± 0.15	255 ± 10 (RT)	
	0.64 ± 0.10	0.30 ± 0.15	225 ± 10	
<i>Fe_{0.881}S</i>		0.31 ± 0.03	305 ± 3	(33)
		0.43 ± 0.04	224 ± 3	
		0.31 ± 0.04	253 ± 4	
<i>Fe_{0.909}S</i>		0.23 ± 0.0	302 ± 10	(33)
		0.00 ± 0.1	274 ± 10	
		0.30 ± 0.1	256 ± 10	
		0	0	
<i>Mackinawite (Fe_{1+x}S, x = 0.04–0.07)</i>	0.2 (4.2 K)			(28)

The second modification of FeS₂ is the orthorhombic mineral marcasite (20); it has a bimolecular unit of dimensions $a = 4.436$ Å, $b = 5.414$ Å, and $c = 3.381$ Å. Marcasite has a slightly different isomer shift (IS) and quadrupole splitting (QS) (Table II). A typical spectrum of a marcasite single crystal is shown in Figure 4. When the amount of marcasite in coal is more than 20% of the total iron disulfide content, its detection using Mössbauer spectroscopy is possible. However, XRD and petrographical techniques seem to be more appropriate for its identification.

Thin films of pyrite prepared by evaporation and deposited on a substrate at room temperature (25) have been studied by Mössbauer and Auger spectroscopies (they consist of microcrystallites of FeS₂). When the substrate is at a temperature of 78 K or lower, FeS₂ tends to condense in an amorphous form with slightly different Mössbauer parameters (26).

While studying several coal macerals, a new Mössbauer spectrum associated with pyrite was observed in three different samples rich in framboidal pyrite (26). The extra Mössbauer doublet showed the same

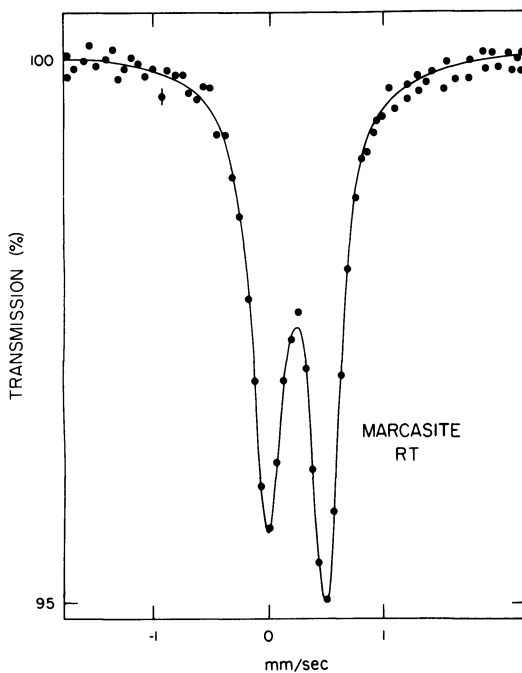


Figure 4. Mössbauer spectrum of a thin single crystal of marcasite at room temperature

magnetic behavior as pyrite (low spin). However, its Mössbauer parameters were different and the isomer shift suggests a smaller electronic density at the nucleus than for FeS_2 , similar to amorphous FeS_2 . The spectrum also may be produced by small particles of Fe_3S_4 . It is to be noted that the spectra observed for these coal macerals were exceptions, and no similar spectra were detected in any other sample (27). Consequently, it is suspected that this is a rare compound in coal.

We have not observed any other iron-bearing sulfides in our study of fresh coals by Mössbauer spectroscopy. Fe_{1-x}S was detected in some heavily weathered coals (27), and the presence of monoclinic pyrrhotite in coal can be inferred in some cases from the magnetic properties. Other minerals like sphalerite, mackinawite, greigite, smythite, chalcocopyrite, troilite, and arsenopyrite were not detectable. Some of these minerals may be detected more easily using scanning electron microscopy (SEM).

Clay Minerals. The clay minerals represent a large percentage of the inorganic matter in coal (15, 34). The principal minerals in clays are layer-lattice silicates (phyllosilicates), except for those of the Palygorskite–Sepiolite group which are chain silicates (35). The crystal structures

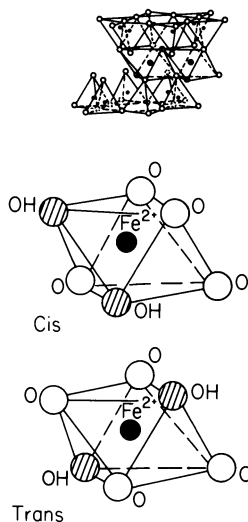


Figure 5. Structure typical of the clay minerals (the drawing represents montmorillonite) ((O) oxygen; (⊕) OH; (●) aluminum, iron, magnesium; (•) silicon)

of layered clays are based on two types of sheets. A tetrahedral sheet typically made of SiO_4 units, and an octahedral sheet typically made of $\text{Al}(\text{O}, \text{OH})_6$ units. In the 1:1 group of minerals, the basic layer is composed of one tetrahedral and one octahedral sheet connected by the oxygens at the apices of the tetrahedra (see Figure 5), giving two ligands around each aluminum cation; the remaining ligands are hydroxyl ions. The layers are electrically neutral and held together by van der Waals forces. Any mineral where only two-thirds of the octahedral positions are occupied by Al^{3+} cations is called dioctahedral. If all the octahedral sites are filled, the mineral is termed trioctahedral. A typical 1:1 dioctahedral mineral is kaolinite, with a chemical composition of $2\text{SiO}_2 \cdot \text{Al}_2\text{O}_3 \cdot 2\text{H}_2\text{O}$ per unit cell. The water in kaolinite exists as hydroxyl groups (36, 37). Kaolinite is identified in coal by XRD. The amount of iron cation substitution is very small, and its identification is sometimes difficult due to surface contamination of the clay grains with iron oxides, principally goethite (38, 39). In very well-characterized kaolinites there is evidence of small amounts of substitutional ferric iron in the lattice (40). The Mössbauer parameters for this ferric iron are given in Table III. At low temperatures and in the presence of an external magnetic field the typical magnetic hyperfine field of Fe^{3+} is observed. Kaolinite was present in all the coal samples we studied, and only XRD and SEM could be used for its identification. Other minerals in the kaolinite group are dickite, nacrite, halloysite, and disordered kaolinite. The trioctahedral members of the kaolinite group are the serpentines. They are very diverse due to variations of order and disorder in the stacking of the layer $(\text{OH})_4\text{Mg}_3\text{Si}_2\text{O}_5$, which is the magnesium homeotype of kaolinite. There are many

Table III. Clay Mineral (Isomer Shifts with Respect to α -Iron)

Name	T	IS (mm/s)	QS (mm/s)	MHF (kOe)	Ref.
Kaolinite	RT	0.36 \pm 0.03	0.50 \pm 0.03	505 \pm 5 (4.2 K)	(39)
				$H_{\text{ex}} = 30$ kOe	
Chamosite	RT	0.38 \pm 0.04	0.78 \pm 0.08		
		1.14 \pm 0.02	2.57 \pm 0.08		
Chlorite	RT	0.17 \pm 0.06	0.78 \pm 0.08		*
		1.13 \pm 0.01	2.67 \pm 0.06		
Talc	RT	1.33 \pm 0.01	2.82 \pm 0.02	505 \pm 5 kOe	*
				25 kOe	
Vermiculite	RT	1.13 \pm 0.03	2.63 \pm 0.03	$(H_{\text{ext}} = 20$ kOe)	*
		0.45 \pm 0.05	0.48 \pm 0.05		
Muskovite	RT	1.07 \pm 0.07	2.58 \pm 0.07		*
		0.37 \pm 0.05	0.75 \pm 0.08		
Glauconite	RT	1.17 \pm 0.03	3.08 \pm 0.07		(39)
		1.00 \pm 0.10	2.66 \pm 0.12		
Nontronite	RT	0.36 \pm 0.05	0.52 \pm 0.12		(103)
		0.38 \pm 0.03	1.21 \pm 0.05		
Montmorillonite	RT	1.14 \pm 0.06	2.30 \pm 0.06		(103)
		0.36 \pm 0.02	0.62 \pm 0.06		
Fayalite	RT	0.38 \pm 0.08	0.50 \pm 0.13		(39)
		1.15 \pm 0.06	2.81 \pm 0.06		
Biotite, annite	RT	1.17 \pm 0.06	2.85 \pm 0.08		(103)
		0.99 \pm 0.07	1.72 \pm 0.10		
Phlogopite	RT	0.47 \pm 0.08	0.52 \pm 0.18		(104)
		0.47 \pm 0.06	0.96 \pm 0.20		
Illite	RT	1.11 \pm 0.05	2.62 \pm 0.08		(103)
		1.09 \pm 0.05	2.18 \pm 0.10		
Illite No. 36 (Morris)	RT	0.52 \pm 0.08	1.05 \pm 0.12	0	*
		0.19 \pm 0.02	0.47 \pm 0.03		
Illite No. 35 (Fhitian)	RT	1.20 \pm 0.10	2.70 \pm 0.20	0	*
		1.10 \pm 0.08	2.40 \pm 0.20		
Illite Coal	RT	0.33 \pm 0.02	0.65 \pm 0.05	0	*
		0.38 \pm 0.04	1.21 \pm 0.08		
Antigorite	RT	1.14 \pm 0.01	2.75 \pm 0.02	0	(105)
		0.34 \pm 0.02	0.43 \pm 0.04		
Antigorite	RT	1.24 \pm 0.05	2.60 \pm 0.06	0	*
		1.27 \pm 0.03	1.92 \pm 0.04		
Antigorite	RT	0.28 \pm 0.06	0.60 \pm 0.08	0	*
		(FeS ₂ ?)			
Antigorite	RT	1.14 \pm 0.07	2.77 \pm 0.07	20–30	*
		1.25 \pm 0.08	2.54 \pm 0.08		
Antigorite	RT	1.10–1.20	2.6–2.8	15	*
Antigorite	RT	1.16 \pm 0.02	2.74 \pm 0.04	4.2 K	(105)
				$H_{\text{ext}} = 30$ kOe	

* The author.

other homeotypes of kaolinite, like chamosite (berthiérine) and aluminiferous silicate and cronstedtite, but they are usually rare in coal.

The minerals belonging to the 2:1 layer structure present a great variety of arrangements. Basically they have an octahedral layer between two tetrahedral layers (35, 36). Four of the ligands around Al^{3+} in the octahedral layer are oxygen and two are hydroxyl ions. The hydroxyls may be at opposite (trans, M1) or adjacent (cis, M2) corners of the octahedron (36, 39). Considerable cation substitution takes place (i.e., iron and magnesium replacement of aluminum), giving a great diversity of structures to these clays.

The mica group of minerals is of great importance because of its abundance in coal. In the micas only three out of every four tetrahedra of the tetrahedral layer are occupied by silicon; the fourth tetrahedron is occupied by aluminum. This produces a deficit of charge for the sheet filled by large ions, generally potassium, that occur between the layers. The bonding due to the potassium is weak enough to allow an easy cleavage of micas. Mineralogically, micas are classified as muscovite (37), a dioctahedral mineral of composition $\text{K Al}_2(\text{Al Si}_3\text{O}_{10})$, or as biotite (37), a trioctahedral mineral of composition $\text{K}(\text{Mg,Fe})_3\text{O}_{10}(\text{OH})_2$. In the muscovite group of minerals there is a large variety of cation replacement. There are several polytypes of muscovite (36), and they have been designated as 1M, 2M₁, 2M₂, and 3T, for one-layer monoclinic muscovite, two kinds of two-layer monoclinic muscovite, and three-layer trigonal muscovite, respectively. Iron can substitute in the octahedral sheet in the ferric or ferrous form, and occasionally in the tetrahedral site. The possibility of oxides coating the micas always should be considered when studying their Mössbauer spectra (39, 40, 41).

A very important clay belonging to the mica group is illite. Illite is a term designated for the mica in soils, unconsolidated sediments, and sedimentary rocks (35, 37). The chemical composition is similar to muscovite but with less than one silicon out of four replaced by aluminum, resulting in a proportionate diminution of K^+ . A partial replacement of the aluminum octahedral ions by Mg, Fe^{2+} , and Fe^{3+} ions is frequent. The 1M and 2M structures are found in illite, which gives a great diversity of compositions. The illites contain any or all muscovite polytypes, and most illites are mixed-layer structures. The total amount of iron is generally small (15). Illites are mainly identified by XRD (15), since the Mössbauer spectra have a great variability, and it is impossible to assign a particular Mössbauer pattern to illite (26, 39, 42, 43). XRD and SEM observations are necessary before any Mössbauer parameter values can be assigned to a particular Mössbauer pattern.

Another difficulty associated with the illites is the smaller amount of iron present in the structure as compared, for example, to chlorite. A Mössbauer spectrum of an illite (Fhitian) from Illinois is shown in Figure

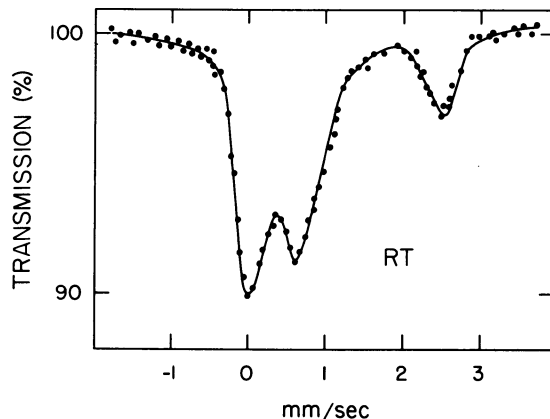


Figure 6. Mössbauer spectrum of a Fhitan illite (some FeS_2 is present)

6. This spectrum cannot be considered typical of all illites but only of this particular sample. In general, there is a great variability of values for the quadrupole splitting and isomer shifts of the illites (39). Some of the iron in illite identified as Fe^{3+} can be low-spin Fe^{2+} , substitutional, or in some cases, pyrite contamination of the clay. In the study of pure clays, one should try to eliminate interfering factors such as oxides and pyrite by using the prescribed treatments given in the literature (38, 39). A typical Mössbauer spectrum of a coal containing illite at room temperature (RT) is shown in Figure 7a with a sample of a Pocahontas coal. The spectrum at low temperatures and with an external field indicates

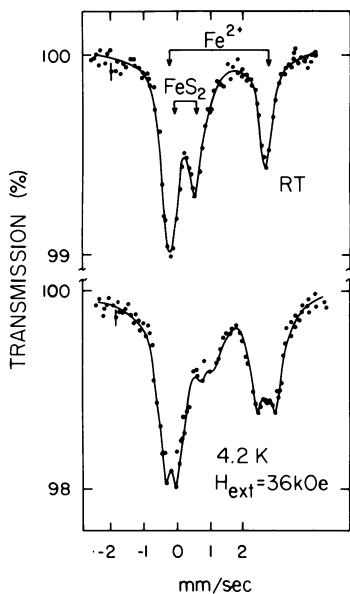


Figure 7. (top) Mössbauer spectrum of a Pocahontas coal (West Virginia) at room temperature. FeS_2 and illite are present. (bottom) Mössbauer spectrum at 4.2 K in the presence of an external magnetic field (36 kOe) parallel to the gamma ray.

the presence of only Fe^{2+} (Figure 7b). In general, the illites appearing in coal show slightly different Mössbauer parameters than other illites (27). A striking result of all our measurements is the observation of very small amounts of Fe^{3+} in any of the coals studied (more than 200). In general, with very few exceptions (heavily weathered coals), divalent iron is the dominant valence state in coal (27).

The montmorillonite group of minerals consists of clay minerals in which the component layers are not tightly bonded by K^+ or Mg^{2+} ions, but contain water molecules instead (35, 37). They are capable of intercalating a large variety of guest molecules between their negatively charged layers. Such minerals are also called smectites. Isomorphous substitution occurs either in the octahedral or tetrahedral layer. The structure of the montmorillonites is similar to mica, except for the interlayer substitution of K^+ ions. Their crystallographic parameters are variable. Most of the montmorillonites are dioctahedral, but hectorite, stevensite, saunonite, and saponite are trioctahedral. The iron in the montmorillonites is predominantly ferric, but Fe^{2+} also appears in their Mössbauer spectra (39).

The minerals classified as chlorites are trioctahedral phyllosilicates with a 2:1 layer structure. They are rich in iron and consequently their Mössbauer spectrum is easily recorded. The general formula for the chlorite group (35, 37) is $(\text{Mg,Fe,Al})_6(\text{Al,Si})_4\text{O}_{10}(\text{OH})_8$. A great variety of these minerals exists because of the numerous isomorphous replacements of cations. It should be noted that chlorites fall into iron chlorites, intermediate, and magnesium chlorites. The structure of chlorite consists of talc and brucite layers stacked in various ways to form polytypes. For true chlorites the basal spacing is fixed at about 14 Å. Mössbauer spectra of chlorites are very similar to those of talc (39). The linewidth is narrow and the M1 and M2 sites are indistinguishable. Substitution of Fe^{2+} in the brucite layer has not been observed. In Figure 8a, a Mössbauer spectrum of an iron-rich chlorite is shown at 4.2 K in the absence of a magnetic field; in Figure 8b the sample is subject to an external magnetic field of 20kOe at 4.2 K. From the Mössbauer spectrum at low temperature and in the presence of an external field it is possible to differentiate chlorite from illite. The Mössbauer parameters for the spectra in Figure 8 are given in Table III. One can also observe the presence of a small amount of Fe^{3+} . The ground state of Fe^{2+} is an orbital singlet, something that has been observed for all clays studied in our laboratory. A way of eliminating chlorite from the coal samples in order to detect other clays is to treat the sample with warm 1N HCl; the less-ordered chlorites will dissolve easily. There is an expandable type of chlorite in which the incomplete brucite sheet forms pillars between the mica layers (35). A dioctahedral chlorite has been identified in soil

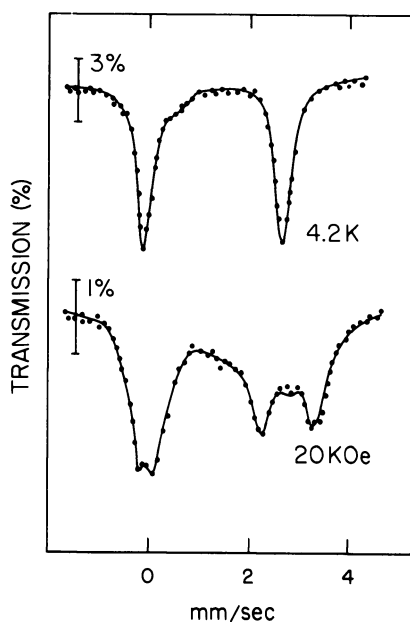


Figure 8. (top) Iron-rich chlorite at 4.2 K (divalent iron is dominant); (bottom) the same sample in the presence of an external magnetic field (20 kOe) parallel to the gamma ray

derived from muscovite schist in Virginia and in British Columbia (37). The vermiculite group of minerals resembles heated mica that has the appearance of little worms (35). The structural formula is $(\text{OH})_2(\text{Mg, Fe})_3(\text{Si}_{4-x}\text{Al}_x)\text{O}_{10}(\text{Mg, Ca})_{x/2}$. The vermiculite of soils and sediments is dioctahedral as well as trioctahedral. In the vermiculites the bonding between layers is weaker than in micas and chlorites, but stronger than in montmorillonites. There is not enough Mössbauer work in the literature on well-characterized vermiculites, and their Mössbauer parameters remain unclear.

Clay minerals also appear in nature as mixed-layer clays consisting of interstratified layers of different minerals. There are three types of mixed-layer structures: (1) regular layers of different types alternate according to a specific law; (2) irregular layers randomly interstratified; and (3) layers segregated within one crystallite into zones of regular and irregular. Mixed-layer clays are quite common in coals (15, 34) and their identification using Mössbauer spectroscopy is very difficult because of the tremendous variability of compositions. XRD and SEM are probably the only techniques that can give some insight on the mixed-clay constituent in coal (15, 34). The usual method utilized to identify and quantify the clay minerals in coal is XRD of the low-temperature ashes (LTA), but due to the poor crystallinity of the clays in the coal, the technique is not very reliable for quantification. The Mössbauer effect is not much of an improvement due to the variability of iron content of

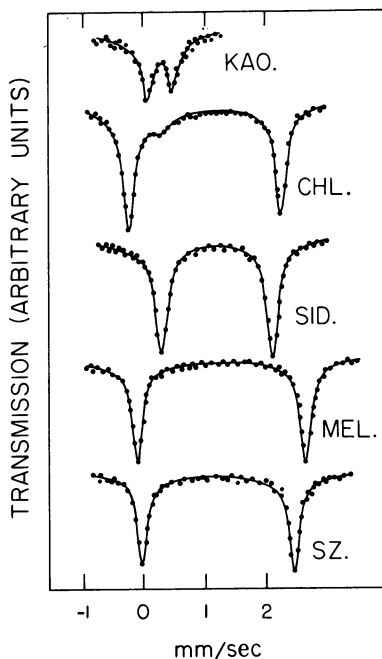


Figure 9. Mössbauer spectra for different iron-bearing minerals in coal at room temperature ((Kao) kaolinite; (CHL) chlorite; (SiD) siderite; (Mel) melanterite; (Sz) szomolnokite)

the clays. Moreover, the qualitative identification of the clays in coal may be affected by the similarities in their spectra, and by the presence of szomolnokite. In Figure 9, a series of spectra of different minerals shows the difficulties involved in identifying the iron species in the coal. Weathering of the coal results in the appearance of iron sulfates; these sulfates can be dissolved in a mild HCl solution (if chlorite is present, it will be partially dissolved). The remaining minerals can be identified by their Mössbauer parameters, compared with well-defined standards. Treating the coal with HNO_3 will dissolve pyrite, giving illite and kaolinite (partial alteration of illite can occur due to the acid treatment). In general, it is recommended to carry out measurements at low temperatures and in the presence of an external field in order to resolve the different iron species in the coal samples. In Figure 10 we show a Mössbauer spectrum of a Waynesburg coal with two different Fe^{2+} sites and pyrite. In Figure 11 the same sample is shown at 4.2 K—one of the Fe^{2+} sites has a well-defined magnetic hyperfine splitting characteristic of szomolnokite (26). (Partial dehydration of $\text{FeSO}_4 \cdot \text{H}_2\text{O}$ to FeSO_4 took place and this sulfate is also found.) The other Fe^{2+} was identified as coal illite.

Carbonate Minerals. The major carbonates in coal are calcite (CaCO_3), siderite (FeCO_3), ankerite [$\text{Ca}(\text{Fe}, \text{Mg}, \text{Mn})(\text{CaCO}_3)_2$], and dolomite [$\text{CaMg}(\text{CO}_3)_2$]. From these carbonates only siderite and

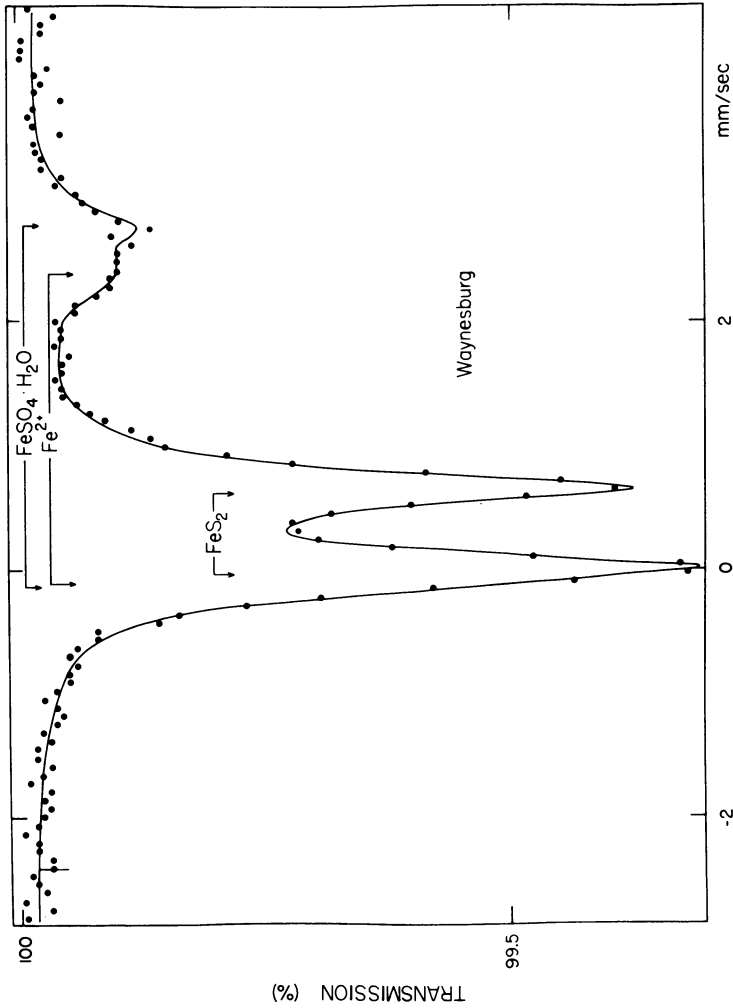


Figure 10. Mössbauer spectrum of a Waynesburg coal at room temperature. Pyrite, szomolnokite, and illite are present.

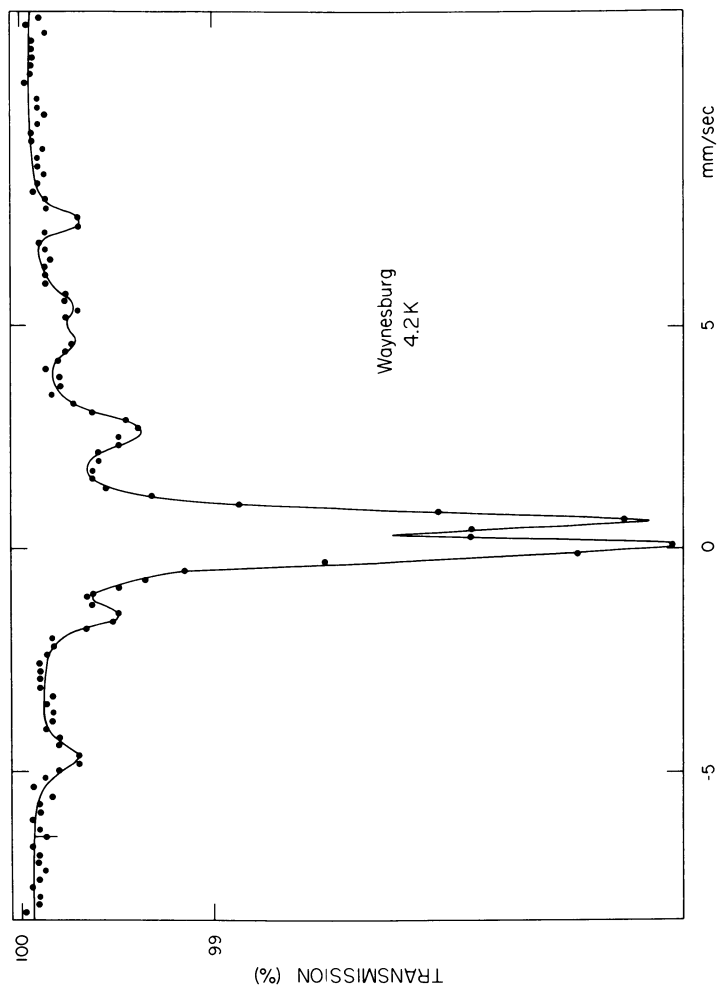


Figure 11. Mössbauer spectrum of the same Waynesburg coal as in Figure 10 at 4.2 K

ankerite are of importance to the Mössbauer spectroscopist. Siderite can appear in coal as nodules and lenticular masses (44). Siderite is associated with the groundmass of the coal and rarely fills in the residues of cell cavities in plant tissues. The presence of siderite in bright clarain coals is evidence of its formation in quiet, anaerobic media rich in CO_2 . Siderite and pyrite usually do not occur together in significant amounts in coal. Ankerite and calcite can occur as veins and in cellular structures (45).

In several coal samples we have observed the presence of siderite or ankerite. The identification of siderite by Mössbauer data is relatively simple since many of these data are available on well-characterized samples (46–49). Siderite has a rhombohedral structure with an octahedron of oxygens around the iron and a small trigonal distortion along the *c*-axis. Neutron diffraction measurements have established that the magnetic moments of Fe^{2+} are pointing along the trigonal axis below T_N (50). The electronic ground state of FeCO_3 is an orbital doublet. Siderite is magnetically ordered at low temperatures ($T_N = 38$ K) with a very distinctive Mössbauer spectrum (46, 48) ($QS = 2.06$ mm/s, magnetic hyperfine field $+ 184$ kOe, and $IS = 1.36$ mm/s). The Mössbauer parameters at room temperature (49) are $QS = 1.798$ mm/s and $IS = 1.24$ mm/s. Ankerite also appears in some coals, and it is difficult to distinguish between ankerite and siderite at room temperature. However, low-temperature measurements allow a clear distinction between the two minerals.

Sulfates. The presence of sulfates in coal is almost always an indication of weathering. The following iron sulfate minerals are associated with coals: szomolnokite ($\text{FeSO}_4 \cdot \text{H}_2\text{O}$), rozenite ($\text{FeSO}_4 \cdot 4\text{H}_2\text{O}$), melanterite ($\text{FeSO}_4 \cdot 7\text{H}_2\text{O}$), coquimbite ($\text{Fe}_2(\text{SO}_4)_3 \cdot X \text{H}_2\text{O}$), roemerite ($\text{FeSO}_4 \cdot \text{Fe}_2(\text{SO}_4)_3 \cdot 12\text{H}_2\text{O}$), and jarosites ($(\text{Na,Fe})\text{Fe}_3(\text{SO}_4)_2(\text{OH})_6$). Melanterite dehydrates to rozenite and rozenite dehydrates to szomolnokite. Some of the sulfate minerals have been reported to form by fixing a portion of the organic sulfur in the LTA (51). Another common sulfate mineral is gypsum (CaSO_4). This last mineral can be produced by the interaction of water with calcite in the presence of iron sulfates (15). The anhydrous ferrous sulfate can be observed in Mössbauer spectroscopy when measurements are carried under vacuum (4). We have detected the presence of ferrous and ferric sulfates in many of the coals we studied (4, 26, 27, 52). In Figure 10, a Mössbauer spectrum of a Waynesburg coal containing szomolnokite can be seen. In general, only very fresh coal will be free of iron sulfates. The amounts of iron sulfates in the coal can be very small, but their contribution to the Mössbauer effect is comparable to that of iron impurities in the clays.

Ferrous sulfate is an orthorhombic crystal with a tetramolecular unit cell. Each Fe^{2+} ion is surrounded by six oxygen atoms occupying the

Table IV. Mössbauer Parameters of the Iron Sulfates

	$T[K]$	IS	QS	MHF (kOe)	Ref.
		(mm/s) ^a	(mm/s)		
$FeSO_4$	RT	1.28 (2)	2.90	185	(27, 53)
	4.7	1.39 (4)	3.64 (4)		(27, 53)
$FeSO_4 \cdot H_2O$	RT	1.18 (2)	2.69 (3)	359	(26, 27)
	78.0	1.33 (3)	3.07 (3)		(26)
	20.0	1.45 (3)	3.09 (3)		(26)
	4.2				(26)
$FeSO_4 \cdot 4H_2O$	RT	1.32 (4)	3.17		(55)
$FeSO_4 \cdot 7H_2O$	RT	1.31	3.20		(55)
	5	3.384	1.391		(63)
$Fe_2(SO_4)_3 \cdot xH_2O$	RT	0.39 (3)	0.60 (5)	550	(58, 59)
				(4.2 K)	
Jarosite	RT	0.43 (2)	1.1–1.2	470–480	(60, 61)
				(4.2 K)	

^a Isomer shifts relative to α -iron.

vertices of a distorted octahedron (53) with a Neel temperature of 21 K. The Mössbauer parameters of $FeSO_4$ are given in Table IV. The most commonly observed ferrous sulfate in coal is szomolnokite, $FeSO_4 \cdot H_2O$. The crystal is monoclinic with four molecules per unit cell (54). Each iron atom has six oxygen neighbors, four of which belong to sulfate ions and the other two to water molecules. This results in a slightly reduced crystal field as compared to the anhydrous case (55). Szomolnokite is antiferromagnetically ordered below 15 K (26). The Mössbauer parameters of szomolnokite are given in Table IV. It is noted that the detection of szomolnokite by Mössbauer spectroscopy (52) is more sensitive than by XRD. Also, observations of sulfates by XRD are carried out on LTA, and in many cases some of the ferrous and ferric sulfates are produced in the ashing process (4, 27).

Rozenite is a monoclinic crystal with four molecular units per unit cell (56, 57). The Fe^{2+} ions are surrounded by a distorted octahedra formed by water and O^{2-} ions. The Mössbauer parameters of rozenite are easily distinguishable from those of $FeSO_4 \cdot H_2O$. No magnetic hyperfine field is observable at 4.2 K (Table IV). Melanterite contains four molecules per unit cell and Mössbauer parameters are given in four molecules per unit cell and is rare in coal; Mössbauer parameters are given in Table IV. The ferric sulfate coquimbite has not been carefully studied by Mössbauer spectroscopy. There are reliable parameters only for the anhydrous phase (58, 59) (Table IV); the isomer shift and magnetic hyperfine field at low temperatures seem to be independent of the amount of water of hydration. However, the quadrupole splitting is highly sensitive to the amount of water of hydration; to identify

coquimbite completely, XRD measurements might become necessary. A number of jarosites of general formula $MFe_3(OH)_6(SO_4)_2$ ($M = Na^+$, K^+ , NH_4^+ , H_3O^+ , $\frac{1}{2}Pb^{2+}$) have been studied (60, 61); they are antiferromagnetically ordered below 60 K (Table IV).

A word of caution concerning the presence of trivalent sulfates in the coal is appropriate here. In general, these sulfates have lines that overlap with the Mössbauer pyrite lines. The result is the detection of a slightly asymmetric pyrite spectrum. If one treats the samples with HCl it will appear as if some of the pyrite has dissolved. Of course this is not true, and is instead the result of the presence of the iron sulfates. The ferric sulfates are easily distinguishable from pyrite when measurements are carried out at low temperatures in the presence of an external magnetic field.

Iron Oxides and Other Minerals. Iron oxides are rare in coal and will appear mainly on heavily weathered coal (27, 34). Small crystals of hematite and magnetite in coal have been observed by SEM, but their total concentration in fresh coal is negligible (62). However, in coal refuse and exposed coals, iron oxides are quite common, and hematite and goethite are detectable in such cases. In general, the identification of iron oxides in the Mössbauer spectrum of a coal should be taken as a result of bad sampling. Other minerals in coal, such as quartz (15, 34), do not contain iron and consequently are undetectable by Mössbauer spectroscopy.

Mössbauer Spectroscopy as a Quantitative Method for Pyritic Sulfur Determination

An accurate knowledge about the amount of sulfur present in a coal is important when selecting it for further utilization, be it combustion, gasification, or liquefaction. Due to the resurgence of coal as a major energy resource, considerable attention has been drawn lately to the standard method of sulfur determination (ASTM D2492-68). The total sulfur in coal is subdivided into its component parts: inorganic and organic, and the inorganic is subdivided further into pyrites and sulfates. The method of differentiation is based on selective solvent leaching. The sulfate sulfur is determined by extracting a weighed sample of coal with dilute HCl; sulfate sulfur is soluble in dilute HCl, pyritic and organic forms of sulfur are not. The pyritic sulfur is determined by extracting a weighed sample of coal with dilute HNO_3 followed by iron determination in the extract (ASTM D2492). A major criticism of the ASTM method is based on problems associated with the coal particle size—in the standard method coal is ground to 60 mesh (250 μm). However, there is no reason why it can not be ground to smaller particle size (this is

actually a common practice in many coal research laboratories). If the particle size is very small or much smaller than the average coal particle, some of the pyrite particles can be totally encapsulated by the coal matrix. Several authors have suggested that this might be a source of error in the pyritic sulfur determination (5). To solve this problem, the Mössbauer effect has been suggested as an alternative method for determining the pyritic sulfur. Considerable controversy exists in the literature on this point, and some very respected coal researchers suggest that the technique is basically sound (65) when applied correctly, and gives as good a value as can be expected due to the natural mineral distribution in a coal seam.

For several years we have been conducting pyritic sulfur analyses in our laboratory, both by Mössbauer spectroscopy and the standard method (in collaboration with the West Virginia Geological Survey). We have found considerable agreement in our studies whenever the same sample was analyzed by both methods (4, 66). Only in a very small number of cases was there some disagreement between the two techniques.

The following paragraphs describe the procedures used in our laboratories for pyritic sulfur determination. A critical review of alternative methods is discussed as well.

Mössbauer Parameters. The quantity measured by Mössbauer spectroscopy is the amount of ^{57}Fe in the coal. To find this quantity several factors should be considered. First, one has to have a good knowledge of the values of the Debye–Waller factors of the Mössbauer source used and the pyrite. Both can be measured in independent experiments. One should record the total gamma-ray spectrum going through the sample and determine the amount of nonresonant (nonMöss-

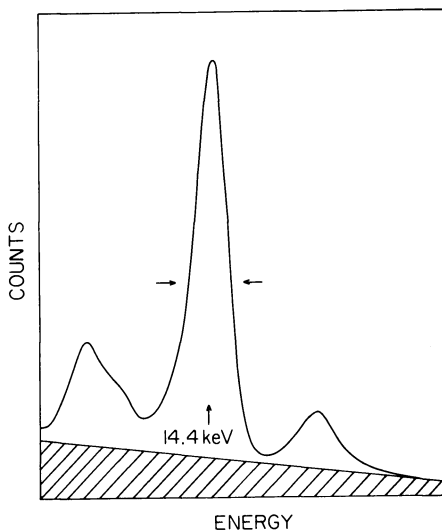


Figure 12. Pulse height spectrum through a thin coal sample (60 mg/cm²). Dashed area is radiation due to scattering of the 122- and 136-keV gamma rays (source ^{57}Co : Pd, 50 mCi).

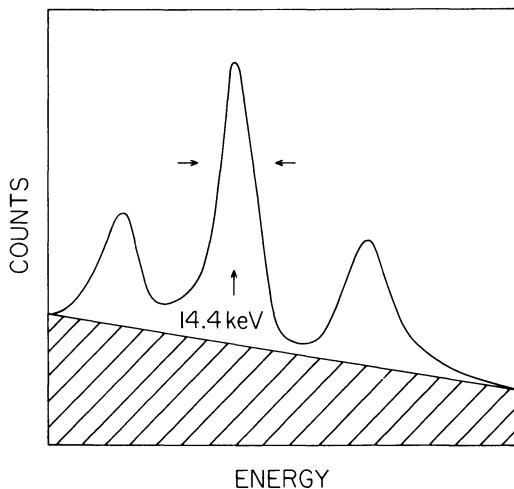


Figure 13. Pulse height spectrum through a thick coal sample (400 mg/cm²). Dashed area is radiation due to scattering of the 122- and 136-keV gamma rays (source ⁵⁷Co: Pd, 50 mCi).

bauer) radiation accurately. The background varies greatly from sample to sample due to the variability in the total mineral content of coals. We have observed variations among different samples as large as 10 to 40%. In Figures 12 and 13 we show the gamma-ray spectra for two different coal samples (50 mCi ⁵⁷Co: Pd source). One notices the large difference in background contributions, mainly due to Compton scattering of the higher energy gamma-rays emitted by the source and the overlap of x-ray peaks with the Mössbauer radiation. In strong sources pile-up effects have to be considered even when the resolution of the detector is high. In summary, for any quantitative measurement a very careful analysis of the background is necessary to avoid mistakes in interpreting the results.

After the background correction is known one has to find the Debye-Waller factors of the source and the absorber (FeS₂). We have determined the Debye-Waller factor of the source using the black absorber technique (67). Several methods were used to determine the Debye-Waller factor of pyrite. A simple method is based on the temperature dependence of this factor. For temperatures where $hw_{\max} \leq 2\pi k_B T$ one can use the Thirring expansion to describe the Debye-Waller factor (68, 69), obtaining for the isotropic case:

$$-\ln f(T) = \frac{E_\gamma}{mc^2} \langle (hw)^{-2} \rangle T + \frac{1}{12} \left(\frac{\hbar}{k_B} \right)^2 T^{-1} - \frac{1}{720} \left(\frac{\hbar}{k_B} \right)^4 \langle w^2 \rangle T^{-3} + \dots \quad (1)$$

where E_γ is the Mössbauer transition energy, \hbar is the Planck constant divided by 2π , k_B is the Boltzmann constant, m is the mass of the Mössbauer atom, and $\langle w^n \rangle$ are the moments of the frequency spectrum given by

$$\langle w^n \rangle = \int_0^\infty g(w) w^n dw \quad (2)$$

where $g(w)$ is the density of the vibrational modes. Each term in Equation 1 may be described by an effective weighed Debye temperature (69)

$$\theta_D(n) = \frac{\hbar}{k_B} [1/3(n+3) \langle w^n \rangle]^{1/n} \quad (3)$$

Using this method, we determined a Debye–Waller factor for pyrite of 0.64 ± 0.04 at room temperature. We also used the effective Debye temperature approach to fit the temperature dependence of the Debye–Waller factor of pyrite (pure and in coal) (4) between room temperature and 78 K. We find a value for the Debye–Waller factor at room temperature of 0.60 ± 0.04 . In a recent publication, a Debye temperature of 610 K was reported for pyrite, based on the analysis of the second-order Doppler shift (SODS) using a Debye model (70). However, comparisons between the expansions for $\ln f$ and $\langle v^2 \rangle$ show the different weights with which high- or low-frequency features determine their temperature dependence (71). The Debye–Waller factor is sensitive to the low frequencies and the SODS to the high frequencies in the phonon spectrum. The effective Debye temperature derived from the SODS will be larger than the one obtained from the Debye–Waller–factor temperature dependence.

In view of the possibility of introducing errors in our evaluation of the Debye–Waller factor of pyrite due to model dependence, we decided to carry our measurements on single crystals of known thicknesses. As a result of those measurements, we obtained a value of $f_{\text{FeS}_2} = 0.58 \pm 0.03$, in good agreement with our former measurements. A value of $f_{\text{FeS}_2} = 0.6$ is used in all of our evaluations of pyritic sulfur using the Mössbauer effect.

Application to Well-Characterized Coals. The sample selected for Mössbauer measurements should be as large as possible, and homogenization of the sample is necessary before measurements are undertaken. The recommended procedures for sampling of the coal should be followed (ASTM procedure D2013-72). The samples should be stored under inert atmosphere or vacuum to avoid weathering. Typical coal samples in our studies are around 300 mg/cm². Several samples should be run, and the

angle between the sample and the gamma-ray direction should be varied to detect any possible inhomogeneity in the distribution of pyrite. In principle, if the pyrite particle size is very large, uncertainties in the pyritic sulfur determination can be appreciable. In all of our coal studies, no evidence of particle size effects was detected. We used the spectral area to determine the amount of ^{57}Fe in the sample. A justification of this method follows in the next section.

Overlap effects due to other iron-bearing minerals are significant, especially if ferric sulfates are present. The Mössbauer spectrum of ferric sulfates usually overlaps with pyrite, which is certainly the reason why some of the pyrite determined by Mössbauer measurements seems to be "soluble" in HCl (5). Care must be taken to treat the samples with HCl prior to the measurements to eliminate the effect of sulfates. In the case of clays, the overlap effect cannot be removed by HCl leaching (except for chlorite). However, by carrying our measurements at low temperatures in the presence of an external magnetic field one can easily distinguish all the iron-bearing minerals in the sample. In our studies, we have not been able to distinguish between pyrite and marcasite, and pyritic sulfur determination includes both types. The error introduced in the evaluation will be related to differences in Debye-Waller factors between the two dimorphs of FeS_2 . Using the intensity for evaluation purposes introduces large errors in the pyritic sulfur determination because the effect of marcasite will be to broaden lines, due to its slightly different isomer shift and quadrupole splitting.

In all of our studies a petrographical analysis of the sample usually was available so that the presence of marcasite could be detected. If marcasite is dominant (a rare case), it will be reflected in a Mössbauer spectrum with an isomer shift more negative than that of pure pyrite. A petrographic examination of the sample is necessary to determine the amount of marcasite by point counting. If marcasite is abundant, XRD will easily detect its presence. In Figure 14, the pyritic sulfur Mössbauer

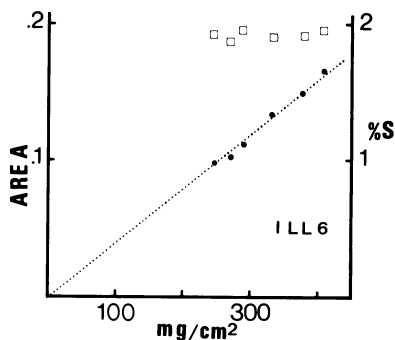


Figure 14. Mössbauer spectral area vs. sample thickness for an Illinois No. 6 coal: (●) the spectral areas, (□) the pyritic sulfur as determined by Mössbauer spectroscopy (scale to the right of the figure). ASTM determination gives a value of 1.95% pyritic sulfur (78).

determination is shown for samples of different thickness (ILL #6). We found excellent agreement between our method and the standard chemical procedures.

During our studies of pyritic sulfur in coal, we selected a few samples where the pyrite was present mainly as euhedral crystals and framboids. The particle size was small and some of the pyrite crystals were encapsulated by the organic matter. When carrying our Mössbauer measurements on 60-mesh samples, we found considerable disagreement with the standard method. However, by working with 220-mesh samples or low-temperature ashes, the agreement between Mössbauer pyritic sulfur determination and the standard method was restored (66).

Spectral Area vs. Mössbauer Absorption Intensity. We consider the spectral area the most sensitive and reliable parameter for determining the amount of ^{57}Fe . The intensity (amplitude of the Mössbauer peak) is not reliable enough because it depends on the linewidth. A broader Mössbauer line will give a smaller intensity without really implying a smaller amount of ^{57}Fe . The spectral area is independent of the source line shape and instrumental velocity resolution. With increasing absorber thickness the spectral area saturates less rapidly than the intensity of Mössbauer peak intensity. The presence of both marcasite and pyrite in a sample will produce a broader Mössbauer line. Consequently, any analysis of the Mössbauer intensity will be erroneous.

The intensity of the Mössbauer absorption is given by (72)

$$N(0) = f_s [-1 - \exp \{-\frac{1}{2} t_a\} I_0(\frac{1}{2} i t_a)] \quad (4)$$

where $I_0(i t_a/2)$ is a zero-order Bessel function of imaginary argument; $t_a = n f_a \sigma_0$, where n is the number of Mössbauer nuclei per cm^2 , σ_0 is the absorption cross section at resonance, and f_a is the Debye-Waller factor of the absorber.

The Mössbauer spectral area has been calculated by several authors using series expansions (73) on t_a or Bessel functions of imaginary argument; both representations are equivalent. We will use the approach of Bykov and Pham Zuy Xien (74) in the following discussion. For a single absorption line the spectral area is given by

$$A = \pi \frac{\Gamma_0}{2} f_s t_a \exp \{-\frac{1}{2} t_a\} [I_0(\frac{1}{2} i t_a) + I_1(\frac{1}{2} i t_a)] \quad (5)$$

where Γ_0 is the natural linewidth, f_s the Debye-Waller factor of the source, and I_1 the first-order Bessel function with imaginary argument.

In the case of pyrite, the Mössbauer spectrum shows a characteristic quadrupole splitting, slightly larger than twice the linewidth. Pyrite is an isotropic crystal, and polarization effects are not important. The total spectral area for the Mössbauer doublet is given, according to Ref. 74, by

$$A = \frac{\Gamma_0}{2} \pi f_s \left\{ K(t_{1a}) + K(t_{2a}) - \frac{K(t_{1a})K(t_{2a})\chi(t_{1a}, t_{2a})}{[\chi(t_{1a}, t_{2a})]^2 + \Delta^2} \right\} \quad (6)$$

Here $t_{ia} = \beta_i t_a$, where β_i is the relative intensity of the i th component, and Δ is the energy difference between the two Mössbauer peaks in units of $\Gamma_0/2$;

$$K(\lambda) \equiv \lambda e^{-\lambda/2} \left[I_0 \left(\frac{\lambda}{2} \right) + I_1 \left(\frac{\lambda}{2} \right) \right]$$

$$\chi(t_{1a}, t_{2a}) = \frac{K(t_{1a})K(t_{2a})}{K(t_{1a}) + K(t_{2a}) - K(t_{1a} + t_{2a})} \quad (7)$$

In our case t_{1a} is equal to t_{2a} . Equation 6 for the spectral area becomes equal to twice the spectral area of one line (as given by Equation 5), only in the limit that $t_a \rightarrow 0$. In coal samples rich in pyrite t_a can have values larger than one, and the error in estimating the amount of ^{57}Fe due to neglect of the overlapping effect becomes significant. In Figure 15, the spectral area vs. thickness (t_a) is shown for pyrite, and the increased discrepancy in values obtained from using Equations 5 or 6 is easily observed. It is to be noted that this effect is even more marked if one is measuring the absorption amplitude. The mathematical expression for the amplitude as a function of t_a becomes extremely cumbersome (74). In pyrite-rich samples it becomes practically impossible to obtain any reliable value for the ^{57}Fe from the Mössbauer intensity.

Quo Vadis? The use of Mössbauer spectroscopy as a quantitative technique in the past has not been very successful. Perhaps the use of the Mössbauer effect to determine the amount of pyritic iron in coal

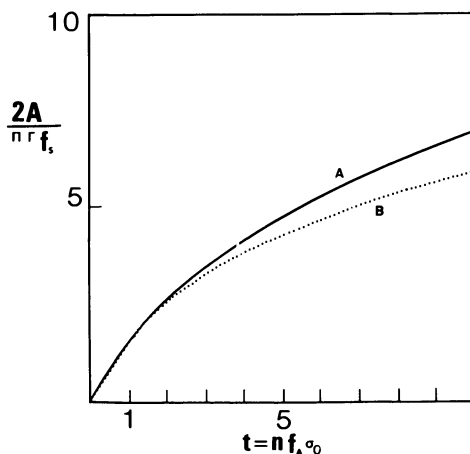


Figure 15. Mössbauer spectral area for pyrite vs. thickness ($t_a = n\sigma_0 f_a$): (A) neglecting overlapping effects; (B) taking the overlapping of the lines into consideration.

represents an exception in what can be considered otherwise as a road covered by failures. Several researchers have suggested recently the use of this technique for pyritic sulfur determination in coal (4, 5, 6). Huffman and Huggins (6) use a standard sample for obtaining the pyritic sulfur. The major shortcoming of their method is the neglect of the nonresonant background. They compensate for it by using an effective Debye-Waller factor of 0.48, smaller than in pyrite. Different approaches have been tried by other authors (76). In some cases the amplitude of the Mössbauer absorption has been suggested as the measurable parameter for determining the amount of pyritic sulfur (77). This approach will render many incorrect results due to overlap and saturation problems. In our laboratory we have used the spectral area and have determined background correction for all samples; in general, a good agreement between the standard ASTM technique and the Mössbauer results has been found. Huggins and Huffman have carried out a comparison of three different techniques for evaluating the pyritic sulfur using the Mössbauer effect (78). In Figure 16 we have plotted their results. The standard deviations from the three techniques when compared to the ASTM value are as follows: Levinson and Jacobs' method $\sigma = 0.12$; Huggins and Huffman's $\sigma = 0.086$; Montano's $\sigma = 0.071$. One can observe that, except for Levinson and Jacobs' method the values of the pyritic sulfur as determined by Mössbauer spectroscopy and the ASTM technique agree fairly well. If we evaluate all the measurements in our laboratory, the agreement is even better. Consequently, it seems unjustifiable to use the Mössbauer effect as a substitute for the standard method. We firmly believe that all of the experimental results indicate that the ASTM method is basically sound. Only in some special cases might there be problems. The standard technique allows use of smaller particle size, and in case of doubt, the use of LTA will give the pyritic sulfur correctly (65). Is there then a future for Mössbauer spectroscopy as a quantitative tool in coal research? Possibly, as a quick method to determine pyritic sulfur

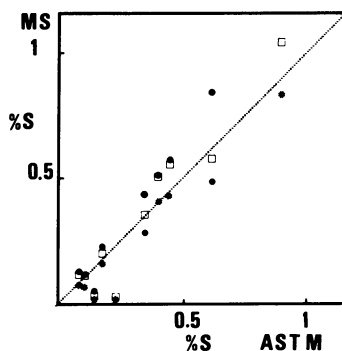


Figure 16. Comparison of pyritic sulfur determinations using three different methods taken from Ref. 75. All the measurements are from Huffman and Huggins. ((●) calculated using Levinson and Jacobs method (5); (□) Huffman and Huggins methods; and (•) Montano's method.)

at coal processing plants or at the mining site. In such cases accuracies of 20 to 30% in pyritic sulfur determination may be permissible. The development of a simple spectrometer to be operated by a nonspecialist is feasible as long as accuracy is not a constraint. This is an area where further work is necessary.

The use of Mössbauer spectroscopy to determine absolute amounts of other iron-bearing minerals in coal is in our opinion not a realistic approach. It is possible to use it as a semiquantitative tool but not for absolute measurements. For pyritic sulfur evaluation the Mössbauer effect will play only a complementary role to the standard (ASTM D 2492) method.

Coal Utilization

Coal can be utilized in many ways—the most common is its direct use as a combustible for steam production. Other uses are related to the iron and steel industry, and to the production of synthetic fuels (gasification and liquefaction). In the following sections a brief discussion of the various utilization schemes of coal are presented.

Combustion. The most common use of coal is in direct combustion—the coal is burned to produce steam which is expanded in a turbine to generate electricity. One of the major problems facing this direct utilization of coal is associated with pollution of the environment. One method of reducing pollution from coal is to clean it prior to its use in a boiler. The cleaning process primarily gets rid of the sulfur, and there are great economic and environmental incentives for doing so. Of all the minerals in coal, pyrite is without a doubt the most deleterious in coal burning. It is one of the major sources of SO₂ pollution of the atmosphere. Several methods exist for cleaning the pyrite prior to the utilization of the coal. Three of these methods are the Hazen Magnex process, the Mayer's process (acid leach, TRW), and an oxidative desulfurization process (air leach PETC). The Mössbauer effect has been applied in some of these methods to study the transformations of pyrite during the cleaning process (77, 79).

After burning the coal, the residual ashes contain α -Fe₂O₃ (end product of the oxidation of FeS₂, siderite, and sulfates) and ferrous and ferric glass phases produced by the clays in the coal. Figure 17 shows a typical Mössbauer spectrum of a coal ash (Pittsburgh coal); the only phase appearing in the spectrum is α -Fe₂O₃. The coal has only FeS₂ and szomolnokite as detectable iron-bearing minerals.

Another major environmental problem related to coal utilization is associated with mining techniques. In the mining and reclamation phases of the coal industry, pyrite (or marcasite) is generally accepted as the

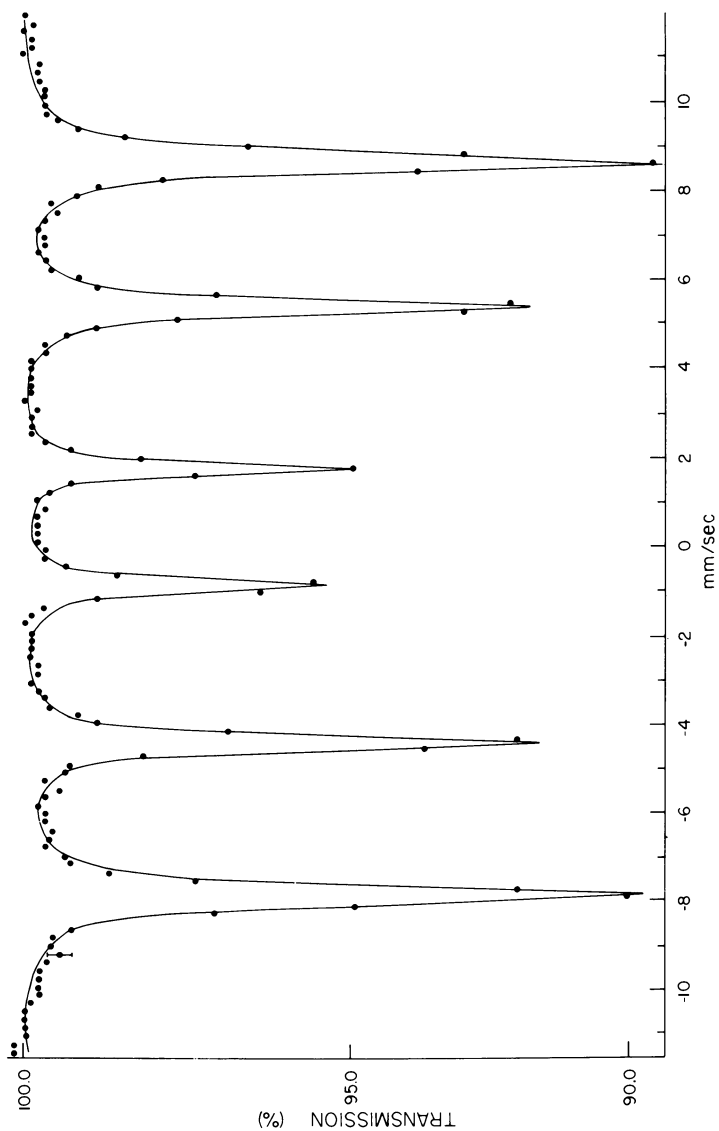


Figure 17. High-temperature ash of a Pittsburgh seam coal

precursor for acid formation. When coal and the associated strata are exposed to the atmosphere, the iron disulfides are oxidized to a series of hydrous iron sulfates which subsequently dissolve in water and produce the acid-mine drainage. However, one of the major problems involved in predicting acid-mine drainage is the lack of correlation between the amount of iron disulfides present in the coal and associated rocks and the resulting amount of acid (34). The evaluation of the acid-producing capabilities of a particular rock section must also take into consideration the neutralizing effect of any calcareous overburden involved in the mining. It seems that biological factors (acidophilic chemoautotrophic bacteria) play an important role in the oxidation of pyrite. Baker (80) has used the Mössbauer effect to study surface reactions on pyrite in the presence of a mixture of chemoautotrophic (*Ferrobacillus ferrooxidans*, *Ferrobacillus sulfooxidans*, and *Thiobacillus thiooxidans*). He observed the presence of ferric sulfate on the surface of pyrite. The Mössbauer effect also was used to study a pyrite lens from a Waynesburg coal (52). This pyrite lens was of interest because about one-third of its surface was covered with a white mineral crust not present on the other two-thirds. The lens was divided into reactive (encrusted) and nonreactive (nonencrusted) portions. A careful chemical and Mössbauer study of these samples revealed a larger percent of pyrite (6.21%) for the non-reactive than for the reactive (2.68%). The presence of szomolnokite in the reactive part was detected by Mössbauer spectroscopy, but escaped detection by other techniques (XRD, SEM). Thus, Mössbauer spectroscopy showed considerable success in identifying the concentration of the acid-mine-drainage producer where other methods failed.

Coke. Coke is a key ingredient in the production of iron and steel (81, 82). The transformation of coal to coke is a chemical and physical process on which much of the world's modern steel industry depends. Coke is basically produced by exposing a properly chosen and prepared coal or blend of coals to sufficiently high temperatures for a long period of time in the absence of air. In the heating process volatile tars and gases are released from the coal; if the coal has the right coking characteristics, a relatively solid structure consisting of carbon and ash is produced. Not much is known about the process taking place during coking. This lack of fundamental knowledge has now become a critical problem. The properties of the coal determine whether it can be used for coking. It is known, for example, that heavily weathered coal is not useful, and the number of coals good for coking is rather limited. The presence of iron minerals in coal allows for the use of Mössbauer spectroscopy to study the transformation of these minerals during high-temperature carbonization. To our knowledge the only Mössbauer study of cokes is the one by Huffman and Huggins (6, 75). They studied

several cokes produced from different coals and were able to detect the presence of iron sulfides (troilite and Fe_{1-x}S), hematite, magnetite, α -iron, and the characteristic ferrous glass spectrum due to the transformations of the clays. Other phases were also observed but not identified. A lot of necessary information is still lacking with respect to the transformation of the iron-bearing minerals during coking; for example, the relation of this transformation to the properties of the coke. This is an area of research where considerable application of Mössbauer spectroscopy can be expected.

Coal Gasification. The total gasification process can be divided into two main reaction stages, coal gasification and char gasification (83). During the coal gasification stage, up to 50% of the original coal mass can be gasified. After this stage is completed, the remaining coal char is much less reactive. The overall process is endothermic; extra heat to sustain it is obtained from combustion of the char with oxygen and increased catalytic methanation, all of which contribute to decrease the thermal efficiency. Catalytic effects must be taken into consideration, even if catalysts are not added to the coal since the mineral matter and trace elements present can have strong catalytic effects on the gasification process (84, 85).

One important aspect of coal gasification is related to the use of the synthesis gas to produce fuels and chemicals (86). The syngas (mixtures of H_2 and CO) is cleaned, catalytically shifted via the water-gas shift reaction to desired H_2 to CO ratio, and the CO_2 and H_2S are removed. There are several applications of the production of fuel from syngas that date back to prewar Germany. The Fischer-Tropsch synthesis (87) is used widely in South Africa for the production of synthetic fuels (SASOL). The synthesis gas reacts over iron catalysts to produce a mixture of hydrocarbons and oxygenates. The choice of catalyst and operating conditions profoundly affects the product distribution in the Fischer-Tropsch synthesis.

The majority of the work on coal gasification reaction has dealt with catalytic enhancement of hydrocarbon liquids and gas production through hydrogenation. It is also evident that a number of serious problems exist in the use of catalysts in coal gasifiers. These problems relate to catalyst recovery, catalyst poisoning, side reactions, and corrosion effects due to vaporization of catalysts.

Mössbauer spectroscopy has been applied recently to characterize catalysts used in the synthesis reaction (88, 89, 90). Bimetallic catalysts have been studied by Vannice and Garten (89). However, all of the work has dealt with the characterization of the catalyst and none with the study of intermediate products. The possibility of using the Mössbauer effect for in situ measurements has not been explored in coal

gasification. There are only a few Mössbauer spectra of coal char reported in the literature, and no systematic study of the transformations taking place in the iron minerals during gasification has been conducted (91). Considerable research remains to be done in this area.

Coal Liquefaction. Liquefaction of coal has been a known process for a number of years (1). It already was used on a commercial scale by the Germans before and during World War II. Researchers working in the area have found that to achieve coal liquefaction, hydrogen must be added at high pressure. The presence of catalysts enhances the liquid yields and helps in removing sulfur (92, 93). Bergius employed an iron oxide-alumina material for removing sulfur during the reaction. Other successful catalysts were found to be the sulfides of iron, nickel, cobalt, molybdenum and tungsten, and a combination of these as such or supported on alumina, kieselguhr, and clay.

The liquefaction of coal is a complex process that involves close interaction between solubilized coal, the hydrogen-donor solvent, and the catalyst. A catalyst for coal liquefaction must satisfy several requirements, but two key aspects are high activity for liquefaction-desulfurization and good aging characteristics (92, 93). The best measures of the performance of a catalyst (which can decline rapidly due to coking, sintering, and metal deposition) are the liquid yield, the liquid properties (i.e., viscosity), and the desulfurization characteristics.

The initial objective in coal liquefaction appears to be the production of low-sulfur boiler fuels for power generators, but it is reasonable to assume that the upgrading of coal liquids will be necessary in the future. The importance of catalysis in the further processing of coal liquids is without question. There are also several problems associated with the conversion of coal to liquids. For example, major effort is needed to reduce the hydrogen consumption; to achieve this reduction more research is necessary on the role played by the catalysts in coal liquefaction. In general, in any processing of coal one must be below the decomposition temperature of the material. The optimal extraction temperature range is about 400°C. Above this temperature the organic matter of coal begins to crack and the amount dissolved decreases. Solvation increases under hydrogen pressure due to partial hydrogenation. The interaction of hydrogen in these reactions is not well understood, but the presence of H₂ has been observed to enhance liquid yield. However, hydrogen is one of the major factors in increasing the cost of coal liquefaction.

It has been shown recently that the mineral matter plays a significant role in the conversion of coal to liquid products (2, 3, 28, 94). The specific effect of each mineral has not been well established, but the iron-bearing minerals seem to be the most important. Pyrite, pyrrhotite, and the liquefaction residues have been shown to affect the yield and hydrogenation

tion (94). The extent of conversion, product viscosity, and hydrogen consumption could be correlated with the mineral content (18). It seems that the addition of mineral matter does not affect the conversion to pyridine solubles (96), but certain species such as iron sulfides (Fe_{1-x}S), liquefaction residue, and CoMo did have an affect upon the conversion to benzene solubles.

Under the conditions generally employed for coal liquefaction, pyrite is transformed into pyrrhotite (variable composition Fe_{1-x}S , $0 < x \leq 0.125$). Some researchers have applied the Mössbauer effect to the study of the liquefaction residues (19, 79, 95). Our interest has been in finding an analytical method to determine the stoichiometry of the iron sulfides present in the liquefaction residues, and to correlate it to the liquid yields and properties.

The most important parameter for identifying the various Fe_{1-x}S compounds is the magnetic hyperfine splitting. It is observed that the magnetic hyperfine field (mhf) differs considerably between the different iron sites in the pyrrhotites, depending on the number of vacancies in their immediate vicinity (32, 33). The magnetic hyperfine field at the iron site is reduced as the number of nearest-neighbor vacancies increases. Ovanesyan et al. (33) have identified three types of iron sites in $\text{Fe}_{0.881}\text{S}$ with a different number of vacancies around them.

The high sensitivity of the Mössbauer effect to detect small changes in the local environment of the iron atoms makes it an ideal tool to study liquefaction residues. To make this tool more useful, one has to develop a method for identifying the pyrrhotites unequivocally. The most common method for determining pyrrhotite composition is XRD. The following expression which relates the d_{102} reflection of hexagonal pyrrhotites to the atomic iron was given by Yund and Hall (97).

atomic percent iron =

$$45.212 + 72.86 (d_{102} - 2.0400) + 311.5 (d_{102} - 204)^2 \quad (8)$$

This relation has been used to determine the stoichiometry of the pyrrhotites in the liquefaction residues. However, poor crystallinity and the presence of more than one phase sometimes make a unique identification difficult.

We have developed a method to determine the stoichiometry of the iron sulfides present in the liquefaction residues. We utilized a set of well-characterized single crystals and powder samples of iron sulfides (Fe_{1-x}S , ranging from Fe_7S_8 to FeS) to obtain a relation between the atomic percent iron and the average magnetic hyperfine field. We define the average magnetic hyperfine field as

$$H_{av} = \frac{1}{A_{total}} \sum_i A_i H_i \quad (9)$$

where A_{total} is the total spectral area, A_i is the spectral area of the i site, and H_i is the respective magnetic hyperfine field.

In Figure 18 we show the result of our calibration using our standards (stars) and liquefaction residues. The liquefaction residues also were analyzed by XRD. This method was applied to all systems where only one phase was present. Presently we have extended our method to cover two-phase systems (98).

The stoichiometry of the liquefaction residues in general depends on the type of coal, the running temperature, and the hydrogen pressure (residence time also may be a factor). The importance of temperature in determining the stoichiometry of the pyrrhotites in the liquefaction residues is illustrated in Figure 19. The spectra of the liquefaction residues of an Illinois No. 6 coal at three different temperatures are shown ($p_{H_2} = 1800$ psig, time = 30 min, solvent SRC II heavy distillate (99)). There is a clear variation of stoichiometry as the temperature increases. At 325°C the presence of pyrite in the spectrum is evident—full conversion has not taken place.

An important factor in determining the stoichiometry of the pyrrhotites is the presence of additives. In Figure 20 the Mössbauer spectra of a West Virginia coal (Blacksville No. 2) are shown. At the top appears the Mössbauer spectrum of the untreated coal. The second spectrum is from the liquefaction residues of the autoclave run without additive

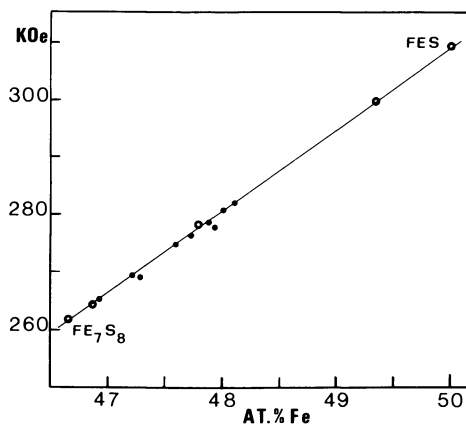


Figure 18. Average magnetic hyperfine field vs. at. % in $Fe_{1-x}S$: (★) pure sulfides; (●) liquefaction residues. The value for FeS corresponds to iron in pyrrhotite without nearest-neighbor vacancies (not troilite).

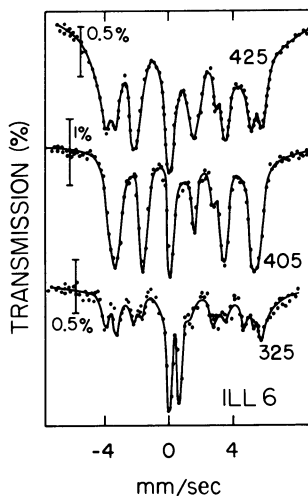


Figure 19. Effect of temperature on the stoichiometry of the liquefaction residues of an Illinois No. 6 coal. At 325°C the presence of pyrite is evident from the figure.

($p_{\text{H}_2} = 1800$ psig, $T = 425^\circ\text{C}$, time = 30 min (99). The two other spectra are runs of the same coal but with 5% pyrite and 5% CoMo, respectively. The change in stoichiometry between the pure coal and the additive plus coal runs is evident. It is noted that the liquid yields increase with the additives (FeS_2 and CoMo).

In a recent study Granoff and the author (19) found a linear correlation between the extent of conversion of the coal to either benzene or THF solubles, and the atomic percent iron in the liquefaction residues. The iron content of the Fe_{1-x}S increased as the conversion of coal to liquid products decreased (see Figure 21). The most reactive coal, in terms of conversion, was Illinois No. 6, and the least reactive was the

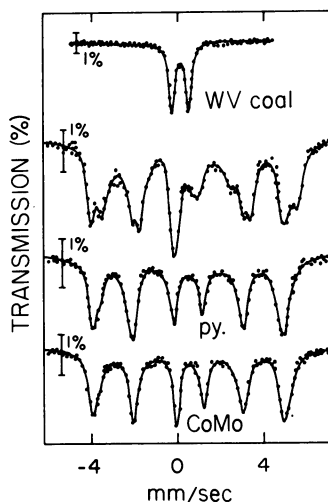
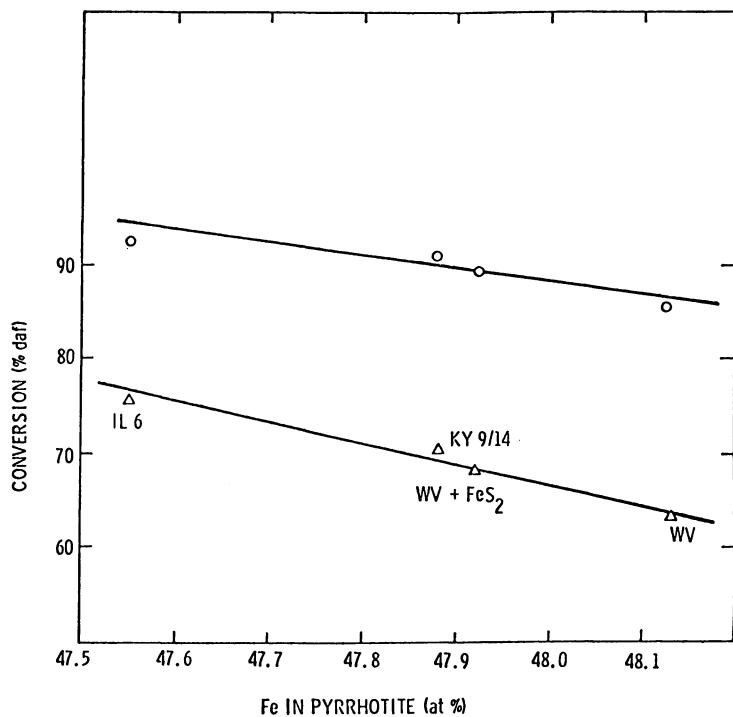


Figure 20. Mössbauer spectrum of a West Virginia coal (Blacksville No. 2); (top specimen) liquefaction residue of this coal; (py) liquefaction residue of a run with pyrite as additive; (CoMo) liquefaction residue of a run with CoMo added to the coal.



Fuel

Figure 21. Conversion to THF (O) and benzene (Δ) solubles as a function of the at. % iron in the pyrrhotite (19)

West Virginia sample. When the West Virginia coal was doped with pyrite (five wt percent based on coal), the conversion to benzene and THF solubles increased, and the resulting liquefaction residue contained a pyrrhotite with a lower atomic percent iron than did the residue from the original experiment with the West Virginia coal. A similar effect was observed when CoMo was added. The experimental evidence to date indicates a good correlation between the atomic percent iron and the number of vacancies in the pyrrhotites, and the conversion of coal to benzene and THF solubles.

The presence of a two-phase system in vacuum tower bottoms (SRC II process) was detected in several Mössbauer runs. The two phases were troilite and a pyrrhotite with atomic percent iron in the range 47.4–47.8. The identification of troilite is relatively simple due to its large magnetic hyperfine field. The great diversity in the pyrrhotite spectra and the difference observed between autoclave and continuous runs required a careful study of the conditions by which pyrrhotite is formed during liquefaction. Its possible catalytic role provides a great

incentive to a careful research of these iron sulfides. In-situ studies of the transformations in the iron sulfides during liquefaction are in progress in our laboratory.

Future of Mössbauer Spectroscopy in Coal Research

A general review of the applications of Mössbauer spectroscopy to coal research is presented in this chapter. Lefelhocz et al. were the first to apply Mössbauer spectroscopy to the study of coal with the purpose of identifying any possible organically bound iron in coal (101). The results of all the Mössbauer work up to date can be explained without considering the presence of these compounds.

The use of Mössbauer spectroscopy as a substitute for the standard techniques for pyritic sulfur determination is not justifiable (in the author's opinion). We can expect Mössbauer spectroscopy to play a secondary role in this area and to be used at best, only as a complementary technique. The future looks brighter in the field of Mössbauer spectroscopy applied to coal utilization, that is, in liquefaction, gasification, coking. There, Mössbauer spectroscopy is at its best, due to its great sensitivity, its applicability to systems with poor crystallinity, and to the very important possibility of studying in-situ processes. We can expect to see this area of research developing into a major field for the application of Mössbauer spectroscopy. The standard usage of Mössbauer in mineralogy is also relevant to coal characterization. It is necessary to develop a well-coordinated research program to understand the iron forms in the clays and how this relates to the coal properties. It is also clear that all of the research involving heterogeneous catalysis in relation to coal conversion is extremely important. In general, we can expect a great increase in the number of Mössbauer spectroscopists carrying out coal-related research.

Acknowledgment

The author wishes to acknowledge the assistance of S. Reddy, J. J. Renton, and A. H. Stiller of West Virginia University. Special thanks go to the West Virginia Geological Survey and to W. Grady of the Coal Research Bureau at West Virginia University. B. Granoff's (Sandia Laboratories) collaboration was invaluable, as was the assistance of former students P. Russell, D. Walker, and W. Dyson. Finally, I wish to thank the West Virginia University Energy Research Center and the U.S. Department of Energy for their support.

Literature Cited

1. Wright, C. H.; Severson, D. E. *Am. Chem. Soc., Div. Fuel Chem., Prepr.* (Boston, Apr., 1972) 16(2), 68.
2. Granoff, B.; Thomas, M. G. *Am. Chem. Soc., Div. Fuel Chem., Prepr.* (Chicago, Aug.-Sept., 1977) 22(6), 183.
3. Granoff, B.; Baca, P. M.; Thomas, M. G.; Noles, G. T. "Sandia Laboratories Report," Albuquerque, NM, 1978, SAND-78-1113.
4. Montano, P. A. *Fuel* 1977, 56, 397.
5. Levinson, L. M.; Jacobs, I. S. *Fuel* 1977, 56, 453.
6. Huffman, G. P.; Huggins, F. E. *Fuel* 1978, 57, 592.
7. Krevelen, D. W. "Coal-Typology-Chemistry-Physics-Constitution"; Elsevier: Amsterdam, 1961.
8. "International Handbook of Coal Petrography," 2nd ed.; CNRS: Paris, 1963.
9. *Am. Soc. Test. Mater. Book ASTM Stand.* 1976, D 388-66.
10. Stach, E.; Taylor, G. H.; Mackowsby, M. Th.; Chandra, D.; Teichmuller, M.; Tiechmuller, R. "Stach's Textbook of Coal Petrology"; Gebrüder Bomtraeger: Berlin, 1975.
11. Grady, W. C. "Petrography of West Virginia Coals," in Carboniferous Coal, Eastern Section of the American Association of Petroleum Geol., 1979.
12. Wender, I. *Catal. Rev. Sci. Eng.* 1976, 14, 97.
13. Given, P. H. *Fuel* 1960, 39, 147.
14. Gluskoter, H. J. *J. Sed. Pet.* 1967, 37, 205.
15. Rao, C. P.; Gluskoter, H. J. *Ill. State Geol. Survey, Circ.* 1973, 476.
16. Grady, W. C. *Pet. Eng., Trans.* 1977, 262, 268.
17. Lau, C. M.; Shumate, K. S.; Smith, E. E. *3rd Symp. Coal Mining Drainage Res., Mellon Inst.* 1970, 114.
18. Illig, E. "Disposable Catalysts in Coal Liquefaction"; DOE: Albuquerque, NM, 1978.
19. Montano, P. A.; Granoff, B. *Fuel* 1980, 59, 214.
20. Wyckoff, R. W. "Crystal Structures"; Interscience: New York, 1963; Vol. 1.
21. Montano, P. A.; Seehra, M. S. *Solid State Comm.* 1976, 20, 897.
22. Guettinger, T. W.; Williamson, D. L. *Phys. Rev. B* 1979, 20, 3938.
23. Burgardt, P.; Seehra, M. S. *Solid State Commun.* 1977, 22, 153.
24. Seehra, M. S.; Seehra, S. S. *Phys. Rev. B* 1979, 19, 6620.
25. Seehra, S. S.; Montano, P. A.; Sen, S. K. *J. Mater. Sci.* 1979, 14, 2761.
26. Russell, P.; Montano, P. A. *J. Appl. Phys.* 1978, 49(3), 1573.
27. Montano, P. A. In "Coal Structure," *Adv. Chem. Ser.* 1981, 192, in press.
28. Vaughan, D. J.; Ridout, M. S. *J. Inorg. Nucl. Chem.* 1971, 33, 741.
29. Schrader, R.; Pietzch, C. *Krist. Tech.* 1969, 4, 385.
30. Stiller, A. H.; McCormick, B. J.; Russell, P.; Montano, P. A. *J. Am. Chem. Soc.* 1978, 100, 2553.
31. Marfunin, A. S.; Mkrtchyan, A. R. *Geochem. Int.* 1967, 4, 980.
32. Hafner, S. S.; Kalvius, M. *Z. Kristallogr.* 1966, 123, 443.
33. Ovanesyanyan, N. S.; Trukhtanov, V. A.; Odinets, G. Yu; Novikov, G. V. *Sov. Phys. JETP* 1971, 33, 1193.
34. Renton, J. J.; Hidalgo, R. V. *Coal Geol. Bull.* 1975, 4 WVGS.
35. Millot, G. "Geologie der Argiles"; Marson: Paris, 1970.
36. Brown, G. "X-ray Identification and Crystal Structure of Clay Minerals"; Mineralogical Society: London, 1961.
37. Carroll, Dorothy. "Clay Minerals: A Guide to Their X-ray Identification"; Geological Society of America: Boulder, CO, 1970.

38. Jefferson, D. A.; Tricker, M. J.; Winterbottom, A. P. *Clays Clay Miner.* 1975, 23, 355.
39. Coey, J. M. D., *Proc. Int. Conf. Mössbauer Spectrosc.*, V2, Cracow, 1975.
40. Bowen, L. H.; Weed, S. B.; Stevens, J. G. *Am. Min.* 1969, 54, 72.
41. Hogg, C. S.; Meads, R. E. *Min. Mag.* 1970, 37, 606.
42. Malathi, N.; Puri, S. P.; Saraswat, I. P. *J. Phys. Soc. Jpn.* 1969, 26, 680.
43. Malathi, S. P.; Puri, S. P.; Saraswat, I. P. *J. Phys. Soc. Jpn.* 1969, 26, 680.
44. Brown, H. R.; Duriel; Schaefer *H.N.S. Fuel* 1960, 39, 59.
45. Kemezys, M.; Taylor, G. H. *J. Inst. Fuel* 1964, 37, 389.
46. Ōno, K.; Ito, A. *J. Phys. Soc. Jpn.* 1964, 19, 899.
47. Okiji, A.; Kanamori, J. *J. Phys. Soc. Jpn.* 1964, 19, 908.
48. Forester, D. W.; Koon, N. C. *J. Appl. Phys.* 1969, 40, 1316.
49. Housley, R. M.; Gonser, U.; Grant, R. W. *Phys. Rev. Lett.* 1968, 20, 1279.
50. Alikhanov, R. A. *JETP* 1959, 9, 1204.
51. Gluskoter, H. P. *Fuel* 1965, 44, 285.
52. Stiller, A. H.; Renton, J. J.; Montano, P. A.; Russell, P. *Fuel* 1978, 57, 447.
53. Ok, H. N. *Phys. Rev.* 1971, B4, 3870.
54. Pistorious, C. A. *Bull. Soc. Chim. Bdg.* 1960, 69, 570.
55. Vertes, A.; Zsoldos, B. *Acta Chim. (Budapest)* 1970, 65, 261.
56. Carg, V. K.; Puri, S. P. *J. Chem. Phys.* 1971, 54, 209.
57. Nascimento, A. R.; Carg, V. K. *J. Chem. Phys.* 1977, 66, 5798.
58. Champion, A. R.; Vaughan, R. W.; Drickhamer, H. G. *J. Chem. Phys.* 1967, 47, 2503.
59. Wignall, J. W. G. *J. Chem. Phys.* 1966, 44, 2462.
60. Hrynkiewicz, A. Z.; Kubisz, J.; Kulgawczk, D. S. *J. Inorg. Nucl. Chem.* 1965, 27, 2531.
61. Takano, M.; Shinjo, T.; Kiyama, M.; Takada, T. *J. Phys. Soc. Jpn.* 1968, 25, 902.
62. Finkelman, R. B., private communication.
63. Grant, R. W.; Wiedersich, H.; Muir, A. H., Jr.; Gonser, U.; Delgass, W. N. *J. Chem. Phys.* 1966, 45, 1015.
64. Greer, R. T. "Proc. Int. Sym. Anal. Chem. Exploration, Mining and Processing of Materials, Johannesburg, S.A., 1976, paper 171.
65. Given, Peter H.; Miller, Robert N. *Fuel* 1978, 57, 381.
66. Montano, P. A.; Stiller, A. H.; Renton, J. J., unpublished data.
67. Steyert, W. A.; Taylor, R. D. *Phys. Rev. A* 1964, 134, 716.
68. Petzold, J. *Z. Phys.* 1961, 163, 71; Sitzgsber. Heiderberg Akad. Wiss., Mat.-naturw. kl 1960/61, 5 abs.
69. Housley, R. M.; Hess, F. *Phys. Rev.* 1966, 146, 517.
70. Nishihara, Yoshikazu Ogawa, Shinji. *J. Chem. Phys.* 1979, 71(9), 3796.
71. Nussbaum, R. H. "Mössbauer Effect Methodology"; Gruverman, I. T., Ed.; Plenum: New York, 1966; Vol. 2.
72. Wegener, Horst "Der Mössbauer Effect"; B. I. Hochschul Tachenbücher: Mannheim, 1965.
73. Lang, G. *Nucl. Instr. Methods* 1963, 24, 425.
74. Bykov, G. A.; Pham, Xuyxien. "Proceedings of the Dubna Conference on the Mössbauer Effect"; Consultants Bureau Enterprises, Inc.: NY, 1963; pp. 2-27.
75. Huggins, F. E.; Huffman, G. P. "Analytical Methods for Coal and Coal Products"; Academic: New York, 1980; Vol. 3.
76. Dovzhenko, N. F.; Smoilovskii, A. N.; Chernyshov, Yu. A. *Khim. Tverd. Topl.* 1977, 5, 73.
77. Levinson, L. M. "Research Project 267-2 Final Report," EPRI FP-1228, 1979.

78. Finhelman, R. "Report on the Analysis of an IL. 6 Standard Coal."
79. Jacobs, I. S.; Levinson, L. M.; Hart, H. R., Jr. *Appl. Phys.* **1978**, *49*(3), 1775.
80. Baker, R. A. "Water Research"; Pergamon: New York, 1972; Vol. 6, p. 9.
81. Graham, J. P. *IISI Proc.* **1969**, pp. 141-148.
82. Dartnell, J. *Ironmaking Steelmaking* **1978**, *5*(N1), 18.
83. Johnson, James L. *Use of Catalysis in Coal Gasification Am. Chem. Soc., Div. Fuel Chem., Chicago, Aug. 1975*.
84. Given, P. H.; Katzman, H. "A Research and Development Program for Catalysis in Coal Conversion Processes," EPRI 207-0-0, 1974.
85. Gray, D. *Fuel* **1978**, *57*, 213.
86. Wender, I. *Catal. Rev.-Sci. Eng.* **1976**, *14*(1), 97.
87. Storch, H. H.; Columbric, N.; Anderson, R. B. "The Fischer-Tropsch and Related Syntheses"; Wiley: New York, 1951.
88. Unmuth, E. E.; Schwartz, L. H.; Butt, J. B. *J. Catal.* **1980**, *61*, 242.
89. Vannice, M. A.; Garten, R. L. *J. Mol. Catal.* **1975/76**, *1*, 201.
90. Delgass, W. N. In "Mössbauer Effect Methodology"; Gruverman, I. H.; Seidel, C. W., Eds.; Plenum: New York, 1976.
91. Hinckley, S. C.; Smith, G. V.; Twardowska, H.; Sakoroschenko, M.; Shiley, R. H.; Griffen, R. A. *Fuel* **1980**, *59*, 161.
92. Oblad, Alex G. *Catal. Rev.-Sci. Eng.* **1976**, *14*(1), 83.
93. Donath, E. E. *Adv. Catal.* **1956**, *8*, 239.
94. "Mineral Matter Effects and Use of Disposable Catalysis in Coal Liquefaction, Project Review Meeting Organized by the Division of Coal Conversion," DOE, Albuquerque, NM, 1978.
95. Keisch, B.; Gibbon, G. A.; Akhtar, S. *Am. Chem. Soc., Div. Fuel Chem. Prepr.* (Anaheim, Mar., 1978), *23*(1-2), 263.
96. Thomas, M. G.; Granoff, B.; Baca, P. M.; Noles, G. T. *Am. Chem. Soc., Div. Fuel Chem., Prepr.* (Anaheim, Mar., 1978) *23*(1), 23.
97. Yund, R. A.; Hall, H. T. *Econ. Geol.* **1969**, *64*, 420.
98. Montano, P. A.; Vipul, Shah, unpublished data.
99. Granoff, B. runs at Sandia Laboratories.
100. Montano, P. A.; Granoff, B.; Reddy, S., unpublished data.
101. Lefelhocz, J. F.; Friedel, R. A.; Kohman, T. P. *Geochim. Cosmochim. Acta* **1967**, *31*, 2261.
102. Stiller, A. H.; McCormick, B. J.; Russell, P.; Montano, P. A. *J. Am. Chem. Soc.* **1978**, *100*, 2553.
103. Coeey, J. M. D. "Clay Minerals and Their Transformations Studied with Nuclear Techniques," unpublished data.
104. Hogath, D. D.; Brown, F. F.; Pritchard, A. M. *Can. Mineral.* **1970**, *10*, 710.
105. Malysheva, T. V. "Effect Mössbauer v Geokimii Kosmochimii"; Nauk.: Moscow, 1975.

RECEIVED June 27, 1980.

Quantitative Investigations of Pyrite and Coal

D. L. WILLIAMSON and T. W. GUETTINGER

Department of Physics, Colorado School of Mines, Golden, CO 80401

D. W. DICKERHOOF

Department of Chemistry/Geochemistry, Colorado School of Mines,
Golden, CO 80401

The application of ^{57}Fe Mössbauer spectroscopy to determine pyritic and total iron concentrations in coals is explored. Two methods, one based on resonance area and the other on resonance intensity, are described and tested. Results are compared with those of the chemical method, ASTM D2492. Several problem areas are identified in both the chemical and Mössbauer methods. Of particular interest here is the illustration of errors in quantitative analysis caused by nonuniform, or granular, Mössbauer absorbers prepared from coal and pyrite.

The investigation of iron-containing compounds in fossil fuels and related materials through the use of ^{57}Fe Mössbauer spectroscopy is an area of research that has come to prominence only recently. Results of Mössbauer work have been reported on coals (1-14), coal ash (2, 5, 12, 15), coal liquefaction residues (6, 11, 16, 17), coke (8, 9), and oil shales (5, 18). Most of this work has been semi-quantitative in nature, although some quantitative methods have been proposed (2, 3, 8, 9, 13, 14). In general, the use of Mössbauer spectroscopy to obtain accurate quantitative information on the absolute concentration of resonant nuclei in a given absorber has proved to be a difficult task. For coals, in particular, two major problems present themselves: first, generalized experimental techniques and procedures have yet to be fully developed, and second, there must be some alternative analytical method for analyzing coals to verify the accuracy of the Mössbauer results. One chemical method, an ASTM standard method, does exist, but recently has come under question in the literature.

0065-2393/81/0194-0177\$08.00/0
© 1981 American Chemical Society

This chapter outlines and illustrates experimentally the factors that we feel must be addressed before reliable quantitative results can be obtained routinely. A factor of considerable importance, which is examined both theoretically and experimentally, is the difficulty of preparing absorbers of uniform thickness. Results from the application of Mössbauer spectroscopy to investigate possible sources of error in the standard ASTM chemical method of analysis are presented also.

Nature of Coal and Its Mineral Matter

Coal is probably one of the least desirable types of materials to be used for analytical analysis. It is a heterogeneous solid of varying composition. It has been described as an organic rock or as a type of strange "fruitcake" (19). Organic material from plants, trees, spores, algae, and other varied sources was mixed in varying proportions, underwent various stages of decay to produce peat-like material, and was buried where it became compressed into a solid mass. This mass then underwent differing degrees of rearrangement to form more condensed structures in a poorly understood process called coalification. The greater the extent of the process, the higher the rank of the resulting coal. During the peat stage and also possibly during the burial stage, various minerals or inorganic matter were deposited and incorporated into the organic mass.

The mineral matter may be found imbedded in the organic matrix as microcrystals, as larger crystals between the grains, or in the cracks of the organic matrix. The latter are easily freed by grinding the coal whereas the former require grinding the coal to an extremely small particle size. The overall picture that emerges is a material of extreme complexity in terms of the organic material present, a wide variability in composition between different coals (and often within different regions of one lump of coal), and a wide variety of compositions and distributions of mineral matter within the coal.

Because of this extreme variability, careful sampling procedures, such as ASTM D2013-72 and D346-75 (20), should be followed. Additionally, if a container of finely ground coal is agitated, such as would occur during handling, the heavier, mineral-rich particles will tend to migrate to the bottom of the container. Consequently, thorough mixing is required prior to withdrawing any sample, and replicate samples should be run whenever possible.

The major classifications of mineral matter found in typical U.S. coals are clay minerals (aluminosilicates), carbonates, pyrite and other metal sulfides, quartz and other silicates, and, especially for lower rank

coals, metal cations coordinated to (or complexed by) some of the functional groups in the organic matrix (21, 22). These occur in different proportions in different coals, and various ones may be completely absent in particular coals.

It should be noted in passing that coal does not contain "ash"; it contains "mineral matter" (21). Ash and mineral matter are not the same, which may lead to some confusion in reporting results since the term "ash-free coal" is often encountered. Because of the chemical changes taking place during the ashing process, the weight of ash normally differs from the weight of the mineral matter. All of the work reported herein is on an "as-determined" basis; that is, the percentages or compositions are based on the entire sample as it was at the time of measurement with no attempt to recalculate it on a dry ash-free (daf) or a dry mineral matter-free (dmmf) basis.

The minerals of primary concern in this study are the iron- and sulfur-containing minerals; paramount among these is pyrite, FeS_2 . True pyrite is a mineral composed of ferrous cations (Fe^{2+}) and disulfide anions (S^{2-}) in cubic lattice. A different packing arrangement (orthorhombic) of the same ions produces the mineral marcasite which also has the formula FeS_2 . The term pyrite is often used in the generic sense to cover both minerals. Marcasite has been considered a relatively rare mineral and is not normally analyzed for since x-ray diffraction or careful Mössbauer interpretation is needed for quantitative determinations. Petrographic analysis can identify its presence and provide an estimate of the concentration. Chemically, it should behave identically to true pyrite, but this is considered an open question by some investigators. In one experiment, no difference was found in the recoilless fractions of coal pyrite and mineral pyrite (14). The term pyrite in this chapter will be used in the generic sense in discussing chemical analyses but in the more restricted sense in discussing the Mössbauer experiments.

Pyrite (and presumably marcasite) can occur in coals in a range of particle sizes, from massive "chunks" several centimeters in diameter to tiny single crystals less than $1 \mu\text{m}$ in diameter (10, 24, 25). It also occurs in clusters of small crystals termed "framboids" from their resemblance to a raspberry; these clusters have been reported in the range of 10–20 μm in diameter. For purposes of comparison, a U.S. No. 325 mesh sieve has openings of about 44 μm in diameter.

Figure 1 shows the similarity of the Mössbauer resonance for pyrite and marcasite. The lower velocity lines overlap almost exactly whereas the higher velocity lines are separated by 0.09 mm/s, or approximately one half the resonance linewidth. Thus a 50–50 mixture of pyrite and marcasite as shown in Figure 1 yields an asymmetric spectrum, with the

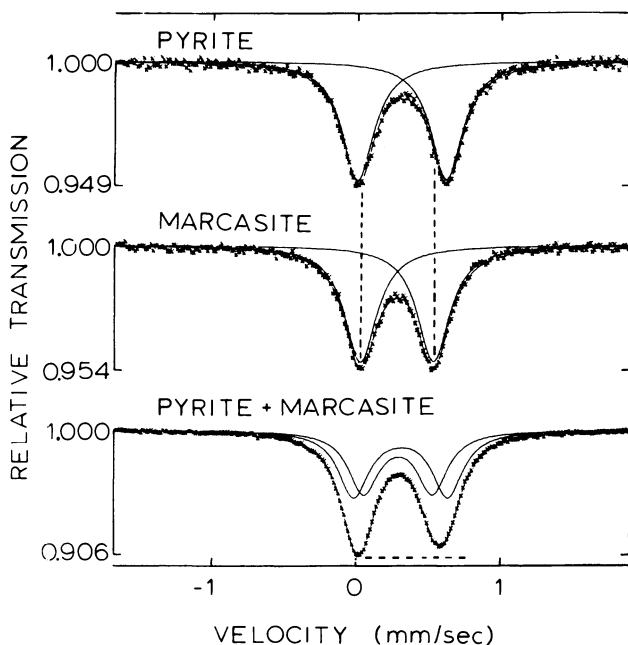


Figure 1. Mössbauer spectra of pyrite and marcasite (natural minerals).

The solid lines are the computer-fitted Lorentzian lines, and the dashed lines are to indicate differences in position and intensity. The isomer shift δ (relative to α -iron) and quadrupole splitting Δ for pyrite (p) and marcasite (m) from the upper two spectra are: $\delta(p) = 0.306(2)$, $\Delta(p) = 0.616(4)$; $\delta(m) = 0.273(2)$, $\Delta(m) = 0.504(3)$, all in mm/s. The composite pyrite + marcasite spectrum was obtained by stacking the absorbers used to generate the upper two spectra. Computer decomposition with two quadrupole pairs as indicated yields erroneous δ and Δ values but approximately the correct relative intensities.

higher velocity component broader and less intense than the lower. We have found no evidence of the dominance of marcasite over pyrite in the coals examined to date.

Figure 2 illustrates a variety of Mössbauer spectra obtained from coals. Although pyrite is usually the most abundant iron-containing mineral present, one coal (Figure 2c) has been found that contains siderite (FeCO_3) and essentially no pyrite. Other compounds most often seen in our work are illites (clay minerals), szomolnokite ($\text{FeSO}_4 \cdot \text{H}_2\text{O}$), and jarosites [$M^+\text{Fe}_3(\text{SO}_4)_2(\text{OH})_6$] where M^+ may be an alkali metal cation, H_3O^+ , or NH_4^+ . The total sulfate content in most coals is very low ($\leq 0.3\%$ by weight), but can be higher in specific coals or in weathered coals because of oxidation of the disulfide ion to sulfate. The Mössbauer parameters (isomer shift and quadrupole splittings) of these compounds and others seen in coals are tabulated in the literature (8, 9, 12, 26, 27).

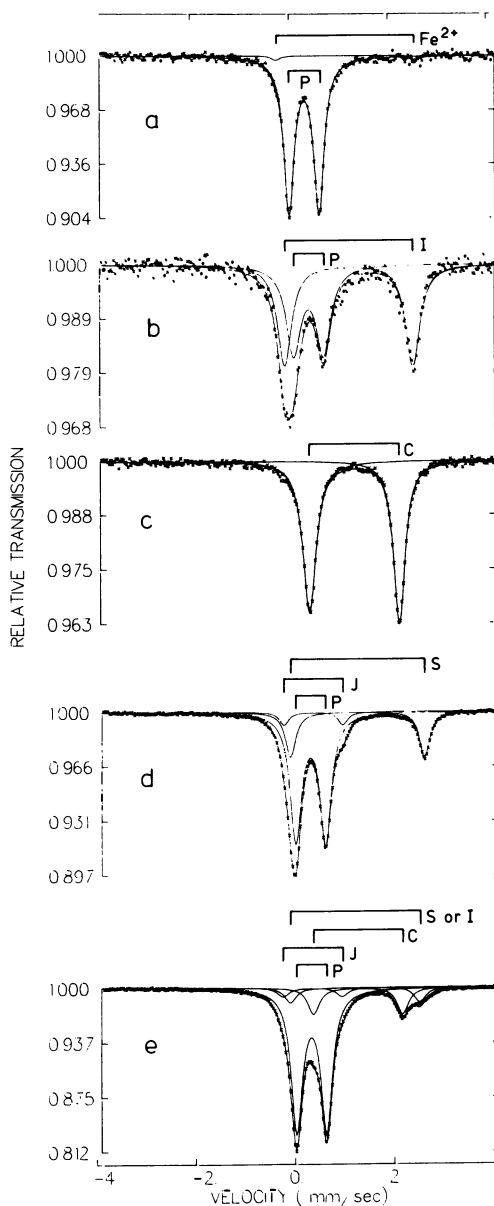


Figure 2. Mössbauer spectra of five U.S. coals.

(a) West Virginia coal containing pyrite (P) and a small amount of ferrous iron (Fe^{2+}); (b) Colorado coal containing approximately equal amounts of pyrite and illite (I); (c) Colorado coal containing siderite (C); (d) West Virginia coal containing mixture of pyrite, szomolnokite (S), and jarosite (J); (e) Ohio coal containing mixture of pyrite, jarosite, siderite (or ankerite), and szomolnokite (or illite). The computer decomposition with superposition of Lorentzian lines are indicated by solid curves. The zero of velocity corresponds to the center of the α -iron calibration.

Chemical and Mössbauer Analyses

ASTM Standard D2492 (28). Sulfur forms are important in industrial uses of coal, especially in coal conversion processes. The forms of sulfur in coals are disulfide (pyritic) sulfur (S_2^{2-}), sulfate sulfur (SO_4^{2-}), organic sulfur bond in the matrix of the coal, and sulfur in the form of sulfide (S^{2-}). The latter is normally absent or present in low concentrations in most coals and is ignored in the ASTM method of analysis; iron sulfides can be detected by Mössbauer spectroscopy but have not been found in any of the coals investigated in this work.

The ASTM method provides a procedure for analyzing for the pyritic and sulfate forms of sulfur, and a way to calculate the organic sulfur content. It depends on having available the results of ASTM Standard D3177, a method for determining the total sulfur content of coal (29). Figure 3 shows ASTM Method D2492 as we employ it. The amount of sulfate sulfur is determined from a gravimetric determination of a $BaSO_4$ precipitate, while the pyritic sulfur is calculated from an analysis of the iron content of a nitric acid (HNO_3) solution. The determination may be by volumetric titration or by atomic absorption (AA). We have employed the latter (30).

Several sources of error exist that can limit the accuracy of this method. It depends on pyrite being completely insoluble in hydrochloric acid (HCl) and then completely dissolved by the HNO_3 . It further requires that the HCl completely dissolve all sulfates and nonpyritic iron-containing compounds (or that the latter also remain insoluble in the HNO_3). Any iron not dissolved by the HCl that eventually dissolves in the HNO_3 will cause the pyritic iron and sulfur values to appear too high,

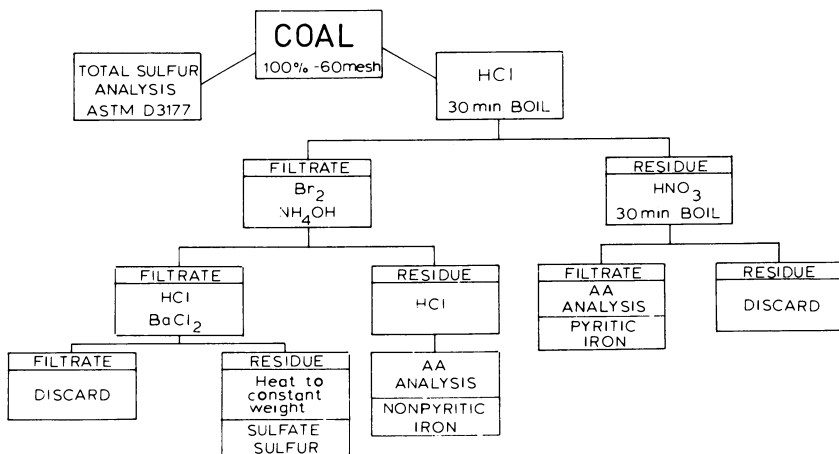


Figure 3. Chemical analysis schematic

and thereby cause the organic sulfur content to appear too low. Any pyrite not dissolved by the HNO_3 will cause a low pyritic sulfur value and a high organic sulfur content. Any nonferrous sulfides present will contribute to the total sulfur value and lead to a high value for the organic sulfur content. Thus, an error in one factor can have repercussions in the calculated values reported for the other sulfur forms.

Some investigators have questioned the accuracy of the method and even suggested the possibility of errors as high as 20% (3, 31, 32). Nonetheless, reports can be found that are supportive of the ASTM procedures (33). Thus, a controversy exists concerning the limits of accuracy of this standard method.

For this work we are concerned with the fate of the iron-containing compounds in coals during the chemical treatments of the ASTM procedure and with comparing the results of Mössbauer and chemical analyses. To obtain a quantitative balance of iron compounds in coals by chemical means, an additional analysis is performed that is not called for in the published ASTM method. This is shown in Figure 3 as an additional analysis for iron and is labeled "nonpyritic iron." Values for nonpyritic iron arise from the presence of species such as szomolnokite, jarosite, or siderite. These have been found in the coals we have investigated, and all have dissolved to a large degree in HCl. They are not identified as separate species by the chemical analysis, but the Mössbauer spectra do show them separately (Figure 2). Chemical analysis gives the gross nonpyritic iron content and the pyritic iron content, and these values are then compared with values determined from Mössbauer analysis.

Mössbauer Analysis Methods. In this section we describe two procedures to obtain total and pyritic iron concentration data from coals. The results are given in the following section where a comparison is made with the chemical analyses.

RESONANCE AREA METHOD. Each Mössbauer spectrum is computer-fitted to a superposition of Lorentzian-shaped lines, each of which is characterized by the number of counts at maximum resonance, N , and the full width at half maximum resonance, Γ . The off-resonance count rate N_∞ is also a fitted parameter of each spectrum. A background correction factor B is determined to account for unwanted counts that are inadvertently included in the resonance spectrum. B is measured by a method introduced in precision recoilless fraction work (34, 35). The count rate through the absorber is obtained with, C_t , and without, C_o , a brass foil filter of 125- μm thickness inserted between absorber and detector. The correction factor is then (34):

$$B = \left[1 - 1.04 \frac{C_t}{C_o} \right]^{-1} \quad (1)$$

The area A of a given resonance line is calculated as:

$$A = B \frac{\pi}{2} \Gamma \frac{N_{\infty} - N}{N_{\infty}} \quad (2)$$

Since Γ is expressed in mm/s, A will also have these units. For coal absorbers, we find B to vary from as low as 1.03 to as high as 1.3, depending on experimental geometry, source strength, and the resolution of the photon detection system.

Mössbauer spectra of coal usually consist of several quadrupole doublets (e.g., see Figure 2). This occurs because there is more than one iron site in the absorber attributable to a mixture of iron-containing compounds and/or nonequivalent crystallographic sites in a single compound. The quadrupole splittings and isomer shifts of ^{57}Fe in the several sites are usually such that the lower velocity components of the quadrupole pairs overlap strongly but the higher velocity components are partially or well resolved (Figure 2). For poorly resolved, multicomponent spectra we often use one or both of the following restrictions in the computer fitting: (1) the intensities of both lines of a quadrupole pair are equal, and (2) all lines have the same linewidth.

The experimental area associated with the i th hyperfine line of the j th site (or phase) is then calculated as:

$$A_{ij} = \frac{B}{N_{\infty}} \frac{\pi}{2} \Gamma_{ij} (N_{\infty} - N_{ij}) \quad (3)$$

with the resonance resulting from the j th site and from all sites given

by $A_j = \sum_i^{\alpha_j} A_{ij}$ and $A = \sum_j^k A_j$, respectively, where α_j is the number of

hyperfine transitions associated with the j th site ($\alpha_j = 2$ for the quadrupole interaction) and k is the total number of sites. The quality of a fit is gauged by the χ^2 -test and by visual inspection.

The theoretical expression connecting resonance area and iron concentration is (36):

$$A_{ij} = \frac{\pi}{2} \Gamma_0 f_s K (T_{ij}) \quad (4)$$

with

$$K(T_{ij}) = T_{ij} e^{-T_{ij}/2} [I_0(T_{ij}/2) + I_1(T_{ij}/2)] \quad (5)$$

and

$$T_{ij} = \sigma_0 a q_{ij} f_j m_j \frac{N_A}{W} \equiv D q_{ij} f_j m_j \quad (6)$$

where I_0 and I_1 are modified Bessel functions of zero and first order, respectively; Γ_0 is the natural linewidth of the Mössbauer gamma ray ($\Gamma_0 = 0.0970$ mm/s (26, 27)); f_s is the source recoilless fraction, ($f_s = 0.660 \pm .003$ for ^{57}Fe in palladium at 295 K (35)); T_{ij} is the effective thickness (unitless) associated with the i th line attributable to the j th site; σ_0 is the Mössbauer resonance cross section ($\sigma_0 = (2.56 \pm .05) \times 10^{-18}$ cm² (37)); a is the isotopic abundance of ^{57}Fe ($a = 0.0214$ (26, 27)); q_{ij} is the transition probability associated with the i th hyperfine line of the j th site; n_j is the concentration of iron atoms in the j th site (in number/cm³); and f_j is the recoilless fraction at the j th iron site. When working with powder absorbers it is convenient to express T_{ij} in terms of mass of iron per unit area associated with the j th site, $m_j = n_j tW/N_A$, where W is the molecular weight of natural iron, N_A is Avogadro's number, and t is the actual thickness of the absorber. Equations 4, 5, and 6 have seen considerable use in the phase analysis of steels and similar alloys (38–41), and they are the expressions used by Huffman and Huggins in their analysis of coals and coke (8, 9). The constant $D = 0.591$ cm²/mg, provided m_j is expressed in units of mg of iron/cm². The uncertainty in D is presently about 2% owing to the experimental uncertainty in σ_0 (37).

Equation 4, 5, and 6 are valid provided the i th line is well resolved from all others and the absorber is of uniform thickness, that is, T_{ij} is constant over the area of the absorber sampled by the gamma-ray beam.

Comparison of the theoretical A_{ij} (Equation 4) to the experimental Lorentzian A_{ij} (Equation 3) shows the Lorentzian fit to yield an area that is 0.2% high at $T = 1.0$, 1.2% high at $T = 3.0$, and 4.9% high at $T = 10.0$ (42). All of our experimental data from coal, to date, yield values of T_{ij} less than 3, so errors from this source are 1% or less.

Our coal absorbers are prepared by compression into a pellet of 2.54-cm diameter by a simple piston and cylinder. If the coal is ground to about -100 mesh or finer, then no binder such as acrylic or epoxy is required to hold the pellet together (each disc is then secured between two pieces of masking tape). Typical weights of coal used range from 0.2 to 2.0 g, yielding discs of about .04 to 0.4 g/cm². For the smaller weights, powdered sugar is added and mechanically mixed to give a pellet of maximum uniformity and convenient thickness. The gamma-ray beam from the source is collimated to strike an absorber area of about 0.3 cm². On this area scale, several of our absorbers have been tested for uniformity in density by gamma-ray and x-ray attenuation through different regions of a given absorber. Uniformity to better than 5% is observed.

We now summarize our procedure:

1. Prepare an absorber disc of known total mass/area = M .
2. Measure the background factor B prior to accumulation of

- the spectrum according to the procedure just described (Equation 1).
3. Computer-fit the spectrum with a superposition of Lorentzian lines using the restrictions just described only if necessary to achieve convergence.
 4. Calculate the A_{ij} according to Equation 3.
 5. Using only the A_{ij} from the best resolved line of each quadrupole pair, compare with A_{ij} of Equation 4 by computer iteration to obtain T_{ij} .
 6. Calculate each m_j from Equation 6 assuming $q_{ij} = 1/2$ for all quadrupole pairs and using the best available value of the recoilless fraction f_j .
 7. Compute the weight concentration of iron in the j th site from $C_j = m_j/M$ and the total iron weight concentration $\sum_j m_j/M$.

The recoilless fractions f_j (hereafter referred to as f -values) needed in this analysis are not known for all the iron sites commonly found in coal, and the values presently available are not known with good precision. In the initial stage of our work on coal, the f -value of pyrite was determined by adding known quantities of -200 mesh ($-74 \mu\text{m}$) pyrite to a given coal. Following the procedure just outlined, values of T for pyrite

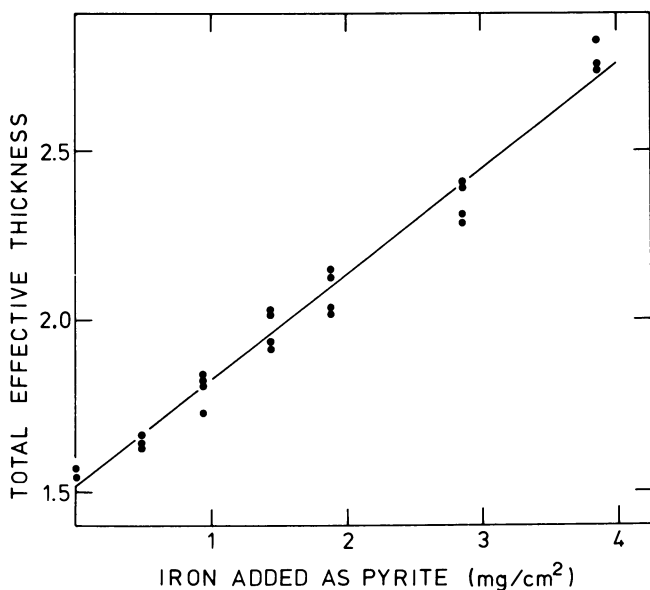


Figure 4. Correlation of total effective thickness (T) of coal absorbers with pyritic iron additions. The data points for a given amount of iron are from duplicate specimens. The straight line is a least-squares fit based on Equation 6.

were obtained as a function of pyrite addition to coal. These are shown in Figure 4 where one can see a scatter of about 5% in the total effective thickness associated with preparation and analysis of duplicate absorbers from the same coal-pyrite mixture. A linear fit to the data using Equation 6 yielded $f(\text{pyrite}) = 0.53 \pm 0.04$, where the error given is two standard deviations as calculated from the least-squares analysis. As described in a later section, this value is not accurate because the effect of absorber granularity was neglected in the analysis; however, it is probably a reasonable *effective f*-value to use in quantitative analysis of coal since it was obtained from samples prepared in a similar manner. Huffman and Huggins (8, 9) obtained a value of $f(\text{pyrite}) = 0.48$ using a very similar procedure, and its application to coal yielded pyritic iron concentrations in reasonable agreement with chemical results.

INTENSITY METHOD. In our laboratory, the time required to accumulate a Mössbauer spectrum from coal is typically on the order of 1–15 h, depending on iron concentration and source strength. Further time is needed to carry out the computer analysis described earlier. The chemical ASTM method requires comparable time. To test a method that greatly reduces the Mössbauer analysis time, we have made preliminary investigations of the use of resonance intensities measured at a few selected constant velocities. Although not practical for studying the detailed nature of iron-containing species in different coals, this method could prove to be valuable for fast, routine monitoring of pyrite and other iron-sulfur compounds in operations where the nature of the coal is not highly variable.

The normalized resonance intensity I_v at the v th constant velocity is calculated as:

$$I_v = B (r_\infty - r_v) / r_\infty \quad (7)$$

where the r_∞ is the count rate measured at an off-resonance velocity (e.g., < -2 mm/s for coals), r_v is the measured count rate at the v th constant velocity, and B is the background factor which is measured as described previously.

Theoretical expressions analogous to Equations 4, 5, and 6 have been developed for I_v (36); however, in contrast to the area relation, peak intensities depend on self-absorption in the source and instrumental line broadening. We have tested the following empirical method: (1) a series of "standard" absorbers was prepared from known quantities of pure pyrite; (2) the intensity of one of the pyrite lines was measured to generate a calibration curve; (3) intensities from coal absorbers were then compared with the calibration to determine the pyritic iron concentration. Figure 5 shows calibration curves generated for pyrite powder

of two different particle sizes. The origin of the size dependence is discussed later. The lines drawn through the data are hand fits and the change in slope is indicative of the saturation of I_0 vs. sample thickness (36). Calibration curves for other iron-containing compounds occurring in coal should be developed to obtain total and fractional iron concentrations; however, we assumed the recoilless fraction at other iron sites to be similar to that in pyrite, and simply used the Figure 5 pyrite calibration to illustrate the possible use of the method. Clearly, corrections should also be made for overlapping resonance lines.

Results. COMPARISON OF RESULTS FOR SEVERAL COALS. Chemical and Mössbauer area analyses of pyritic iron and total iron concentrations in a variety of U.S. coals are presented in Table I. Our experimental f -value of 0.53 was used for the pyritic iron determinations, and it was also assumed to be valid for all other iron-containing compounds. The "total wt % iron" values from the ASTM method are the sum of values from the pyritic and nonpyritic iron analyses shown in Figure 3. Because

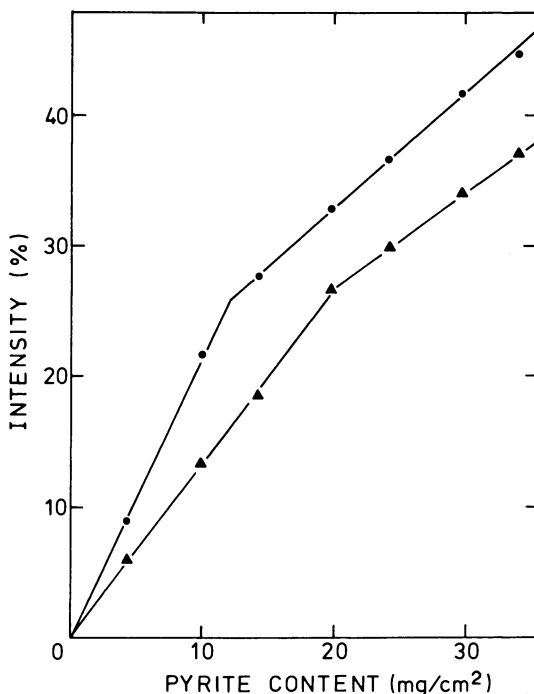


Figure 5. Mössbauer resonance intensity obtained from pyrite absorbers prepared from granules having the average size indicated ((●) 19 μ ; (▲) 48 μ). The intensity was measured at a constant velocity corresponding to maximum resonance of one of the pyrite lines, corrected for background, and normalized according to Equation 7.

Table I. Analysis of Various U.S. Coals by ASTM Method and the Mössbauer Area Method^a

Coal ^b	Mesh	Pyritic Wt % Iron		Total Wt % Iron	
		ASTM	Mössbauer	ASTM	Mössbauer
IM8	-100 (-149 μm)	1.44	1.20	2.13	1.71
	-325 (-44 μm)	1.63	2.37	2.44	3.09
	-100	1.66 ^c		2.36 ^c	
	-325	1.85 ^c		2.64 ^c	
RB	-100	0.75	0.26	0.96	0.29
	-325	1.03	1.75	1.40	1.94
BC	-100	0.00	0.00	0.23	0.39
LN	-100	0.05	0.08	0.12	0.16
LV	-100	2.11	2.03	2.44	2.16
KY9	-200 (-74 μm)	1.33	1.67	1.95	2.10
OP7	-270 (-53 μm)	2.19	2.39	2.93	3.14
IL6	-270	1.49	1.74	2.25	2.10
	-100	1.29	1.31	1.40	1.34
WV	-100			1.38 ^d	
	-100			1.97 ^c	
	-100	1.34 ^e		2.03	1.90
	-100	1.50	1.62	1.93 ^d	
KY	-100			2.03 ^e	
	-100	1.42 ^e		2.03 ^e	
	-100	1.36	1.49	1.64	1.52
IL	-100			1.64 ^d	
	-100	1.55 ^e		1.68 ^e	

^a An *f*-value of 0.53 was used for all iron-containing compounds. The samples were ground such that 100% passed through the U.S. mesh sieve indicated. Aliquots for Mössbauer and chemical analyses were taken from same sample of ground coal.

^b Coal identification: IM8 = Pittsburgh No. 8 Ireland Mine, West Virginia (bituminous); RB = Rosebud Seam, Colstrip, Montana (subbituminous); BC = Bear Coal Company Mine, Colorado; LN = Lennox Bed, Edna Mine, Colorado (bituminous); LV = Lovilla Seam, Lovilla, Iowa (subbituminous); KY9 = Kentucky No. 9, Fies Mine, Kentucky (bituminous); OP7 = Oak Park No. 7 Mine, Lower Freeport (No. 6-A), Ohio (bituminous); IL6 = Illinois No. 6 (bituminous); WV = Blacksville No. 2, Pittsburgh Seam, West Virginia; KY = Kentucky No. 9/14, Colonial; IL = Illinois No. 6, River King.

^c Used TFA in place of HCl in ASTM method.

^d Commercial laboratory atomic absorption analysis for total iron.

^e Commercial laboratory (different from *d*) ASTM analysis.

of a rather large variety of factors that could cause errors, several of which are described here and in a later section, a single set of results for a given coal should not be taken as definitive. When viewed as a collection, however, several systematic, albeit qualitative, features can be observed:

1. The overall agreement is reasonable over a range of concentrations from about 0.1 to 3 wt % iron. The results are comparable to those of other workers (2, 8, 9).
2. On the average, the pyritic iron determined by the Mössbauer method is higher than that determined by the ASTM

- method by about 25% (relative to the ASTM values and using only the -325-mesh results for the IM8 and RB coals), with individual differences up to 70%.
3. On the average, the total iron content determined by the Mössbauer method is only about 5% higher than that determined by the ASTM method (relative to the ASTM values and using only the -325-mesh results for the IM8 and RB coals), with individual differences as large as 70%, however.
 4. For two coals, IM8 and RB, mesh size affects both the Mössbauer and ASTM results. The finer mesh material results in substantially higher pyritic and total iron for both methods. (The large difference for the RB coal is probably attributable in part to difficulty in obtaining a small representative sample from this particular coal because of rather large pyrite particles.)

Possible explanations for some of these trends can be offered. The higher pyritic iron values from the Mössbauer area method could be caused by the use of too low an f -value appropriate to pyrite. Measurements described later indicate that the true f -value of pyrite may be as high as 0.80 (as opposed to $f = 0.53$ used here). On the other hand, the ASTM method could be missing some of the pyrite for two reasons: the HCl treatment (Figure 3) dissolves some of the pyrite (or perhaps marcasite) and/or the HNO₃ treatment (Figure 3) does not dissolve all of the pyrite. These effects were demonstrated by Levinson and Jacobs (3) and are supported further here. For example, the finer mesh IM8 (bituminous) and RB (subbituminous) coals yielded higher ASTM pyritic iron (Table I), presumably because more of the pyrite was freed from the coal matrix. Additional evidence for these problems is presented below.

The average agreement on total iron between the Mössbauer and ASTM analyses, combined with the higher Mössbauer results on pyritic iron, would be consistent with either (or a "combination") of the following possibilities: (1) the ASTM results are correct and the Mössbauer decomposition into pyritic and nonpyritic iron is in error because the f -value of 0.53 is too low for pyrite and too high for the nonpyritic iron compounds (but such that on the average it represents a good "effective" value and yields a correct total iron content) or (2) the Mössbauer results are correct and the chemical determination is in error because the HCl treatment dissolves some of the pyrite to give a low value of pyritic iron (but the total iron value is correct since the HNO₃ dissolves all remaining iron-containing compounds).

Complicating these over-simplified pictures is the effect of mesh size seen for the first two coals listed in Table I. The implication for the chemical analysis is that finer grinding frees more of the iron-containing compounds from the coal for the acids to dissolve. In the case of the

Mössbauer analysis, the finer grinding reduces the average thickness of the iron-containing crystallites, thereby allowing for the preparation of a more uniform absorber and the generation of a larger resonance area even though the same total concentration of iron is present in the coal. Further evidence for this effect is given here, and it is explored in more detail, theoretically and experimentally, in a later section. For the IM8 and RB coals used in these experiments, it appears that the -60-mesh size specified in the ASTM procedure is not fine enough for accurate analysis. In general, it would be good practice to specify the mesh size used in a coal analysis by either of these methods if the ASTM standard -60-mesh size is not used.

The ASTM method calls for the use of two acids. In an attempt to improve the penetration of the first acid into the coal matrix to remove the nonpyritic iron, trifluoroacetic acid (TFA) was substituted for HCl in several experiments. TFA plus hydrogen peroxide (H_2O_2) has been shown by Deno et al. (43) to be effective in degrading the aromatic structures in coals. We did not add the H_2O_2 to avoid oxidation (and thereby the dissolving) of the pyrite. The results of Table I for IM8 coal by chemical analysis show increased values of pyritic iron and total iron for both mesh sizes. The nonpyritic iron value is almost identical to that from the HCl extraction, so the TFA would not seem to offer an advantage over the HCl in the first step. Some of the TFA may remain absorbed onto the coal or it may have degraded the organic matrix to a larger extent so that the combination of TFA followed by HNO_3 is more effective in removing pyritic iron than is the prescribed combination of HCl followed by HNO_3 (Figure 3). The HNO_3 is an oxidizing agent as is H_2O_2 , so it may be that the TFA remaining on the coal becomes more effective in attacking the coal structure only in the HNO_3 solution. The results are still lower than those of the -325-mesh Mössbauer analysis, so there still may be some undissolved pyrite remaining after this treatment (see discussion of Sample 8, Figure 6, in the next section).

MÖSSBAUER ANALYSIS OF A COAL AFTER VARIOUS TREATMENTS. The IM8 coal was subjected to a more detailed study, and these results are shown graphically in Figure 6. It should be emphasized that not all of the weight concentrations shown (C_j) have been normalized to the weight of the original coal sample. They represent the Mössbauer effect measured on the original coal and several different products derived from it so that C_j is the concentration in the particular sample and not necessarily in the original coal. For example, the coal can be said to contain organic matter, pyrite, and other inorganic or mineral matter. After the treatment with the first acid, it may contain only organic matter and pyrite. Thus the nature of the sample has changed and the fraction of pyrite may increase even though the actual mass of pyrite remains unchanged. Weight relationships between the different products and the

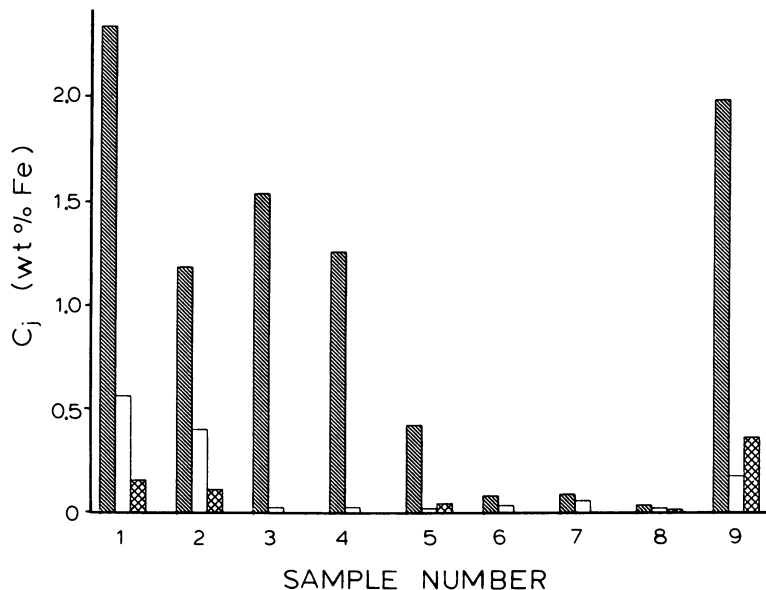


Figure 6. Iron concentrations obtained using Mössbauer area method after various treatments of IM8 coal.

The subscript j refers to each of the three iron species indicated ((▨) pyritic iron; (□) nonpyritic ferrous iron; (▩) ferric iron). All samples other than No. 1 employed -100 -mesh coal. Sample identification: (1) as received (-325 mesh); (2) as received (-100 mesh); (3) residue after 30-min boil in HCl; (4) residue after 30-min boil in TFA; (5) residue after 1-h boil in HNO₃; (6) residue after 8-h boil in HNO₃; (7) residue after HCl and HNO₃ treatments (ASTM); (8) residue after TFA and HNO₃ treatments; (9) residue after low-temperature ashing.

original coal were not obtained in these early experiments. Relative changes in the values for the three iron-containing compounds are significant, however.

Samples 1 and 2 in Figure 6 show the effect of particle size differences (related data are also listed in Table I). Both are the same bituminous coal but ground to pass through different sieve sizes and prepared as absorbers with identical mass per unit area. Sample 1 was ground to -325 mesh and Sample 2 to -100 mesh. Although all C_j 's increase for the finer mesh size, note that the pyrite value increases more in relation to the nonpyritic iron components, perhaps indicating finer particle sizes for these phases relative to pyrite.

Samples 3 and 4 show the iron-containing compounds present in the residues after treatment of the coal with either boiling HCl or TFA for the 30-min time period called for in the ASTM procedure. The ferric iron component has been removed by both acids, but a small amount of a nonpyritic ferrous iron component remains, thereby indicating a small

source of error in the ASTM method: it can result in a low sulfate sulfur value and, perhaps, a larger value for pyritic iron if the HNO_3 later dissolves this component. The error may be larger than indicated by the graph if the f -value of the ferrous iron site is substantially lower than that of pyrite.

It may be noted that the pyrite values for Samples 3 and 4 are both larger than for the original -100-mesh coal. This could result from the loss of mineral matter and possibly small organic molecules from the coal, thereby causing the pyrite to become a larger fraction of the total remaining sample. The size of the difference seems rather large, however, and should not be taken as accurate in view of the large difference between Samples 1 and 2.

Sample 5 shows the effect of treating IM8 coal with only HNO_3 for 1 h at a boil and at the concentration specified in the ASTM procedure. Apparently, a considerable amount of pyrite dissolves but both ferrous and ferric iron compounds remain in the residue. Sample 6 is the residue from a similar treatment except that an 8-h time period was used. This did remove all of the ferric iron, but some pyrite and some nonpyritic ferrous iron still remain.

Sample 7 is the final residue from the application of the complete ASTM procedure. (This residue is represented by the rectangle at the extreme right in Figure 3.) The combination of the two acids $\text{HCl} + \text{HNO}_3$ can be seen to be more effective than either acid alone. A small quantity of undissolved pyrite and ferric iron species still remain in the residue even with this treatment. This is evidence that the ASTM procedure does not remove all of the iron from this coal. The magnitude of the error or a generalization to other coals must await further work. It may be that both treatments have extracted all the readily available pyrite and the remaining crystals are deeply imbedded in some tough organic matrix. It should also be noted that if these are extremely small microcrystals, their Mössbauer resonance could be yielding an enhanced value of C_j over that of the presumably larger particles in the original coal (see section on absorber granularity). Particle size effects should always be kept in mind.

Sample 8 shows the results for a residue similar to that in Sample 7 except that TFA was substituted for the HCl . It appears to have reduced the pyrite and nonpyritic ferrous iron component still further. The C_j values are both nearly 1/3 those of Sample 7. Some ferric iron was detected in addition. This small amount could have been present in the other samples but remained undetected, masked by the more dominant pyrite resonance. As the pyrite concentration is lowered to values approaching that of the other components, it becomes easier to see and identify the other species.

Taken as a whole, these results provide clear evidence that sources of error do exist in the ASTM procedures. If unextracted iron is present in the residue for one coal, it can be present in the residues of other coals. Analysis of the residues at various stages of the ASTM procedure by Mössbauer spectroscopy offers a convenient way to monitor the existence of these sources of error. More careful and detailed experiments are now underway to attempt to achieve an iron balance through all of the steps of the ASTM procedure.

The bar graphs shown as Sample 9 are from a residue resulting from a low-temperature ashing (LTA) experiment. The C_j 's are normalized to the weight of ash and not to the weight of the original coal. The feature of most interest would be whether or not the iron compounds underwent any alteration during the ashing. The pyrite did not undergo extensive changes as no iron oxides were detected, but measurable changes in the nonpyritic ferrous iron species did occur. The C_j relative to pyrite for the -325-mesh coal are 0.24 and 0.07 for the nonpyritic ferrous and ferric iron, respectively. For the ash, the values are 0.09 and 0.18; that is, a reversal in relative concentrations of the nonpyritic ferrous and ferric iron sites has occurred because of LTA. Similar effects have been demonstrated by Montano (2, 12).

RESULTS FROM THE MÖSSBAUER INTENSITY METHOD. Results from the application of the resonance intensity method described earlier are presented in Table II for several of the same coals characterized in Table I. The agreement is encouraging. Both calibration curves presented in Figure 5 are used for comparison. Note that in every case

Table II. Results of Mössbauer Analysis
Fraction of Iron as FeS_2

<i>Coal (mesh)</i>	<i>Mössbauer</i>		<i>ASTM</i>
	<i>Intensity Method</i>	<i>Area Method</i>	
IM8 (-100)	0.76	0.70	0.68
IM8 (-325)	0.80	0.77	0.67
RB (-325)	0.90	0.90	0.74
BC (-100)	0.00	0.00	0.00
LN (-100)	0.55	0.50	0.42
LV (-100)	0.90	0.94	0.86
KY9 (-200)	0.96	0.80	0.68

^a Comparison is made with area method and chemical ASTM method. Both the 19- μ m and 48- μ m calibration curves of Figure 5 are used. See Table I for coal identification. The absorbers are identical to those used to obtain the results in Table I.

except one (BC coal), the total wt % iron, obtained from the 19- μm and 48- μm calibrations, spans the values obtained from the Mössbauer area method. The differences between the intensity and area methods in the fractional amount of pyritic iron are readily explained by our present neglect of overlap corrections. For example, the larger fractions for the IM8 and KY9 coals using the intensity method result from neglect of some ferric iron resonance at the velocity selected for pyrite determination, 0.62 mm/s relative to the center of a metallic iron calibration (see Figure 2d). Also, we emphasize that prior knowledge of the full resonance spectra aided in these particular measurements. For example, if we had looked for pyritic iron in the BC coal (pyrite-free, see Figure 2b) at the above velocity, a fractional amount of about 0.2 would have been detected simply because of the overlap of the FeCO_3 resonance at this velocity. However, such overlaps are amenable to correction since the line shape is known. An important point to keep in mind here is that the data obtained from the intensity method are found in a much shorter time than those using the area method.

To test further the utility of the intensity method and to examine the particle size problem associated with RB coal (Table I) in more detail, we examined the effect of grinding time of the coal in a mechanical grinder. A 50-g quantity of -14-mesh coal was placed in the grinder and subsamples of about 2 g were removed after increasingly longer grinding times. The data obtained at the two velocities corresponding to the well-resolved pyrite and sulfate lines are shown in Figure 7. Less than 1-h was required to obtain the data shown; approximately 40 h would have

of Coals by Resonance Intensity Method*

<i>Total Wt % Iron</i>			
<i>Mössbauer</i>		<i>Area Method</i>	<i>ASTM</i>
<i>Intensity Method</i>			
<i>19 μm</i>	<i>48 μm</i>		
1.28	2.06	1.71	2.13
2.15	3.22	3.09	3.44
1.46	2.32	1.94	1.40
0.20	0.33	0.39	0.23
0.12	0.22	0.16	0.12
1.68	2.65	2.16	2.44
1.55	2.42	2.10	1.95

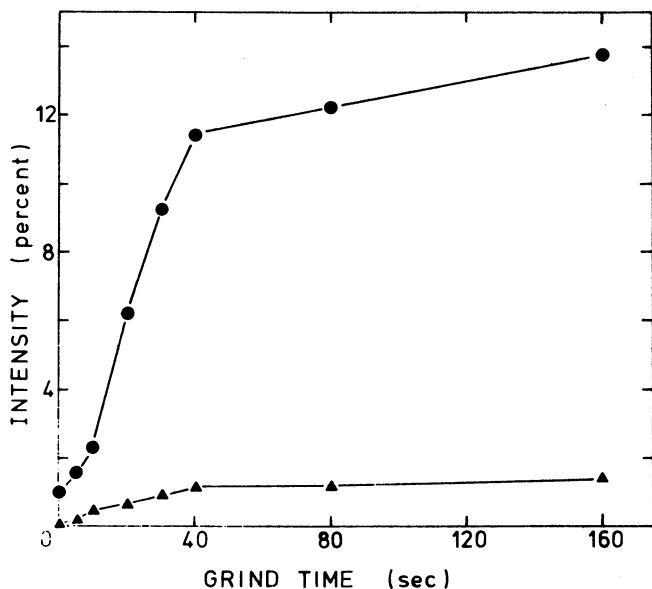


Figure 7. Mössbauer intensities from RB coal according to Equation 7 for samples ground for different times in a mechanical grinder. The intensities were measured at constant velocities corresponding to maximum resonance of the higher velocity pyrite (FeS_2 (●)) and sulfate ($\text{FeSO}_4 \cdot \text{H}_2\text{O}$ (▲)) lines (see Figure 8). All absorbers were prepared with identical mass per unit area. The solid lines are drawn to guide the eye.

been required with the area method to obtain comparable statistics. For both pyrite and sulfate iron, there is a rapid increase in intensity during the initial stages of grinding followed by a relatively slow increase at longer grind times. The ratio of pyrite intensity to sulfate intensity remains the same within statistical uncertainty throughout the time period. This implies that both the pyrite and sulfate exhibit the same particle size effect and that pyrite is not being converted to sulfate during the grinding. The dramatic change in the Mössbauer resonance of the original coal compared to the coal ground for 160 s is shown in Figure 8. These spectra were obtained with the same amount of coal in the absorber (0.20 g/cm^2). The resonance, in addition to being quantitatively larger for the finely ground coal attributable to a more uniform absorber, is qualitatively different. The A-component is not observed in the fine coal simply because of the dominance of the pyrite and sulfate. Thus, the A-component (perhaps ankerite) is distributed in the original coal as much smaller particles than the pyrite or sulfate. These results show the impracticality of obtaining quantitative Mössbauer data from roughly ground or bulk

coal, for example, by backscatter techniques (at least for coals like the RB) but, on the other hand, suggest a means of searching for and studying less-common iron-containing compounds in coal.

Problems in Quantitative Mössbauer Analysis

Based on our preliminary work on coal described above, and to some extent by the work of others (1-16), the present problems affecting the application of Mössbauer spectroscopy to quantitative determinations of iron concentrations in coal (and other fuel materials) are: absorber granularity, background radiation corrections, imprecise or unknown f -values, polycrystalline texture effects, and the associated computer decomposition of strongly overlapping spectral components. These are discussed briefly in the following sections.

Absorber Granularity. The consequence of preparing a Mössbauer absorber from powdered material containing small crystals or granules of iron-containing compounds is a nonuniform absorber with respect to the

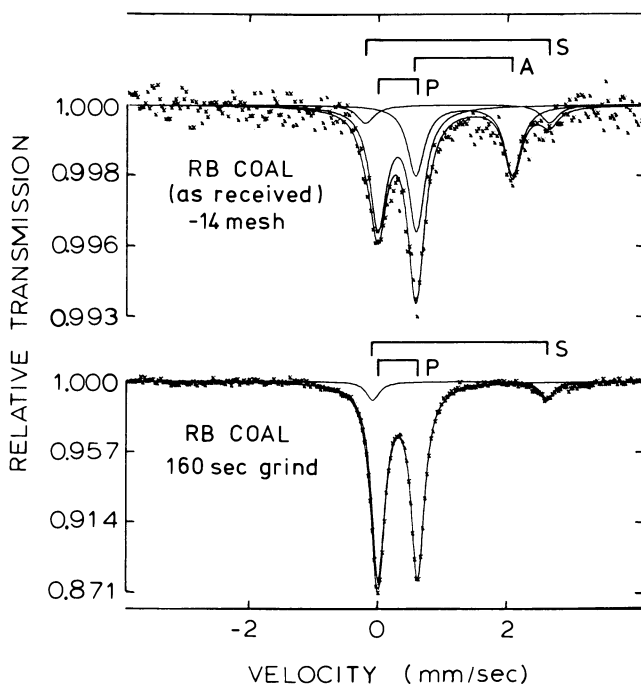


Figure 8. Mössbauer spectra from RB coal of different particle size. The solid curves represent the computer decomposition with superpositions of quadrupole pairs corresponding to pyrite (P), szomolnokite (S), and an iron carbonate-like component (A). Note the different ordinate scales.

optical path of the gamma-rays. Because of electronic absorption, the thinner parts of the absorber will be given a different weight than the thicker ones, and this combined with the nonlinear resonance area vs. thickness behavior (Equation 4) will cause the observed intensity or area to be smaller than that for a uniform absorber. Bowman et al. (44) have treated theoretically the effect of granular absorbers on resonance intensity and linewidth. Abe and Schwartz (38, 39) considered the effect on resonance area. In these studies (38, 39, 44) small variations from uniformity and a single granule size in the absorber were assumed. We have extended the theory to examine larger deviations from uniformity and to consider the more realistic situation of a distribution of granule sizes. We summarize some experimental observations on pyrite and state some results of theoretical work, the details of which (45) will be presented elsewhere.

The theoretical approach involves an average of the Mössbauer resonance area A , Equation 4, over all thicknesses encountered by the gamma-rays in passing through a granular absorber. The resulting average, $\langle A \rangle$, for a single resonance line can be expressed in a form similar to Equation 4, with analytical correction terms added to account for deviations from uniformity, or it can be left in a more general integral form appropriate to highly nonuniform absorbers. Comparisons of calculations of $\langle A \rangle$ for a simple granule shape, and different size distributions from these two types of expressions are displayed in Figure 9 as a function of the ratio of the average thickness of a granule, $\langle x \rangle$, to the total average thickness of the absorber, T . Based on the theoretical results presented in Figure 9, several conclusions may be drawn:

1. The resonance area $\langle A \rangle$ decreases with increasing granule thickness for a fixed average absorber thickness. The size of the effect is such that large errors in calculating the iron concentration or the f -value from $\langle A \rangle$ are possible if one does not account for granularity. For example, note that at $\langle x \rangle / T = 1$, for $T = 4$, $\langle A \rangle$ is reduced by about 20% relative to what it would be for a uniform thickness absorber. However, it is reduced by only about 10% for $T = 1$ for the same $\langle x \rangle / T = 1$. Thus the iron concentration determined from the experimental area probably contains less error if both the effective thickness and the granule size are small.
2. A first-order granularity correction reasonably accounts for the effect in the region where $\langle x \rangle / T \leq 1$. For example, at $\langle x \rangle / T = 1$ the difference between the first-order correction curve and the general evaluation curve is about 3% for $T = 4$ and only 1.5% for $T = 1$ (valid for a resolved two-line resonance such as from pyrite).

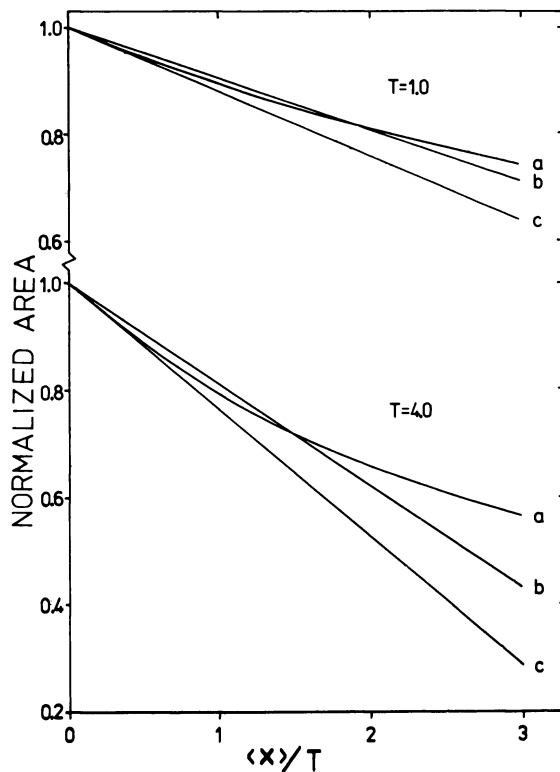


Figure 9. Theoretical resonance area (normalized to the value for a uniform absorber, Equation 4) for absorbers composed of granules of right cylindrical shape whose axes are parallel to the gamma-ray beam.

The calculations are appropriate to a two-line resonance like that of pyrite, and the area plotted is for one of the lines. $\langle x \rangle / T$ is the ratio of average effective granule thickness to the total effective thickness of the absorber. Curve a assumes a Gaussian distribution of granule thickness with Gaussian width $\sigma = \langle x \rangle / 2$; Curve b uses first-order granularity correction and assumes a single thickness for all granules; Curve c uses first-order granularity correction and assumes a Gaussian distribution, $\sigma = \langle x \rangle / 2$.

3. The presence of a Gaussian size distribution causes the area to decrease faster with increasing average particle size than it does for granules of a single size. Compare Curves b and c.

To demonstrate experimentally the effect of absorber granularity as suggested in Figure 9, we prepared a series of pure pyrite absorbers of various concentrations and different but known granule sizes and distributions.

The effect of granularity is illustrated dramatically in Figure 10, which shows the Mössbauer spectra of 19.7 mg FeS_2/cm^2 absorbers (i.e., same average concentration) of $\langle d \rangle = 19 \mu\text{m}$ and $125 \mu\text{m}$ average particle size. The resonance area of the sample with 19- μm granules is a factor of 2.6 times larger than that with the 125- μm granules. This effect clearly does not result from a background radiation effect since B from Equation 1 was found to be only 1.05 for the $\langle d \rangle = 19 \mu\text{m}$ absorber and even smaller (1.04) for the $\langle d \rangle = 125 \mu\text{m}$ absorber.

Figure 11 shows the experimental area A of one of the lines of pyrite plotted in a manner analogous to Figure 9. The 33.91-mg FeS_2/cm^2 absorbers were obtained by stacking the other three samples. The vertical arrows indicate the average thickness, $t_A = (\text{mass of pyrite}/\text{cm}^2)/\rho$, for each sample weight, where $\rho = 5.013 \text{ g}/\text{cm}^3$ is the density of pyrite. Thus $\langle d \rangle/t_A = 1$ would correspond approximately to $\langle x \rangle/T = 1$ in Figure 9. The correspondence is not exact because in Figure 9 we have

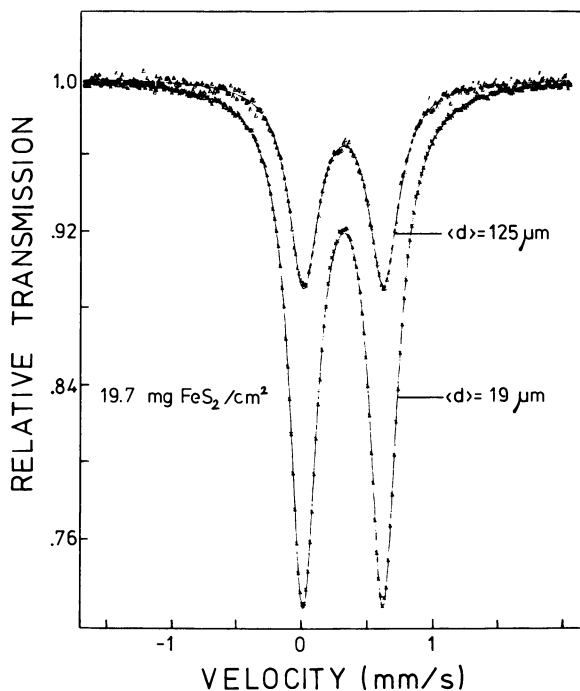


Figure 10. Mössbauer spectra from pure pyrite absorbers of identical average concentration ($19.7 \text{ mg}/\text{cm}^2$) but different average granule size $\langle d \rangle$. The solid lines are least-squares computer fits and the zero of velocity corresponds to the center of the α -iron calibration.

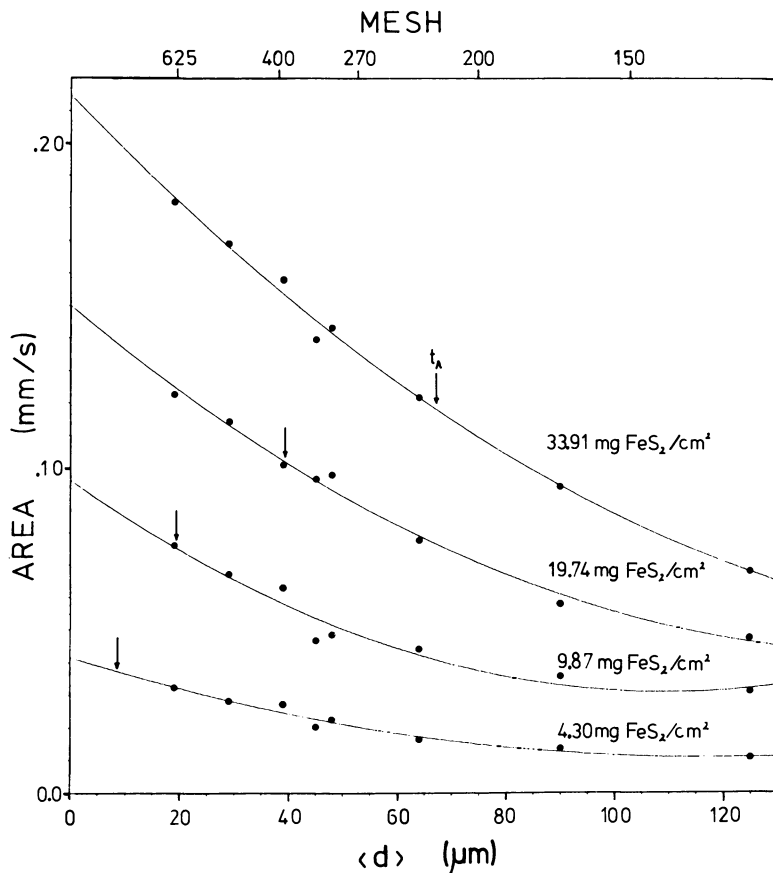


Figure 11. Experimental Mössbauer resonance area of one of the lines of pyrite for various concentrations (in mg/cm^2) and various average granule sizes $\langle d \rangle$.

The area was calculated using Equation 3. The arrows indicate the average thickness of pyrite t_A for each absorber concentration. The solid lines are least-squares fits to Equation 8. The data for $33.91 \text{ mg FeS}_2/\text{cm}^2$ was obtained by stacking absorbers (of the same $\langle d \rangle$) of the other weights.

assumed an idealized particle shape. The solid lines passing through each set of data at constant weight are least-squares polynomial fits of the form:

$$A = A_0 + A_1 \langle d \rangle + A_2 \langle d \rangle^2 \quad (8)$$

This behavior is consistent with the theoretical results presented in Figure 9. Note that the intercept A_0 is the area that would be obtained

with a uniform absorber as given by Equation 4. T was evaluated from Equation 4 for the four experimental intercepts (Figure 11) and then used to evaluate the f -value of pyrite (Equation 6). This yielded $f = 0.80 \pm 0.08$, where the main source of error is attributable to uncertainty in the extrapolation of the data in finding each A_0 .

The size of the slopes A_1 in Figure 11 is found to be in reasonable agreement with our theoretical predictions; close agreement was not expected in view of our use of idealized particle shapes in the calculations. More realistic models of granule shape and size distributions are being developed. Our results to date show that to avoid a significant granularity effect, absorbers must be prepared such that $\langle x \rangle / T \ll 1$, often a difficult task with coal. On the other hand, our semi-quantitative agreement between simple theoretical first-order corrections and experiment for absorbers with $\langle x \rangle / T \leq 1$ suggests that one should pursue further improvements. These could lead to the practical application of granularity corrections to quantitative Mössbauer analysis of pyrite in coals.

Background Correction. The size of the background radiation contribution relative to total count rate in the gamma-ray counting channel is likely to be highly variable with absorbers made of coals because of wide variations in mineral matter content. The size of the background correction also will be affected by the granule sizes of the mineral matter. These effects are illustrated in Figure 12, which shows the background factor B measured for pure pyrite absorbers with the filter method described in an earlier section (Equation 1). The absorbers are the same ones generated for the granularity study described in the preceding section. The observed trends are expected: both the increase in B with average mass per unit area in the optical path of the gamma-ray beam and the increase in B with decreasing granule size for a constant mass per unit area result from increased electronic absorption of the 14.4-keV gamma-rays.

Because of the nonlinear behavior of the resonance area with iron concentration in the absorber, the errors produced from a neglect of the background are compounded as the concentration increases. Using Equations 3 and 4 one can calculate the error in the effective thickness T caused by neglect of B ; for example, neglect of a 10% background correction at $T = 5$ causes an error of 18% in T and therefore in the iron concentration as well (Equation 6).

Although the filter method as used here is convenient and fast, it should not be regarded as highly accurate as it does neglect some additional possible contributions to the background (34, 46). The ultimate accuracy to be realized in quantitative coal analysis by Mössbauer spectroscopy is likely to be limited by this problem.

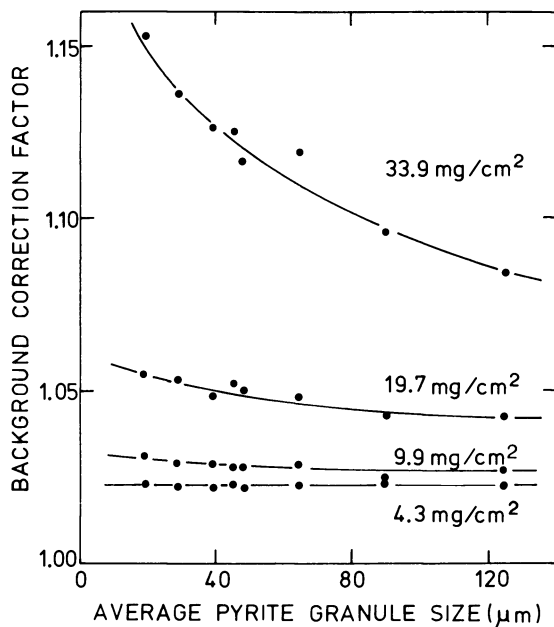


Figure 12. Background correction factor B vs. average size of pyrite granules in absorbers of different average concentration. B was found using the filter method described in an earlier section (Equation 1). The set of absorbers was the same as that used to obtain the experimental areas shown in Figure 11.

Recoilless Fractions. Table III summarizes the available room-temperature f -values of iron-containing compounds that commonly occur in coal. We comment briefly on some of the values listed. The single-crystal pyrite results of Suzdalev et al. (47) are based on resonance area measurements and the use of an expression similar to Equation 4, but one which includes an overlap correction. Their results (47) are open to question since the observed difference in pyrite line intensities was not found in more recent studies (50, 51).

Montano (2), using coal samples containing pyrite and szomolnokite, measured the temperature dependence of the resonance areas, extracted the effective thicknesses, and fitted the variations with the Debye model to obtain the f -values shown. We note, however, that the validity of a simple one-parameter Debye model for pyrite is open to question (52), and that the Debye temperature of 285 K corresponding to $f = 0.60$ is much lower than values obtained by other methods (50, 52, 53).

The value of $f = 0.48$ for pyrite (8, 9) was obtained by preparing standard absorbers of -400-mesh pyrite mixed with coconut charcoal to

Table III. Mössbauer f -Values of Iron Compounds Commonly Occurring in Coals^a

Compound	f -Value	Reference
Pyrite (FeS ₂)	$f_{//} = 0.7, f_{\perp} = 0.5^b$	47
Pyrite	0.60 (± 10 –15%)	2
Pyrite	0.48	8, 9
Pyrite	0.53 ± 0.04	this work
Pyrite	0.80 ± 0.08	this work
Marcasite	$f(\text{marc})/f(\text{pyrite}) = 0.96 \pm 0.06$	this work
Szomolnokite (FeSO ₄ · H ₂ O)	0.59 (± 10 –15%)	2
Siderite (FeCO ₃ [10% Mg])	$0.60 \leq f_{\perp} \leq 0.80^c$	48
Siderite (FeCO ₃)	$0.60 \leq f_{//} \leq 1.0$	
Siderite (FeCO ₃)	0.47 ± 0.05	49

^a All values listed are those for room temperature.

^b // and \perp refer to the body diagonal directions of the cubic pyrite lattice.

^c // and \perp refer to the C -axis of the rhombohedral lattice.

simulate the coal environment. The experimental resonance areas were compared with Equation 4 to yield effective thicknesses vs. pyrite content. No corrections were made for background radiation or absorber granularity. The use of $f = 0.48$ produced results for coals which when compared with chemical results (8, 9) yielded differences of about 20% on the average.

Our determination of $f = 0.53 \pm .04$ for pyrite was described in an earlier section. It included background corrections but no granularity correction. Since -200 -mesh (-74μ) pyrite was used, Figure 9 or 11 suggests a correction for granularity of as high as 1.5 to the effective thickness and therefore to the f -value. This is then consistent with our second value of $f = 0.80 \pm .08$ obtained from pure pyrite powder absorbers as described in the beginning of this section. Similarly, the Huffman and Huggins value of 0.48 would be increased substantially if background and granularity corrections were included in the analysis.

The f -value of marcasite compared to pyrite (ratio = $0.96 \pm .06$) was found from powder absorbers prepared and measured under similar conditions: granule sizes sieved to the same range ($-270, +400$ mesh) and measured with the same source and same geometry. The similarity of the resonance areas of these pyrite and marcasite absorbers is illustrated in Figure 1.

The reported f -values of FeCO₃ (48, 49) are not in agreement. Also, Goldanskii et al. (49) find a significant angle dependence in f from natural-mineral single-crystal specimens, and the value of 0.47 given in Table III is their calculated average over several angles; they suggest

that it should be the f -value appropriate to a polycrystalline absorber (49). Note that our use of $f = 0.53$ in the analysis of a coal containing only FeCO_3 (BC coal, Table I) yielded a value for the iron content of 0.39 wt % compared to the chemical result of 0.23 wt %. This suggests that a larger f -value for FeCO_3 might be appropriate, but this requires further study.

Absorber Texture and Spectral Resolution. The existence of a "texture" or nonrandom orientation of iron-containing crystallites in a Mössbauer absorber can cause problems in quantitative analysis because of its effect on the transition probabilities q_{ij} or the f -values f_j in Equation 6. This is attributable to the possible angle dependence of q_{ij} in the presence of magnetic and quadrupole hyperfine interactions, or the possible angle dependence of f_j caused by lattice vibrational anisotropy of iron sites of low symmetry (54–59). For example, a polycrystalline metallic iron foil with nonrandom domain orientation or a textured powder absorber of FeCO_3 will yield a total resonance area that is different from that with a random distribution of domains or crystallites (55, 57). Attempts to generate randomly oriented powder samples of FeCO_3 have been mostly unsuccessful and have led to discrepancies regarding interpretation of unequal line intensities (58, 59).

The possibility of effects of nonrandom orientation of iron-containing crystallites in coal Mössbauer absorbers should be considered in view of the inherent, highly textured nature of coal, particularly if one is considering in-situ measurements of coal deposits or the study of bulk (unground) specimens. In a recent experiment (51) it was demonstrated that angle-dependent effects associated with the quadrupole resonance or the f -value of pyrite are negligible. This result is useful in that it allows one to obtain quantitative information from either of the two pyrite resonance lines (since $q_{1j} = q_{2j} = 1/2$ when $j = \text{pyrite}$ in Equation 6), one of which is often obscured by resonance from other iron compounds in the coal. It also appears to validate the often used assumption of equal intensities for the pyrite lines in computer decomposition of asymmetric spectra due to overlapping resonance lines. However, even for perfectly random absorbers (no texture), the latter assumption for pyrite or any iron-containing compound exhibiting a quadrupole splitting must be used with caution in quantitative work because of the inherent nonlinearity (saturation) of resonance area vs. effective thickness (Equation 4). This problem of spectral resolution combined with thickness saturation has been pointed out and illustrated before (60). An accurate decomposition of poorly resolved coal spectra could require the use of the correct, but more complicated, transmission integral expression for the line shape (60). Although we have not yet explored their use, modifications of the area expression used here (Equation 4)

are available to account exactly for overlap of two lines separated by some amount Δ (36) and to account approximately for line broadening caused, for example, by a small distribution of isomer shifts or quadrupole splittings (39, 61).

Summary

These investigations support the ability of ^{57}Fe Mössbauer spectroscopy to provide values of pyritic and nonpyritic iron concentration in coals which are in average agreement with chemical analysis values. However, the limits of accuracy of the techniques cannot yet be established. This is attributable in part to uncertainties in both the chemical method and in the interpretation of Mössbauer data. Of the several problems considered in this work, absorber nonuniformity appears to us to be a major source of error. Another is the present uncertainty in the recoilless fractions of the various iron-containing compounds in coal and the practice of assuming a single value of this parameter for all such species. The use of $f \approx 0.5$ to 0.6 by us and others yields reasonable agreement with chemical results. Such f -values should be regarded as useful, effective values and not true values until further systematic measurements are made. The treatment of granularity of pyrite in Mössbauer absorbers as presented here indicates that the true f -value of pyrite could be substantially higher than those presently in use. We do not advocate the use of this higher value ($f = 0.80$) until it is substantiated by other methods described in the literature. Our theoretical granularity corrections are being improved and tested with coals of known pyrite size distributions. Parallel investigations are underway to define more precisely the limits of accuracy of the ASTM chemical method and to delineate special precautions regarding mesh size and rank of coal. Applications of the quantitative techniques developed here to other fuel materials such as oil shale are in order.

Although the Mössbauer resonance intensity method as described here will certainly be laboratory-dependent, and also subject to granularity corrections, our preliminary findings indicate its possible utility for fast, routine determinations of pyrite in coal. Corrections for line overlap, data reduction based on calibration curves, and the experimental manipulations associated with this method are all amenable to automation. Although not yet constructed, a microcomputer-controlled constant-velocity system has been designed to select appropriate velocities sequentially, route detector signals to various counters, record and reset the contents of the counters, time each operation, and process the data. With this improvement, an analysis time on the order of 1 min/sample appears feasible.

Acknowledgments

The initial stage of this work was supported under DOE Contract ERDA E(49-18)-2047, and later work was supported in part by a grant from the Colorado Energy Research Institute. We also are grateful for the financial support from the Mining and Mineral Resources Research Center of the Colorado School of Mines, and for the assistance from several Colorado School of Mines undergraduates, particularly Mike Taravella, Bill Branch, and Donna Turner.

Literature Cited

1. Lefelhocz, J. F.; Friedel, R. A.; Kohman, T. P. *Geochim. Cosmochim. Acta* 1967, 31, 2261.
2. Montano, P. A. *Fuel* 1977, 56, 397.
3. Levinson, L. M.; Jacobs, I. S. *Fuel* 1977, 56, 453.
4. Smith, G. V.; Liu, J.; Saporochenko, M.; Shiley, R. *Fuel* 1978, 57, 41.
5. Russell, P. E.; Montano, P. A. *J. Appl. Phys.* 1978, 49, 1573.
6. Jacobs, I. S.; Levinson, L. M.; Hart, H. R. *J. Appl. Phys.* 1978, 49, 1775.
7. Stillert, A. H.; Renton, J. J.; Montano, P. A.; Russell, P. E. *Fuel* 1978, 57, 447.
8. Huffman, G. P.; Huggins, F. E. *Fuel* 1978, 57, 592.
9. Huggins, F. E.; Huffman, G. P. In "Analytical Methods for Coal and Coal Products", C. Karr, Jr., Ed.; Academic: New York, 1979, Vol. 3, p. 371.
10. Lee, R. J.; Huggins, F. E.; Huffman, G. P. *Scanning Electron Microsc.* 1978, 1, 561.
11. Keisch, B.; Gibbon, G. A.; Akhtar, S. *Fuel Proc. Tech.* 1977/1978, 1, 269.
12. Montano, P. A. *Amer. Chem. Soc., Div. Fuel Chem., Prepr.* (Washington, D.C., Sept., 1979) 24, 218.
13. Dovzhenko, N. F.; Smoilovskii, A. M.; Chernyshov, Yu. A. *Khim. Tverd. Topl.* 1977, 11, 73 (English translation in *Solid Fuel Chem.* 1977, 11, 61).
14. Levinson, L. M. "EPRI Report, FP-1228 Research Project 267-2," 1979.
15. Hinckley, C. C.; Smith, G. V.; Twardowska, H.; Saporoschenko, M.; Shiley, R. H.; Griffen, R. A. *Fuel* 1980, 59, 161.
16. Jacobs, I. S.; Levinson, L. M. *J. Appl. Phys.* 1979, 50, 2422.
17. Montano, P. A.; Granoff, B. *Fuel* 1980, 59, 214.
18. Cole, R. D.; Liu, J.; Smith, G. V.; Hinckley, C. C.; Saporoschenko, M. *Fuel* 1978, 57, 514.
19. Neavel, R. C. *Amer. Chem. Soc., Div. Fuel Chem., Prepr.* (Washington, D.C., Sept., 1979) 24, 73.
20. *Annu. Book ASTM Stand.* Part 26, Designations D2013-72 and D346-75.
21. Gluskoter, H. J. In "Trace Elements in Fuels," *Adv. Chem. Ser.*, 1975, 123, p. 1.
22. Kiss, L. T.; King, T. N. *Fuel* 1977, 56, 340.
23. Given, P. H. *Fuel* 1976, 55, 256.
24. Greer, R. T. *Energy Sources* 1978, 4, 23.
25. Greer, R. T. In "Coal Desulfurization, Chemical and Physical Methods," *ACS Symp. Ser.* 1977, 64, p. 1.
26. Stevens, J. G.; Stevens, V. E., Eds. "Mössbauer Effect Data Index"; Plenum: New York, 1970-1978.
27. *Mössbauer Eff. Ref. Data J.*, 1978-1980, 1-3.
28. *Annu. Book ASTM Stand.* Part 26, Designation D2492-79.
29. *Ibid.*, Designation D3177-75.

30. Gladfelter, W. L.; Dickerhoof, D. W. *Fuel* 1976, 55, 360.
31. Edwards, A. H.; Jones, J. M.; Newcombe, W. *Fuel* 1964, 43, 55.
32. Burns, M. S. *Fuel* 1970, 49, 126.
33. Given, P. H.; Miller, N. M. *Fuel* 1978, 57, 397.
34. Housley, R. M.; Erickson, N. E.; Dash, G. *Nucl. Instr. Meth.* 1964, 27, 29.
35. Nussbaum, R. H.; Howard, D. G.; Nees, W. L.; Steen, C. F. *Phys. Rev.* 1968, 173, 653.
36. Bykov, G. A.; Hien, P. Z. *Sov. Phys. JETP* 1963, 16, 646.
37. Johnson, D. P. *Phys. Rev.* 1970, B1, 3551.
38. Abe, N.; Schwartz, L. H. *Mater. Sci. Eng.* 1974, 14, 239.
39. Abe, N.; Schwartz, L. H. In "Mössbauer Effect Methodology", Gruverman, I. J., Ed.; Plenum: New York, 1973; Vol. 8, p. 249.
40. Williamson, D. L.; Schupmann, R. G.; Materkowski, J. P.; Krauss, G. *Metall. Trans.* 1979, 10A, 379.
41. Williamson, D. L.; Nakazawa, K.; Krauss, G. *Metall. Trans.* 1979, 10A, 1351.
42. Trooster, J. M.; Vieggers, M. P. A. *Mössbauer Eff. Ref. Data J.* 1978, 1, 154.
43. Deno, N. C.; Greigger, B. A.; Stroud, S. G. *Fuel* 1978, 57, 455.
44. Bowman, J. D.; Kankeleit, E.; Kaufmann, E. N.; Persson, B. *Nucl. Instr. Meth.* 1967, 50, 13.
45. Guettinger, T. W., M.S. Thesis, Colorado School of Mines, 1979.
46. Housley, R. M. *Nucl. Instr. Meth.* 1965, 35, 77.
47. Suzdalev, I. P.; Vinogradov, I. A.; Imshennik, V. K. *Sov. Phys. Solid State* 1972, 14, 1136.
48. Housley, R. M.; Conser, U.; Grant, R. W. *Phys. Rev. Lett.* 1968, 20, 1279.
49. Goldanskii, V. I.; Makarov, E. F.; Suzdalev, I. P.; Vinogradov, I. A. *Sov. Phys. JETP* 1970, 31, 407.
50. Finklea III, S. L.; Cathey, L.; Amma, E. L. *Acta. Cryst.* 1976, A32, 529.
51. Guettinger, T. W.; Williamson, D. L. *Phys. Rev.* 1979, B20, 3938.
52. Anderson, C. T. *J. Amer. Chem. Soc.* 1937, 59, 486.
53. Nishihara, Y.; Ogawa, S. *J. Chem. Phys.* 1979, 71, 3796.
54. Housley, R. M.; Grant, R. W.; Gosner, U. *Phys. Rev.* 1969, 178, 514.
55. Rosencwaig, A.; Ron, M.; Kidron, A.; Shechter, H. *J. Phys. Chem. Solids* 1969, 30, 359.
56. Stöckler, H. A.; Sano, H. In "Mössbauer Effect Methodology", Gruverman, I. J., Ed.; Plenum: New York, 1970; Vol. 5, p. 3.
57. Housley, R. M. In "Mössbauer Effect Methodology", Gruverman, I. J., Ed.; Plenum: New York; Vol. 5, p. 109.
58. Pfannes, H. D.; Conser, U. *Appl. Phys.* 1973, 1, 93.
59. Nagy, D. L. *Appl. Phys.* 1978, 17, 269.
60. Shenoy, G. K.; Friedt, J. M.; Maletta, H.; Ruby, S. L. In "Mössbauer Effect Methodology", Gruverman, I. J., et al., Eds.; Plenum: New York, 1974; Vol. 9, p. 277.
61. Johnson, D. P.; Dash, J. G. *Phys. Rev.* 1968, 172, 983.

RECEIVED June 27, 1980.

Mössbauer Effect Study of Victorian Brown Coal

J. D. CASHION and B. MAGUIRE

Department of Physics, Monash University, Clayton, Victoria, 3168, Australia

L. T. KISS

Herman Research Laboratories, State Electricity Commission,
Richmond, Victoria, 3121, Australia

Mössbauer spectra using ^{57}Fe were taken of low-rank, low-sulfur brown coals from the Latrobe Valley, Victoria, Australia, having a typical water content of 67%. Spectra at 78 K on bed-moist samples showed at least six poorly resolved quadrupole split doublets, one due to pyrite and/or marcasite, and the others, which do not fit any known spectra, most probably due to different hydrolyzed iron carboxylates. Dried samples gave completely different spectra with generally one intense quadrupole split doublet and one or more relaxed magnetic splittings. The isomer shifts typically moved $+0.1\text{--}0.2\text{ mm s}^{-1}$ on drying. However, the most dramatic change was an increase of nearly an order of magnitude in the absorption dip, showing that the water molecules are bonded intimately to the iron atoms in the bed-moist state.

The principal aim of this investigation was to determine the chemical state or states of nonpyritic iron in various brown coals from the Latrobe Valley in Victoria, Australia. Samples were selected to cover the known variations from the field, with concentrations of iron varying from 0.07 to 1.8% on a dry basis.

The nature of any organically bound iron was of particular interest. Lefelhocz et al. (1) tentatively assigned one of their iron spectra to organic iron, but this was subsequently determined to be a clay site (2, 3). Recent detailed Mössbauer effect investigations (4, 5, 6, 7) on coals from the U.S. northeastern fields have not shown any evidence of

organically bound iron. Schafer (8) studied the oxidation of carboxylates in Victorian brown coal, but his report does not contain any details of the Mössbauer spectra or parameters obtained.

The coals used in this investigation are of much lower rank (67% carbon) than the U.S. coals that have been studied. The Victorian coals are much higher in phenolic and carboxylic functional groups and have a low sulfur concentration ($<0.4\%$), with a low level of sulfur being present as pyrite or marcasite, FeS_2 . Possibly the largest difference from the U.S. samples is the high water content of about 67% as mined, and care has been taken to maintain the samples in this condition. When left open to the air, the coals rapidly lose moisture down to a concentration of about 15%. Samples dried below this value readily absorb moisture when exposed to the atmosphere. For the bed-moist samples, Mössbauer spectroscopy is one of the few techniques that can analyze the states of the iron without requiring drying, dissolution, or some other change to the sample.

The water in bed-moist coal is contained in several different forms and an approximate classification in order of decreasing ease of removal is (9): free water in macropores and interstices, capillaries, and water on the walls of pores too small to have a meniscus. This last type can be divided further into multilayer and monolayer water, with the monolayer water being bonded to oxygen-containing hydrophilic sites on the coal by hydrogen bonds. Schafer (10) showed that carboxylic acid groups, particularly in the salt form, are the most significant hydrophilic site, with the Fe^{2+} salt being the most efficient, followed by Mg^{2+} , Ca^{2+} , Cu^{2+} , Ba^{2+} , Al^{3+} , Fe^{3+} , Na^+ , and K^+ in order. The phenolic hydroxyl groups are less efficient than the carboxylic groups.

Sample Preparation and Experimental Details

The bed-moist samples were received in air-tight containers. Absorbers were made by quickly scraping off the outer, slightly oxidized and blackened layers until a uniform brown region was obtained. This was scraped into Lucite containers to a thickness of $1/\mu$ (where μ is the atomic absorption coefficient) of typically 3–4 mm, and then sealed. The whole operation took approximately 2–3 min, and no blackening of the coal was observed in this time. Separate absorbers were also made of some of the outer blackened layers.

One sample was received in an already oxidized form and two samples had been crushed, dried, and compressed into briquettes. These samples were allowed to remain in equilibrium with the atmosphere.

All the Mössbauer runs were taken with a $^{57}\text{CoRh}$ source using a conventional constant-acceleration drive with data collection into either a 1024 or 512 channel analyzer. All the samples were run at 78 K, with some runs also being made at room temperature and at 4.2 K. Counting time for the bed-moist samples was usually on the order of 1 week with over 10^7 counts per channel. However, for most of these spectra this was

inadequate to resolve the many small overlapping lines, so the number of data points was reduced to 170 by summing the data in groups of three adjacent channels. This gave up to 4×10^7 counts per channel, corresponding to a standard deviation of less than 0.02%. Curve fitting was then carried out by standard least-squares techniques using single Lorentzian lines, or in some cases, magnetic- or quadrupole-split spectra, where they could be used reasonably.

Results

A list of the samples studied together with some of their relevant data are given in Table I. Chemical analysis indicated that only three of the samples contained detectable amounts of FeS_2 that could be in the form of either pyrite or marcasite. Our spectra on these samples gave parameters that corresponded to pyrite, but with the poor resolution obtained we would not rule out the possibility of some marcasite as well. Consequently, we shall refer to the FeS_2 somewhat loosely as pyrite in this chapter, but with the interpretation that it includes the possibility of both pyrite and marcasite.

The total iron concentrations on a dry basis ranged from 0.07 to 1.77%, but we note that with a 67% water content, the effective iron concentration is much less. The pH of most of the dried samples was not measured. The labeling of the first six samples refers to the bore holes from which they were taken.

Bed-moist Samples. Attempts to take spectra of these samples at room temperature resulted in very small absorption dips from which it was difficult to discern any structure. Consequently the major effort was put into liquid nitrogen spectra, all of which gave at least five poorly

Table I. Details of the Coal Samples Examined*

Sample	Form	Depth (m)	Fe as FeS_2 (Dry Basis (%))	Total Fe (Dry Basis (%))	pH
M2275	Bed-moist	15.7–16.0	0.21	0.58	3.6
LY1280	Bed-moist	24.6–25.0	0.00	0.07	3.4
H1317	Bed-moist	52.0–52.8	0.00	0.22	5.1
N3372	Bed-moist	54.7–55.0	0.00	0.34	4.5
M2276	Bed-moist	44.3–44.6	0.00	1.77	4.6
C92	Partially dried	—	0.09	0.15	4.2
Top-oxidized	Dried	—	—	—	—
#15	Briquette	—	0.36	0.42	—
#19	Briquette	—	0.00	0.80	—

*Dashes indicate that the information was neither known nor measured. Iron concentrations are quoted on a dry basis.

Table II. Parameters of the Doublets Observed for the Bed-moist Samples at 78 K^a

Site	IS (mm s ⁻¹)	QS (mm s ⁻¹)	Percentage Absorption					
			M2275	LY1280	H1317	N3372	M2276	C92
1	+0.15 (4)	0.51 (4)	60	67	62	37	33	43
2	+0.16 (6)	1.20 (6)	—	—	—	19	—	10
3	+0.21 (6)	0.91 (6)	11	—	9	19	—	18
4	+0.22 (2)	0.00 (4)	22	25	21	19	18	14
5	+0.27 (9)	1.25 (9)	—	8	—	—	16	—
6	+0.38 (5)	0.61 (5)	7	—	—	—	—	8
Single lines								
7	-0.76 (6)	—	—	—	—	7	—	—
8	-0.21 (6)	—	—	—	—	—	17	—
9	-0.04 (6)	—	—	—	—	—	8	—
10	+1.02 (6)	—	—	—	7	—	4	7
11	+1.37 (6)	—	—	—	—	—	5	—

^a The single lines probably belong to doublets whose other member has not been positively identified. Isomer shifts are relative to iron metal at room temperature and the quadrupole splitting is $1/2e^2qQ$. The numbers in parentheses indicate the error in the last figure.

resolved and overlapping lines in the region between -0.04 and $+0.09$ mm s⁻¹ with respect to iron metal. The dominant absorption peak for each sample varied between 0.1 and 0.4%, and peaks were identified down to 0.03%. Typical linewidths (FWHM) were about 0.32–0.35 mm s⁻¹, with only a few lines being significantly narrower than this.

Two sets of peaks were observed for all of the samples and dominated most of the spectra—a quadrupole-split doublet with an isomer shift of $+0.15$ mm s⁻¹ (all shifts will be quoted with respect to iron at room temperature) and a splitting of 0.51 mm s⁻¹, and a single-line or possibly an unresolved quadrupole-split doublet at $+0.22$ mm s⁻¹. A total of five quadrupole-split doublets were identified, and their parameters are given in Table II together with details of the samples for which they were observed. The percentage absorption values given are the fraction of the total absorption present in that resonance. Sample inhomogeneities inevitable in the small samples used in Mössbauer spectroscopy can alter these numbers considerably so that their accuracy is certainly not better than $\pm 10\%$.

In addition, Table II lists several other lines that are undoubtedly the unmatched halves of further doublets, but whose other half is either superimposed on a stronger line or hidden in the wings. Apparently there are no strong peaks at larger velocities as would be the case if, for example, high-spin Fe²⁺ were present, but some spectra did show either very weak peaks or relaxation effects. Further spectra, preferably at 4.2 K, are required to resolve this.

Figure 1 shows spectra of four of the samples, and the differing and generally poor resolution can be seen clearly. The number of channels after folding has been reduced to 170 for all of these spectra. In Figures 1a and b we see two of the characteristic spectra from M2275 and LY1280 dominated by the three peaks mentioned earlier. The spectrum of H1317 is similar to these two. Figure 1c shows the spectrum of N3372 which had the poorest resolution of all the samples studied, while Figure 1d shows the spectrum of M2276 which contains more than three times the iron concentration of any of the other samples. This larger iron concen-

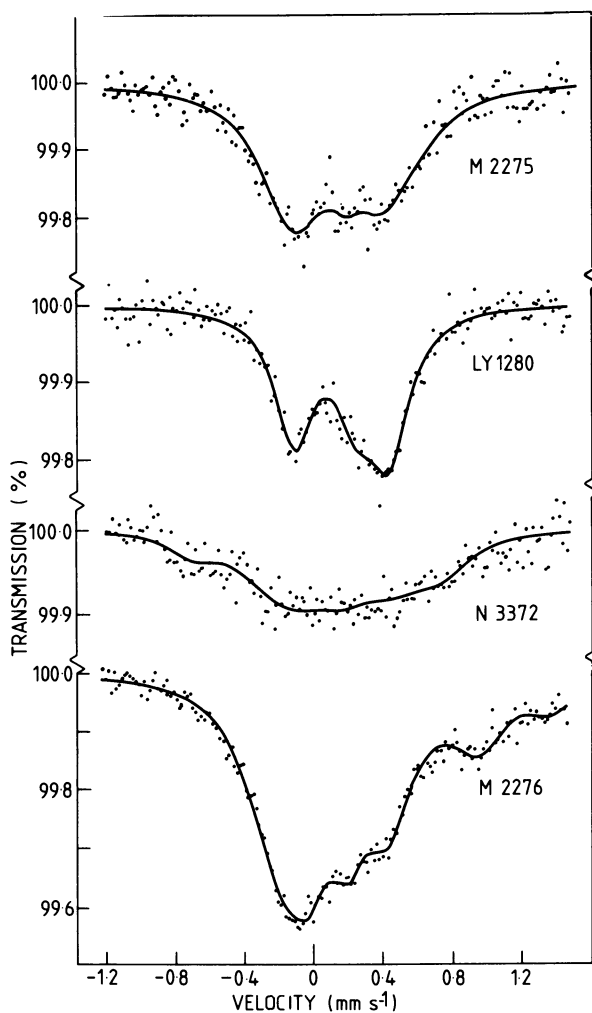


Figure 1. Mössbauer spectra of bed-moist samples of (a) M2275 (b) LY1280, (c) N3372, and (d) M2276 taken at 78 K (note the different vertical scales for each spectrum)

tration is known to alter the types of iron compounds formed as will be discussed in the next section.

Dried Samples. Sample C92 showed a spectrum similar to those of the bed-moist samples and is included with them in Table II. Its spectrum is intermediate between those shown in Figures 1b and c. However, the top oxidized sample (Figure 2) showed a completely different spectrum with a much larger recoilless fraction. This was characteristic of most of the dried samples which generally had an intense central doublet and a weaker contribution from one or more hyperfine fields, the latter usually showing signs of electronic relaxation.

In an effort to shed some light on the marked difference between the spectra of the bed-moist and dried samples, we ran an absorber made from the outer blackened section of the M2276 sample which had shown the largest previous dip of 0.4%. The difference between this spectrum (Figure 3) and the bed-moist spectrum (Figure 1d) was startling. The maximum percentage effect had increased by almost a factor of ten to 3.5% and the outer wings now showed strong evidence of electronic relaxation effects. Clearly the water molecules had been intimately bonded to the iron atoms to produce such a large change, and this will be discussed further in the next section.

The briquetted samples showed spectra similar to each other, consisting of a very intense doublet (4% dip), and relaxation effects corresponding to a magnetic hyperfine splitting. Sample 15 also had a large

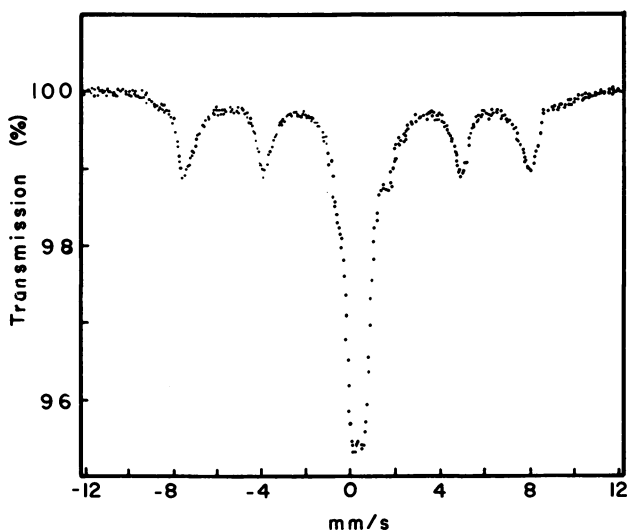


Figure 2. Mössbauer spectrum of the top-oxidized sample taken at 78 K

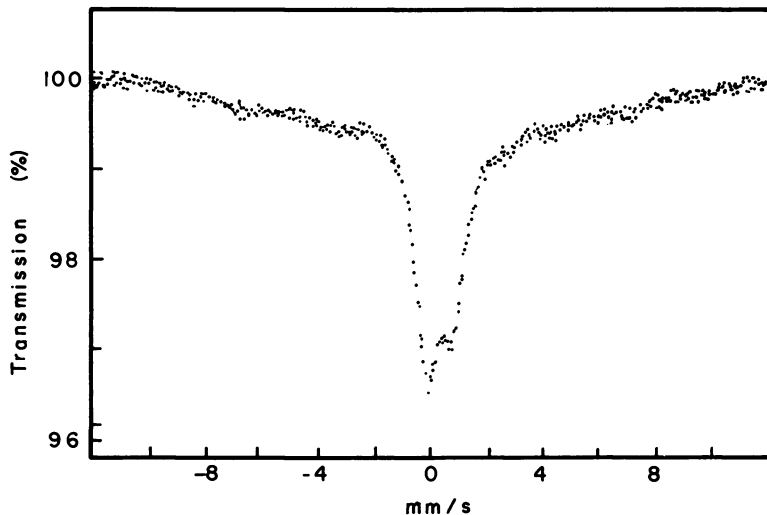


Figure 3. Mössbauer spectrum taken at 78 K of a sample of M2276 which had been slightly oxidized on exposure to the air

additional line of intensity 1% at $+2.7 \text{ mm s}^{-1}$ clearly associated with another line near zero velocity superimposed on the main doublet. The observed parameters for all of these samples are given in Table III.

Table III. Parameters Observed for the Dried Coal Samples^a

Sample	Temp (K)	IS (mm s^{-1})	QS (mm s^{-1})	Hyperfine Field (T)	Absorption (%)
#15	300	0.34 (4)	0.45 (4)	0	54
		1.3 (1)	2.8 (1)	0	8
		0.3 (2)	*	probably ~ 33	38
#29	300	0.35 (4)	0.60 (4)	0	30
		0.3 (2)	*	34 (4)	70
		0.51 (4)	0.78 (4)	0	30
Dried M2276	78	0.4 (2)	*	43 (2)	70
		0.6 (3)	*	55 (2)	
		0.57 (3)	0.32 (3)	0	36
		0.4 (2)	$-0.5 (2)$	33 (4)	9
Top-oxidized	78	0.5 (1)	$-0.5 (1)$	48 (1)	35
		0.3 (3)	*	55 (3)	20
		0.20 (4)	0.40 (4)	0	Partially dried cleaned coal
0.31 (4)	0.62 (4)	0			
0.46 (2)	0.89 (3)	0			
0.48 (3)	0.96 (5)	0			

^a Values marked (*) could not be determined but are not necessarily zero. For other explanations, see Table II.

Interpretations and Discussion

Chemical measurements on Latrobe Valley coals have shown (8) that, at low concentrations, the nonpyritic iron is usually present as low-spin iron(II) bonded to carboxylates, but at higher concentrations, oxyhydroxides may start forming. It was expected that Sample M2276 was the only one to be in this regime.

It was assumed initially that the spectra of our coals should closely resemble those from the U.S. coals, so assignment of the peaks commenced by considering both the parameters obtained there (4, 5, 6, 7) and data on oxides and hydroxides (11) and clays (12). The only site in Table II that definitely could be assigned on this basis was Site 6, which is clearly attributable to pyrite. Its observation in Samples M2275 and C92 correlated with the initial chemical analyses carried out at the Herman Research Laboratories, although our quantitative value is much lower presumably because of an inhomogeneous distribution.

Sites 1–5 could not be assigned to any of more than 50 compounds considered, and this indicated either new types of iron compounds such as organically bonded iron or alteration of the parameters from known compounds resulting from the high water content. Site 4 could correspond to Fe^{3+} in a symmetric electronic environment or perhaps chalcopyrite $(\text{Cu,Fe})\text{S}_2$, although this compound commonly produces a magnetically split spectrum at 78 K. One organically bonded compound of the former type that has the same parameters is hydrated ferric oxalate, $(\text{C}_2\text{O}_4)_3\text{Fe}_2 \cdot 5\text{H}_2\text{O}$.

The remaining sites do not correlate with known parameters for other carboxylates, although most hydrolyzed iron(III) carboxylates have isomer shifts of 0.2–0.5 mm s^{-1} and quadrupole splittings of 0.2–1.0 mm s^{-1} (see, e.g., Refs. 13–20). The parameters for these sites also cover the region of low-spin iron(II) compounds. We believe that all of these sites correspond to organically bonded iron and that the high moisture content and multiplicity of different ligands are altering parameters from the previously observed values for these compounds. This belief is supported by measurements that we have carried out on a separate project involving catalytic hydrogenation of some Latrobe Valley coals that have been dried, crushed to –60 mesh, and floated with CCl_4 to remove most of the mineral matter (21). In addition to the pyrite peaks at an isomer shift of $+0.31(4)$ mm s^{-1} and a quadrupole splitting of $0.62(4)$ mm s^{-1} , these coals showed three other doublets which are also listed at the bottom of Table III and no evidence of Sites 1–5 in Table II. Typical absorption dips were about 3%, but the linewidths were broader than the bed-moist samples, being between 0.35–0.50 mm s^{-1} .

The characteristic six-coordinated bonding of iron probably allows considerable competition between water and carboxylate ligands. The

changes observed between the spectra of bed-moist and dried M2276 also indicate that the water must be intimately bonded to the iron. The change of an order of magnitude in the Debye–Waller factor for a 14-keV gamma ray is totally unexpected and shows that the iron environment in the bed-moist coals must be decidedly “sloppy.”

The quadrupole-split doublets of the dried samples are all shifted to more positive isomer shifts than those of the bed-moist samples. This trend is also evident from the other project measurements. However, assigning the peaks is again difficult with organically bonded iron probably producing the intense central doublets in the spectra from Samples 15 and 29. The doublet with the splitting of 2.8 mm s^{-1} in Sample 15 is attributable to szomolnokite, $\text{FeSO}_4 \cdot \text{H}_2\text{O}$ arising from oxidation of the sulfide. Note that the prominent doublet in the oxidized M2276 spectrum does not correspond to any of the doublets in the original sample.

Four values of hyperfine field could be discerned in the relaxed wings of these samples, with only the top-oxidized sample giving any clean splittings. In Sample 15, the dip was so weak and relaxation sufficiently fast that the field value is only an estimate, but Sample 29 showed a maximum value of 34 T. The oxidized M2276 showed splittings out to 55T while the top oxidized sample showed three fields of 33 T, 48 T, and 55 T, with the 48-T field being well resolved (Figure 2). We believe that the 48-T field results from goethite, $\alpha\text{-FeOOH}$, with a small particle size, similar to that observed by Goodman and Berrow (22) in their study of Scottish peats. The critical size for superparamagnetism in $\alpha\text{-FeOOH}$ is about 4 nm, and x-ray diffraction measurements are consistent with the conjecture of small particle sizes. The 55-T field is probably attributable to hematite, $\alpha\text{-Fe}_2\text{O}_3$, although liquid helium experiments are required to rule out magnetite, Fe_3O_4 . The 33-T field probably results from trivalent iron bonded to organic material, with the iron–iron separation being the right distance to give relaxation effects at liquid nitrogen temperatures. Surprisingly, a spectrum of the oxidized M2276 sample taken at 4.2 K failed to show any sharpening of the relaxation.

Conclusions

The initial aim of this project was to investigate the usefulness of Mössbauer spectroscopy for characterizing coals in the bed-moist condition. The results show a clearly observable difference between the sample expected to contain oxyhydroxides and those lower in iron which only contain carboxylates. The spectra observed are markedly different from those obtained on higher-rank U.S. coals for which only information on minerals and clays has been obtained.

The drying of the coal altered the observed Mössbauer spectrum completely, increasing both the Debye–Waller factor and the isomer

shift. These changes are consistent with a change from a labile, loosely bound environment to a tightly constrained site.

The enormity of the change both in the shape of the spectrum and the size of the Debye-Waller factor when the coal is dried opens up the possibility to study on a microscopic scale the poorly understood process of the drying of coal. Chemical measurements usually determine total water content or changes in water content, and as pointed out by Allardice and Evans (9), care must be taken not to confuse thermal release of chemically combined water with accelerated diffusion of water out of micropores because of an increase in temperature. With iron carboxylates being the most active hydrophilic site, it appears that Mössbauer spectroscopy is well placed to investigate selectively at least one of the different varieties of bound water.

Further experiments at liquid helium temperatures and in applied magnetic fields are required to aid in the interpretation of the bed-moist spectra and to confirm the assignments of the magnetically split spectra. Another possible extension of this work would be a study of the changes in the coal during the briquetting process.

Acknowledgments

This work was carried out under contract to the Victorian State Electricity Commission and was supported by the Australian Research Grants Committee. The coal samples were supplied by courtesy of the Victorian Brown Coal Council. We wish to thank P. E. Clark, F. P. Larkins, and K. S. Murray for helpful discussions. We are grateful to G. P. Huffman for forwarding a copy of his review before publication.

Literature Cited

1. Lefelhocz, J. F.; Friedel, R. A.; Kohman, T. P. *Geochim. Cosmochim. Acta* 1967, 31, 2261-2273.
2. Kohman, T. P.; Ulmer, J. D. USAEC Report NYO-844-81, Sec.II.A.4, 1970, pp. 31-36.
3. Kohman, T. P.; Karol, P. J.; Kamarchik, P. USAEC Report COO-3236-3, Sec.II.A.1, 1971, pp. 5-16.
4. Huffman, G. P.; Huggins, F. E. *Fuel* 1978, 57, 592-604.
5. Huggins, F. E.; Huffman, G. P. "Analytical Methods for Coal and Coal Products"; Karr, C., Jr., Ed.; Academic: New York, 1979; Vol. 3, pp. 371-423.
6. Jacobs, I. S.; Levinson, L. M.; Hart, H. R., Jr. *J. Appl. Phys.* 1978, 49, 1775-1780.
7. Russell, P. E.; Montano, P. A. *J. Appl. Phys.* 1978, 49, 4615-4617.
8. Schafer, H. N. S. *Fuel* 1977, 56, 45-46.
9. Allardice, D. J.; Evans, D. G. "Analytical Methods for Coal and Coal Products"; Karr, C., Jr., Ed.; Academic: New York, 1978, Vol. 1, pp. 247-262.
10. Schafer, H. N. S. *Fuel* 1972, 51, 4-9.
11. Bowen, L. H. *Mössbauer Eff. Ref. Data J.* 1979, 3, 76-94.

12. Ericsson, T.; Wappling, R.; Punakivi, K. *Geol. Foeren. Stockholm Foerh.* 1977, 99, 229–244.
13. Duncan, J. F.; Kanekar, C. R.; Mok, K. F. *J. Chem. Soc.* 1969, A, 480–482.
14. Malathi, N.; Puri, S. P. *J. Phys. Soc. Jpn.* 1970, 29, 108–111.
15. Takano, M. *J. Phys. Soc. Jpn.* 1972, 33, 1312–1317.
16. Lupu, D.; Barb, D.; Filoti, G.; Morariu, M.; Tarina, D. *J. Inorg. Nucl. Chem.* 1972, 34, 2803–2810.
17. Rumbold, B. D.; Wilson, G. V. H. *J. Phys. Chem. Solids* 1973, 34, 1887–1891.
18. Long, G. J.; Robinson, W. T.; Tappmeyer, W. P.; Bridges, D. L. *J. Chem. Soc. Dalton* 1973, 573–579.
19. Dezsi, I.; Pardavi Hordath, M.; Molnar, B. *Chem. Phys. Lett.* 1973, 22, 384–386.
20. Steger, H. F. *J. Inorg. Nucl. Chem.* 1975, 37, 39–43.
21. Cashion, J. D.; Clark, P. E.; Cook, P. S.; Larkins, F. P.; Marshall, M. In “Nuclear and Electron Resonance Spectroscopies Applied to Materials Science”; Kaufmann, E. N.; Shenoy, G. K., Eds.; North-Holland: New York, 1981; in press.
22. Goodman, B. A.; Berrow, M. L. *J. Phys. (Paris)* 1976, 37(C6), 849–855.

RECEIVED June 27, 1980.

Qualitative and Quantitative Analysis of Iron-Bearing Minerals in Fossil Fuels and Petroleum Source Rock by Iron-57 Mössbauer Spectroscopy

R. E. KARL¹ and J. J. ZUCKERMAN

Department of Chemistry, University of Oklahoma, Norman, OK 73019

The Mössbauer techniques described here have important advantages over current methods for analyzing coal and petroleum source rock. During the first stage of analysis, the iron-containing minerals are identified by comparing the line positions with values for pure mineral samples. In the second stage, absorption intensities are used to determine relative amounts of mineral, and in the final step, absolute amounts of the mineral iron in the sample are found. In oil shales, four iron-containing minerals are predominant: pyrite, dolomite, siderite, and illite. The results are related to those from x-ray diffraction analysis where the correspondence is not always complete.

Any spectroscopic method is intrinsically capable of yielding only three types of information: (1) identity—on the basis that identical systems behave in an identical way; (2) purity, or the composition of a physical mixture—on the basis that physical mixing does not alter spectroscopic properties; and (3) information concerning structure, bonding, and the forces between molecules. It is a strange commentary that the application of Mössbauer spectroscopy to the first two of this list of three possibilities has come rather late, for these analytical applications would

¹ Current address: Degussa Hanau, Postfach 1351, 6540 Hanau 1, West Germany.

seem to be the most simple and straightforward, but interest in the systematics of chemical and mineralogical analysis by Mössbauer spectroscopy is developing only now.

Mössbauer Spectroscopy

The Mössbauer effect is ideally suited, among spectroscopic techniques, for analysis because of the high energy of its exciting line, which is expressed in wave numbers (cm^{-1}) in Table I, for easy comparison. The penetrating nature of the gamma rays makes Mössbauer spectroscopy effective for situations in which the materials to be analyzed are in a dilute matrix, such as rock or coal, which will be largely transparent to the exciting gamma ray. These and other advantages of using the Mössbauer effect to analyze iron minerals are listed in Table II.

The Mössbauer effect was discovered in 1957, and its principles have been described in a number of excellent texts (1, 2, 3), including its more recent applications to geology and mineralogy (1, 4, 5). Thermal (6) and magnetic (7) methods, scanning electron microscopy (8), x-ray powder diffraction (9-12), and infrared spectroscopy (13) have been applied to the detection and analysis of the mineral components of coal, but the Mössbauer method has some unique advantages not found in other techniques. However, there are also formidable technical problems that will need to be overcome.

Using the Mössbauer technique for analysis, no preconcentration or chemical treatment steps are necessary, with their attendant possible alteration of chemical state or environment. The exciting line in ^{57}Fe Mössbauer spectroscopy is a gamma ray of 14.4-keV energy to which

Table I. Spectroscopic Energies

<i>Spectroscopy</i>	<i>Typical Energy of Radiation (cm^{-1})</i>
X-ray: inner electronic states } Photoelectron: electronic states }	10,000,000
Visible-ultraviolet: valence electronic states	10,000
Infrared-Raman: vibrational states	1,000
Microwave: rotational states	10
Electron spin resonance: electron spin states in a magnetic field	0.1
Nuclear magnetic resonance: nuclear spin states in a magnetic field	0.001
Mössbauer: nuclear states	100,000,000

Table II. Mössbauer Spectroscopy in the Analysis of Iron Minerals

No preconcentration or chemical treatment
 Carbonaceous and rock matrix transparent to the exciting line (14.4-keV) gamma ray
 Applicable to crystalline or amorphous solids
 Method sensitive to tiny amounts of iron
 No isotopic enrichment
 High specific activity ^{57}Fe Mössbauer sources available
 High count rate spectrometers available
 Small quantities of sample
 Mineral of greatest interest, pyrite, has an intense and simple doublet spectrum

the carbonaceous coal or coal process product matrix will be transparent. There is no requirement for crystallinity, and iron in amorphous solids resonates as well. In techniques based upon x-ray diffraction, on the other hand, crystallites of size ≤ 200 nm give diffuse lines, and crystallites ≤ 100 nm in diameter give no pattern at all during reasonable collection times. The ^{57}Fe nuclide is the most easily studied, and has the most extensive Mössbauer literature (1-5). Powerful ^{57}Fe gamma-ray sources of high specific activity are available commercially at reasonable costs, and spectra can be developed rapidly using recently developed high count rate spectrometers. Modern Mössbauer instrumentation can be secured at very reasonable costs compared with the corresponding costs for infrared or nuclear magnetic resonance spectrometers. These advanced instruments and data reduction methods have made results more reliable. The technique is uniquely sensitive to small amounts of iron in large amounts of matrix material such as coal. Pyrite (cubic FeS_2), with an intense and characteristically simple doublet spectrum, is particularly easy to detect and analyze.

The parameters of interest are:

1. the isomer shift (IS) which reflects the electron density at the iron nucleus;
2. the quadrupole splitting (QS) in which the separation of the doublet peaks is a function of the site symmetry at the iron nucleus;
3. the Zeeman (magnetic) splitting to a six-line pattern with 3:2:1:1:2:3 intensity from which the magnetic field at the iron nucleus can be calculated; and
4. the area under the resonance absorption which is related to the number of iron atoms present and to the tightness of their binding into the lattice.

Quadrupole splitting values often vary strongly with temperature, aiding spectral line assignments in complex, overlapping spectra. Magnetic interactions can be strongly enhanced at reduced temperatures, or

eliminated above the Curie or Néel temperature, again aiding assignment. As in other forms of spectroscopy, fingerprint spectra can identify particular species present. Iron(II) to iron(III) ratios are generally easier to obtain than with traditional wet chemical methods, and accurate weight percentages can be determined (1, 4, 5).

The Mössbauer parameters for most of the iron-sulfur minerals and compounds likely to be found in coals and petroleum source rock already have been obtained. Iron pyrite and marcasite yield doublet spectra, while the spectra of the other iron sulfides are magnetically split at room temperature. Iron metal itself and many of its oxides, hydroxides, carbides, etc., give ambient temperature magnetic spectra, but iron(II) in clay minerals and sulfates and their hydrates gives simple doublet spectra. The data in the literature are scattered, with some dating from the 1960's just after the Mössbauer effect was first studied. There are differences outside of the experimental errors assigned to the numerical data among laboratories, and there are several cases of more serious discrepancies in the general appearance of the spectra reported for the same material. The authenticity and purity of the natural mineral samples examined is obviously in question in several cases, and the data taken before a decade ago should be rerun using a modern spectrometer with up-to-date calibration and computation techniques.

Current Analytical Methods

The qualitative analysis of coal and petroleum source rock generally employs the x-ray powder diffraction (XRD) technique (9-12) in which complex pattern recognition is crucial to reliable detection. Quantitative analysis relies upon careful measurement of XRD peak heights in whole rock analysis, which has proved notoriously difficult to do. The current American Society for Testing and Materials (ASTM) method for the determination of sulfur in coal (14) is based upon a wet chemical procedure (15) in which total sulfur and only two of its three forms, sulfate and pyritic, are determined. The third form, organic sulfur is calculated by difference:

$$\text{Organic S} = \text{Total S} - (\text{Sulfate S} + \text{Pyritic S})$$

The sulfate and pyritic sulfur together are known as mineral sulfur (16, 17, 18), which is bound predominantly to iron. The HCl-soluble iron sulfates are separated from the HNO₃-soluble iron sulfides in pulverized and sieved coal samples.

The ASTM method of analysis, although based upon thermodynamic principles, is in fact controlled by kinetic factors. Several known effects can contribute to systematic errors in the results. First, small crystallites of the mineral sulfur forms may be completely encapsulated in the carbonaceous material within sieved ($250\ \mu\text{m}$) pieces, and thus survive both the HCl- and HNO_3 -digestion stages (19–22). The carbonaceous environment of these crystallites is combustible, and their sulfur content would contribute to the total sulfur analysis, but not to the mineral sulfur content. Thus the net effect is to overestimate the organic sulfur content. Second, iron minerals and compounds other than pyrite itself may remain behind as insoluble residues from the HCl treatment. Their sulfur content is likely to be less than that of FeS_2 , but their iron contribution is calculated as though it were derived from a material of the composition FeS_2 . In addition, finely divided FeS_2 , especially in the more reactive orthorhombic marcasite form, may in fact dissolve during the HCl treatment to liberate H_2S and not be reported as mineral sulfur. The sulfate sulfur present may, in any case, have been derived only from the oxidation of less stable or surface forms of pyrite during the weathering of mined coal in storage or transport, or even during the grinding and handling steps in the laboratory, and may not be an intrinsic component of the raw coal. Performing the HCl- and HNO_3 -digestions simultaneously on different coal samples, rather than sequentially, can actually yield negative results for pyrite (23). Errors in the pyritic or sulfate determinations will accumulate in the organic sulfur calculation for which no reliable independent method of analysis exists (15).

The determination of the sulfur content of coals (24) has increased in importance in recent years, and is a concern of both the coal-producing industries and governmental regulating and energy agencies. Analysis for inorganic or mineral sulfur forms directly through the application of ^{57}Fe Mössbauer spectroscopy to iron-containing minerals in coals could replace the current, wet-chemical ASTM method with a sensitive, accurate spectroscopic technique. It is capable not only of providing quantitative data on the total amounts of iron-sulfur minerals present in coals and coal process products, but of identifying and determining quantitatively the relative amounts of the individual iron-sulfur minerals present. Almost all the mineral sulfur is present as FeS_2 in the form of pyrite or its less stable dimorph, marcasite. Much of the remainder consists of variously hydrated forms of FeSO_4 (16, 17, 18, 24). A reliable, differential analytical method for these two types of iron-sulfur minerals would itself constitute a significant improvement over what is currently available.

In addition, quantitative determination of the mineral assemblage and iron partitioning in oil shales is important for the influence these materials have on the retorting characteristics of the shale (25, 26, 27).

Mössbauer Spectra of Coals and Coal Process Products

The Mössbauer spectra of coals and coal products were first recorded in 1967 (28), and recently interest has revived, both here (29–37) and in the Soviet Union (38). The published data are both scattered and sparse, but include ambient temperature spectra of sieved raw coal (28, 29, 38), vitrain and fusain samples of ranks from lignite to anthracite (28), and cryogenic spectra of high- and low-pyrite-content coals (31). In addition, data for heat-treated coals (29), the residues from the low-temperature ashing process (31), are available. The iron(II)/iron(III) ratios in pyrite ores also have been determined (40), along with iron in the Athabasca tar sands (41) and iron partitioning in oil shale (42).

The information from the studies on coal published so far confirms that FeS_2 , either in the form of pyrite or marcasite, is by far the predominant iron-sulfur mineral in coal, and that the iron(II) sulfate hydrates can be distinguished from FeS_2 in oxidized and weathered coal samples (28). It is claimed that some (ca. 20%) of the FeS_2 is removed during the HCl-digestion stage of the current ASTM procedure, and that small amounts (ca. 5%) of an iron-bearing species that is probably FeS_2 remain behind after HNO_3 -digestion (32, 33, 34).

Technical Problems

There are several practical problems that have to be solved before Mössbauer spectroscopy can be applied in a routine way to the analysis of iron minerals in coal and petroleum source rock. Some of these are associated with the spectroscopic method itself, while others arise because of the nature of the iron minerals and the materials in which they are found.

Coal. Coal is an air- and moisture-sensitive material whose mineral composition begins to change once it is dug. Weathered coal will give different results from fresh, dry samples protected from the atmosphere and water. What is termed coal embraces an enormous number of materials, with different mineral compositions and contents. Thus, generalizing results from one coal to another will be hazardous, and the difficulty of choosing representative samples for study from a mass of heterogeneous material will have to be addressed carefully.

Iron-Sulfur Minerals. Mineral samples have been wrongly identified by optical means in large numbers of cited cases, and Mössbauer spectra for mislabeled iron-sulfur minerals are scattered throughout the literature. The densities of pyrite and the other iron-sulfur minerals of interest are much greater than those of the carbonaceous materials that make up their matrix, and there could be settling and loss during sampling. The most important of these minerals, FeS_2 , is also much

harder than coal itself and may be lost systematically during grinding, riffing, and sieving. FeS_2 , especially in its more reactive marcasite dimorphic form, is rather easily oxidized in moist air to iron(II) and iron(III) sulfates in different hydrated phases (17, 43). Although usually absent in fresh coals, sulfate sulfur can become abundant in weathered coal samples. The amount of sulfate sulfur reported in the chemical analyses of many coals is merely a function of the time since collection of the fresh material, and the manner in which it was stored and handled (17). Mössbauer spectroscopy has been used in the Soviet Union to follow the changes in pyrite on flotation (44) and fine grinding (45, 46). The advanced stages of oxidation produce the thermodynamically more stable iron oxides. In addition, iron in coal has been found as the nonsulfur-containing siderite (FeCO_3) and ankerite ($2\text{CaCO}_3 \cdot \text{MgCO}_3 \cdot \text{FeCO}_3$) as well as in many clay minerals; sulfur may be present as the noniron sulfide minerals galena (PbS) and sphalerite (ZnS) as well as the sulfate minerals gypsum ($\text{CaSO}_4 \cdot 2\text{H}_2\text{O}$) and barite (BaSO_4) (16, 17, 18). Of course, only the iron-bearing materials can be detected by the Mössbauer effect.

The Mössbauer Technique. While the Mössbauer spectra of coals (28) and other natural minerals (1-5) were recorded in the last decade, reaching the goal of developing a method for quantitative analysis and the ability to identify individual iron-bearing species by this technique will require more sophisticated apparatus to record spectra and compute routines for fitting the data. Some iron(II) compounds may show no spectra at ambient temperatures during normal data collection times, so low-temperature runs are necessary. The quadrupole splitting values in some cases are strongly temperature-dependent, and magnetic interactions may begin to predominate at low temperatures. Liquid-helium temperatures may be necessary to identify unequivocally certain iron minerals. Long count times and very powerful sources are necessary to resolve shoulders arising from minor components. Mössbauer spectra of materials giving rise to quadrupole-split lines can be affected by the particular orientation of the crystallites in the sample being studied. Nonrandom orientations can give rise to doublet lines of unequal areas, which might lead to the misassignment of a pair of lines arising from the same material to two different spectral features in a complex spectrum, or instead, skew quantitative estimates of the amount of that component in a complex mixture. Deciding upon relative amounts of components by weight from Mössbauer data is not straightforward. The area under each resonance depends upon the recoil-free fraction, related to the Debye temperature or the tightness of binding of the iron nucleus at its particular site, in addition to merely the number of atoms of each type present. In general, the lattice dynamics will not be the same at

each site, so site population ratios could be difficult to obtain. It must be assumed that no isotope fractionation has occurred during geological times, so that ^{57}Fe is in fact 2.19% by weight at each site. The recoil-free fraction can in principle be determined by several methods for each component iron mineral of coal, but in practice the determinations are rather laborious and are fraught with large errors (1-5). This fact, combined with the question of whether these values, which depend somewhat upon particle size (1-5), are the same for pure synthetic materials and those found naturally, may defeat attempts to obtain site population ratios in some cases. Another feature of the problem is the similar spectral parameters reported for pyrite and marcasite, whose Debye temperatures are close as well (47).

Computation Methods. Computer-fitting of a complex spectrum will be necessary. Several choices confront the analyst, and assumptions must be made in the fitting procedures, especially initially. Implicit in any analysis is the assumption that the ^{57}Fe isotope is equally abundant at each site. Either the recoil-free fractions of each suspected component must be known reliably, or set equal. Line shapes must be assumed to be Lorentzian, even though they begin to deviate from the ideal as the thickness of the sample increases (saturation effects) and as the mover system vibrates, causing the line shapes to become Gaussian. Linewidths of the individual components of doublets or sextets usually must be set equal. The close overlap of two or more Lorentzian curves will give an envelope of non-Lorentzian shape. To resolve two overlapping peaks accurately, the peak separation should be greater than the full-width at half-height. For peaks only 0.20 mm/s apart, for example, the standard deviation in the area estimates can be very large.

Constraints often must be placed on the fitting procedure, especially in the initial stages, in order to have the fit converge. The number of superimposed patterns and their multiplicity are estimated, and half-widths and intensities can be constrained to be equal. However, achieving convergence even after stepwise reestimation and the removal of the constraints does not always guarantee that a unique fit to the spectrum has been achieved.

These technical problems are summarized in Table III.

Approaches to the Solutions of the Technical Problems

The attempt to overcome these apparent difficulties to produce a reliable analytical method for mineral sulfur is worthwhile at this time, and solutions are at hand for each of the technical problems just outlined.

Sampling. The handling of air- and moisture-sensitive materials is commonplace in inorganic and organometallic chemistry, and reliable techniques for recording Mössbauer spectra of extremely unstable

Table III. Technical Problems

Representative sampling
 Iron minerals more dense and harder than coal and petroleum source rock matrices
 Air- and moisture-sensitivity of coal and rock iron minerals
 Oxidation of FeS₂ and iron (II) minerals
 Particle size and orientation effects
 Mineral composition-dependent spectral parameters
 Resonance area dependence on number of ⁵⁷Fe nuclei, recoil-free fraction
 Lack of reliable recoil-free fraction data for iron minerals
 Synthetic vs. natural samples
 Complex magnetically and quadrupolar split spectra
 Fitting overlapping spectra
 Reliable data for each pure component
 Constraints and assumptions
 Recoil-free fractions set equal
 Lorentzian line shape vs. saturation
 Linewidths set equal
 Line intensities in doublet spectra set equal
 Line intensities in magnetically split spectra set 3:2:1:1:2:3
 Non-Beer's law behavior (saturation)

compounds have been developed. Fresh samples can be handled in an inert-atmosphere glovebox using conventional techniques, and grinding, pulverization, riffing, and sieving can be carried out under inert-atmosphere conditions as well. Interior portions of chunk material can be chosen to ensure freshness, since only gram quantities are necessary for spectral analysis.

Iron-Sulfur Minerals. Optically authenticated samples of mineral specimens in the small quantities required for our experiments are obtained from the Smithsonian Institute, the U.S. Geological Survey, from corresponding state surveys, or from commercial sources. Chemical analysis by the ASTM (14) and x-ray powder methods (9-12) are used to characterize further the mineral samples, which are then characterized by Mössbauer spectroscopy, including the isomer shift, quadrupole splitting, resonance area, and line multiplicity. Beer's law plots of resonance area vs. concentration in coal-like charcoal matrices are constructed for each material. The Beer's law plots are calibrated vs. source-absorber distance in the experimental setup, temperature of the absorber, weight of the absorber, and thickness of the absorber. Utilizing the whole sample avoids problems of density or hardness separation of iron minerals during sample preparation.

Qualitative Analysis by Mössbauer Spectroscopy. The problem of assigning the spectra of mineral samples to their component parts has been examined extensively, and treatments with worked examples are found in the standard textbooks on the subject (1-5). Sulfate minerals

Table IV. Approaches to the Solutions of the Technical Problems

Representative sampling of interior portion or use of freshly dug material
 Inert-atmosphere handling of samples
 Comparison spectra of authentic minerals
 Spectral dependence of varying mineral composition determined
 Variable-temperature runs
 simplify magnetically split spectra
 identification by temperature dependence of area
 identification by magnetic transition temperature

have been detected in the presence of pyrite in coal in one study (31), and the use of Mössbauer spectroscopy as a fingerprint technique in mineralogy and geochemistry has now reached a high level of development (4, 5).

Quantitative Analysis by Mössbauer Spectroscopy. This subject is of great potential interest in ferrous metallurgy (48) and the study of corrosion (49), and methods have been worked out for mixtures of iron compounds (50). Intensive development of methods for characterizing minerals and lunar samples (51) has more recently taken place (4, 5). Soviet workers have, for example, claimed the determination of pyrite in Donets coal (38). It is clear that accurate methods for both the quantitative analysis and speciation of pyrite and other iron minerals in raw coals and petroleum source materials can now be developed.

The approaches to the solutions of the technical problems are summarized in Table IV.

A Portable Analyzer for Pyrite

It is possible using currently available technology to design an inexpensive, battery-operated, portable analyzer for pyrite, with no moving parts, based on the Mössbauer effect. Small, freshly pulverized samples could be analyzed rapidly by this backscatter spectrometer without weighing or sieving. Such a device would contain a powerful, fixed ^{57}Fe Mössbauer source with a gamma-ray tuned precisely to the wing of the pyrite doublet least subject to interference from other iron-bearing minerals in coal. Baseline, off-resonance calibration for each sample would be achieved by mounting the source on a piezoelectric crystal subjected to an intermittent oscillating voltage which would vibrate the crystal and shift the source gamma-ray away from any possible interfering resonance. A conversion electron detector could be read out continuously as a digital ratio of the on- and off-resonance signals. An error analysis program would digitally display the percentage of pyritic sulfur as successive significant figures developed during the course of analysis. Such portable devices have been developed extensively

for x-ray analyses of sulfur in fuel oil and lead in gasoline (52). A pyrite meter based on a pyrite ^{57}Co source recently has been proposed (53). An earlier suggestion utilized a $^{119\text{m}}\text{SnO}_2$ source to find cassiterite in the field (54).

Survey of Coals

The following spectra form an anthology made possible by samples from the Oklahoma Geological Survey. The coals are all from Craig County in Northeast Oklahoma. Approximate analytical data and forms of sulfur from the ASTM method were provided with each sample. The typical spectrum shown in Figure 1 is dominated by the doublet for pyrite/marcasite, and contains the right wing of a second doublet, whose position is constant at 2.50 ± 0.01 mm/s for all coal spectra in which it appears. The left wing is buried somewhere under the pyrite resonances, and there is little doubt that it arises from an iron(II) sulfate. Four forms of this material are known: the orthorhombic anhydrous salt (55, 56, 57), and the mono-(szomolnokite) (58, 59, 60), tetra-(rozenite) (61), and hepta-(melanterite) (60, 62–71) hydrates. We studied samples of iron(II) sulfate in its various forms, and found four species with almost equal isomer shift values of 1.14–1.16 mm/s, but different quadrupole splitting magnitudes in the range 2.70–3.62 mm/s. We attempted to synthesize each form separately, and although to our knowledge there are no reliable

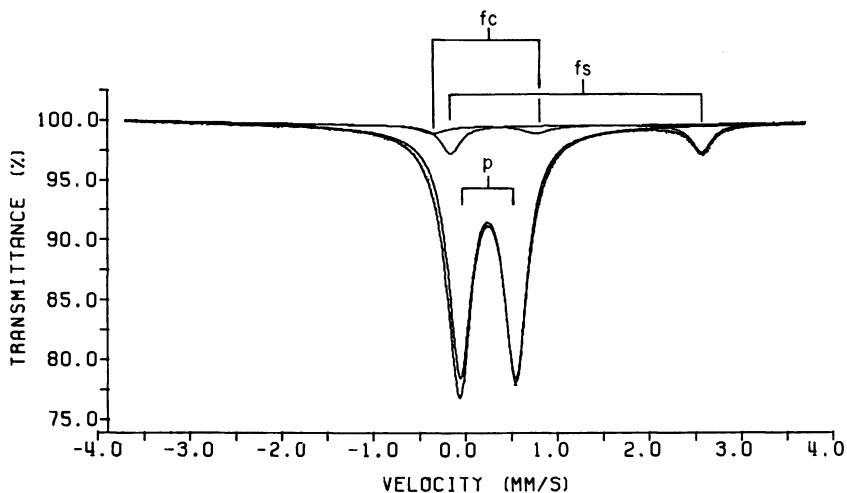


Figure 1. Coal sample from Craig County, Oklahoma containing pyrite/marcasite (p) plus high-spin iron(II) sulfate monohydrate (fs). A second line from an iron(III) sulfate (fc) can be seen in the fit.

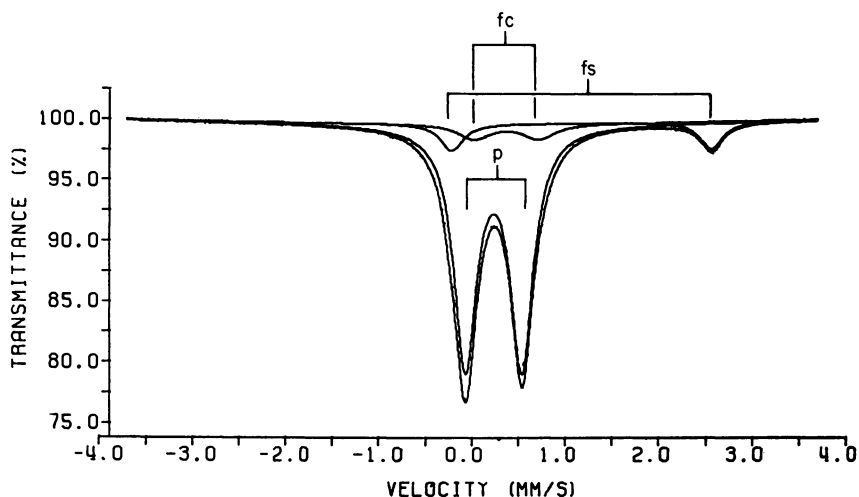


Figure 2. The Craig County, Oklahoma coal shown in Figure 1 with the iron(II) sulfate doublet fit inside the slightly more intense iron(III) sulfate doublet ((*p*) pyrite/marcasite; (*fs*) iron(II) (ferrous) sulfate; (*fc*) iron(III) (ferric) sulfate)

data linking Mössbauer parameters to each pure form, we can assign the small doublet to the monohydrated iron(II) sulfate form using our own data and those from the literature just cited.

The situation becomes more complex on closer examination, since in almost all of these coal samples an additional weak absorption line in the range 0.68–0.79 mm/s is detected. Again, this is the higher velocity component of a quadrupolar doublet, but in this case, no well-founded identification is possible, apart from its assignment as an iron(III) compound (probably sulfate). This assignment is likely on the basis of chemical intuition, but is supported only on the position of the high velocity line, since there is simply no way to determine the correct position of the second component of the doublet which lies under the pyrite/marcasite absorptions and overlaps with the iron(II) sulfate lines. In the solution shown in Figure 1, this iron(III) line has been placed to lower velocities of the iron(II) lines, leading to isomer shift values of about 0.15–0.20 mm/s and a quadrupole splitting value of about 1.1 mm/s. A second solution, shown in Figure 2, places the iron(III) doublet inside the iron(II) doublet, leading to an isomer shift of 0.30–0.35 mm/s and a quadrupole splitting of 0.7 mm/s. The Mössbauer values for the anhydrous iron(III) sulfate (68,72) and that with nine waters of hydration (coquimbite), for which no Mössbauer data seem to have been reported, do not allow us to distinguish the two possibilities, nor do the goodness-of-fit criteria from the spectra. We believe we can

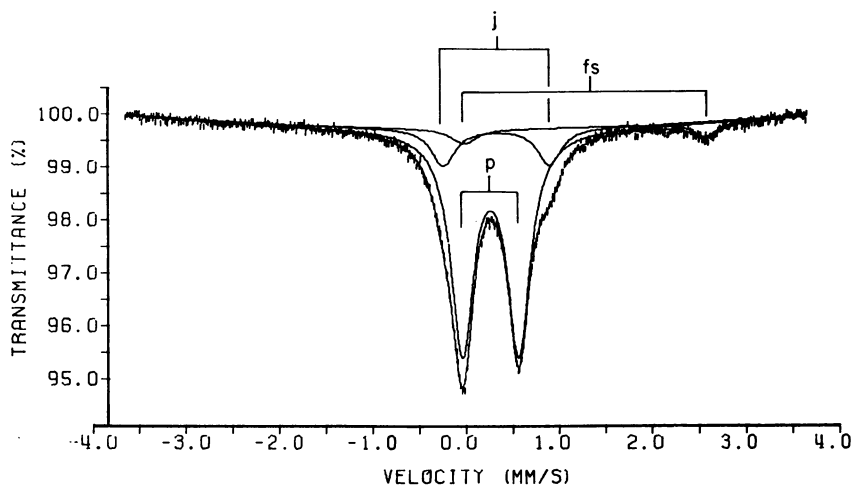


Figure 3. A Craig County, Oklahoma coal containing jarosite ((p) pyrite/marcasite; (fs) iron(II) (ferrous) sulfate; (j) jarosite)

rule out the presence of jarosite, $(\text{Na,K})\text{Fe}_3(\text{SO}_4)_2(\text{OH})_6$, since the line arising from this mineral should appear at higher velocities (73, 74).

In Figure 3 a shoulder arising from jarosite on the high-velocity side of the right-wing of the pyrite/marcasite doublet can be seen easily. Once more, other possible solutions exist, but in this case switching the low-velocity components as in Figure 4 leads to a worsening in χ^2 and misfit parameters.

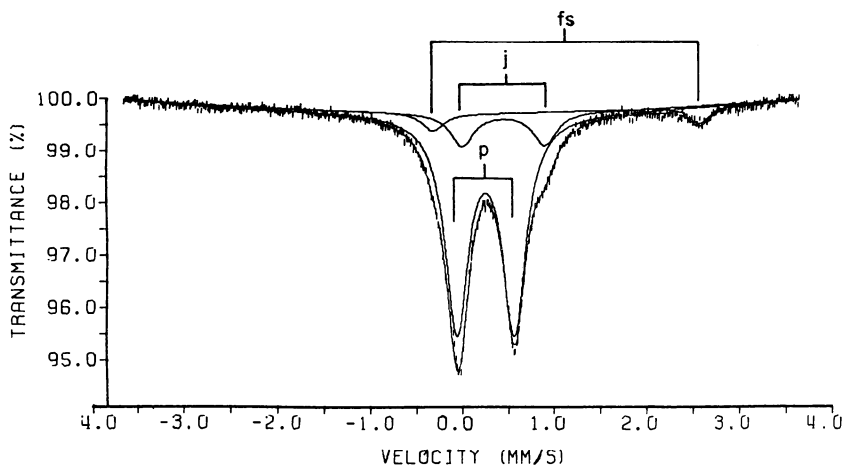


Figure 4. The same coal sample spectrum depicted in Figure 3 with the low-velocity components of the two weak doublets reversed. The fit is worse ((p) pyrite/marcasite; (fs) iron(II) (ferrous) sulfate; (j) jarosite).

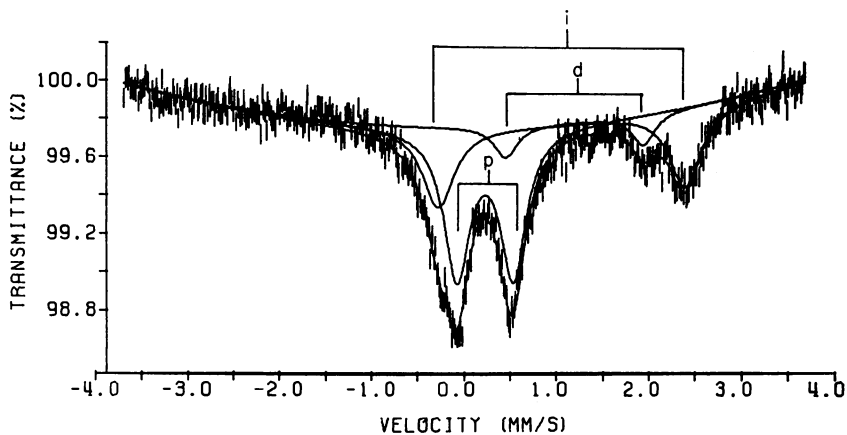


Figure 5. A low-mineral coal from Craig County fit to only three components: pyrite (*p*), dolomite (*d*), and illite (*i*)

In addition to the minerals already mentioned, we have been able to identify dolomite/ankerite, $(\text{Ca,Mg,Fe})\text{CO}_3$, and illite, $(\text{Al,Fe,Mg})_2(\text{Si,Al})_4\text{O}_{10}(\text{OH})_2$, in these Oklahoma coals. Figure 5 shows a low mineral coal that gave a statistically poor spectrum. Dolomite was identified from the position of its weak doublet ($\text{IS} = 1.13$; $\text{QS} = 1.48$ mm/s), and the more intense, larger-magnitude quadrupole splitting assigned to the high-spin iron(II) component of illite ($\text{IS} = 1.01$; $\text{QS} = 2.70$ mm/s), or a similar clay mineral. The two main absorption lines

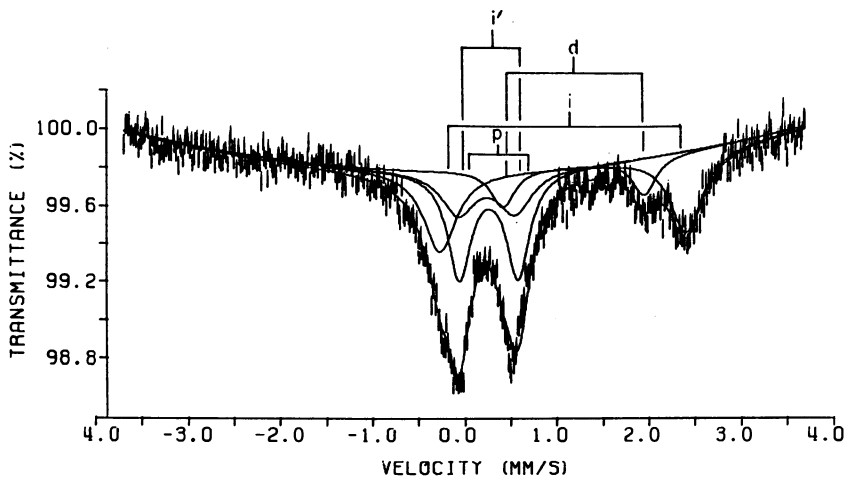


Figure 6. The same spectrum depicted in Figure 5 fit to four components, including the second iron component of illite (*p*) pyrite/marcasite; (*i*) illite; (*d*) dolomite; (*i'*) illite second iron site

were first fit as one doublet, and the parameters coincided with those of pyrite with satisfactory χ^2 and misfit values. However, illite is known to contain a second iron site, which gives rise to smaller isomer shift and quadrupole splitting values and is variously assigned as iron(III) or low-spin iron(II) or as a pyrite impurity. Taking into account this second illite component leads to the four-parameter fit shown in Figure 6 in which the positions of the dolomite and the high-spin iron(II) lines of illite are unchanged. The lines arising from the second iron site in illite coincide almost exactly with the pyrite/marcasite doublet. The consequence of this is that the first fit (Figure 5) has overestimated the amount of pyrite in the sample by three times.

Survey of Oil Shales

The focus of our work has been on shales from the Green River formation in Rio Blanco, Garfield, and Mesa Counties in western Colorado supplied by the Laramie Energy Technology Center. From the Mössbauer spectra four iron-bearing minerals can be identified: pyrite/marcasite, dolomite, illite, and magnesium siderite, $(\text{Fe, Mg})\text{CO}_3$. Figure 7 has a sample which shows all four. Pyrite/marcasite predominates, with siderite next in intensity. Dolomite gives rise to a weak doublet, and the high-spin iron(II) component of illite is the weak doublet with the largest quadrupole splitting. The second doublet from illite under the pyrite/marcasite lines was not separately identified. This qualitative analysis agreed with the results from XRD on the same sample.

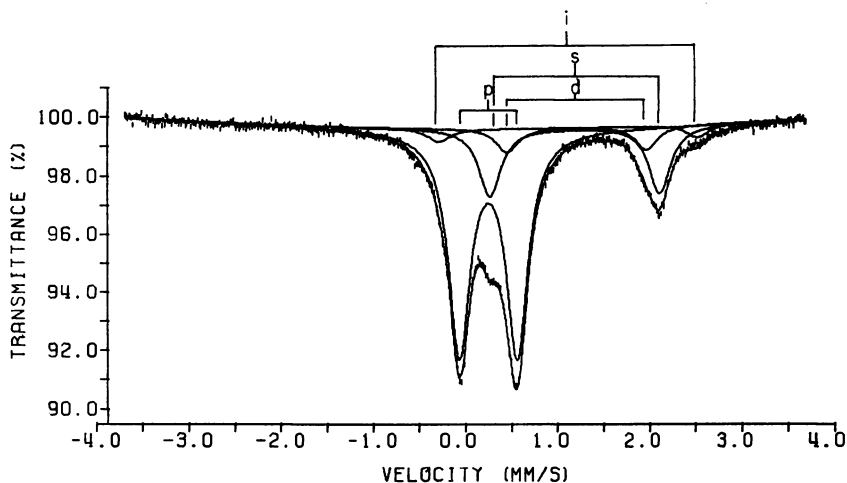


Figure 7. A Green River, Colorado oil shale containing pyrite (p), siderite (s), dolomite (d), and illite (i), in that order of relative intensity. The second doublet from illite was not identified.

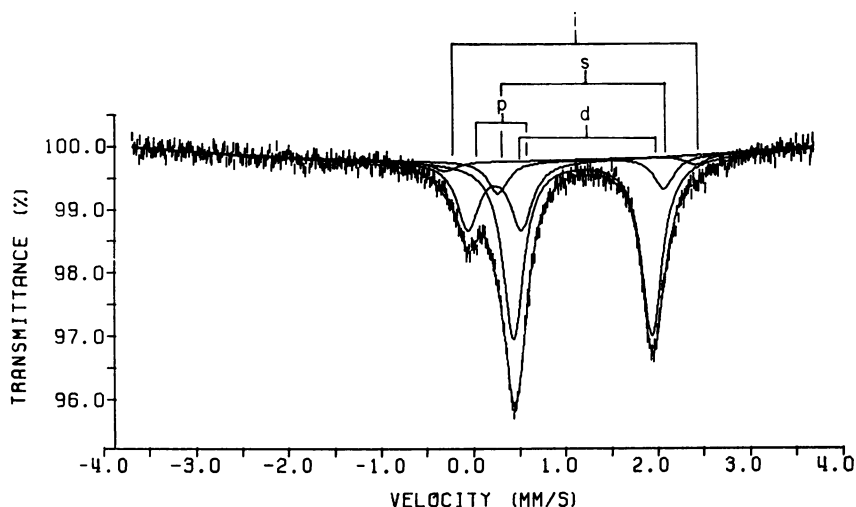


Figure 8. A shale in which dolomite (*d*) predominates, and which contains pyrite/marcasite (*p*), siderite (*s*), and high-spin iron(II) from illite (*i*), in that order of relative intensity

However, the correspondence between the XRD and Mössbauer results is not always as complete as in the foregoing example. The sample whose spectrum appears in Figure 8 was identified by XRD as containing dolomite only, and the dolomite doublet pattern is certainly the most intense, but a second doublet is clearly visible whose parameters identify

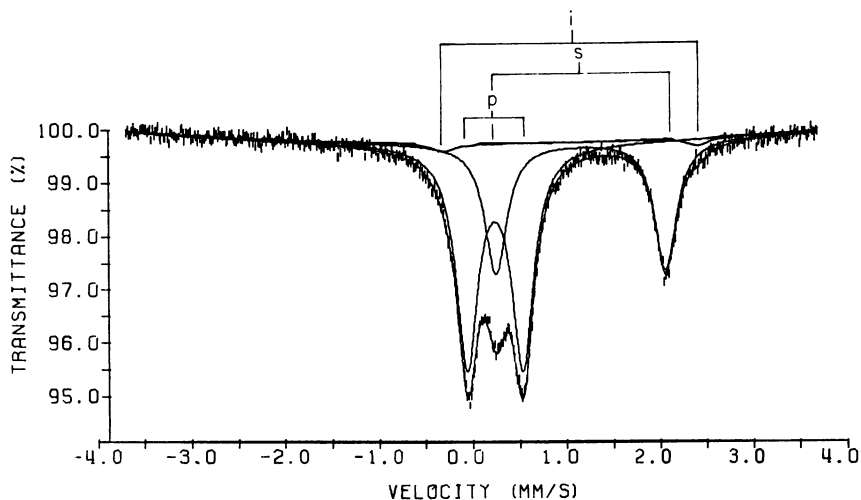


Figure 9. A shale with predominantly pyrite/marcasite (*p*) and siderite (*s*) with only a trace of illite (*i*)

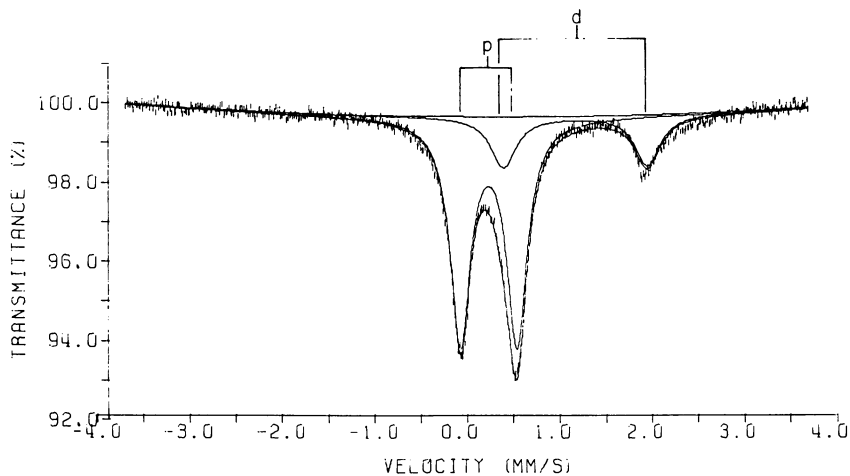


Figure 10. A shale spectrum fit only to pyrite/marcasite (p) and dolomite (d)

it as pyrite/marcasite. In addition, a satisfactory fit is only achieved by assuming the presence of two additional doublet patterns compatible with those of siderite and the high-spin iron(II) in illite.

It is instructive to record here briefly some examples of the spectra of the Green River shales. Figure 9 shows a material containing predominantly pyrite/marcasite and siderite, with only a trace of illite. The spectrum in Figure 10 can be fit by assuming a predominant pyrite/marcasite component plus some dolomite, but a more satisfactory fit is obtained by assuming the presence of siderite and illite as in Figure 11. The sample in Figure 12 contains three components that give a spectrum with pyrite/marcasite, dolomite, and siderite, in that order of intensity, while the sample in Figure 13 contains the four components dolomite, pyrite/marcasite, siderite, and illite, in that order of intensity. In Figure 14 the four components are siderite, dolomite, pyrite/marcasite, and illite, in that order of intensity.

Quantitative Analysis

Some idea of the correspondence of the Mössbauer and XRD results for oil shales can be gathered from the plot in Figure 15 of the Mössbauer resonance area analysis for pyrite/marcasite and the data for pyrite from XRD peak height analysis. As discussed in the earlier sections of this chapter, poorly crystallized materials or very small particles will be missed by the XRD method, but not by the Mössbauer technique, where strongly overlapping lines are the chief difficulty. The best least-squares line through the points in Figure 15 cuts the abscissa above the origin,

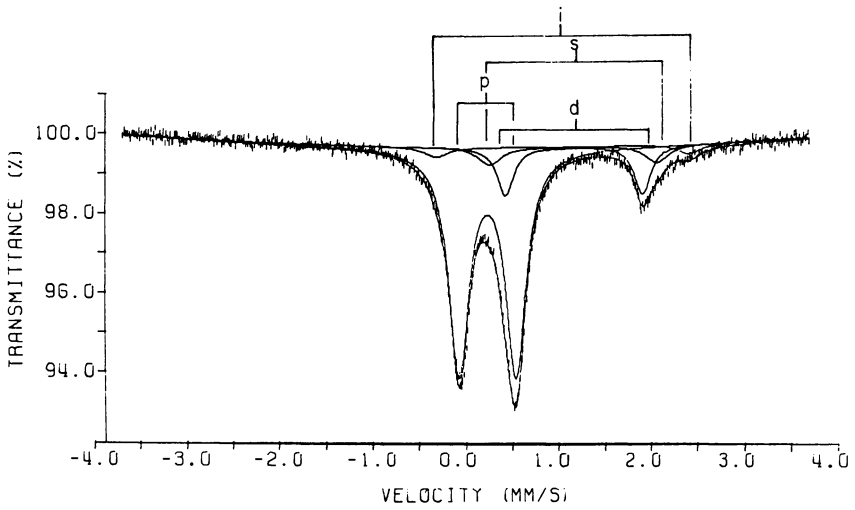


Figure 11. The same spectrum as depicted in Figure 10 fit to siderite (s) and illite (i) as well ((p) pyrite/marcasite; (d) dolomite)

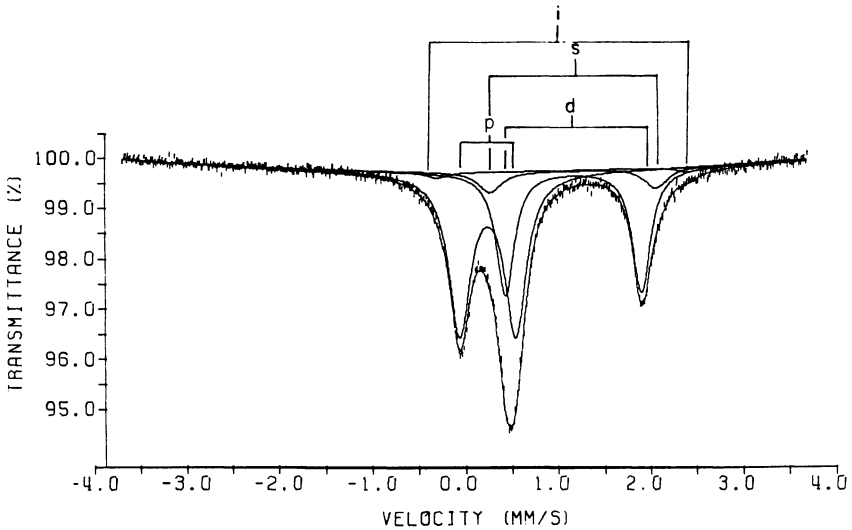


Figure 12. A shale spectrum fit to three components: pyrite/marcasite (p), dolomite (d), and siderite (s), in that order of relative intensity

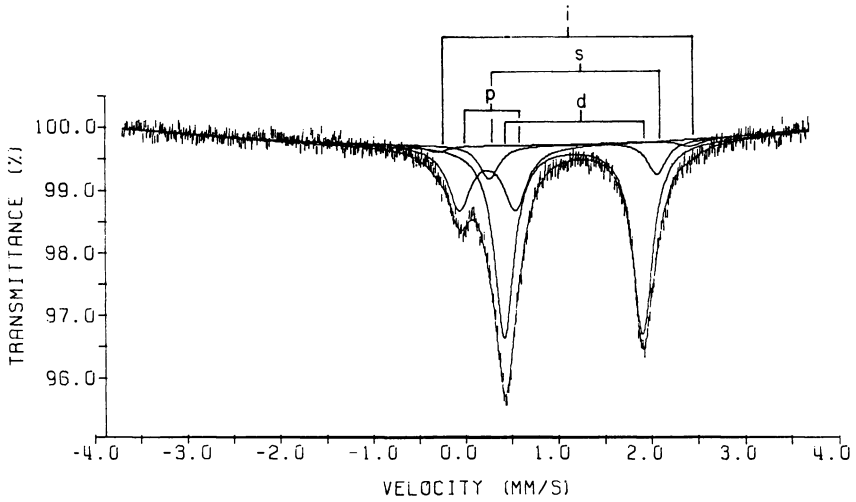


Figure 13. A shale spectrum fit to four components: dolomite (d), pyrite/marcasite (p), siderite (s), and illite (i), in decreasing relative order of intensity

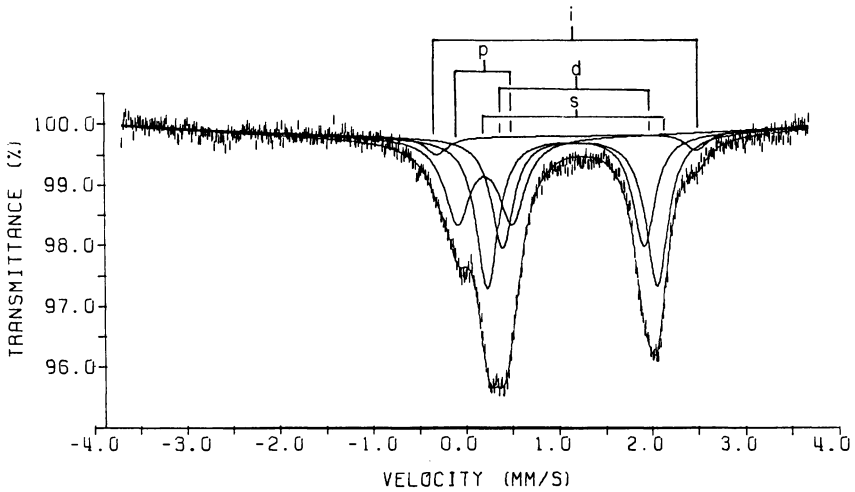


Figure 14. A shale spectrum fit to siderite (s), dolomite (d), pyrite/marcasite (p), and illite (i), in that order of relative intensity

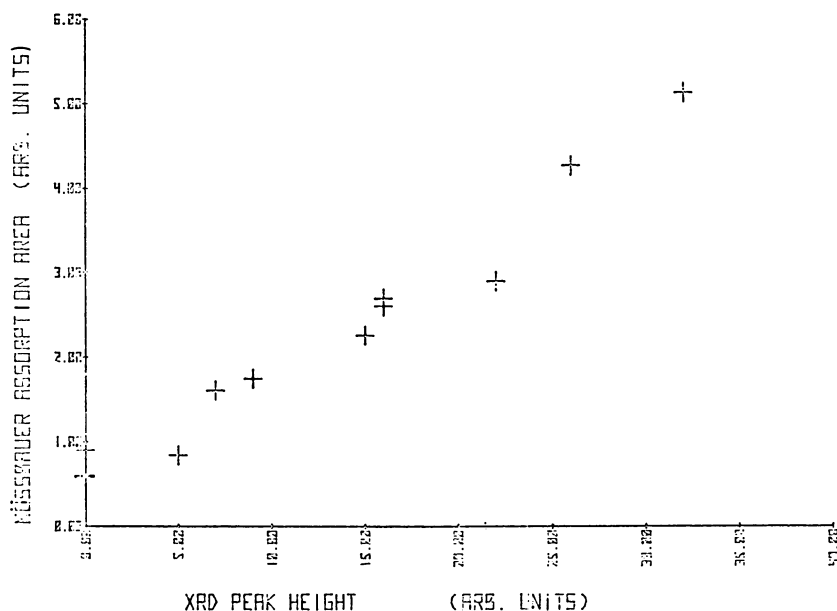


Figure 15. Plot of the Mössbauer resonance areas for pyrite/marcasite vs. the XRD peak heights for pyrite in oil shales

supporting the idea that XRD analysis does not detect all the pyrite present, despite the fact that no attempt was made in the Mössbauer analyses to distinguish the marcasite and subtract it.

Plots for dolomite, siderite, and illite are considerably worse, which is expected since the composition of these minerals is variable, but the Mössbauer technique detects the iron content only.

For coal, a direct comparison of the Mössbauer and ASTM methods applied to the same samples leads to the plot in Figure 16. Our Mössbauer results for synthetic mixtures of pyrite with carbon black gave values very close to this least-squares line, ruling out a large systematic error in the ASTM values.

The variation of the recorded quadrupole splitting values with amount of mineral present in coal and oil shale is very small, as shown in Figure 17.

For the quick analysis envisioned by the portable pyrite meter discussed previously, the whole spectrum would not be recorded; only the count rates at the absorption maxima and the off-resonance count rate are needed. Interference with other absorption lines in coal is usually low. A source emitting gamma-rays tuned to one of the wings of the pyrite doublet is proposed here. This stationary source would record the count rate at that maximum, and then be vibrated at a

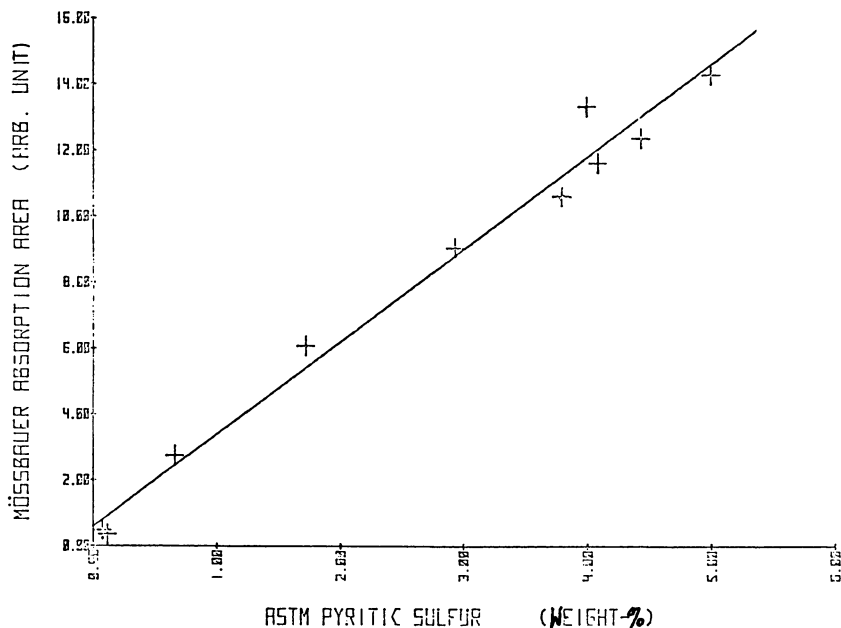


Figure 16. Comparison of the Mössbauer resonance areas for pyrite/marcasite and the ASTM pyritic sulfur results for Craig County, Oklahoma coals

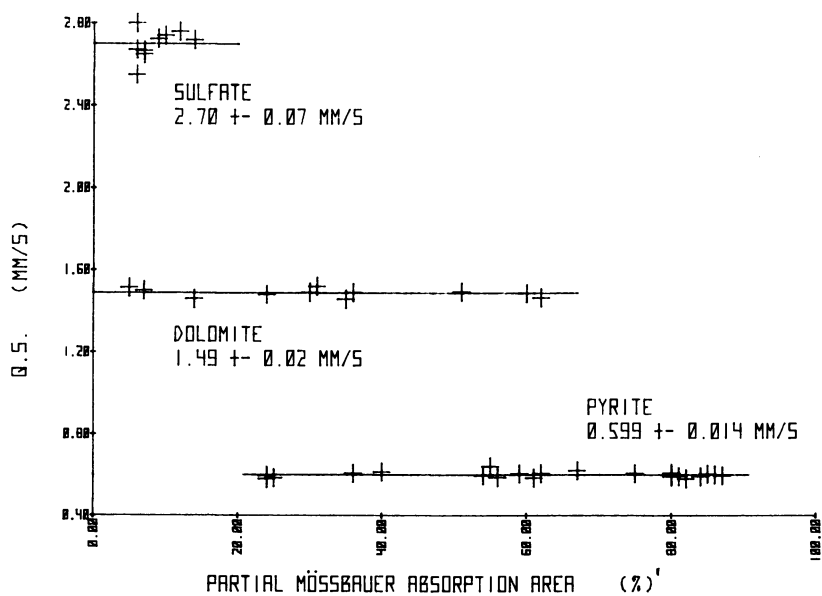


Figure 17. Lack of variation in the magnitude of the quadrupole splitting values with relative amount of minerals in coal and oil shales

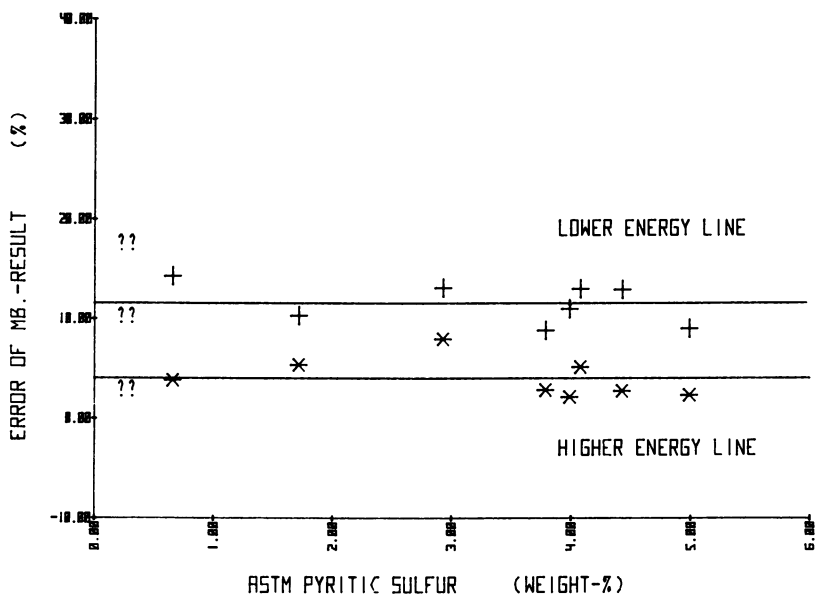


Figure 18. Overestimation of the amounts of pyrite/marcasite in coal vs. the ASTM pyritic sulfur values for the high- and low-velocity wings of the Mössbauer doublet

velocity appropriate to record the baseline values. Comparison of the two count rates would give the pyrite content directly. This technique would overestimate the amount of pyrite/marcasite present, and we have calculated the error limits for each of the wings of the pyrite doublet. In Figure 18 the values for several spectra are plotted against the corresponding ASTM pyritic sulfur values. The lower velocity pyrite line suffers more interference because of its overlap with the iron(II) sulfate resonance ($12 \pm 2\%$), while use of the higher velocity line leads to an overestimate of only $4 \pm 2\%$. The portable analyzer could take into account this overestimate in the calculations performed by its micro-processor, with reproducibility being the only criterion for the choice of which line to use. In the case of the very low mineral content coal shown in Figures 5 and 6, this method would result in a relative threefold overestimation of pyrite/marcasite. However, the absolute values are 0.1 and 0.3%, and therefore, the error might not be as serious.

Further Work

To put the Mössbauer method of analysis on a firmer footing, we need to develop information on the following questions:

1. the Mössbauer parameters for the iron(II) sulfate in all four of its forms;
2. the identification of the low-spin iron(II) or iron(III) sulfate present in coal and its Mössbauer parameters;
3. the recording of reliable Mössbauer parameters for the iron(III) or low-spin iron(II) in illite;
4. the relative recoil-free fractions for all the minerals of interest in coal and oil shale so that quantitative estimation of the iron distribution in these complex mineral assemblages can be carried out.

Acknowledgments

Our work is supported by the Energy Resources Center and Mining and Minerals Research and Resources Institute of the University of Oklahoma, the Oak Ridge Associated Universities Short-Visit Research Participation Travel Contract Program, U.S. Department of Energy, and the Laramie Energy Technology Center, U.S. Department of Energy. We thank the Oklahoma Geological Survey, Norman, OK, the University of Oklahoma Schools of Petroleum and Geological Engineering and Geology and Geophysics, the Continental Oil Company–Consolidation Coal Company, Ponca City, OK, the Phillips Petroleum Company, Bartlesville, OK, and the Pittsburgh Energy Technology Center, Pittsburgh, PA for the donation of coal samples, and the Laramie Energy Technology Center for the donation of oil shales.

Literature Cited

1. Greenwood, N. N.; Gibb, T. C. "Mössbauer Spectroscopy"; Chapman & Hall: London, 1971.
2. Gibb, T. C. "Principles of Mössbauer Spectroscopy"; Chapman & Hall: London, 1976.
3. Gütlich, P.; Link, R.; Trautwein, A. "Mössbauer Spectroscopy and Transition Metal Chemistry"; Springer-Verlag: New York, 1978.
4. Bancroft, G. M. "Mössbauer Spectroscopy: An Introduction for Inorganic Chemists and Geochemists"; Halsted, John Wiley and Sons: New York, 1973.
5. Gonser, U., Ed. "Mössbauer Spectroscopy in Lunar Geology and Mineralogy"; Springer-Verlag: New York, 1975.
6. O'Gorman, J. V.; Walker, P. L., Jr. *Fuel* 1973, 52, 71.
7. Richardson, J. T. *Fuel* 1972, 51, 150.
8. Greer, R. J. In "Scanning Electron Microscopy/IIT 1977"; Johari, O., Ed.; IIT Research Institute: Chicago, 1977; Vol. 1, p. 79.
9. Mitra, G. B. *Fuel* 1954, 33, 316.
10. Pollack, S. S. *Fuel* 1971, 50, 453.
11. Schehl, R. R.; Friedel, R. A. "U.S. Bureau of Mines Technical Progress Report No. 71," Washington, D.C., 1973.
12. Benson, J. E.; Jacobson, R. A. *Abstr. Inst. Sci. Probls. Coal Util.* 1977, May.

13. Estep, P. A.; Kovach, J. K.; Karr, C., Jr. *Anal. Chem.* **1968**, *40*, 353.
14. *Am. Soc. Test. Mater. Book ASTM Stand., D-2492* **1974**, 507-511.
15. Shimp, N. F.; Kuhn, J. K.; Helfinstine, R. J. In "Energy Sources"; Crane, Russak and Co.: New York, 1977; p. 93.
16. Gluskoter, H. J. In "Trace Elements in Fuel," *Adv. Chem. Ser.* **1975**, *141*, 1.
17. Gluskoter, H. J. In "Energy Sources"; Crane, Russak & Co.: New York, 1977; p. 125.
18. Ward, C. K. Circular No. 498, Illinois State Geological Survey, Urbana, IL, 1977.
19. Brown, H. R.; Burns, M. S.; Durice, R. A.; Swaine, D. J. *Fuel* **1964**, *43*, 409.
20. Edwards, A. H.; Jones, J. M.; Newcombe, W. *Fuel* **1964**, *43*, 55.
21. Mayland, H. *Fuel* **1966**, *45*, 97.
22. James, R. G.; Severn, M. I. *Fuel* **1968**, *47*, 476.
23. Burns, M. S. *Fuel* **1970**, *49*, 126.
24. Lowry, H. H., Ed. "Chemistry of Coal Utilization"; John Wiley & Sons: New York, 1945; Vols. 1 and 2; 1963, Suppl. Vol.
25. Desborough, G. A.; Pitman, J. K. "Rocky Mtn. Assoc. Geol. Guidebook to the Energy Resources of the Piceance Creek Basin, Colorado, 25th Field Conf.," 1974; pp. 81-89.
26. Desborough, G. A.; Pitman, J. K. *U.S. Geol. Survey Open-file Rep.* **75-219**, 1975, p. 26.
27. Desborough, G. A.; Mountjoy, W.; Frost, I. C. *U.S. Geol. Survey Open-file Rep.*, 1975, p. 75-156.
28. Lefelholcz, J. F.; Friedel, R. A.; Kohman, T. P. *Geochim. Cosmochim. Acta* **1967**, *31*, 2261.
29. Smith, C. V.; Liu, J.-H.; Saporoschenko, M.; Shirley, R. *Fuel* **1978**, *57*, 41.
30. Schafer, H. N. S. *Fuel* **1977**, *56*, 45.
31. Montano, P. A. *Fuel* **1977**, *56*, 397.
32. Levinson, L. M.; Jacobx, I. S. *Fuel* **1977**, *56*, 453.
33. Jacobs, I. S.; Levinson, L. M.; Hart, H. R., Jr. *J. Appl. Phys.* **1978**, *49*, 1775.
34. Levinson, L. M. EPRI Report FP-1228, Oct., 1979.
35. Keisch, B.; Gibbon, G. A.; Akhtar, G. *Fuel Process. Technol.* **1977/78**, *1*.
36. Russell, P.; Montano, P. A. *Abstr. Inst. Sci. Probs. Coal. Util.* **1977**, May.
37. Huffman, G.; Huggins, F. *Abstr. Inst. Sci. Probs. Coal. Util.* **1977**, May.
38. Kovzhenko, N. F.; Smoilovskii, A. N.; Chernyshov, Yu. A. *Khim. Tverd. Topl.* **1977**, *73*.
39. Shumeiko, V. P.; Goryunova, N. P. *Khim. Tverd. Topl.* **1976**, 148.
40. Puro, R. K. *Ind. J. Pure Appl. Phys.* **1972**, *10*, 841.
41. Clausen, B. S.; Mørup, S.; Topøe, H.; Cooper, B. *Proc. Int. Conf. Mössbauer Spectrosc.*, Bucharesti, Romania **1977**, *1*, 319.
42. Cole, R. D.; Liu, J.-H.; Smith, G. V.; Hinckley, C. C.; Saporoschenko, M. *Fuel* **1978**, *57*, 514.
43. Gluskoter, H. J.; Simon, J. A. "Sulfur in Illinois Coals," Circular No. 432, Illinois State Geological Survey, Urbana, IL, 1968.
44. Solozhenkin, P. M.; Voitkovskii, Yu. B.; Generalov, O. N.; Siderov, S. V. *Dokl. Akad. Nauk Tadzh. SSR* **1974**, *17*, 39.
45. Avvakumov, E. G.; Boldyrev, V. V.; Kosobudskii, I. D.; Pavlyukhin, Yu. T. *Izv. Sib. Otd. Akad. Nauk SSSR, Ser. Khim. Nauk* **1973**, 132.
46. Tyulenev, G. V.; Marks, G. L.; Krechman, A. F.; Varnek, V. A. *Izv. Sib. Otd. Akad. Nauk SSSR, Ser. Khim. Nauk* **1976**, 21.
47. Temperley, A. A.; LeFevre, H. W. *Bull. Am. Phys. Soc.* **1963**, *8*, 470.
48. Dubois, J. M.; LeCaër, G.; Offroy, C. *Rev. Metall.* **1977**, *74*, 621.
49. Meisel, W.; Kreysa, G. *Z. Chem.* **1972**, *12*, 301.
50. Meisel, W.; Kreysa, G. *Z. Anorg. Chem.* **1973**, *395*, 31.

51. Gay, P.; Bancroft, G. M.; Brown, M. G. *Proc. Apollo 11 Lunar Ser. Conf. Geochim. Cosmochim. Acta Suppl.* 1970, 1, 481.
52. Ziegler, C. A., Ed. "Applications of Low Energy X- and Gamma-Rays"; Gordon and Breach: New York, 1971.
53. Jaggi, N. K.; Rao, K. R. P. M. *Fuel* 1979, 58, 688.
54. Klumpp, W.; Hoffmann, K.-N. *Z. Phys.* 1969, 227, 254.
55. Ok, H. N. *Phys. Rev.* 1971, B4, 3870.
56. Zimmermann, R.; Trautwein, A.; Harris, F. E. *Phys. Rev.* 1975, B12, 3902.
57. Brady, P. R.; Duncan, J. F.; Mok, K. F. *Proc. Phys. Soc.* 1965, 287, 343.
58. Gallagher, P. K.; Johnson, D. W.; Schrey, F. *J. Am. Ceram. Soc.* 1970, 53, 666.
59. Neto, K. S.; Garg, V. K. *J. Inorg. Nucl. Chem.* 1975, 37, 2287.
60. Garg, V. K.; Puin, S. P. *J. Chem. Phys.* 1971, 54, 209.
61. Fluck, E.; Kerler, W.; Neuwirth, W. *Angew. Chem. Int. Ed. Engl.* 1963, 2, 277.
62. DeBenedetti, S.; Land, G.; Ingalls, R. *Phys. Rev. Lett.* 1961, 6, 60.
63. Kerler, W.; Neuwirth, W. *Z. Phys.* 1971, 54, 209.
64. Nozik, A. J.; Kaplan, M. *Phys. Rev.* 1967, 159, 273.
65. Chandra, K.; Puri, S. P. *Phys. Rev.* 1968, 169, 272.
66. Tamul, J. J.; York, L. A.; Seykora, E. J. *Nucl. Instr. Methods* 1970, 84, 317.
67. Mosback, H.; Poulsen, K. G. *Acta Chem. Scand.* 1971, 25, 2421.
68. Kopcewicz, M.; Kotlicki, A. *Phys. Stat. Solid* 1971, b44, K127.
69. Lipka, J.; Silek, J.; Cirak, J.; Prejsa, M. *Radiochem. Radioanal. Lett.* 1974, 20, 59.
70. Bristoti, A.; Kunrath, J. I.; Viecaro, P. J.; Bergter, L. *J. Inorg. Nucl. Chem.* 1975, 37, 1149.
71. Baker, R. A. *Water Res.* 1972, 6, 9.
72. Hoynkiewicz, A. Z.; Kubisz, J.; Kulgaqczuk, D. S. *J. Inorg. Nucl. Chem.* 1975, 27, 2513.
73. Herzenberg, C. L.; Jones, D. *J. Geophys. Res.* 1966, 71, 2661.

RECEIVED June 27, 1980.

Mössbauer Spectroscopic Analysis of Iron Oxides in Soil

LAWRENCE H. BOWEN and STERLING B. WEED

Departments of Chemistry and Soil Science, North Carolina State University, Raleigh, NC 27650

Iron oxides in well-oxidized soils exist primarily in the form of aluminum-substituted goethite (α -FeOOH) and hematite (α -Fe₂O₃). These microcrystalline oxides often occur in low abundance and may be concentrated for analysis by boiling with 5M NaOH. This chapter is a Mössbauer study of the consequences of this treatment in a variety of soil clays containing both goethite and hematite. The iron oxide is concentrated appreciably, while aluminum incorporation is not markedly affected. The Mössbauer results for aluminum substitution in goethite generally agree with aluminum content chemically determined after treatment with base. Hematite samples give better agreement before treatment. Detection of hematite and goethite by x-ray diffraction agrees qualitatively with the Mössbauer data.

Iron oxides and oxyhydroxides are widely occurring in soil clays (1). Although often dilute, they significantly influence the physical and chemical properties of the soils because of their mode of occurrence as finely divided particles or possibly as coatings on silicate minerals. Because of this mode of occurrence, standard techniques of analysis such as x-ray diffraction are of limited use. Mössbauer spectroscopy gives unique information about the iron oxide constituents of soils (2, 3), and is particularly useful in distinguishing the two major natural forms of hematite (α -Fe₂O₃) and goethite (α -FeOOH) from their differing magnetic hyperfine interactions. Two effects complicate spectral analysis: small particle size produces superparamagnetic relaxation (4) and substitution of nonmagnetic ions, especially Al³⁺, into the oxide lattice, reduces the magnitude, and broadens the distribution of magnetic fields (5). These

0065-2393/81/0194-0247\$05.00/0
© 1981 American Chemical Society

effects are interrelated, since aluminum substitution also reduces particle size (5). Mössbauer spectroscopy has the potential for analyzing not only the crystalline forms of the iron oxides, but their degree of aluminum substitution and particle size as well.

The first step in studying the iron oxide fraction of soils is often boiling with 5M NaOH to remove preferentially silicates and aluminum oxides (6). However, such drastic treatment might well affect the nature of the remaining oxides, in particular their aluminum substitution and particle size. The present study was initiated to determine these effects from the resulting changes in the Mössbauer spectra. The clay fractions, in which the iron oxides are most abundant, from a variety of soils were studied before and after chemical concentration. Mössbauer spectra at room temperature and at 78 K were obtained, and results from these spectra were compared with chemical and x-ray diffraction analyses.

Experimental

The methods used were the same as those reported by Bigham et al. (3). The soils (Table I) were fractionated by standard sedimentation procedures (7). In most cases only the clay ($< 2\mu\text{m}$) fraction was studied. Samples A606 and A608 were used as silt plus clay ($< 20\mu\text{m}$). The analyses of iron and aluminum in the oxides were carried out by atomic absorption spectroscopy on the extracts from multiple extractions of nonsilicate oxides by treatment with sodium dithionite–citrate–bicarbonate (DCB) (8). The x-ray diffraction studies of the clays were carried out using Cu K_{α} radiation with a diffracted beam monochromator. Mössbauer spectra were obtained with an approximate 10-mCi ^{57}Co -Rh source, using samples containing 5–10 mg Fe/cm², mixed with powdered polyethylene. Velocity calibration was achieved by accumulating laser interferometer data in every sixteenth channel of the 512-channel analyzer. For low-temperature runs, source and absorber were both cooled. All Mössbauer spectra were computer-fit to sums of Lorentzian lines with the positions constrained by the hyperfine interaction parameters. Certain widths and intensities were constrained also, for example, to make the spectra symmetrical.

The concentration of the iron oxide fraction was effected using boiling 5M NaOH (6) with both the solution/solid ratio and extraction time doubled. After boiling, the samples were washed with water, 0.5M HCl, 0.3M KCl, and water again before being dispersed and freeze-dried.

Results

The samples studied are divided into four groups for discussion purposes. Group A contains three clays with poorly crystallized iron oxides (appreciable doublet observed in the 78 K Mössbauer spectrum and relaxation-broadened magnetic peaks). Group B consists of four North Carolina soils with goethite present but no hematite. Group C

Table I. Soil Materials

<i>Sample No.</i>	<i>Description and Source</i>
9	Grossarenic Ochraquult; loamy, siliceous, thermic. Ap horizon. North Carolina Coastal Plain. (McColl series).
13	Typic Paleudult; clayey, kaolinitic, thermic. Ap horizon. North Carolina Coastal Plain. (Faceville series).
A606	Typic Hapludult; fine-loamy, siliceous, thermic. B horizon. North Carolina Piedmont. (Durham series, profile I).
A608	Typic Hapludult; fine-loamy, siliceous, thermic. B horizon. North Carolina Piedmont. (Durham series, profile II).
A675	Humic Paleudult; clayey, kaolinitic, thermic. B horizon. North Carolina Piedmont. (Davison-Applying intergrade).
A685	Humic Paleudult; clayey, kaolinitic, thermic. B horizon. North Carolina Piedmont. (Davidson-Georgeville intergrade).
A906	Oxisol. B horizon. Brazil.
A915	Andept. Volcanic ash. Guatemala.
A924	Typic Paleudult. A1 horizon. Amazon basin; Yurimaguas, Peru.
A927	Typic Paleudult. B1 horizon in same soil profile as 924. Amazon basin; Yurimaguas, Peru.
B154	Humic Paleudult; clayey, kaolinitic, thermic. B horizon. North Carolina Piedmont. (Davidson series).
B157	Typic Acrorthox; clayey, oxidic, isohyperthermic. B horizon. Puerto Rico (Nipe series).
B158	Laterite sample from Australia. (Sample L, obtained from I. J. Ibang, N. C. State University, Raleigh, N. C.)
B159	Laterite sample from Australia. (Sample Q, obtained from I. J. Ibang, N. C. State University, Raleigh, N. C.)

samples contain hematite as the major iron oxide species. Finally, in Group D are four clay samples with both hematite and goethite observed in the Mössbauer spectra.

The results are tabulated by groups in Tables II–XI. In each group the chemical and x-ray diffraction analyses are given first, followed by the Mössbauer data. It should be noted that the weight percent iron, although calculated on the basis of the total clay, was determined from the material extracted by DCB (8) and thus reflects the iron in oxide form, the so-called free iron oxides easily reduced by dithionite. Silicate iron, if present, would not be extracted. The aluminum content also gives that amount extracted by DCB and is presented as mole percent, calculated assuming the moles of aluminum plus iron equal 100%. Thus the value will reflect the aluminum incorporation in the iron oxide lattice only if no other form of aluminum is extracted. In fact, poorly crystallized aluminum oxyhydroxides are somewhat soluble in the citrate solution used to complex the reduced iron (7). Therefore, an unspecified amount of aluminum extracted in the DCB treatment of the untreated

clays must come from a source other than the iron oxides. This would not be true for the treated clays, since easily solubilized aluminum would be removed by the alkali treatment (6). Mössbauer data presented include the quadrupole splitting parameter $\Delta \equiv 1/2 e^2qQ$, the linewidth at half-maximum Γ (for magnetic components only the outermost pair of peaks is reported), the internal magnetic field H (really the magnetic flux density B), and the relative area of the respective peaks RA , which is the sum of peak intensity times linewidth over all lines. The isomer shifts are not reported individually, but all corresponded to the range expected for high-spin Fe^{3+} , about 0.36 ± 0.05 mm/s relative to metallic iron.

Group A. In this group are three samples labeled poorly crystalline on the basis of the appreciable doublet observed at 78 K in the Mössbauer spectrum. The results are in Tables II and III. Of the common iron oxides and oxyhydroxides, only lepidocrocite, γ - $FeOOH$, is not magnetically ordered at the liquid-nitrogen temperature (2). The iron oxide contents of these clays were very low, even after treatment of the clay with alkali, and x-ray diffraction spectra of the iron oxides, if present, were very weak and diffuse. Only goethite was detected in A924 and A927; no crystalline iron oxide was detected in A915. The Andept (A915) is a very young soil forming on volcanic ash. Hence, little crystalline clay has formed, halloysite being the only layer silicate present. However, the two Ultisol samples (A924 and A927) contain the better crystalline kaolinite in addition to small amounts of vermiculite, indicating a more advanced weathering state. The lack of magnetically oriented iron oxide in the Andept, even after concentration, most likely indicates that the iron oxide has extremely small particle size. In the two Ultisol samples, the magnetic component at 78 K is enlarged considerably by concentration. It is likely that some of the iron was present in the kaolinite structure (9) and would be removed as newly precipitated oxide by the acid wash following base concentration (10). The near-constant field values of the magnetic component, indicating particle

Table II. Composition of Group A (Poorly Crystallized) Oxides

<i>Soil</i>	<i>Iron Oxides in X-Ray*</i>	<i>Weight % Iron</i>	<i>Mole % Aluminum</i>
A915	none	3.4	33
A915C ^b	none	10.8	6
A924	g (?)	2.7	15
A924C	g	4.9	20
A927	g (?)	3.4	23
A927C	g	12.8	17

* The diffraction peaks of goethite (g), if observed, were broad and weak.

^b The designation C refers to samples concentrated with NaOH.

Table III. Mössbauer Results at 78 K for Group A Clays

Sample	Magnetic Component				Doublet		
	Δ (mm/s)	Γ (mm/s)	H (kG)	RA (%)	Δ (mm/s)	Γ (mm/s)	RA (%)
A915 ^a					0.68	0.58	100
A924	(-0.2) ^b	1.80	456	24	0.68	0.64	76
A927C	-0.29	1.56	452	78	0.65	0.55	12
A927	-0.20	1.70	468	63	0.56	0.68	37
A927C	-0.25	1.79	470	91	0.60	0.56	9

^a The concentrated Sample 915C was not analyzed, but had only slight evidence of magnetic peaks.

^b Fixed parameter.

size and aluminum incorporation in this material which is almost definitely aluminum-substituted goethite from the observed field (5), remain the same. Any recrystallization occurring during the NaOH treatment should reduce the aluminum incorporation and thus increase the observed *H*. Sample A924 had a measurable reduction in linewidth (Table III), but this is probably attributable to the lack of precision in determining Γ for samples with dilute magnetic peaks. As representative of the broadened magnetic spectra observed, Sample A927C is shown in Figure 1. The doublet, although only 9% of the total area, is readily observed, and is probably part of the superparamagnetic goethite spectrum. Particle size on the basis of Shinjo's results on pure goethites (4) and Golden et al.'s studies of substituted goethites (5) is likely to be about 100 Å or less. This is supported by the very diffuse x-ray reflections, indicative of small particle size. Only goethite was identified by either x-ray or Mössbauer techniques.

Group B. The four samples in this group are listed in Table IV and the Mössbauer results in Table V. Again, the content of extractable iron oxides was low in the untreated clays, causing some uncertainty regarding the type of oxide present as determined by x-ray diffraction. These also had kaolinite as the dominant layer silicate mineral, and reduction of the doublet area by concentration in three samples (Table V) was probably attributable to extraction of some iron from the kaolinite structure. Again, the magnetic field values for goethite hardly changed on concentration, indicating that little dissolution/reprecipitation occurred during base treatment. The same three samples (A608, 9, 13) also showed less aluminum in the treated materials (Table IV), which could be attributable to the presence of gibbsite or poorly crystalline aluminosilicates in the original samples. The linewidths for the magnetic component (presumed to be goethite) were large, indicating small particle size even after concentration with base. The observed quadrupole splitting of the doublet in these samples generally increased on concentration

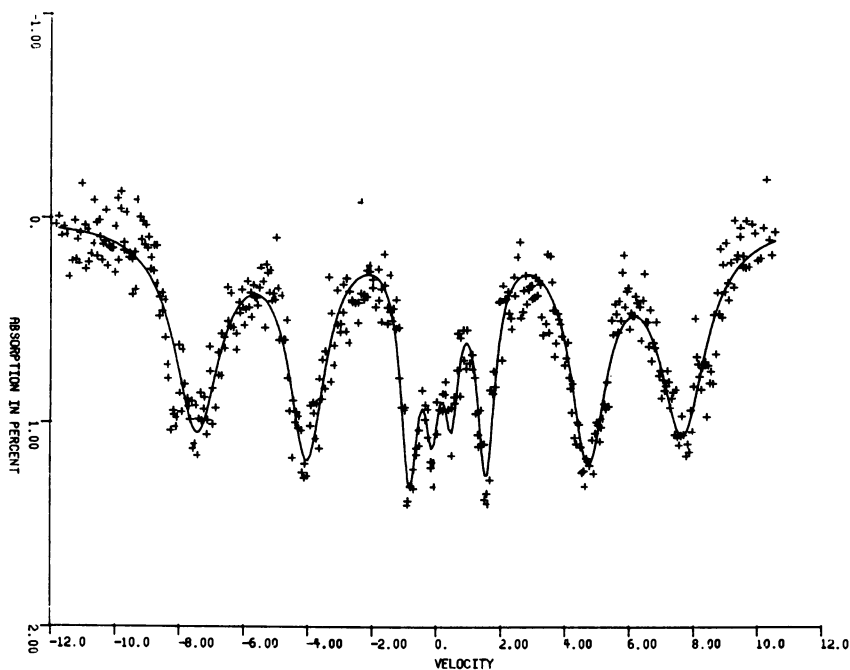


Figure 1. Mössbauer spectrum of concentrated oxide fraction from soil clay A927C at 78 K

with base (Table V). The doublet parameters are expected to change, since in the samples before concentration they are a superposition of Fe^{3+} in the form of kaolinite and superparamagnetic goethite, whereas after concentration the former is removed. The Δ values after concentration seem somewhat large for goethite, but the weak intensity and relaxation-broadened linewidths make the observed Δ values imprecise. Also, each

Table IV. Composition of Group B (Goethite-Rich) Oxides

Soil	Iron Oxides in X-Ray ^a	Weight %	Mole % Aluminum
A606	g (?)	5.2	33
A606C	g	16.7	34
A608	g	2.9	37
A608C	g	5.7	28
9	g (?)	2.0	45
9C	g	15.8	24
13	g	3.7	40
13C	g	18.3	24

^a Weak diffraction peaks of goethite are indicated by g.

Table V. Mössbauer Results at 78 K for Group B Clays

Sample	Magnetic Component			RA (%)	Doublet		
	Δ (mm/s)	Γ (mm/s)	H (kG)		Δ (mm/s)	Γ (mm/s)	RA (%)
A606	-0.22	1.56	436	89	0.63	0.66	11
A606C	-0.29	1.39	440	84	0.73	0.65	16
A608	-0.27	1.48	448	81	0.60	0.70	19
A608C	-0.24	1.46	441	86	0.84	0.98	14
9	-0.30	1.28	461	79	0.64	0.71	21
9C	-0.27	1.34	459	94	0.72	0.71	6
13	-0.23	1.68	463	79	0.65	1.04	21
13C	-0.22	1.79	460	91	0.80	1.09	9

of these materials has a weathered muscovite component (dioctahedral vermiculite) that may contain some iron and would not be removed by the base treatment.

Group C. The three samples in this group (Table VI) had larger iron oxide content both before and after concentration. Two of the samples were studied at room temperature and exhibited magnetic components (Table VII). The spectrum of B158 is shown in Figure 2. The field value is much too large for goethite and indicates hematite with aluminum substitution. Sample B154 had broader magnetic lines and lower field than B158, indicating smaller particle size. At 78 K the hematite lines (Table VIII) of all these samples were sharp and predominant. Sample A906 had about 20% relative area in the form of a doublet, which remains after concentration. Sample B154 had a second magnetic component present, with parameters in agreement with aluminum-substituted goethite. The concentration step in this case appears to convert the small amount of doublet to goethite, with a corresponding increase in H . This is to be expected if a small amount of goethite crystallization occurred on treatment with base, the newly crystallized material being low in aluminum substitution.

Table VI. Composition of Group C (Hematite-Rich) Oxides

Soil	Iron Oxides in X-Ray ^a	Weight % Iron	Mole % Aluminum
A906	H,g	9.3	24
A906C	H,g	39.6	24
B154	H,g (?)	7.7	19
B154C	H,g	43.4	9
B158	H,g	22.5	9
B158C	H,g	56.8	5

^a Strong lines for hematite are indicated by H, weaker lines for goethite by g.

Table VII. Mössbauer Results at Room Temperature for Group C Clays

Sample	Magnetic Component			RA (%)	Doublet		
	Δ (mm/s)	Γ (mm/s)	H (kG)		Δ (mm/s)	Γ (mm/s)	RA (%)
B154	-0.17	1.25	478	62	0.55	0.44	38
B154C	(-0.2) ^a	1.12	474	62	0.59	0.58	38
B158	-0.21	0.56	498	84	0.55	0.50	16
B158C	-0.21	0.72	493	84	0.56	0.54	16

^a Fixed parameter.

X-ray diffraction results showed lines characteristic of hematite in all samples and weak peaks which could indicate some goethite (the goethite lines are generally obscured by silicate minerals). In the concentrated Sample B154C goethite was definitely present, in agreement with the Mössbauer results. Samples B158C and A906C also showed weak goethite lines. An attempt was made to fit the Mössbauer spectrum of B158C to two sets of magnetic lines, but no improvement was obtained. A stronger source and/or longer counting times would be needed therefore to detect the presence of a small amount of goethite when hematite is predominant.

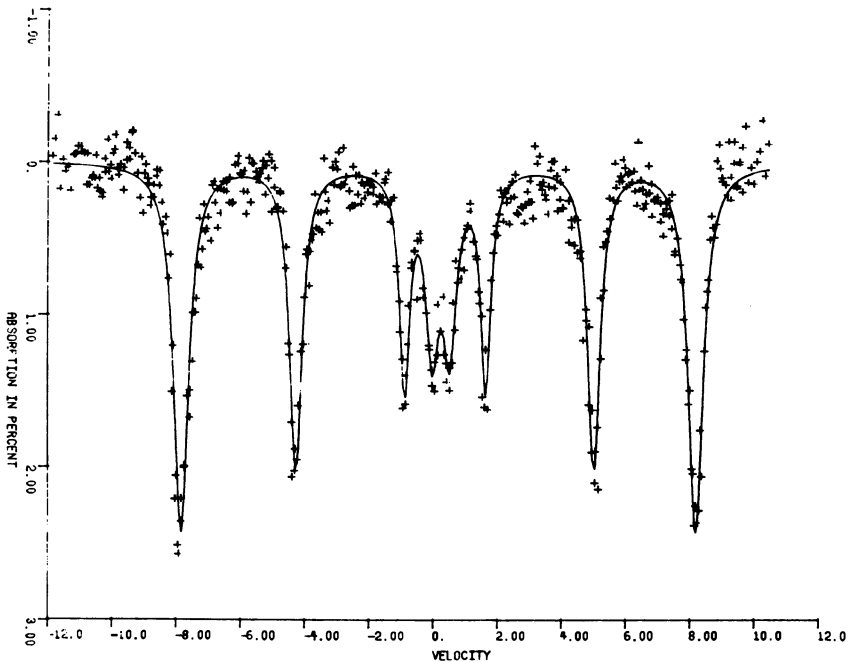


Figure 2. Mössbauer spectrum of soil clay B158 at room temperature

Table VIII. Mössbauer Results at 78 K for Group C Clays

Sample	Magnetic Components				Doublet		
	Δ (mm/s)	Γ (mm/s)	H (kG)	RA (%)	Δ (mm/s)	Γ (mm/s)	RA (%)
A906	-0.19	0.51	518	78	0.70	0.81	22
A906C	-0.19	0.52	517	84	0.70	0.90	16
B158	-0.19	0.47	523	100	—	—	0
B158C	-0.18	0.53	521	100	—	—	0
B154	-0.17	0.54	514	57	—	—	0
	-0.19	1.08	470	34	0.55	(0.54)	9
B154C	-0.20	0.48	516	56	—	—	0
	-0.28	1.21	478	44	—	—	0

Group D. This group (Table IX) contains four samples with both hematite and goethite clearly present in their Mössbauer spectra. Iron content varied from about 7 to 25%. As generally observed in the previous samples, the aluminum extracted by DCB decreased after base concentration. Room-temperature Mössbauer spectra were obtained for two of these (Table X). Only one, B159, showed a weak magnetic component. After concentration, both samples showed some magnetic component characteristic of hematite with reduced field. At 78 K (Table XI), all samples had sharp hematite lines in addition to a second magnetic component characteristic of relaxation-broadened goethite, plus a small doublet. To fit these complex spectra, the linewidths of all hematite peaks were constrained equally and the doublet linewidth was constrained to that of hematite. The spectrum of Sample B159 at room temperature is shown in Figure 3. The spectral data for B159 and B159C are shown in Figures 4 and 5, illustrating the elimination of the doublet by concentration. The x-ray patterns obtained for B157C, B159C, and A685C also showed both hematite and goethite present in significant amounts.

Table IX. Composition of Group D Oxides

Soil	Iron Oxides in X-Ray*	Weight % Iron	Mole % Aluminum
A675	G	6.6	24
A675C	G,h (?)	31.8	16
A685	H,G	8.8	14
A685C	G,h	32.8	10
B157	G,H	24.9	27
B157C	G,H	47.7	16
B159	H,g (?)	15.2	16
B159C	H,g	49.5	11

* Dominant oxide in terms of diffraction intensity is labeled H (hematite) or G (goethite). Weaker peaks are indicated by lower case h and g.

Table X. Mössbauer Results at Room Temperature for Group D Clays

Sample	Magnetic Component			RA (%)	Doublet		RA (%)
	Δ (mm/s)	Γ (mm/s)	H (kG)		Δ (mm/s)	Γ (mm/s)	
B157	—	—	—	0	0.54	0.41	100
B157C	(-0.2) [*]	1.86	475	30	0.57	0.65	70
B159	(-0.2) [*]	0.79	486	18	0.56	0.46	82
B159C	(-0.2) [*]	0.76	492	30	0.57	0.63	70

^{*} Fixed parameter.

Although the Mössbauer relative area for goethite was similar in A685C and B159C (Table XI), the goethite x-ray peaks were more prominent in A685C. This agrees with the smaller linewidth of the latter, indicating better crystallization. The original clay B157 showed x-ray lines characteristic of the aluminum oxide gibbsite; this probably accounts for the appreciable reduction in aluminum content upon base concentration (Table IX). The reduction in relative area of the doublet upon base concentration for all of these samples (Table XI) could be attributable either to removal of silicate iron or to changes in goethite particle size. The near constancy of the field values before and after concentration argues against the latter, although the goethite relative area did increase with decreased doublet area in three cases.

Aluminum Incorporation in Iron Oxides. Golden et al. (5) obtained a linear correlation between aluminum content of goethites and the Mössbauer H at 78 K. Aluminum substitutions calculated by this correlation, $H(78\text{ K}) = 500 - 1.77 (\% \text{ aluminum})$, are compared in Table XII with values determined by DCB extraction. For Group B, the goethite-rich samples, the correlation is excellent if the DCB results on

Table XI. Mössbauer Results

Sample	Hematite			
	Δ (mm/s)	Γ (mm/s)	H (kG)	RA (%)
A675	-0.17	0.49	517	33
A675C	-0.16	0.51	512	30
A685	-0.16	0.55	517	37
A685C	-0.17	0.45	520	30
B157	(-0.2) ^b	0.61	513	17
B157C	-0.17	0.50	516	16
B159	-0.18	0.56	515	35
B159C	-0.21	0.58	513	43

^b Doublet width constrained equal to hematite width.

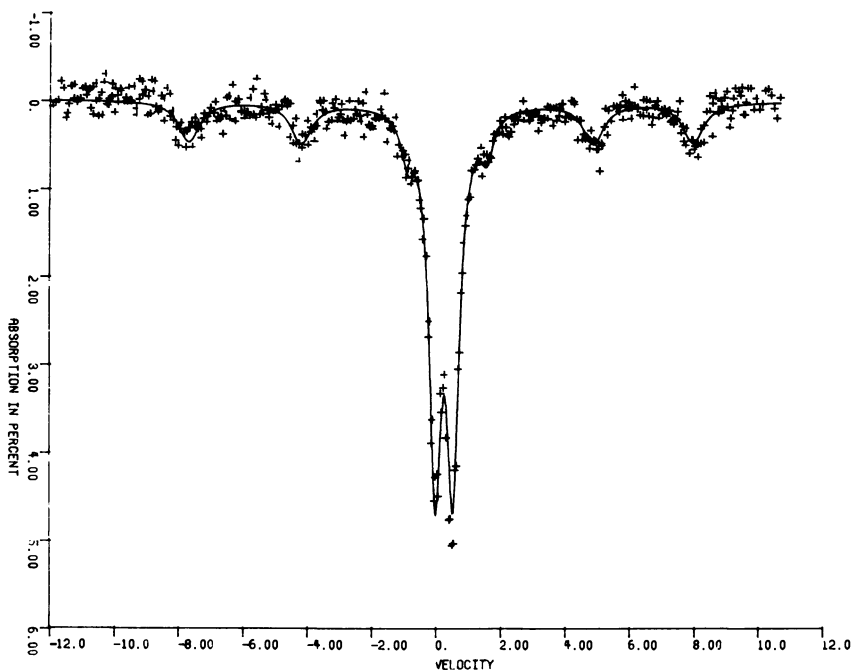


Figure 3. Mössbauer spectrum of soil clay B159 at room temperature

the concentrated samples are used. Most of these originally must have contained aluminum in some other form soluble in the DCB treatment. The correlation is not as good for the samples from Group D, the Mössbauer values generally being somewhat larger. This result could indicate the hematite component was lower in aluminum, making the average equal to the DCB value.

at 78 K for Group D Clays

<i>Goethite</i>				<i>Doublet</i>		
Δ	Γ	H	RA	Δ	Γ	RA
(mm/s)	(mm/s)	(kG)	(%)	(mm/s)	(mm/s)	(%)
-0.23	1.28	468	57	0.59	(0.49) ^a	10
-0.16	1.35	462	67	0.61	(0.51) ^a	3
-0.23	1.18	467	52	0.59	(0.55) ^a	11
-0.25	1.34	471	66	0.67	(0.45) ^a	4
-0.22	1.35	463	76	0.69	(0.61) ^a	7
-0.27	1.42	466	84	—	—	0
-0.20	1.34	469	59	0.57	(0.56) ^a	6
-0.18	1.51	465	57	—	—	0

^a Fixed parameter.

Table XII. Comparison of Aluminum Content in Goethite from Mössbauer Field Data with DCB Extraction

Sample	Mole % Aluminum (Mössbauer) ^a	Mole % Aluminum (DCB)
Group B		
606 (606C) ^b	36 (34) ^b	33 (34) ^b
608	29 (33)	37 (28)
9	22 (23)	45 (24)
13	21 (23)	40 (24)
Group D 675		
685	18 (21)	24 (16)
B157	21 (19)	27 (16)
B159	18 (20)	16 (11)

^a From H (78 K) = 500 - 1.77 (% aluminum).

^b The results for the NaOH-concentrated sample are given in parentheses following the results for the untreated clay.

Thus an attempt was made to estimate the aluminum content in hematite for those samples with magnetic components at room temperature (Table XIII). It should be noted that the field values for hematite at 78 K are relatively independent of aluminum content and thus are not

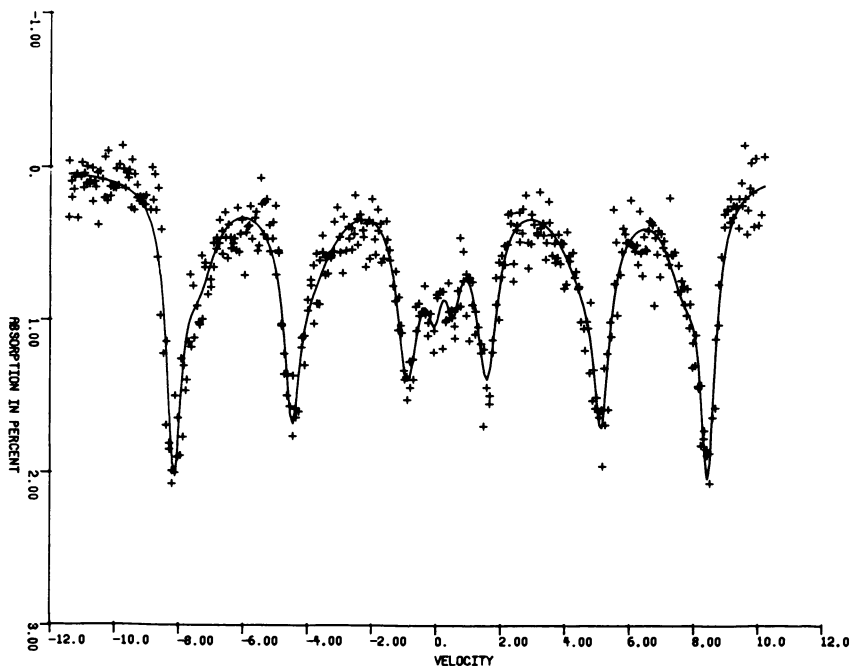


Figure 4. Mössbauer spectrum of soil clay B159 at 78 K

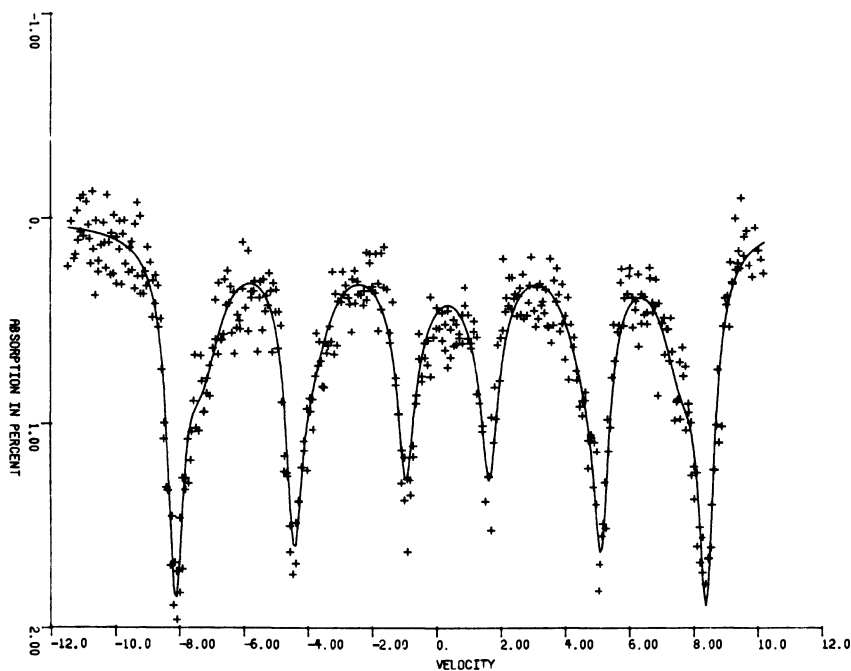


Figure 5. Mössbauer spectrum of concentrated oxide fraction from B159C at 78 K

suitable. The early data of Janot and Gibert (11) on synthetic bauxites gives a slope of H (300 K) vs. % aluminum of about -0.9 . Clearly this is too small to account for the observed low fields.

Data from our laboratory (12) on synthetic aluminous hematites indicate a more negative slope. Based on these data we used a correlation line of H (300 K) = $513 - 1.07$ (% aluminum). These results overestimate the mole percent aluminum in all cases. Part of this is most

Table XIII. Comparison of Aluminum Content in Hematite from Mössbauer Field Data with DCB Extraction

Sample	Mole % Aluminum (Mössbauer) ^a	Mole % Aluminum (DCB)
B154 (B154C) ^b	33 (36)	19 (9)
B158	14 (19)	9 (5)
B157	— (36)	27 (16)
B159	25 (20)	16 (11)

^a From H (300 K) = $513 - 1.07$ (% aluminum).

^b The results for the NaOH-concentrated sample are given in parentheses following the results for the untreated clay.

likely attributable to the fact that H is really nonlinear at higher aluminum concentrations. Also, it may be that particle size is a more important parameter in determining the magnetic field for hematite than for goethite. However, the results of Kundig et al. (13) do not indicate any drastic reduction of field with particle size for pure hematites. Mössbauer results also do not show the low aluminum content for hematite in Samples B157 and B159 proposed earlier on the basis of the goethite spectra.

Peak Area Ratios. For those samples from Groups C and D studied at both room temperature and 78 K, some information about changes occurring upon concentration can be obtained from the ratio R of peak area at room temperature to that at 78 K. This ratio should be the same for a given clay before and after concentration if the iron-containing material is unchanged, and should increase if the effective particle size increased upon concentration. Complications are caused by changes in relative proportions of doublets and magnetic components. Also, low intensities and broad lines make determination of the areas imprecise. Thus, these ratios can be interpreted only qualitatively.

Two of the samples had no significant change in ratio upon concentration, B154 with $R \approx 0.6$ before and after, and B159 with $R \approx 0.5$. The lower R for B159 is consistent with its higher percentage goethite. Sample B158, which was primarily hematite of low aluminum concentration, had a decrease in R upon concentration, from 0.8 to 0.6. This indicates a reduction in particle size, which is consistent with the line broadening observed at room temperature (Table VII). For Sample B157, R increased from 0.5 to 0.6 upon concentration, indicating an increase in particle size. This is consistent with the reduced area of the doublet component at both 78 K (Table XI) and room temperature (Table X). Why these effects occur in opposite directions is not clear, but B157 had a larger goethite component than the other samples.

Conclusions

Mössbauer spectroscopy in conjunction with chemical treatment and x-ray diffraction can give much useful information about the iron oxides in soil. Concentration of the oxide fraction by treatment with boiling NaOH has little effect on the iron oxides—neither on their particle size nor on their aluminum substitution. For a few soils with poorly crystalline oxides, Mössbauer spectra below 78 K would be useful, but in most cases the oxides give characteristic spectra at 78 K. The effects of aluminum substitution on the Mössbauer spectra of hematite need further study.

Acknowledgment

The contributions of Betty Ayers in preparing the samples, carrying out the concentration procedure, and analyzing for iron and aluminum were essential for this work and are gratefully acknowledged.

Literature Cited

1. Schwertmann, U.; Taylor, R. M. In "Minerals in Soil Environments"; Dixon, J. B.; Weed, S. B., Eds.; Soil Science Society America: Madison, WI, 1977; pp. 145-180.
2. Bowen, L. H. *Mössbauer Effect Ref. Data J.* 1979, 2, 76.
3. Bigham, J. M.; Golden, D. C.; Bowen, L. H.; Buol, S. W.; Weed, S. B. *J. Soil Sci. Soc. Amer.* 1978, 42, 816.
4. Shinjo, T. *J. Phys. Soc. Jpn.* 1966, 21, 917.
5. Golden, D. C.; Bowen, L. H.; Weed, S. B.; Bigham, J. M. *J. Soil Sci. Soc. Amer.* 1979, 43, 802.
6. Norrish, K.; Taylor, R. M. *J. Soil Sci.* 1961, 12, 294.
7. Jackson, M. L. "Soil Chemical Analysis-Advanced Course"; Univ. Wisconsin; Madison, 1974.
8. Mehra, O. P.; Jackson, M. L. *Clays Clay Miner.* 1960, 5, 317.
9. Jefferson, D. A.; Tricker, M. J.; Winterbottom, A. P. *Clays Clay Miner.* 1975, 23, 355.
10. Bigham, J. M. Ph.D. Thesis, North Carolina State University, Raleigh, 1977. (Univ. Microfilms, Ann Arbor, MI (Diss. Abstr. 7729662)).
11. Janot, C.; Gibert, H. *Bull. Soc. Miner. Fr. Crystallogr.* 1970, 93, 213.
12. Weed, S. B.; Bowen, L. H.; DeGrave, E. Unpublished results. North Carolina State University, Raleigh, 1980.
13. Kundig, W.; Bömmel, H.; Constabaris, G.; Lindquist, R. H. *Phys. Rev.* 1966, 142, 327.

RECEIVED June 27, 1980.

Applications of Mössbauer Spectroscopy in the Steel Industry

G. P. HUFFMAN and F. E. HUGGINS

U.S. Steel Corporation, Research Laboratory, Monroeville, PA 15146

Applications of Mössbauer spectroscopy in three principal areas of interest to the steel industry are reviewed: (1) characterization and processing of iron ore; (2) investigations of coal and its derivatives; and (3) analysis of steel products. The ore section discusses the use of Mössbauer spectroscopy for characterization of raw and processed iron ores, with emphasis on the direct-reduction process. Topics reviewed in the coal section include Mössbauer determinations of pyritic sulfur and iron-phase mineralogies in coal, and investigations of mineral transformations during weathering, coking, and combustion. In the steel section, traditional topics such as the iron-carbon system are reviewed briefly, and more detailed discussions are given of recent work on internally nitrided high-strength low-alloy (HSLA) steels, and electron and x-ray re-emission Mössbauer studies of surface and subsurface oxidation.

Iron is an important, usually dominant, constituent of most materials of interest to the steel industry. It is therefore not surprising that Mössbauer spectroscopy finds many applications of both a fundamental and practical nature in steel research. In this chapter we will summarize some of these applications.

Three principal areas will be covered. The first section describes applications of Mössbauer spectroscopy in the characterization and processing of ores, with emphasis on studies related to the direct reduction of iron ore. The second section deals with the primary fuel source of the steel industry, coal, and its important derivative, coke. Several problems of current concern in the steel industry are discussed in this

section, including Mössbauer investigations of oxidized or weathered coal, studies of mineral transformations that occur during coking and their relation to coke quality, and the pivotal role played by iron in controlling ash melting and deposition during high-temperature combustion. The final section deals with Mössbauer studies of steel products. Because there is obviously a very wide range of applications in this area, this section focuses primarily on relatively recent investigations in the area of surface analysis, precipitation strengthening, and internal solute oxidation. More traditional areas, such as studies of the iron-carbon system and quantitative phase analysis of steels, are discussed only briefly, but extensive references are given.

Characterization and Processing of Iron and Other Ores

Raw and Beneficiated Ores. Iron ore may be defined as any naturally occurring iron-bearing formation that contains iron in sufficient quantity and satisfactory form to allow its economic recovery. Therefore, what constitutes a suitable iron ore significantly depends on such economic factors as the proximity of steel-making facilities and the availability and cost of fuel and transportation.

Most of the iron ore currently mined contains from 25 to 50% iron. Consequently, concentration of the iron-bearing phases, by such methods as magnetic separation or washing and flotation, is usually required (1). The type of beneficiation processes required for a particular ore depends on its iron-phase distribution, which is readily determined from Mössbauer spectroscopy. Spectra of some typical ores are shown in Figures 1 and 2. The absorption peaks derived from magnetite, hematite, goethite, and siderite are indicated. An ore that has magnetite as its principal iron-bearing constituent can be beneficiated by magnetic separation without prior treatment. This is certainly the case for the taconite-magnetite ore of Figure 1 (top spectrum). (Taconite is the general name given to most ores now mined in the Minnesota ore fields. It consists principally of a mixture of silica and various iron oxides.) Direct magnetic beneficiation would probably also be suitable for the Indian ore sample of Figure 1 (bottom), provided the hematite component is intimately associated with the magnetite, as is often the case.

In recent years, leaner, more highly weathered ores, such as the taconite ore with the spectrum shown in Figure 2 (top), have become important sources of iron. For such ores, "magnetic roasting" treatments are required prior to magnetic beneficiation. Such treatments consist of approximately 1 h in a reducing atmosphere (H_2 -CO) at 400° to 500°C. This converts essentially all the iron to magnetite, as illustrated by the lower spectrum of Figure 2. The magnetite in this instance is a non-stoichiometric form ($Fe_{3-x}O_4$), as evidenced by the B/A site ratio of 1.14.

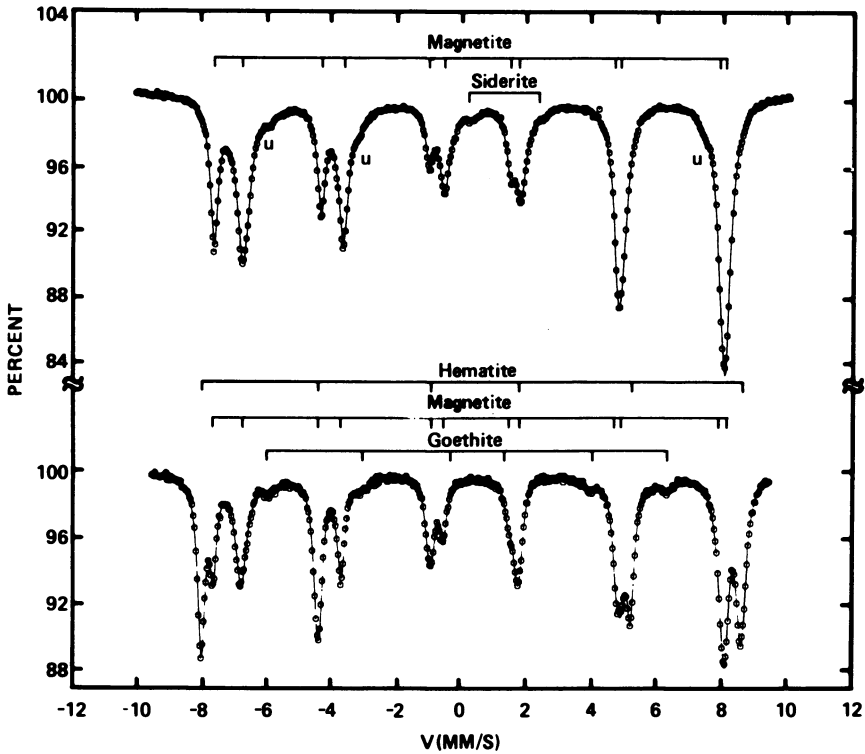


Figure 1. Mössbauer spectra of a taconite-magnetite ore (top) and of an Indian iron ore (bottom)

Sinter Quality. After beneficiation of the ore, typically to more than 90% iron oxide, it is usually subjected to one of several agglomeration processes to convert it to a suitable "burden" material for the blast furnace. Sintering is perhaps the most widely used agglomeration process (1). The finely divided, beneficiated ore is intimately mixed with a finely divided fuel such as coke breeze. Flux (limestone, dolomite) required for proper blast-furnace operation is also normally added to the mixture, which is then passed on a continuously moving bed through an ignition furnace. This causes the fuel to be combusted and the ore particles to be sintered together into porous, coherent lumps called "sinter."

Mössbauer spectra of two sinters, one of which gave good performance in the blast furnace, the other poor, are shown in Figure 3. Both sinters exhibit absorption peaks from hematite, calcium- and magnesium-substituted magnetite, and a set of broad paramagnetic peaks derived from glass and calcium ferrite. These data indicate that the poor sinter contains approximately twice as much glassy material as the good sinter (28% of the iron in paramagnetic phases for the poor sinter vs. 13% for the good sinter). This result is in accord with scanning-electron and

optical microscopy, which show the poor sinter to consist of abundant hematite, magnetite, and ferrite crystals in a glassy matrix which fills essentially all of the space between crystallites, while the good sinter exhibits a much more porous morphology. The poor reducibility of the glass-rich sinter presumably arises because of its low porosity.

Investigation of Direct-Reduction Processes. There has been much interest in recent years in direct-reduction processes during which beneficiated ores are reduced to essentially a metallic state. Such highly reduced material can be used directly in electric furnaces in place of more expensive scrap, providing metallics relatively free of contaminants. Alternatively, if it is used as burden material in the blast furnace, the high state of reduction permits significant decreases in coke usage.

There are numerous direct-reduction techniques (1, 2, 3), but the shaft-furnace reduction process is perhaps the most popular. The beneficiated ore is first mixed with a very small amount ($\sim 1/2\%$) of a binder such as bentonite, rolled into pellets, and indurated at 1300° to 1350°C in air. This induration process converts all iron to hematite and produces sintering between the hematite particles. The indurated pellets are then

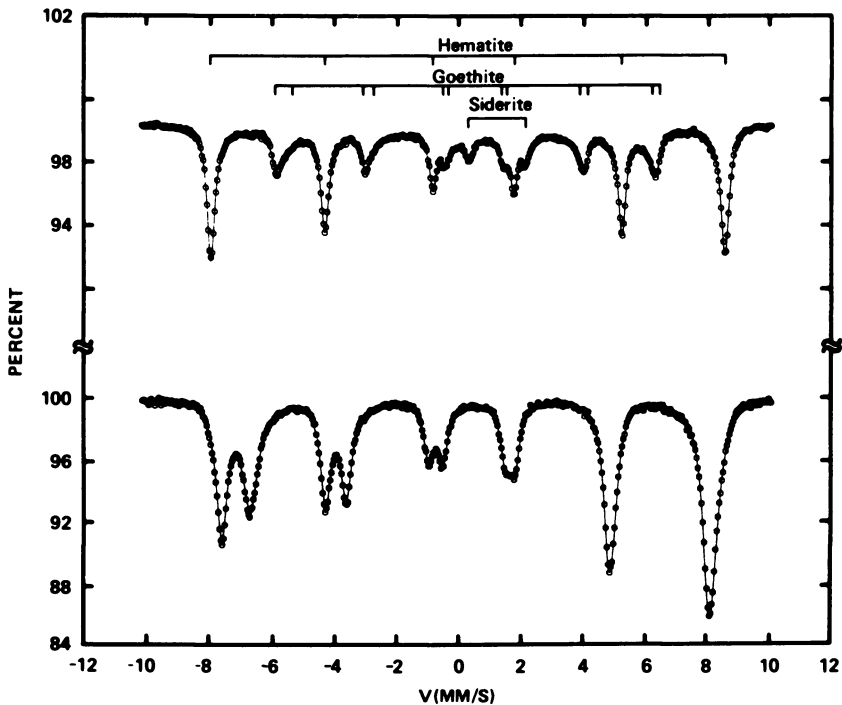


Figure 2. Mössbauer spectra of a highly weathered taconite ore before (top) and after (bottom) "magnetic roasting"

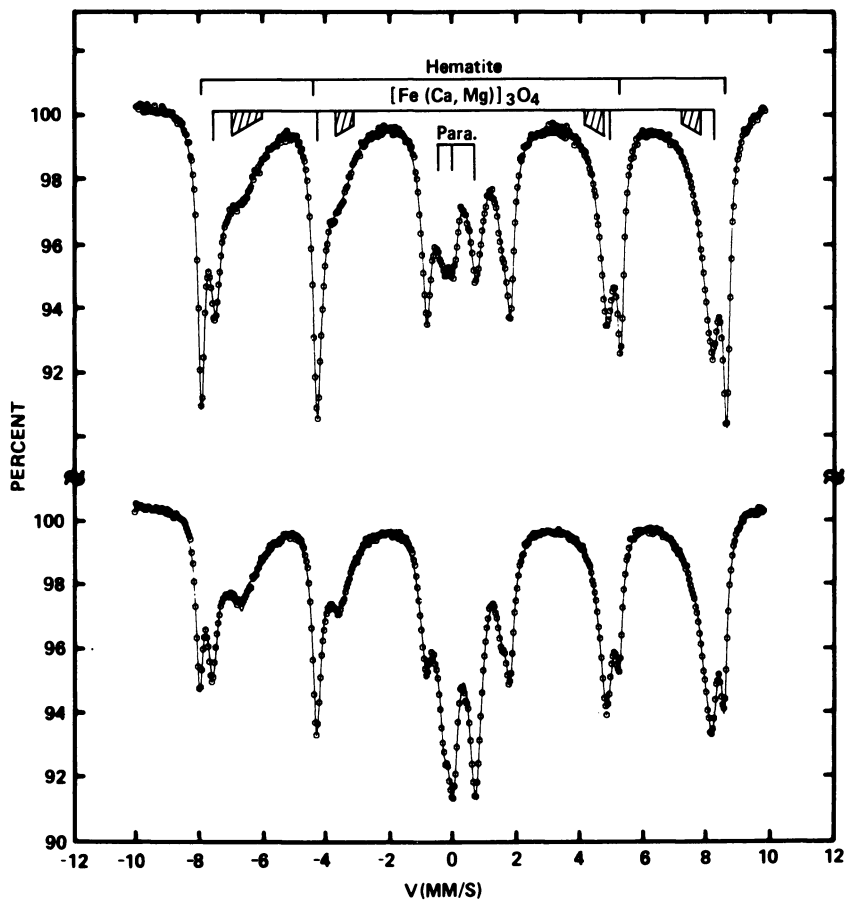


Figure 3. Spectra of two sinter samples that exhibited good (top) and poor (bottom) performance in the blast furnace

loaded into the top of a large shaft-reduction furnace, illustrated in Figure 4. The reducing gas is normally $>90\%$ $\text{H}_2 + \text{CO}$ ($\text{H}_2:\text{CO} \sim 1$ to 3). Total pellet transit time through the furnace is typically on the order of $\frac{1}{2}$ to 1 h.

Work at U.S. Steel (4) has established that Mössbauer spectroscopy is the best method available for monitoring the iron-phase distribution of direct-reduced pellets. This is illustrated in Figure 5, which shows spectra obtained from pellets reduced by several somewhat different methods. The iron-phase percentages determined for these three samples show that their total oxygen contents have been reduced by 35%, 85%, and 100%. (For all such results reported in this chapter, the peak areas have been

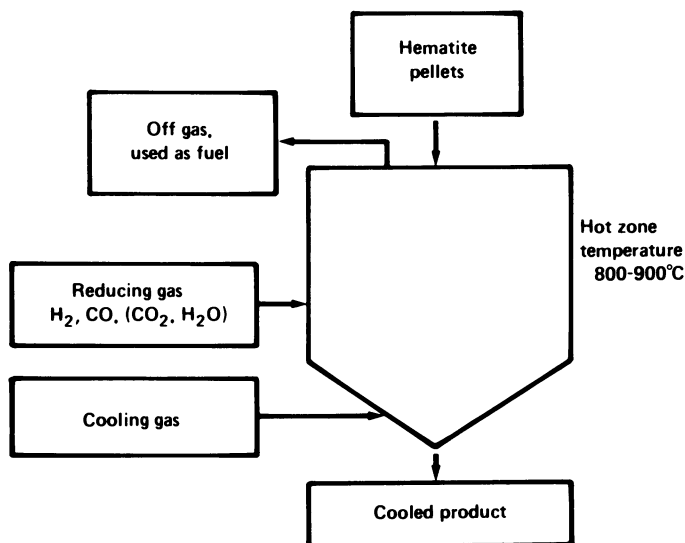


Figure 4. Schematic of a shaft-reduction furnace

converted to effective thicknesses, which are used to calculate the iron-phase percentages. As we have emphasized elsewhere (5), serious errors can result from using peak areas directly to calculate such percentages. Unless otherwise noted, equality of recoilless fractions is assumed for the absorbing phases.) Normally, the reduction of the iron-bearing phases is close to 100%. Table I shows the range and typical values of the weight percentages of metallic iron, cementite, wustite, and magnetite determined by Mössbauer analyses of a large suite of reduced pellets produced by a variety of reduction processes. Over a period of years, such Mössbauer determinations have been compared with the results of chemical analysis for metallic, ferrous, and ferric iron, oxygen, and carbon on numerous occasions, and the agreement is normally very good (4).

One problem encountered in direct-reduction technology is the rather marked tendency of some reduced pellets to reoxidize during storage and shipment. This occurs because the reduced pellets consist principally of

Table I. Mössbauer Analyses of Reduced Pellets

Compound	Wt % ^a	
	Process Ranges	Typical
Metallic Iron	42-84	68
Cementite	8-48	22
Wustite	0-10	3
Magnetite	0-10	1

^a Corrected for gangue content.

fine grains of metallic iron sintered together in a highly porous mass with large surface areas of metal ($\sim 0.5\text{--}1.0\text{ m}^2/\text{g}$) available for reoxidation. In the worst cases, such reoxidation may become pyrophoric.

An investigation was conducted at U.S. Steel to determine what factors control such reoxidation and how it can be avoided (6). A simple test was devised to determine the relative stabilities of various reduced pellets. A single pellet is heated to 450°C in an inert atmosphere, the inert atmosphere is replaced by air, and the subsequent temperature rise of the pellet is measured. Pellets exhibiting temperature rises of more than 100°F are considered to be unstable to reoxidation.

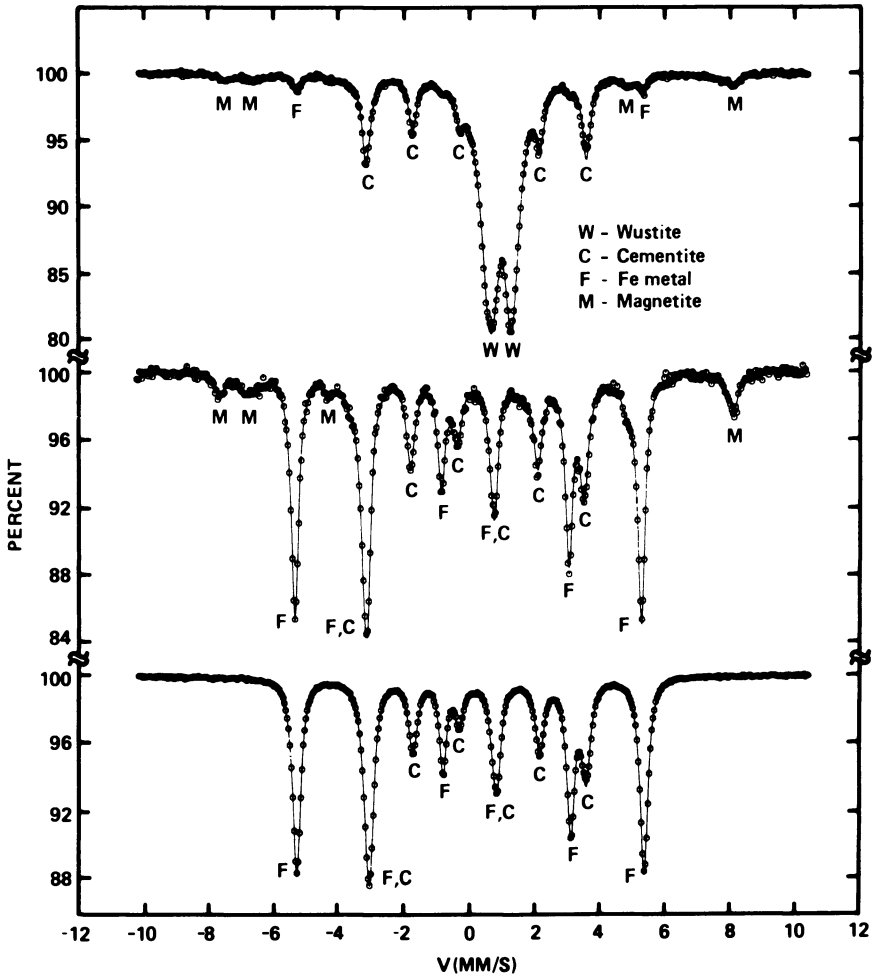


Figure 5. Mössbauer spectra of direct-reduced pellets exhibiting reductions in oxygen content of 35 (top), 85 (middle), and 100% (bottom)

It was found that such unstable pellets could be "passivated" by mild reoxidation treatments (6). Numerous unstable pellets were selected, their surface areas per gram were determined by a gas-absorption technique, and they were subjected to short (~15–60 min) reoxidation treatments in CO₂/CO mixtures (CO₂/CO ≥ 4) at 400°C to convert a portion of the metallic iron to magnetite. Mössbauer spectra of these reoxidized pellets were similar in appearance to the middle spectrum of Figure 5. Assuming that the magnetite is present chiefly as a thin layer on the metal grains making up the pellet, an approximate formula for the magnetite thickness can be written:

$$Z_{\text{mag}} = (\text{wt } \% \text{ Fe}_3\text{O}_4) \times 10^2 / \rho_{\text{mag}} S \quad (1)$$

Here, Z_{mag} is the magnetite thickness (Å), ρ_{mag} is the density of magnetite (g/cm³), S is the surface area per g (m²/g), and the weight percentage of magnetite is determined from the Mössbauer measurement.

Following this passivation treatment, the temperature rise in the pellet-stability test, ΔT , was redetermined. The results are summarized in Figure 6, which shows the dependence of ΔT on the thickness of the passivating magnetite layer produced by reoxidation of three initially unstable pellets. The dashed curve is the result of a theoretical calculation by Speich (6), using known thermodynamic quantities and other measured pellet parameters. The amount of iron and cementite oxidized during the pellet stability test, and therefore the amount of heat released, increases with increasing internal surface area and decreases with increasing thickness of the passivating oxide layer. Consequently, the thickness of the magnetite layer required for passivation increases with increasing surface area per gram.

Other Types of Ore. Iron-57 Mössbauer spectroscopy also can be quite useful in the characterization and processing of other types of ore. An example is provided by work conducted on titanium-bearing sands (7), for which the processing objective was to liberate the titanium. The top spectrum in Figure 7 was obtained from a high-gradient magnetic-separation product of the sand. It is seen that the titanium is present in the form of ilmenite, FeTiO₃, which is mixed with nearly pure hematite in an exsolution structure. The ferric quadrupole doublet presumably arises from the small ferric component in the ilmenite phase. The transformation of this "feed material" after a 1-h reduction in H₂ at 800°C is shown by the lower spectrum in Figure 7. It is seen that most of the iron has been converted to iron metal, with only a small ilmenite remnant. H₂ reduction for somewhat longer times or at somewhat higher temperatures is sufficient to convert all iron to metallic form. Chemical leaching processes, which can also be followed by Mössbauer spectroscopy, are then used to remove the metallic iron, leaving the titanium behind as rutile, TiO₂.

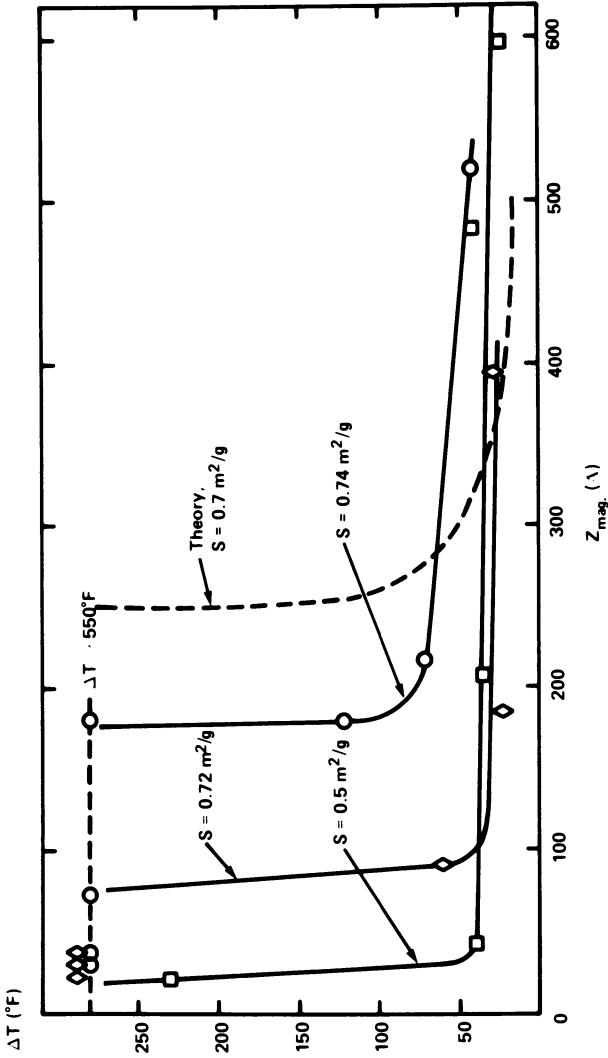


Figure 6. Temperature increase measured in the pellet stability test vs. thickness of the passivating magnetite layer for pellets of several surface areas per gram

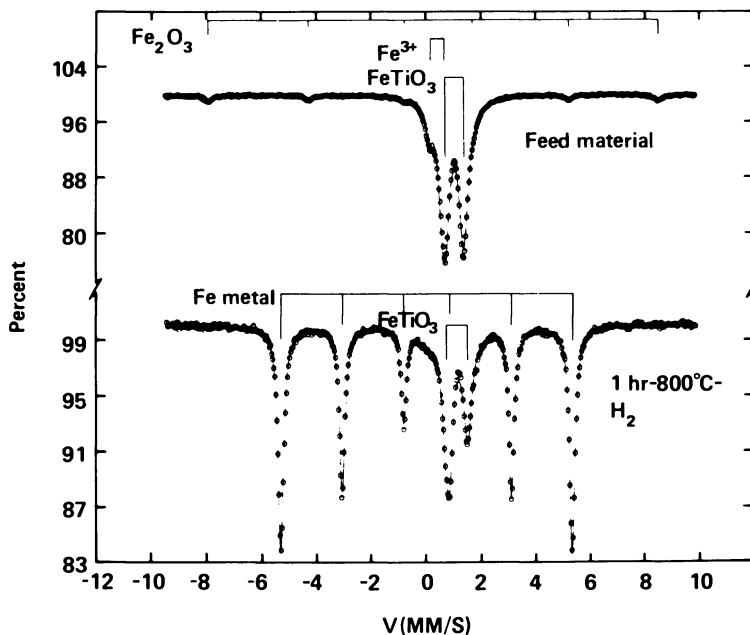


Figure 7. Spectra of the magnetic separation product of a titanium-rich sand before (top) and after (bottom) a reduction treatment in H_2 .

Investigation of Coal, Coke, and Ash

In this section, we summarize some aspects of the Mössbauer analysis of coal and its derivatives that are of particular relevance to the steel industry. Other chapters in this volume summarize additional aspects of the numerous Mössbauer investigations of coal that have been conducted in recent years (8-14).

Coal Mineralogy—Pyritic Sulfur Determinations and Paleoenvironmental Considerations. Typical spectra of several fresh, deep-mined bituminous coals are shown in Figure 8. Pyrite (FeS_2) is present in virtually all coals and is the dominant iron-bearing phase in approximately 70% of the samples we have investigated. The Pittsburgh seam coal, the spectrum of which appears at the top of Figure 8, contains essentially all its iron in pyrite. Ferrous clay minerals, principally illite and, to a lesser extent, chlorite and montmorillonite (rarely), are the second most abundant iron-bearing minerals in fresh coals. The middle spectrum of Figure 8 is typical of a clay-rich coal. Approximately 90% of the coals we have investigated contain ferrous clay, and it is the dominant iron-bearing species in perhaps 20%. The carbonate phases siderite ($FeCO_3$) and occasionally ankerite [$(Ca,Mg,Fe)CO_3$] occur in approximately half the coals investigated and are dominant in perhaps 10%. The sulfate

phases jarosite $[(\text{Na,K})\text{Fe}_3(\text{SO}_4)_2(\text{OH})_6]$ and szomolnokite $(\text{FeSO}_4 \cdot \text{H}_2\text{O})$ are also frequently observed in minor amounts in deep-mined coals.

Several methods have been developed for determining the pyritic sulfur content of coal by Mössbauer spectroscopy. In the method developed at this laboratory (8,9), the absorption area under the pyrite doublet is converted to an effective thickness X_{pyr} , which is divided by the area density of the absorber, yielding a Mössbauer mass-absorption coefficient for pyrite,

$$\mu_{\text{pyr}} \left(\frac{\text{cm}^2}{\text{g}} \right) = X_{\text{pyr}}/d \quad (2)$$

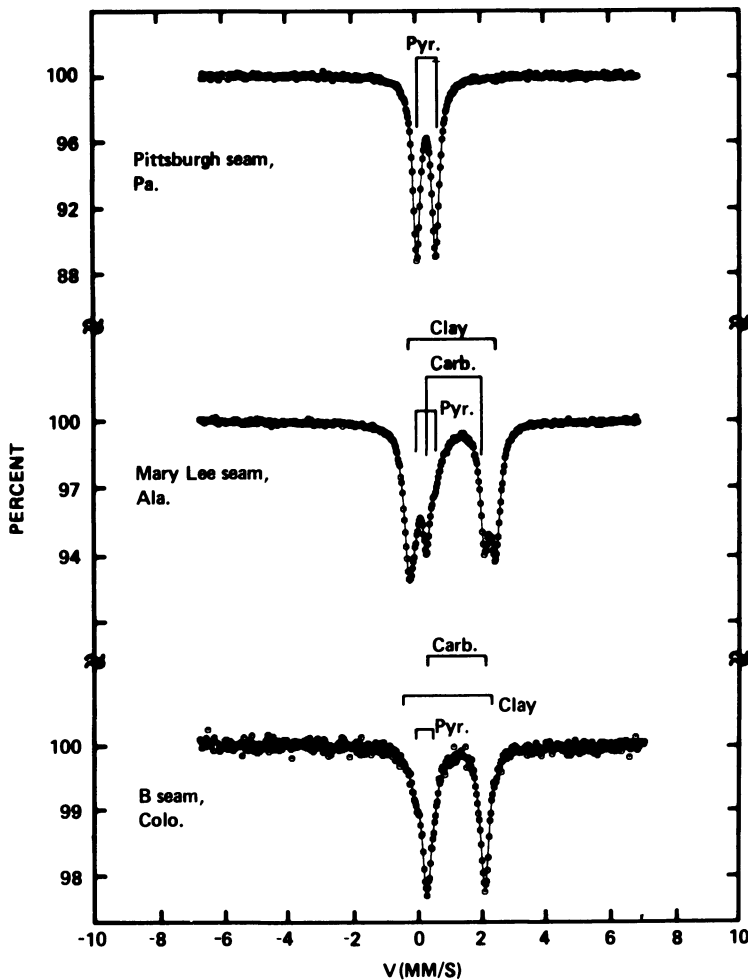


Figure 8. Mössbauer spectra of three coals rich in pyrite (top), the clay mineral, illite (middle), and the carbonate mineral, siderite (bottom)

Calibration data obtained from a set of samples of accurately known pyrite content have established a linear relationship between pyritic sulfur content and this mass-absorption coefficient (8), namely,

$$\text{wt } \% S_{\text{pyr}} = 0.394 \mu_{\text{pyr}} \quad (3)$$

As discussed in more detail in our earlier papers (8,9) and elsewhere in this volume, pyritic sulfur values determined by Mössbauer spectroscopy are usually somewhat larger and more accurate than those determined by the standard ASTM method.

Over a period of several years, we have investigated the mineralogies of raw coal samples taken from a large variety of U.S. seams, using both Mössbauer spectroscopy and a scanning-electron microscopy technique known as automatic image analysis (15,16). Recently these techniques have been used to determine detailed mineralogies of a suite of drill-core samples from the Sewickley seam in Pennsylvania (17). It appears that such data, in particular the iron phase distributions, can be of significant value in aiding geologists to make paleoenvironmental reconstructions of the original peat deposit. Such reconstructions are used to delineate the regions of best coal quality in a deposit, which normally means lowest total sulfur. The Mössbauer determination of pyritic sulfur is clearly of interest in this connection. Of more significance, however, is the observation that the samples of lowest sulfur content contain the highest percentages of iron-bearing carbonates and clays, whereas the samples of highest sulfur content usually contain very little or none of these phases, but exhibit comparatively large percentages of the sulfate phases jarosite and szomolnokite. Consequently, abundant iron-bearing carbonates and clay minerals apparently reflect freshwater peat deposition, whereas a high content of iron sulfates reflects a more brackish, marine environment which gives rise to high-sulfur, low-quality coal. This trend between iron-bearing minerals and sulfur abundance is consistent with Eh-pH diagrams (9,18).

Oxidized Coal. For various reasons the use of strip-mine coal in the production of metallurgical coke is increasing. Oxidation of strip-mine coal by natural weathering processes is highly probable because of its near-surface location. Such oxidation, if extensive, makes coal unsuitable for coking (19), and is often difficult to detect. Recent studies at this laboratory have established that the principal effect of weathering on the minerals in coal is to convert a significant fraction of the pyrite to iron oxyhydroxide, principally goethite. This is illustrated in Figure 9, which shows Mössbauer spectra obtained from samples of a strip-mine coal. The designations "outcrop," "middle," and "high wall," specify coal obtained at locations where the seam is exposed at the surface, approximately halfway into the strip pit, and from the deepest part of the pit,

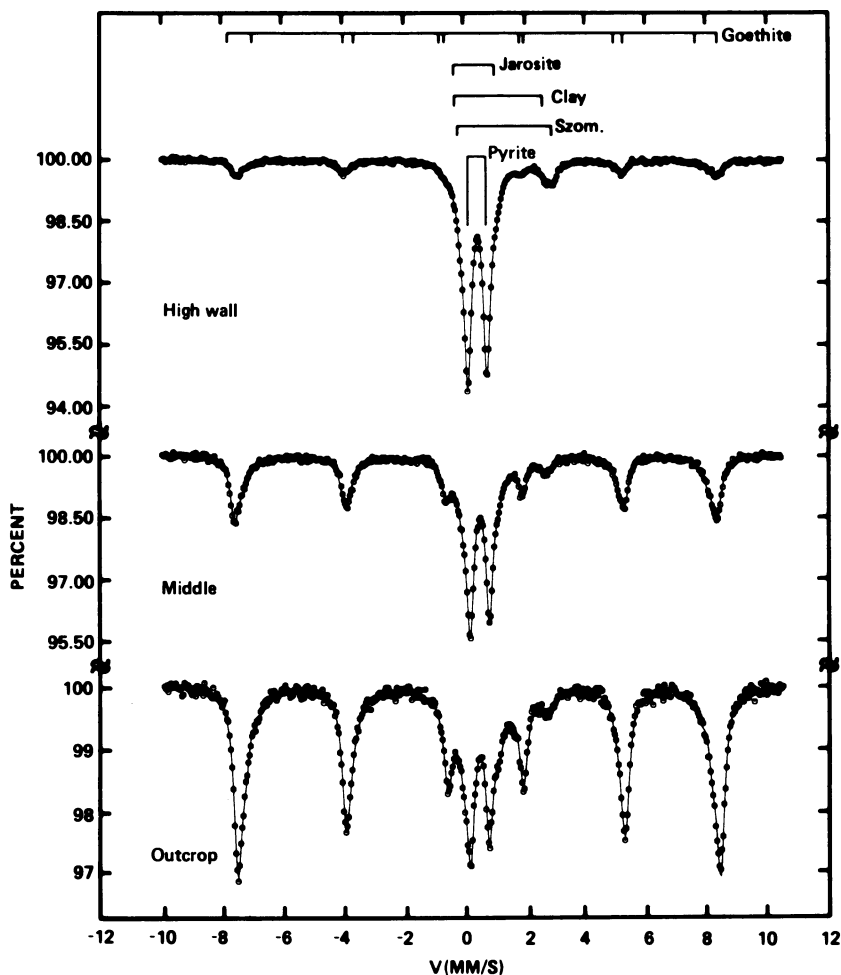


Figure 9. Spectra of oxidized strip-mine coal from the Middle Kittanning seam, illustrating the transformation of pyrite to goethite with increased weathering (all spectra obtained at 77 K)

respectively. All spectra shown in Figure 9 were obtained at 77 K, because the goethite in these coals is superparamagnetic and therefore gives very poorly resolved peaks at room temperature. A more detailed description of this work, including comparison of the Mössbauer $\text{FeOOH}/(\text{FeS}_2 + \text{FeOOH})$ ratio with other coal-oxidation parameters, is given elsewhere (20).

Mineral Transformations During Coking. Coking consists of heating a coking bituminous coal or blend of coals in an air-tight slot-shaped oven. The coal is charged cold into the ovens, and from 15 to 20 h are required for the charge to reach the so-called "pushing temperature" of

approximately 1000° to 1100°C. During this period, the volatile matter of the coal is distilled off and collected in the form of coke-oven gas and other substances, leaving behind the solid, highly porous carbon residue called coke. (The principal constituents of coke-oven gas are H₂ (~50%), CH₄ (~30%), and CO (~5%).) About 15% of the coal mined in the U.S. is converted to coke for use by the basic steel industry.

The iron-bearing phases in coal are significantly transformed during coking (8,9). This is illustrated by the coke spectra shown in Figures 10 and 11. The top spectrum of Figure 10 was obtained from coke made from the Pittsburgh seam coal of Figure 8; the bottom spectrum of Figure 10 was taken from a coke made with Pittsburgh seam coal obtained from a different location. The latter coal also had pyrite as its dominant phase, but contained approximately 13% of its iron in illite.

In the case of the lower coke sample of Figure 10, the pyrite has been reduced to a mixture of pyrrhotite and troilite (8),



For the upper coke sample of Figure 10, however, the pyrite has been reduced to a mixture of iron sulfide and metallic iron; that is,

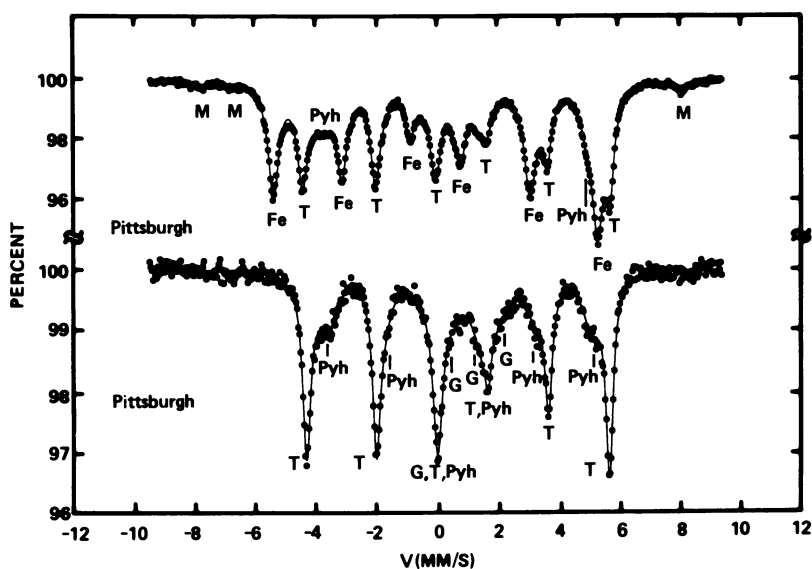
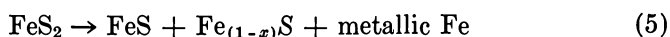


Figure 10. Spectra of two coke samples prepared from pyrite-rich Pittsburgh seam coal ((Fe) iron metal; (Pyh) pyrrhotite; (T) troilite + pyrrhotite; (G) glass and poorly crystalline silicates; (M) magnetite; (W) wustite, containing calcium and magnesium)

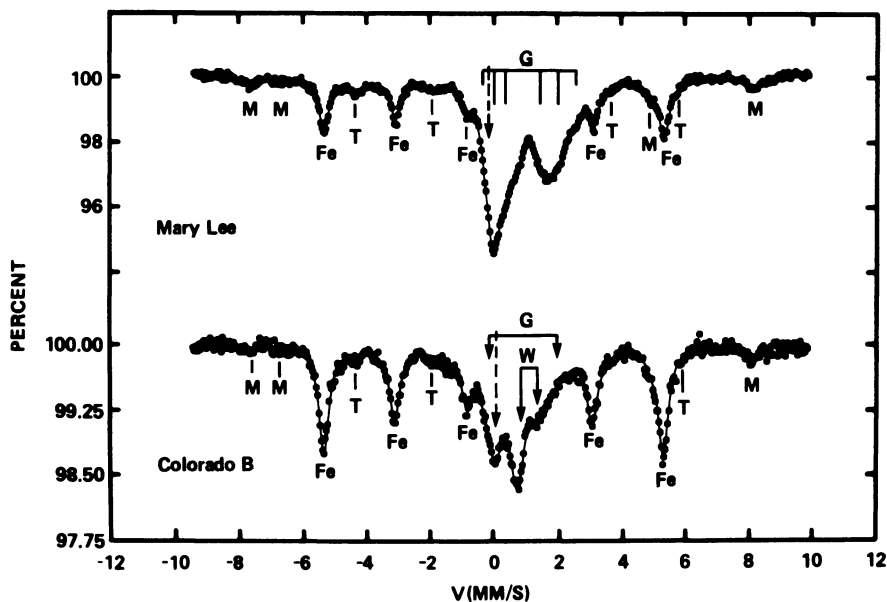


Figure 11. Spectra of cokes prepared from the clay-rich Mary Lee seam coal (top) and from the carbonate-rich Colorado B seam coal (bottom). (Peak labels as in Figure 10.)

The origin of this differing behavior of pyrite during coking is not thoroughly understood at this time. However, it appears to be a function of coking temperature and time, and of the composition of the evolved gas. Because of the economic advantages of lower-sulfur coke in steel-making, alterations of the coking process to favor Reaction 5 would be desirable.

The transformations of the ferrous clay and iron carbonate phases are illustrated in Figure 11, which shows spectra obtained from cokes prepared from the Mary Lee and Colorado B seam coals of Figure 8. Illite, the principal ferrous clay mineral, transforms to glass or poorly crystalline material which gives rise to the broad quadrupole contribution labeled G in Figure 11. Siderite, the principal iron carbonate phase, is reduced to metallic iron. Ankerite, however, appears to be reduced to a calcium- and magnesium-substituted wustite, indicated by the doublet labeled W. Also shown in Figure 11 is a dashed arrow denoting the location of an unassigned single peak. This component is seen in many coke spectra and is believed to have a variable origin. In some cokes, it appears to arise from austenitic iron-carbon, whereas in others it seems more likely to be an unresolved component of the glass spectrum. More detailed discussions of mineral transformations during coking, and of quantitative iron sulfide measurements by Mössbauer spectroscopy, may be found elsewhere (8, 9, 21).

Investigation of Factors Controlling Ash and Slag Deposits. In addition to coke-making, coal has many combustion applications in the steel industry, such as combustion in industrial boiler systems and firing of kilns used for the induration of iron-ore pellets (1, 22). The formation of damaging ash and slag deposits during direct combustion of coal often can be a major problem. Traditionally, the propensity of coals to form such deposits has been assessed by means of a standard ASTM ash fusion test (23), which defines a series of melting points, and by various empirical formulae (24). Recent investigations at this laboratory (25) have concentrated on phase analysis of ash samples quenched from high temperatures in either reducing (60% CO–40% CO₂) or oxidizing (air) atmospheres. These studies show that significant partial melting of ash occurs at temperatures far below the “initial deformation temperature” (IDT) determined in the ASTM test (23), which frequently is considered to be the temperature at which melting begins.

Mössbauer data are particularly useful for ashes quenched from a reducing atmosphere, because iron is the principal flux in this condition. For ashes of typical composition, a definite sequence of iron-bearing compounds and ferrous glass associated with the iron-rich corner of the FeO–Al₂O₃–SiO₂ phase diagram (26), shown in Figure 12, is observed

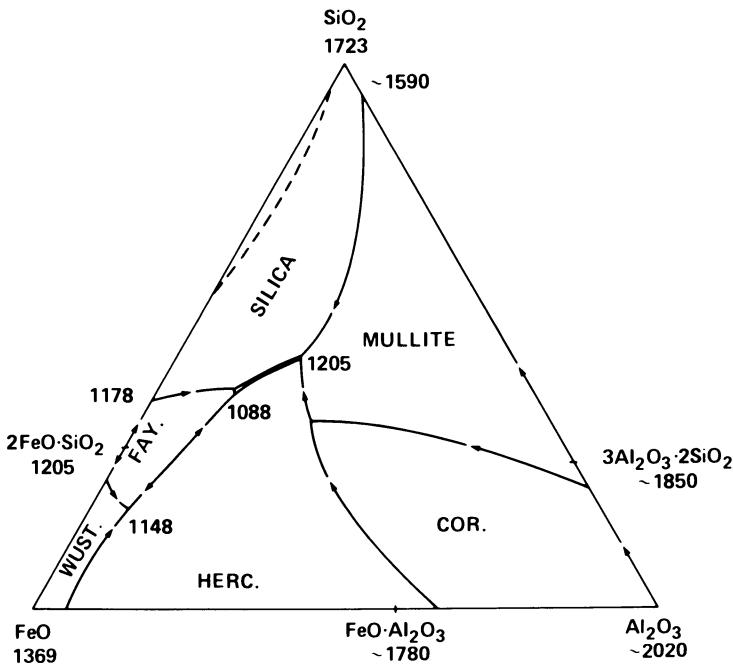


Figure 12. The FeO–Al₂O₃–SiO₂ phase diagram. Several key liquidus temperatures are indicated.

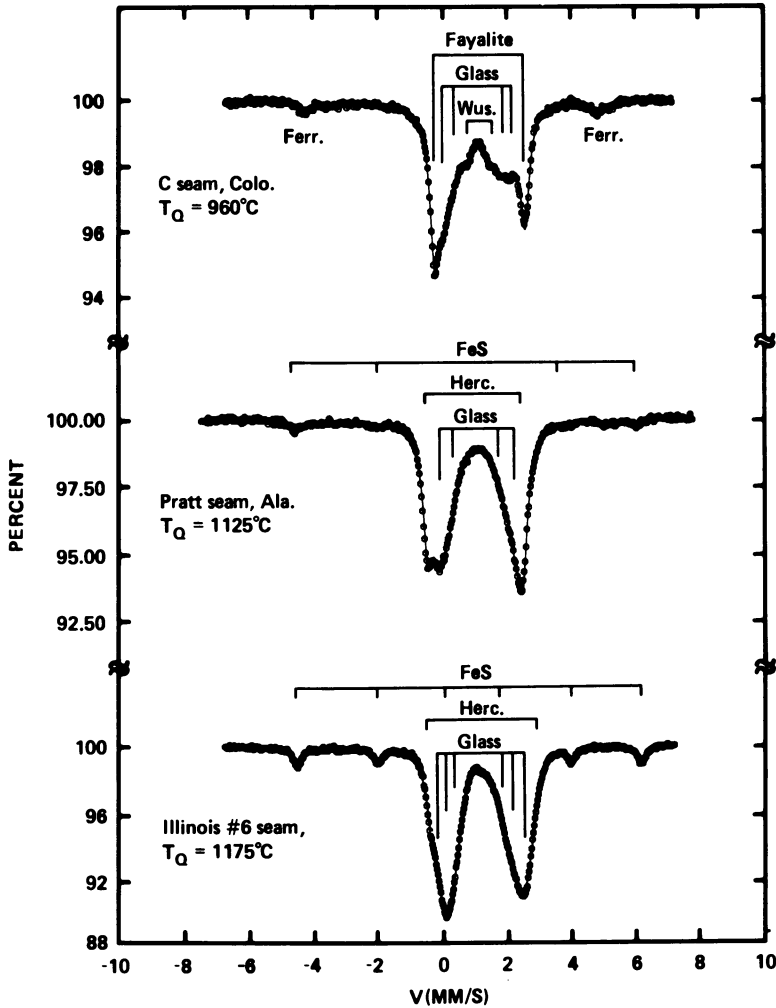


Figure 13. Spectra of ash samples quenched from high temperatures in a reducing atmosphere. The top spectrum was obtained at room temperature and the lower spectra at 77 K.

as a function of increasing temperature. The results are summarized in Figure 13, which shows typical Mössbauer spectra of several ashes quenched from various temperatures in a reducing atmosphere, and in Figure 14, which is a schematic representation of the iron-phase percentages as a function of temperature, typical of most of the ashes investigated. (Typical ash compositions are 40 to 60% SiO_2 , 20 to 30% Al_2O_3 , and 5 to 15% FeO , with the balance contributed by CaO , K_2O , MgO , etc.)

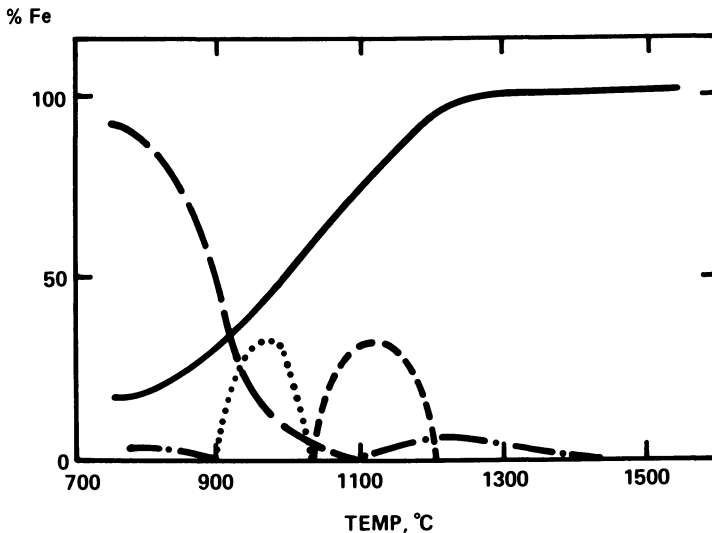


Figure 14. Typical temperature dependence of the percentages of iron contained in various phases in ash samples quenched from a reducing atmosphere (60% CO-40% CO₂) ((—) glass; (---) wustite, ferrite; (· · ·) fayalite; (- · -) iron sulfide; (---)hercynite, Fe-Al spinel)

Below 850°C, most of the iron is present as wustite and iron-rich ferrite phases derived from iron-rich minerals in the coal (pyrite, siderite, etc.), with a smaller amount contained in glass or poorly crystalline phases derived principally from illite. Above approximately 900°C, wustite reacts strongly with quartz- and kaolinite-derived aluminosilicates to form fayalite and silicate melts. The top spectrum of Figure 13 is typical of samples quenched from this temperature range. Melting accelerates and fayalite disappears as the temperature is increased to approximately 1100°C. Depending on the aluminum content (kaolinite in the original mineralogy), significant amounts of hercynite (FeAl₂O₄) or other refractory aluminum-spinels may form in the range from 1100° to 1200°C, retarding assimilation of iron into the molten phase. At temperatures above approximately 1200°C, however, most of the iron has been incorporated into glass phases. The middle and lower spectra of Figure 13 are typical of ashes quenched from this temperature range.

As seen in Figures 13 and 14, iron sulfide, formed by reaction of ferrous iron with sulfur from CaS, is also frequently observed. Usually the amount of iron sulfide is minor, but for certain ashes of high iron and calcium contents, iron sulfide and wustite are the dominant iron-bearing phases observed at all temperatures. Melting appears to be controlled in these cases by the binary FeO-FeS phase diagram. A more detailed discussion of this and other points will be given elsewhere (25).

Mössbauer Analysis of Steels

Applications of Mössbauer spectroscopy to the problems of steel analysis and ferrous metallurgy constitute one of the largest Mössbauer research areas, and several reviews on this topic have been written (27–30). Consequently, this section will concentrate primarily on several relatively new utilizations of Mössbauer spectroscopy in the analysis of steels, with only a brief review of more traditional areas.

The Iron–Carbon System and Austenite–Martensite–Carbide Determinations. Most steels consist principally of iron and carbon, and not surprisingly, the iron–carbon system has been studied extensively by Mössbauer spectroscopy. Some of the principal results of these studies may be discussed conveniently by referring to Figure 15, which shows spectra of a low- and high-carbon steel after annealing at 1100°C, quenching into ice brine, and aging at room temperature for a week. The high-temperature (above 750° to 900°C, depending on the carbon con-

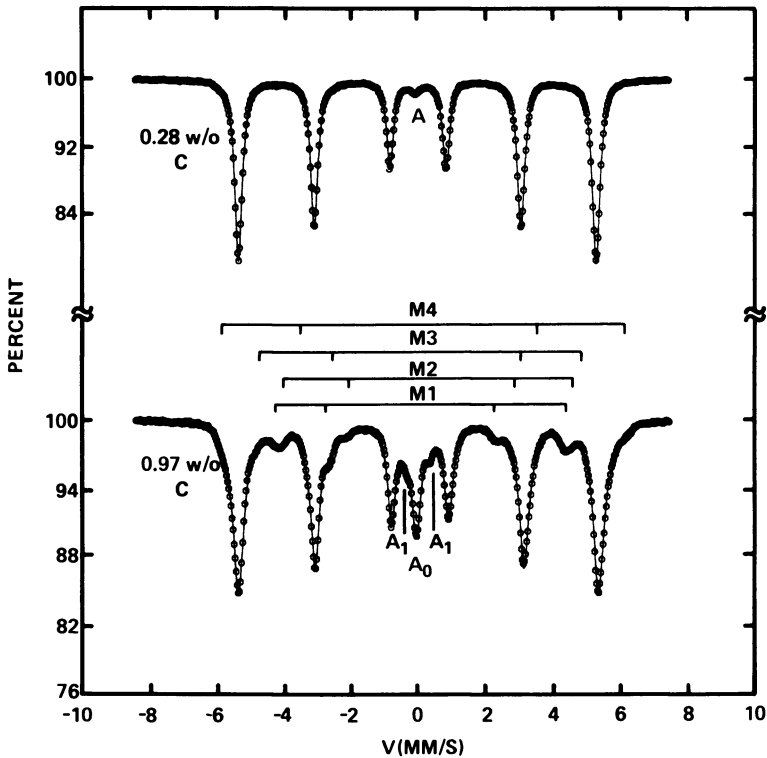


Figure 15. Spectra of a low- (top) and high- (bottom) carbon steel, quenched from 1100°C, exhibiting retained austenite contents of 1.3 and 10.4%, respectively

tent) phase of steel is a face-centered cubic solid solution of carbon in iron called austenite. On cooling below the so-called M_s temperature, austenite transforms to a body-centered tetragonal solid solution called martensite (31). Normally, the transformation of austenite to martensite during cooling is incomplete. Both the amount and the form of the retained austenite significantly affect mechanical properties.

Because austenite is paramagnetic and martensite is ferromagnetic at room temperature, they are easily distinguished in Mössbauer spectra. (Only a few papers will be individually referenced in this section. The reader is referred to the review articles (27–30) noted earlier for more extensive metallurgical bibliographies.) Recent discussions of austenite determination by transmission and backscattering Mössbauer spectroscopy have been given by Schwartz et al. (29, 32) and by Flinn et al. (27, 33). They conclude that Mössbauer spectroscopy gives somewhat more accurate results than x-ray diffraction (XRD), provided corrections for effective thickness and other technique-related effects are made. Additionally, it is frequently applicable in cases where XRD is ineffective, as discussed later.

Recently, Schwartz and Kim (34) used electron re-emission Mössbauer (ERM) spectroscopy to establish that the amount of austenite at the surface of a 1095 steel was only half that in the bulk. They have also used ERM spectroscopy to investigate fracture surfaces in Fe–9Ni–0.1C steel (35), and established that the austenite in the steel is transformed to martensite to a depth of 300 μm below the fracture surface. Such measurements would be very difficult by XRD.

Austenite–martensite percentages are also of interest in other types of steel. Many austenitic stainless steels undergo partial transformation to martensite during deformation. The degree of transformation depends critically on prior heat treatment and composition (36). The spectrum of Figure 16 was obtained from a highly deformed area of a wheel cover hot-pressed (temperatures of approximately 100°C) from Type 301 stainless steel which was completely austenitic prior to pressing. The very broad martensite peaks are fit by three magnetic components, reflecting the high alloying content of the steel (17 wt % chromium, 7 wt % nickel). Investigation of several Type 301 steels revealed that formability increased with increasing transformation of austenite to martensite, presumably because of additional energy dissipation and work hardening (36). Again the XRD method would be difficult because of deformation and texture effects.

Returning to Figure 15, both the austenite and martensite spectra exhibit structure arising from carbon in solution. The austenite spectrum consists of a singlet (A_0) arising from iron atoms with no carbon nearest neighbor, and a doublet (A_1) derived from iron atoms having one carbon

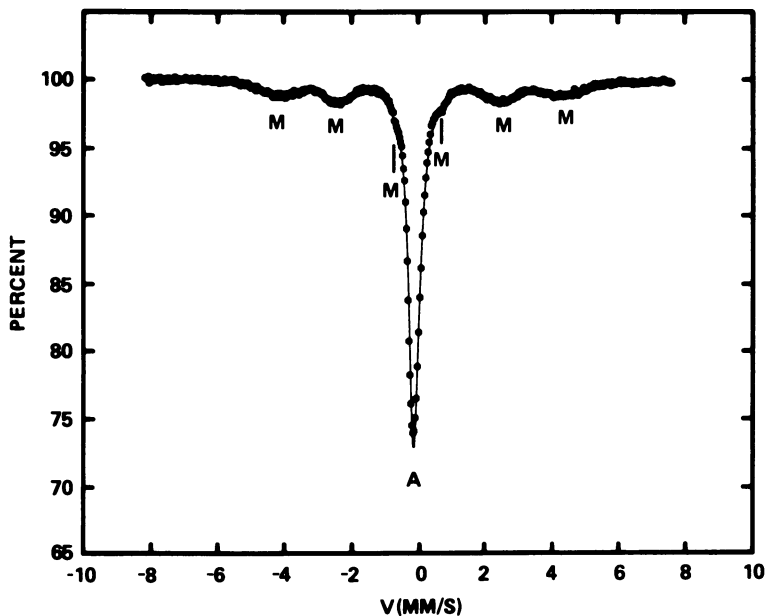


Figure 16. Spectrum of a highly deformed section of a wheel cover hot-pressed from Type 301 stainless steel. The deformation has transformed 23% of the steel to martensite.

nearest neighbor. Examination of the relative percentages of iron atoms having zero or one carbon nearest neighbor reveals that carbon atoms do not occupy adjacent sites, indicating a strong repulsion between carbon atoms in austenite (37).

The martensite spectrum for high-carbon steels is quite complex. As seen in Figure 15, there are at least four distinct magnetic satellite components derived from iron atoms with various configurations of carbon neighbors. There have been many attempts to interpret Mössbauer spectra of martensite (37-41). All investigators agree that significant tempering involving clustering of carbon atoms occurs in relatively short times (\sim hours) at room temperature. There also appears to be general agreement that the M_1 and M_2 satellite components arise from iron atoms that are dipolar and planar nearest neighbors of carbon atoms in octahedral interstices. There is little agreement, however, with regard to the origin of the remaining satellite peaks or the atomic arrangement of the carbon atoms. The original articles should be consulted for further discussion (37-41).

Tempering at somewhat elevated temperatures (300° to 500°C) normally causes the formation of cementite, as illustrated in Figure 17. A recent, detailed Mössbauer study of cementite formation during tem-

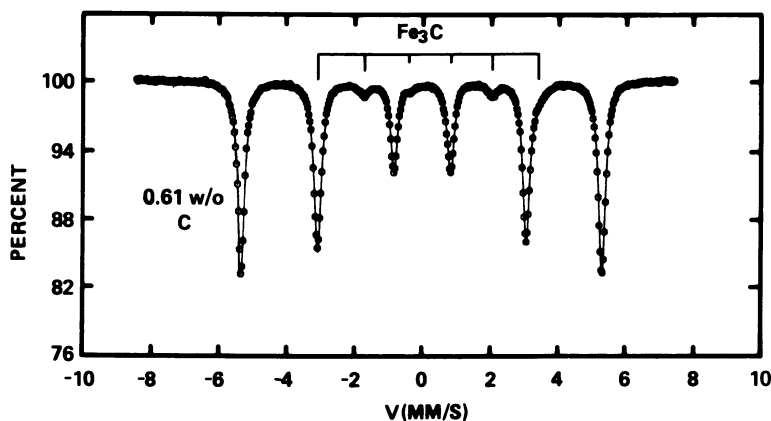


Figure 17. Spectrum of a steel quenched from 1100°C and subsequently tempered at 400°C for 3 h; 7% of the iron is contained in cementite

pering has been published by Williamson et al. (42). Common alloying elements such as manganese, chromium, and silicon also may be incorporated into cementite and other carbide structures; such mixed carbide phases usually give rise to quadrupole doublets at room temperature (27, 43).

Finally, it is worth noting that many of the studies of the iron-carbon system described in this section have been largely duplicated for the iron-nitrogen system (40, 44, 45).

Investigations of Internally Nitrided Steels. Much effort has been devoted in recent years to the development of precipitation-strengthened, high-strength low-alloy (HSLA) steels. HSLA steels that are strengthened by precipitation of fine dispersions of internal solute nitride phases have been studied extensively at this laboratory. In this section, some of the results obtained by Mössbauer analysis of such internally nitrided alloys (46, 47, 48) are summarized.

The nitride precipitates normally take the form of thin coherent platelets lying along (100) ferrite planes. In the transmission electron microscope, they give rise to a characteristic tweed contrast, as shown in Figure 18. Because the platelets are extremely fine (1 to 3 atom layers thick, 10 to 50 Å in diameter), conclusive identification of their stoichiometry is difficult. Figure 19 illustrates how Mössbauer spectroscopy can be used for such stoichiometry identification (46, 47). The top spectrum was obtained from an iron-2.9 at. % molybdenum alloy prior to nitriding; the arrows labeled (*n,m*) denote the outermost peaks derived from iron atoms with *n* molybdenum nearest neighbors and *m* molybdenum next-nearest neighbors. The remaining spectra were obtained after the alloy was nitrided to various levels at 500°C in an NH₃-H₂ atmosphere. As

the nitrogen level increases, the molybdenum satellite peaks disappear. They are replaced by a very weak set of peaks indicated by dashed arrows; as discussed later, these arise from iron atoms in the ferrite matrix that are nearest neighbors to nitrogen atoms in the platelets.

The nitrogen level is measured gravimetrically, and at each level of nitrogenation the amount of molybdenum remaining in solution, C_{Mo} , is determined from the expression

$$C_{Mo} = 100 \left\{ 1 - \exp \left[\frac{\ln P(0,0)}{14} \right] \right\}$$

where $P(0,0)$ is the Mössbauer-determined fraction of ferrite atoms which have no molybdenum nearest neighbors or next-nearest neighbors. Comparison of the molybdenum removed from solution with the amount of absorbed nitrogen for many samples led to the conclusion that the stoichiometry of the nitride was MoN. Similarly, the stoichiometry of the most stable nitride in the iron-titanium-nitrogen system was established as TiN.

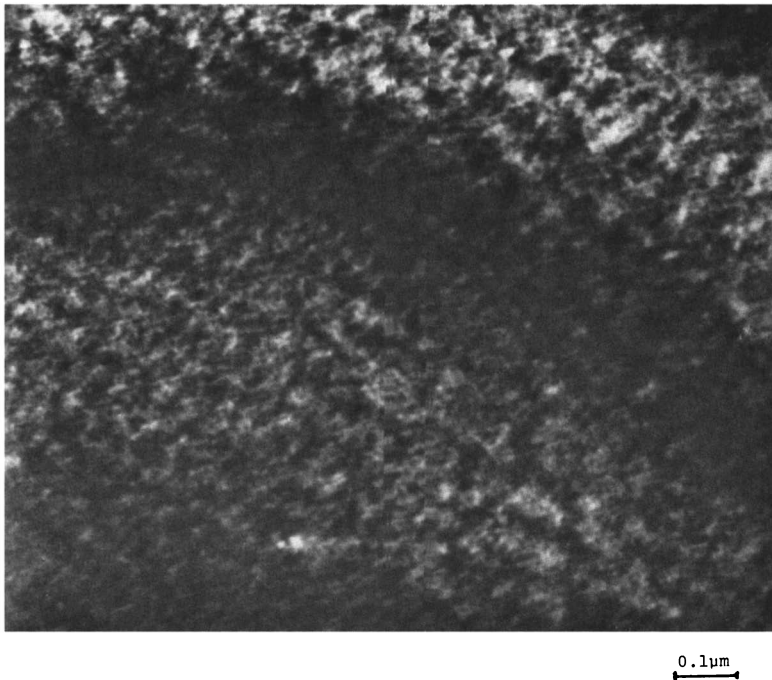
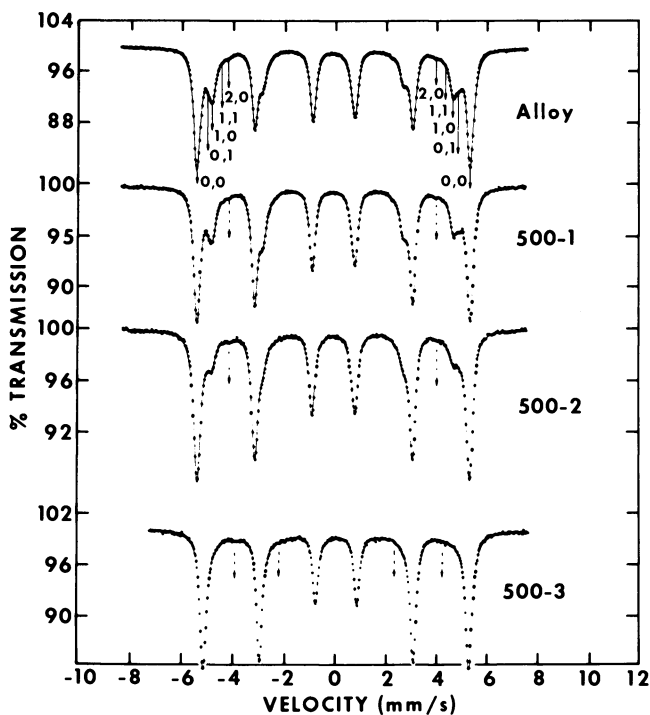


Figure 18. Characteristic tweed microstructure exhibited by an inter-nitrided iron-titanium alloy



Acta Metallurgica

Figure 19. Spectra of iron-2.9 at. % molybdenum alloy before (top) and after nitriding to various levels at 500°C. Nitrogen contents (at. %) are: 500-1-0.93%; 500-2-1.73%; 500-3-2.75% (46).

The nitride platelets formed in the iron-titanium-nitrogen system are much more stable and significantly smaller than those in the iron-molybdenum-nitrogen system (46). Consequently, iron atoms neighboring titanium and nitrogen in the platelets can be readily detected and studied.

The spectrum of an iron-titanium alloy containing 1.9% titanium is shown at the top of Figure 20; satellite peaks derived from iron atoms with one and two titanium nearest neighbors or next-nearest neighbors are indicated. (The change in the hyperfine field and isomer shift produced by a nearest neighbor titanium atom is not sufficiently different from that produced by a next nearest neighbor titanium atom to be distinguished (51).) The lower spectrum of Figure 20 was obtained after the alloy was nitrided at 400°C to a very high nitrogen level (5.4 at. % nitrogen). The upper spectrum of Figure 21 was taken after the alloy was nitrided to a high level and subsequently equilibrated at a low nitrogen activity at 500°C; this treatment was found to produce a TiN_2 stoichiometry for numerous alloys of various titanium contents (48, 49). Finally,

the lower spectrum of Figure 21 was obtained after the alloy was nitrided and subsequently reduced in H_2 at $400^\circ C$ to remove all nitrogen in excess of the TiN level.

Mössbauer, transmission electron microscopy, and other measurements on this and more dilute iron-titanium-nitrogen alloys have significantly clarified the internal solute nitride structure and its relation to bulk mechanical properties (48). For samples reduced to the TiN level, the Mössbauer results are in good agreement with a model proposed by D. H. Jack (50), illustrated in Figure 22. The TiN takes the form of approximately circular, monolayer platelets lying along (100) ferrite planes, in which the nitrogen atoms occupy octahedral interstices surrounded by four planar titanium nearest neighbors and two dipolar iron nearest neighbors in the ferrite matrix; these iron atoms give rise to the

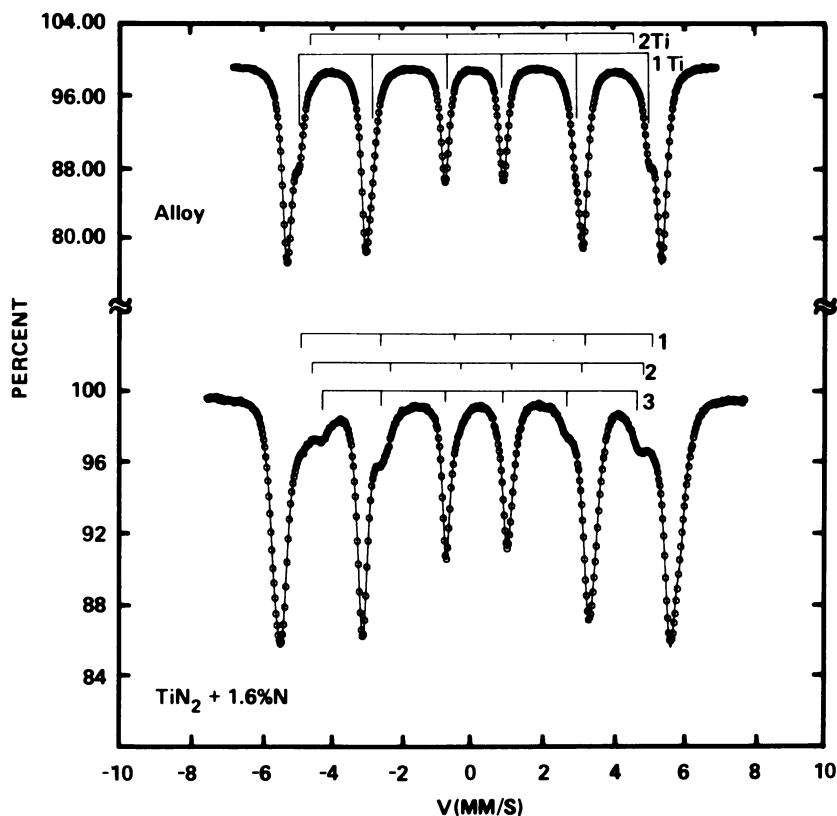


Figure 20. Spectra of an iron-1.9 at. % titanium alloy before (top—295 K) and after (bottom—77 K) nitrogeneration to a high level (5.4 at. % nitrogen)

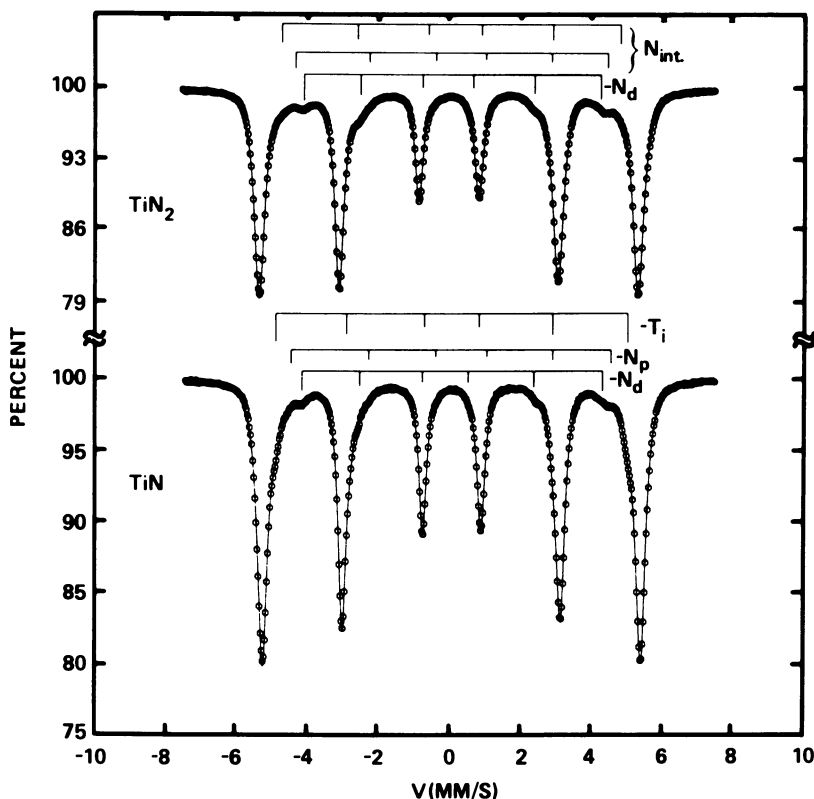


Figure 21. Spectra of the iron-titanium-nitrogen alloy at the TiN_2 level (top) and at the TiN level (bottom)

satellite peaks labeled N_d in Figure 21. There are two other principal types of iron atoms present:

1. Iron atoms that are either nearest neighbor or next-nearest neighbor to titanium atoms in the monolayer. The next-nearest iron atoms occur in the second atomic planes above and below the monolayer, and the nearest neighbor iron atoms are located in the first atomic planes above and below the square monolayer in the ferrite sites around its perimeter. These produce the component labeled titanium in the lower spectrum of Figure 21; its Mössbauer parameters are quite close to those observed for iron atoms with one titanium nearest neighbor or next-nearest neighbor in the untreated alloy.
2. Iron atoms in the plane of the monolayer that are planar nearest neighbors to nitrogen atoms on its perimeter, and give rise to a satellite component labeled N_p .

Estimates of the thickness and diameter of the TiN platelets can be made from the percentages of iron atoms contributing to the satellite components. For monolayers, it is seen from Figure 22 that the percentage of iron atoms having a dipolar nitrogen nearest neighbor, P_d , should be twice the titanium percentage. This has been observed for several Fe-TiN alloys after nitriding and reducing at 400°C and 500°C. Similarly, estimates of platelet diameter can be made from the percentages P_{Ti} and P_P (48). For the TiN sample of Figure 21, the satellite percentages indicate a thickness of one monolayer and a diameter of approximately 10 Å.

Aging the Fe-TiN samples at elevated temperatures in H_2 causes thickening and growth of the TiN platelets, producing changes in mechanical properties. Platelet growth can be monitored by Mössbauer spectroscopy. For example, the average platelet thickness $\langle n \rangle$ is given by

$$\langle n \rangle = 2 \times \text{at. \% Ti}/P_d$$

The TiN-level sample of Figure 21 was aged for 1 to 33 h in H_2 at 600°C, and Mössbauer data were obtained at each stage. Figure 23 shows the

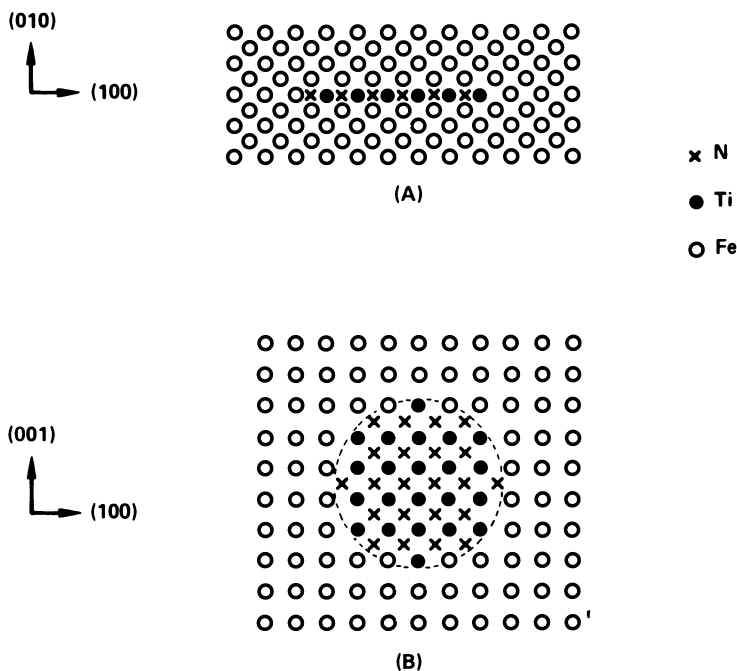


Figure 22. Model of a circular TiN monolayer platelet lying on a (100) ferrite plane viewed (a) edge on and (b) face on

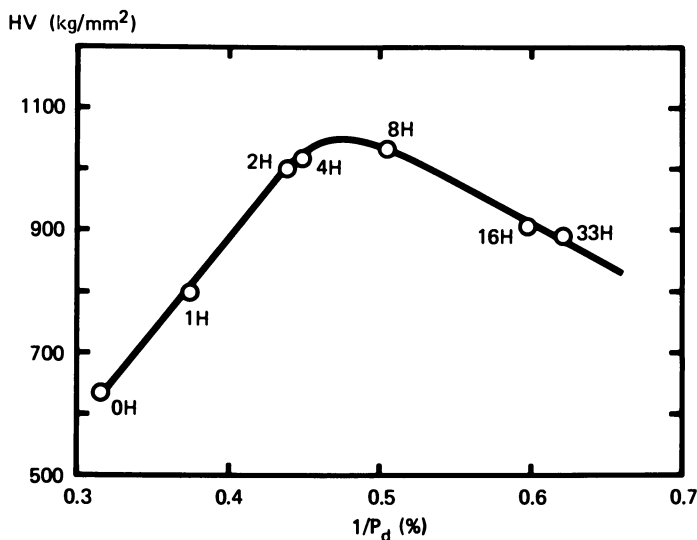


Figure 23. Hardness values of the 1.9 at. % TiN level samples aged from 0 to 33 h in H_2 vs. the inverse of the percentage of iron atoms that are dipolar nearest neighbors to nitrogen atoms in the TiN platelets

mechanical hardness plotted against $1/P_d$. The peak hardness value occurs at an average platelet thickness of approximately two atomic layers. This is in accord with electron microscopy, which indicates that transformation to an incoherent "bulk" TiN structure occurs when the platelet thickness exceeds two layers.

In spectra obtained from alloys in which the precipitates have the TiN_2 structure (Figure 21, top), the satellite component N_d again arises from dipolar iron nearest neighbors to nitrogen atoms in the platelet. The components N_{int} are believed to arise from an ordered arrangement of interfacial nitrogen atoms which occupy every fourth interstitial site in the two ferrite planes immediately above and below the central TiN monolayer (48). At nitrogen levels above the TiN_2 level (bottom, Figure 20), all peaks are markedly broadened, and assignment of satellite components is inconclusive. An important observation, however, is that no iron nitride phases are detected, reflecting the markedly increased nitrogen solubility of ferrite containing dispersed titanium nitrides relative to that of pure iron.

Investigation of Surface and Subsurface Oxides in Steels. Electron and x-ray re-emission Mössbauer (ERM and XRM) spectroscopy provide excellent methods for surface and subsurface analysis of steel. For ^{57}Fe , ERM spectroscopy samples approximately the top 0.5 μm of an iron-rich surface, whereas XRM samples approximately the top 20 μm .

The ERM technique has been investigated more extensively (52–61). A theory of ERM spectroscopy developed at this laboratory (54) provides analytical expressions that allow the conversion of ERM spectral area percentages to surface-layer thicknesses. This theoretical method has been used in studies of surface oxide layers on iron (55, 56, 59) and in a ^{119}Sn ERM investigation of surface layers on tinplate (57). A chapter reviewing the ERM technique is contained in this volume (60). An earlier review article describing the use of ERM, XRM, and transmission spectroscopy in the analysis of surface-treated steels is also available (58).

In this section, we summarize several practical applications of these techniques in the analysis of surface and subsurface oxides in steel. We first consider the oxidation of silicon during the annealing of nonoriented electrical sheet steel (61). These steels, which typically contain approximately 4 at. % silicon, 0.5 at. % aluminum, and 0.3 at. % manganese, are subjected to a variety of annealing treatments to achieve desired magnetic properties. Normally, these treatments are conducted in $\text{H}_2\text{-N}_2\text{-H}_2\text{O}$ or "HNX" atmospheres at approximately 800°C (decarburization anneal) and 1000°C (grain-growth anneal). Investigations here (61) and elsewhere (62) have established that internal solute oxidation during such annealing treatments can significantly degrade magnetic properties.

Several typical ERM and XRM spectra of samples treated in relatively wet ($\text{H}_2\text{O}/\text{H}_2 = 0.15$) and dry ($\text{H}_2\text{O}/\text{H}_2 = 0.02$) HNX atmospheres are shown in Figures 24 and 25. Samples annealed completely in dry HNX exhibited only peaks from unoxidized iron (top, Figure 24); the arrows labeled 0, 1, and 2 denote the outer peaks arising from iron atoms in the ferrite matrix that have 0, 1, or 2 solute atoms as nearest neighbors. For samples treated in wet HNX, silicon is removed from solution and incorporated into the ferrous silicate phase, fayalite (Fe_2SiO_4 ; peaks labeled Fa in Figures 24 and 25). The lower spectrum of Figure 24 not only exhibits a significant amount of fayalite, but also shows the existence of a surface magnetite layer estimated from its spectral area percentage (54) to be 540 Å thick. This indicates a large $\text{H}_2\text{O}/\text{H}_2$ ratio (> 0.5) in the cracked natural gas atmosphere in which this sample was annealed.

The fayalite peaks are most prominent in the ERM spectra, and are either much weaker or undetectable in the XRM spectra, indicating that fayalite is contained primarily in the top several microns of most samples. From the relatively small intensities of the satellite peaks attributable to silicon in solution exhibited by the XRM spectra, it is seen that silicon has been significantly depleted from the ferrite matrix to depths of 20 to 30 μm . The micrographs of Figure 26 show that this relatively deep removal of silicon from solution is associated with the formation of small

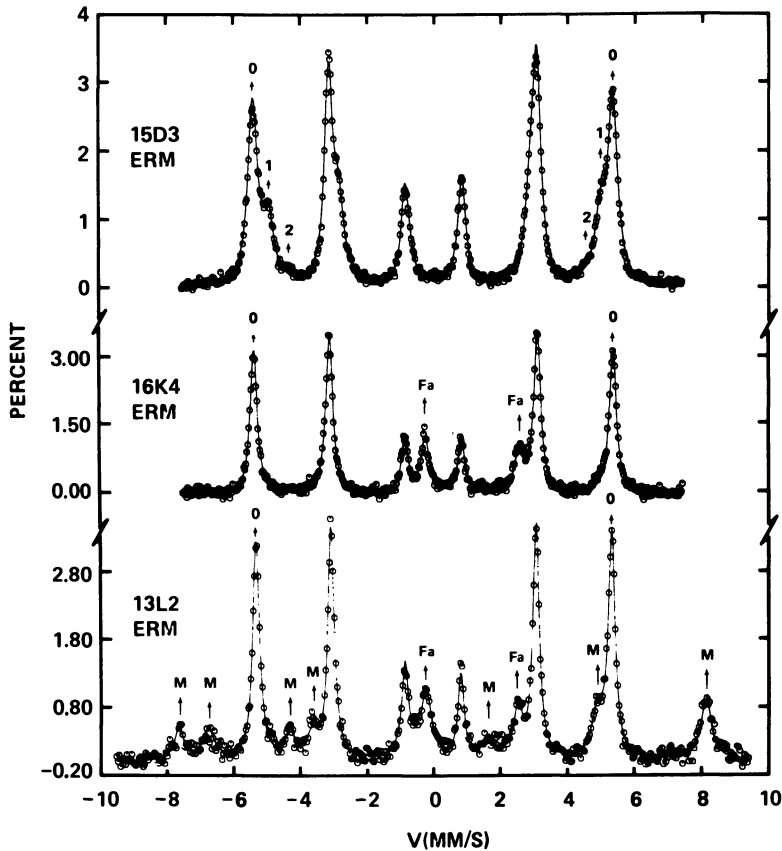


Figure 24. ERM spectra of several samples of nonoriented silicon-steels annealed as follows: Sample 15D3—5 min, dry HNX ($H_2O/H_2 = 0.02$), 800°C ; Sample 16K4—5 min, wet HNX ($H_2O/H_2 = 0.15$), 980°C ; Sample 13L2—30 min, cracked natural gas ($H_2O/H_2 > 0.5$), 840°C

internal oxide inclusions (principally SiO_2) which have a marked affinity for grain boundaries.

The surface oxide layer and the grain boundaries apparently become more permeable to oxygen when fayalite is formed. The deleterious effect of fayalite formation is illustrated in Figure 27, which shows a correlation between magnetic permeability and the ERM-determined percentage of iron contained in fayalite. The two solid data points represent samples subjected to an initial 5-min anneal in wet HNX, followed by a longer annealing treatment in dry HNX that converts fayalite to iron plus SiO_2 , but produces no significant recovery of magnetic properties.

Removal of solute elements from solid solution to form internal solute oxides is a common problem encountered in the annealing of many types of steel. Figure 28 provides an example of such oxidation during box annealing of a steel containing 1.7 at. % manganese (63). The surface oxide layers are determined from the ERM spectrum area percentages (54) to be quite thick in this instance ($Z_{\text{hem}} = 1070 \text{ \AA}$; $Z_{\text{mag}} = 2310 \text{ \AA}$). More serious, however, is the fact that the XRM spectrum shows an almost complete depletion of manganese from solution to a depth of $20 \mu\text{m}$. Serious impairment of physical properties and appearance results from such oxidation.

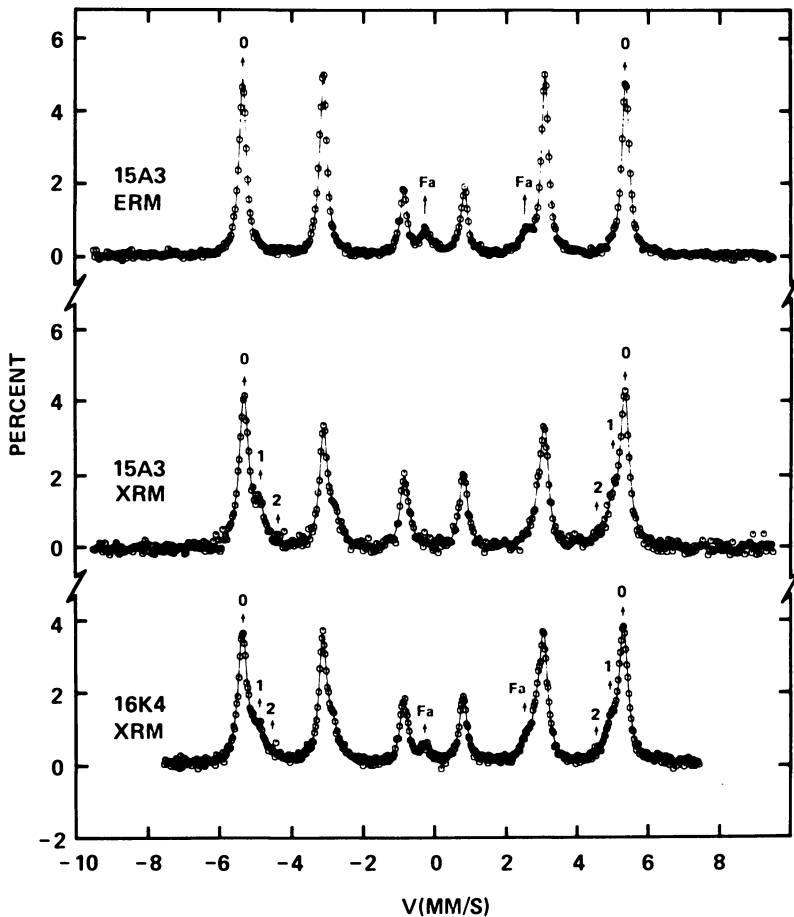


Figure 25. ERM (top) and XRM (middle) spectra of silicon-steel annealed 5 min in wet HNX at 800°C ; XRM spectrum (bottom) of Sample 16K4, the ERM spectrum of which appears in Figure 24

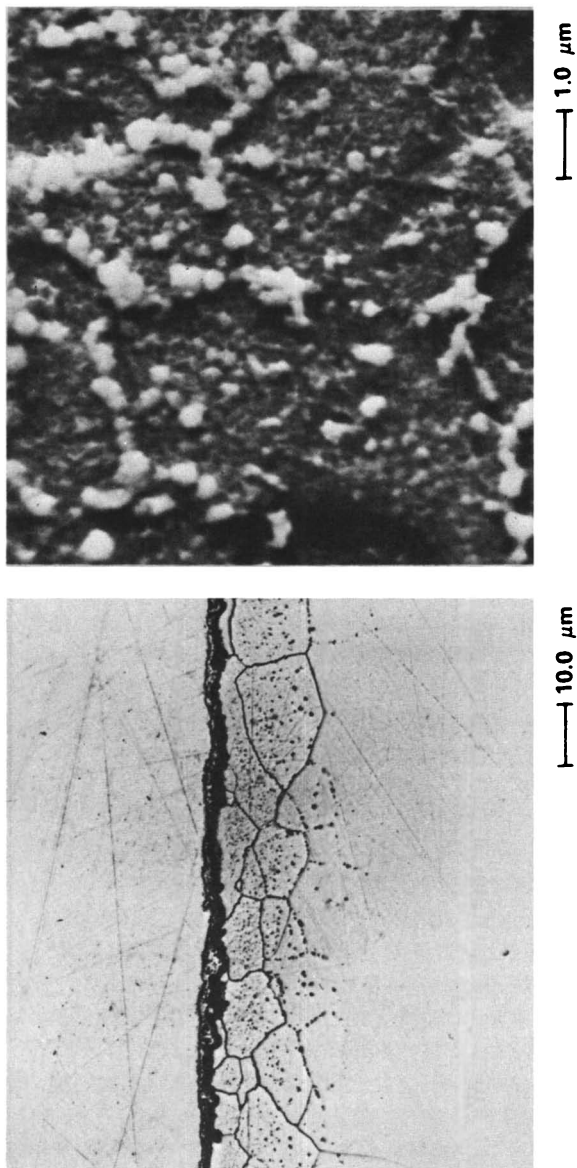
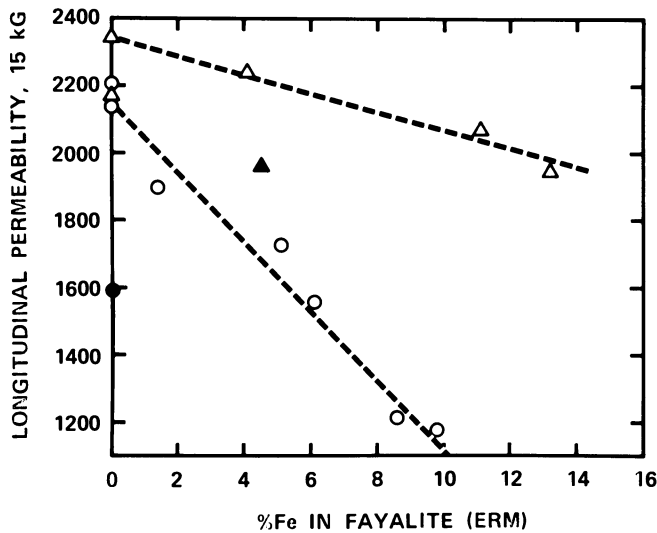


Figure 26. Optical ($\times 850$) and SEM ($\times 8500$) micrographs of the polished and etched edge of an internally oxidized silicon-steel showing concentration of oxide particles along grain boundaries (61)



Journal of Applied Physics

Figure 27. Permeability vs. the ERM-determined percentage of iron in fayalite (61) ((○) 5-min anneal at 1475°F; (△) 5-min anneal at 1800°F)

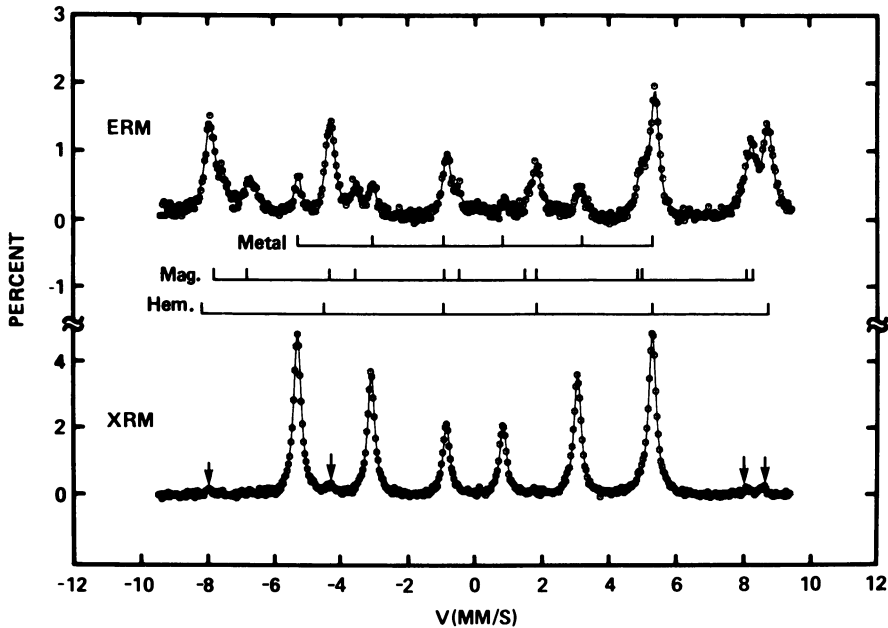


Figure 28. ERM and XRM spectra of an annealed steel containing 1.7 at. % manganese illustrating the nature of the surface oxide layer and the removal of manganese from solution by internal oxidation. The surface oxide peaks are just detectable (arrows) in the XRM spectrum.

In many cases, the oxide scales of interest on steel are too thick for ERM spectroscopy to provide really useful information. XRM spectroscopy is more useful here, and some typical XRM spectra of relatively thick oxide scales are shown in Figures 29 and 30. The XRM spectra in Figure 29 illustrate the nature of oxide scales formed during hot-rolling. If the hot-rolled coil is cooled rapidly, the scale is predominantly wustite (lower spectrum); for slower cooling rates, the scale is transformed to magnetite (upper spectrum). It is found that descaling is more easily accomplished for the magnetite than for the wustite scale.

Figure 30 shows spectra obtained from the protective oxide layer formed on USS COR-TEN, a structural steel, during three months of atmospheric exposure (63). From the relative percentages contributed to the XRM spectrum by the steel substrate and the ferric oxyhydroxide layer, the thickness of the layer is estimated to be 13 μm . Identification of the superparamagnetic oxyhydroxide phases required a low-temperature transmission spectrum of the extracted oxide layer (lower spectrum, Figure 30), which showed it to consist of 67% $\beta\text{-FeOOH}$ and 33% $\gamma\text{-FeOOH}$.

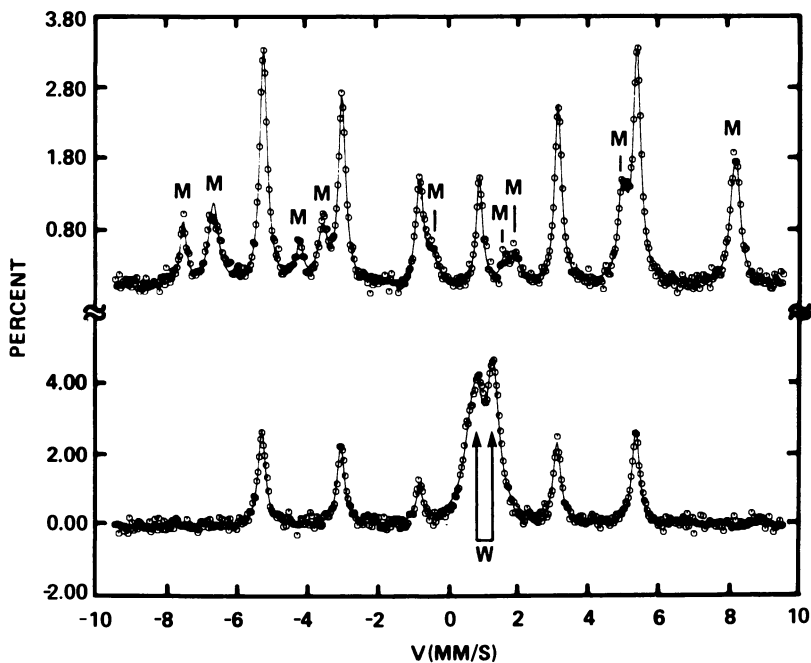


Figure 29. XRM spectra illustrating different types of oxide scales formed during hot-rolling

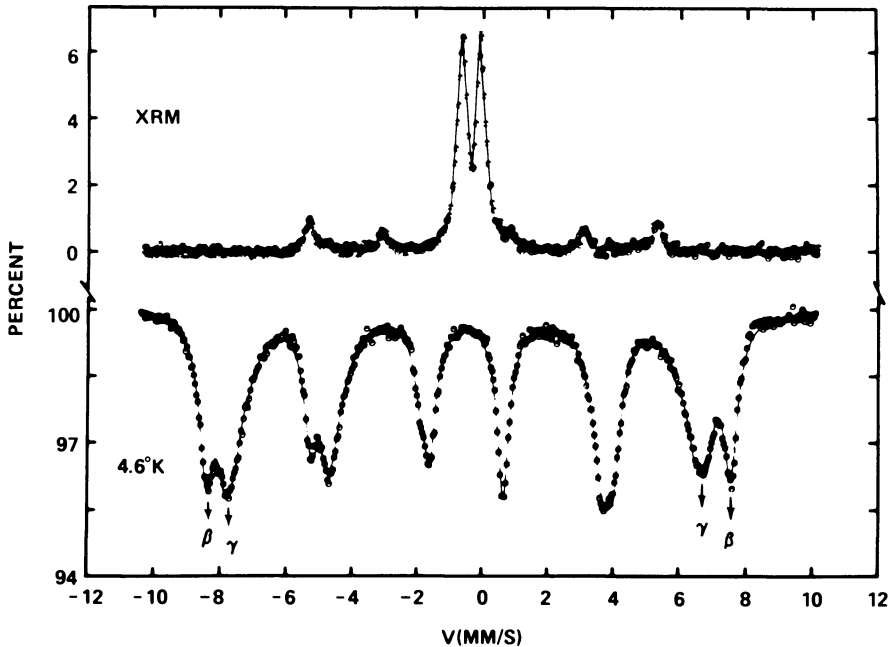


Figure 30. Analysis of the protective oxide layer on COR-TEN requires both XRM and low-temperature transmission spectra

Summary

Iron is an important and frequently dominant constituent of the raw materials (iron and other ores), of the principal fuel source (coal and coke), and of the many products of the steel industry. In this chapter, we have attempted to give examples of the applications of Mössbauer spectroscopy in each of these important areas. Because of the scope of the subject, no application has been treated in any detail. Nevertheless, it is hoped that some of the principal contributions of Mössbauer spectroscopy in each area have been highlighted properly, and that sufficient references have been given to allow the reader to pursue any particular topic in more detail.

Literature Cited

1. McGannon, H. E., Ed. "The Making, Shaping, and Treating of Steel"; U.S. Steel Corp.: Pittsburgh, PA, 1971.
2. *Stahl Eisen*. 1970, 90, 1531.
3. Teller, L.; Mozer, I.; Turcotte, S. F. *Iron Steel Eng.* 1974, 51, 33.
4. Huffman, G. P.; Dunmyre, G. R., unpublished data.

5. Huffman, G. P.; Schwerer, F. C.; Fisher, R. M.; Nagata, T. *Proc. Lunar Sci. Conf., 5th, Geochim. Cosmochim. Acta, Suppl.* 5 1974, 2279.
6. Speich, G. R.; Huffman, G. P.; Schwerer, F. C., unpublished data.
7. Huffman, G. P.; Dunmyre, G. R., unpublished data.
8. Huffman, G. P.; Huggins, F. E. *Fuel* 1978, 57, 592.
9. Huggins, F. E.; Huffman, G. P. In "Analytical Methods for Coal and Coal Products"; Clarence Karr, Jr., Ed.; Academic: New York, 1979; Vol. 3, p. 371.
10. Levinson, L. M.; Jacobs, I. S. *Fuel* 1977, 56, 453.
11. Jacobs, I. S.; Levinson, L. M.; Hart, H. R. *J. Appl. Phys.* 1978, 49, 1775.
12. Montano, P. A. *Fuel* 1977, 56, 397.
13. Russel, P. E.; Montano, P. A. *J. Appl. Phys.* 1978, 49, 4615.
14. Smith, G. V.; Lui, J.-H.; Saporoschenko, M.; Shiley, R. *Fuel* 1978, 57, 41.
15. Lee, R. J.; Huggins, F. E.; Huffman, G. P. *Scanning Electron Microsc.* 1978, 1, 561.
16. Huggins, F. E.; Kosmack, D. A.; Huffman, G. P.; Lee, R. J. *Scanning Electron Microsc.* 1980, 1, 531.
17. Huggins, F. E.; Huffman, G. P.; Lee, R. J., unpublished data.
18. Garrels, R. M.; Christ, C. L. "Solutions, Minerals, and Equilibria"; Harper: New York, 1965.
19. Gray, R. J.; Rhoades, A. H.; King, D. T. *Trans. AIME* 1976, 260, 334.
20. Huggins, F. E.; Kosmack, D. A.; Huffman, G. P.; Lowerhaupt, D. E. *Int. J. Coal Geology*, 1980, 1, 75.
21. Huggins, F. E.; Huffman, G. P.; Lee, R. J., unpublished data.
22. Nigro, J. C.; Zahl, R. K. *Shillings' Min. Rev.* 1976, 65(24), 1.
23. *Am. Soc. Test. Mater., Book ASTM Stand.* 1976, 26, 263.
24. Winegartner, E. C., Ed. "Coal Fouling and Slagging Parameters"; ASME Spec. Publ., 1974.
25. Huffman, G. P.; Huggins, F. E.; Dunmyre, G. R., *Fuel*, in press.
26. Levin, E. M. et al., Eds. "Phase Diagrams for Ceramists"; Amer. Ceram. Soc.: Columbus, OH, 1964; 241.
27. Flinn, P. A. "Metallurgical Applications of the Mössbauer Effect," *Proc. 5th Int. Conf. Mössbauer Spec.*, 1975, 2, 275.
28. Fujita, F. E. In "Topics in Applied Spectroscopy: Mössbauer Spectroscopy"; Gonser, U., Ed.; Springer-Verlag: Berlin, 1975; Vol. 5, p. 201.
29. Schwartz, L. H. In "Applications of Mössbauer Spectroscopy"; Cohen, R. L., Ed.; Academic: New York, 1976; Vol. 1, p. 37.
30. Foct, J.; LeCaer, G. *Bull. Cercle Etud. Met.* 1977, 13, 381.
31. Hansen, M.; Anderko, K. "Constitution of Binary Alloys"; McGraw-Hill: New York, 1958; p. 353.
32. Abe, N.; Schwartz, L. H. *Mater. Sci. Eng.* 1974, 14, 239.
33. Chow, H. K.; Welse, R. F.; Flinn, P. A. "Mössbauer Effect Spectrometry for Analysis of Iron Compounds," USAEC Report, NSEC-4023-1, 1969.
34. Schwartz, L. H.; Kim, K. J. *Metall. Trans.* 1976, 7A, 1567.
35. Kim, K. J.; Schwartz, L. H. *Mater. Sci. Eng.* 1978, 33, 5.
36. Ludwigson, D. C.; Brickner, K. G. *Sheet Met. Ind.* 1976, 245.
37. Genin, J. R.; Flinn, P. A. *Trans. Met. Soc. AIME* 1968, 242, 1419.
38. Moriya, T.; Ino, H.; Fujita, F. E.; Maeda, Y. *J. Phys. Soc. Jpn.* 1968, 24, 60.
39. Choo, W. K.; Kaplow, R. *Acta Met.* 1973, 21, 725.
40. DeCristofaro, N.; Kaplow, R. *Metall. Trans.* 1977, 8A, 35.
41. Ino, H.; Ito, T. *J. Phys. Colloq. C2* 1979, 40, Suppl. 3, C2-644.
42. Williamson, D. L.; Schupmann, R. G.; Materkowski, J. P.; Krauss, G. *Metall. Trans. A* 1979, 10A, 379.
43. Huffman, G. P.; Errington, P. R.; Fisher, R. M. *Phys. Status Solidi* 1967, 22, 473.

44. Moriya, T.; Sumitomo, Y.; Ino, H.; Fujita, F. E.; Maeda, Y. *J. Phys. Soc. Jpn.* **1973**, *35*, 1378.
45. Foct, J. *J. Phys. Colloq. C6* **1974**, *35*, Suppl. 12, C6-487.
46. Huffman, G. P.; Podgurski, H. H. *Acta Metall.* **1975**, *23*, 1367.
47. Huffman, G. P.; Podgurski, H. H. In "Mössbauer Effect Methodology"; Gruverman, I. J.; Seidel, C. W., Eds.; Plenum: New York, 1976; Vol. 10, p. 183.
48. Huffman, G. P.; Lally, J. S.; Cuddy, L. J., submitted for publication in *Acta Metall.*
49. Podgurski, H. H.; Davis, F. N. *Acta Metall.* **1981**, *29*, 1.
50. Jack, D. H. *Acta Metall.* **1976**, *24*, 137.
51. Vincze, I.; Gruner, G. *Phys. Rev. Lett.* **1972**, *28*, 178.
52. Spijkerman, J. J. In "Mössbauer Effect Methodology"; Gruverman, I. J., Ed.; Plenum: New York, 1971; Vol. 7, p. 85.
53. Simmons, G. W.; Kellerman, E.; Leidheiser, H. *Corros.* **1973**, *29*, 227.
54. Huffman, G. P. *Nucl. Instrum. Methods* **1976**, *137*, 267.
55. Huffman, G. P.; Podgurski, H. H. *Oxid. Met.* **1976**, *10*, 377.
56. Graham, M. J.; Mitchell, D. F.; Channing, D. A. *Oxid. Met.* **1978**, *12*, 247.
57. Huffman, G. P.; Dunmyre, G. R. *J. Electrochem. Soc.* **1978**, *125*, 1652.
58. Huffman, G. P. In "Applications of Mössbauer Spectroscopy"; Cohen, R. L., Ed.; Academic: New York, 1980; Vol. 2, p. 189.
59. Huffman, G. P.; Podgurski, H. H. *Oxid. Met.*, in press.
60. Tricker, M. J., Chapter 3 in this volume.
61. Huffman, G. P.; Stanley, E. B. *J. Appl. Phys.* **1979**, *50*, 2363.
62. Geiger, A. J. *J. Appl. Phys.* **1979**, *50*, 2366.
63. Huffman, G. P., unpublished data.

RECEIVED June 27, 1980.

Novel Iron-Sulfur Clusters

ECKARD MÜNCK

Gray Freshwater Biological Institute, Department of Biochemistry,
University of Minnesota, P.O. Box 100, Navarre, MN 55392

*Three novel iron-sulfur clusters have emerged during the past few years from the study of various biological systems. Two of the new centers are components of the molybdenum- and iron-containing protein (nitrogenase) of the biological nitrogen fixation system. During the past few months Mössbauer data and x-ray diffraction studies have given evidence for a cluster containing three spin-coupled iron atoms and (probably equimolar amounts of) sulfide. We characterized this center in detail for two ferredoxins from *A. vinelandii* and *D. gigas*. The new group also was present in aconitase from beef-heart mitochondria and in glutamate synthase from *E. coli*. This chapter focuses mainly on the spectroscopic evidence for this new three-iron center.*

During the past 15 years a fascinating subfield of modern biochemistry, the family of iron-sulfur proteins, has developed. During the past decade this discipline has matured into a sophisticated branch of modern research, and it has spawned the vigorous pursuit of designing structural models for the metal centers discovered in the proteins. This work culminated with the syntheses of [2Fe-2S] and [4Fe-4S] centers by R. H. Holm's group (1). About five years ago it appeared that the fundamental units had been discovered. Some strange EPR spectra, however, were signaling that additional structures remained to be characterized. Indeed, three novel iron-sulfur centers were found since 1975. Two of the new structures reside on the molybdenum- and iron-containing protein (MoFe protein) of nitrogenase; they seem to be specific ingredients to carry out the biological nitrogen fixation process. The third novel cluster, a spin-coupled center containing three iron atoms and inorganic sulfur, was discovered very recently; during the past four months we found this structure to be present in four different proteins

and enzymes, and at present it appears that this new center may be distributed widely in nature. Since Mössbauer spectroscopy has been an indispensable tool in characterizing this center and since the decisive clues were furnished by this technique, we will focus in this chapter on this novel structure. Moreover, we will have the opportunity to employ and discuss some new Mössbauer methodologies that promise to be fruitful in unraveling the spectral intricacies of multimetal systems.

In the following we briefly summarize nomenclature and salient spectral features of the familiar iron-sulfur centers, mention the novel centers of nitrogenase, and proceed, in the third section, with a brief history of two proteins that contain the new three-iron center. In the fourth section we discuss recent Mössbauer and EPR data, and in the fifth section we present a discussion of the principal results and an outline of some interesting future work.

It should be emphasized that the work presented here is the result of a fruitful cooperation between the Mössbauer group at the Gray Freshwater Biological Institute with other groups, in particular those of W. H. Orme-Johnson, M.I.T., and A. V. Xavier, University of Lisbon, Portugal.

Familiar Centers and the Clusters of Nitrogenase

In this section we will briefly review the pertinent features of [2Fe-2S] and [4Fe-4S] centers and of the cofactor centers and P-clusters of nitrogenase. We will not discuss rubredoxin, although an interesting (geometrical) twist regarding the simplest iron-sulfur center (one iron atom, no inorganic sulfur) was reported recently (2).

[2Fe-2S] Clusters. The history of the elucidation of the structure of the [2Fe-2S] centers by means of spectroscopic techniques is a beautiful example of how techniques such as the Mössbauer effect, EPR, ENDOR, NMR, magnetic susceptibility, and various optical methods can be combined in a very powerful way. A lucid review has been given by Palmer (3). The most important biophysical property of the [2Fe-2S] centers is their ability to mediate reversible one-electron transfer by utilizing two stable oxidation states. In the oxidized form the centers have a diamagnetic ($S = 0$) ground state; upon a one-electron reduction the famous EPR feature at $g = 1.94$ is observed, a signal resulting from an $S = 1/2$ ground state. In 1966 Gibson and co-workers (4) proposed a very elegant model involving antiferromagnetic coupling (via sulfur bridges) of the two iron atoms for the observed EPR features. This model was confirmed experimentally by Dunham et al. (5) and Münck et al. (6); the decisive clue was the observation of positive and negative magnetic hyperfine fields with Mössbauer spectroscopy. Recently, the salient features of the proposed structure for the [2Fe-2S] centers were

confirmed by x-ray diffraction studies of the ferredoxin from *Spirulina platensis* (7); this work also establishes that the compounds synthesized by Holm's group are close structural models of the active centers found in the electron transfer proteins.

[4Fe-4S] Clusters. Clusters of the cubane [4Fe-4S] type are stabilized by proteins in three oxidized states, although a given protein apparently utilizes only a single redox pair. In the *Chromatium vinosum* high-potential iron protein (HiPIP) the cluster operates at a midpoint potential of +420 mV. In the oxidized form an axial EPR signal is observed at $g_z = 2.12$ and $g_{\perp} = 2.04$ (see Orme-Johnson and Sands (8)); upon a one-electron reduction a diamagnetic cluster ground state results. In contrast, most other proteins stabilize the [4Fe-4S] center at a midpoint potential of about -400 mV. In the latter case (examples are the ferredoxins from *Bacillus polymyxa* and *Bacillus stearothermophilus*) the oxidized state is diamagnetic while the reduced state ($S = 1/2$) yields a signal at $g = 1.94$ (typical g -values are $g_z = 2.06$, $g_y = 1.92$, and $g_x = 1.88$ as observed for the *B. polymyxa* protein; see Ref. 8). The occurrence of three oxidation states for the [4Fe-4S] clusters has been rationalized by Carter et al. (9) by the three-state hypothesis which proposes that the clusters of reduced HiPIP and the oxidized ferredoxins are in equivalent diamagnetic states. The ferredoxins can be reduced into the EPR-active (+1) state (here we use the new rules for the nomenclature of iron-sulfur centers (10)). Note that the average g -value for reduced ferredoxin is $g_{av} < 2$, while $g_{av} > 2$ is for oxidized HiPIP. There are many examples in the literature where signals around $g = 2.01$ have been observed in iron-sulfur proteins under oxidizing conditions. These features often have been referred to as "HiPIP-type" signals, and frequently it was concluded (or tacitly assumed) that a [4Fe-4S] cluster in the (+3) oxidation level is present. In the next section we discuss a three-iron center as the source of many of the reported signals.

The P-Cluster of Nitrogenase. The P-clusters of nitrogenase are iron-sulfur centers with unique spectroscopic properties (the symbol P indicates that these centers (four per molecule) reside on the protein component of the MoFe protein, in contrast to the M-centers, discussed later, which belong to the iron- and molybdenum-containing cofactor (FeMo-co) of nitrogenase). The elucidation of their structural features so far has been entirely in the realm of Mössbauer spectroscopy. Zimmermann et al. (11) and Huynh et al. (12) have published detailed analyses of Mössbauer spectra of nitrogenase from *Azotobacter vinelandii* (11) and *Clostridium pasteurianum* (12). All evidence favors the P-clusters to be variants of familiar [4Fe-4S] centers. Spectroscopically, however, the P-clusters are quite unique. In the native protein (as isolated) the P-clusters are diamagnetic. According to the Mössbauer data one of the iron sites (labeled Fe²⁺) is clearly recognizable as high-

spin ferrous in character (this reminds one of the trapped ferrous valence state observed for reduced $[2\text{Fe}-2\text{S}]$ centers); no such site has been observed for standard $[4\text{Fe}-4\text{S}]$ clusters. A one-electron oxidation of the P-clusters yields an electronic ground state with half-integral electronic spin, $S \geq 3/2$; curiously, this state is EPR-silent (Zimmermann et al. (11) have rationalized this observation). At present it is not clear what chemical features distinguish the P-clusters from other $[4\text{Fe}-4\text{S}]$ centers. It appears that these spectroscopically unique structures have a $[4\text{Fe}-4\text{S}]$ core, as indicated by core extrusion experiments (11, 13) which yielded three to four $[4\text{Fe}-4\text{S}]$ clusters, in accordance with conclusions reached from Mössbauer spectroscopy (four clusters per molecule) and redox titrations (11). This suggests that the unique spectroscopic features signal different ligations of the P-cluster iron atoms. Such differences could include expansion to five-coordination or replacement of thiolate ligands by other nucleophiles.

If we tentatively accept the idea that the P-clusters are variants of $[4\text{Fe}-4\text{S}]$ centers, an intriguing question arises: To what oxidation level in Carter's scheme does the native diamagnetic state, P^{N} , belong? It seems obvious to associate the oxidation state P^{N} with the diamagnetic (+2) state. However, the average isomer shift $\delta_{\text{av}} = 0.65$ mm/s suggests an oxidation level even more reduced than the (+1) state which has $\delta \approx 0.58$ mm/s, that is, the oxidation state of super-reduced ferredoxin, the (+0) state, is implicated. This is in accordance with the observation of transient $g = 1.94$ signals under oxidizing conditions. (So far we have not been able to prove unambiguously that these signals result indeed from the P-clusters; the low concentration of the $g = 1.94$ centers and the presence of about 30 iron atoms impose formidable difficulties.) The P-clusters can be reversibly oxidized into the state P^{OX} (see Figure 1); recent Mössbauer experiments, in collaboration with W. H. Orme-Johnson and M. H. Emptage, have yielded a midpoint potential of about -250 mV for the $\text{P}^{\text{OX}}/\text{P}^{\text{N}}$ couple (for the *A. vinelandii* protein). This value for the potential seems to be considerably high for a (+1)/(+0) couple. On the other hand, -250 mV is very low for a (+3)/(+2) couple, the only other possible assignment for the $\text{P}^{\text{OX}}/\text{P}^{\text{N}}$ pair. It is clear that much interesting research needs to be done.

The Cofactor Center of Nitrogenase (M-Centers). In 1975 it was shown (14) by combined EPR and Mössbauer studies that the prominent EPR features at $g = 4.32, 3.67,$ and 2.01 observed for the *A. vinelandii* MoFe protein result from an $S = 3/2$ spin-coupled cluster (M-center) that contains at least four iron sites. (There are two apparently identical M-centers per protein molecule.) Subsequently, Rawlings et al. (15) proved that the M-centers contain those metal atoms that comprise the EPR-active component of the iron- and molybdenum-containing cofactor (FeMo-co) of nitrogenase. X-ray absorption fine structure studies (16)

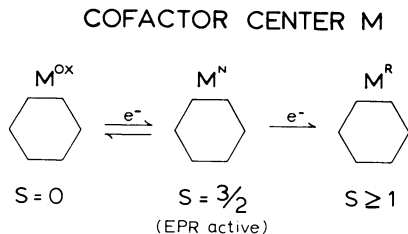
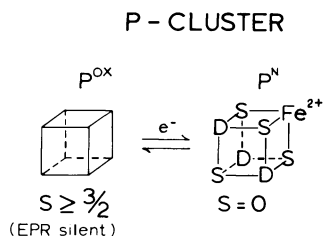


Figure 1. Stable oxidation states of the cofactor centers and P-clusters of nitrogenase.



The hexagon symbol was used to indicate a structure with (most probably) six iron atoms; no structural features are suggested. The cubane structure depicted for the P-clusters is very probable but not an established fact. The symbol *D* represents three iron atoms that give rise to a Mössbauer quadrupole doublet *D*; the Fe^{2+} site yields a doublet labeled Fe^{2+} (see Refs. 11, 12, 14).

on the molybdenum of isolated FeMo-co and of holoprotein strongly suggest that the M-centers contain iron, molybdenum, and sulfur. The exact stoichiometric ratios of these three elements are at present the subject of intensive research in many laboratories. By combining Mössbauer and EPR spectroscopy on holoproteins (12, 17, 18) and FeMo-co (15), it was found that each M-center most likely contains six iron atoms and one molybdenum. This number agrees quite well with values (about 7 iron atoms) obtained recently by chemical analysis of FeMo-co (13). The M-center, in the protein, can be stabilized in three distinct oxidation states (see Figure 1). So far the reduced state M^R has been observed only when nitrogenase is prepared under nitrogen fixing conditions. The diamagnetic state M^{OX} is attained by oxidation in air or with redox dyes such as thionine.

Many laboratories have made considerable efforts to assess whether isolated cofactor material contains amino acids serving as external ligands to the M-centers and whether any organic component is present at all. Currently it appears that no such components are present and that the cofactor is removed from the protein as an anion. It has been shown recently that none of the ingredients of the original extraction procedure of Shah and Brill is absolutely required (B. K. Burgess, W. E. Newton, and E. I. Stiefel, private communication). Apparently, buffer and solvent molecules coordinate to the M-centers in FeMo-co to replace ligands furnished by the protein. This is quite surprising since Mössbauer and EPR studies demonstrate the structural similarity of the FeMo-co cluster to the protein-bound M-centers. Reports from various laboratories suggest the presence of about four sulfur atoms in FeMo-co. Since precise

sulfur analyses are extremely difficult to obtain in the presence of molybdenum, these findings, as most results for FeMo-co, should be considered as tentative. We should like to point out that the observed isomer shifts of the M-centers do not demand a sulfur coordination of the iron atoms (nor do they rule out a sulfur environment, see Ref. 19). This should not discourage chemists from continuing to design cofactor models by cleverly combining and modifying [4Fe-4S] cubes; however, other iron coordinations are worth consideration. One might contemplate the possibility that some iron atoms of FeMo-co are linked by oxo-bridges. It should be possible to elucidate this point by labeling the protein with ^{18}O or ^{17}O . (Mass spectroscopy and spin-echo modulation experiments could provide useful information.)

Background on Two Ferredoxins

In 1971 LeGall's group in Marseille isolated a very interesting ferredoxin from the sulfate-reducing bacterium *Desulfovibrio gigas*. The basic subunit of this protein has 57 amino acids (6 cys) of known sequence (20). The ferredoxin is isolated in two different oligomeric forms. Fd II is a tetramer formed from identical monomers. It has been reported (21) that Fd II mediates electron transfer between cytochrome c_3 and the sulfite reductase system, while another oligomeric form, the trimeric Fd I, can serve as a carrier in the phosphoroclastic reaction. The magnetic properties of the iron-sulfur centers in the two oligomeric forms are drastically different (22). Reduced Fd I exhibits EPR features at $g_x = 1.92$, $g_y = 1.94$, and $g_z = 2.07$, signals indicative of [4Fe-4S] centers in the (+1) state. In sharp contrast, Fd II exhibits a nearly isotropic signal around $g = 2.01$ in the oxidized state; this signal vanishes upon a one-electron reduction. The midpoint potentials of Fd I and Fd II were determined to be at -455 mV and -130 mV, respectively. Although there are notable differences between HiPIP and Fd II in g -values and redox potential, the entire pattern of EPR observations was interpreted by Cammack et al. (22) as indicating [4Fe-4S] clusters stabilized in different redox pairs in Fd I and Fd II, according to Carter's three-state scheme (see the second section). The idea of a [4Fe-4S] center stabilized in different redox pairs by the same monomeric unit has caused considerable excitement.

Shethna and subsequently Yoch and Arnon have isolated a ferredoxin (MW 14400) from *A. vinelandii* containing 6-8 iron atoms and about equal amounts of labile sulfur. Subsequently, Sweeney et al. (23) reported potentiometric titrations of the protein, and suggested the presence of two [4Fe-4S] cores that are EPR-active in the oxidized state and that are each reduced by a one-electron step into an EPR-silent state.

They proposed that the two clusters operated in the (+3)/(+2) states as does HiPIP, although the two centers have drastically different midpoint potentials (+320 mV and -450 mV). Both centers, in the oxidized state, exhibit nearly isotropic EPR signals around $g = 2.01$. Howard et al. (24) interpreted their cluster displacement experiments as indicative of two [4Fe-4S] centers, while Averill et al. (25) found evidence for only one such cluster. In 1979, Stout (26) reported the analysis of an x-ray diffraction study at 4-Å resolution, suggesting the presence of one [2Fe-2S] cluster and one [4Fe-4S] center. We were quite excited about this report since it suggested that something new was to be discovered: Since familiar [2Fe-2S] centers are EPR-active only in the reduced state, and since the presumed [2Fe-2S] center yielded an EPR signal in the oxidized state, the published data suggested that either a higher oxidation state of a [2Fe-2S] center was attained or that a new structure was present. According to present spectroscopic evidence (27, 28) and a recent reinterpretation of the electron density map at 2.5-Å resolution, a novel three-iron center is present in the two ferredoxins.

Spectroscopic Evidence for a New Three-Iron Center

Together with co-workers W. H. Orme-Johnson and M. H. Emptage we have studied a ^{57}Fe -enriched sample of the ferredoxin from *A. vinelandii* (27). Shortly after we submitted the *Azotobacter* work we started a study of Fd II, together with A. V. Xavier, J. J. G. Moura, and I. Moura (28). In the following we treat both proteins but we focus mainly on Fd II since the presence of only one cluster facilitates the analysis considerably. The reader may keep in mind that the results were obtained during the past few months and that many details need to be worked out. All chemical, Mössbauer, and EPR data reported here on Fd II were taken on the selfsame sample; iron and spin concentrations are quoted per monomer. The Mössbauer data were taken on a sample with ^{57}Fe in natural abundance. (The sulfate-reducing *D. gigas* bacteria produce sulfide which precipitates iron in the growth medium and thus precious dollars if ^{57}Fe were used.)

The Fd II sample was analyzed for eight stable amino acids; their distribution was found to fit the known sequence. Thus, the sample was pure in protein and the protein concentration was therefore known. Iron analyses yielded repeatedly, to within 3%, 3 iron atoms/monomer. The Mössbauer data will prove the absence of any discernable iron impurity. An EPR spectrum of oxidized Fd II is shown in Figure 2. We studied the EPR saturation behavior of the sample over a wide range of temperatures and found that only one EPR-active species is present. A good representation of the observed spectrum was obtained by choosing

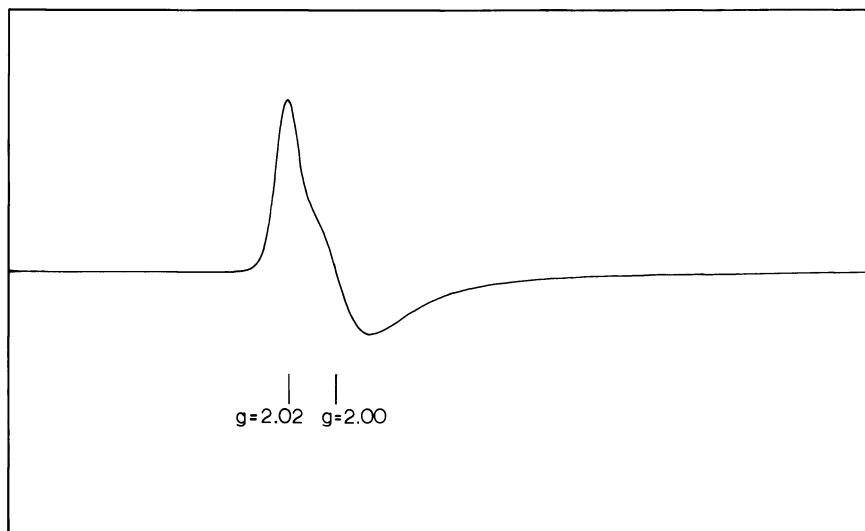


Figure 2. EPR spectrum of oxidized Fd II from *D. gigas* recorded at 6 K. The derivative of the absorption is plotted vs. the magnetic induction.

$g_1 = 2.02$, $g_2 = 2.00$, and $g_3 = 1.97$ for spectral simulations. We quantitated the spectra at 6, 8, and 12 K against a copper-EDTA standard and found a spin concentration of 0.93 ± 0.12 spins/3 iron atoms. Thus, if one can establish that all iron atoms in the sample are connected with the EPR-active center, it follows that a center with 3 covalently linked iron atoms is present. The Mössbauer data will provide the answer.

Figure 3A shows a Mössbauer spectrum of oxidized Fd II taken at 77 K. The solid line is a least-squares fit generated by assuming that only one species is present, that is, by assuming that all iron atoms in the sample are equivalent. The quality of the fit, the symmetry of the spectrum, and the sharpness of the absorption lines (0.27 mm/s) support this assumption. Also, there is no evidence for any iron impurity. The Mössbauer parameters $\Delta E_Q = (0.54 \pm 0.03)$ mm/s and $\delta = (0.27 \pm 0.03)$ mm/s are practically the same as those observed for oxidized rubredoxin (29). In particular, the isomer shift suggests a tetrahedral coordination of sulfur atoms. Moreover, the data show that the iron atoms are high-spin ferric ($S = 5/2$) in character. Isolated $S = 5/2$ iron obviously is not present; otherwise, an EPR signal typical of the ferric ion should be observed.

Figure 4 shows a spectrum of the sample taken at 1.5 K. A broad spectrum exhibiting paramagnetic hyperfine structure is observed, in accordance with the information from EPR which shows slow electronic

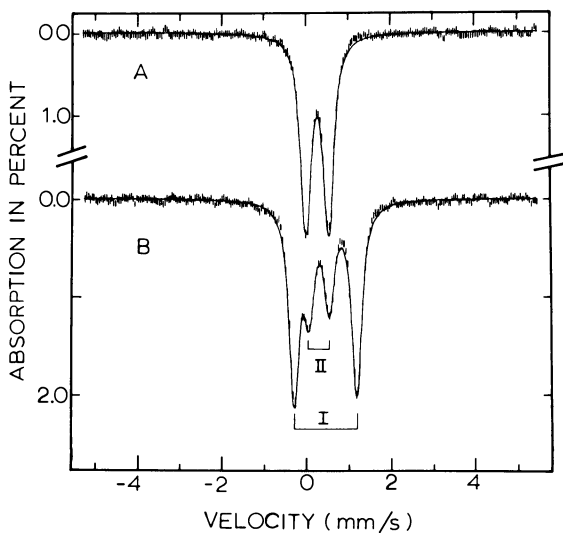


Figure 3. Zero-field Mössbauer spectra of Fd II from *D. gigas*. The sample had 26mM iron with ^{57}Fe in natural abundance: (A) spectrum of oxidized, EPR-active Fd II taken at 77 K; (B) spectrum of reduced Fd II taken at 4.2 K. The solid lines are the result of a least-squares fitting of the quadrupole doublets to the data.

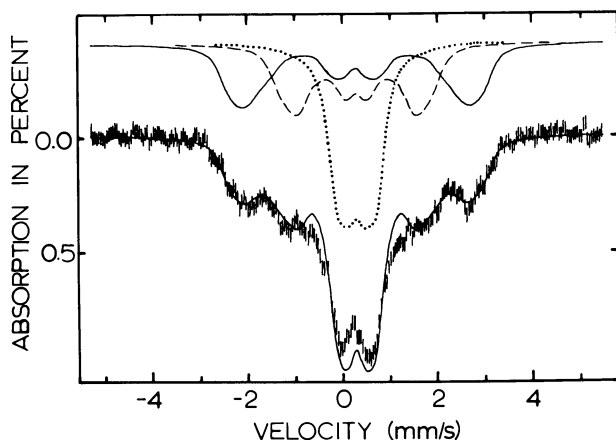


Figure 4. Mössbauer spectrum of oxidized Fd II taken at 1.5 K in a parallel field of 600 G. The solid line plotted over the data is the result of adding three theoretical spectra computed from Equation 1 using the parameters quoted in Table I.

spin relaxation below 10 K. Note that the doublet-type spectrum around zero velocity is quite different from the doublet observed in Figure 3A. Before we discuss the spectral decomposition indicated in Figure 4, we present some data taken on the ferredoxin from *A. vinelandii* (the protein was labeled iron-sulfur protein III by Shethna, but here we will label it Av III for brevity).

A Mössbauer spectrum of semi-reduced Av III is shown in Figure 5. In the semi-reduced state the high-potential center of Av III is reduced while the low-potential center is in the oxidized, EPR-active state. The spectrum shows essentially two components: an intense quadrupole doublet (indicated by the bracket) and a magnetic component (traced out by the solid line). The quadrupole doublet has to be associated with the high-potential center. In most respects this center behaves indeed like an HiPIP-type [4Fe-4S] cluster. We will not discuss this component here any further, but will concentrate on the magnetic material.

To evaluate the magnetic spectrum the following remarks might be helpful. For a system with $S = 1/2$ exhibiting an isotropic Zeeman term and isotropic magnetic hyperfine interaction, the internal magnetic field produced by the doublet is $\vec{H}_{\text{int}} = -A\langle\vec{S}\rangle/g_n\beta_n$. For an isotropic system the expectation value of the electronic spin $\langle\vec{S}\rangle$ will be parallel (or antiparallel) to the applied magnetic field \vec{H} . Thus \vec{H}_{int} will be parallel to \vec{H} also, regardless of the orientation of the molecule relative to the applied field. Since \vec{H}_{int} is (essentially) the quantization axis of the nucleus, the nuclear $\Delta m = 0$ lines will be quenched when a sample is studied in a field applied parallel to the observed gamma radiation. In transverse field the $\Delta m = 0$ lines will have maximum intensity. If we record a Mössbauer spectrum in parallel and transverse field and subtract the "transverse" spectrum from that obtained in parallel field, we will

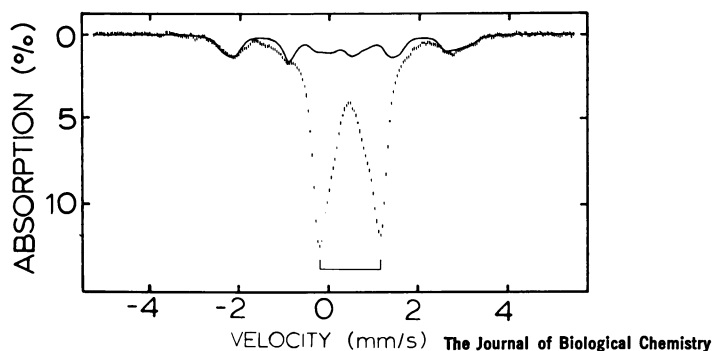
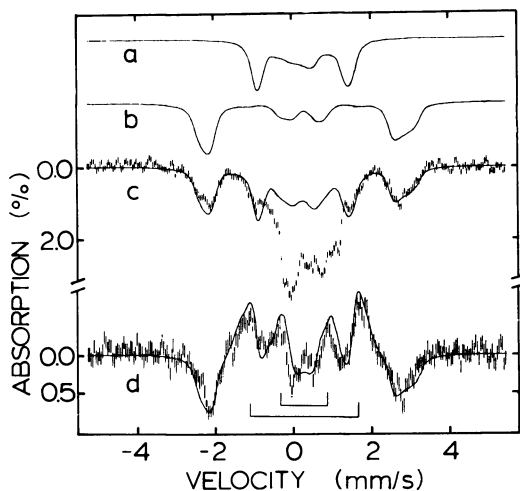


Figure 5. Mössbauer spectrum of ^{57}Fe -enriched ferredoxin from *A. vinelandii* taken at 4.2 K in a 500-G parallel field (27). The bracket indicates a doublet resulting from the high-potential [4Fe-4S] center. The solid lines in Figures 5 and 6 are theoretical spectra for Sites 1 and 2, computed with the parameters of Table I.



The Journal of Biological Chemistry

Figure 6. Mössbauer spectra of the oxidized low-potential center of Av III (27).

Spectrum c was obtained by removing the contribution of the high-potential center quadrupole doublet, using methods as described in Ref. 11. Spectra a and b are theoretical spectra belonging to Sites 1 and 2. Spectrum d is a difference spectrum, obtained by subtracting a 4.2-K spectrum taken in transverse field from that of Figure 5. The solid line in d is a theoretical difference spectrum computed with the parameters of Table I.

generate a difference spectrum with the positions of the two nuclear $\Delta m = 0$ lines clearly identified. For Av III this procedure has an obvious benefit: the high-potential center that yields the intense doublet in Figure 5 is diamagnetic, and therefore, its spectrum is practically insensitive to the direction of a weak (500 G) applied field. Thus, its contribution cancels when the difference spectrum is formed. A difference spectrum obtained for Av III, shown in Figure 6d, should be attributable entirely to the EPR-active, low-potential center. Note that the spectrum exhibits two sets of $\Delta m = 0$ lines (indicated by the brackets), proving the presence of at least two magnetically nonequivalent subsites. From the difference spectrum the general features of the two magnetic components are obtained quite readily. We computed theoretical spectra for the two subcomponents from the spin Hamiltonian ($S = 1/2$).

$$\hat{H} = \beta \vec{H} \cdot \vec{g} \cdot \vec{S} + \vec{S} \cdot \vec{A} \cdot \vec{I} - g_n \beta_n \vec{H} \cdot \vec{I} + \frac{eQV_{zz}}{12} [3I_z^2 - I(I+1) + \eta(I_x^2 - I_y^2)] \quad (1)$$

The g -values for Av III were taken from the EPR data, $g_x = g_y = g_z = 2.01$. ΔE_Q is independent of temperature and is known from the high-

temperature data. The magnetic hyperfine coupling constants of the two identified sites are found from the total splittings (or the splittings of the $\Delta m = 0$ pairs). To account for some details of the line shape we found it necessary to introduce some magnetic anisotropy. The solid lines in Figures 6a and b are theoretical spectra of Sites 1 and 2; the curve in Figure 6d is a theoretical difference spectrum, while the sum of both spectra is displayed in Figure 5. The spectral parameters are listed in Table I.

In strong applied fields the sign of \vec{H}_{int} can be determined. We have studied samples of Fd II and Av III in fields up to 60 kG and found that $A < 0$ for Site 1 while $A > 0$ for Site 2 (see Table I). Since the magnetic hyperfine coupling constants of single high-spin ferric irons are always negative, the observation of a positive coupling constant gives strong evidence for spin coupling (5, 6).

At this stage of the analysis we have clearly identified two iron sites that are associated with the $S = 1/2$ center. Since there is only one EPR signal present and since two field-dependent magnetic Mössbauer spectra are observed, both iron sites must participate in a spin-coupled complex. However, there is one problem: two $S = 5/2$ irons cannot be coupled to yield the observed half-integral system spin $S = 1/2$; a third half-integral spin is required.

The Fd II spectrum of Figure 4 is very similar to the magnetic spectrum of the Av III low-potential center except that the magnetic splittings of Sites 1 and 2 differ less for Fd II, yielding a less-resolved spectrum. However, the missing spin shows up quite nicely in Fd II: The third iron site, traced by the dotted line in Figure 4, is characterized by a very small magnetic hyperfine interaction, $A \approx 3.5$ MHz. We have just completed a series of high-field studies of oxidized Fd II. The data show that $A < 0$ for Site 1 while $A > 0$ for Site 2, but the sign of A for

Table I. Hyperfine Parameters for Oxidized Three-Iron Centers^a

Site No.	A. Vinelandii <i>Ferredoxin</i>			D. gigas <i>Fd II</i>		
	1	2	3	1	2	3
A_x (MHz)	-37	+17	4	-27	+29	(+)3.5
A_y (MHz)	-42	+17	4	-44	+16	(+)3.5
A_z (MHz)	-45	+17	4	-44	+16	(+)3.5
ΔE_Q (mm/s)	+0.63	+0.63	0.6	+0.54	+0.54	+0.54
δ (mm/s)	0.27	0.27	0.3-0.4	0.27	0.27	0.27

^a Isomer shifts are quoted at 77 K relative to iron metal at room temperature. To account for the details of line shape some magnetic anisotropy seems to be required. However, within the limited resolution microheterogeneities could have similar effects. The sign of A for Site 3 is extremely difficult to determine and should be considered as tentative. For the simulations of the Av III spectra we used $\eta = 0.7$ and a linewidth of 0.3 mm/s; for Fd II we used $\eta = 1$ and 0.4 mm/s for the linewidth. For further details see Refs. 27 and 28.

Site 3 is extremely difficult to determine. First, in order to assess the shape of the high-field spectra of Site 3 one has to understand the features of the high-field spectra of Sites 1 and 2 in detail; unfortunately, the broad spectra indicate the presence of magnetic anisotropies as well as micro-heterogeneities (the latter also seem to be indicated by the high-field tail of the EPR spectrum of Figure 2). Second, since the magnetic splitting is very small for Site 3, magnetic anisotropies could result in positive and negative components of the A tensor. If we assume an isotropic A tensor for Site 3, the high-field data on Fd II suggest $A > 0$. (Because of the small hyperfine field the nuclear $\Delta m = 0$ lines of the Site 3 spectrum overlap with the $\Delta m = \pm 1$ lines. Thus, this site is not discernible in the difference spectrum in Figure 6d.)

The theoretical spectra shown in Figures 4 and 6 fit the data quite nicely. The parameters quoted in Table I are tentative and certainly not unique. We believe, however, that they represent the essential features of the observed spectra.

At this stage of the analysis we have obtained, in our view, compelling evidence for the existence of a novel three-iron center. The case can be strengthened further by studying the one-electron reduced centers.

A Mössbauer spectrum of reduced Fd II, taken at 4.2 K in zero applied field, is shown in Figure 3B. The one-electron reduction has transformed the spectra of all irons of Figure 4 into two sharp quadrupole doublets. Doublet I has $\Delta E_Q = (1.47 \pm 0.03)$ mm/s and $\delta = (0.46 \pm 0.02)$ mm/s while Doublet II has $\Delta E_Q = (0.47 \pm 0.03)$ mm/s and $\delta = (0.30 \pm 0.02)$ mm/s (isomer shifts are quoted relative to iron metal at 298 K). A least-squares fit to the data (Figure 3B) showed, somewhat fortuitously, that the two sites are in the ratio of 2.0:1.

The spectra shown in Figure 7 show that the three-iron centers have a very distinctive Mössbauer signature. Figure 7A shows again the zero-field spectrum of Figure 3B; a spectrum taken in a parallel field of 600 G is shown in Figure 7B. Note that both quadrupole doublets have virtually disappeared and that the weak external field has induced sizeable magnetic hyperfine interactions. This observation proves immediately that the electronic ground state of the reduced cluster is paramagnetic, that is, $S \geq 1$. (The spin must be an integer because the cluster is reduced by a one-electron step.) Furthermore, it is very clear that the centers under consideration have no spectral resemblance to HiPIP as suggested in the literature; reduced HiPIP has $S = 0$ (and four iron sites).

Figure 8 shows a spectrum of reduced Fd II taken at 4.2 K in a parallel field of 10 kG. A beautifully resolved magnetic hyperfine pattern is observed. We found that the hyperfine fields are essentially saturated in applied fields of about 2 kG. For $H > 10$ kG we observed a pattern

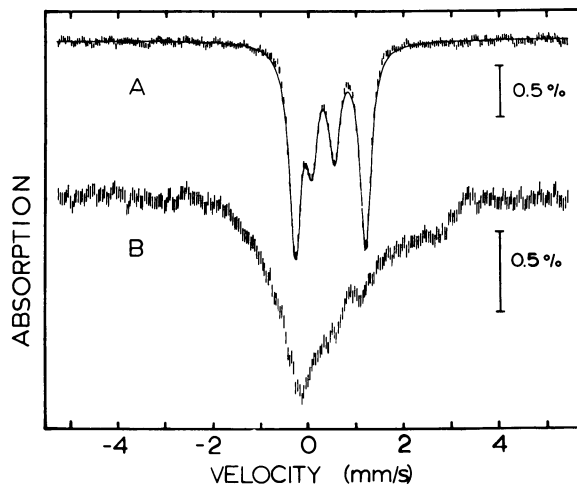


Figure 7. Mössbauer spectrum of reduced Fd II taken at 4.2 K.

The spectrum shown in Figure 7A is identical to that of Figure 3B. The spectrum of Figure 7B was obtained in an external field of 600 G. The broadening of the spectrum in a weak applied field is attributable to the presence of sizable induced internal magnetic fields, a distinctive feature of reduced three-iron centers.

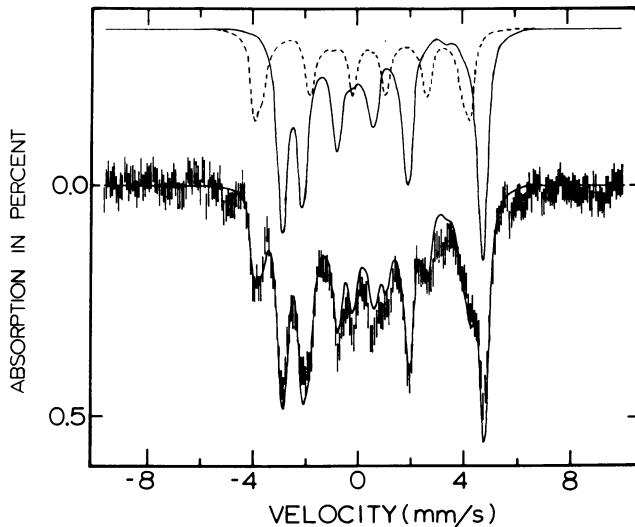


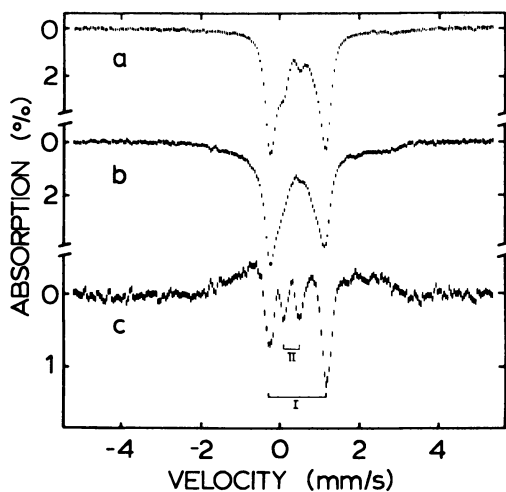
Figure 8. Mössbauer spectrum of reduced Fd II taken at 4.2 K in a parallel field of 10 kG. Also shown is a theoretical curve and decomposition into two subcomponents of area ratio 2:1. The subcomponent corresponding to Site I is traced by the solid line. For convenience, the spectra were computed from a spin Hamiltonian with $S = 2$.

of inward- and outward-moving absorption lines, showing again the presence of negative and positive hyperfine fields, that is, the effects of spin-coupling. This pattern of moving lines allowed us to identify the absorption lines of each subcomponent. The data analysis revealed that the two iron sites of Doublet I remain indistinguishable even in strong applied fields, that is, the spectrum in Figure 8 is a superposition of two spectra with an intensity ratio of 2:1. The line assignment of the decomposition shown in Figure 8 was facilitated by comparing the Fd II spectra with the spectra observed for the $[\text{S}_2\text{MoS}_2\text{Fe}(\text{PhS})_2]^{2-}$ anion which presently is under study in our laboratory. The values for ΔE_Q and δ of this compound match those found for Site II; the high-field spectra also have a close resemblance (30).

Isomer shift and quadrupole splitting of the Site II iron ($\delta = 0.30$ mm/s) identify this site as high-spin ferric in character. Previously we have argued, giving physical and chemical arguments (27), that the iron of Site II is a subsite of a spin-coupled cluster and not an isolated ferric ion. The high-field studies on Fd II prove this assertion to be correct; Site II has $A > 0$ and thus participates in spin-coupling. At present the system spin of the reduced three-iron centers is not known. J. J. G. Moura has performed room-temperature susceptibility studies of reduced Fd II using the NMR method at 270 MHz. The diamagnetic corrections are now being assessed so the room-temperature susceptibility of the reduced three-iron center should be available soon.

To explore the physics of the spectra in Figures 7 and 8 a bit more, let us assume that $S = 2$, the value presently indicated. The fact that a sizable internal magnetic field is observed in applied fields of only 100 G shows that the electronic relaxation rate is slow at 4.2 K. Furthermore, since the magnetic hyperfine fields saturate already in weak applied fields, the lowest electronic spin levels are two closely spaced states of energy separation Δ (for Fd II we found $\Delta = 0.35 \text{ cm}^{-1}$); for the high-spin ferrous iron the physics of such situations has been discussed in detail (2, 29, 31, 32). The distinctive feature of the reduced three-iron centers is the observation that the values for Δ are much smaller than those for other compounds. This can be used to identify the presence of reduced three-iron clusters in proteins with more than one metal center. Let us discuss this for reduced Av III.

In reduced Av III both iron centers are EPR-silent. The HiPIP-type $[4\text{Fe}-4\text{S}]$ center is in the same diamagnetic state as observed (in Figure 5) for semi-reduced Av III; in addition, the low-potential center has become reduced. A Mössbauer spectrum of a sample taken in zero field at 4.2 K is shown in Figure 9a; the spectrum in Figure 9b was taken in a parallel field of 500 G. Note that the application of a 500-G field has elicited a magnetic component, most conspicuously in the velocity range



The Journal of Biological Chemistry

Figure 9. Mössbauer spectra of fully reduced Av III, taken at 4.2 K (a) in zero-field and (b) in a parallel field of 600 G (27). The spectrum in (c), obtained by subtracting the spectrum in (b) from that in (a), should be compared with that shown in Figure 7A.

from +2 mm/s to +4 mm/s. We know from the semi-reduced sample that the high-potential center is in a diamagnetic state. Thus, by subtracting the spectrum of Figure 9b from that shown in Figure 9a its contribution will cancel. The resulting difference spectrum, displayed in Figure 9c, is practically identical to that obtained when the same procedure is used for the Fd II data of Figure 7. Therefore, the spectrum of reduced Fd II and the spectrum of the reduced low-potential center of Av III are almost identical. (The observation that the tiny absorption feature at +0.5 mm/s in Figure 9a broadens in a weak magnetic field provided us with the first clue of the existence of three-iron centers.)

The theoretical spectra in Figure 8 were simulated using a spin Hamiltonian with $S = 2$. In applied fields of moderate strengths the electronic system has an easy axis of magnetization, and Sites I and II are characterized by internal magnetic fields of -237 kG and $+250$ kG, respectively. We refrain at present from publishing a complete set of hyperfine parameters; the ambiguity problem commonly associated with multiparameter fits requires more detailed studies. (A set of parameters used to simulate the 10-kG spectrum may be obtained from the author.)

Discussion

In the preceding section we discussed in some detail the Mössbauer results obtained for Fd II and the low-potential center of the ferredoxin

from *A. vinelandii*. In the following we summarize and elaborate on some of the salient features of the new three-iron centers. We will focus mainly on Fd II; except for minor details the same conclusions apply for Av III.

At temperatures above 15 K, where the electronic spin relaxation is fast, all three iron sites of oxidized Fd II exhibit the same quadrupole doublet. The observed isomer shifts, $\delta = 0.27$ mm/s, strongly suggest high-spin ferric-type iron in a tetrahedral environment of sulfur atoms. Although such an environment, by analogy with well-characterized compounds, is strongly implicated, we cannot rule out a site with three thiolate ligands and, for example, one oxygenic or nitrogeneous ligand; no suitable reference compounds are available for comparison. While all three iron atoms seem to be equivalent when only ΔE_Q and δ are considered, the low-temperature data reveal drastic differences between the iron sites when the magnetic properties are taken into account. Not only do the A values have different signs, a strong indication of spin-coupling, but their magnitudes also differ appreciably. There are essentially two possibilities for rationalizing the vastly different splittings. First, the intrinsic A values might be different for the three sites, that is, ligand geometry and covalency effects are at the root of the observed differences. However, this is unlikely because these would affect the values of δ and ΔE_Q , at least to some observable extent. Since δ indicates tetrahedral environments of sulfur atoms, one would expect the intrinsic A values to be close to those observed for rubredoxin (29) and desulfuredoxin (1), that is, $A \approx -22$ MHz (defined by $A \vec{S}_1 \cdot \vec{I}$ with $S_1 = 5/2$). In our view, the observed difference in the magnetic splittings reflects the mechanism of spin-coupling. What is measured are A values referring to the coupled system spin; namely, $\vec{S} \cdot \vec{A} \cdot \vec{I}$ where $S = 1/2$. It is well known from the analysis of the spin-coupling of the [2Fe-2S] centers (4, 5, 6) that essentially one measures the components of the intrinsic internal fields along the direction of the system spin, which defines the frame of reference. T. A. Kent and B. H. Huynh, in our laboratory, are presently studying the problem of coupling three $S = 5/2$ spins to a resultant spin $S = 1/2$. To produce an $S = 1/2$ ground state, at least three different coupling constants are required. It appears that the experimental results, both the signs and magnitudes of the A values, are nicely explained in such a model.

Upon reduction by a one-electron step, all three irons of Fd II experience profound changes. Evidently the electron entering the cluster is essentially accommodated by those two iron atoms that give rise to Doublet I. The observed isomer shift for the two Site I irons, $\delta = 0.47$ mm/s, is just between the values observed for ferric ($\delta = 0.3$ mm/s) and ferrous ($\delta = 0.7$ mm/s) rubredoxin (29). Both irons of Site I are roughly at the oxidation level $\text{Fe}^{2.5+}$ while the iron of Site II remains

Fe^{3+} in character. The observation that the two Site I iron atoms are indistinguishable even in the well-resolved high-field spectra suggests that they reflect two sites in equivalent (chemical and geometrical) environments.

Numerous HiPIP-type EPR signals around $g = 2.01$ have been reported in the literature. In particular, an EPR signal similar to those observed in Fd II and Av III has been reported for oxidized aconitase from beef-heart mitochondria (33), an important enzyme operating in the Krebs cycle. H. Beinert and J.-L. Dreyer of the University of Wisconsin have provided us with a sample of the reduced enzyme. The low concentration of ^{57}Fe has put some restrictions on the Mössbauer investigation. (We used a 2-mM sample with ^{57}Fe in natural abundance; ^{57}Fe -enriched beef hearts are much more expensive than beef Wellington.) The distinctive signature of the three-iron centers, however, was apparent: Two spectra obtained at 4.2 K in zero field and 600 G are practically identical to those shown for Fd II in Figure 7. Together with the EPR information, the Mössbauer data strongly implicate a three-iron center in aconitase. We found no evidence for any other iron component. In particular, we found no evidence of a high-spin ferrous component alluded to in many biochemistry text books.

Recently we studied another protein that exhibits an HiPIP-type EPR signal in the oxidized state. The enzyme glutamate synthase from *E. coli* has a complex subunit structure and at least four prosthetic groups (34). Using similar difference spectroscopy as discussed in the previous section, we found that the enzyme contains a cluster with the spectroscopic properties of three-iron centers. (This work was performed in cooperation with W. H. Orme-Johnson and A. Rendina.)

So far we have concentrated entirely on the spectroscopy of the three-iron centers and have not mentioned the results of core extrusion experiments. This technique has been applied to both Av III (27) and aconitase (35) with the result that $[2\text{Fe}-2\text{S}]$ centers are recovered in high yields. We suspect that the three-iron centers may decompose to yield $[2\text{Fe}-2\text{S}]$ cores under the experimental conditions. Averill et al. (25) have reported that the absorption spectrum of the Av III protein in 80% dimethylsulfoxide with 10 mM benzenethiol could not be simulated as the sum of $[2\text{Fe}-2\text{S}]$ and $[4\text{Fe}-4\text{S}]$ centers. Furthermore, the spectra changed slowly with time. It would be interesting to know at what stage of the extrusion procedure the three-iron centers decompose. Experimental data on this question might shed some light on structural features of the three-iron centers. Also, if the third iron atom remains on the protein, interesting isotopic-labeling experiments would be useful if (at least partially) reversible conditions could be found.

What is the structure of the new three-iron centers? Based on x-ray diffraction studies at 2.5-Å resolution, Stout et al. (36) reinterpreted the data on Av III and found that a three-iron center best fits the electron density map. They also report that the cluster is distinctly planar and that it cannot be modeled with [2Fe-2S] or [4Fe-4S] structures. The proposed model has not been refined crystallographically, but what seems to emerge is a planar structure of three iron atoms linked by three sulfurs. Six contacts (mostly cysteines) with the protein are suggested. For details the reader is referred to the article by Stout et al. (36).

We pointed out earlier that Cammack et al. (22) have suggested that the centers of Fd I and Fd II are [4Fe-4S] clusters stabilized at different oxidation levels by the protein environments. We are presently studying an Fd I sample with Mössbauer and EPR spectroscopy. Although the studies are not completed, we can unequivocally state that the center that gives rise to the EPR signal at $g_x = 1.92$, $g_y = 1.94$, and $g_z = 2.07$ is indeed a [4Fe-4S] center. Thus the monomeric unit can accommodate, in the proper oligomeric form, three-iron centers and [4Fe-4S] clusters. It might appear that the tetrameric form of the protein accommodates three-iron centers, while the trimeric oligomer folds into a conformation that can accept [4Fe-4S] centers. However, we found that the Fd I sample has about 25% of its iron in the form of three-iron centers. According to the purification standards the sample is homogeneous in trimers, that is, there is no evidence for a (tetrameric) Fd II contaminant. Since even molecules such as rubredoxin and insulin can accommodate [4Fe-4S] centers under the proper conditions, much work needs to be done to identify the physiologically active centers of Fd I. It is clear that some exciting protein chemistry lies ahead. At present, extreme caution needs to be exercised in assessing the physiological significance of the chemical and spectroscopic observations for Fd I and Fd II.

Finally, we have reported here the presence of a novel three-iron center in four proteins. There is quite a variety of proteins with magnetic properties that also suggest the presence of the three-iron center. Among them are the ferredoxins from *P. ovalis* (37), *R. rubrum* (38), *M. flavum* (39), *M. smegmatis* (40), and *T. thermophilus* (41).

Acknowledgment

The work on Av III was performed in collaboration with W. H. Orme-Johnson of the Massachusetts Institute of Technology and his postdoctoral associates M. H. Emptage and J. Rawlings. The studies on the *D. gigas* ferredoxins are the result of a cooperation with A. V. Xavier, J. J. G. Moura, and I. Moura, visiting scientists at the Gray Freshwater

Biological Institute from the University of Lisbon, Portugal. The *D. gigas* bacteria were grown in J. LeGall's laboratory in Marseilles, France. Finally, I am grateful to my postdoctoral associates B. H. Huynh and T. A. Kent who did most of the spectroscopic work described here.

Addendum

Recently we have demonstrated (42) that the magnetic properties of the oxidized three-iron centers can be explained with a simple model of three high-spin ferric ions ($S = 5/2$) exchange-coupled to a system spin $S = 1/2$. The results show that the three sites have intrinsic magnetic interactions like rubredoxin; the differences in the hyperfine fields observed for the three sites reflect the geometrical features of spin-coupling. In particular, the small hyperfine field observed for Site 3 is attributable to an almost perpendicular orientation of the local spin to the system spin. Furthermore, the model suggests strongly that the three-iron center is a single, covalently linked structure; it should not be considered as a $[2\text{Fe}-2\text{S}]$ cluster weakly coupled to a third iron atom.

Together with H. Beinert and J.-L. Dreyer we have continued the Mössbauer studies of aconitase. Data obtained for oxidized and reduced aconitase clearly show the presence of a three-iron center.

Literature Cited

1. Holm, R. H.; Ibers, J. A. In "Iron-Sulfur Proteins"; Lovenberg, W., Ed.; Academic: New York, 1977; Vol. 3, Chap. 7.
2. Moura, I.; Huynh, B. H.; LeGall, J.; Hausinger, R. P.; Xavier, A. V.; Münck, E. *J. Biol. Chem.* 1980, 255, 2493-2498.
3. Palmer, G. In "Iron-Sulfur Proteins"; Lovenberg, W., Ed.; Academic: New York, 1973; Vol. 2, Chap. 8.
4. Gibson, J. H.; Hall, D. O.; Thorneley, J. H. M.; Whatley, F. R. *Proc. Natl. Acad. Sci. U.S.A.* 1966, 56, 987.
5. Dunham, W. R.; Bearden, A. J.; Salmeen, I. T.; Palmer, G.; Sands, R. H.; Orme-Johnson, W. H.; Beinert, H. *Biochim. Biophys. Acta* 1971, 253, 134-152.
6. Münck, E.; Debrunner, P. G.; Tsibris, J. C. M.; Gunsalus, I. C. *Biochemistry* 1972, 11, 855-863.
7. Tsukihara, T. K.; Fukuyama, K.; Katsube, Y.; Tanaka, N.; Matsuura, Y.; Kakuda, K.; Wada, K.; Matsubara, H., presented at the 6th Int. Biophys. Congr., Kyoto, Japan, 1978.
8. Orme-Johnson, W. H.; Sands, R. H. In "Iron-Sulfur Proteins"; Lovenberg, W., Ed.; Academic: New York, 1973; Vol. 2, Chap. 5.
9. Carter, C. W.; Kraut, J.; Freer, S. T.; Alden, R. A.; Sieker, L. C.; Adman, E. T.; Jensen, L. H. *Proc. Natl. Acad. Sci. U.S.A.* 1972, 69, 3526.
10. *Eur. J. Biochem.* 1979, 93, 427
11. Zimmermann, R.; Münck, E.; Brill, W. J.; Shah, V. K.; Henzl, M. T.; Rawlings, J.; Orme-Johnson, W. H. *Biochim. Biophys. Acta* 1978, 537, 185-207.
12. Huynh, B. H.; Henzl, M. T.; Christner, J. A.; Zimmermann, R.; Orme-Johnson, W. H.; Münck, E. *Biochim. Biophys. Acta* 1980, 623, 124-138.

13. Kurtz, D. M.; McMillan, R. S.; Burgess, B. K.; Mortenson, L. E.; Holm, R. H. *Proc. Natl. Acad. Sci. U.S.A.* 1979, 76, 4986.
14. Münck, E.; Rhodes, H.; Orme-Johnson, W. H.; Davis, L. C.; Brill, W. J.; Shah, V. K. *Biochim. Biophys. Acta* 1975, 400, 32-53.
15. Rawlings, J.; Shah, V. K.; Chisnell, J. R.; Brill, W. J.; Zimmermann, R.; Münck, E.; Orme-Johnson, W. H. *J. Biol. Chem.* 1978, 253, 1001-1004.
16. Cramer, S. P.; Hodgson, K. O.; Gillum, W. O.; Mortenson, L. E. *J. Am. Chem. Soc.* 1978, 100, 3398-3407.
17. Huynh, B. H.; Münck, E.; Orme-Johnson, W. H. *Biochim. Biophys. Acta* 1979, 576, 192.
18. Huynh, B. H.; Orme-Johnson, W. H.; Münck, E. *J. Phys. (Paris)* 1979, 40, C2-526.
19. Wolff, T. E.; Berg, J. M.; Hodgson, K. O.; Frankel, R. B.; Holm, R. H. *J. Am. Chem. Soc.* 1979, 101, 4140.
20. Bruschi, M. *Biochem. Biophys. Res. Commun.* 1979, 91, 623-628.
21. Moura, J. J. G.; Xavier, A. V.; Hatchikian, E. E.; LeGall, J. *FEBS Lett.* 1978, 89, 177-179.
22. Cammack, R.; Rao, K. K.; Hall, D. O.; Moura, J. J. G.; Xavier, A. V.; Bruschi, M.; LeGall, J.; DeVille, A.; Gayda, J. P. *Biochim. Biophys. Acta* 1977, 490, 311, 321.
23. Sweeney, W. V.; Rabinowitz, J. C.; Yoch, D. C. *J. Biol. Chem.* 1975, 250, 7842-7847.
24. Howard, J. B.; Lorsbach, T.; Que, L. *Biochem. Biophys. Res. Commun.* 1976, 70, 582-588.
25. Averill, B. A.; Bale, J. R.; Orme-Johnson, W. H. *J. Am. Chem. Soc.* 1978, 100, 3034-3043.
26. Stout, C. D. *Nature* 1979, 279, 83-84.
27. Emptage, M. H.; Kent, T. A.; Huynh, B. H.; Rawlings, J.; Orme-Johnson, W. H.; Münck, E. *J. Biol. Chem.* 1980, 255, 1793.
28. Huynh, B. H.; Moura, J. J. G.; Moura, I.; Kent, T. A.; LeGall, J.; Xavier, A. V.; Münck, E. *J. Biol. Chem.* 1980, 255, 3242-3244.
29. Debrunner, P. G.; Münck, E.; Que, L.; Schulz, C. E. In "Iron-Sulfur Proteins"; Lovenberg, W., Ed.; Academic: New York, 1977; Vol. 3, Chap. 10.
30. Tieckelmann, R. H.; Silvis, H. C.; Kent, T. A.; Huynh, B. H.; Waszczak, J. V.; Teo, B.-K.; Averill, B. A. *J. Am. Chem. Soc.* 1980, 102, 5550.
31. Zimmermann, R.; Spiering, H.; Ritter, G. *Chem. Phys.* 1974, 4, 133.
32. Zimmermann, R.; Huynh, B. H.; Münck, E.; Lipscomb, J. D. *J. Chem. Phys.* 1978, 69, 5463.
33. Ruzicka, F. J.; Beinert, H. *J. Biol. Chem.* 1978, 253, 2514.
34. Rendina, A. R.; Orme-Johnson, W. H. *Biochemistry* 1979, 17, 5388.
35. Kurtz, D. M.; Holm, R. H.; Ruzicka, F. J.; Beinert, H.; Coles, C. J.; Singer, T. P. *J. Biol. Chem.* 1979, 254, 4967-4969.
36. Stout, C. D.; Gosh, D.; Pattabhi, V.; Robbins, H. *J. Biol. Chem.* 1980, 255, 1797.
37. Hase, T.; Wakabayashi, S.; Matsubara, H.; Ohmori, D.; Suzuki, K. *FEBS Lett.* 1978, 91, 315-319.
38. Yoch, D. C.; Carithers, R. P.; Arnon, D. I. *J. Biol. Chem.* 1977, 252, 7453-7460.
39. Yates, M. G.; O'Donnell, M. J.; Lowe, D. J.; Bothe, H. *Eur. J. Biochem.* 1978, 85, 291-299.
40. Hase, T.; Wakabayashi, S.; Matsubara, H.; Imai, T.; Matsumoto, T.; Tobari, J. *FEBS Lett.* 1979, 103, 224-228.
41. Onishi, T.; Blum, H.; Sato, S.; Nakazawa, K.; Hoh-nami, K.; Oshima, T. *J. Biol. Chem.* 1980, 255, 345.
42. Kent, T. A.; Huynh, B. H.; Münck, E. *Proc. Natl. Acad. Sci. U.S.A.* 1980, 77, 6574.

RECEIVED June 27, 1980.

Mössbauer Effect in Zinc-67

WILLIAM T. VETTERLING

Department of Physics, Harvard University, Cambridge, MA 02138

Recent developments in the use of ^{67}Zn as a Mössbauer isotope are reviewed. Methods are discussed for the construction and calibration of two appropriate velocity drives. A historical review is followed by a summary of results on the pressure and temperature dependence of the resonance, the spectrum characteristics for the zinc chalcogenides, the Goldanskii-Karyagin effect, quadrupole interactions in ZnO and zinc metal, and isomer shift systematics (including the second-order Doppler shift from zero-point motion).

Only recently, instrumentation and techniques have been developed to provide ^{67}Zn resonances with sufficient reliability, and in enough circumstances, to make them appropriate tools for chemical studies. Although the present body of information so derived is not large, it is a timely project to summarize what has been learned so that such investigations may become more routine. This chapter indicates the particular problems that slowed progress with the isotope for many years, and describes procedures for overcoming them. In particular, two successful transducer designs are described and the means by which accurate low-temperature velocity calibrations may be achieved. Then a summary of experimental progress is followed by a discussion of the recent investigations.

General Properties

The 93.3-keV level of ^{67}Zn , with a half-life of 9.1 μs , represents a resonant system with extraordinarily small fractional width. The natural linewidth of 0.16 $\mu\text{m/s}$ corresponds to a Q of about 2×10^{15} . Consequently, the very early efforts to develop narrow Mössbauer sources and absorbers included work on this isotope (1). However, many years have

0065-2393/81/0194-0329\$05.00/0
© 1981 American Chemical Society

elapsed since the time of these experiments, and only in the past few years have reliable methods been established to deal with it. The slow progress may be traced primarily to four problems.

First, the transition energy of 93 keV and atomic mass of 67 lead to a free recoil energy of 0.069 eV. In the limit of low temperature, a zinc compound with a Debye temperature of 300 K is expected to show a recoil-free fraction of only 1.6%. (In this context, "low" temperature means lower than about 50 K, where the recoil-free fraction is reduced by a factor of two). At liquid-nitrogen temperatures the fraction f is reduced by a factor (0.17.) In fact, all successful ^{67}Zn experiments to date have been performed below 43 K.

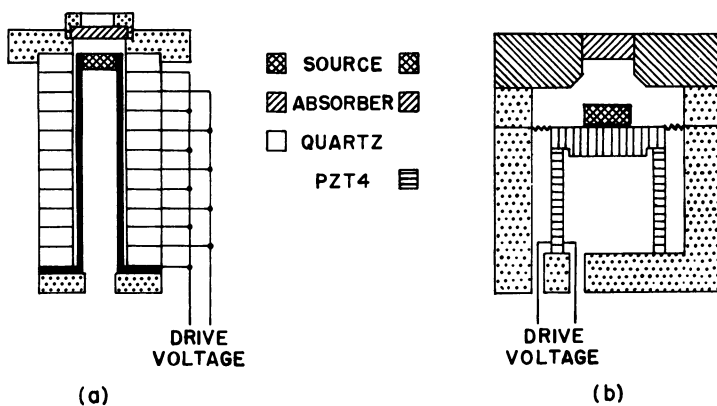
Second, the small fractional effects, even at 4.2 K, require the collection of many gamma rays for adequate statistical precision. Even with a moderately active source (10–20 mCi), the counts collected over the three-day half-life of the ^{67}Ga parent would be inadequate at counting rates of about $10^3/\text{s}$. One must work at rates well over $10^5/\text{s}$ for consistent success, and this places demands on the single-channel analysis and multichannel scaling systems.

Third, the natural linewidth of this isotope is only $0.16 \mu\text{m}/\text{s}$, while the isomer shifts measured so far span a range of about $180 \mu\text{m}/\text{s}$. The small linewidth requires, at the very least, the use of a very "stiff" mount for sources and absorbers, to avoid differential motions due, for example, to boiling cryogenes. However, an equally serious problem is the large isomer shift-to-linewidth ratio, which makes necessary the use of an extremely stable modulation and triggering system, and a great deal of velocity resolution. A large number of multiscalar channels must be scanned in one modulation cycle, and therefore an unusually fast channel advance system is needed.

Finally, ^{67}Zn has a natural abundance of only 4%, and suitably enriched absorbers are valued at several dollars per milligram. An absorber of ZnO with two radiation-length thicknesses (at 93 keV) and 1 cm^2 area has a value of several thousand dollars.

Instrumentation

The problem of developing a stiff transducer system with adequate range, for use at liquid-helium temperature, has been dealt with primarily in two ways. The first is the use of x-cut quartz plates. A single plate of this type has a range of only about $10 \mu\text{m}/\text{s}$ (2), but drives have been made by stacking them with interleaved electrodes of alternating polarity (3) (see Figure 1a). The properties of the individual transducers are well known and, provided that one can make reliably stiff joints between them, the resulting drive may be considered to produce at known velocity for a given applied ac voltage. Such a calibration remains suspect,



Physical Review

Figure 1. Transducers for use with ^{67}Zn : (a) stacked-quartz plates; (b) PZT-4 cylinder (5)

however, until checked by more fundamental means. Even at full voltage at 100 Hz, these drives generate a displacement of only 5000 Å. (The problems involved in bonding quartz plates can be circumvented by using larger single pieces of properly cut quartz, as has been demonstrated recently by Forster et al. (4).)

A second form of drive may be constructed from commercially produced cylinders of PZT (lead-zirconate-titanate). Cylinders of 1.27-cm o.d. and 1.27-cm length have been used to produce drive velocities in excess of $200 \mu\text{m/s}$ (5, 6, 7) (see Figure 1b). The motion is generated by applying sinusoidal voltages of up to 340 V peak-to-peak between electrodes on the inner and outer surfaces of the cylinder, thus causing a longitudinal contraction and elongation. This transducer makes no pretense of having a known calibration. Indeed, the velocity may not even be precisely constant around the circumference of the cylinder, and one must screen a stock of such cylinders (with a phonograph cartridge as a sensor) to find examples with adequate uniformity. As shown in Figure 1b, the source and absorber are mounted as an integral package, with the source fastened with frozen water or vacuum grease to an endcap on the transducer. The PZT cylinder itself was maintained under a force of about 1.5×10^6 dyn (measured at room temperature) by a concentrically ribbed Be-Cu diaphragmatic spring to maintain contact with the cylinder and to suppress higher modes of vibration.

Radiation is usually detected with a NaI(Tl) detector, using a wide-band amplifier and a high-speed, single-channel analyzer to discriminate the desired gamma rays. Initial count rates of $2 \times 10^5/\text{s}$ or higher are appropriate so that 10^{10} – 10^{11} counts total will be collected in the life of a single 20-mCi source.

The multichannel scaling system represents a fundamental limitation to present systems. To obtain adequate velocity sweep, one uses drive frequencies of 100 Hz or higher. In a single cycle, an analyzer with a minimum dwell time of 10 μs can sweep through 1000 channels. Thus in sweeping from zero to maximum positive velocity, it covers only 250 channels. A line of 0.32- $\mu\text{m/s}$ observed width (the theoretical minimum) and an isomer shift of 100 $\mu\text{m/s}$ would have poor definition under these circumstances. The resonances discovered so far at large isomer shift have been considerably broadened and so have not fully encountered this limitation. The method of using a "region-of-interest" spectrometer has not been applied, although the very recent introduction of novel interferometric velocity measurement techniques may make it possible to do so (7). A limitation of such a spectrometer may be the complicated response of the piezoelectric and ferroelectric transducers to nonsinusoidal driving waveforms of the frequencies required for obtaining adequate velocity range.

One may avoid large line displacements in certain investigations by choosing an absorber matched relatively closely in isomer shift to the sources. (We will specify later in this chapter a set of possible absorbers that span the presently known range of shifts.) Moreover, the usual technique of multichannel scaling may be modified (4, 8, 9). In one alternate system, a scalar is run at very high speed, and the detection of a gamma ray initiates the transfer of the present scalar contents into a first-in first-out (FIFO) buffer. The series of numbers produced is used by a computer to specify memory addresses which it increments. The method allows channel-advancing to occur effectively at the maximum count rate of the scalar, since each advance is not necessarily accompanied by two memory cycles as in the usual multichannel scaling scheme. Dwell times as short as 100 ns have been achieved, easily allowing the use of 1024 multiscalar channels at the typical drive frequencies of several hundred Hertz.

Calibration

Use of the ^{67}Zn Mössbauer resonance in chemical applications requires that one be able to establish a velocity calibration for the drive. As we pointed out earlier, the displacements involved make conventional position measurements difficult, and the drives do not span an adequate velocity range to allow comparison to the well-known ^{57}Fe resonance. However, drive calibration is now possible by at least three independent means. The first two rely on the fact that the ground state spin of ^{67}Zn is 5/2, so that it develops a three-line quadrupole-split structure in the presence of the field gradients that exist in its noncubic compounds, such

as ZnO and zinc. (The excited state has spin 1/2 and remains unsplit.) The third method involves a rather unconventional interferometric measurement.

Frequency modulation has been used to produce sidebands to calibrate the quadrupole splitting in ZnO (10). The quadrupole coupling constant was determined to be $e^2qQ/h = 2.408 \pm 0.006$ MHz. Independent measurement with a pulsed-radiofrequency, time-sharing NMR spectrometer measured this constant to be $e^2qQ/h = 2.409 \pm 0.010$ MHz by observing the orientation dependence of the $m = 1/2$ line in a single crystal of ZnO (11). (The latter measurement was performed at room temperature.)

The quadrupole splitting also has been measured for a zinc metal absorber. This was done originally using the ZnO splitting, just described, as the velocity reference (12). The first-order measurement then made it possible to find the resonance using pulsed Fourier transform nuclear quadrupole moment (NQR) techniques, with the result that $e^2qQ/h = 13.620 \pm 0.008$ MHz (13).

Therefore, a measurement of the quadrupole structure of either ZnO or zinc provides a transducer calibration. Moreover, these two calibrations apply to the extremes of presently known isomer shifts. A similar measurement for the hexagonal form of ZnS, as we shall see, would offer a more accurate calibration for the central part of the range of these shifts.

A very recent contribution to the technique of ^{67}Zn spectroscopy was the development of an interferometric system capable of accurately and quickly providing absolute measurements of the very small displacements involved (7). The device is based on a double-frequency laser with two stabilized and orthogonal polarized modes. The two modes are mixed to provide a measurable 565-MHz beat. Another portion of the light has its two modes separated spatially by a birefringent crystal and reflected respectively from mirrors attached to the Mössbauer source and absorber. The reflected waves are mixed to provide a second 565-MHz beat, out of phase with the first. The phase difference is a measure of the source-absorber displacement, and can be used to measure displacements up to 158 nm. The system achieves 0.6-nm resolution at frequencies up to 200 Hz.

Experimental Background

Experiments with the ^{67}Zn isotope use ^{67}Ga as the parent, with a half-life of 78.3 h. About 32% of the decays involve emission of 93.3-keV gamma rays, as a result of transitions from the spin-1/2 first excited state to the spin-5/2 ground state of ^{67}Zn . The number of materials used as absorbers is somewhat limited. The best resonances have been observed

with ZnO absorbers, and this remains the material of choice when investigating new sources. Moreover, the enriched material kept on inventory at Oak Ridge is in this form.

The first success with ^{67}Zn was reported in 1960, using a 92.4%-enriched ZnO absorber and a source produced by deuteron bombardment and annealment of a sintered ZnO source. A 0.3% resonance was observed through Zeeman splitting of the absorber (14, 15). The use of Zeeman splitting was a necessary feature of the experiments in the period before adequate means of velocity modulation were available. A resonance of 0.026% depth was observed by similar methods in 1961 for polycrystalline metallic zinc enriched to 33% in ^{67}Zn . In this case the source and absorber were formed of a single piece, with one face irradiated by 6.7-MeV protons to produce the ^{67}Ga parent (16). No structure was observed, and no resonance whatsoever was observed with natural zinc, β' -brass, or copper + 1.5% zinc (enriched to 71%).

A quartz transducer was first used in 1962, again using a 33%-enriched ZnO absorber and a deuteron-irradiated ZnO source (2). The total scan was $\pm 5 \mu\text{m/s}$, and a 0.2% resonance of twice theoretical width was found. In 1970, well-resolved hyperfine spectra were produced with depths of 0.2% and widths 3 to 5 times the theoretical minimum (3). Sources were sintered disks of ZnO enriched to 90% in ^{68}Zn , irradiated with deuterons or ^3He particles, and annealed. Absorbers were ZnO disks enriched to 90% in ^{67}Zn , and the transducer was a stacked-quartz plate design. The quadrupole coupling in this case was determined to be $e^2qQ/h = 2.47 \pm 0.03 \text{ MHz}$, and was reported to have an asymmetry factor 0.23 (although this factor is now known to be much smaller—probably zero).

Concurrent work by Russian researchers (17) used very similar techniques to find $e^2qQ/h = +2.32 \pm 0.11 \text{ MHz}$ and an asymmetry parameter of 0.19 ± 0.04 . The line depths reached 0.13%, with widths down to $0.6 \mu\text{m/s}$. The temperature dependence of the shift was measured from 4.2 to 43 K, and the report also described the first resonance found with nonidentical source and absorber. An isomer shift of $21 \pm 2 \mu\text{m/s}$ was reported for a 33%-enriched ZnO absorber with a source of ^{67}Ga in a MgO source matrix.

The excited-state magnetic moment $\mu_{\text{ex}} = (0.58 \pm 0.03)\mu_{\text{N}}$ was determined in 1973 (18, 19). In this case the source was an alpha-irradiated single crystal of ZnO mounted on the end of an Alnico bar that was progressively magnetized. A measurement of the energy-level splitting in this report was followed in the same year by the use of frequency modulation for a more accurate determination (10). The result was $e^2qQ/h = 2.408 \pm 0.006 \text{ MHz}$ with an asymmetry parameter of $\eta = 0.00_{-0.0}^{+0.07}$.

A broader range of sources and absorbers was used in a study begun in 1974, the primary purpose of which was to observe the resonance for all of the zinc chalcogenides (5). In most cases an enriched ZnO absorber was used, with sources made by diffusing ^{67}Ga activity into sintered zinc chalcogenide pills. However, resonances were also observed with a copper source matrix, and with absorbers of natural ZnS and zinc metal. A PZT-4 transducer was used, and the quadrupole interaction in zinc metal was measured. The spectrum of zinc metal showed a well-resolved quadrupole-split spectrum with an isomer shift of $16.6 \pm 0.5 \mu\text{m/s}$ with respect to a Cu(^{67}Ga) source, and the quadrupole coupling constant was reported as $e^2qQ/h = 13.8 \pm 0.4 \text{ MHz}$ (12). This study was paralleled by a concurrent study of the nuclear magnetic resonance for the same compounds (11). In this work, the chemical shifts for ^{67}Zn in the zinc chalcogenides were measured relative to a nuclear g -factor of $\gamma = 2\pi(266.2) \text{ rad/s/G}$, and a method called rotary saturation recovery was developed to study the spin-lattice relaxation $T_{1\rho}$ of ^{67}Zn in the rotating frame at 305 K. The results are tabulated in Table I. The temperature dependence of $T_{1\rho}$ from 80 to 310 K for ZnS and ZnSe agreed well with the theory for relaxation by quadrupole interactions with lattice phonons. A high-temperature probe was used to observe a Knight shift (again relative to the g -factor just given) of $(0.418 \pm 0.003\%)$ at 430°C in dispersed molten-zinc droplets. This measurement was performed independently with higher precision in 1978, and a suspected increase of the shift with temperature was confirmed (20). A measurement of the quadrupole interaction constant in a single crystal of ZnO also was made, and is discussed elsewhere in this chapter.

Even more recently, resonances of natural width have been seen with monocrystalline sources and absorbers of ZnO (21). The observed width was $(0.36 \pm 0.04) \mu\text{m/s}$ before a correction of $0.03 \mu\text{m/s}$ attributable to absorber thickness broadening was made. The absorber in this case was natural ZnO with a thickness of $58 \text{ mg } ^{67}\text{Zn}/\text{cm}^2$, and the line depth was only 0.17%. Source activity was generated in situ in a separate natural crystal by 11-MeV deuteron bombardment, and the transducer was of the stacked-quartz variety.

Table I. Chemical Shift and Spin-Lattice Relaxation Time $T_{1\rho}$ in the Rotating Frame for the Zinc Chalcogenides

	<i>Chemical Shift</i>	$T_{1\rho}$
ZnO	$-(10.3 \pm 1.6) \times 10^{-4}$	$2.03 \pm 0.15 \text{ s}$
ZnS	$-(11.3 \pm 0.7) \times 10^{-4}$	$1.25 \pm 0.10 \text{ s}$
ZnSe	$-(10.3 \pm 0.7) \times 10^{-4}$	$0.78 \pm 0.06 \text{ s}$
ZnTe	$-(08.2 \pm 0.8) \times 10^{-4}$	$0.49 \pm 0.03 \text{ s}$

The same research group recently has repeated the measurement of the quadrupole splitting in zinc metal using techniques similar to those in Ref. 12, except that the ^{67}Ga activity was produced by alpha bombardment of copper foils (22). The results were somewhat smaller, but later NQR measurements favored the earlier value (13).

A very comprehensive report (4) of the most recent work in Germany includes isomer shifts for absorbers of ^{67}ZnO , ^{67}ZnS (both wurtzite and sphalerite), $^{67}\text{ZnSe}$, $^{67}\text{ZnTe}$, and $^{67}\text{ZnF}_2$, as measured with single-line sources of ^{67}Ga in copper. The sources were produced by bombardment of copper foils by 35-MeV alpha-particles. Unlike the experiments described in Ref. 13, the zinc chalcogenides were used as absorbers, rather than as source matrices. However, the isomer shift measurements were consistent with the earlier results and indicated no after-effects of the electron capture decay. The resonance observed for ZnF_2 has the largest positive value (considered as a source with respect to a ZnO absorber) presently known. Further contributions of this work were the inference of values of Debye temperatures θ_M for the zinc chalcogenides (as determined from the recoil-free fraction and the known value of θ_M for ZnO), the observation that the isomer shifts bear a linear relation to the Pauling electronegativities, and the tentative identification of the value $\langle r^2 \rangle \approx +11 \times 10^{-3} \text{ fm}^2$ as a calibration for isomer shifts, on the basis of comparison with tin(IV) chalcogenides.

The development of a ^{67}Zn spectrometer with a double-frequency interferometer for absolute velocity calibration (described earlier) has offered the possibility of performing direct velocity measurements, rather than referring results to velocities extrapolated from known quadrupole splittings in ZnO and zinc (7). Moreover, the device has a sufficiently short measuring interval to allow the possibility of employing the velocity feedback techniques with more conventional electromechanical drives. It has not yet been used comprehensively, but preliminary experiments were done with enriched cubic ZnS crystal absorbers and polycrystalline (^{67}Ga) sources (obtained by proton bombardment of ZnO). A Ge(Li) detector was used at count rates of 70,000/s, and the drive was a cylinder of PZT-5A. Results in this initial trial were consistent with the known ZnO quadrupole splitting and showed an isomer shift of $-54.7 \pm 1.0 \mu\text{m/s}$, in agreement with results in Ref. 5.

The most recent reports on ^{67}Zn spectroscopy have been directed at the use of the resonance for highly sensitive energy-shift measurements. The work began with a look at the precise variations in the (^{67}Ga) ZnO vs. ZnO isomer shift with changes in the form and heat treatment of the samples (6). The sources were single crystals of ZnO that had been irradiated with 10-MeV deuterons and annealed in oxygen. The absorbers were natural or enriched powders, or natural single crystals, annealed at various temperatures between 700° and 1200°C . It was shown that the

variations in isomer shift resulting from grinding or sintering of the samples could be a significant fraction (up to 30%) of the natural linewidth, and that measurements based on the absolute measurements of this shift should rely on the use of enriched single-crystal absorbers. In a subsequent paper, this group applied similar techniques to measure the angular dependence of the gravitational red-shift (23). The red-shift, in this case, was measured over vertical distances of only 1 m, and the fractional energy shift of about 1×10^{-16} was measured to a precision of 10%.

Results

Because of the novelty of the techniques involved in these studies, the range of properties investigated is limited. Included are: (1) the effect of pressure on the ZnO spectrum; (2) the temperature dependence of the isomer shift and the second-order Doppler shift resulting from zero-point motion; (3) the isomer shifts for the zinc chalcogenides, copper, MgO, ZnF₂, and zinc metal; (4) the lattice anisotropy and the Goldanskii-Karyagin effect and; (5) the quadrupole interaction in zinc and zinc oxide. We will discuss these in order.

Pressure Dependence. deWaard and Perlow observed the influence of pressure on a ⁶⁶ZnO source that was annealed after deuteron irradiation and compressed in a steel cylinder to a pressure of approximately 40 kbar (3). While measuring the three central lines of the spectrum they noted: (a) a shift of $-0.11 \mu\text{m/s}$ for the central line; (b) a $(4 \pm 2)\%$ reduction of the splitting of the outer two lines; (c) a 25% broadening of the central line; and (d) a reduction of the ratio of center-line to outer-line intensity from 3.6 ± 0.5 to 2.4 ± 0.3 . While the source of these effects could not be stated with certainty, it was remarked that all were consistent with a reduction by about 8% of the quadrupole splitting in the source. The 40-kbar pressure is known to produce a 3% change in the lattice spacing, so that the inverse-cubic dependence of the quadrupole interaction on distance would lead one to expect an interaction of this size. However, a uniform compression would lead to an expected change of opposite sign, so we must conclude that the compression is nonuniform.

Temperature Dependence. The effect of temperature on the measured isomer shift for ZnO was investigated by Beskronny, Lebedev, and Ostanevich (17) and was found to be given by $\delta\nu/\nu = -\alpha(T_a^4 - T_s^4)$, with $\alpha = (0.141 \pm 0.012) \times 10^{-20} \text{ K}^{-4}$. This result is within about 20% of the value predicted from the known heat capacity of ZnO.

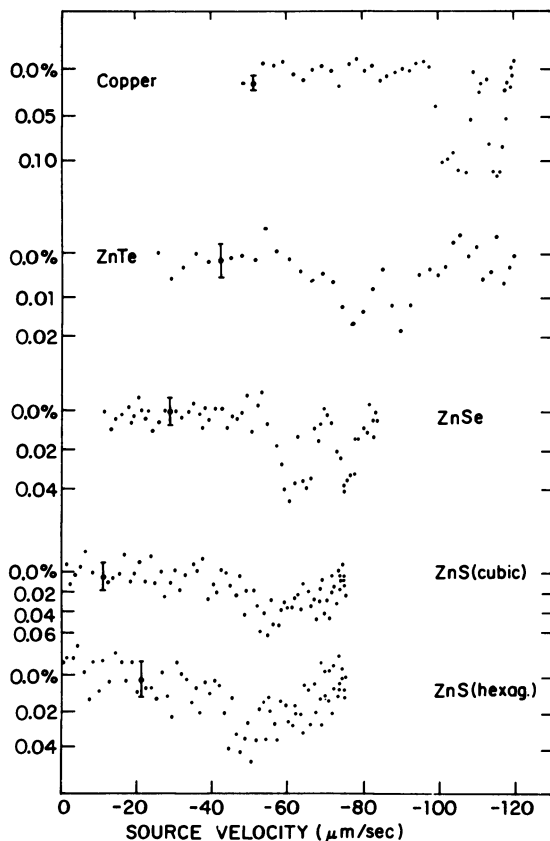
Unique to ⁶⁷Zn, perhaps, is the possibility of observing the contribution of zero-point motion to the second-order Doppler shift. Before it was appreciated that hyperfine interactions could produce shifts of Möss-

bauer resonances, this factor was cited as a possible explanation for the absence of observed resonances. A simplified analysis indicated that such shifts might be given by

$$\frac{\Delta E}{E} = -\frac{1}{2} \frac{\langle v^2 \rangle}{c^2} = -\frac{1}{c} (15 \mu\text{m/s}) \frac{\theta_D}{M}$$

where M is the host atomic mass and θ_D is its Debye temperature. This formulation predicts shifts much larger than the natural linewidth. However, a more rigorous analysis showed that in the case of monatomic hosts the shifts will be considerably smaller (24). Exact computer calculations for one-dimensional lattices, both monatomic and diatomic, agree that the zinc chalcogenides will be much less differentiated by the zero-point motion shift than this equation would predict (25). The calculations took into account the unequal sharing of energy between the two species in a diatomic lattice, and between host and impurity in a monatomic lattice. Nevertheless, it has yet to be established that these shifts may not, in some particular cases, contribute to the observed shift and therefore be important to a proper assessment of chemical effects. Also, despite the very small size of the effect, it may be informative to find a manner of explicitly verifying its presence and magnitude. For example, in a ZnO vs. ZnO experiment there may be a shift because the enriched absorber is primarily ^{67}Zn while the source matrix is ^{66}Zn . In this case the shift will be only about $-0.08 \mu\text{m/s}$, and therefore not easily observed. Any shift of this size, even with proper statistical precision, could be confused by a distortion of the drive velocity. The temperature-dependence data quoted earlier, for example, extrapolate to a value of about $-0.08 \mu\text{m/s}$ when both source and absorber are at 4 K. This result is probably too large to be attributable to the zero-point motion shift because the absorber was only 33% enriched in ^{67}Zn . Moreover, the results of deWaard and Perlow show a shift differing in both magnitude and sign from the expected value (3).

Isomer Shifts. The first measurements performed on a series of chemical compounds were done by Griesinger, Pound, and Vetterling (5, 25, 26). The studies were initiated in order to compare the lines from different chalcogenides of zinc, and particularly, to investigate the possibility of producing narrow single-line sources and absorbers from the cubic members of the group (ZnTe, ZnSe, and sphalerite). As a result, isomer shifts were measured for a variety of source-absorber combinations. Some of the absorption spectra are shown in Figure 2, and the related isomer shifts are indicated in Figure 3a. It is interesting to see to what degree these agree with the over-simplified calculation of zero-point motion shift shown in Figure 3b. A more realistic model, such as Lipkin's (24), produces the results shown in Figure 3c, which do little



Physical Review

Figure 2. The ^{67}Zn Mössbauer absorption spectra for ^{67}Ga diffused into the various hosts indicated (5). The absorber in all cases is enriched ZnO .

to explain the large range of observed shifts. Indeed, these large shifts may be seen to result most probably from the usual contact interaction, insofar as the plot of isomer shift vs. lattice spacing in Figure 4 is seen to be linear. The mean spacing is taken to be $(M_{\text{av}}/\rho)^{1/3}$, where ρ is the host density and M_{av} is the average atomic mass, and small corrections are made for the zero-point motion shift. A linear dependence has been observed previously for a variety of semiconductors (27, 28, 29) and has been given an interpretation in terms of bonding by Antoncik (30). It has been noted for both substitutional and interstitial ^{129}I in diamond, silicon, and germanium, and for substitutional and interstitial ^{119}Sn in diamond, silicon, germanium, and alpha-tin. For both isotopes, the substitutional and interstitial nuclei showed linear dependences on spacing with slopes of opposite sign. (The identification of peaks in these

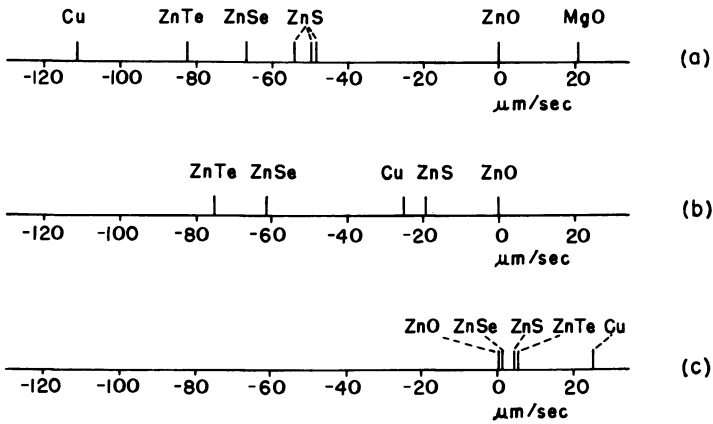


Figure 3. Observed and theoretical isomer shifts for a ZnO absorber and a ^{67}Ga source in various hosts: (a) observed shifts (b) shifts predicted on the basis of the mean energy per atom; (c) shifts predicted by a more realistic lattice model.

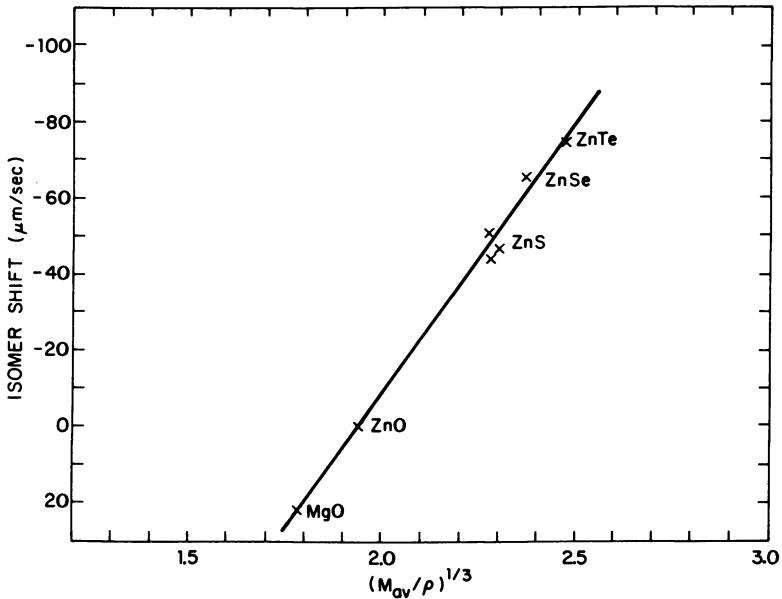


Figure 4. Isomer shift vs. mean lattice spacing (5)

Physical Review

Mössbauer spectra as resulting from substitutional or interstitial nuclei has been questioned by recent channeling experiments (31).)

A second set of measurements on the chalcogenides of zinc was made recently by Forster, Potzel, and Kalvius (4). In this case, the samples were enriched in ^{67}Zn and used as absorbers rather than as source matrices, while a monochromatic source of $\text{Cu}(^{67}\text{Ga})$ was used for all. The purpose of these measurements was to evaluate any possible aftereffects of the parent decay process, and to improve the spectral resolution. The results were essentially in agreement with those reported by Griesinger et al. (5), showing center shifts that increased monotonically for absorbers from ZnO to ZnTe . The shifts were shown to bear a linear correlation with the Pauling electronegativity of the ligands bonded to the divalent zinc atom.

Accepting the role played by the usual contact interaction, one may look further into the nature of these shifts (4,5). The bonding in divalent zinc involves $4s$ and $4p$ electrons which may be removed from the zinc site by ligands of high electronegativity. In the case of the $4s$ electrons, this removal corresponds to a decrease in the contact electron density. The $4p$ electrons, however, operate indirectly via shielding of s -orbitals, so that their removal corresponds to an increase in contact electron density. Theoretical calculations suggest that the effect of the $4s$ electrons is much larger (32) so that the isomer shift is a direct measure of $4s$ charge transfer in the bond. The observed sign of the isomer shift variations with lattice spacing and electronegativity imply a positive sign for the nuclear factor $\Delta\langle r^2 \rangle$. The compounds with smaller lattice spacings and larger electronegativities show the largest shifts compared to a free zinc atom. Since the isomer shift for a copper host is at the opposite end from ZnF_2 in the presently observed range, we may take it to represent the situation most resembling the free atom. The same is true for zinc metal, which was found to have a relatively small ($16.6 \pm 0.5 \mu\text{m/s}$) isomer shift with respect to a $\text{Cu}(^{67}\text{Zn})$ source. When it becomes established to what degree the electron density at the nucleus is affected by the participation of the $4s$ electrons in the conduction band, then these measurements will determine a scale for assessing $4s$ charge transfer in other zinc compounds.

Apart from the zinc chalcogenides, isomer shifts have been reported for various isolated source and absorber combinations. A comprehensive listing of these values is contained in Table II.

Goldanskii-Karyagin Effect. There may be some information available from a consideration of integrated line intensities, when the spectra are sufficiently well resolved to determine them accurately. This has been pointed out by Potzel, Forster, and Kalvius for the case of zinc metal (22). The three hyperfine lines in the spectrum of a completely

Table II. Isomer Shifts^a

Host for ⁶⁷ Ga	Absorber	Isomer Shift ($\mu\text{m/s}$)	Reference
MgO	ZnO	21 ± 2	17
ZnO	ZnO	0.0 ± 0.05	5
ZnS (cubic)	ZnO	-54 ± 4	5
ZnS (hexag)	ZnO	-50 ± 4	5
ZnSe	ZnO	-66.4 ± 1	5
ZnTe	ZnO	-82 ± 3	5
Cu	ZnO	-111 ± 3	5
Cu	ZnS (nat.)	-63 ± 3	5
Cu	Zn	-16.6 ± 0.5	12
Cu	ZnO	-106.4 ± 0.1	4
Cu	ZnS (cubic)	-56.8 ± 0.1	4
Cu	ZnS (hexag)	-57.5 ± 0.2	4
Cu	ZnSe	-48.7 ± 0.1	4
Cu	ZnTe	-30.1 ± 0.2	4
Cu	ZnF ₂	-165 ± 15	4

^a These shifts are the measured values, uncorrected for contributions from second-order Doppler shifts.

randomly oriented zinc metal powder normally would have equal intensity. However, there is a strong anisotropy in the mean-squared displacement $\langle x^2 \rangle$ of the zinc atoms in the metal, and this results in a variation in the intensities via the Goldanskii-Karyagin effect (33, 34). The data collected to date have not been definitive, but the effect may well yield valuable information in the future, as sample-producing techniques improve.

Quadrupole Interactions. The zinc compounds studied divide themselves between fcc and hcp structures. In fact, in proceeding through the chalcogenides, we pass from the hexagonal crystal ZnO to the cubic crystal ZnTe. ZnS exists in both cubic (sphalerite) and hexagonal (wurtzite) forms, while ZnSe is cubic. Zinc metal, itself, is hexagonal. For both zinc and ZnO, well-resolved structure from the quadrupole interaction has been observed. This structure results from the fact that the ⁶⁷Zn ground state has spin 5/2 and splits into three levels in an electric field gradient. The excited state has spin 1/2 and remains unsplit. The splitting is such that the lines are spaced by a ratio of 2:1.

Table III summarizes the measurements of this interaction for zinc and ZnO. The information may be combined with that from other studies to infer the magnitude of the local electric field gradient in each. For example, a straightforward comparison of the observed splittings shows that

$$\frac{(eq)_{Zn}}{(eq)_{ZnO}} = 5.656 \pm 0.004$$

If we use the best value for the ^{67}Zn ground-state quadrupole moment $Q = 0.150 \pm 0.015$ barns (35), derived from atomic hyperfine structure measurements and uncorrected for atomic shielding, we arrive at values for the field gradients:

$$\begin{aligned}(eq)_{Zn} &= (3.75 \pm 0.37) \times 10^{17} \text{ V/cm}^2 \\ (eq)_{ZnO} &= (0.66 \pm 0.06) \times 10^{17} \text{ V/cm}^2\end{aligned}$$

The result for zinc is consistent with the theoretically calculated values of $(eq)_{Zn} = 4.43 \times 10^{17} \text{ V/cm}^2$ (36) and $(eq)_{Zn} = (4.05 \pm 0.60) \times 10^{17} \text{ V/cm}^2$ (37). In these calculations a factor of $\gamma_\infty = -13.96$ was used for the Sternheimer antishielding for lattice ions and distant conduction electrons, while a factor about 60% as large was used for the shielding of the plane wave component of the conduction electrons. A simple calculation for ZnO (3), based on a lattice of point charges and computed from expressions given by deWette (38), was found to give $(eq)_{ZnO} = (0.5 \pm 0.11) \times 10^{17} \text{ V/cm}^2$. This is also good agreement, despite the neglect of contributions from higher multipoles to the lattice sum.

Conclusion

This chapter has summarized the techniques responsible for success with the ^{67}Zn isotope in recent years, and the Mössbauer effect parameters and properties to the extent that they have been determined. In many cases the information is not specifically chemical in nature, but

Table III. Quadrupole Interactions^a

Sample	Temperature (K)	e^2qQ/h (MHz)	$\Delta\nu$ (MHz)	Reference
ZnO	4.2	2.470 ± 0.030	0.7420 ± 0.0090	3
ZnO	4.2	2.320 ± 0.110	0.7000 ± 0.0300	17
ZnO	4.2	2.750 ± 0.030	0.8250 ± 0.0090	19
ZnO	4.2	2.408 ± 0.006	0.7233 ± 0.0018	10
ZnO	300	2.409 ± 0.010	0.7236 ± 0.0030	11
Zn	4.2	13.800 ± 0.400	4.1400 ± 0.1200	12
Zn	4.2	12.400 ± 0.200	3.7200 ± 0.0700	22
Zn	4.2	13.620 ± 0.008	4.0860 ± 0.0020	13

^a The splitting $\Delta\nu$ is that between the center line and the more widely spaced outer line.

is foundational to progress in such areas. Zinc compounds are certainly of enormous practical interest, and for this reason will undoubtedly capture the attention of the Mössbauer-effect community. Yet the major attraction of this isotope may be its extremely narrow linewidth which makes it singularly sensitive, to the extent that the scale of isomer shifts covers a range several hundred times the minimum observable linewidth. It has the smallest fractional linewidth of any of the Mössbauer isotopes, and is a system to which we can look for measurement of minute chemical or physical effects, perhaps not observable with any other Mössbauer isotope.

Literature Cited

1. Pound, R. V.; Rebka, G. A. *Phys. Rev. Lett.* **1960**, *4*, 397.
2. Alfimenkov, V. P.; Ostanevich, Yu. M.; Ruskov, T.; Strelkov, A. V.; Shapiro, F. L.; Wu-Kuang, Yen. *Sov. Phys. JETP* **1962**, *15*, 713.
3. deWaard, H.; Perlow, G. J. *Phys. Rev. Lett.* **1970**, *24*, 566.
4. Forster, A.; Potzel, W.; Kalvius, G. M. *Z. Physik* **1980**, *B37*, 209.
5. Griesinger, D.; Pound, R. V.; Vetterling, W. T. *Phys. Rev.* **1977**, *B15*, 3291.
6. Katila, T.; Riski, K. J.; Yla-Jaaski, J. *J. Phys.* **1980**, *41*, C1-121.
7. Beckhoff, H.; Paffe, J.; Duelberg, R. *J. Phys.* **1980**, *41*, C1-119.
8. Forster, A.; Halder, N.; Kalvius, G. M.; Potzel, W.; Asch, L. *J. Phys.* **1976**, *37*, C6-725.
9. Forster, A.; Potzel, W.; Kalvius, B. M. *AIP Conf. Proc.* **1977**, *38*, 29.
10. Perlow, G. J.; Potzel, W.; Kash, R. M.; deWaard, H. *J. Phys.* **1974**, *35*, C6-197.
11. Hayes, C. E. Ph.D. Thesis, Harvard Univ., Cambridge, MA, 1973.
12. Vetterling, W. T.; Pound, R. V. *AIP Conf. Proc.* **1977**, *38*, 27.
13. Kaufmann, E. N.; Brookeman, J. R.; Canepa, P. C.; Scott, T. A.; Rasmussen, D. H.; Perepezko, J. H. *Sol. State Comm.* **1979**, *29*, 375.
14. Nagle, D. E.; Craig, P. P.; Keller, W. E. *Nature* **1960**, *186*, 707.
15. Craig, P. P.; Nagle, D. E.; Cochran, D. R. F. *Phys. Rev. Lett.* **1960**, *4*, 561.
16. Aksenov, S. I.; Alfimenkov, V. P.; Lushchikov, V. I.; Ostanevich, Yu. M.; Shapiro, F. L.; Wu-Kuang, Yen. *Sov. Phys. JETP* **1961**, *13*, 62.
17. Beskronny, A. I.; Lebedev, N. A.; Ostanevich, Yu. M. *J. Inst. Nucl. Res., Dubna, USSR* **1971**.
18. Perlow, G. J. In "Perspectives in Mössbauer Spectroscopy"; Plenum: New York, 1973; p. 221.
19. Perlow, B. J.; Campbell, L. E.; Conroy, L. E.; Potzel, W. *Phys. Rev.* **1973**, *B7*, 4044.
20. Bucklish, R.; Ploumbidis, D. *Phys. Rev.* **1978**, *B17*, 4160.
21. Potzel, W.; Forster, A.; Kalvius, B. M. *J. Phys.* **1974**, *35*, C6-725.
22. Potzel, W.; Forster, A.; Kalvius, G. M. *Phys. Lett.* **1978**, *67A*, 421.
23. Helisto, P.; Katila, T.; Niemi, A.; Riski, K. J.; Yla-Jaaski, J. *Proc. Int. Conf. Gen. Relativ. Gravitation, 9th, Jena, DDR, 1980*.
24. Lipkin, H. J. *Ann. Phys.* **1963**, *23*, 28.
25. Vetterling, W. T., Ph.D. Thesis, Harvard Univ., Cambridge, MA, 1976.
26. Griesinger, D., Ph.D. Thesis, Harvard Univ., Cambridge, MA, 1976.
27. Hafemeister, D. W.; deWaard, H. *Phys. Rev.* **1973**, *B7*, 3014.
28. Weyer, B.; Nylandsted-Larsen, A.; Deutch, B. I.; Andersen, J. U.; Antoncik, E. *Hyp. Int.* **1975**, *1*, 93.

29. Weyer, G.; Deutch, B. I.; Nylandsted-Larsen, A.; Andersen, J. U.; Nielsen, H. L. *J. Phys.* **1974**, *35*, C6-297.
30. Antoncik, E. *Hyp. Int.* **1976**, *1*, 329.
31. Kemerink, G. J.; Boerma, D. O.; de Waard, H.; de Wit, J. C.; Drentje, S. A. *J. Phys.* **1980**, *41*, C1-435.
32. Freeman, A. J.; Ellis, D. E. In "Mössbauer Isomer Shifts"; Shenoy, G. K.; Wagner, F. E., Eds.; North Holland: New York, 1978.
33. Karyagin, S. V. *Sov. Phys. Solid State* **1966**, *8*, 1387.
34. Karyagin, S. V. *Sov. Phys. Solid State* **1968**, *9*, 1979.
35. Laulainen, N. S.; McDermott, M. N. *Phys. Rev.* **1969**, *177*, 1606.
36. Pattnaik, P. C.; Thompson, M. D.; Das, T. P. *Phys. Rev.* **1977**, *B16*, 5390.
37. Mohaptra, N. C.; Pattnaik, P. C.; Thompson, M. D.; Das, T. P. *Phys. Rev.* **1977**, *B16*, 3001.
38. deWette, F. W. *Phys. Rev.* **1961**, *123*, 103.

RECEIVED June 27, 1980.

Covalency of Neptunium(IV) Organometallics from Neptunium-237 Mössbauer Spectra

D. G. KARRAKER

E. I. du Pont de Nemours & Company, Savannah River Laboratory,
Aiken, SC 29808

The isomer shifts in ^{237}Np Mössbauer spectra arise from the shielding of neptunium's 6s orbitals by the inner 5f orbitals. In covalent bonding, ligand contributions to the 5f electron density increase the shielding, and the ^{237}Np isomer shift reflects differences in bond character among covalently bonded ligands. The large difference in isomer shift (3.8 cm/s) between ionic neptunium(IV) and neptunium(III) compounds permits a good determination of ligand bonding differences in neptunium(IV) organometallic compounds. The Mössbauer spectra for about 20 neptunium(IV) organometallic compounds, principally cyclopentadienyl (Cp) compounds of the general composition $\text{Cp}_x\text{NpX}_{4-x}$ ($x = 1, 2, 3$; $\text{X} = \text{Cl}, \text{BH}_4, {}^n\text{Bu}, \text{Ph}, \text{OR}, \text{acac}$), show both the differences in σ bonding among the X ligands, as well as the covalent effect of the Cp ligands.

The ^{237}Np Mössbauer effect has been especially valuable for chemical and physical studies of solid neptunium compounds. The isomer shift in ^{237}Np has a very wide range—from -6.9 to $+3.5$ cm/s, and excellent resolution can be obtained without excessively elaborate equipment. Neptunium forms compounds in five valence states, plus the metallic state, so a wide range of compounds and intermetallic materials can be prepared for Mössbauer studies. Examples of some past Mössbauer studies are magnetic properties of some neptunium compounds (1-4) and localization of 5f electrons in neptunium intermetallics (5). This chapter outlines the theory and experimental procedure for ^{237}Np Mössbauer studies and presents the application of the ^{237}Np Mössbauer effect to determine covalent effects in neptunium organometallic compounds.

0065-2393/81/0194-0347\$05.00/0

© 1981 American Chemical Society

²³⁷Np Mössbauer Effect

Description. Stone and Pillinger (6) discovered the Mössbauer effect of ²³⁷Np at the Savannah River Laboratory, and the experimental techniques were further developed by the group at Argonne National Laboratory, then directed by G. M. Kalvius. The physics of ²³⁷Np has been summarized in three excellent reviews (7, 8, 9) and will be discussed here only briefly.

The gamma ray used in the ²³⁷Np Mössbauer effect results from the 59.5-keV, 5/2⁻ → 5.2⁺ E1 transition in ²³⁷Np (*t*^{1/2}, 63 ns). The 59.5-keV level is accessible from the α-decay of ²⁴¹Am, β-decay from ²³⁷U, or the electron-capture decay from ²³⁷Pu. The half-life of ²⁴¹Am (433 years) makes it the obvious choice for a Mössbauer source.

Hyperfine Interactions. Hyperfine interactions refer to the interaction of the ²³⁷Np nucleus with the surrounding electromagnetic field (internal or external). The interpretation of ²³⁷Np Mössbauer spectra depends on the analysis of hyperfine effects. The Hamiltonian for the Mössbauer effect system has three terms:

$$H_{\text{hf}} = H_{\text{IS}} \pm H_{\text{Q}} \pm H_{\text{M}}$$

where H_{IS} refers to interactions of the central field with the nucleus; H_{Q} represents the interaction between the quadrupole moment with the electric field gradient; and H_{M} is the interaction of magnetic fields with the nucleus. The splitting of the excited and ground states by hyperfine fields is illustrated in Figure 1 for single unsplit levels, quadrupole-split levels, magnetically split levels, and combined magnetic- and quadrupole-split levels (10).

Isomer Shift. The central field interaction is the result of the Coulomb interaction of the electronic charge with the nuclear charge. This interaction determines the isomer shift. The central field interactions, which lead to the isomer shift in the Mössbauer effect, are spherically symmetric and depend principally on *s* orbitals. For the ²³⁷Np Mössbauer effect, 6*s* orbitals are shielded from the nucleus by the inner 5*f* orbitals (Figure 2). Increases in the electron density in the 5*f* orbitals increase the shielding of the 6*s* orbitals and produce a more positive isomer shift. The 6*d* and 6*p* electrons can also shield the 6*s* orbitals, but their contributions are small compared to the effect of 5*f* shielding. An obvious example of the effect of 5*f* electron density on the isomer shift is the difference in the isomer shift for neptunium compounds of different valences, which amount to 2–4 cm/s between consecutive valences and a range over 10 cm/s between Np⁷⁺ and Np³⁺ (Figure 3).

Given these large differences in isomer shifts between valences, covalent effects on bonding also can be identified by isomer shifts (11). Covalency requires the overlap of ligand orbitals with the 5*f* orbitals,

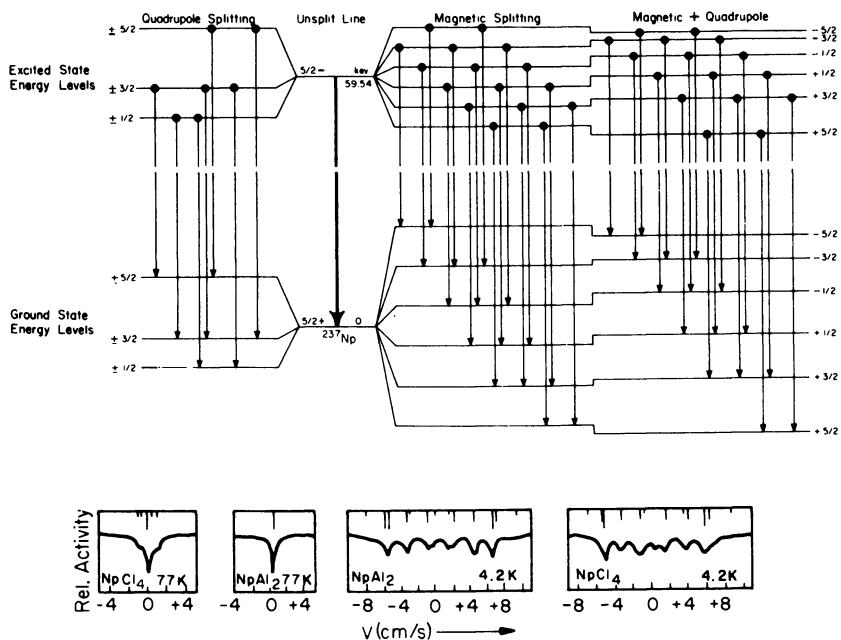


Figure 1. Splitting of the ground state and 59.5-keV level of ^{237}Np in magnetic and electric fields

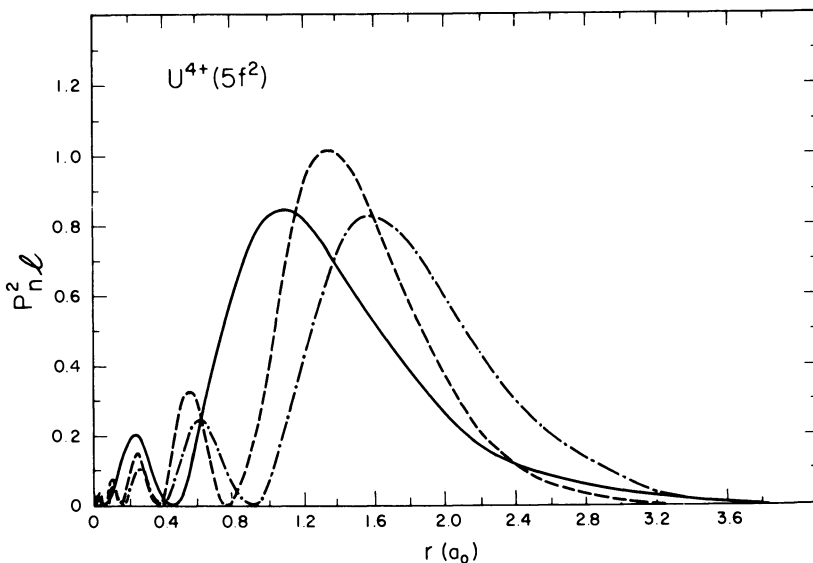


Figure 2. Radial charge density for U^{4+} ((—) 5f; (---) 6s; (- · -) 6p) (courtesy of N. M. Edelstein, Lawrence Berkeley Laboratory, Berkeley, CA)

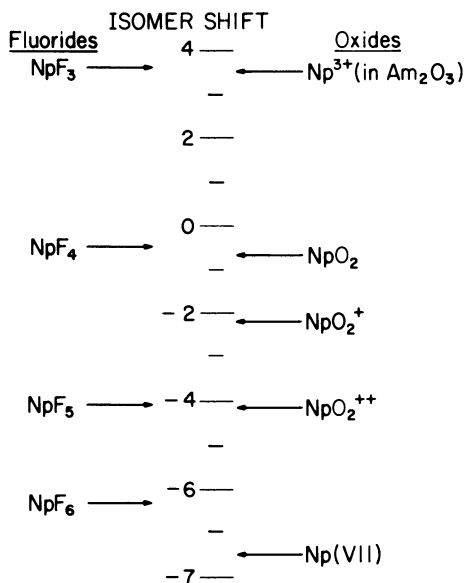


Figure 3. Isomer shifts of neptunium fluorides and neptunium oxides

which increases the 5f electron density with a consequent positive increase in the isomer shift. The comparison of isomer shifts between neptunium fluorides and oxygen-bonded neptunium compounds (Figure 3) shows the strong shift toward lower valence of the NpO_2^{2+} and NpO_2^+ compounds compared to that of NpF_6 and NpF_5 . The electron density contributed to the 5f orbitals of the Np^{6+} and Np^{5+} ions by the tightly bonded oxygen ligands results in an isomer shift toward lower valence. For the Np^{4+} , the contribution of oxygen ligands is small because it becomes more difficult for the orbitals to overlap in the larger Np^{4+} ion. In the still larger Np^{3+} ion, essentially no difference in the isomer shifts occurs between a fluoride and an oxygen ligand environment.

Quadrupole Interaction. The interaction of the nuclear quadrupole tensor and the electric field gradient tensor from the ionic environment surrounding the neptunium ion can result in Stark (electric field) splitting of the nuclear levels, or quadrupole splitting. In general, quadrupole splitting requires the alignment of the z-component of the electric field gradient of the unfilled 5f electron shell (8). This alignment must be produced by an external field; otherwise, rapid rotation of the electric field gradient allows only an average to be observed.

Quadrupole interactions can be reduced to combinations of two components—the electric field gradient and the asymmetry parameter η (12). For a neptunium ion in a site with an n-fold rotation or rotation–reflection axis with $n > 2$, the asymmetry parameter $\eta = 0$, and the

resonance is split into five equally spaced lines. At the other extreme, where $\eta = 1$, the resonance is split into three lines. Intermediate values of η are represented by unequal, five-line spectra. In all cases, the central resonance of the quadrupole spectrum has the same isomer shift as the unsplit resonance would have (Figure 1).

Magnetic Interaction. The interaction of the nuclear energy levels with a magnetic field (internal or external) results in magnetic splitting of the ^{237}Np Mössbauer spectra (Figure 1). Normally, a paramagnetic ion will have a magnetic field at the nucleus because of its unpaired electrons. At room temperature, the direction of the field changes too rapidly for the nucleus to respond. At low temperatures, the relaxation time is greatly decreased, often to the point where the ^{237}Np Mössbauer spectrum is magnetically split. When the absorbing compound becomes ferromagnetic or antiferromagnetic, the relaxation time becomes infinite on the ^{237}Np Mössbauer time scale, and a large magnetic splitting normally results. Pure magnetic splitting has a 16-line pattern (Figure 1), but as the energies of some of the resonances are nearly the same, the spectrum usually shows only eight to ten lines. The average of two symmetrically split lines determines the isomer shift in magnetically split spectra. Occasionally, quadrupole splitting also may be imposed on magnetic splitting, but since the magnetic splitting is normally much greater than quadrupole splitting, no serious complication is introduced in interpreting the spectrum. Where quadrupole and magnetic splitting are nearly equal, as for some NpO_2^{2+} or NpO_2^+ compounds, assignment of the resonances becomes very difficult.

Intermediate Relaxation Effects. The discussion of hyperfine interactions involves the assumption that the hyperfine fields are time independent. For some compounds, time-dependent effects (intermediate relaxation) influence the Mössbauer spectrum.

The electrons in the unfilled shell of the neptunium ion can be considered to alternate between "spin-up" and "spin-down" positions under the influence of external fields on the ion. The electronic relaxation time is the period required for the spin flip. If the relaxation time is slow, compared to the Larmor precession frequency of the nucleus and the lifetime of the excited state, the nucleus will see a static field, and the spectrum will be magnetically split. Fast relaxation times average the field on the nucleus to zero, and single-line or quadrupole spectra will result. Intermediate relaxation times are of the same order of magnitude as the Larmor precession frequency and the excited-state lifetime, and result in a loss of resolution of the Mössbauer spectrum, often so much so that the spectrum becomes an uninterpretable smear (Figures 4 and 5). Relaxation is considered to occur principally through spin-lattice and spin-spin interactions, although other mechanisms have been con-

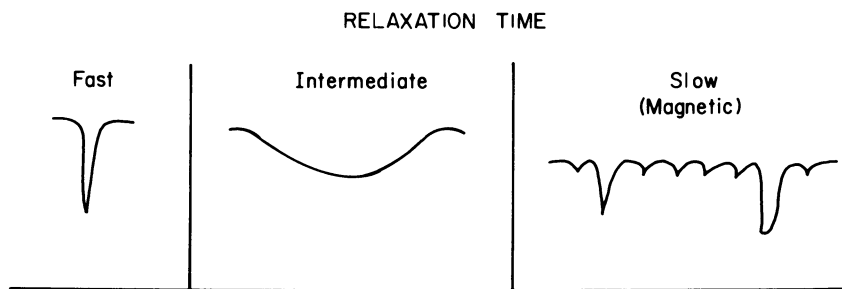


Figure 4. Relaxation effects on ^{237}Np Mössbauer spectra

sidered (13). Physical methods of avoiding intermediate relaxation effects depend on changing the experimental conditions to favor faster (higher temperatures) or slower (external magnetic fields, lower temperatures) relaxation times. In practice, such methods are not easy to apply and not necessarily successful. However, in some cases, intermediate relaxation effects can be avoided by changing the chemical compound to a similar compound that retains the features under study. Substitution of a bulkier ligand or cation [MeCp for Cp, $\text{N}(\text{C}_2\text{H}_5)_4^+$ for Cs^+] often reduces relaxation effects without affecting the object of the study. Bulkier ligands increase the distance between neptunium ions, thus reducing the spin-spin interactions that affect relaxation.

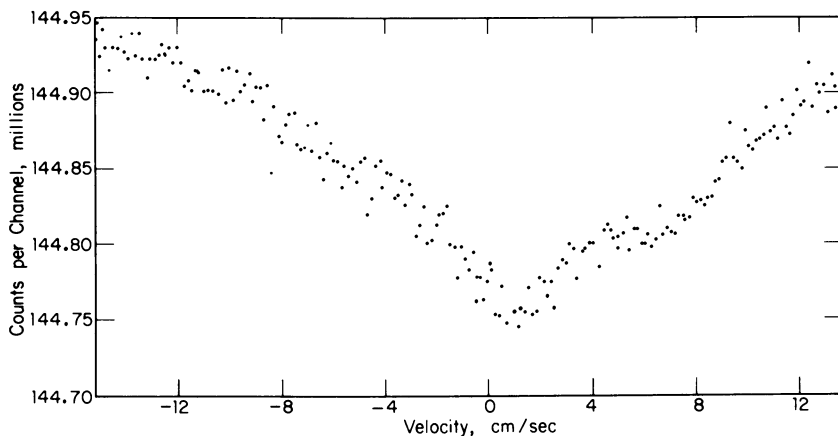


Figure 5. Mössbauer spectrum of $\text{Np}(\text{MeCp})_3\text{Cl}$

Experimental

Techniques. The experimental apparatus and techniques for ^{237}Np Mössbauer spectroscopy have been included in earlier reviews (7, 8, 14, 15, 16). The instrumentation used in Mössbauer studies has always been similar among different workers, but there were some differences in sources, detectors, standardization of spectra, etc., particularly before

1972. In recent years some techniques have become standard; they will be emphasized in the next section.

Instrumentation. ^{237}Np Mössbauer experiments usually have used a conventional constant-acceleration spectrometer in transmission geometry (17). The spectrometer must achieve relatively high velocities (± 20 cm/s) while operating at liquid-helium temperatures. The recoilless fraction for ^{237}Np Mössbauer effect is decreased severely above helium temperatures for most absorbers, so the source-absorber equipment requires a liquid-helium dewar, preferably one capable of maintaining helium temperatures for 3–4 days. A convenient velocity calibration can be obtained from an NpAl_2 absorber, which has a well-characterized, magnetically split spectrum at 4.2 K.

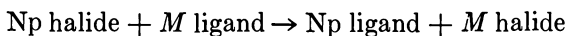
Sources. The most convenient source is ^{241}Am metal as a 5% alloy in cubic thorium metal matrix. A 433-year ^{241}Am source lasts indefinitely; one such source has been used satisfactorily at the Savannah River Laboratory for about ten years. About 3 mg ^{241}Am in a source yields counting rates above 10^4 counts/channel-min. Sources in earlier work used ^{237}U (6.75 d), and the use of ^{237}Pu (44.6 d) has been considered, but the half-lives of both isotopes are quite inconvenient. The ^{241}Am -Th source has the narrowest experimental linewidth yet achieved, about 0.1–0.2 cm/s (14).

Standards. The single-line spectrum of NpAl_2 at 77 K is the recommended zero of isomer shift (18). This zero can be determined with more precision than a zero based on the single resonance line of NpO_2 . The NpO_2 resonance is broadened by a weak magnetic splitting below 25 K, and is thus much less satisfactory, though often used in early work. In practice, the centroid of the NpAl_2 spectrum at 4.2 K is normally used as zero isomer shift. As noted before, the magnetically split spectra of NpAl_2 can provide simultaneously a convenient velocity calibration.

Detectors. Two detectors are in use— $\text{NaI}(\text{Tl})$ scintillation crystals and $\text{Ge}(\text{Li})$ semiconductors, and both are satisfactory. The detector in current use at Savannah River Laboratory is an $\text{NaI}(\text{Tl})$ scintillation counter. This counter has been quite satisfactory over several years of service and avoids the liquid-nitrogen cooling necessary for $\text{Ge}(\text{Li})$ detectors. The window of the single-channel analyzer is adjusted to accept the 59.54 keV photopeak for all three detectors.

Absorbers. ^{237}Np can be obtained in gram quantities to prepare absorbers for study. The specific activity of ^{237}Np is 1.57×10^6 $\alpha\text{d}/\text{min}\cdot\text{mg}$, and quantities greater than a few mg should be handled in a glove box or other form of containment to prevent contamination of the laboratory with alpha activity. Most neptunium organometallic compounds are decomposed by water and oxygen (often violently), so preparation of the compounds, absorbers, etc., is performed in an inert-atmosphere glove box. The absorbers are usually prepared by (1) packing the powdered sample in a plastic holder, (2) covering the powder with a plastic plug, and (3) wrapping the assembly with adhesive polyester tape. The absorber is removed from the glove box and wrapped with an additional layer of plastic tape to prevent the spread of alpha activity. Normally, about 50 mg Np/cm^2 is adequate for most materials. Crystalline solids, such as NpCl_4 , NpBr_4 , NpCl_3 , etc., have larger recoilless fractions than the essentially amorphous neptunium organometallic compounds, which can require 3–4 days to develop an acceptable spectrum.

Compounds. The neptunium organometallic compounds used in this study were prepared (most for the first time) by using the general procedures developed in the synthesis of the analogous uranium compounds. Some modification of the procedures was necessary since Np^{4+} is more easily reduced than U^{4+} . The basic reaction used in nearly all preparations is



where M is an alkali or Tl. In general, metallated ligands are strong reducing agents, so often an Np^{3+} organometallic is the major product rather than the desired Np^{4+} organometallic. Adjustment of experimental conditions occasionally was successful in obtaining the desired Np^{4+} product.

²³⁷Np Isomer Shift and Covalency

NpCp₃X Compounds. The first actinide organometallic compound prepared was tris(cyclopentadienyl) uranium(IV) chloride, $\text{U}(\text{C}_5\text{H}_5)_3\text{Cl}$ (hereafter C_5H_5^- is abbreviated Cp) (19), and its preparation was succeeded by the preparation of Cp compounds of the 3+- and 4+-valent actinide ions up to Cf^{3+} (20). With few exceptions, the organometallic compounds of the actinides include the Cp ligand in their structure; by reacting UCp_3Cl (or NpCp_3Cl) with an alkali metal ligand compound, such as Li^nBu , LiPh , NaO^nBu , etc., the ligand replaces the chloride ion, forming NpCp_3^nBu , NpCp_3Ph , $\text{NpCp}_3\text{O}^n\text{Bu}$, etc. Quite a variety of compounds have been prepared in this manner from UCp_3Cl , most of which can also be prepared from NpCp_3Cl . Substituted Cp ligands, such as $\text{CH}_3-\text{C}_5\text{H}_4^-$ (MeCp), form analogous compounds.

The isomer shifts in ²³⁷Np Mössbauer spectra of these compounds normally are displaced from an ionic Np^{4+} isomer shift toward the Np^{3+} isomer shift. Using the variety of compounds that can be prepared as derivatives of the NpCp_3^+ moiety and selecting appropriate standards, a comparison of the bonding properties of the ligands can be obtained from their ²³⁷Np Mössbauer spectra. Compounds containing one or two Cp ligands per Np^{4+} ion also have been prepared. These compounds afford a measure of the effect on the ²³⁷Np isomer shift of adding one, two, or three Cp ligands.

Unfortunately, the ²³⁷Np Mössbauer spectra of NpCp_3X compounds are strongly affected by intermediate relaxation effects. Attempts to counter relaxation effects by synthesizing compounds that substitute MeCp for Cp or $\text{C}_6\text{H}_4\text{C}_2\text{H}_5$ for $-\text{C}_6\text{H}_5$, etc., often succeeded in obtaining interpretable, although not necessarily ideal, spectra. Figure 6 shows the spectra of NpCp_3BH_4 and $\text{Np}(\text{MeCp})_3\text{BH}_4$, illustrating a successful example where an isomer shift could be obtained from the spectrum of the substituted compound but not from the parent compound. Analysis of the results in terms of the ligand's properties involves the assumption

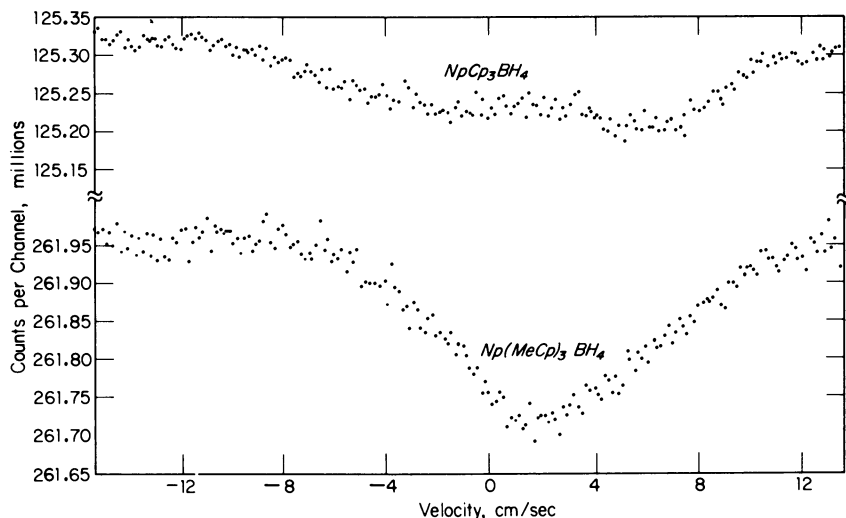


Figure 6. Mössbauer spectra of $NpCp_3BH_4$ and $Np(MeCp)_3BH_4$

that the effect of substituted ligands and unsubstituted ligands on the isomer shifts is the same; data given later in this chapter support this assumption. The ^{237}Np Mössbauer spectrum of $NpCp_3OCH(CH_3)_2$ is shown in Figure 7, and spectra for $Np(acac)_2Cl_2 \cdot THF$ ($acac = CH_3COCHCOCH_3$) and $Np(acac)_2(MeCp)_2$ are shown in Figures 8 and 9, respectively. The latter two spectra allow a comparative isomer shift for Cp_2NpX_2 compounds to be derived. Mössbauer parameters for $NpCp_nX_{4-n}$ compounds are shown in Table I.

To compare the contributions of the ligands, the assumption is made that Cl^- and BH_4^- ions make no covalent contributions, and that $NpCp_3Cl$ or $Np(MeCp)_3BH_4$ and $NpCl_4$ can be used as reference compounds. To determine the effect of two Cp ligands, $Np(acac)_2Cl_2 \cdot THF$ was used as a reference, since the acac ligands made a strong negative change in the normal Np^{4+} isomer shift. The isomer shifts assigned to each ligand are shown in Table II.

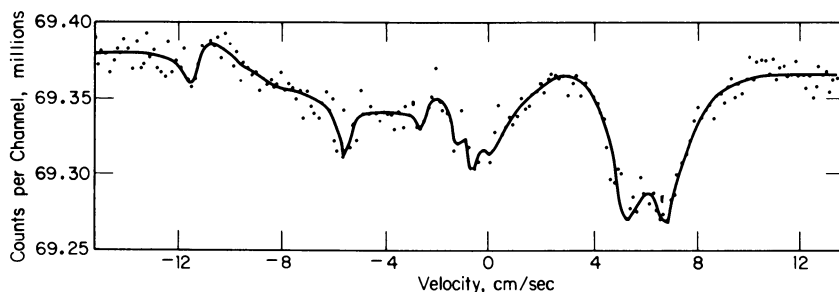


Figure 7. Mössbauer spectrum of $NpCp_3OCH(CH_3)_2$

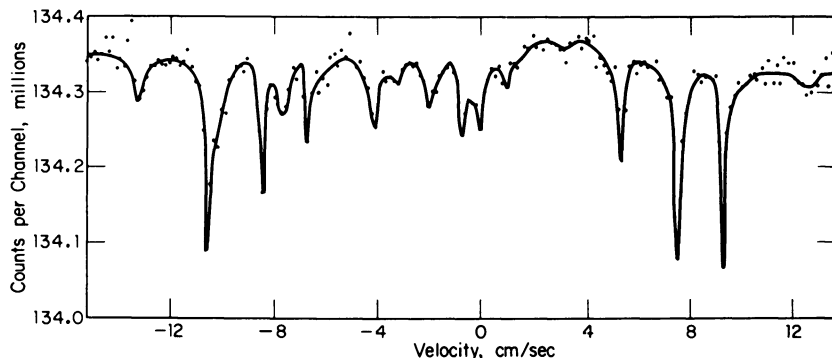


Figure 8. Mössbauer spectrum of $Np(acac)_2Cl_2 \cdot THF$

Table I. Mössbauer Parameters

Compound	Isomer Shift ^a δ (cm/s)
$NpCp_3Cl$	1.4 ± 1.0
$Np(MeCp)_3BH_4$	1.45 ± 0.4
$NpCp_3^nBu$	0.27 ± 0.07
$NpCp_3C_6H_4C_2H_5$	0.42 ± 0.28
$Np(MeCp)_3O^iPr$	0.93 ± 0.07
$NpCp_3O^iPr$	0.86 ± 0.2
$NpCp_3OCH(CF_3)_2$	0.79 ± 0.3
$NpCp_3^iBu$	0.86 ± 0.3
$Np(MeCp)Cl_3 \cdot 2THF$	-0.31 ± 0.07
$Np(acac)_2Cl_2 \cdot THF^b$	-1.47 ± 0.07
$Np(MeCp)_2(acac)_2$	-0.53 ± 0.07
$NpCl_4^b$	-0.35 ± 0.05
$NpCl_3^b$	3.54 ± 0.05

^a Referred to $NpAl_2 = 0$.

Table II. ²³⁷Np Isomer

Bond	Compound
$Cp-NpX_3$	$Np(MeCp)Cl_3 \cdot 2THF$
Cp_2-NpX_2	$Np(acac)_2(MeCp)_2$
Cp_3-NpX	$NpCp_3Cl$
	$Np(MeCp)_3BH_4$
$R-NpCp_3$	$NpCp_3^nBu$
$Ar-NpCp_3$	$NpCp_3C_6H_4C_2H_5$
$RO-NpCp_3$	$Np(MeCp)_3O^iPr$
	$NpCp_3O^iPr$
	$NpCp_3OCH(CF_3)_2$
	$NpCp_3O^iBu$
$(acac)_2-NpCl_2$	

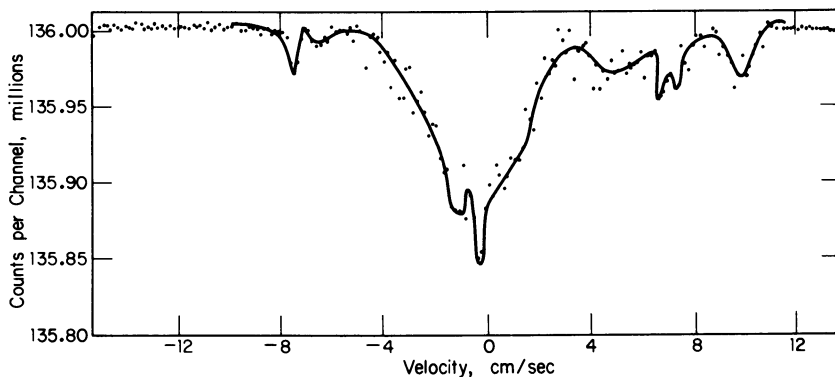


Figure 9. Mössbauer spectrum of $Np(acac)_2(MeCp)_2$

for $Np-Cp_n-X_{4-n}$ Compounds

Quadrupole Coupling Constant $eqQ/4$ (cm/s)	Magnetic Hyperfine Constant $g_0\mu_N H_{eff}$ (cm/s)	Reference
		21
		22
	5.8 ± 0.2	22
	5.5 ± 0.4	22
5.0 ± 1.0	5.7 ± 0.2	22
	5.4 ± 0.5	22
	5.7 ± 0.5	22
	5.2 ± 0.06	22
	5.15 ± 0.06	22
0.97 ± 0.15	7.92 ± 0.15	} this work
-0.42 ± 0.05	4.74 ± 0.05	
0.49 ± 0.05		7

^b Included for comparison.

Shifts for Ligands

δ (cm/s)	Reference	$\Delta\delta$
-0.31	$NpCl_4$	+0.04
-0.53	$Np(acac)_2Cl_2 \cdot THF$	+0.94
1.4	$NpCl_4$	+1.75
1.45	$NpCl_4$	+1.80
0.27	$NpCp_3Cl$	-1.13
0.42 ± 0.3	$NpCp_3Cl$	-0.98
0.93	$NpCp_3Cl$	-0.47
0.86	$NpCp_3Cl$	-0.56
0.79	$NpCp_3Cl$	-0.61
0.86	$NpCp_3Cl$	-0.56
-1.47	$NpCl_4$	-1.13

Table III. Isomer Shifts of NpCp_4

<i>Compound</i>	<i>Isomer Shift (cm/s)^a</i>
NpCp_4	0.72 ± 0.02
$\text{Np}(\text{MeCp})_4$	0.71 ± 0.07
$\text{Np}(\text{COT})_2$	1.94 ± 0.05
$\text{Np}(\text{EtCOT})_2$	1.90 ± 0.10
$\text{Np}(\text{BuCOT})_2$	1.94 ± 0.05

^a Referred to $\text{NpAl}_2 = 0$.

The isomer shift differences in Table II show that only Cp ligands make a positive covalent contribution. Moreover, the Cp_3Np^+ moiety is unusually stable; $\text{Cp}_2\text{Np}^{2+}$ shows about half the isomer shift difference of the Cp_3Np^+ unit, and the effect of a single Cp ligand is so slight that Cp in NpCpCl_3 is probably σ -bonded. The isomer shift differences show clearly that alkyl, aryl, and alkoxide ligands are σ -bonding. The alkyl and aryl ligands are very strongly σ -bonding, equivalent to about 25% of the difference in the Np^{3+} - Np^{4+} isomer shifts. The isomer shift differences of the alkoxide ligands average 0.55 cm/s, about half the alkyl-aryl shift difference, and are consistent with the greater stability of the $\text{Np}-\text{OR}$ bond. The precision of the data does not allow a distinction between the isomer shifts of the alkyl and aryl ligands, or among the alkoxide ligands. The chemical stability of NpCp_3Ph and NpCp_3Ar compounds depends on the covalent contribution of the three Cp ligands offsetting the strong electron-withdrawing nature of the $\text{Np}-\text{R}$ and $\text{Np}-\text{Ar}$ bonds.

Bond Length and Isomer Shift. The ^{237}Np Mössbauer isomer shifts (Table III) of NpCp_4 - and $\text{Np}(\text{COT})_2$ -type compounds (COT = $\text{C}_8\text{H}_8^{2-}$, the cyclooctatetraenyl dianion) show anomalously small isomer shifts for the NpCp_4 compounds, when compared to $\text{Np}(\text{COT})_2$ or NpCp_3Cl ($\delta = 1.4$). The substitution of a fourth Cp ligand into NpCp_3Cl would not be expected to decrease the isomer shift to 0.72 cm/s (NpCp_4). The COT and Cp ligands are 10- and 5-electron donors, respectively, so NpCp_4 and $\text{Np}(\text{COT})_2$ both have the same electron density available for bonding.

An explanation for this apparent anomaly is found by considering the metal-carbon bond lengths of the uranium analogues of these compounds. The average uranium-ring distances have been determined crystallographically to be 2.65 Å for $\text{U}(\text{COT})_2$, 2.74 Å for (UCp_3Cl) , and 2.81 Å for UCp_4 (26). The bond distances for the isostructural $\text{Np}-\text{COT}$ and $\text{Np}-\text{Cp}$ compounds should be slightly, but not significantly smaller. The addition of a fourth Cp ligand to the UCp_3^+ moiety creates sufficient ligand repulsion that the uranium-ring carbon distance of UCp_4 is 0.07 Å greater than that of UCp_3Cl , and 0.16 Å longer than that of

and $\text{Np}(\text{COT})_2$ Compounds

<i>Magnetic Coupling Constant $g_{0N\mu} H_{\text{eff}}$ (cm/s)</i>	<i>Quadrupole Coupling Constant $g_{0\mu N} H_{\text{eff}}$ (cm/s)</i>	<i>Reference</i>
—	1.66 ± 0.02	21
—	1.29 ± 0.08	22
6.12 ± 0.05	-0.46 ± 0.05	23
6.15 ± 0.10	-0.5 ± 0.02	24
6.10 ± 0.05	0.46 ± 0.05	24

$\text{U}(\text{COT})_2$. As applied to the covalency of the neptunium compounds, the longer bond distance decreases the overlap of the neptunium 5*f* and ligand orbitals and is reflected in a smaller covalent isomer shift.

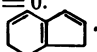
A second example of the effect of bond distance is found by comparing the isomer shift range of Np^{3+} organometallics (Table IV) with the isomer shift range of Np^{4+} organometallics. The extreme range of isomer shifts for Np^{3+} organometallics is about 0.4 cm/s, while Np^{4+} organometallics have isomer shifts covering a range of about 2.5 cm/s. The probable explanation lies in the sizes of the neptunium ions— Np^{4+} has an ionic radius of 0.98 Å; Np^{3+} an ionic radius of 1.04 Å (27). The 5*f* orbitals of the Np^{3+} ion are spatially less accessible than those of Np^{4+} , and the smaller interaction between the 5*f* and ligand orbitals is reflected in small isomer shift effects.

The results of ^{237}Np Mössbauer spectra provide a picture of the bonding of ^{237}Np organometallics and their uranium analogues that could be obtained by no other method. In essence, Mössbauer results give a view of the compound from the position of the neptunium nucleus; the work summarized in this chapter shows that the ^{237}Np isomer shift results are consistent with available data and provide a useful picture of the bonding in actinide organometallics.

Table IV. Isomer Shifts of $\text{Np}(\text{III})$ Organometallics

<i>Compound</i>	<i>Isomer Shift (cm/s)^a</i>	<i>Quadrupole Coupling Constant $eqQ/4$ (cm/s)</i>	<i>Reference</i>
$\text{NpCp}_3 \cdot 3\text{THF}$	3.65 ± 0.10		21
$\text{NpIn}_3 \cdot \text{THF}^b$	3.55 ± 0.10		22
$\text{KNp}(\text{COT})_2 \cdot 2\text{THF}$	3.92 ± 0.10	0.75 ± 0.10	25
NpCl_3	3.54		7

^a Referred to $\text{NpAl}_2 = 0$.

^b In = indenyl, .

Acknowledgment

The author is indebted to J. A. Stone for over a decade of advice, counsel, and experimental assistance. This chapter was prepared in connection with work under Contract No. DE-ACO9-76SR00001 with the U.S. Department of Energy.

Literature Cited

1. Stone, J. A.; Jones, Jr., E. R. *J. Chem. Phys.* 1971, 54, 1713.
2. Dunlap, B. D.; Brodsky, M. B.; Kalvius, G. M.; Shenoy, G. K.; Lam, D. J. *J. Appl. Phys.* 1969, 40, 1495.
3. Jones, Jr., E. R.; Hendricks, M. E.; Stone, J. A.; Karraker, D. G. *J. Chem. Phys.* 1974, 60, 2088.
4. Stevens, J. L.; Jones, Jr., E. R.; Karraker, D. G. *J. Chem. Phys.* 1976, 64, 1492.
5. Dunlap, B. D.; Lander, G. H. *Phys. Rev. Lett.* 1974, 33, 1046.
6. Stone, J. A.; Pillinger, W. L. *Phys. Rev. Lett.* 1964, 13, 200.
7. Pillinger, W. L.; Stone, J. A. "Mössbauer Effect Methodology"; Gruverman, I. J., Ed.; Plenum: New York, 1968; Vol. 4, pp. 217-236.
8. Kalvius, G. M. "Plutonium 1970 and Other Actinides, Proceedings of the 4th International Conference on Plutonium and Other Actinides, Santa Fe, NM, October 5-9, 1970"; Miner, W. N., Ed.; Metallurgical Society of American Institute of Mining, Metallurgical and Petroleum Engineers, Inc.: New York, pp. 296-330.
9. Dunlap, B. D.; Kalvius, G. M. In "Actinides Electronic Structure and Related Properties"; Freeman, A. J., Darby, Jr., J. B., Eds.; Academic: New York, 1974; p. 237.
10. Stone, J. A.; Pillinger, W. L. *Phys. Rev.* 1968, 165, 1319.
11. Karraker, D. G. In "Organometallics of the f-Elements"; Marks, T. J., Fischer, R. D., Eds.; D. Reidel: Dordrecht, Holland, 1979; p. 395.
12. Cohen, M. H.; Reif, F. *Solid State Phys.* 1957, 5, 345.
13. Wickman, H. H. "Mössbauer Effect Methodology"; Gruverman, I. J., Ed.; Plenum: New York, 1966; Vol. 2, pp. 39-66.
14. Dunlap, B. D.; Kalvius, G. M.; Ruby, S. L.; Brodsky, M. B.; Cohen, D. *Phys. Rev.* 1968, 171, 316.
15. Stone, J. A. In "Applications of the Mössbauer Effect in Chemistry and Solid State Physics," *Tech. Rep. Ser. I.A.E.A.* 1966, 50, 179.
16. Stone, J. A. In "Mössbauer Effect Data Index"; Stevens, J. G., Stevens, V. E., Eds.; Plenum: New York, 1972; pp. 33-49.
17. Krankeleit, E. *Rev. Sci. Instrum.* 1964, 35, 194.
18. Cohen, R. L.; Kalvius, G. M. *Nucl. Instrum. Methods* 1970, 86, 209.
19. Reynolds, L. T.; Wilkinson, G. *J. Inorg. Nucl. Chem.* 1956, 2, 246.
20. Kanellakopoulos, B. In "Organometallics of the F-Elements"; Marks, T. J., Fischer, R. D., Eds.; D. Reidel: Dordrecht, Holland, 1979; pp. 1-36.
21. Karraker, D. G.; Stone, J. A. *Inorg. Chem.* 1972, 11, 1742.
22. *Ibid.*, 1979, 18, 2205.
23. Karraker, D. G.; Stone, J. A.; Jones, Jr., E. R.; Edelstein, N. *J. Am. Chem. Soc.* 1970, 92, 4841.
24. Karraker, D. G. *Inorg. Chem.* 1973, 12, 1105.
25. Karraker, D. G.; Stone, J. A. *Inorg. Chem.* 1973, 12, 1105.
26. Baker, E. C.; Halsted, G. W.; Raymond, K. N. *Struct. Bonding (Berlin)* 1976, 25, 23.
27. Shannon, R. D.; Prewitt, C. T. *Acta Crystallogr., Sect. B* 1969, 25, 925.

RECEIVED June 27, 1980.

Characterization of Novel Antimony Compounds by Antimony-121 Mössbauer Spectroscopy

R. V. PARISH and OWEN PARRY

Department of Chemistry, University of Manchester Institute of Science and Technology, Manchester, M60 1QD, England

*The products of reaction of $SbCl_5$ with $R_2C:NH$ and $R_2C:N^+Li^-$ ($R = \text{phenyl or substituted phenyl}$) were investigated. Infrared and ^{121}Sb Mössbauer spectroscopy suggest that three different types of compounds are formed. One type appears to be the ketiminium salt $[R_2C:NH_2][SbCl_6]$ (δ_{InSb} ca. 5.7 mm s^{-1} , e^2qQ_0 zero), presumably formed by adventitious hydrolysis. The second group of products, most surprisingly, are antimony(III) derivatives, probably $[R_2C:NH_2][SbCl_4]$. This oxidation state is indicated unambiguously by the Mössbauer spectra (δ_{InSb} ca. -8 mm s^{-1} , e^2qQ_0 ca. 10 mm s^{-1}), but might otherwise have escaped detection. The final group of compounds has δ_{InSb} ca. 5.3 mm s^{-1} , e^2qQ_0 ca. 10 mm s^{-1} , consistent with the presence of an $Sb-C$ bond, and these materials appear to be the first examples of *o*-metallated derivatives involving antimony, for example, $Ph(\overset{\cdot}{C}_6H_4)C:NHSbCl_4$.*

This investigation arose from a visit to the University of Manchester Institute of Science and Technology by Dr. Ken Wade of Durham University, to describe some work he had been doing on complexes of ketimines, $R_2C:NH$, with main-group acceptors (1). The Durham group also was concerned with the interaction of the ketimines or their lithium derivatives, $R_2C:N^+Li^-$, with $SbCl_5$ (2), and we suggested that ^{121}Sb Mössbauer spectroscopy might aid the characterization of the products. Accordingly, Dr. Wade sent us ten samples for investigation, the Mössbauer data for which were indeed invaluable, as we describe in the following

0065-2393/81/0194-0361\$05.00/0

© 1981 American Chemical Society

sections. A brief review of the Mössbauer technique with ^{121}Sb is given also; more detailed treatments have been presented by Bowen (3), Bancroft and Platt (4), and Greenwood and Gibb (5).

^{121}Sb Mössbauer Spectroscopy

Mössbauer spectroscopy with ^{121}Sb is a frustrating experience. Sources usually have only low activity, and the spectra are complex and inherently poorly resolved. It is tedious to obtain good spectra.

The source material is the 50-year $^{121\text{m}}\text{Sn}$, usually in the form of CaSnO_3 . This isotope is produced by neutron irradiation of ^{120}Sn [$^{120}\text{Sn}(n,\gamma)^{121\text{m}}\text{Sn}$], but the cross section is small and low activities are obtained even after years of irradiation. From the higher-energy state, $^{121\text{m}}\text{Sn}$ decays directly to the 37.2-keV level of ^{121}Sb , which is the Mössbauer-active state. The source also emits considerable x-radiation, centered at 26 keV, and the normal method of detection is to monitor the escape peak (8 keV) of an Xe/CO_2 or Xe/CH_4 proportional counter or a $\text{NaI}(\text{Tl})$ scintillator. In the present work, a high-resolution, hyperpure germanium LEPS detector (Ortec) was used to monitor the 37.2-keV gamma ray directly.

The moderately high energy of the gamma radiation results in relatively small recoil-free fractions, especially for molecular compounds. Measurements normally must be made at liquid-nitrogen temperatures or below. Most of the data reported here refer to 4.2 K. We have worked with a vertical-drive cryostat with both source and absorber immersed in liquid helium. To improve baseline linearity, the source was kept stationary and the Doppler motion was applied to the absorber. Isomer shifts were measured relative to InSb .

The Mössbauer transition is from a ground state with $I = 5/2$ to an excited state with $I = 7/2$. Quadrupole interaction therefore gives an eight-line spectrum (Table I; 12 lines are present if the electric field gradient is not axially symmetric, $\eta \neq 0$). Unfortunately, the natural

Table I. Mössbauer Transitions in ^{121}Sb for $e^2qQ_g = 1.00 \text{ mm s}^{-1}$, $\eta = 0$

Position (mm s^{-1})	Intensity	$ m_I _{(g)}$	$ m_I _{(ex)}$
-0.3936	0.0119	5/2	3/2
-0.2021	0.0714	5/2	5/2
-0.1893	0.0357	3/2	1/2
-0.0936	0.1191	3/2	3/2
-0.0393	0.2143	1/2	1/2
+0.0564	0.1191	1/2	3/2
+0.0850	0.2500	5/2	7/2
+0.0979	0.1786	3/2	5/2

linewidth is large (2.1 mm s^{-1}), and fully resolved spectra are never obtained (see Figure 1). However, the shape of the broad absorption envelope readily reveals the sign of the quadrupole coupling constant (e^2qQ_g ; Q_g is the quadrupole moment of the ground-state nucleus), and a rough estimate of its magnitude usually can be made. Computer fitting must be made with eight lines whose positions are constrained by the isomer shift, e^2qQ_g , and the ratio of ground- and excited-state quadrupole moments $Q_{\text{ex}}/Q_g = 1.34$, while the intensities are constrained to those for a random powder (Table I). It is therefore necessary to grind the samples carefully to avoid orientation effects. If the electric field gradient is not axially symmetric, an appropriate calculation of line positions and intensities must be made, preferably by solution of the quadrupole Hamiltonian (6). In the present work e^2qQ_g is small ($\leq 10 \text{ mm s}^{-1}$), and the shape of the spectrum is relatively insensitive to moderate values of the asymmetry parameter ($< \text{ca. } 0.6$); therefore, we have used only the eight-line fitting procedure. The isomer shift can be determined precisely (ca. $\pm 0.05 \text{ mm s}^{-1}$), but, owing to the poor resolution, e^2qQ_g is much less well defined (ca. $\pm 0.8 \text{ mm s}^{-1}$ or worse).

The shape of the spectrum also can be affected by the thickness of the sample. The optimum thickness is 5–10 mg cm^{-2} of natural antimony. For higher values, saturation effects can occur, giving relative enhancement of the weaker lines. To obtain accurate values of e^2qQ_g under these conditions, the transmission integral described by Shenoy et al. (7) should be used. This procedure enormously increases the computation time, even with Cranshaw's ingenious time-saving modification (8), and should be attempted only after preliminary fitting by the normal method. Using the transmission integral for relatively small values of e^2qQ_g (ca. 10 mm s^{-1}) and samples of moderate thickness results in an approximate 5% decrease in the fitted value (9, 10). The transmission integral was not used in the present work.

For ^{121}Sb , $\delta R/R$ is relatively large and negative. The isomer shift is very sensitive to small electronic changes, and the two oxidation states are well differentiated. Since $\delta R/R$ is negative, antimony(III) gives the more negative isomer shift, and InSb provides a useful rough dividing point—shifts for antimony(III) being more negative than for InSb and those for antimony(V) more positive. For each oxidation state the isomer shift is sensitive to the nature of the groups bonded to the antimony, normally becoming more positive with increasing electronegativity. Typical ranges of values are shown in Table II.

Quadrupole coupling is normally small in antimony(V) unless the ligands differ appreciably in electronegativity, and substantial splittings are seen primarily in organoantimony compounds. The presence of one Sb—C bond (or two in cis positions) gives e^2qQ_g equal to 10–14 mm

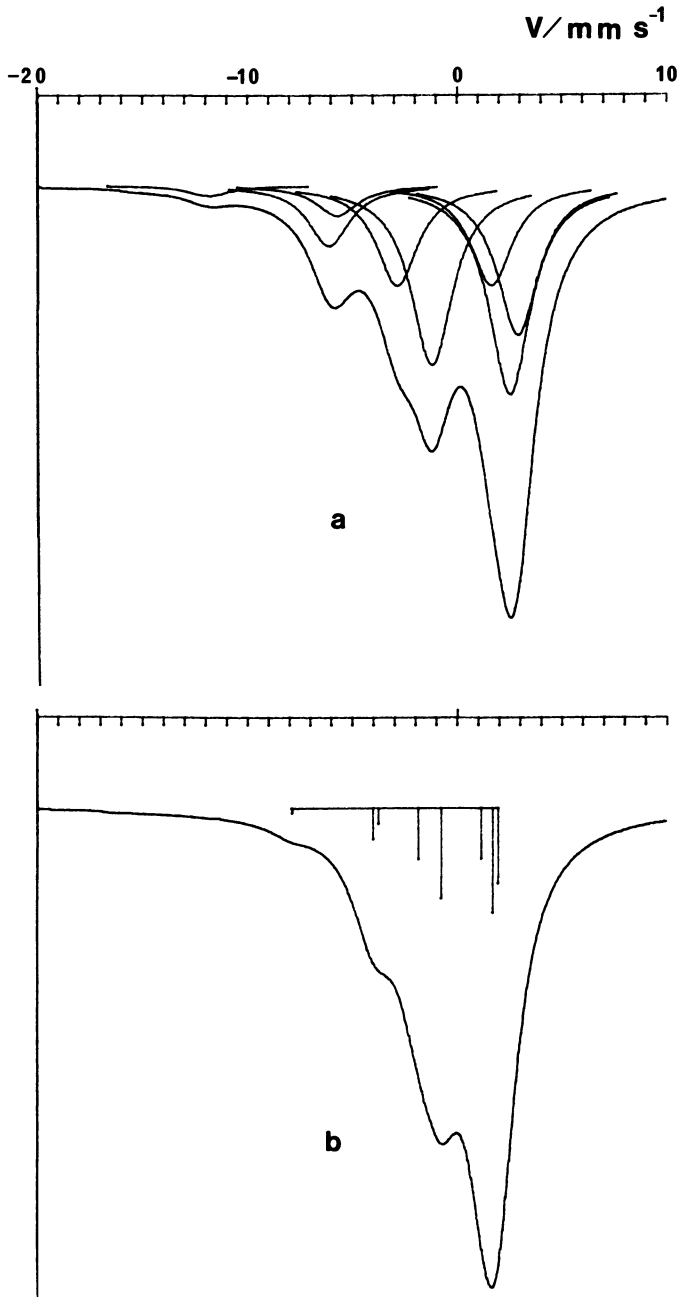


Figure 1. Calculated ^{121}Sb Mössbauer spectra for $\delta = 0$, $\Gamma = 2.4 \text{ mm s}^{-1}$, and $e^2qQ_q = +30 \text{ mm s}^{-1}$ (a) and $+20 \text{ mm s}^{-1}$ (b). In (b) the peak positions are indicated with half intensity. Note the dramatic reduction in resolution as e^2qQ_q decreases.

Table II. Typical Ranges for ^{121}Sb Mössbauer Parameters

	δ_{InSb} (mm s^{-1})	e^2qQ_g (mm s^{-1})
"Inorganic" antimony (III)	-8 to -2	0 to +18
"Inorganic" antimony (V)	+2 to +12	0 to ± 5
Organoantimony (III)	-2 to 0	+15 to +18
Organoantimony (V)	0 to +6	0 to +30

s^{-1} (positive in the first case, negative in the second, because Q_g is negative), and a trans C—Sb—C arrangement gives values of 22–27 mm s^{-1} . Values for particular structures can be estimated by using the point-charge treatment (4). For antimony(III) there is usually a large negative contribution to the electric field gradient from the lone pair, which usually outweighs that from the ligands, and e^2qQ_g values of 5–19 mm s^{-1} are found. The range reflects differences in the hybridization of the antimony atom and the wide variety of structures. In a few compounds containing the SbCl_6^{3-} ion the antimony atom occupies a site of octahedral symmetry; the lone pair is now forced to have 100% 5s character, e^2qQ_g becomes zero, and the isomer shift is reduced correspondingly to about -11 mm s^{-1} (11).

Preliminary Investigation

The ten samples supplied by Dr. Wade were examined initially by infrared spectroscopy. Marked differences were found in the N—H and C=N stretching regions of the spectra, 3000–34,000 cm^{-1} and 1550–1700 cm^{-1} , respectively. On this basis the samples were divided into three groups. The first (Group I, two samples) shows three absorption peaks in the N—H stretching region, at about 1600 and 1660 cm^{-1} . These samples were prepared by direct treatment of SbCl_5 with $\text{R}_2\text{C:NH}$. The second group (II, three samples) has only one strong N—H stretching band, but four peaks in the 1550–1700 cm^{-1} region, of which the one at about 1660 cm^{-1} is of medium-weak intensity. This group, and the third, were obtained by interacting SbCl_5 with $\text{R}_2\text{C:NLi}$. The third group (III, five samples) shows very broad N—H absorption and three broad bands in the C=N region. The shape of the N—H band suggests the hydrogen-bonding effects seen in amine salts. The spectra are thus all more complex than expected for simple adducts of the type $\text{R}_2\text{C:NH} \cdot \text{SbCl}_5$. Representative spectra for samples derived from $\text{Ph}_2\text{C:NH}$ or $\text{Ph}_2\text{C:NLi}$ are shown in Figure 2.

Chemical analysis showed that the compounds of Group I had an Sb:Cl ratio of 1:6, while all the other compounds gave a ratio of 1:4 (Table III). Although analyses for hydrogen are probably the least

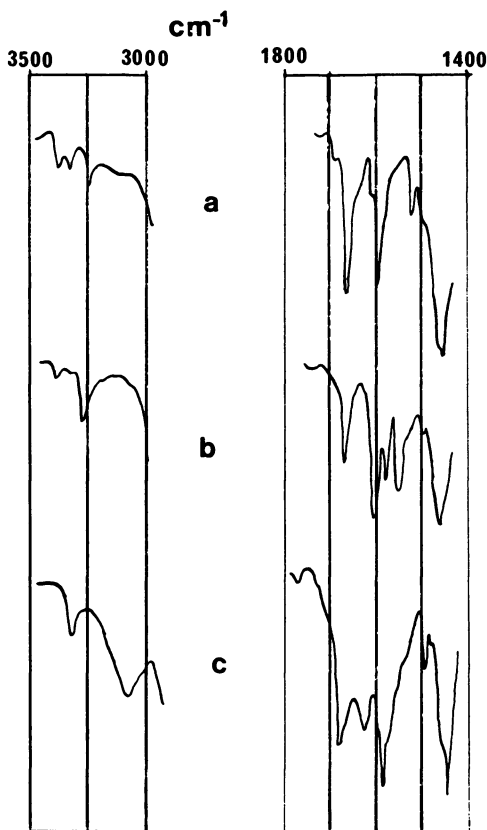


Figure 2. Infrared spectra in the N—H and C=N stretching regions for samples derived from (a) $\text{Ph}_2\text{CNH}/\text{SbCl}_5$, Group I; (b) $\text{Ph}_2\text{CNLi}/\text{SbCl}_5$, Group II; and (c) $\text{Ph}_2\text{CNLi}/\text{SbCl}_5$, Group III

reliable, the atom ratios are consistently higher for Groups I and III, and lower for Group II than expected for the simple adducts $\text{R}_2\text{C}:\text{NH} \cdot \text{SbCl}_5$. Thus, none of the compounds are of this form, confirming deductions made previously from the infrared spectra.

Mössbauer Spectra

The ^{121}Sb Mössbauer spectra also showed differences among the samples, and confirmed the grouping deduced from the infrared spectra. Representative spectra are shown in Figure 3. The compounds of Group I show sharp, symmetrical singlet spectra, centered around $+6 \text{ mm s}^{-1}$. Group II gives a slightly lower isomer shift, but the shape of the absorption envelope clearly demonstrates a small but definite quadrupole

splitting, with e^2qQ_g positive. Thus, these two groups both contain antimony(V), but differ in the symmetry of the antimony environment. The remaining samples, very surprisingly, showed major resonances at about -8 mm s^{-1} , and thus are unambiguously derivatives of trivalent antimony. In two cases additional signals were seen also.

Antimony(III) Species (Group III)

All five samples of Group III showed resonances in the antimony(III) region (Table IV, Figure 4). All have an e^2qQ_g of about $+10 \text{ mm s}^{-1}$ (as explained earlier, these values are accurate to only about $\pm 1 \text{ mm s}^{-1}$). The positive sign is consistent with the presence of a stereochemically active lone pair. From the analytical data it seems likely that these compounds could contain SbCl_4^- anions, and the infrared spectra are also consistent with the presence of $\text{R}_2\text{C:NH}_2^+$ cations. Comparison with the (rather limited) data for other salts of these anions (Table IV) confirms this suggestion and rules out other types of coordination. The identifi-

Table III. Analytical Data for $\text{R}_2\text{C:NH/SbCl}_5$ and $\text{R}_2\text{C:NLi/SbCl}_5$ Products^a

R	Group	% C	% H	% N	% Cl	% Sb
C_6H_5	I	31.6 (14.5)	2.5 13.8	2.9 1.1	38.9 6.1	21.9 1.0)
<i>p</i> - $\text{CH}_3\text{C}_6\text{H}_4$	I	39.4 (21.0)	3.7 23.7	2.5 1.1	35.1 6.3	18.9 1.0)
C_6H_5	II	35.2 (12.9)	2.1 9.3	2.8 0.9	32.5 4.0	(27.4) ^b 1.0)
<i>p</i> - $\text{CH}_3\text{C}_6\text{H}_4$	II	38.1 (15.0)	3.0 14.2	2.9 1.0	29.9 4.0	25.6 1.0)
C_6H_5	II	33.7 (13.0)	2.4 11.1	2.9 1.0	33.4 4.4	26.1 1.0)
C_6H_5	III	34.9 (12.7)	2.7 11.8	3.2 1.0	31.7 3.9	27.8 1.0)
<i>p</i> - $\text{CH}_3\text{C}_6\text{H}_4$	III	37.7 (15.4)	3.4 16.7	2.7 0.9	30.1 4.2	24.7 1.0)
<i>p</i> - FC_6H_4	III	34.8 (14.4)	2.3 11.5	2.8 1.0	27.9 3.9	24.3 1.0)
C_6H_5 , <i>m</i> - $\text{CH}_3\text{C}_6\text{H}_4$	III	35.9 (14.1)	3.2 15.1	2.8 0.9	28.8 3.8	25.6 1.0)

^a Figures in parentheses are the atom ratios.

^b By difference.

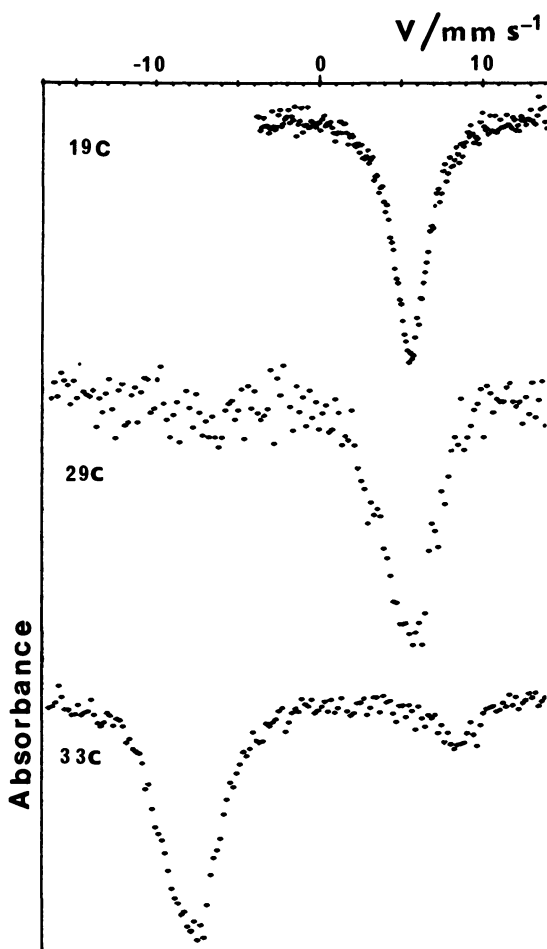


Figure 3. ^{121}Sb Mössbauer spectra for representative compounds of groups I (top), II (middle), and III (bottom)

cation of this oxidation state of the antimony would have been very difficult without the Mössbauer data, and probably would have been overlooked.

Further confirmation was obtained from an electrical conductivity measurement on $[\text{Ph}_2\text{C}:\text{NH}_2][\text{SbCl}_4]$, which behaved as a 1:1-electrolyte in nitromethane ($\Lambda_\infty = 81.4 \text{ S cm}^2 \text{ mol}^{-1}$).

One compound showed slight contamination with an antimony(V) compound, probably an oxide species produced by hydrolysis. The *p*-tolyl compound gave a broad asymmetric spectrum, appearing to require a negative value for e^2qQ_g . This is unusual for antimony(III), although

not unknown (13, 16). However, satisfactory fittings could not be achieved with a negative e^2qQ_g , even by relaxing the $\eta = 0$ constraint. Acceptable fits were obtained by assuming that the spectrum was a composite of two overlapped spectra, each with e^2qQ_g positive. One sub-spectrum showed parameters similar to those of the other compounds of this group. The second component had a more positive isomer shift and probably a larger value of e^2qQ_g (large errors are associated with these values which are close to those reported for SbCl_3). The adduct $R_2C:NH \cdot \text{SbCl}_3$ probably would have similar parameters.

Antimony(V) Species (Group I)

The two compounds of Group I gave sharp singlet Mössbauer spectra (Table V) with small linewidths. Quadrupole coupling must be zero or very small. For the adduct $R_2C:NH \cdot \text{SbCl}_5$, e^2qQ_g would be very small since the ketimine would probably be a relatively poor donor, comparable to Cl^- . Data for related complexes are shown in Table V.

Table IV. ^{121}Sb Mössbauer Data for Antimony(III) Complexes (Group III)

	δ_{InSb}^a (mm s^{-1})	e^2qQ_g (mm s^{-1})	Γ (mm s^{-1})	Ref.
$[\text{Ph}_2\text{CNH}_2][\text{SbCl}_4]$ (77 K)	-8.03 (4)	+8.0 (5)	2.5	
$[\text{Ph}_2\text{CNH}_2][\text{SbCl}_4]$	-8.08 (6)	+10.2 (8)	2.5	
$[(p\text{-FC}_6\text{H}_4)_2\text{CNH}_2]\text{-}$ $[\text{SbCl}_4]^b$	-7.16 (3)	+10.1 (3)	2.6	
$[(m\text{-tol})\text{PhCNH}_2]\text{-}$ $[\text{SbCl}_4]$	-7.92 (2)	+10.2 (2)	2.7	
	(+8.50 (10))	—	2.7 15%	
$[(p\text{-tol})_2\text{CNH}_2]\text{-}$ $[\text{SbCl}_4]$	-7.73 (7)	+8.2 (7)	2.7 60%	
$[\text{Et}_4\text{N}][\text{SbCl}_4]$	-5.29 (11)	+12.8 (10)	2.3 40%	
	-8.17 (10)	+8.9 (20)		12
	-7.47 (10)	+10.6 (10)		13
$[\text{C}_5\text{H}_5\text{NH}][\text{SbCl}_4]$	-8.10 (10)	+11.3 (20)		12
	-7.98 (10)	+9.1 (10)		13
$(\text{NH}_4)_2[\text{SbCl}_5]$	-6.52 (10)	+11.2 (20)		14
$(\text{NH}_4)_3[\text{SbCl}_6]$	-8.7 (2)	0		11
$\text{Cs}_3[\text{SbCl}_6]$	-9.6 (2)	0		11
$\text{PhNH}_2 \cdot \text{SbCl}_3$	-6.3 (1)	+12.0 (10)		15
SbCl_3	-5.24	+12.2		11
	-5.9 (1)	+13.9 (10)		13

^a Figures in parentheses are the standard errors of the fitting procedure.

^b η about 0.9.

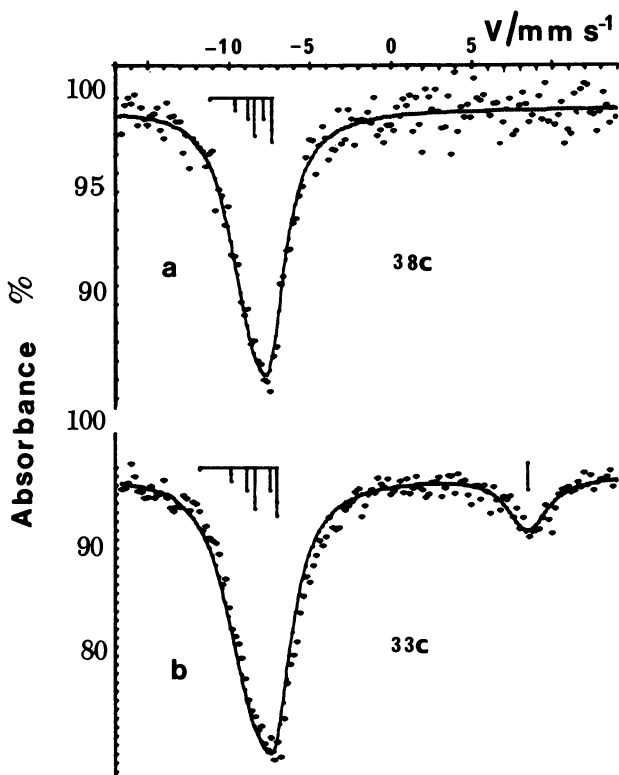


Figure 4. ^{121}Sb Mössbauer spectra of (a) $[\text{Ph}_2\text{CNH}_2][\text{SbCl}_6]$ and (b) $[\text{Ph}(\text{m-tol})\text{CNH}_2][\text{SbCl}_6]$. The bar spectra show the line positions with intensities halved.

Table V. ^{121}Sb Mössbauer Data for Antimony(V) Halide Complexes (Group I)

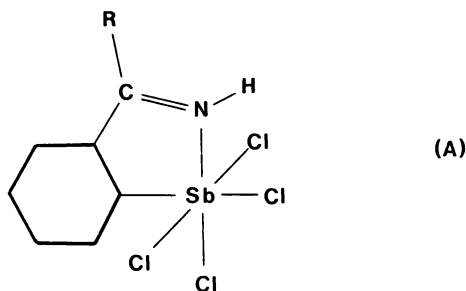
	δ_{InSb} (mm s^{-1})	e^2qQ_{Sb} (mm s^{-1})	Γ (mm s^{-1})	Ref.
$[\text{Ph}_2\text{CNH}_2][\text{SbCl}_6]$	+5.74 (5)	0	2.5	
$[(p\text{-tol})_2\text{CNH}_2][\text{SbCl}_6]$	+5.75 (1)	0	2.5	
$\text{Rb}[\text{SbCl}_6]$	+5.8 (2)	0		11
$\text{SbCl}_5 \cdot \text{DMF}$	+6.6 (2)	0		17
	+6.16 (4)	± 4.5		18
$\text{SbCl}_5 \cdot \text{NCMe}$	+5.9 (2)	0		17
	+5.86 (4)	-6.9 (30)		18
$\text{SbCl}_5 \cdot \text{NCCMe}_3$	+5.85 (6)	-7.23 (44)		18
$\text{SbCl}_5 \cdot \text{NO}_2\text{Me}$	+5.64 (4)	-8.94 (20)		18

However, the analytical data show an Sb:Cl ratio of 1:6, suggesting the presence of SbCl_6^- anions. The Mössbauer spectra are consistent with such a formulation, for which zero quadrupole coupling is expected.

Antimony(V) Species (Group II)

The remaining antimony(V) compounds show distinct quadrupole coupling with a negative electric field gradient (Table VI, Figure 5). This observation requires the presence of at least one ligand that is an appreciably better donor than Cl^- . As shown previously, it is unlikely that $\text{R}_2\text{C:NH}$ would be a sufficiently good donor. The analytical data show that one chloride of SbCl_5 has been replaced, and the method of preparation (from $\text{R}_2\text{C:N}^-\text{Li}^+$) suggests the formulation $\text{R}_2\text{C:NSbCl}_5$. This stoichiometry, involving either five-coordinate or, by dimerization, six-coordinate antimony, would be compatible with the Mössbauer data, with the reasonable assumption that the anion $\text{R}_2\text{C:N}^-$ is a good donor to antimony. Unfortunately, there are no data for comparable compounds with covalent Sb—N bonds.

This formulation is, however, not compatible with the infrared spectrum, which shows a single N—H stretching band. An alternative structure is one in which an Sb—C bond has been formed in an *o*-metalation reaction, for example, Structure A. Similar products have been



found in analogous reactions of tin compounds (1). Bromination, followed by hydrolysis, gave the *o*-bromoketones $\text{RC}_6\text{H}_4\text{COC}_6\text{H}_3\text{BrR}$ ($R = \text{H, Me}$), and the ^1H NMR spectra are consistent with the *o*-metallated structure (2). The only other compounds containing one Sb—C bond for which Mössbauer data are available appear to be the anions PhSbX_5^- (10). The chloro anion has slightly more negative isomer shifts and larger quadrupole coupling constants than the present compounds, but the effects of chelation on the electric field gradient attributable to the ketimine group cannot be assessed.

The diphenyl compound was found to be a nonconductor in nitromethane.

Table VI. ^{121}Sb Mössbauer Data for Organoantimony(V) Compounds (Group II)

	δ_{InSb} (mm s^{-1})	e^2qQ_{Sb} (mm s^{-1})	Γ (mm s^{-1})	Ref.
$\text{Ph}_2\text{CNSbCl}_4$	+5.29 (4)	+10.9 (4)	2.5	
$\text{Ph}_2\text{CNSbCl}_4$	+5.34 (5)	+9.4 (6)	2.4	
$(p\text{-tol})_2\text{CNSbCl}_4$	+5.29 (5)	+9.7 (5)	2.6	
$\text{Ph}_4\text{As}[\text{PhSbCl}_5]$	+4.47 (3)	+11.8 (3)		10
$\text{Me}_4\text{N}[\text{PhSbCl}_5]$	+4.22 (2)	+11.3 (2)		10
$\text{NH}_4[\text{PhSbCl}_5]$	+4.04 (2)	+11.5 (3)		10
$\text{Ph}_4\text{As}[\text{PhSbBr}_5]$	+3.21 (3)	+9.9 (3)		10
$\text{Me}_4\text{N}[\text{PhSbBr}_5]$	+3.46 (4)	+10.8 (4)		10

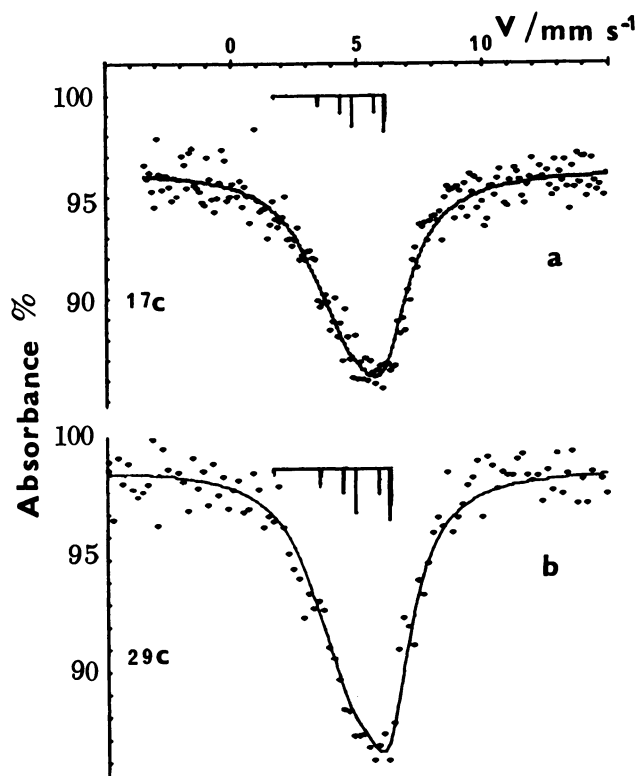


Figure 5. ^{121}Sb Mössbauer spectra of (a) $(p\text{-tol})(\text{CH}_3\text{C}_6\text{H}_4)\text{CNHSbCl}_4$ and (b) $\text{Ph}(\text{C}_6\text{H}_4)\text{CNHSbCl}_4$. The bar spectra show the line positions with intensities halved.

Conclusion

The interaction of $R_2C:NH$ with $SbCl_5$ might be expected to yield the simple adduct $R_2C:NH \cdot SbCl_5$. The properties of the products examined here are consistent with this formulation as ketiminium hexachloroantimonate(V) salts, $[R_2C:NH_2][SbCl_6]$. Thus, the analytical data reveal six chlorine atoms per antimony and a higher hydrogen content than expected for the simple adduct. The Mössbauer spectra indicate an antimony(V) species with high effective symmetry. It would appear that adventitious hydrolysis has occurred during the preparation.

When $SbCl_5$ reacts with $R_2C:NLi$, products of two types are formed. In the majority of cases, reduction to antimony(III) occurs, and the isolated product appears to be a tetrachloroantimonate(III) salt, $[R_2C:NH_2][SbCl_4]$. This formulation is consistent with the analytical data ($Sb:Cl = 1:4$, hydrogen content rather high), with the Mössbauer and infrared spectra, and with the electrical conductivity of the diphenyl compound. The substituted methyleneaminolithium compounds, $R_2C:NLi$, might well function as reducing agents, possibly leading to the ketazine $R_2C:NN:CR_2$, in which case sufficient chlorine is available to form the anion.

In three experiments a substituted antimony(V) species was obtained. Analysis clearly indicated one ketoimino group and four chlorine atoms per antimony, and the Mössbauer spectrum showed an asymmetric environment for the antimony atom with one good donor ligand. The best formulation for these products seems to be as the *o*-metallated derivatives A, which is also consistent with the chemical and NMR evidence (2). It is likely that the compounds are formed by facile rearrangement of the ketimino-antimony intermediate $R_2C:NSbCl_4$, as in the related reactions of tin derivatives (1).

Acknowledgment

The award of an S.R.C. Studentship to Owen Parry is gratefully acknowledged.

Literature Cited

1. Fitzsimmons, B. W.; Othen, D. G.; Shearer, H. M. M.; Wade, K.; Whitehead, G. *J. C. S. Chem. Comm.* 1977, 215.
2. El Arian, A.; Edwards, J. H.; Wade, K.; unpublished data.
3. Bowen, L. H. *Mössbauer Eff. Data Index* 1972, 71.
4. Bancroft, G. M.; Platt, R. H. *Adv. Inorg. Chem. Radiochem.* 1972, 15, 59.
5. Greenwood, N. N.; Gibb, T. C. "Mössbauer Spectroscopy"; Chapman & Hall: London, 1971.
6. Robinette, R.; Cosgrove, J. C.; Collins, R. L. *Nucl. Instr. Meth.* 1972, 105, 509.

7. Shenoy, G. K.; Freidt, J. M.; Maletta, H.; Ruby, S. L. *Mössbauer Eff. Methodol.* **1973**, *9*, 277.
8. Cranshaw, T. E. *J. Phys. (E)* **1974**, *7*, 122.
9. McAuliffe, C. A.; Niven, I. E.; Parish, R. V. *J. C. S. Dalton* **1977**, 1901.
10. Bertazzi, N.; Gibb, T. C.; Greenwood, N. N. *J. C. S. Dalton* **1976**, 1153.
11. Birchall, A.; Della Valle, B.; Martineau, E.; Milne, J. B. *J. Chem. Soc. (A)* **1971**, 1855.
12. Birchall, T.; Ballard, J. G.; Milne, J. B.; Moffett, W. D. *Can. J. Chem.* **1974**, *52*, 2375.
13. Donaldson, J. D.; Southern, J. T.; Tricker, M. J. *J. C. S. Dalton*, **1972**, 2637.
14. Birchall, T.; Della Valle, B. *Can. J. Chem.* **1971**, *49*, 2808.
15. Bowen, L. H.; Taylor, K. A.; Chin, H. K.; Long, G. G. *J. Inorg. Nucl. Chem.* **1974**, *36*, 101.
16. Devart, J. P.; Sanchez, J. P.; Freidt, J. M.; Shenoy, G. K. *J. Phys.* **1974**, *C6*, 35.
17. Vertes, A.; Burger, K. *J. Inorg. Nucl. Chem.* **1972**, *34*, 3665.
18. Freidt, J. M.; Shenoy, G. K.; Burgard, M. *J. Chem. Phys.* **1973**, *59*, 4488.

RECEIVED June 27, 1980.

Application of Iodine-127 Mössbauer Spectroscopy to Some Anions and Cations of Iodine

THOMAS BIRCHALL and RONALD D. MYERS

Department of Chemistry and Institute for Materials Research,
McMaster University, 1280 Main Street West,
Hamilton, Ontario L8S 4M1

Iodine-127 Mössbauer spectra were recorded for a number of cations and anions of iodine. A reasonable correlation was found between the quadrupole coupling constants and ligand electronegativity; however, the fluoro anions deviate from this correlation. Isomer shifts were referenced against H_5IO_6 and a revised empirical relationship between isomer shift and the orbital occupation numbers h_s and h_p was found. It is recommended that CuI be used as a universal standard for both ^{127}I and ^{129}I measurements.

Iodine Mössbauer spectroscopy has been used to obtain information about the structure and bonding of iodine-containing systems, and the results have been reviewed in a number of books (1-4). Two isotopes of iodine are available for study: namely, ^{127}I , the naturally occurring stable isotope in 100% abundance, and ^{129}I , a radioisotope with a half-life of 1.7×10^7 y. By far the greatest use, for chemical studies, has been made of the latter isotope because of the superior resolution that it offers. The excited-state lifetime is $t_{1/2} = 16.8(2)$ ns, which results in a natural linewidth of $2\Gamma_0 = 0.59$ mm s^{-1} for ^{129}I (5), whereas ^{127}I has $t_{1/2} = 1.86(11)$ ns for a natural linewidth of $2\Gamma_0 = 2.54$ mm s^{-1} (6). However, the 129-isotope suffers a disadvantage in chemical investigations since one must carry out chemical reactions with a radioisotope on a small scale, and it is rare that the products of such reactions are chemically analyzed. This disadvantage does not arise for the naturally occurring 127-isotope, and the paucity of chemical studies with this isotope is undoubtedly attributable to the large natural linewidth coupled with the high transition

0065-2393/81/0194-0375\$05.00/0
© 1981 American Chemical Society

energy, 57.60(2) keV. This results in lower recoil-free fractions and necessitates carrying out measurements at liquid-helium temperatures. However, the ground-state quadrupole moment is quite large (-0.79 barn) and $^{127}Q_e/^{127}Q_g = 0.892$ (7), which means that even moderate distortions from cubic symmetry result in some splitting of the spectrum into the eight component lines ($^{127}I_e = 7/2$; $^{127}I_g = 5/2$). Such spectra, even with the large natural linewidths, now can be successfully computer-fitted to give reliable hyperfine parameters. It is important, however, that these programs have a provision for full transmission integral procedures to be applied in the fitting. Such programs have been described previously (8, 9).

Empirical Relationships

The interpretations of the Mössbauer parameters obtained from the ^{127}I spectra, and other nuclei (e.g., ^{129}I , ^{125}Te , ^{129}Xe), have relied heavily on empirical relationships. These have allowed the conversion of isomer shifts and quadrupole coupling constants into s and p orbital populations. For example, U_p , the p electron imbalance, has been related to the measured quadrupole coupling constant by:

$$U_p = \frac{-e^2 q_{\text{mol}}^{127} Q_g / h}{e^2 q_{\text{at}}^{127} Q_g / h} \quad (1)$$

where $e^2 q_{\text{at}}^{127} Q_g / h = 2293$ MHz is the value for an iodine atom, which is known from nuclear quadrupole resonance measurements (10). The isomer shift has been related to h_s and h_p , the magnitudes of the electron holes in the iodine $5s$ and $5p$ orbitals relative to the closed shell of the iodide ion, by:

$$\text{Isomer shift } \delta = K[-h_s + \gamma(h_s + h_p)(2 - h_s)] \quad (2)$$

It has been assumed that $5d$ electrons do not influence the isomer shift parameter. To use Equation 2 one must first evaluate the constants K and γ ; the best value for γ appears to be 0.07 (2, 3, 4). Using the isomer shifts and quadrupole coupling constants obtained from the ^{127}I spectra of HI (anhydrous), I_2 , $\text{K}[\text{ICl}_2] \cdot \text{H}_2\text{O}$, ICl , and $\text{K}[\text{ICl}_4] \cdot \text{H}_2\text{O}$, Perlow and Perlow (11) calculated a value for $2K\gamma$ of -0.56 mm s^{-1} . This leads to the isomer shift expression:

$$\begin{aligned} ^{127}\delta_{\text{ZnTe}} = & -4.0[-h_s + 0.07(h_p + h_s)(2 - h_s)] + 0.16 = \\ & + 3.44 h_s - 0.56 h_p + 0.16 \end{aligned} \quad (3)$$

Equation 3 is then used exclusively to describe the bonding in a wide variety of iodine compounds. Similar expressions are derived for ^{129}I ,

and only occasionally are these simple expressions questioned (12). In establishing Equation 3 it was assumed that no *s* electrons are involved in the bonds to iodine (11). This may not be a good assumption, particularly for anhydrous HI. Also, in establishing the value for $2K\gamma$ there appears to be some question as to which value was used for the isomer shift of iodine. The isomer shift of I_2 relative to I^- was -0.58 mm s^{-1} rather than the -0.74 mm s^{-1} shown in Figure 1 of Ref. 11. However, this error may have been partially compensated for by the fact that the isomer shift for $^{127}I_2$ relative to $Zn^{127m}Te$ measured by Perlow and Perlow (11) appears to be much too negative. This error shows up clearly in the plot of $\delta^{127}I$ vs. $\delta^{129}I$ where it is seen that only I_2 deviates seriously from the best fit to the data (2). Several measurements have been reported for $^{129}I_2$, and all are in reasonable agreement in regard to its isomer shift relative to $Zn^{129m}Te$; a value of 0.9 mm s^{-1} is found (2, 3, 12). Conversion of this value to the ^{127}I equivalent using the data of Jones and Warren (13) gives -0.31 mm s^{-1} for $^{127}I_2$. Relative to the I^- standard of Perlow and Perlow (11), an isomer shift of -0.47 mm s^{-1} is found for $\delta^{127}I_2$ which is much closer to the value used to establish Equation 3, but is much more positive than the measured value. These discrepancies are further complicated by the lack of internal consistency in the original work. For example, the data using the $ZnTe$ source are preferred over those obtained using the H_6TeO_6 source (11), yet it is interesting to note that with the latter source, $\delta I_2 - \delta KI$ is -0.48 mm s^{-1} , which is in rather good agreement with the value calculated from the ^{129}I data.

In view of the uncertainties in some of the reported data that have been used to establish the empirical relationships of Equations 1 and 3, we felt that a reinvestigation of the spectra of a number of simple compounds was warranted. From these measurements we make recommendations as to a suitable reference material against which all ^{127}I chemical shifts would be reported. To test the empirical relationships just mentioned, we have chosen to investigate the $[X-I-Y]^-$ series of anions where *X* and *Y* can be F, Cl, Br, or I. These linear anions provide us with a series of compounds, all with the same geometry about iodine, in which systematic changes in the ligands attached to iodine can be correlated with the Mössbauer parameters. A new isomer shift expression is derived from data that are internally consistent and that correlate exceptionally well with existing ^{129}I measurements.

Experimental

Spectra were recorded using an Elscint AME-40 drive system operating in the constant-acceleration mode with automatic folding of the triangular waveform. The transmitted radiation was detected, amplified, analyzed, and stored in a Tracor-Northern multichannel analyzer operating in the up-down

multiscaling mode. The folded spectra generally were accumulated in 256 channels. The gamma rays were detected using a Harshaw NaI(Tl) 2-mm-thick crystal and matched photomultiplier tube. A somewhat thicker crystal would have been more efficient for the 57.6-keV ^{127}I gamma rays.

Source materials that have been used for ^{127}I measurements are ZnTe, H_6TeO_6 , and Te (11). The telluric acid matrix probably has the highest recoilless fraction of these three materials, but ZnTe is easy to prepare. Mixing the appropriate quantities of zinc and ^{127m}Te (a slight excess of zinc is generally used) in a quartz tube, sealing under vacuum, heating to red heat ($\sim 800^\circ\text{C}$), and subsequent slow cooling produces good crystals of $\text{Zn}^{127m}\text{Te}$. These can then be finely powdered and pressed into a suitable source holder. If one has access to a high flux reactor then sources are easily produced. However, good quality sources are commercially available, and we have used sources purchased from New England Nuclear that have proved to be very satisfactory. A nominally 10-mCi $\text{Zn}^{127m}\text{Te}$ source was used for most of the measurements reported here.

Samples were finely ground powders, intimately mixed with boron nitride, or alumina, and sandwiched in a copper ring (i.d. 18 mm) between thin aluminum foils. The samples contained approximately 30 mg of iodine cm^{-2} . Both source and sample were immersed in liquid helium (4.2 K) in a research cryostat manufactured by the Janis Research Company. This was equipped with a Cryogenic Research Company temperature controller, which in these measurements was used solely to ensure that the source and sample were immersed in liquid helium: a calibrated Allen-Bradley 47-ohm, $\frac{1}{4}$ -watt carbon resistor was used to monitor the temperature. The source-detector distance was 10 cm, which resulted in 57.6-keV gamma-ray count rates that varied from 5 to 10 counts s^{-1} channel $^{-1}$, depending upon the chemical composition of the absorber. The velocity scale was calibrated using an iron foil absorber against a $^{57}\text{Co}/\text{Rh}$ source.

All spectra were computer-fitted using a program previously described (9) that incorporates full transmission integral procedures. In the fitting procedure, the source linewidth was fixed at the natural value, $\Gamma_{\text{nat}} = 1.27 \text{ mm s}^{-1}$, while the absorber linewidth was allowed to vary: in the quadrupole split spectra the individual lines were constrained to have equal but variable width. The isomer shift, quadrupole coupling constants, η , and thickness (T_a) were allowed to vary, though in the initial fitting stages η was fixed at zero and allowed to go free only in the later stages. When two iodine sites were present, the intensities of the two sites were initially assumed to be equal to the atomic ratios in the molecule, but this constraint was later removed since it is unlikely that the different iodine sites would have the same recoil-free fractions. This generally resulted in an improvement in the value of $\chi^2/\text{degree of freedom}$.

Isomer Shift Calibration

The chemical isomer shift is given by:

$$^{127}\delta = A \{ |\psi_s(0)|_A^2 - |\psi_s(0)|_S^2 \} \frac{\delta R}{R} \quad (4)$$

where A is a constant, $\{ |\psi_s(0)|_A^2 - |\psi_s(0)|_S^2 \}$ is the difference in s electron density between absorber and source, and $\delta R/R$ is a nuclear

term that depends on the difference in nuclear radii of excited and ground states. Various estimates of $\delta R/R$ exist ranging from -5.6×10^{-5} to -4.8×10^{-4} (14, 15). There appears to be no general agreement as to the absolute value for $\delta R/R$, but at least all agree upon the sign being negative. This means that increases in chemical isomer shift correspond to decreases in *s* electron density at the ^{127}I nucleus.

To interpret isomer shift data and to compare new data with old, it is necessary that some suitable reference substance be chosen to serve as a universal standard. Agreement on the reporting of isomer shift data appears to be universal for ^{57}Fe , ^{119}Sn , and ^{121}Sb , but this is not so for ^{127}I or ^{129}I . Previous workers have reported shifts relative to the source used, and although the sources may be nominally the same the quality might vary considerably. This makes it very difficult to compare data from one laboratory to another, particularly for ^{127}I , where the shifts are much smaller than the natural linewidth. Stevens (16) has collected shift data for the various isotopes in an attempt to provide reliable values.

The following criteria determine the usefulness of a material as a reference substance:

1. It must be a single line absorber, that is, the nucleus of interest must be in a cubic environment.
2. The linewidth should be as close to natural as possible.
3. The compound must be stable and easily obtainable.
4. The recoil-free fraction should be high, and any other elements present in the compound should not be strong gamma-ray absorbers.

We attempted to prepare a sample of $\text{Na}_3\text{H}_2\text{IO}_6$ which has been suggested as a possible reference substance. Two preparative procedures were tried: oxidation of $[\text{IO}_3]^-$ with chlorine in strongly basic (NaOH) solution resulted in the disodium salt; titration of H_5IO_6 with NaOH , followed by crystallization also failed to yield the trisodium salt. Indeed a pH titration of H_5IO_6 shows that two protons are removed easily, and only at high pH are two more protons titrated. Therefore, the disodium salt appears to be the most likely product in a simple acid-base reaction. It is interesting to note that the x-ray measurements on the $[\text{IO}_6]^{5-}$ ion were in fact carried out on the diammonium salt (17). None of the previous workers who used $\text{Na}_3\text{H}_2\text{IO}_6$ indicate the origin of the compound. In view of the uncertainty of its composition, $\text{Na}_3\text{H}_2\text{IO}_6$ does not appear to be a suitable reference material.

It has always been assumed that the iodine environment is octahedral in the $[\text{IO}_6]^{5-}$ ion and tetrahedral in the periodate ion $[\text{IO}_4]^-$. However, Helmholtz (17) reports different iodine-oxygen bond lengths in $[\text{NH}_4]_2\text{[H}_3\text{IO}_6]$, but because of the large errors in those lengths, the iodine environment was described as octahedral within experimental error. In

the case of the periodate ion, the arrangement about iodine is described as disphenoid tetrahedral within the error of the measurement (18). It would appear that more accurate x-ray measurements should be made on these materials to accurately establish the geometry at iodine. The alkali metal iodides would be suitable references were it not for the difficulty of obtaining them in an anhydrous form and for the fact that they are easily oxidized to iodine. Any iodine reference should be usable for both ^{127}I and ^{129}I measurements. Again alkali iodides would appear to be convenient for 129 measurements since the radioisotope is commercially available in this form, but unfortunately only in solution. However, this is easily converted to Cu^{129}I in a pure form which can be easily dried and is very stable; the iodine environment is reportedly tetrahedral, suggesting that this would be a possible reference material for both 127 and 129 measurements.

Currently we are examining several of these substances but so far we are only able to report data for H_5IO_6 . These have been fitted to a single line although the linewidth Γ_{nat} is rather on the high side at 2.46 mm s^{-1} , suggesting that the iodine environment may be distorted slightly. We have chosen to use this as our reference zero but it is clear that careful measurements must be made on the other substances discussed.

Results and Discussion

Our results have been separated into Tables I and II. Table I contains data for iodine, iodine cations, and H_5IO_6 , while Table II contains results for the $[\text{X—I—Y}]^-$ series of compounds. In these tables we also include literature data for $\text{K}[^{127}\text{ICl}_2] \cdot \text{H}_2\text{O}$, $^{127}\text{I}_2$ (11), as well as some ^{129}I data (3, 12) for comparison purposes. Various comparisons

Table I. ^{127}I Mössbauer Data for

Compound	Isomer Shift (mm s^{-1})	$e^2q^{127}\text{Q}_g/h$ (MHz)	η
I_2	-1.30 ± 0.04	-2193 ± 18	0.17 ± 0.04
	-1.28 ± 0.13^a	-2238 ± 20	0.12 ± 0.02
	-1.60 ± 0.04^b		
$[\text{I}_2][\text{Sb}_2\text{F}_{11}]$	-1.38 ± 0.03^a	-2154 ± 18	0.16 ± 0.03
	-1.12 ± 0.05	-1858 ± 36	0.08 ± 0.11
$[(\text{C}_5\text{H}_5\text{N})_2\text{I}]\text{NO}_3$	-1.62 ± 0.03	-3159 ± 18	0.08 ± 0.04
	-1.64 ± 0.03^a	-3239 ± 20	0.03 ± 0.03
$\text{IO}_2\text{F}_3 \cdot \text{SbF}_5$	-0.23 ± 0.03	$+308 \pm 90$	—
H_5IO_6	0	0	—
	$(+1.03 \pm 0.09)^d$		
$\text{Na}_3\text{H}_2\text{IO}_6$	$(+1.02 \pm 0.01)^b$		

^a Ref. 11 (H_6TeO_6 source).

^b Ref. 11 (ZnTe source).

of ^{127}I and ^{129}I isomer shifts have been made (2, 13), and we find that our data correlate quite well with those of Jones and Warren (13). They find the ratio $\delta^{127}\text{I}/\delta^{129}\text{I}$ to be -0.345 , and we have used this value to convert ^{129}I chemical shifts to their ^{127}I equivalents when we need to make a comparison.

Iodine and the $[\text{I}_2]^+$ Cation

Comparing our data for iodine (I_2) with the literature data measured at 4.2 K one notes (Table I) that there is excellent agreement for $e^2q^{127}\text{Q}_g/h$ and η parameters, but poor agreement with the value for the isomer shift. This value has been accepted to be -0.58 mm s^{-1} relative to ZnTe , or -1.60 mm s^{-1} relative to $\text{Na}_3\text{H}_2\text{IO}_6$ (11). We find a value of -1.30 mm s^{-1} relative to H_5IO_6 , which is the same as that measured by Perlow and Perlow (11) (-1.28 mm s^{-1} relative to $\text{Na}_3\text{H}_2\text{IO}_6$) using a telluric acid source. Our value agrees well with the ^{129}I data after conversion to this ^{127}I equivalent.

Oxidation of iodine with antimony pentafluoride produces $[\text{I}_2]^+[\text{Sb}_2\text{F}_{11}]^-$, whose vibrational spectra and x-ray crystal structure have been reported (19). The Mössbauer spectrum shows the same shape as for iodine, indicating a negative value for the quadrupole coupling constant. Both the isomer shift and the quadrupole coupling constant are less negative than for I_2 . Since $\delta R/R$ is negative for ^{127}I , the more positive isomer shift for $[\text{I}_2]^+$ means that the s electron density at iodine has decreased. The most reasonable interpretation of the changes on oxidation is to be found in a simple molecular orbital description of the bonding. In I_2 there is one net $\sigma(p_z)$ bond and the highest energy orbitals that are filled are a degenerate set of π_g^* antibonding orbitals of p_x and p_y char-

Iodine and Some Iodine Ions

T_a	Γ (mm s^{-1})	U_p	h_p ($h_s = 0$)	h_p ($h_p = U_p$)
1.85 ± 0.15	1.04 ± 0.07	0.96	0.80	0.03
1.67 ± 0.18	1.01 ± 0.96	0.81	0.44	0.06
1.42 ± 0.10	1.69 ± 0.10	1.38	1.44	-0.01
2.87 ± 0.26	0.82 ± 0.05			
2.46 ± 0.33	0.11 ± 0.01			

^c Ref. 12 (converted from ^{129}I data).

^d Isomer shift of H_5IO_6 relative to ZnTe source.

Table II. ^{127}I Mössbauer Data and Orbital

Compound	Isomer Shift ^a (mm s^{-1})	$e^2q^{127}Q_0/h$ (MHz)	η
$\text{Cs}[\text{I}_3]$	-1.64 ± 0.04^b	-2515 ± 20	
	-1.29 ± 0.04^b	-1460 ± 14	
	-1.16 ± 0.04^b	-820 ± 25	
$[(\text{CH}_3)_4\text{N}][\text{BrI}_2]$	-1.81 ± 0.11	-2583 ± 55	
	-0.64 ± 0.13	-1580 ± 75	
$[(\text{C}_2\text{H}_5)_4\text{N}][\text{ClI}_2]$	-1.40 ± 0.07	-2769 ± 37	
	-1.22 ± 0.12	-1264 ± 75	
$[(\text{CH}_3)_4\text{N}][\text{BrICl}]$ $\text{K}[\text{ICl}_2] \cdot \text{H}_2\text{O}$	-1.42 ± 0.05	-3048 ± 18	
	-1.28 ± 0.04^c	-3189 ± 20	
$\text{Cs}[\text{ClIF}]$ $\text{Cs}[\text{BrIF}]$	-1.64 ± 0.05	-3029 ± 36	0.16 ± 0.03
	-1.53 ± 0.05	-2769 ± 18	0.24 ± 0.02
$[(\text{C}_2\text{H}_5)_4\text{N}][\text{IBr}_2]$ I^-	-1.36 ± 0.05	-2695 ± 36	0.19 ± 0.03
	-0.86^c		

^a Isomer shifts are measured relative to H_5IO_6 .

^b Ref. 19 (converted from ^{129}I data).

acter. Oxidation results in the removal of a π_g^* electron with a net increase in the p bond order, and the iodine-iodine distance shortens from 2.66 to 2.55 Å (19). This increase in p -bonding electron density shields the s electrons, reduces the s electron density, and makes the isomer shift more positive. Removal of this antibonding π electron means that the iodine-iodine bond in $[\text{I}_2]^+$ has acquired π character. The p electron imbalance U_p is related to the electron occupation numbers U_x , U_y , U_z of the p_x , p_y , and p_z orbitals by Equation 5 (2, 3, 10). For each iodine in I_2 ,

$$U_p = -U_z + \frac{U_x + U_y}{2} \quad (5)$$

becomes equal to $-U_z + 2$, while for $[\text{I}_2]^+$, $U_p = -U_z + 1.75$. In our fitting procedure the small value found for η has a large error associated with it and hence we assume that $U_x = U_y = 1.75$. Therefore, U_p is reduced, and we observe a decrease in the quadrupole coupling constant from -2193 MHz for I_2 to -1858 MHz for $[\text{I}_2]^+$. Using Equation 1 this leads to a value of 0.81 for U_p and U_z is therefore $1.75 - 0.81 = 0.94$. These values for U_x , U_y , and U_z give us a value for h_p , the number of p holes, from Equation 6 (2),

$$h_p = 6 - (U_x + U_y + U_z) \quad (6)$$

of 1.56. Calculation of h_p from Equation 3 gives a value of 0.43, not in very good agreement with the h_p value estimated here.

Occupation Numbers for $[X-I-Y]^-$ Anions

Γ ($mm\ s^{-2}$)	T_a	U_p	h_p ($h_s = 0$)	h_p ($h_p = U_p$)
		1.10	1.48	-0.06
		0.64	0.78	-0.02
		0.36	0.52	-0.03
1.43 ± 0.20	0.84 ± 0.09	1.13	1.82	-0.11
1.43 ± 0.20		0.69	-0.52	0.20
1.47 ± 0.17	1.49 ± 0.14	1.21	1.00	0.03
1.47 ± 0.17		0.55	0.64	-0.01
1.58 ± 0.14	1.49 ± 0.10	1.33	1.04	0.05
		1.39	0.76	0.10
			1.40	0.00
2.47 ± 0.17	1.45 ± 0.07	1.32	1.48	-0.03
2.25 ± 0.16	1.75 ± 0.09	1.21	1.26	-0.01
1.95 ± 0.17	1.21 ± 0.08	1.18	0.92	0.04

^c Ref. 10 (H_6TeO_6 source).

^d Ref. 10 (ZnTe source).

Dipyridine Iodine(I) Nitrate

The isomer shift of $[I(py)_2]NO_3$ is more negative than I_2 or I^- indicating a higher s electron density at the iodine nucleus. It is clear from this that the electron removed to produce the cation cannot be a $5s$ electron and that the bonds to pyridine are largely of p , with perhaps some d , character. A large negative quadrupole coupling constant (Figure 1) is observed that is slightly smaller than that found by Jones (12) from measurements made with the 129 isotope. The p electron imbalance, estimated from the coupling constant, is quite large at 1.38 and is to be expected from an iodine cation linearly coordinated by two electro-negative pyridine nitrogens. Electron density of s and p character in the $x-y$ plane, under the influence of the positive charge, is contracted, leading to a higher s electron density and thus accounting for the negative isomer shift.

 $IO_2F_3 \cdot SbF_5$

It has been suggested that IO_2F_3 is an oxygen-bridged trimer (20) with three terminal fluorines, one doubly bonded oxygen, and two bridging oxygens around each iodine. The iodine sits in a distorted octahedral geometry. This molecule behaves as a Lewis acid in forming an adduct with SbF_5 which is probably polymeric. We have examined the Mössbauer spectrum of this adduct in an attempt to obtain some information about the geometry at iodine. The spectrum shown in Figure 2 is a somewhat quadrupole-split line at relatively high isomer shift

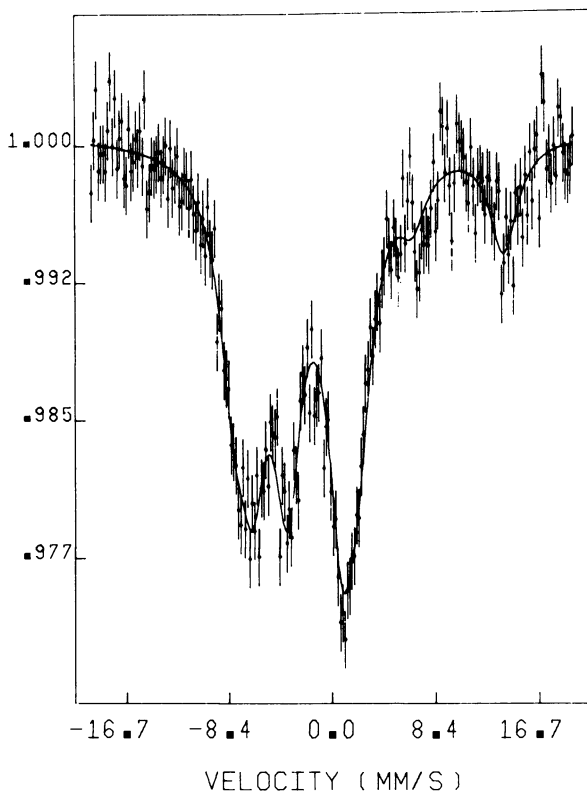


Figure 1. The ^{127}I Mössbauer spectrum of $[(\text{C}_5\text{H}_5\text{N})_2\text{I}]\text{NO}_3$ at 4.2 K

characteristic of an iodine (VII) species. It would appear from the spectrum that the quadrupole coupling constant is positive. This suggests that the oxygen bridged arrangement for the $[\text{IO}_2\text{F}_4]$ unit may well be in a trans configuration. Further measurements are being carried out on these and related iodine oxyfluoride systems.

Polyhalide Anions $[\text{X—I—Y}]^-$

Relatively few anions of this type have been studied by Mössbauer spectroscopy. Early work on $[\text{}^{127}\text{I}\text{Cl}_2]^-$ revealed well-resolved spectra (11) while studies of $[\text{I}_3]^-$ gave well-resolved spectra only when the 129 isotope was employed (3, 21). We have examined all of the possible $[\text{X—I—Y}]^-$ species, where X and/or Y may be F, Cl, Br, or I, except $[\text{I}_3]^-$ and $[\text{ICl}_2]^-$. The data are summarized in Table II where we have included ^{129}I data for $[\text{I}_3]^-$ (3), and $[\text{}^{127}\text{I}\text{Cl}_2]^-$ data (11). All of these anions are essentially linear. The structures of $\text{Cs}[\text{I}_3]$ (22), $\text{Cs}[\text{I}_2\text{Br}]$

(23), and $\text{Cs}[\text{IBr}_2]$ (24) have been reported, and vibrational spectroscopy has been used to infer linearity in a number of other instances (25). The Mössbauer data for $\text{Cs}[\text{F—I—Cl}]$ and $\text{Cs}[\text{F—I—Br}]$ are the first spectroscopic evidence for the existence of these ions, the preparations of which have been described (26). We were unable to synthesize $\text{Cs}[\text{F—I—I}]$.

Figure 3 shows the spectrum of $[(\text{CH}_3)_4\text{N}][\text{BrICl}]$ which is typical of all of these anions apart from those containing two iodine sites. All of the spectra are similar, with the line attributable to transition number 2 (1, 2) being well-resolved at high positive velocity. This means that the quadrupole coupling constant is negative for all of these compounds as would be expected for a central iodine with the X and Y halogens along the z axis and the nonbonding electron pairs in the x-y plane.

It is apparent from Table II that the quadrupole coupling constant for the central iodine increases with the electronegativities of the terminal halogens. For example, $e^2q^{127}Q_e/h$ for $[\text{I}_3]^- < [\text{IBr}_2]^- < [\text{ICl}_2]^-$ and

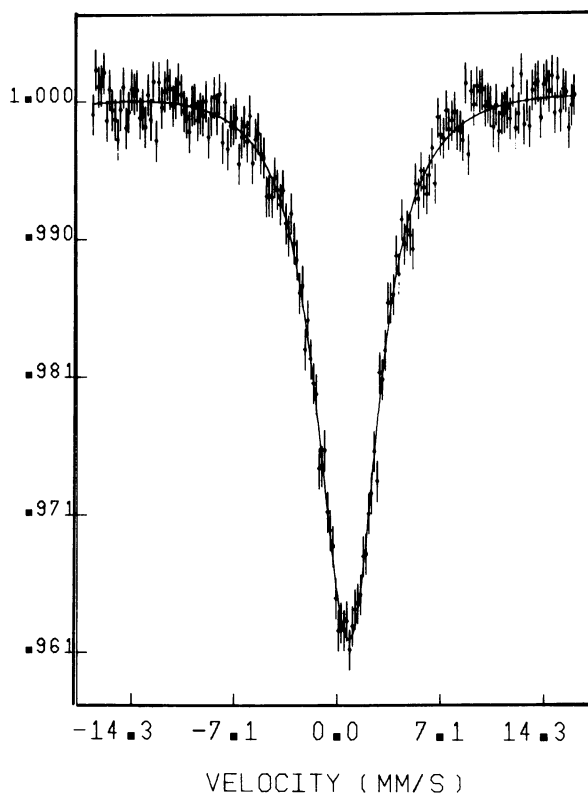


Figure 2. The ^{127}I Mössbauer spectrum of $\text{IO}_2\text{F}_3 \cdot \text{SbF}_5$ at 4.2 K

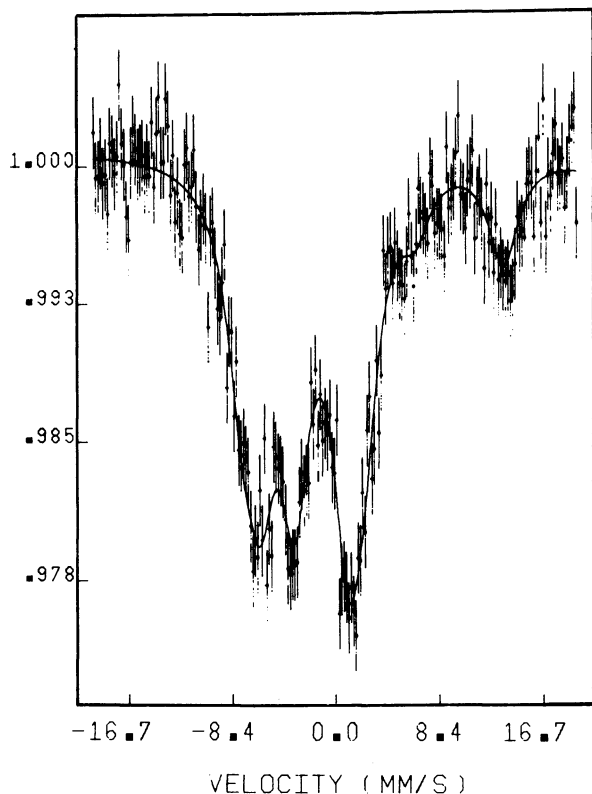


Figure 3. The ^{127}I Mössbauer spectrum of $[(\text{CH}_3)_4\text{N}][\text{BrICl}]$ at 4.2 K

$[\text{I}_3]^- < [\text{I}_2\text{Br}]^- < [\text{I}_2\text{Cl}]^-$. Only the fluoro anions do not follow this pattern. These trends are further illustrated in Figure 4 where we plotted U_p against the sum of the electronegativities of the terminal halogens. We used Pauling electronegativities, though a similar correlation is obtained using the Allred–Rochow values. The fluoro anions $[\text{FICl}]^-$ and $[\text{FIBr}]^-$ both deviate markedly from the least-squares fit, having much lower quadrupole coupling constants and hence U_p values than would have been expected. In fact, their quadrupole coupling constants are about 100 MHz smaller than the parent ICl and IBr molecules (26). In β -ICl there is, in addition to the short I—Cl bond (2.351 Å), another longer I—Cl bond (2.939 Å), which is almost colinear with the first. Other I—Cl molecules in the crystal have an iodine atom, rather than a chlorine atom, colinear with the ICl bond, and therefore, there are two iodine environments in this crystal (27). A similar situation applies in α -ICl (28). The first of these iodine sites should have a quadrupole coupling constant similar to that in $[\text{ICl}_2]^-$ while the other

should resemble that of the central iodine in $[\text{I}_2\text{Cl}]^-$. In the ^{129}I Mössbauer spectrum of ICl , Pasternak and Sonnino (26) attribute additional lines to impurities, but perhaps these were in fact from the other site. A similar interaction, though probably weaker, is also likely in IBr . The diatomic molecule IF is not isolable, probably because of the weakness of the $\text{I}-\text{F}$ bond and the stability of the disproportionation products. Thus, when the reaction between ICl and CsF takes place to produce

$\text{Cs}[\text{FICl}]$, the secondary bond in ICl ($\text{Cl}-\overset{1\text{ry}}{\text{I}}-\overset{2\text{ry}}{\text{Cl}}^-$) is replaced by a much weaker $\text{I}-\text{F}$ interaction. It is also likely that the F^- would interact with more than one ICl molecule so that its potential electronegativity is not reached and the withdrawal of electron density along the bonding axis is less than expected. A similar situation probably pertains to $\text{Cs}[\text{FIBr}]$. The fluoro anions also show significantly higher asymmetry parameters than the other compounds. This could mean that these fluoro anions are not linear or that additional interactions with the iodine atom exist that are off the z axis. These latter interactions could arise from the fluorine bridging just suggested. However, because the quadrupole coupling constant is still large and negative we can take this as good evidence that the $\text{F}^- \text{---} \text{IX}$ ($\text{X} = \text{Cl}, \text{Br}$) interaction is pre-

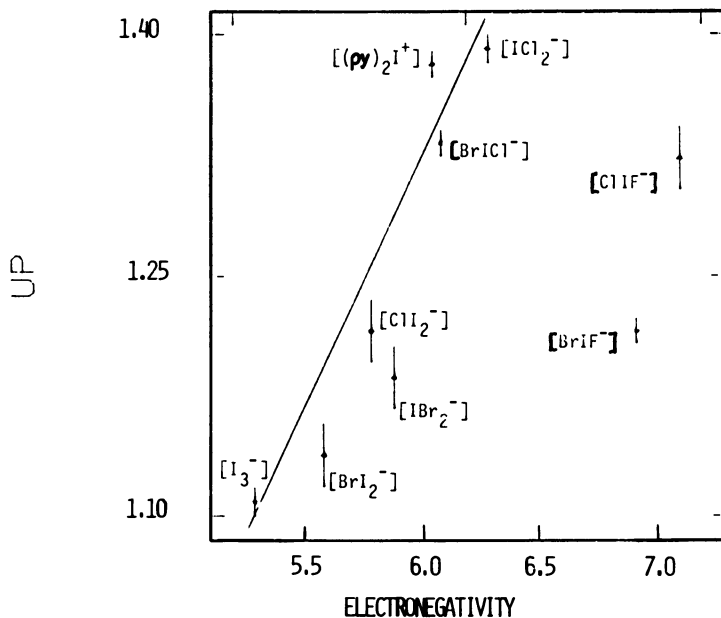


Figure 4. Plot of U_p vs. the sum of the Pauling electronegativities of the terminal halogens $[\text{X}-\text{I}-\text{Y}]^-$. The line drawn is the best least-squares fit to the data excluding the fluoro anions.

dominately a linear one as in the well-characterized anions $[I_3]^-$ (22), $[I_2Br]^-$ (23), and $[IBr_2]^-$ (24).

In the iodine-chlorine series of compounds it was claimed that the quadrupole coupling was attributable entirely to the I—Cl bond (26). Jones (12) has already commented upon this and our results clearly show that the quadrupole coupling depends upon the nature of all coordinated ligands. For example, quadrupole couplings for anions containing an I—I bond range from -2515 MHz to -2769 MHz, for an I—Br bond from -2585 MHz to -3048 MHz, and for an I—Cl bond from -2765 MHz to -3189 MHz.

Isomer shift data are much harder to interpret than are the quadrupole coupling constants. Unlike the latter, the isomer shifts depend upon the source, the reference compound used, and upon whether the source and absorber are at the same temperature. Since our data are internally consistent and are in substantial agreement with ^{129}I shifts, where they are available, it should be possible to evaluate the isomer shifts in terms of the empirical relationships referred to earlier. We have included the ^{129}I shifts for $Cs[I_3]$ reported by de Waard and Spanhoff (29) after converting them to their 127 equivalents by multiplying by -0.345 as indicated earlier.

To evaluate the constants in Equation 2 isomer shift is usually plotted against U_p for a series of compounds. If the bonding is of p character only, then $U_p \equiv h_p$ and Equation 2 reduces to Equation 7,

$$\delta = 2K\gamma h_p \quad (7)$$

and a plot of δ vs. h_p (i.e., U_p) gives a line of slope $= 2K\gamma$. Since $\gamma = 0.07$ (2, 4, 30), the value for K may be calculated. We have plotted the isomer shift data against U_p in Figure 5, the straight line representing a least-squares fit to all the data. The slope of this line is -0.50 ± 0.09 mm s^{-1} with an intercept of -0.90 ± 0.1 mm s^{-1} . In view of the scatter of the data, the intercept is gratifyingly close to the measured shift for I^- , namely, -0.86 mm s^{-1} relative to $[IO_6^{5-}]^-$ (11). The slope of the line is more positive than that usually accepted, -0.56 mm s^{-1} (11), but identical to Ehrlich and Kaplan's value of -0.50 mm s^{-1} (30). A slightly smaller value, -0.48 mm s^{-1} , also has been used by Pasternak and Sonnino (26). Hence the value of K is -3.57 mm s^{-1} and Equation 2 becomes

$$\begin{aligned} {}^{127}\delta_{I^-} &= -3.57 [-h_s + 0.07(h_p + h_s)(2 - h_s)] \\ &= +3.07 h_s - 0.50 h_p \end{aligned} \quad (8)$$

or

$${}^{127}\delta_{[IO_6^{5-}]^-} = +3.07 h_s - 0.50 h_p - 0.90 \quad (9)$$

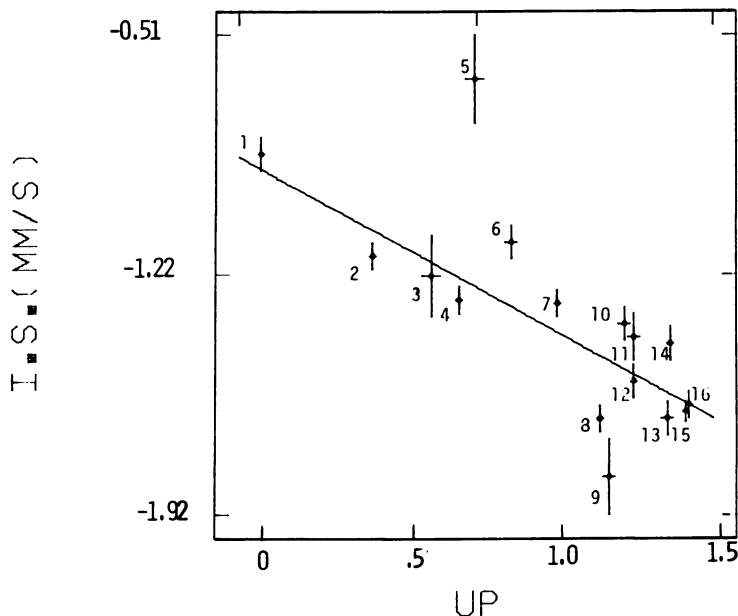


Figure 5. Plot of isomer shift vs. U_p .

The line drawn is the best least-squares fit to the data. (1) I^- ; (2) $[I-I-I]^-$; (3) $[Cl-I-I]^-$; (4) $[I-I-I]^-$; (5) $[Br-I-I]^-$; (6) $[I_3]^+$; (7) I_2 ; (8) $[I-I-I]^-$; (9) $[Br-I-I]^-$; (10) $[IBr_2]^-$; (11) $[Cl-I-I]^-$; (12) $[Br-I-F]^-$; (13) $[Cl-I-F]^-$; (14) $[Br-I-Cl]^-$; (15) $[(py)_2I]^+$; (16) $[ICl_2]^-$.

It is apparent from Figure 5 that there is a considerable scatter of these data. For $[I_3]^-$ and $[ICl_2]^-$, uncertainty either in the referencing of the literature shifts and/or their conversion from ^{129}I data could be the cause of their deviation from the straight line, but it would appear that -1.60 mm s^{-1} is the more correct value for $K[ICl_2] \cdot H_2O$. The largest deviations are observed for the two sites in $[Br-I-I]^-$ where the two isomer shifts are strongly correlated in the fitting procedure. If these two isomer shifts are constrained to be equal, an isomer shift value of -1.36 mm s^{-1} is found which correlates better with the line drawn. However, there is no reason to expect these two shifts to be the same, and indeed a lower χ^2 is obtained when the two isomer shifts are allowed to go free in the fitting procedure. Perhaps a ^{129}I spectrum should be recorded for this anion in order to obtain better resolution and thereby check this point. The fluoro anions also deviate slightly, but this probably can be attributed to additional interactions between anions via fluorine bridges, as discussed previously for the quadrupole coupling constants. Equation 9 then can be used to calculate h_p , assuming that $h_s = 0$, or to estimate h_s by equating h_p and U_p , and these calculated values are listed

in the tables. One can see that there is little agreement between the values for U_p and h_p calculated this way. The difference between these two parameters cannot be accounted for by attributing either s involvement or π character to the bonds. Negative values for h_s can have no meaning, while π character to the bonding is usually invoked when $h_p > U_p$; yet the only compound studied where π character is clearly involved, for example, $[\text{I}_2]^+[\text{Sb}_2\text{F}_{11}]^-$, has $h_p < U_p$.

Conclusions

We have demonstrated that one can obtain useful chemical information from Mössbauer measurements with the ^{127}I isotope. This isotope clearly offers advantages over the radioisotope ^{129}I from a preparative point of view. In the $[\text{X}-\text{I}-\text{Y}]^-$ series we found a reasonable correlation between the quadrupole coupling constants and the electronegativities of the attached ligands. The exceptions to this appear to occur with the fluoro systems where intermolecular interactions seem likely via fluorine bridges.

From these data we abstract a revised value for the constant K which leads to a new correlation between the isomer shift and the number of s and p holes in the iodine valence shell. The assumption that only p bonding occurs in these iodine systems may not be a good one since the occupation numbers calculated from the quadrupole coupling constants and the isomer shifts do not, in general, agree very well. It appears that other systems in which the geometry remains the same but where systematic changes can be made to the ligands attached to the central iodine need to be examined to further test these empirical relationships. One such system would be based on the square planar $[\text{IX}_4]^-$ ion, and we are currently examining such a series of compounds.

Finally, one standard isomer shift reference compound must be chosen for both ^{127}I and ^{129}I isomer shifts. Careful measurements must be made on some simple compounds to determine their linewidths and recoil-free fractions very accurately. From a chemical point of view it would appear that cuprous iodide, CuI , is the best choice. We are in the process of carrying out such measurements.

Acknowledgments

The Natural Sciences and Engineering Research Council of Canada is thanked for financial support, and K. Reubenbauer is thanked for helpful discussions.

Literature Cited

1. Perlow, G. J. In "Chemical Applications of Mössbauer Spectroscopy"; Goldanskii, V. I.; Herber, R. H., Eds.; Academic Press: New York, 1968; p. 400.
2. Greenwood, N. N.; Gibb, T. C., Eds. "Mössbauer Spectroscopy"; Chapman and Hall: London, 1971; p. 462.
3. deWaard, H. In "Mössbauer Effect Data Index"; Stevens, J. G.; Stevens, V., Eds.; Plenum: New York, 1973; p. 447.
4. Gibb, T. C. "Principles of Mössbauer Spectroscopy"; Chapman and Hall: London, 1977; p. 77.
5. Sanders, R.; deWaard, H. *Phys. Rev.* **1966**, *146*, 907.
6. Geiger, J. S.; Graham, R. L.; Bergström, I.; Brown, F. *Nucl. Phys.* **1965**, *68*, 352.
7. Perlow, G. J.; Ruby, S. L. *Phys. Lett.* **1964**, *13*, 198.
8. Shenoy, G. K.; Friedt, J. M. *Phys. Rev. Lett.* **1973**, *31*, 419.
9. Ruebenbauer, K.; Birchall, T. *Hyperfine Interact.* **1979**, *7*, 125.
10. Das, T. P.; Hahn, E. L. In "Nuclear Quadrupole Resonance Spectroscopy"; Seitz, F.; Turnbull, D., Eds.; Academic Press: New York, 1958.
11. Perlow, G. J.; Perlow, M. R. *J. Chem. Phys.* **1966**, *45*, 2193.
12. Jones, C. H. W. *J. Chem. Phys.* **1975**, *62*, 4343.
13. Jones, C. H. W.; Warren, J. L. *J. Chem. Phys.* **1970**, *53*, 1740.
14. Jung, P.; Triftshäuser, W. *Phys. Rev.* **1968**, *175*, 512.
15. Ruby, S. L.; Shenoy, G. K. *Phys. Rev.* **1969**, *186*, 326.
16. Gettys, W. L.; Stevens, J. G. *J. Phys. (Paris) Coll.* **1980**, *41*, C1-137.
17. Helmholz, L. *J. Amer. Chem. Soc.* **1937**, *59*, 2036.
18. Hazlewood, E. A. *Z. Krist.* **1938**, 439.
19. Davies, C. G.; Gillespie, R. J.; Ireland, P. R.; Sowa, J. M. *Canad. J. Chem.* **1974**, *52*, 2048.
20. Krasznai, J. J., Ph.D. Thesis, McMaster Univ., 1975.
21. Ehrlich, B. S.; Kaplan, M. *J. Chem. Phys.* **1969**, *51*, 603.
22. Mooney, R. C. L. *Z. Krist.* **1935**, *90*, 143.
23. Breneman, G. L.; Willet, R. D. *Acta Cryst.* **1969**, *B25*, 1073.
24. Davies, J. E.; Nunn, E. K. *J. Chem. Soc. Chem. Commun.* **1969**, 1374.
25. Popov, A. I. In "M.T.P. International Review of Science, Inorganic Chemistry"; Emeleus, H. J.; Gutmann, V., Eds.; Butterworths: London, 1972; Vol. 3, p. 53.
26. Birchall, T.; Myers, R. D. *J. Chem. Soc. Dalton Trans.* **1980**, in press.
27. Carpenter, G. B.; Richards, S. M. *Acta Cryst.* **1962**, *15*, 360.
28. Boswijk, K. H.; van der Heide, J.; Vos, A.; Wiebenga, E. H. *Acta Cryst.* **1956**, *9*, 274.
29. de Waard, H.; Spanhoff, F. L., unpublished data.
30. Ehrlich, B. S.; Kaplan, M. *J. Chem. Phys.* **1969**, *50*, 2041.

RECEIVED June 27, 1980.

Note Added in Proof

The x-ray crystal structure of $\text{IO}_2\text{F}_3 \cdot \text{SbF}_5$ recently has been reported (Edwards, J. E.; Hana, A. A. K., *J. Chem. Soc. Dalton Trans.* **1980**, 1734.). The structure analysis has shown that the adduct exists in the solid state as dimers, $(\text{IO}_2\text{F}_3 \cdot \text{SbF}_5)_2$, such that the two antimony atoms and two iodine atoms are at opposite corners of a rhombus, and the oxygen atoms are in the cis configuration.

Tellurium-125 and Iodine-129 Mössbauer Study of the High-Pressure Phase Transition of Tellurium

U. LADEWIG, B. PERSCHIED, K. FRANK, and G. KAINDL

Institut für Atom- und Festkörperphysik, Freie Universität Berlin,
D-1000 Berlin 33, West Germany

The effects of pressure up to 80 kbar on the isomer shift and electric-quadrupole interaction of ^{125}Te and dilute ^{129}I probe atoms in tellurium were investigated by Mössbauer spectroscopy with the 35.5-keV and 27.8-keV gamma transitions of ^{125}Te and ^{129}I , respectively. With increasing pressure both nuclear gamma resonances are shifted to higher transition energies (increasing isomer shift), which corresponds to increasing electron densities at the nuclei. The strength of the electric-quadrupole interactions decreases in both cases. The results are interpreted on the basis of pressure-induced changes of the chemical bonding in tellurium and clearly show that tellurium becomes more isotropic with increasing pressure. Mössbauer spectra of the high-pressure phase of tellurium support a noncubic lattice structure, in agreement with recent crystallographic data.

For many years scientists have been strongly interested in the chalcogens sulfur, selenium, tellurium, and polonium because of their widely different physical and chemical properties. In particular, the semiconductor tellurium, which stands between semiconducting selenium and metallic polonium, received much attention after a pressure-induced semiconductor–metal transition was observed (1, 2).

Recently, calculations of the effects of pressure on the electronic structure of tellurium became available (3, 4), motivating an experimental study of the hyperfine interaction parameters of tellurium as a function of pressure. In principle, both the isomer shift and the electric

field gradient tensor studied as a function of pressure are expected to provide sensitive tests for these calculations. This was demonstrated previously for tellurium at atmospheric pressure (5).

Controversial proposals concerning the lattice structure of the metallic high-pressure phase of tellurium have been published (6-9). Both the simple cubic structure of α -polonium and the rhombohedral structure of β -polonium were suggested. Both suggestions would make sense since the trigonal structure of tellurium at ambient pressure could be obtained from both by only small distortions. The results of a previous ^{125}Te high-pressure Mössbauer experiment by Berman et al. (10) supported the cubic lattice structure. However, Aoki et al. (11) recently redetermined the lattice structure of metallic tellurium as monoclinic, which contradicts the conclusion reached in the Mössbauer work of Berman et al.

To clarify the controversy and to get further insight into structural and electronic changes of tellurium under pressure, Mössbauer experiments at pressures up to about 80 kbar were performed. This chapter summarizes results that have been obtained both with the 35.5-keV gamma resonance of ^{125}Te and the 27.8-keV gamma resonance of ^{129}I , studying the effects of pressure on tellurium absorbers and ^{129}Te Mössbauer sources, respectively. A short report of preliminary results with the ^{129}I probe is presented elsewhere (12).

Experimental

Sources and Absorbers. The measurements with the ^{125}Te probe were performed as Mössbauer absorber experiments using a single-line source of $\text{Sn}^{125m}\text{Te}$. The absorber was prepared by imbedding tellurium powder (enriched to 97.7% in ^{125}Te) in epoxy resin to produce a small pill suitable for the employed high-pressure technique. It contained about 2 mg/cm² of ^{125}Te . The single-line SnTe source was produced by neutron activation of 10 mg of $^{119}\text{Sn}^{124}\text{Te}$ (enriched to 99.2% in ^{124}Te and 91.0% in ^{119}Sn) in a thermal neutron flux of 9×10^{13} n/cm²s for a period of 4 weeks. Enriched ^{119}Sn was used to minimize the production of disturbing activity from an activation of tin. The 35.5-keV Mössbauer level of ^{125}Te is populated in the decay of ^{125m}Te ($T_{1/2} = 58$ days).

The studies with dilute ^{129}I probes in tellurium were performed as Mössbauer source experiments using a single-line Cu^{129}I absorber and a tellurium source containing the ^{129m}Te (enriched to 99.2% in ^{128}Te) for a period of about 2 weeks in a thermal neutron flux of 9×10^{13} n/cm²s. This resulted in a conversion of less than 1 ppm of the ^{128}Te atoms to ^{129m}Te . The first excited state of ^{129}I is populated by β -decay of ^{129m}Te ($T_{1/2} = 34$ days). The radioactive tellurium powder was imbedded in epoxy resin to form a small pill for the high-pressure measurements. Cu^{129}I used as the single-line absorber was prepared by precipitation from a Na^{129}I solution with CuSO_4 . The absorber contained 12 mg/cm² of the long-lived ^{129}I isotope ($T_{1/2} = 1.7 \times 10^7$ years). To reduce the background radiation from the Cu^{129}I absorber (mainly 29.8-keV K_α x-rays from ^{129}Xe), an indium foil was used as a critical absorber during the experiments with ^{129}I .

High-Pressure Mössbauer Spectrometer. The high-pressure technique used in the present experiments is based on an opposed-anvil device with sintered B_4C anvils. The gamma rays, detected by an intrinsic germanium detector, pass through the anvils in the axial direction. With this pressure device quasi-hydrostatic pressures up to about 100 kbar can be produced in a sample volume of 4-mm diameter and 0.5-mm thickness. The high-pressure clamp is loaded at room temperature with a hydraulic press and subsequently cooled to liquid-helium temperature in a helium bath dewar. The pressure is determined in situ by measuring the pressure-dependent superconducting transition of lead placed inside the high-pressure cell. The high-pressure clamp is suited for applying pressure to either the absorber or the source of a Mössbauer transmission setup. In the case of an absorber experiment, the source is moved and the gamma rays must pass through both B_4C anvils in the axial direction. When the source is pressed the gamma rays must pass only through one anvil, and the absorber (cooled to 50 K) is moved inside the vacuum chamber of the dewar. Details of the high-pressure system used are described elsewhere (13).

Experimental Results. Mössbauer spectra of ^{125}Te in tellurium were recorded at seven different pressures in the range 0 to 72 kbar with both the $Sn^{125m}Te$ source and the tellurium absorber at 4.2 K. Two representative spectra at 0 kbar and at 72 kbar, respectively, are shown in Figure 1. Both spectra exhibit a well-resolved electric-quadrupole splitting attributable to the interaction of the electric-quadrupole moment of the $3/2^+$ excited state of ^{125}Te with the electric field gradient tensor in $Te(Q(3/2^+) = -0.31 b)$. It is obvious from Figure 1 that the electric-quadrupole interaction does not vanish in the high-pressure phase of tellurium (see spectrum at 72 kbar) as claimed in Ref. 10.

The solid lines in Figure 1 represent the results of least-squares fits of two Lorentzian lines to the data. The results of the least-squares fit analysis for isomer shift and electric-quadrupole splitting ΔE_Q are plotted in Figure 2 as

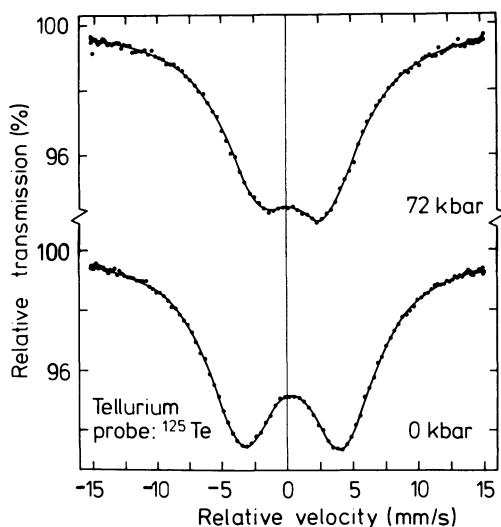


Figure 1. Mössbauer spectra of tellurium at pressures of 0 (bottom) and 72 (top) kbar both taken at 4.2 K with the 35.5-keV gamma resonance of ^{125}Te . The $Sn^{125m}Te$ source also was kept at 4.2 K.

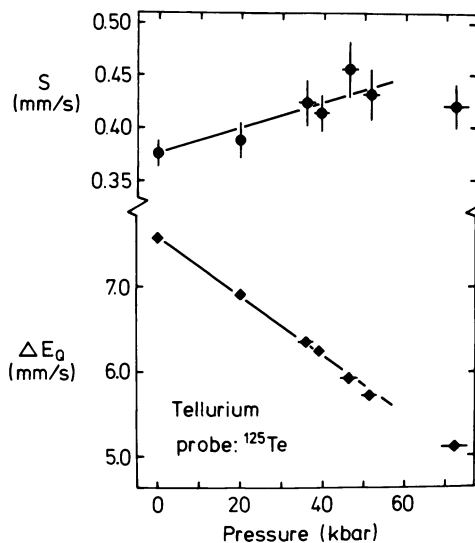


Figure 2. Pressure dependence of the electric-quadrupole splitting ΔE_Q and the isomer shift S of the 35.5-keV gamma resonance of ^{125}Te .

a function of pressure. Over the entire pressure range studied, the electric-quadrupole splitting decreases with increasing pressure, while the isomer shift increases in the low-pressure phase of tellurium and seems to decrease in the high-pressure phase. Note that the $3/2-1/2$ Mössbauer resonance of ^{125}Te allows neither a determination of the sign of the electric-quadrupole interaction nor an analysis of the individual components of the electric field gradient tensor [V_{zz} , $\eta = (V_{xx} - V_{yy})/V_{zz}$] from polycrystalline spectra as presented here.

In addition, dilute ^{129}I atoms were used as probes to study pressure-induced changes of electronic and structural properties of tellurium. Two typical spectra are presented in Figure 3, taken at 0 kbar and at 65 kbar (high-

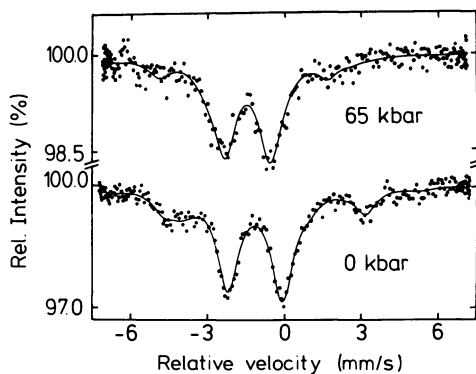


Figure 3. Mössbauer spectra of tellurium at pressures of 0 (bottom) and 65 kbar (top) taken at 4.2 K with the 27.8-keV gamma resonance of ^{129}I (12). The Cu^{129}I absorber was kept at 50 K.

pressure phase), respectively. The spectra exhibit a large isomer shift and a well-resolved electric-quadrupole splitting resulting from the interaction of the electric field gradient at the ^{129}I nucleus with the electric-quadrupole moments of the two nuclear states involved ($Q(7/2) = -0.533 b$; $Q(5/2) = -0.685 b$). In accordance with the ^{125}Te case, a nonvanishing electric-quadrupole interaction is observed at ^{129}I in the high-pressure tellurium phase. Because of the $5/2-7/2$ spin sequence of the 27.8-keV resonance of ^{129}I , values for both the main component V_{zz} and the asymmetry parameter η of the electric field gradient tensor can be obtained from an analysis of the polycrystalline spectra.

In the least-squares fitting procedure used, the positions and relative intensities of the 12 hyperfine components were obtained from a diagonalization of the interaction Hamiltonian. Assuming a polycrystalline sample, this results in a misfit of the line intensities as has been found previously by other authors (24, 25). By analyzing a spectrum with high statistical accuracy of tellurium at ambient pressure we were able to show that this misfit cannot be removed by introducing a texture of the sample, an anisotropic recoil-free fraction, or even a combination of both. A satisfactory fit of data could be obtained only by allowing for a second iodine site with different hyperfine interaction parameters. Similar results were obtained recently by Boolchand et al. (14), who attributed the second interaction to a TeO_2 contamination of the sample. The solid lines in Figure 3 represent the results of such least-squares fits using two sets of V_{zz} , η , and S as the essential parameters. In the fits of the high-pressure spectra, the fraction of the contamination was kept constant at the value determined from the ambient pressure spectrum.

The results of this analysis are presented in Figure 4 as a function of pressure. The transition from trigonal tellurium at low pressures to the high-pressure phase is evident in the observed discontinuity of V_{zz} and S at a pressure of about 50 kbar. The magnitude of V_{zz} decreases over the entire pressure range studied, similar to the ^{125}Te case. The asymmetry parameter decreases only slightly without a significant change of slope at the phase transition. In both phases the isomer shift increases with pressure.

Discussion

The results for isomer shift and electric-quadrupole interaction as a function of pressure give information on pressure-induced changes of the chemical bonding of tellurium and of dilute iodine impurities in tellurium. The crystal structure of trigonal tellurium consists of hexagonal arrays of helical chains of atoms, with the axis of the helical chains pointing into the trigonal c -axis. The main effect of pressure on the structure of this highly anisotropic substance is a decrease in the interchain distances. In the pressure range 0 to 40 kbar, the interchain distances decrease by about 5% while the intrachain distances decrease only by about 1% (15).

The bonding in trigonal tellurium is predominantly π -like in character, where the bonding orbitals to the nearest-neighbor atoms in the same chain involve p_x and p_y orbitals. In the weak interchain bonding, the lone-pair p_z orbital is involved (16, 17).

The electric field gradient at the tellurium nucleus in trigonal tellurium is predominantly of molecular origin (5). Therefore, in a LCAO-MO picture, the electric field gradient and the isomer shift will be

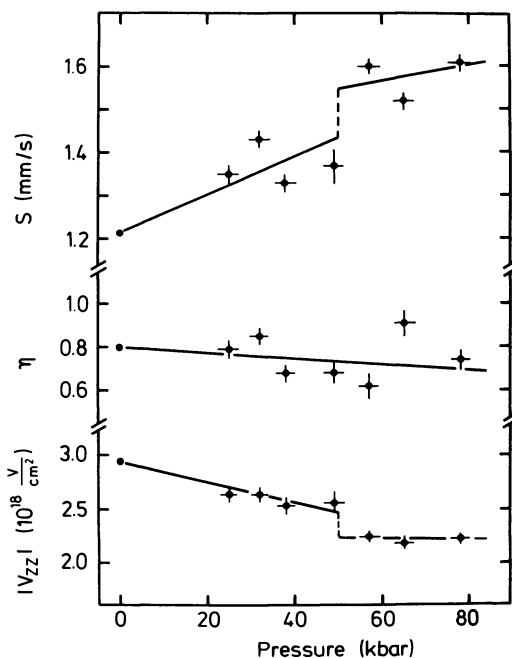


Figure 4. Pressure dependence of the magnitude of the electric field gradient V_{zz} , of the asymmetry parameter η , and of the isomer shift S of the 27.8-keV resonance of ^{129}I (12).

described in the framework of the theory of Townes and Dailey (18), which has been slightly extended to include the isomer shift in the case of s - p elements (19). Using the population numbers n_s , n_x , n_y , and n_z of the s , p_x , p_y , and p_z valence orbitals, respectively, the isomer shift can be described by the relation

$$S = S' + b(2 - n_s) + a[6 - (n_x + n_y + n_z)] \quad (1)$$

The isomer shift S' corresponds to fully occupied $5s$ and $5p$ shells. In this model, the electric field gradient tensor components are given by

$$V_{zz} = U_p \cdot V_{zz}^{\text{at}} \quad (2)$$

and

$$\eta = 3/2 \frac{n_x - n_y}{U_p} \quad (3)$$

In this relation, U_p is defined as the p -electron imbalance

$$U_p = -n_z + \frac{1}{2} (n_x + n_y), \quad (4)$$

and V_{zz}^{at} refers to the atomic electric field gradient attributable to one p_z hole.

In the case of ^{125}Te probes in tellurium, the sign of V_{zz} as well as η have been determined from Mössbauer experiments with single-crystal tellurium absorbers at ambient pressure: $V_{zz} = -(5.43 \pm 0.02) 10^{18}$ V/cm² and $\eta = 0.64 \pm 0.04$ (20). For tellurium, the atomic electric field gradient is $V_{zz}^{\text{at}} = 11.69 \times 10^{18}$ V/cm² (21), and the isomer shift parameters in Equation 1 have been determined as $a = 0.45 \pm 0.01$ mm/s and $S' = -0.31 \pm 0.05$ mm/s (relative to SnTe) (22). The bonding in tellurium has mainly p character, so $n_s = 2$ (fully occupied $5s$ shell) may be assumed. This results in values of $n_x = 1.24$, $n_y = 1.44$, $n_z = 1.81$, and $U_p = -0.46$ from an analysis of the electric field gradient tensor and the isomer shift in tellurium.

The observed pressure-induced increase of the isomer shift of the 35.5-keV gamma resonance of ^{125}Te in the trigonal tellurium phase corresponds to an increase of the electron density $\rho(0)$ at the nucleus, since the change of the mean-square nuclear charge radius $\Delta\langle r^2 \rangle$ is known to be positive for this gamma transition. This is opposite to the theoretical prediction in Ref. 23 based on a simple Wigner-Seitz model, which does not take into account changes in the population numbers of the p orbitals. The observed increase in the isomer shift can be explained by a decrease in the p -orbital occupation, $n_p = n_x + n_y + n_z$, which corresponds to increasing covalency with decreasing volume. This does not rule out that there is also an additional but smaller negative contribution attributable to a pure Wigner-Seitz-cell effect as predicted in Ref. 23. An indication for this is given by the observed decrease of the isomer shift of dilute ^{125}Te probe atoms in iron metal (24).

The present high-pressure data on ^{125}Te in polycrystalline tellurium do not allow a separate evaluation of the components V_{zz} and η of the electric field gradient tensor. The experimental observation is a strong decrease in the electric-quadrupole splitting of the $3/2^+$ excited state of ^{125}Te , $\Delta E_Q = 1/2 eQV_{zz}(1 + 1/3 \eta^2)^{1/2}$ with increasing pressure (Figure 2). This corresponds to a similarly strong decrease in the magnitude of V_{zz} , since the factor $(1 + 1/3 \eta^2)^{1/2}$ (with $\eta = 0.64$ at $P = 0$ kbar) cannot account for more than about 20% of the observed decrease of ΔE_Q in the worst case. The decrease in the magnitude of V_{zz} (with negative sign) correspond to a decrease in U_p . This is exactly what is expected from the increasing strength of the interchain bonding in tellurium with decreasing volume, which simply means that the anisotropy decreases with increasing pressure in tellurium (3, 15). Since the p_z orbital is involved in the interchain bonding, the occupation number n_z will decrease much faster with increasing pressure than $1/2 (n_x + n_y)$, causing the observed change in U_p (see Equation 4). This supports the conclusion

drawn from the observed isomer shift changes and shows that the decrease of the sum $n_p = n_x + n_y + n_z$ is caused mainly by a decrease in n_z .

In the case of ^{129}I probe atoms in polycrystalline tellurium, both components of the electric field gradient tensor, V_{zz} and η , can be obtained from an analysis of the electric-quadrupole-split spectra of the $5/2^+ - 7/2^+$ transition of ^{129}I . As in the ^{125}Te case, the isomer shift parameters in Equation 1 have been determined as 1.5 ± 0.1 mm/s and $S' = -0.17 \pm 0.02$ mm/s (relative to CuI) (25), and the atomic electric field gradient is known to be $V_{zz}^{\text{at}} = 12.09 \times 10^{18}$ V/cm² (25). With these parameters an analysis of our zero-pressure Mössbauer spectrum of ^{129}I in tellurium results in the following p -orbital population numbers: $n_x = 1.83$, $n_y = 1.72$, $n_z = 1.53$. They correspond to $U_p = 0.24$, which is in good agreement with previous results (21, 25, 26).

Obviously, the p_z orbital is involved mainly in the chemical bonds between the iodine impurity and tellurium, which means that the bonding is predominantly a σ type (25). As in the ^{125}Te case, the observed increase in the isomer shift of the 27.8-keV gamma resonance of ^{129}I corresponds to an increase of $\rho(0)$, since $\Delta\langle r^2 \rangle$ is also positive for this gamma transition. Again, the increase of $\rho(0)$ is interpreted as being caused by a decrease of the total p -orbital population $n_p = n_x + n_y + n_z$. It should be mentioned that, as in the ^{125}Te case, the isomer shift of the ^{129}I gamma resonance decreases with increasing pressure for dilute ^{129}I probes in iron (27).

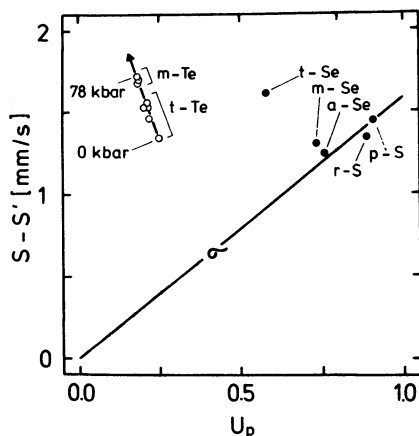


Figure 5. Plot of the difference of the isomer shift S of ^{129}I in various chalcogen hosts and the isomer shift S' of an I^- configuration as a function of the imbalance U_p of $5p$ electrons.

The solid line corresponds to pure σ bonding of iodine. The arrow indicates the effect of pressure on the tellurium host. The values of the sulfur and selenium hosts are from Ref. 25. (a) amorphous; (m) monoclinic; (p) plastic; (r) orthorhombic; (t) trigonal; (○) this work; (●) Kim and Boolchand.

The decrease of the positive z component of the electric field gradient tensor V_{zz} shows that predominantly $n_x + n_y$ are causing this decrease of n_p . Again, the effect of pressure makes the bonding more isotropic and therefore diminishes U_p . This situation is represented graphically in Figure 5, where the difference of the isomer shift S of ^{129}I in various chalcogen hosts and the isomer shift S' is plotted as a function of U_p (25). In addition, the results of the present high-pressure experiments on ^{129}I in tellurium are included. It is obvious that with increasing pressure the π -bonding contributions increase as stated previously, making the bonding more isotropic.

A more detailed interpretation of the experimental results including the observed pressure dependence of the asymmetry parameter η (Figure 4) should be based on the results of band-structure calculations for trigonal tellurium as a function of pressure (3), and for the monoclinic high-pressure phase of tellurium (4).

A final note concerning the controversy on the structure of the metallic high-pressure phase of tellurium mentioned in the introduction: both the present ^{125}Te and ^{129}I data clearly rule out a cubic structure for this phase as proposed in Ref. 10.

Acknowledgment

This work was supported by the Sfb-161 of the Deutsche Forschungsgemeinschaft and by the Kernforschungszentrum Karlsruhe. The authors acknowledge valuable discussions with G. Wortmann and the constant technical support of D. Sobanski.

Literature Cited

1. Bridgman, P. W. *Phys. Rev.* **1935**, *48*, 893.
2. Bridgman, P. W. *Proc. Am. Acad. Arts Sci.* **1952**, *81*, 167.
3. Starkloff, T.; Joannopoulos, J. D. *Phys. Rev. B* **1979**, *19*, 1077.
4. Doerre, G.; Joannopoulos, J. D. *Phys. Rev. Lett.* **1979**, *43*, 1040.
5. Coker, A.; Lee, T.; Das, T. P. *Phys. Rev. B* **1976**, *13*, 55.
6. Kalkina, S. S.; Vereshagin, J. F.; Shulenin, B. M. *Sov. Phys.-JETP (Engl. Transl.)* **1964**, *18*, 1422.
7. Jamieson, J. C.; McWhan, D. B. *J. Chem. Phys.* **1965**, *43*, 1149.
8. Vezzoli, G. C. *Z. Kristallogr.* **1971**, *134*, 305.
9. Donohue, J. *Z. Kristallogr.* **1974**, *139*, 159.
10. Berman, I. V.; Brandt, N. B.; Kuzmin, R. N.; Opalenko, A. A.; Slobodchikov, S. S. *Sov. Phys.—JETP Lett. (Engl. Transl.)* **1979**, *10*, 237.
11. Aoki, K.; Shimomura, O.; Minomura, S. *J. Phys. Soc. Jpn* **1980**, *48*, 551.
12. Ladewig, U.; Frank, K.; Kaindl, G.; Perscheid, B. In "The Physics of Selenium and Tellurium"; Gerlach, E., Grosse, P., Eds.; Springer Verlag: Berlin, 1979; p. 23.
13. Frank, K., Diplom Thesis, Freie Universität Berlin, 1979, unpublished.
14. Boolchand, P.; Bresser, W.; Ehrhart, G. preprint, *Phys. Rev. B*, in press.
15. Keller, R.; Holzapfel, W. B.; Schultz, H. *Phys. Rev. B* **1977**, *16*, 4404.
16. Martin, R. M.; Lucovsky, G.; Helliwell, K. *Phys. Rev. B* **1976**, *13*, 1383.

17. Joannopoulos, J. D.; Schlüter, M.; Cohen, M. L. *Phys. Rev. B* **1975**, *11*, 2186.
18. Townes, C. H.; Dailey, B. P. *J. Chem. Phys.* **1949**, *17*, 782.
19. Bancroft, G. M.; Platt, R. H. "Advances in Inorganic Chemistry and Radiochemistry"; Academic: New York, 1972; Vol. 15, p. 59.
20. Boolchand, P.; Robinson, B. L.; Iha, S. *Phys. Rev. B* **1970**, *2*, 3463.
21. Pasternak, M.; Bukshpan, S. *Phys. Rev.* **1967**, *163*, 297.
22. Cheyne, B. M.; Johnstone, J. J.; Jones, C. H. W. *Chem. Phys. Lett.* **1972**, *14*, 545.
23. Williamson, D. L.; Dale, J. H.; Josephson, W. D.; Roberts, L. D. *Phys. Rev. B* **1978**, *17*, 1015.
24. Ladewig, U.; Perscheid, B.; Kaindl, G., unpublished data.
25. Kim, C. S.; Boolchand, P. *Phys. Rev. B* **1979**, *19*, 3187.
26. Langouche, G.; Van Rossum, M.; Schmidt, K. P.; Coussement, R. *Phys. Rev. B* **1974**, *9*, 848.
27. Frank, K.; Ladewig, U.; Perscheid, B.; Kaindl, G.; Reintsema, S. R.; Pattyn, H. *J. Magn. Magn. Mat.* **1980**, *15-18*, 641.

RECEIVED August 14, 1980.

Recent Investigations of Spin Crossover

P. GÜTLICH

Institut für Anorganische und Analytische Chemie, Johannes Gutenberg-Universität, D-6500 Mainz, West Germany

A brief introduction of the phenomenon of spin crossover in transition metal complexes is followed by a discussion of the results from Mössbauer effect measurements on the metal dilution effect in the solid solutions $[Fe_xM_{1-x}(2-pic)_3]Cl_2 \cdot EtOH$ ($M = Zn, Co$) and $[Fe_xM_{1-x}(phen)_2(NCS)_2]$ ($M = Mn, Co, Ni$). It is shown that the spin transition behavior changes markedly with the iron concentration. It is also demonstrated that the nature of the crystal solvent molecules as well as the method of sample preparation influence the spin crossover behavior. A presentation of some examples for structural changes accompanying spin crossover concludes this review.

The phenomenon of spin crossover, otherwise called magnetic crossover or high-spin (HS) \rightleftharpoons low-spin (LS) transition, observed in certain first-row transition metal complexes has been described extensively and reviewed in a number of articles (1-6).

In terms of ligand field theory, spin crossover occurs in transition metal complexes with d^4 - d^8 electron configuration, if the difference between the net ligand field strength and the mean spin pairing energy, after taking into account all kinds of relevant perturbations such as low-symmetry field components, spin-orbit interaction, configuration interaction, and covalency effects, becomes comparable to thermal energy $k_B T$. On thermodynamic grounds, spin crossover is anticipated if the difference in the Gibbs free energy (G) of the two spin states involved is on the order of $k_B T: \Delta G = G(HS) - G(LS) = \Delta H - T\Delta S \approx k_B T$. The enthalpy change $\Delta H = H(HS) - H(LS)$ is positive going from the low-spin to the high-spin state, and reflects essentially the difference in the electronic energies of the two spin states. The entropy change $\Delta S = S(HS) - S(LS)$ is also positive for the conversion from low-spin to high-spin. It has been found in various instances (7, 8) that only a

smaller fraction of the total entropy change arises from the spin multiplicity change, namely, $\Delta S_{el} = R[\ln(2S+1)_{HS} - \ln(2S+1)_{LS}]$. The major part of ΔS is due to contributions from the changes in both intramolecular and intermolecular vibrations. There is a critical temperature, called transition temperature T_c , where $\Delta H = T\Delta S$ and $\Delta G = 0$, and the two spin states coexist in equal amounts (see Figure 1).

Spin crossover has been observed mostly in the solid state, but also has been found in liquids. In particular, numerous examples of spin crossover have become known for iron(II) complexes with nitrogen donor ligands (5). Many spin crossover systems also have been found in the complex chemistry of iron(III), such as the dithiocarbamates (9), monothio- β -diketonates with $[\text{FeS}_3\text{O}_3]$ chromophore (10–13), and monothiocarbamate complexes with $[\text{FeS}_3\text{O}_3]$ chromophore (14), to name a few. The phenomenon also has been established for a good number of cobalt(II) complexes (3, 15), to a lesser extent for nickel(II) complexes (3, 15), and in a few cases for manganese(II) compounds (16). Quite recently, the first report on spin crossover in a cobalt(III) ($3d^6$) complex, in the solid state as well as in solution, has appeared in the literature (17, 18).

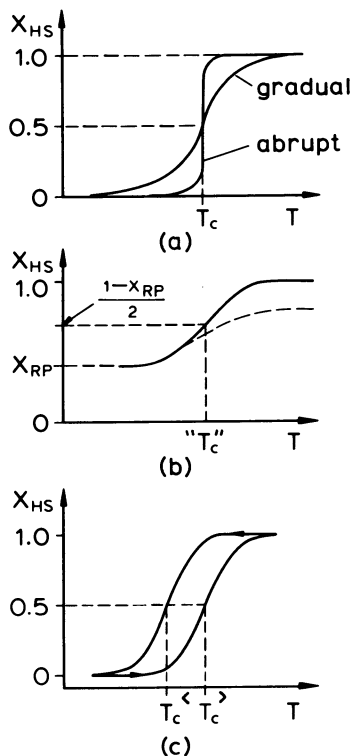


Figure 1. Schematic of various types of spin crossover behavior.

The $x_{HS}(T)$ term is the fraction of high-spin molecules as a function of temperature. (a) Gradual and abrupt spin transition, respectively; (b) incomplete spin transition (RP is the residual fraction of high-spin molecules); (c) spin transition with hysteresis ($T_c^<$ and $T_c^>$ are the transition temperatures in the cooling and heating modes, respectively).

The method most commonly used to detect spin crossover is the measurement of the magnetic susceptibility, which reflects the anomalous magnetic behavior as a function of temperature. For crossover systems of iron, ^{57}Fe Mössbauer spectroscopy has proven to be a powerful technique; it enables one to follow directly the changes of the concentrations of the coexisting spin states with temperature (19). Other techniques have been employed successfully; for example, vibrational spectroscopy to follow the changes in the relative intensities of characteristic vibrational modes (such as the metal–ligand stretching, for which $\nu(\text{HS}) < \nu(\text{LS})$ upon spin conversion (7, 8, 20, 21, 22, 50); uv/vis spectroscopy to detect changes in the ligand field parameters (9, 13, 24, 25, 26); x-ray structure analysis to reveal changes in the lattice parameters (the metal–ligand bond length is known to increase by about 0.1–0.2 Å going from low spin to high spin) and eventually structural phase changes accompanying spin crossover (27–32); heat capacity measurements to determine the thermodynamic parameters ΔH and ΔS for the spin conversion and the nature of the transition (first or higher order) (7, 8); and relaxation measurements to determine spin state lifetimes and thermodynamic quantities (33, 34).

Various types of the spin crossover characteristics, expressed in terms of the fraction x_{H} of molecules in the high-spin state as a function of temperature, have been observed (see Figure 1): (1) “abrupt” transition within a few Kelvin as, for instance, in $[\text{Fe}(\text{phen})_2(\text{NCS})_2]$ (phen = 1,10-phenanthroline) (35, 36), or “gradual” transition extended over a large temperature range as, for instance, in $[\text{Fe}(2\text{-CH}_3\text{-phen})_3]X_2$ (phen = 1,10-phenanthroline) (37, 38) (see Figure 1a); (2) transitions that are incomplete on either the low-temperature end, merging into a plateau of what is called “residual paramagnetism” (RP), or in the high-temperature region (see Figure 1b) (examples of both types will be given later); (3) spin transitions showing hysteresis of the width $\Delta T = T_c < - T_c >$ (see Figure 1c), examples of which are reported in Refs. (39 and 40).

The spin crossover behavior may be highly susceptible to various influences, such as intraligand substitution, ligand replacement, nature of the uncoordinated anion and the crystal solvent molecule, deuteration, metal dilution, and method of sample preparation. To learn more about the driving force and the mechanism of the spin transition in solids, particularly to test the idea of Sorai and Seki of the spin transition taking place in a cooperative manner through a coupling between the spin state and the lattice vibrational modes (7, 8), we have focused our attention on the effect of metal dilution (41–47), the effect of changing the crystal solvent molecule (40), and the influence of deuteration (48) and crystal imperfections (36) in iron(II) spin crossover systems. The essential results will be reviewed here.

Effect of Metal Dilution

Solid Solutions of $[\text{Fe}_x\text{Zn}_{1-x}(\text{2-pic})_3]\text{Cl}_2 \cdot \text{C}_2\text{H}_5\text{OH}$. MÖSSBAUER MEASUREMENTS. Systematic investigations of the effect of metal dilution on the spin transition behavior by means of Mössbauer spectroscopy were initiated in our laboratory some years ago, hoping to find experimental support for the cooperative domain model of Sorai and Seki (7, 8). We started with the spin crossover system $[\text{Fe}(\text{2-pic})_3]\text{Cl}_2 \cdot \text{C}_2\text{H}_5\text{OH}$ (2-pic = 2-picolyamine), for which the temperature-dependent ${}^5T_2(O_h) \rightleftharpoons {}^1A_1(O_h)$ transition has been established by Renovitch and Baker (49). This system appeared to be particularly suited for the metal dilution work for two reasons: (1) The Mössbauer spectra as a function of temperature exhibit two well-resolved quadrupole doublets for the high- and low-spin states of iron(II), respectively (see Figure 2), demonstrating that the two spin states coexist in chemical equilibrium and have lifetimes of $\geq 10^{-8}$ s, the quadrupole precession time of the excited nuclear state. (2) The compound forms solid solutions with zinc and cobalt, respectively, over the entire concentration range. The most important result of the measurements on the series $[\text{Fe}_x\text{Zn}_{1-x}(\text{2-pic})_3]\text{Cl}_2 \cdot \text{C}_2\text{H}_5\text{OH}$ ($1.0 \geq x \geq 0.0009$) (41, 42) becomes apparent from the four representative Mössbauer spectra shown in Figure 3: At a given temperature (101 K in the present case of Figure 3), the relative intensity of the quadrupole doublet of the iron(II) high-spin state, ${}^5T_2(O_h)$, increases with decreasing iron concentration. Figure 4 shows the temperature dependence of the area fraction of the high-spin quadrupole doublet x_H , evaluated from the spectra of $[\text{Fe}_x\text{Zn}_{1-x}(\text{2-pic})_3]\text{Cl}_2 \cdot \text{C}_2\text{H}_5\text{OH}$ with different iron concentrations x . Figure 4 also indicates that the slope of the spin conversion curve at the spin transition temperature T_c diminishes with dilution, and that the spin transition is complete at the low- and high-temperature ends for all concentrations. Figure 6 demonstrates the nearly linear decrease of the spin transition temperature $T_c(x)$ with decreasing iron concentration.

No substantial differences have been observed in the isomer shift, apart from the shift due to the second-order Doppler effect, or in the quadrupole splitting of the high-spin state in the solid solutions with variable x at a given temperature. Thus the electronic structure of the iron(II) ion is not altered significantly by partial substitution of iron(II) by zinc(II).

DRIVING FORCE AND POSSIBLE MECHANISM OF THE SPIN TRANSITION. As has been pointed out earlier (7, 8, 41), a discussion of the relative stability of the spin states involved in spin crossover should be based on the free energy $G = H - TS$ and its change $\Delta G = \Delta H - T\Delta S$ accompanying the change in spin state. The ΔH and ΔS terms include contribu-

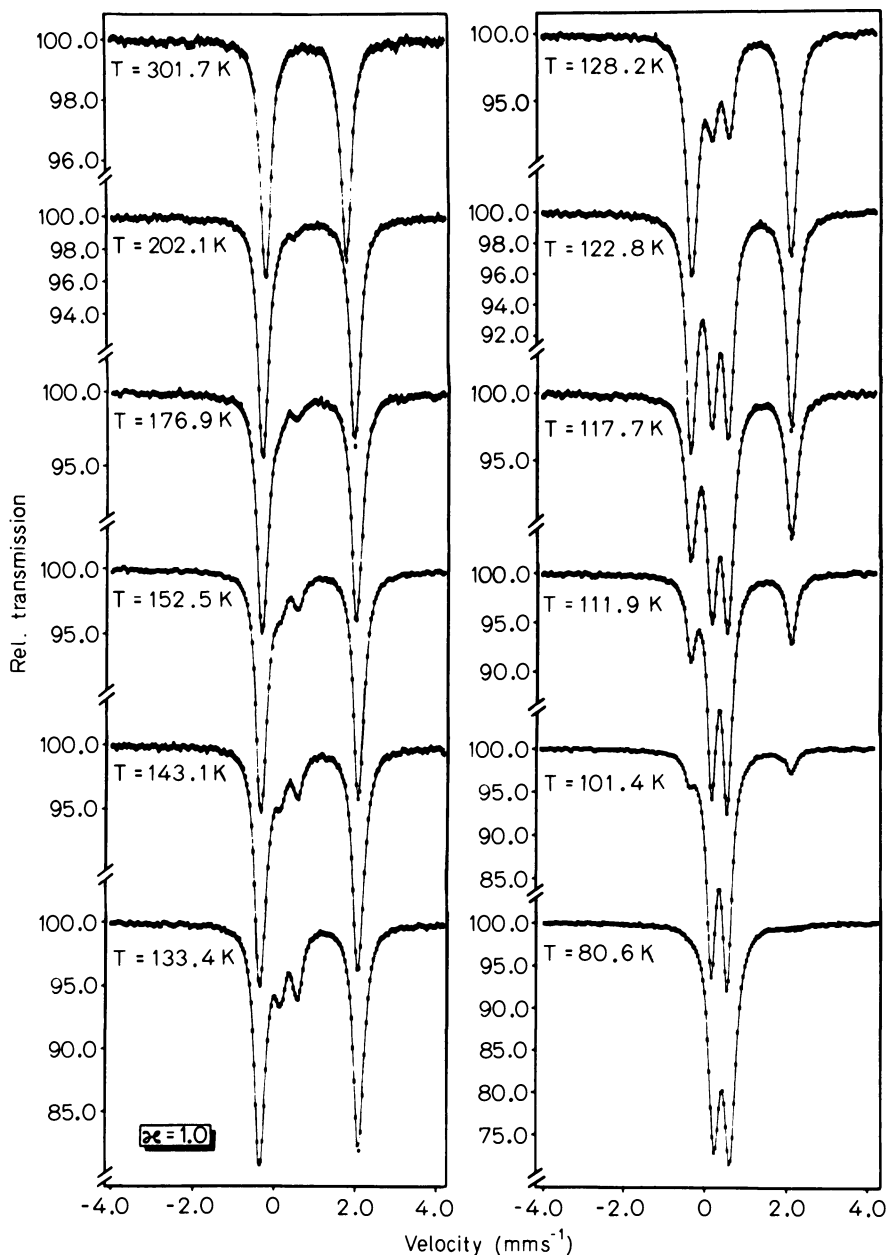


Figure 2. The ^{57}Fe Mössbauer spectra of $[\text{Fe}(\text{2-pic})_3]\text{Cl}_2 \cdot \text{C}_2\text{H}_5\text{OH}$ (2-pic = 2-picolyamine) at various temperatures (41). The inner two lines refer to the quadrupole doublet of the low-spin state $^1\text{A}_1$ (O_h), the outer two lines to that of the high-spin state $^5\text{T}_2$ (O_h) of iron(II).

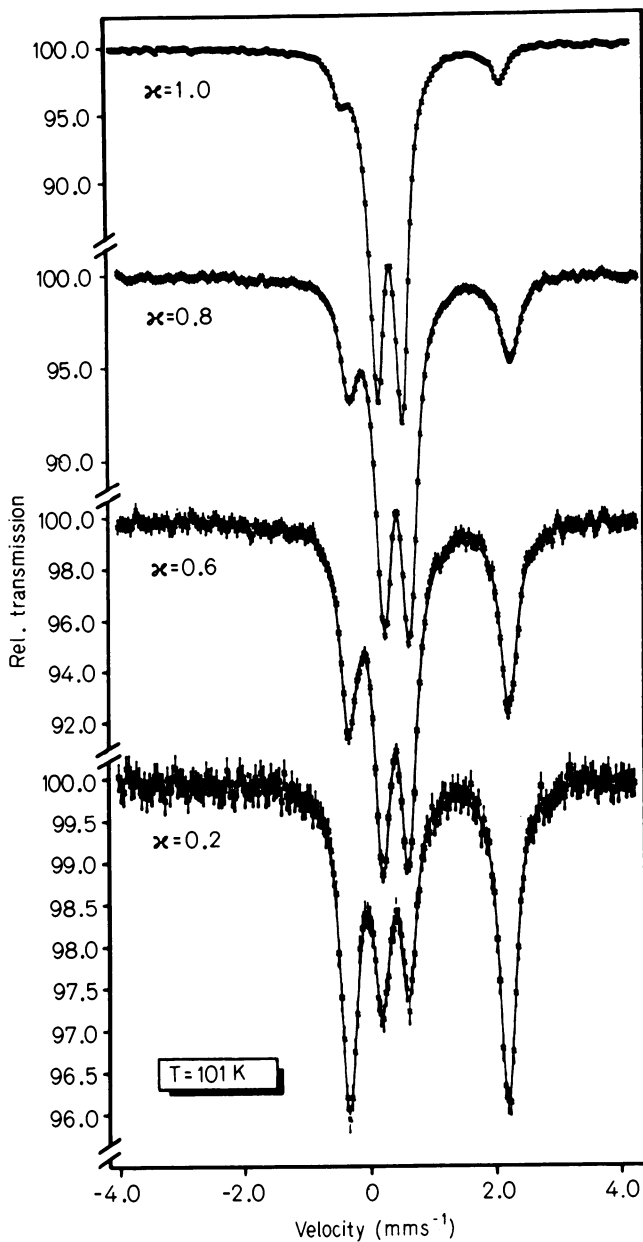


Figure 3. Concentration dependence of ^{57}Fe Mössbauer spectra of $[\text{Fe}_x\text{Zn}_{1-x}(2\text{-pic})_3]\text{Cl}_2 \cdot \text{C}_2\text{H}_5\text{OH}$ at 101 K (41)

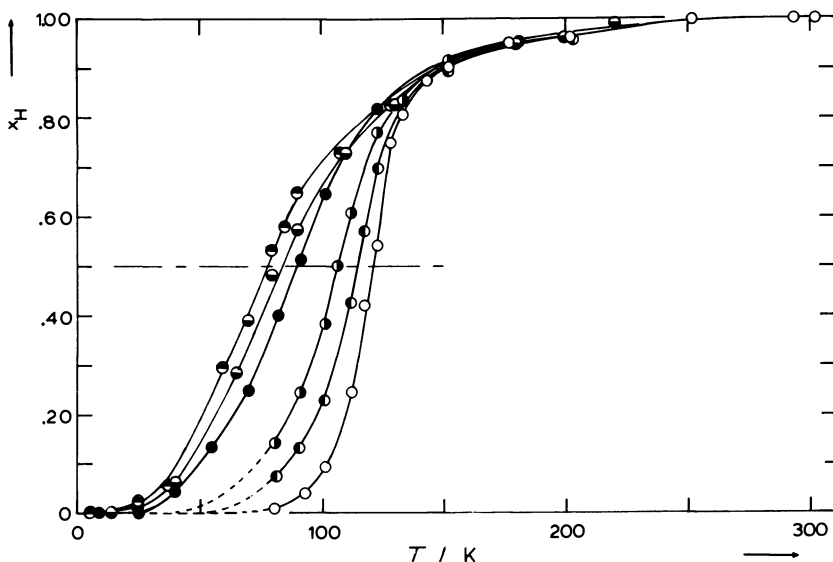


Figure 4. Temperature dependence of the area fraction x_H of the high-spin quadrupole doublet in ^{57}Fe Mössbauer spectra of $[\text{Fe}_x\text{Zn}_{1-x}(\text{2-pic})_3]\text{-Cl}_2 \cdot \text{C}_6\text{H}_5\text{OH}$ with variable iron concentration x (41, 42): (●) $x = 0.0009$; (●) $x = 0.029$; (●) $x = 0.2$; (●) $x = 0.6$; (●) $x = 0.8$; (○) $x = 1.0$.

tions from all degrees of freedom; the most important ones to account for the temperature dependence of ΔG stem from changes in electronic structure and vibrational modes.

For a ${}^1A_{1g}(O_h) \rightleftharpoons {}^5T_{2g}(O_h)$ spin crossover system at absolute zero temperature, the electronic ground state of iron(II) is separated by $\epsilon = E({}^5T_{2g}) - E({}^1A_{1g})$ from the high-spin state (cf. Figure 8); $\epsilon \approx \Delta H$, if $p \cdot \Delta V$ is sufficiently small. From infrared (7, 8) and Mössbauer spectroscopy (40), the energy difference $\epsilon \approx \Delta H$ of the iron atom has been confirmed to be nearly constant over a wide temperature range. At finite temperatures, the entropy term $T\Delta S$ plays an important role. The predominant contributions to the total entropy change arise from changes in electronic structure, $\Delta S_{\text{el}} = R[\ln(2S+1)_{\text{HS}} - \ln(2S+1)_{\text{LS}}]$, and in vibrational frequencies, ΔS_{vib} , mainly of intramolecular modes. As both contributions ΔS_{el} and ΔS_{vib} are positive going from the low-spin to the high-spin state, it is conceivable that the spin transition occurs even if the enthalpy change is essentially constant. Thus, the gain in entropy must be considered the main driving force responsible for the spin transition from the low-spin state to the high-spin state.

The mechanism of the spin transition in the crystalline state is still much in the dark, and the following qualitative description is not more than a hypothetical picture, supported, however, by the results of our

metal dilution work as well as by infrared (7, 8) and x-ray crystal structure investigations. Sorai and Seki (7, 8) originally suggested that the spin transition in a crystalline spin crossover system takes place in a cooperative manner involving a significant coupling between the electronic state that changes spin, and the phonon system encompassing the intramolecular and intermolecular region. The group of molecules that changes spin induced by a "primary" spin change is called a cooperative domain. At sufficiently low temperatures, all the molecules reside in the low-spin state with characteristic normal modes of vibrations. If the temperature rises, a certain number of molecules change from low-spin to high-spin due to thermal excitation. As a consequence, some normal modes of vibrations will be modulated to some extent. It is known from temperature-dependent infrared spectroscopy (7, 8, 21, 22, 23) that the frequencies of the metal-ligand stretching vibrations are markedly reduced in the high-spin state as compared to the low-spin state; the reason is a significant reduction in the extent of π -backbonding which decreases the metal-ligand bond strength. This decrease is paralleled by an increase in the bond length by some 0.2 Å, as has been observed recently in a variable-temperature x-ray crystal structure analysis of the $[\text{Fe}(2\text{-pic})_3]\cdot\text{Cl}_2 \cdot \text{C}_2\text{H}_5\text{OH}$ (30). Through the modulated normal modes the information of a "primary" spin change is communicated to neighboring complex modules. Their vibrational modes will be changed by the incoming perturbation wave; at a certain threshold they may change over to the high-spin state. This "secondary" spin change in turn subsequently modulates the vibrational modes further and carries the spin change information further into the lattice of a cooperative domain.

On the basis of this picture, the effect of substituting iron(II) for zinc(II) in the $[\text{Fe}_x\text{Zn}_{1-x}(2\text{-pic})_3]\text{Cl}_2 \cdot \text{C}_2\text{H}_5\text{OH}$ system is self-explanatory: The zinc(II) ions, having a closed d^{10} configuration, cannot change spin and have different bond properties than iron complex molecules (this should influence the spin transition behavior).

A remarkable step forward in the efforts to gain a deeper insight into the mechanism of the spin phase transition recently has been achieved by Mikami, Konno, and Saito (30). They determined the crystal structure of $[\text{Fe}(2\text{-pic})_3]\text{Cl}_2 \cdot \text{C}_2\text{H}_5\text{OH}$ at 298, 150, and 90 K, that is, above and below the transition temperature. The crystals were found to be monoclinic, $\text{P}2_1/c$ with $Z = 4$ in the two spin states. They also found eminent changes in iron-nitrogen bond lengths, namely, 2.195 Å for the high-spin state and 2.013 Å for the low-spin state on the average. Most important in the context of the cooperative domain model is their observation that all the amino nitrogen atoms of the cationic complexes on the one side, and the ethanol molecule on the other, are hydrogen bonded to Cl^- ions, forming a two-dimensional hydrogen bond network

along which the spin change information is likely to travel. The same type of two-dimensional hydrogen-bonding network has been observed for the methanolate $[\text{Fe}(2\text{-pic})_3]\text{Cl}_2 \cdot \text{CH}_3\text{OH}$ (32), which also exhibits spin crossover (40).

Most interesting is the observation of Mikami et al. (30) that the ethanol molecules in $[\text{Fe}(2\text{-pic})_3]\text{Cl}_2 \cdot \text{C}_2\text{H}_5\text{OH}$ are disordered in the high-temperature high-spin phase occupying three orientational positions. The population in the three sites changes with temperature, whereby a gradual ordering occurs on lowering the temperature. One of the three sites is favored over the other two and has 100% occupancy at 90 K, that is, in the structure of the low-spin state. The authors conclude that the cooperative nature of the spin transition may be accounted for in terms of an interaction of the spin phase transition and the order-disorder transition of the ethanol molecule through hydrogen bonding. Further support for this conclusion has been obtained in studies of the deuterium isotope effect in the deuterated solvates $[\text{Fe}(2\text{-pic})_3]\text{Cl}_2 \cdot \text{Sol}$ (Sol = $\text{C}_2\text{H}_5\text{OD}$, CH_3OD), which will be discussed in a later section.

INTERPRETATION USING A PHENOMENOLOGICAL THERMODYNAMIC MODEL. Following the suggestion of Sorai and Seki (7, 8) that the spin transition is cooperative in nature, we have attempted to interpret the results of the metal dilution studies on $[\text{Fe}_x\text{Zn}_{1-x}(2\text{-pic})_3]\text{Cl}_2 \cdot \text{C}_2\text{H}_5\text{OH}$ on the basis of a phenomenological thermodynamic model (43). We assume that a "primary" spin change is followed spontaneously by "secondary" spin changes in $n-1$ surrounding molecules. The n molecules of like spin are considered to form a "cooperative" domain. The domain size n may be taken as a measure of the cooperative interaction strength. For simplicity, we assume the number n to be the same for high- and low-spin domains in a given system, but to vary with the iron concentration, $n(x)$. Interactions between the domains, irrespective of the spin state, are considered to be negligible. The systems $[\text{Fe}_x\text{Zn}_{1-x}(2\text{-pic})_3]\text{Cl}_2 \cdot \text{C}_2\text{H}_5\text{OH}$ are treated as temperature-dependent chemical equilibria between high- and low-spin domains, for which the effective enthalpy and entropy changes, $\Delta H_{\text{eff}}(x) = n(x)\Delta H^\circ(x)$ and $\Delta S_{\text{eff}}(x) = n(x) - \Delta S^\circ(x)$ ($\Delta H^\circ(x)$ and $\Delta S^\circ(x)$ are the respective changes for one mole of the complex molecules), may be evaluated from straightforward Arrhenius plots, $\ln K = \ln x_{\text{H}}/(1-x_{\text{H}}) = f(T)$ (43); cf. Figure 5. The values for ΔH_{eff} and ΔS_{eff} thus obtained vary between about 13 kJ mol⁻¹ and 110 J mol⁻¹ K⁻¹, respectively, for the pure iron compound, and between about 2.5 kJ mol⁻¹ and 30 J mol⁻¹ K⁻¹, respectively, for the highly diluted ($x = 0.0009$) system.

The transition temperature as a function of x , $T_c(x) = \Delta H_{\text{eff}}(x)/\Delta S_{\text{eff}}(x)$, takes on values between 120 K for the pure iron compound and 77 K for the system with $x = 0.0009$; the agreement with experimental

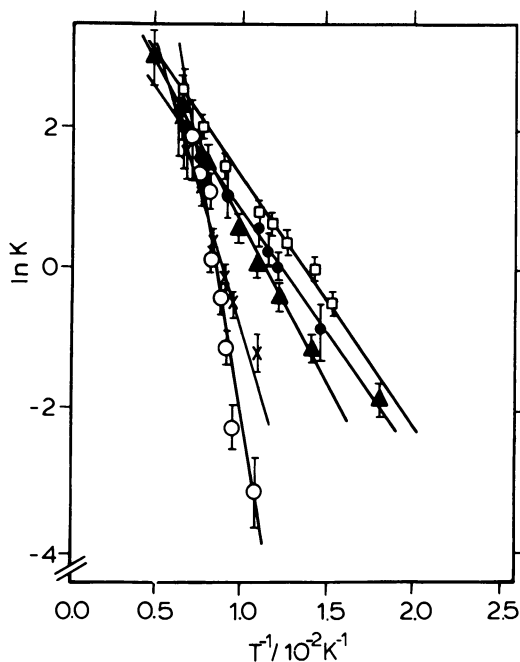


Figure 5. Plot of $\ln K = \ln x_H / (1 - x_H)$ vs. $1/T$ for various iron concentrations x in the solid solutions $[\text{Fe}_x \text{Zn}_{1-x} (2\text{-pic})_3] \text{Cl}_2 \cdot \text{C}_2\text{H}_5\text{OH}$ (43): (●) $x = 0.0009$; (□) $x = 0.029$; (▲) $x = 0.2$; (×) $x = 0.6$; (○) $x = 1.0$.

T_c data is very good. The dependence of T_c on the iron concentration x may be described by the expression

$$T_c(x) = \frac{\Delta H^\circ(x)}{\Delta S^\circ(x)} = \frac{\Delta H^\circ_{\text{Fe}} + \Delta H^\circ_{\text{coop}}(x)}{\Delta S^\circ_{\text{Fe}} + \Delta S^\circ_{\text{coop}}(x)} = \frac{\Delta H^\circ_{\text{Fe}} + Ax^\alpha}{\Delta S^\circ_{\text{Fe}} + Bx^\beta} \quad (1)$$

The $\Delta H^\circ_{\text{Fe}}$ and $\Delta S^\circ_{\text{Fe}}$ terms arise from the changes in electronic state, intramolecular vibrations, and intramolecular electron-phonon interactions, and are considered to be independent of x . The $\Delta H^\circ_{\text{coop}}$ and $\Delta S^\circ_{\text{coop}}$ terms refer to changes in intermolecular vibrations and intermolecular electron-phonon interactions. The A and B correspond to $\Delta H^\circ_{\text{coop}}$ and $\Delta S^\circ_{\text{coop}}$, respectively, in the pure iron compound ($x = 1$); $\alpha > 0$ and $\beta < 0$ serve as damping factors to account for the decrease of $\Delta H^\circ_{\text{coop}}$ and $\Delta S^\circ_{\text{coop}}$ with decreasing x . From an adjustment of Equation 1 to the experimental data of $T_c(x)$ (see Figure 6) it is found, for example, that $\Delta H^\circ_{\text{Fe}} \approx 2000 \text{ J mol}^{-1}$, $A \approx 850 \text{ J mol}^{-1}$, $\Delta S^\circ_{\text{Fe}} \approx 25 \text{ J mol}^{-1} \text{ K}^{-1}$ (43).

Another feature of this phenomenological thermodynamic model is that it enables one to estimate the domain size $n(x)$ from the measured concentration dependence of $\Delta H_{\text{eff}}(x)$ and $\Delta S_{\text{eff}}(x)$ (43). Fitting the expressions

$$\Delta H_{\text{eff}}(x) = \Delta H^\circ(x) \cdot n(x) = (\Delta H^\circ_{\text{Fe}} + Ax^\alpha)(1 + n_0x^\gamma) \quad (2)$$

$$\Delta S_{\text{eff}}(x) = \Delta S^\circ(x) \cdot n(x) = (\Delta S^\circ_{\text{Fe}} + Bx^\beta)(1 + n_0x^\gamma) \quad (3)$$

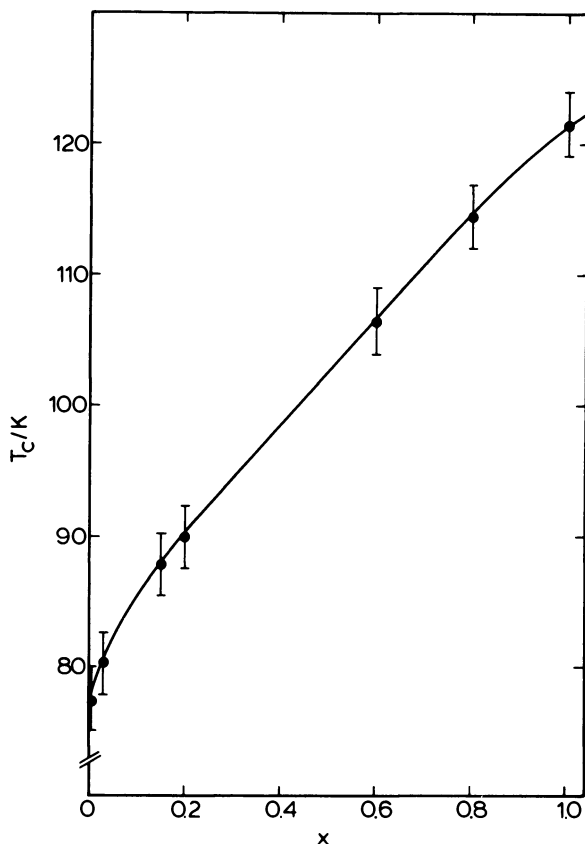


Figure 6. Concentration dependence of the transition temperature $T_c(x)$ for the high-spin/low-spin transition in the solid solutions $[\text{Fe}_x\text{Zn}_{1-x}(2\text{-pic})_3]\text{Cl}_2 \cdot \text{C}_2\text{H}_5\text{OH}$. The experimental points are taken from Refs. 41 and 42. The solid curve has been calculated using Equation 1 and the parameters $\Delta H_{\text{Fe}}^\circ = 1944 \pm 43 \text{ Jmol}^{-1}$, $A = 861 \pm 46 \text{ Jmol}^{-1}$, $\alpha = 0.79 \pm 1.14$, $\Delta S_{\text{Fe}}^\circ = 25.3 \pm 0.3 \text{ Jmol}^{-1} \text{ K}^{-1}$, $B = -2.1 \pm 0.4 \text{ Jmol}^{-1} \text{ K}^{-1}$ and $\beta = 0.51 \pm 0.10$.

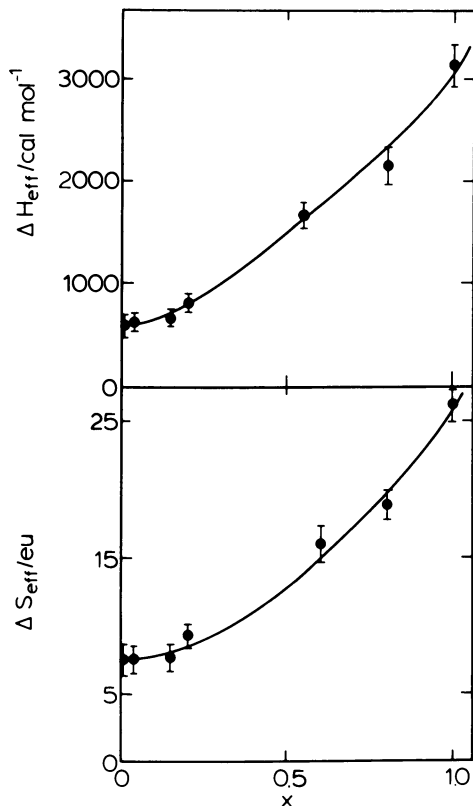


Figure 7. Effective change of enthalpy, $\Delta H_{\text{eff}}(x)$, and entropy, $\Delta S_{\text{eff}}(x)$, of the high-spin/low-spin transition in the solid solutions $[\text{Fe}_x\text{Zn}_{1-x}(\text{2-pic})_3]\text{Cl}_2 \cdot \text{C}_2\text{H}_5\text{OH}$ as a function of the iron concentration x .

The data points are derived from the $\ln K$ vs. $1/T$ plots (see Figure 5) using the experimental $x_H(T)$ data from Refs. 41 and 42. The solid curves have been calculated using Equations 2 and 3 and the following "best-fit" values (43): (top) $\Delta H_{\text{Fe}}^\circ = 2465 \pm 250 \text{ J mol}^{-1}$; $A = 836 \pm 1588 \text{ J mol}^{-1}$; $\beta = 0.90 \pm 0.03$; $\gamma = 1.61 \pm 0.33$; $\eta_0 = 2.9 \pm 1.5$; (bottom) $\Delta S_{\text{Fe}}^\circ = 30.9 \pm 4.6 \text{ J mol}^{-1} \text{ K}^{-1}$; $B = 3.3 \pm 18.8 \text{ J mol}^{-1} \text{ K}^{-1}$; $\alpha = 0.43 \pm 0.47$; $\gamma = 1.76 \pm 0.52$; $\eta_0 = 2.2 \pm 1.4$.

to the experimentally determined data of $\Delta H_{\text{eff}}(x)$ and $\Delta S_{\text{eff}}(x)$ (see Figure 7) yields an average domain size of $n(x=1) = 3.5$ for the pure iron compound $[\text{Fe}(\text{2-pic})_3]\text{Cl}_2 \cdot \text{C}_2\text{H}_5\text{OH}$. The values of $\Delta H_{\text{Fe}}^\circ \approx 2450 \text{ J mol}^{-1}$, $A \approx 840 \text{ J mol}^{-1}$, and $\Delta S_{\text{Fe}}^\circ \approx 31 \text{ J mol}^{-1} \text{ K}^{-1}$ are close to those obtained from the $T_c(x)$ fit just described. The expansion of the domain size with the concentration x , approximated by $n(x) = 1 + n_0 x^\gamma$, decreases rather strongly with falling iron concentration ($\gamma \approx 1.7$).

Solid Solutions of $[\text{Fe}_x\text{Co}_{1-x}(\text{2-pic})_3]\text{Cl}_2 \cdot \text{C}_2\text{H}_5\text{OH}$. Mössbauer studies on solid solutions with the isomorphous cobalt(II) compound

(45) lead to findings similar to those in the Fe/Zn/2-pic system. The series of temperature-dependent spectra of the system $[\text{Fe}_{0.65}\text{Co}_{0.35}(\text{2-pic})_3]\text{Cl}_2 \cdot \text{C}_2\text{H}_5\text{OH}$ reproduced in Figure 8 proves again that the high- (outer two lines) and low-spin states (inner two lines) coexist in chemical equilibrium. Figures 9 and 10 demonstrate the effect of metal dilution in the Fe/Co/2-pic system. As in the Fe/Zn/2-pic systems, the high-spin state becomes increasingly favored with decreasing iron concentration. The transition temperature $T_c(x)$ is shifted to lower temperatures and the slope at T_c becomes less steep with decreasing x . However, there is a difference between the two mixed-crystal systems as can be seen from Figure 11: The transition temperature $T_c(x)$ is higher in the case of the Fe/Co/2-pic system than in the Fe/Zn/2-pic system at all concentrations. This difference is probably due to the different bond properties of the pure cobalt matrix as compared to the pure zinc matrix; there is a higher degree of π -backbonding in the cobalt compound with an open d -shell than in the zinc compound with a closed d -shell, giving rise to stronger metal–ligand bonds and thus to a more rigid lattice in the cobalt matrix than in the zinc matrix. This in turn decreases the relative stability of the high-spin state ${}^5T_2(\text{O}_h)$ of iron(II) in the cobalt matrix, at a given temperature and a given iron concentration, as compared to that in the zinc matrix. An ionic size effect is not likely to apply here because the ionic radii of Co^{2+} and Zn^{2+} are nearly equal, and, from this point of view alone, the capability of stabilizing iron(II) in either the high- or low-spin state should not differ significantly in the two hosts.

The effective enthalpy and entropy changes as a function of x , $\Delta H_{\text{eff}}(x)$ and $\Delta S_{\text{eff}}(x)$, for the spin transition in $[\text{Fe}_x\text{Co}_{1-x}(\text{2-pic})_3]\text{Cl}_2 \cdot \text{C}_2\text{H}_5\text{OH}$ are plotted in Figure 12. The values are considerably higher than the corresponding ones in $[\text{Fe}_x\text{Zn}_{1-x}(\text{2-pic})_3]\text{Cl}_2 \cdot \text{C}_2\text{H}_5\text{OH}$.

The quadrupole splitting of the low-spin state, ${}^1A_1(\text{O}_h)$, of iron(II) in the cobalt host shows the same behavior as in the zinc host, namely, it is independent of temperature and of iron concentration x ($\Delta E_Q(x) = 0.38\text{--}0.45 \text{ mms}^{-1}$ for the low-spin state in the cobalt matrix, $\Delta E_Q(x) = 0.39\text{--}0.44 \text{ mm s}^{-1}$ in the zinc matrix). The quadrupole splitting of the high-spin state, ${}^5T_2(\text{O}_h)$, of iron(II) is also independent of the iron concentration in the two hosts (about 2.05 mm s^{-1} on the average at room temperature), but varies with temperature (cf. Figure 13), which is well-known for iron(II) high-spin compounds (51). Following Ingalls' treatment (51) we have adjusted the expression

$$\Delta E_Q(T) = \frac{1}{2} e^2Q(1 - R) \langle r^{-3} \rangle_{\text{ed}} \alpha_{\text{MO}}^2 F(\delta_{\text{tet}}, \alpha_\lambda^2 \lambda_0, T, \epsilon_r) + \Delta E_Q^{\text{const}} \quad (4)$$

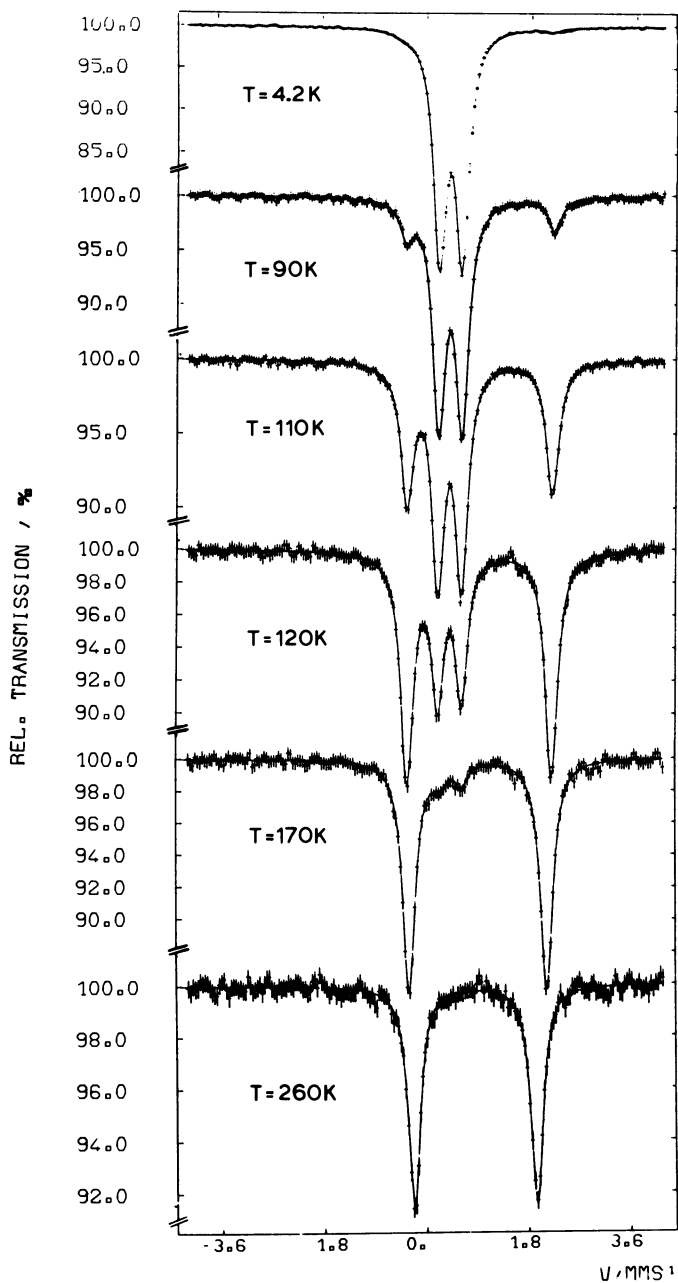


Figure 8. The ^{57}Fe Mössbauer spectra of $[\text{Fe}_{0.65}\text{Co}_{0.35}(\text{2-pic})_3]\text{Cl}_2 \cdot \text{C}_2\text{H}_5\text{OH}$ as a function of temperature (45)

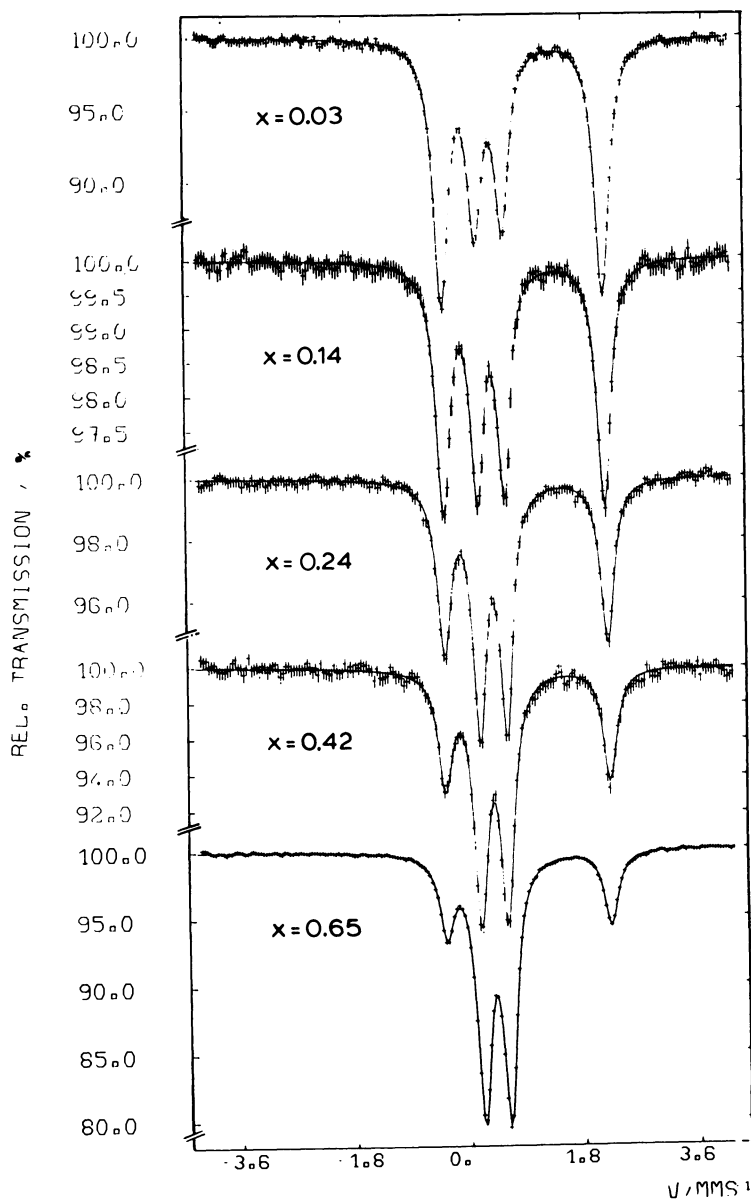


Figure 9. The ^{57}Fe Mössbauer spectra of $[Fe_xCo_{1-x}(2-pic)]_3Cl_2 \cdot C_2H_5OH$ at 100 K as a function of iron concentration x (45)

to the experimental data of $\Delta E_Q(T)$ for the high-spin quadrupole doublet (45). The δ_{tet} and ϵ_r terms are the parameters of tetragonal and rhombic distortion, respectively. The α_{MO}^2 and $\alpha\lambda^2$ terms are covalency factors reducing the expectation value of $\langle r^{-3} \rangle_{3d^6}$ and the spin-orbit coupling parameter λ_0 of a free $3d$ ion, respectively. The other quantities in Equation 4 have the usual meaning (38, 42, 51). The calculation was carried out as described in Refs. 42 and 51, and the results obtained for the fit parameters are listed in Table I. Although the error limits vary, and are very large in some cases, it appears as though there is a certain correlation between δ_{tet} , ϵ_r , and $\Delta E_Q^{\text{const}}$, and the iron concentration x : (1) At both ends of x , $x \rightarrow 0$ and $x \rightarrow 1$, both crystal field distortion parameters δ_{tet} and ϵ_r tend to be largest, whereas they seem to pass through a minimum at $x \approx 0.5$. (2) The temperature-independent contribution to the quadrupole splitting, $\Delta E_Q^{\text{const}}$, seems to show the reverse, namely, it is minimal at both ends of the concentration range and maximal at $x \approx 0.5$.

The measured chemical shift is also independent of the iron concentration, as in the case of the $[\text{Fe}_x\text{Zn}_{1-x}(\text{2-pic})_3]\text{Cl}_2 \cdot \text{C}_2\text{H}_5\text{OH}$ systems (41, 42). Its variation with temperature (see Figure 14) is due to the well-known influence of the second-order Doppler effect.

Solid Solutions of $[\text{Fe}_x\text{M}_{1-x}(\text{phen})_2(\text{NCS})_2]$. The ${}^1\text{A}_1(\text{O}_h) \rightleftharpoons {}^5\text{T}_2(\text{O}_h)$ spin crossover has been known to occur in $[\text{Fe}(\text{phen})_2(\text{NCS})_2]$ (phen = 1,10-phenanthroline) for a long time (35). The spin transition

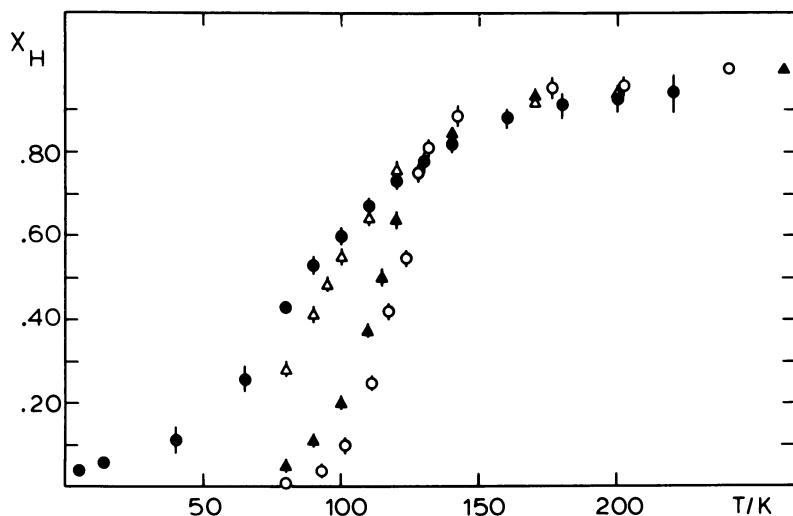


Figure 10. Temperature dependence of the area fraction x_H of the high-spin quadrupole doublet in the Mössbauer spectra of $[\text{Fe}_x\text{Co}_{1-x}(\text{2-pic})_3]\text{Cl}_2 \cdot \text{C}_2\text{H}_5\text{OH}$ (45): (●) $x = 0.006$; (△) $x = 0.14$; (▲) $x = 0.65$; (○) $x = 1$.

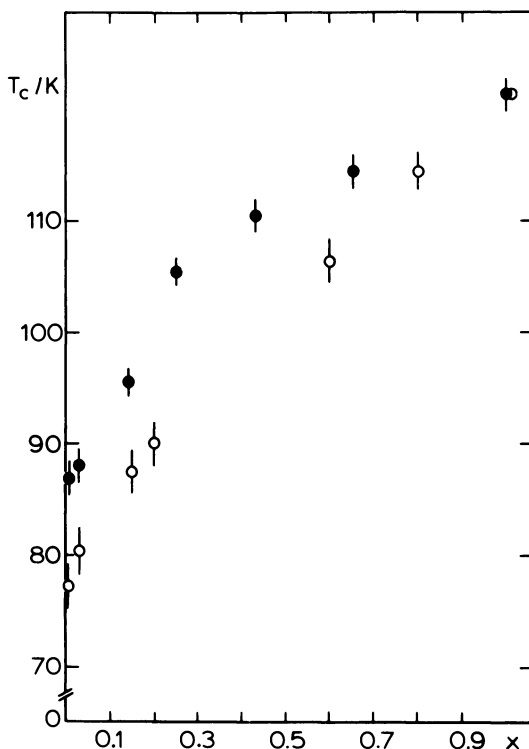


Figure 11. Concentration dependence of the transition temperature $T_c(x)$ of the solid solutions $[Fe_xM_{1-x}(2-pic)_3]Cl_2 \cdot C_2H_5OH$ ($M = Co$ (●), Zn (○)) (41, 42, 45).

Table I. Best-Fit Values for the Tetragonal (δ_{tet}) and Rhombic (ϵ_r) Ligand Field Distortions, and for the Temperature-Independent Contribution to the Quadrupole Splitting, ΔE_Q^{const} , as a Function of the Iron Concentration in $[Fe_xCo_{1-x}(2-pic)_3]Cl_2 \cdot C_2H_5OH$, Obtained from Fitting Equation 4 to the Experimental Points of $\Delta E_Q(x)$ of the High-Spin Quadrupole Doublet^a

x	α_λ^2	δ_{tet} (cm^{-1})	ϵ_r (cm^{-1})	ΔE_Q^{const} ($mm\ s^{-1}$)	α_{MO}^2
0.0060	0.7 ^b	-214 ± 1	280 ± 1	1.018 ± 0.003	0.7 ^b
0.0214	0.7 ^b	-352 ± 1	435 ± 13	0.599 ± 0.017	0.7 ^b
0.0286	0.7 ^b	-236 ± 67	290 ± 108	0.950 ± 0.270	0.7 ^b
0.1426	0.7 ^b	-185^b	201 ± 10	0.973 ± 0.169	0.7 ^b
0.2498	0.7 ^b	-157 ± 21	119 ± 68	1.357 ± 0.114	0.7 ^b
0.4245	0.7 ^b	-150 ± 1	93 ± 22	1.373 ± 0.008	0.7 ^b
0.6538	0.7 ^b	-165 ± 51	114 ± 173	1.276 ± 0.268	0.7 ^b
1.0	0.7 ^b	-256 ± 119	329 ± 184	0.828 ± 0.453	0.7 ^b

^a The covalency factors α_λ^2 and α_{MO}^2 were kept fixed to 0.7 (45).

^b Parameter value kept fixed.

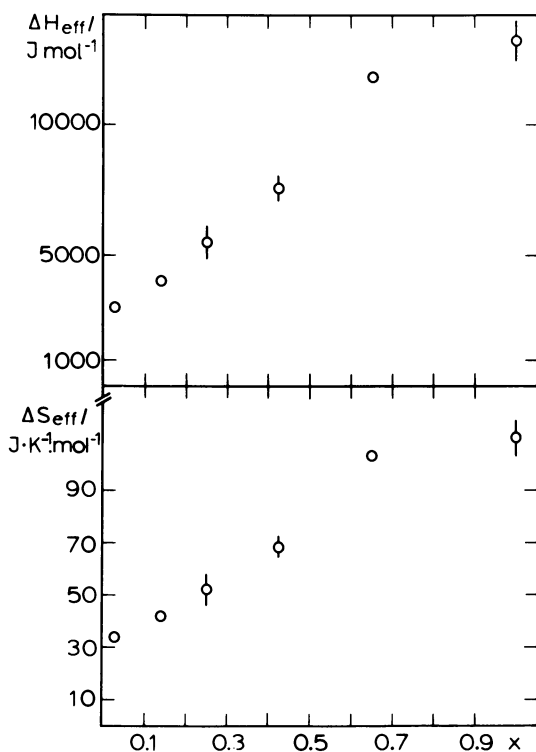


Figure 12. Effective change of enthalpy, $\Delta H_{eff}(x)$, and entropy, $\Delta S_{eff}(x)$, of the spin transition in $[\text{Fe}_x\text{Co}_{1-x}(\text{2-pic})_3]\text{Cl}_2 \cdot \text{C}_2\text{H}_5\text{OH}$ as a function of the iron concentration (45).

is very sharp (within a few Kelvin) near 175 K. This spin crossover system has been studied extensively by a number of research groups using various techniques (7, 8, 20, 21, 22, 53–59). Mössbauer effect studies have been reported by Dézsi et al. (54) and König et al. (53).

Sorai and Seki (7, 8) performed precise heat capacity measurements on $[\text{Fe}(\text{phen})_2(\text{NCS})_2]$. The results led them to the conclusion that the nature of the spin transition is first-order. They also suggested that the spin transition takes place through a coupling between the electronic state and the vibrational modes of the lattice surroundings, and that the spin conversion occurs quasi-simultaneously in a group of molecules that form a so-called cooperative domain. Sorai and Seki concluded from the abrupt spin transition that the cooperative coupling in this system is strong, leading to large domains of about 100 molecules, according to their estimate.

The idea of a cooperative spin transition has been well supported by the metal dilution studies on $[\text{Fe}(\text{2-pic})_3]\text{Cl}_2 \cdot \text{C}_2\text{H}_5\text{OH}$, as described

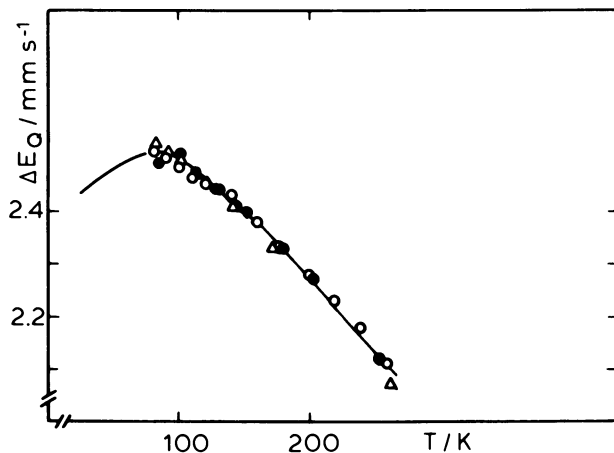


Figure 13. Quadrupole splitting of the high-spin state of iron(II) as a function of temperature in $[\text{Fe}_x\text{Co}_{1-x}(\text{2-pic})_3]\text{Cl}_2 \cdot \text{C}_2\text{H}_5\text{OH}$ for three different iron concentrations (45). The solid line has been calculated for the undiluted compound $[\text{Fe}(\text{2-pic})_3]\text{Cl}_2 \cdot \text{C}_2\text{H}_5\text{OH}$ (40); (O) $x = 0.006$; (Δ) $x = 0.654$; (\bullet) $x = 1.0$.

in earlier sections. In the framework of this cooperative domain model, $[\text{Fe}(\text{2-pic})_3]\text{Cl}_2 \cdot \text{C}_2\text{H}_5\text{OH}$, with a more gradual spin transition behavior than $[\text{Fe}(\text{phen})_2(\text{NCS})_2]$, may be considered a “weakly coupled” system, for which the domain size has been estimated to be 4–6 molecules (43, 44). Recently we have undertaken Mössbauer effect studies on $[\text{Fe}_x-$

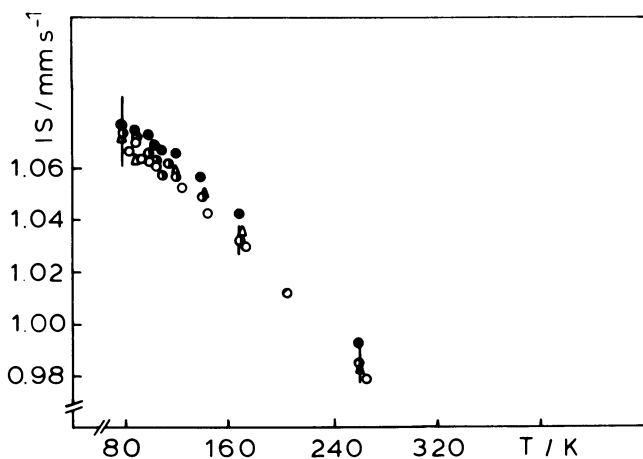


Figure 14. Temperature dependence of the measured chemical shift of the high-spin quadrupole doublet of iron(II) in $[\text{Fe}_{0.14}\text{Co}_{0.86}(\text{2-pic})_3]\text{Cl}_2 \cdot \text{C}_2\text{H}_5\text{OH}$ (45): (O) $x = 0.029$; (\bullet) $x = 0.250$; (\odot) $x = 0.425$; (Δ) $x = 0.654$.

$M_{1-x}(\text{phen})_2(\text{NCS})_2$], with $M = \text{Mn, Co, Ni, Zn}$ to see how metal dilution affects the spin transition characteristics of a "strongly coupled" spin crossover system (47).

All the mixed crystals were prepared by coprecipitation (47). The x-ray powder patterns of the pure compounds [$M(\text{phen})_2(\text{NCS})_2$] with $M = \text{Fe, Mn, Co, and Ni}$ show that these compounds are isomorphous with each other but not with [$\text{Zn}(\text{phen})_2(\text{NCS})_2$]. We therefore studied the [$\text{Fe}_x\text{Zn}_{1-x}(\text{phen})_2(\text{NCS})_2$] system at very low iron concentrations ($x = 0.001$ and $x = 0.01$) only, where good solid solutions could be prepared.

SPIN TRANSITION CHARACTERISTICS IN [$\text{Fe}_x\text{M}_{1-x}(\text{PHEN})_2(\text{NCS})_2$]. A few representative Mössbauer spectra for the system [$\text{Fe}_x\text{Mn}_{1-x}(\text{phen})_2(\text{NCS})_2$] are shown in Figure 15. The spectra reveal the same general feature as in the case of [$\text{Fe}_x\text{M}_{1-x}(\text{2-pic})_3$]Cl₂ · C₂H₅OH, namely, at a given temperature the area fraction of the high-spin quadrupole doublet increases with decreasing iron concentration, irrespective of the nature of the M^{2+} metal ion; that is, the relative stability of the high-spin state of iron(II) increases upon iron dilution.

More instructive are the spin conversion curves $x_H(T)$, determined for the temperature range 300–4.2 K and for various iron concentrations, as shown in Figures 16, 17, and 18. The spin conversion for the undiluted ($x=1$) [$\text{Fe}(\text{phen})_2(\text{NCS})_2$], which is also plotted in Figures 16, 17, and 18 for comparison, refers to the sample prepared by the precipitation method (36). The spin transition in this sample is rather gradual compared to the abrupt spin transition in a sample prepared by the extraction method (36); the reason lies in the difference in crystal size and quality. This phenomenon will be dealt with in more detail later.

In the case of [$\text{Fe}_x\text{Mn}_{1-x}(\text{phen})_2(\text{NCS})_2$] the transition temperature T_c shifts to lower values with dilution, and the residual paramagnetism (RP) increases systematically with decreasing x (see Figure 16). The sharp transition in the undiluted [$\text{Fe}(\text{phen})_2(\text{NCS})_2$] becomes increasingly gradual upon dilution. It appears that in the limit of infinite dilution, the spin crossover would be totally lost, and all the isolated [$\text{Fe}(\text{phen})_2(\text{NCS})_2$] molecules embedded in the manganese host should stabilize in the $^5T_2(O_h)$ ground state. It may be significant to note here that the metal dilution studies on [$\text{Fe}_x\text{Zn}_{1-x}(\text{2-pic})_3$]Cl₂ · C₂H₅OH (41, 42) showed that, even though the transition temperature T_c is lowered and the slope at T_c diminishes with increasing dilution, the temperature-dependent high-spin \rightleftharpoons low-spin crossover is still observable even at the lowest iron concentrations under study. The results that experiments on the mixed-crystal systems have in common is that some cooperative interactions appear to be necessary to induce and/or to effect the spin crossover.

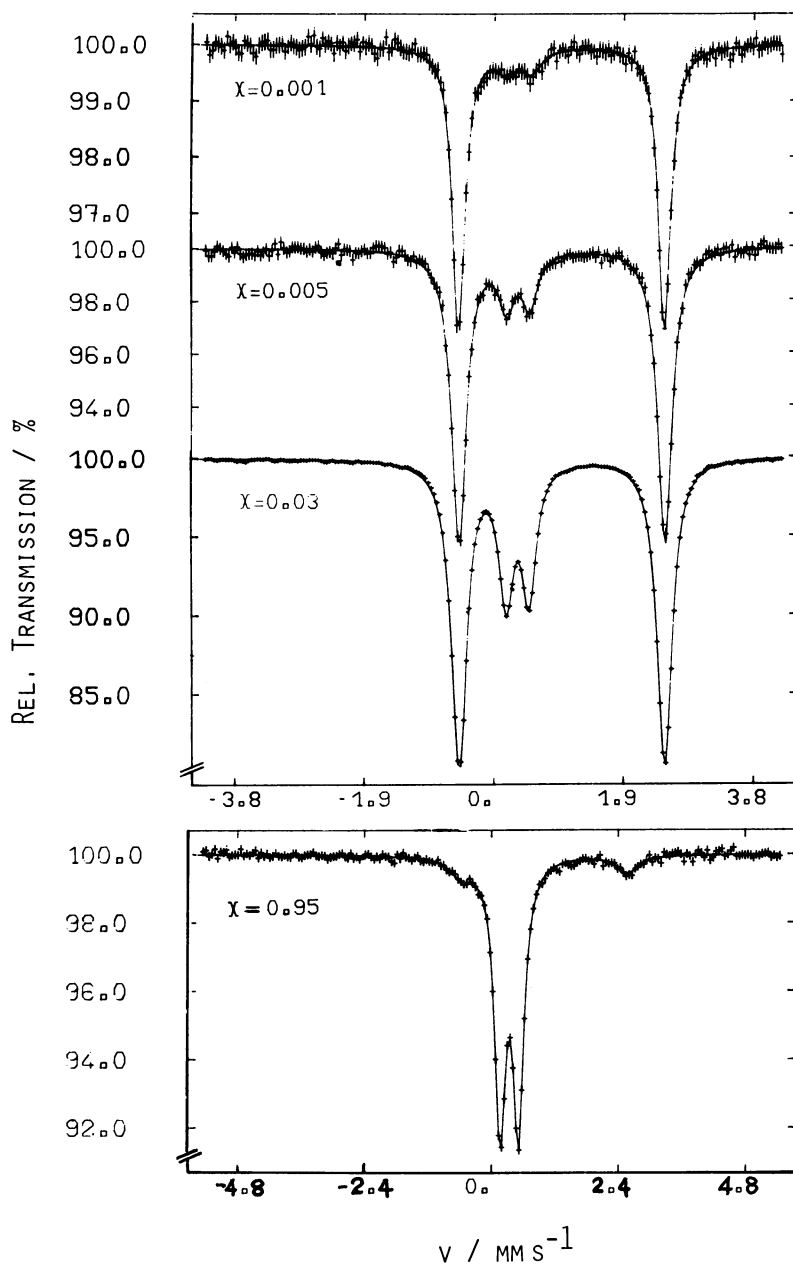


Figure 15. The ^{57}Fe Mössbauer spectra of $[\text{}^{57}\text{Fe}_x\text{Mn}_{1-x}(\text{phen})_2(\text{NCS})_2]$ at 5 K as a function of iron concentration (47)

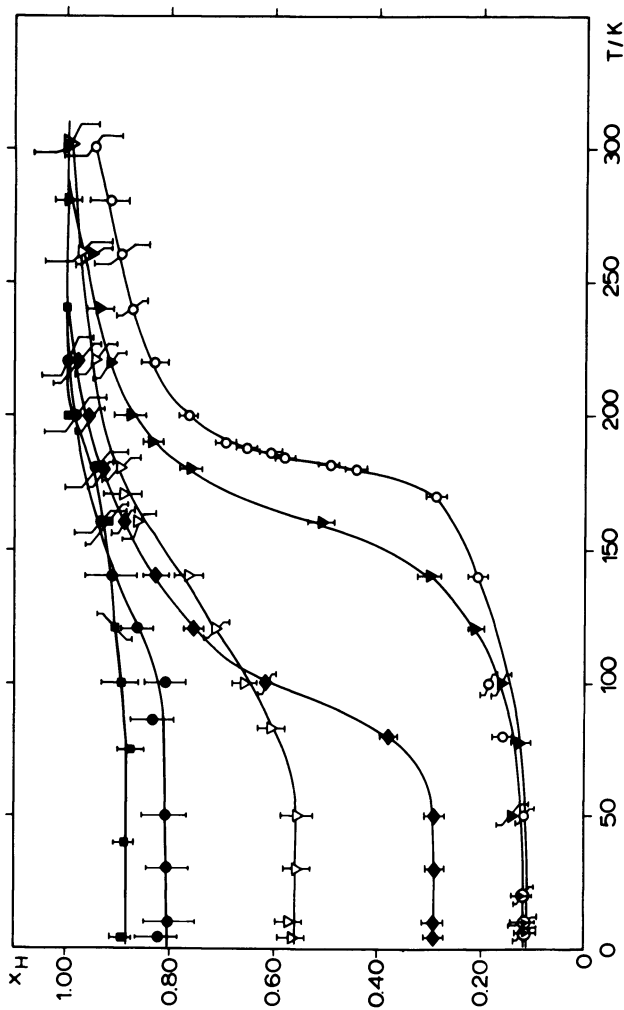


Figure 16. Temperature dependence of the area fraction x_H of the high-spin quadrupole doublet in the Mössbauer spectra of mixed crystals of $[\text{Fe}_x\text{Mn}_{1-x}(\text{phen})_2(\text{NCS})_2]$ (47); (\bullet) $x = 0.001$; (\circ) $x = 0.14$; (∇) $x = 0.24$; (\blacklozenge) $x = 0.51$; (\blacktriangledown) $x = 0.75$; (\circ) $x = 1.00$.

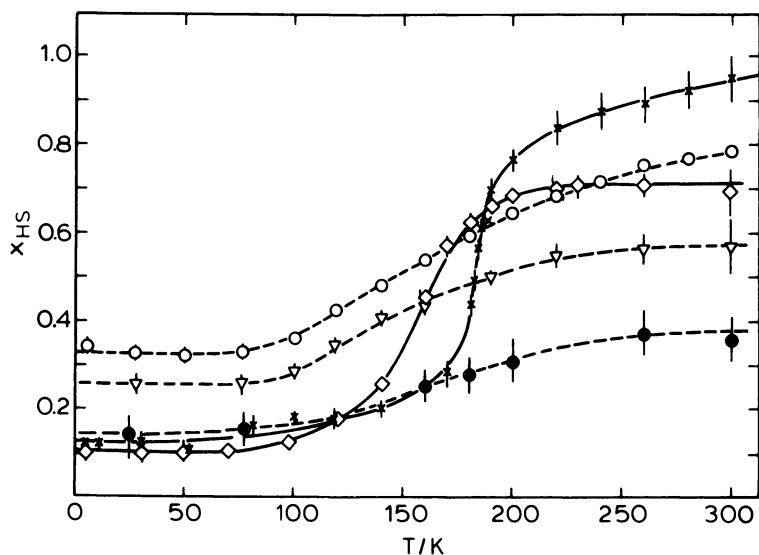


Figure 17. Temperature dependence of the area fraction x_H of the high-spin quadrupole doublet in the Mössbauer spectra of mixed crystals of $[Fe_xCo_{1-x}(phen)_2(NCS)_2]$ (47): (●) $x = 0.001$; (▽) $x = 0.01$; (○) $x = 0.14$; (◇) $x = 0.5$; (×) $x = 1.0$.

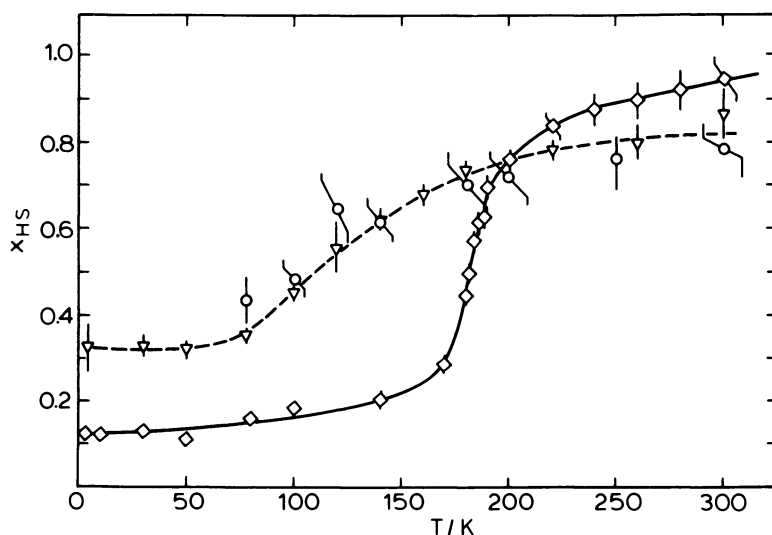


Figure 18. Temperature dependence of the area fraction x_H of the high-spin quadrupole doublet in the Mössbauer spectra of highly diluted solid solutions of $[Fe_xZn_{1-x}(phen)_2(NCS)_2]$ (47): (▽) $x = 0.01$; (○) $x = 0.001$; (◇) $x = 1.0$.

It is likely that the systematic increase in the residual paramagnetism, as reflected in the increase of the high-spin area fraction x_H in the low-temperature Mössbauer spectra of $[\text{Fe}_x\text{Mn}_{1-x}(\text{phen})_2(\text{NCS})_2]$ is due to the lattice constants of $[\text{Mn}(\text{phen})_2(\text{NCS})_2]$ as compared to the iron compound, caused by the fact that $r(\text{Mn}^{2+}) > r(\text{Fe}^{2+})$. As a consequence, the iron–nitrogen bond lengths of the iron complex molecule embedded in the manganese host tends to increase, and the concomitant reduction in the crystal field strength at the iron site leads to a stabilization of the high-spin state.

Drickamer et al. (60) have used similar arguments to explain the observation, also by Mössbauer spectroscopy, that FeS_2 , when diluted into MnS_2 , stabilizes predominantly in the high-spin state at atmospheric pressure, whereas pure FeS_2 is known to possess a ${}^1A_1(O_h)$ ground state. The fraction of Fe^{2+} ions in the high-spin state was found to increase with dilution. Samples of the system $\text{Fe}_x\text{Mn}_{1-x}\text{S}_2$, when subjected to moderate pressures, were made to exhibit a high-spin \rightleftharpoons low-spin crossover. Similar results were obtained with samples containing 2% ${}^{57}\text{Fe}$ in MnSe_2 and MnTe_2 , respectively.

To prove the validity of this argument of the ionic size effect on the relative stability of the high-spin and low-spin states, we also studied the mixed-crystal series of $[\text{Fe}_x\text{Co}_{1-x}(\text{phen})_2(\text{NCS})_2]$ and $[\text{Fe}_x\text{Ni}_{1-x}(\text{phen})_2(\text{NCS})_2]$ and the highly diluted solution $[\text{Fe}_x\text{Zn}_{1-x}(\text{phen})_2(\text{NCS})_2]$ by means of Mössbauer spectroscopy. The spin conversion curves, $x_H(T)$, for the iron/cobalt and the iron/zinc systems are shown in Figures 17 and 18. In the cobalt, nickel (not shown), and zinc lattices, the spin crossover does not go to completion, leaving a residual paramagnetism at temperatures well below T_c and a substantial residual diamagnetism (RD) at temperatures well above T_c . The transition is no longer sharp as in the pure $[\text{Fe}(\text{phen})_2(\text{NCS})_2]$, again indicating that the cooperative strength seems to be weakened on dilution.

In the case of $[\text{Fe}_x\text{Co}_{1-x}(\text{phen})_2(\text{NCS})_2]$, the residual paramagnetism decreases with dilution in the samples with low iron concentration (see Figure 17). However, the residual diamagnetism at the high-temperature end increases with metal dilution, and it appears that the spin crossover phenomenon becomes totally quenched at infinite dilution. This would imply that the isolated $[\text{Fe}(\text{phen})_2(\text{NCS})_2]$ molecules accommodated in the lattice of the cobalt compound tend to stabilize in the low-spin ${}^1A_1(O_h)$, contrary to what is observed for the $[\text{Fe}_x\text{Mn}_{1-x}(\text{phen})_2(\text{NCS})_2]$ mixed crystals. A similar partial stabilization of the low-spin state, ${}^2T_2(O_h)$, in the case of tris(1-pyrrolidinecarbodithioato)iron(III) diluted in the corresponding cobalt(III) lattice also has been reported (61). Here, too, it was assumed that the structure of the iron(III) complex molecule

is modified slightly (presumably with shortening of the iron–sulfur bond) to approach that of the cobalt(III) host lattice which has a shorter metal–sulfur bond.

According to the Mössbauer spectra of the $[\text{Fe}_x\text{Ni}_{1-x}(\text{phen})_2(\text{NCS})_2]$ mixed crystals, the low-spin state of iron(II) seems to be more easily stabilized in the nickel host than in the cobalt host.

In the solid solutions of $[\text{Fe}_x\text{Zn}_{1-x}(\text{phen})_2(\text{NCS})_2]$, the spin crossover behavior is almost independent of the iron concentration in the range $x = 0.001\text{--}0.01$ (see Figure 18). However, the transition is much more gradual than in the undiluted system, with a high residual paramagnetism fraction below T_c and a nearly 20% residual diamagnetism fraction at the high-temperature end, as in the cobalt and nickel mixed crystals. The residual paramagnetism fraction is much higher than in the corresponding cobalt or nickel hosts with comparable iron concentrations.

These observations seem to show qualitatively that the amount of residual paramagnetism in the $[\text{Fe}_x\text{M}_{1-x}(\text{phen})_2(\text{NCS})_2]$ systems is correlated with the relative ionic radii of the M^{2+} and Fe^{2+} ions. The ionic radii are known to follow the order: Mn^{2+} (0.82 Å) > Fe^{2+} (0.74 Å) \approx Zn^{2+} > Co^{2+} (0.72 Å) > Ni^{2+} (0.70 Å). From the Mössbauer effect studies (47) it appears that the host lattices with $r(\text{M}^{2+}) > r(\text{Fe}^{2+})$ favor the stabilization of the high-spin state of iron(II) as in the case of $[\text{Fe}_x\text{Mn}_{1-x}(\text{phen})_2(\text{NCS})_2]$, and the host lattices with $r(\text{M}^{2+}) < r(\text{Fe}^{2+})$ favor the stabilization of the low-spin state of iron(II) as in $[\text{Fe}_x\text{Co}_{1-x}(\text{phen})_2(\text{NCS})_2]$ and $[\text{Fe}_x\text{Ni}_{1-x}(\text{phen})_2(\text{NCS})_2]$. This ionic size effect may be rationalized in terms of an alteration of the iron–nitrogen bond length with a concomitant change in the crystal field strength at the iron site. In the case of $r(\text{M}^{2+}) > r(\text{Fe}^{2+})$, a kind of negative lattice pressure acting on the $[\text{FeN}_6]$ chromophore causes the iron–nitrogen bond to increase and the crystal field strength to decrease, which increases the tendency to stabilize the high-spin state; in the case of $r(\text{M}^{2+}) < r(\text{Fe}^{2+})$, a positive lattice pressure acting on the $[\text{FeN}_6]$ chromophore forces the iron–nitrogen bond to decrease and the crystal field strength to increase, which tends to favor the low-spin state.

The most important conclusion from these metal dilution studies, in $[\text{Fe}_x\text{M}_{1-x}(2\text{-pic})_3]\text{Cl}_2 \cdot \text{C}_2\text{H}_5\text{OH}$ as well as in $[\text{Fe}_x\text{M}_{1-x}(\text{phen})_2(\text{NCS})_2]$, is that a cooperative interaction exists between the electronic state of the iron ion and the surrounding lattice, although the true nature of this interaction and details of the spin transition are still much in the dark.

MÖSSBAUER PARAMETERS OF $[\text{FeM}_{1-x}(\text{PHEN})_2(\text{NCS})_2]$. Figures 19, 20, and 21 show that the magnitude and temperature dependence of the quadrupole splitting of the high-spin state of iron(II) in $[\text{Fe}_x\text{M}_{1-x}(\text{phen})_2(\text{NCS})_2]$ are similar for all iron concentrations in each mixed-crystal

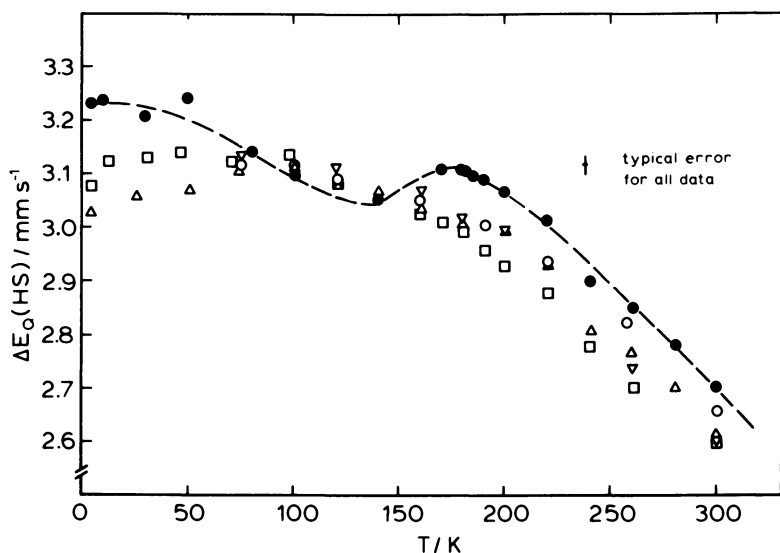


Figure 19. Temperature dependence of the quadrupole splitting of the high-spin state of iron(II) in the mixed crystals of $[\text{Fe}_x\text{Co}_{1-x}(\text{phen})_2(\text{NCS})_2]$ (47). The dashed line refers to the undiluted $[\text{Fe}(\text{phen})_2(\text{NCS})_2]$ (precipitated), for which an anomaly in the $\Delta E_Q(\text{HS})$ vs. T curve was observed near T_c (36); (●) $x = 1.0$; (□) $x = 0.5$; (Δ) $x = 0.14$; (○) $x = 0.01$; (∇) $x = 0.001$.

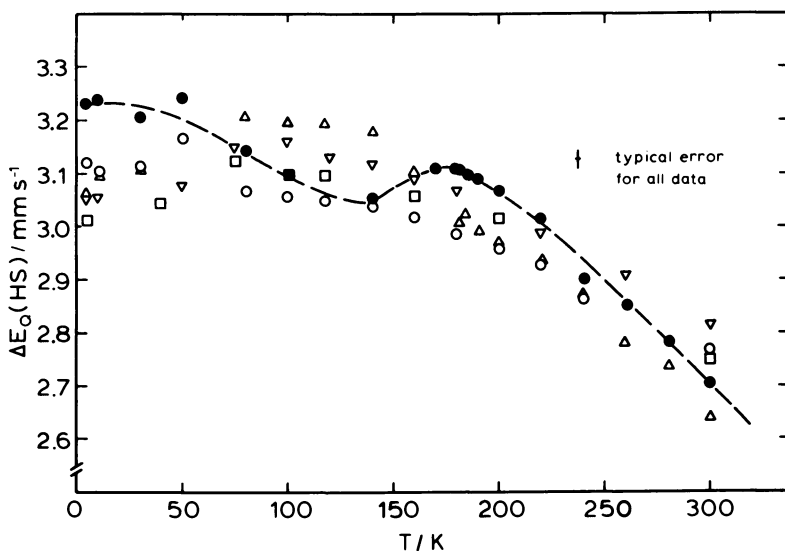


Figure 20. Temperature dependence of the quadrupole splitting of the high-spin state of iron(II) in the mixed crystals of $[\text{Fe}_x\text{Mn}_{1-x}(\text{phen})_2(\text{NCS})_2]$ (47): (●) $x = 1.0$; (Δ) $x = 0.95$; (○) $x = 0.51$; (∇) $x = 0.24$; (□) $x = 0.001$.

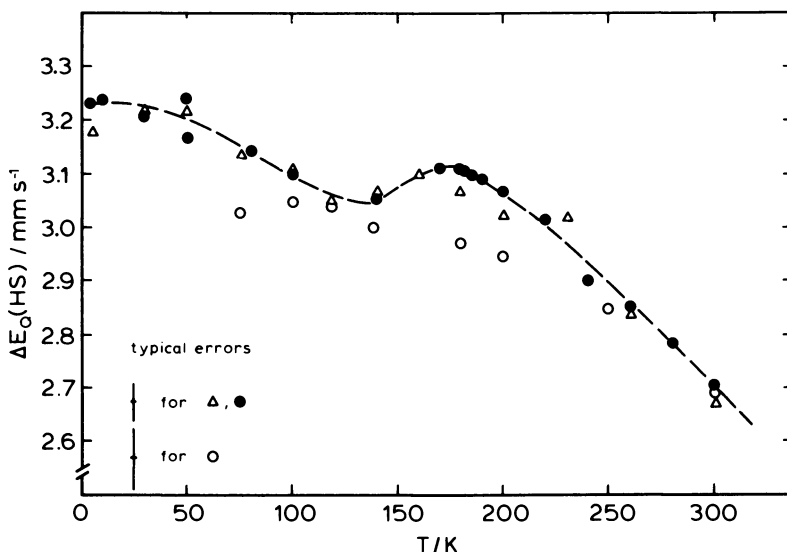


Figure 21. Temperature dependence of the quadrupole splitting of the high-spin state of iron(II) in the highly diluted solid solutions of $[\text{Fe}_x\text{Zn}_{1-x}(\text{phen})_2(\text{NCS})_2]$ (47): (●) $x = 1.0$; (△) $x = 0.01$; (○) $x = 0.001$.

series, and when comparing series having a different host metal M^{2+} with each other. This indicates that, as in the case of the $[\text{Fe}_x\text{M}_{1-x}(2\text{-pic})_3]\text{-Cl}_2 \cdot \text{C}_2\text{H}_5\text{OH}$ series, the electronic environment around the iron(II) ion is not very different in all the mixed crystals. However, it is interesting to note that the anomaly in the temperature dependence of $\Delta E_Q(\text{HS})$ found in the pure $[\text{Fe}(\text{phen})_2(\text{NCS})_2]$ prepared by the precipitation method (36) no longer appears in the mixed-crystal series with $M = \text{Co}$, Mn , Ni (see Figures 19 and 20), but is still present in the highly diluted solid solution of $[\text{Fe}_{0.01}\text{Zn}_{0.99}(\text{phen})_2(\text{NCS})_2]$ (see Figure 21).

The magnitude and temperature dependence of the measured chemical shift of the high-spin state are also very similar in these systems; the temperature dependence may be rationalized as being mainly due to the second-order Doppler shift.

The temperature dependence of the chemical shift of the low-spin doublet is less pronounced, and the quadrupole splitting also remains fairly constant.

Highly Diluted Solutions of $[\text{}^{57}\text{Fe}_x\text{M}_{1-x}(\text{bipy})_3](\text{ClO}_4)_2$ ($M = \text{Mn}$, Ni , Zn) and $[\text{}^{57}\text{Fe}_x\text{M}_{1-x}(\text{phen})_3](\text{ClO}_4)_2$ ($M = \text{Ni}$, Zn). The low-spin complexes $[\text{Fe}(\text{phen})_3](\text{ClO}_4)_2$ and $[\text{Fe}(\text{bipy})_3](\text{ClO}_4)_2$ (bipy = 2,2'-dipyridyl) are known to have crystal field potentials (V_{CF}) at the iron site not very far from the critical crossover point, $V_{\text{CF}} = \bar{P}$ (\bar{P} = mean spin-pairing energy) (62, 63). However, apparently the difference (V_{CF}

$-\bar{P}$) is considerably larger than kT , so that the high-spin state of iron(II) is not thermally populated to any measurable extent at room temperature.

Stimulated by what we have learned in the metal dilution studies on the real crossover systems $[\text{Fe}(2\text{-pic})_3]\text{Cl}_2 \cdot \text{C}_2\text{H}_5\text{OH}$ and $[\text{Fe}(\text{phen})_2(\text{NCS})_2]$, namely, the important result that the relative stability of the high-spin state increases markedly on metal dilution and that, in the case of $r(M^{2+}) > r(\text{Fe}^{2+})$, the low-spin state eventually may become totally lost at infinite dilution, we recently performed Mössbauer effect studies on the highly diluted solid solutions $[\text{}^{57}\text{Fe}_x\text{M}_{1-x}(\text{bipy})_3](\text{ClO}_4)_2$ ($M = \text{Mn, Ni, Zn; } x \leq 0.005$) and $[\text{}^{57}\text{Fe}_x\text{M}_{1-x}(\text{phen})_3](\text{ClO}_4)_2$ ($M = \text{Ni, Zn; } x \leq 0.005$) (46). The purpose was to see whether the normal low-spin state of the $[\text{Fe}(\text{phen})_3]^{2+}$ complex molecule eventually turns over to the high-spin state when sufficiently diluted in a matrix with $r(M^{2+}) > r(\text{Fe}^{2+})$. Although only $[\text{Fe}(\text{phen})_3](\text{ClO}_4)_2$ and $[\text{Fe}(\text{bipy})_3](\text{ClO}_4)_2$ are isomorphous with each other, we did not expect any difficulty in preparing all the systems under study, since the very small fraction of iron ions ($x \leq 0.005$) should be easily accommodated in normal lattice sites of the host.

Some representative Mössbauer spectra recorded of the $[\text{}^{57}\text{Fe}_x\text{M}_{1-x}(\text{bipy})_3](\text{ClO}_4)_2$ ($M = \text{Fe, Ni, Zn, Mn; } x \leq 0.005$) series at room temperature are reproduced in Figure 22. The spectra show only one quadrupole doublet, which is unambiguously assigned to the low-spin state of iron(II) in all cases. The difference in the free energies of the high- and low-spin states, respectively, $\Delta G = G(\text{HS}) - G(\text{LS})$, may have decreased in these solid solutions, similarly to the observations in the a priori spin crossover systems discussed in the two previous sections. The reduction in ΔG , however, is not strong enough to populate the high-spin state thermally to any noticeable extent. From these results we have estimated ΔG to be at least about 1200 cm^{-1} .

The linewidth and the quadrupole splitting stay nearly the same on going from the pure iron compounds to the highly diluted systems; this is quite similar to the results observed with the spin crossover systems discussed in the last two sections. However, the isomer shifts observed in the present systems appear to become slightly more positive in the order of $M = \text{Fe} < \text{Ni} < \text{Zn} < \text{Mn}$ in the Fe/M/bipy systems, and of $M = \text{Fe} < \text{Ni} < \text{Zn}$ in the Fe/M/phen systems. The effect is very weak in the former series, but distinctly outside the error limits in the latter one. The increasing tendency of the isomer shift parallels the increase in the ionic radius of the M^{2+} ions, namely, $\text{Fe}(0.61 \text{ \AA in the low-spin state}) < \text{Ni}(0.70 \text{ \AA}) < \text{Zn}(0.74 \text{ \AA}) < \text{Mn}(0.82 \text{ \AA})$ (64). It is quite likely that the relatively small $[\text{Fe}(\text{phen})_3]^{2+}$ complex molecule, when accommodated in a normal lattice site of the $[\text{M}(\text{phen})_3](\text{ClO}_4)_2$ host, tends to expand isotropically without affecting noticeably the quadrupole inter-

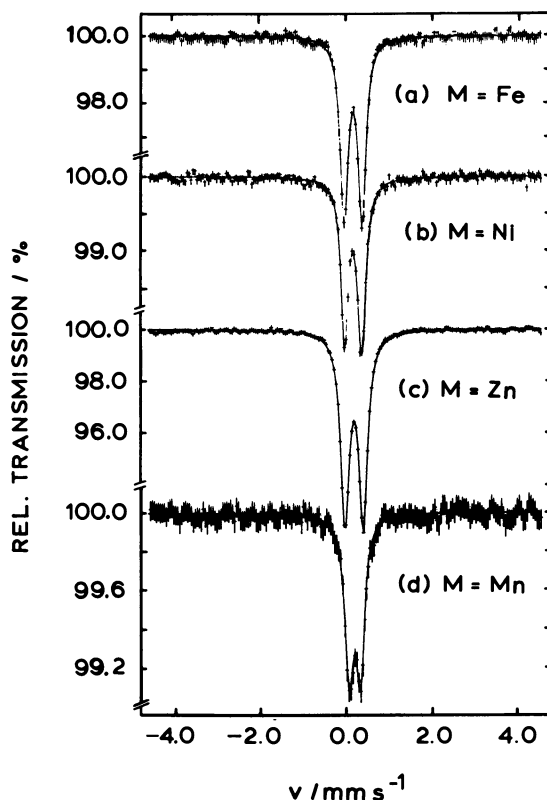


Figure 22. Mössbauer spectra of the solid solutions $[^{57}\text{Fe}_x\text{M}_{1-x}(\text{bipy})_3](\text{ClO}_4)_2$ ($\text{M} = \text{Ni}, \text{Zn}, \text{Mn}; x \leq 0.005$) at room temperature. Spectrum a refers to the pure iron compound for comparison (46).

action. An increase in the iron–nitrogen bond length would be accompanied by a reduction of the extent of $d_{\pi}-p_{\pi}$ back-donation, which in turn causes the electron density at the iron nucleus to decrease due to more effective shielding by the $3d$ electrons; thus the isomer shift is expected to become more positive.

In this context we should again refer to the metal dilution studies of Drickamer et al. (60), which showed a nearly quantitative spin state conversion low-spin \rightleftharpoons high-spin of iron in FeS_2 when diluted into MnS_2 , MnSe_2 , and MnTe_2 , respectively.

Influence of Crystal Solvent Molecules in $[\text{Fe}(2\text{-pic})_3]\text{Cl}_2 \cdot \text{Sol}$

In the framework of a cooperative spin transition mechanism as discussed earlier, it is expected that the nature of the crystal solvent molecules eventually present in the lattice of a spin crossover system

influences the spin transition characteristics. This occurs supposedly through a combined action of both the change in hydrogen-bond formation between the ligand and the intervening solvent molecule and a change in the relevant phonon system caused by different packing geometry and/or possible crystallographic change. To prove this we chose the $[\text{Fe}(2\text{-pic})_3]\text{Cl}_2 \cdot \text{Sol}$ system, where $\text{Sol} = \text{C}_2\text{H}_5\text{OH}$, CH_3OH , H_2O , $2\text{H}_2\text{O}$, and measured their Mössbauer spectra as a function of temperature (40). In another series of experiments we studied the deuterium isotope effect on the spin crossover behavior in $[\text{Fe}(2\text{-pic})_3]\text{Cl}_2 \cdot \text{Sol}$, where $\text{Sol} = \text{C}_2\text{H}_5\text{OD}$, CH_3OD (48).

Spin Crossover in the Solvates $[\text{Fe}(2\text{-pic})_3]\text{Cl}_2 \cdot \text{Sol}$ ($\text{Sol} = \text{C}_2\text{H}_5\text{OH}$, CH_3OH , H_2O , $2\text{H}_2\text{O}$). The ethanolate, the methanolate, and the monohydrate of $[\text{Fe}(2\text{-pic})_3]\text{Cl}_2$ have been found to exhibit spin crossover, whereas the dihydrate is low spin at all temperatures under study (40). A series of temperature-dependent Mössbauer spectra of the methanolate is reproduced in Figure 23. The area fraction of the high-spin doublet as a function of temperature is plotted in Figure 24.

From the spin conversion curves in Figure 24 it is clear that the nature of the intervening crystal solvent molecule influences the spin transition characteristics in a very pronounced way. The relative stability of the high-spin state decreases in the following order of "Sol" molecules: $\text{C}_2\text{H}_5\text{OH}$, $> \text{CH}_3\text{OH} > \text{H}_2\text{O} > 2\text{H}_2\text{O}$. In particular, significant differences are noticeable with respect to (1) the strength of the cooperative effect as reflected in the slope of the spin conversion curve, (2) the phase transition temperature, and (3) a hysteresis effect. The methanolate shows a rather gradual spin transition, whereas the ethanolate and the monohydrate change spin rather abruptly. This implies that the strength of the cooperative interaction differs from one solvate to another, and supports the previous suggestion (7, 41) that the spin phase transition is governed mainly by a significant coupling between the electronic state and the lattice phonon system.

Particularly interesting is the hysteresis effect observed in the monohydrate with an enormously large width of about 90 K; it indicates clearly the first-order nature of the spin transition in $[\text{Fe}(2\text{-pic})_3]\text{Cl}_2 \cdot \text{H}_2\text{O}$. There are only a few other examples of a hysteresis effect observed so far in spin crossover systems (39, 65–69).

Quite recently, single-crystal x-ray structure analysis has been performed on the ethanolate (30, 32, 70), the methanolate (31, 32), and the dihydrate (31) of $[\text{Fe}(2\text{-pic})_3]\text{Cl}_2$. The space groups found at room temperature are: $P2_1/c$ (monoclinic with $Z = 4$) for the ethanolate (30, 70), $Pbca$ (orthorhombic with $Z = 8$) for the methanolate (31), and $P1$ (triclinic with $Z = 2$) for the dihydrate (31). Thus the structures of

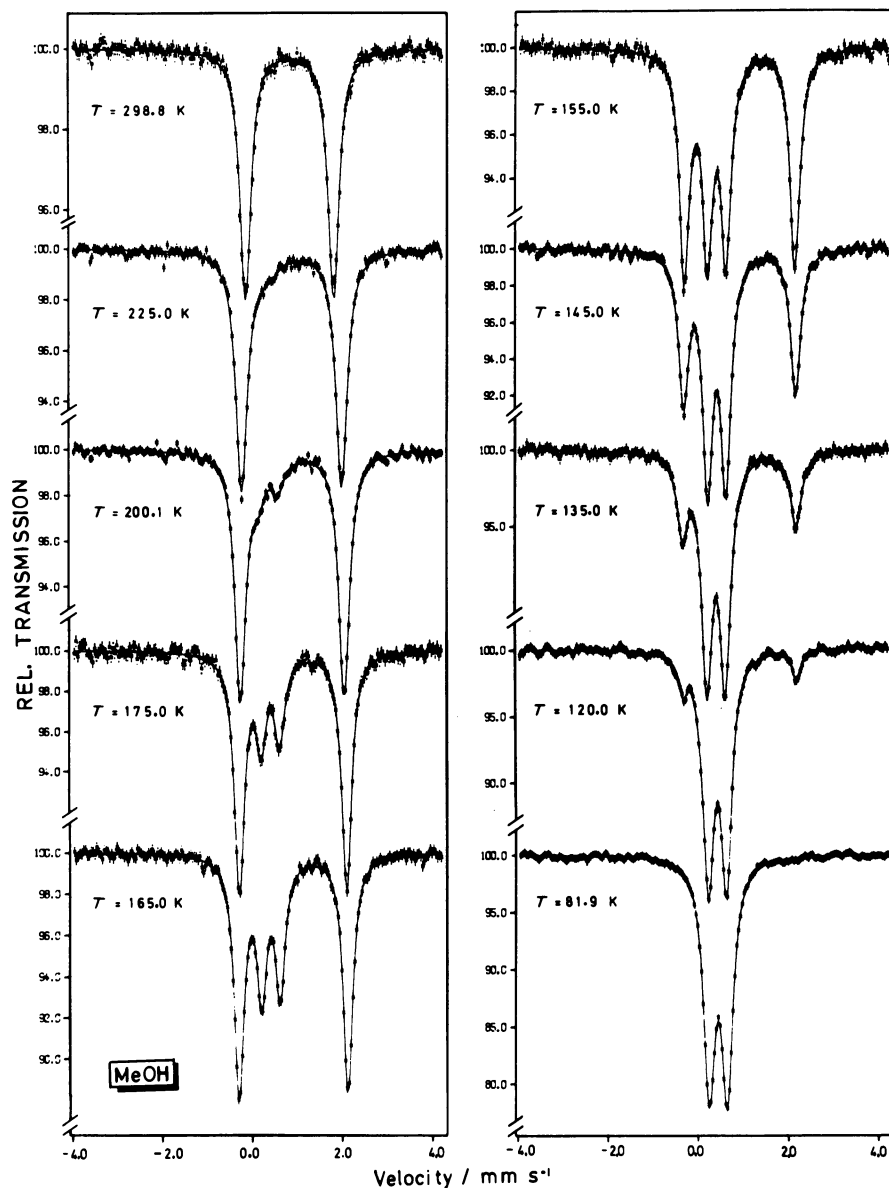


Figure 23. The ^{57}Fe Mössbauer spectra of $[\text{Fe}(\text{2-pic})_3]\text{Cl}_2 \cdot \text{CH}_3\text{OH}$ at various temperatures (40). The inner two lines represent the low-spin doublet, the outer two lines the high-spin doublet of iron(II).

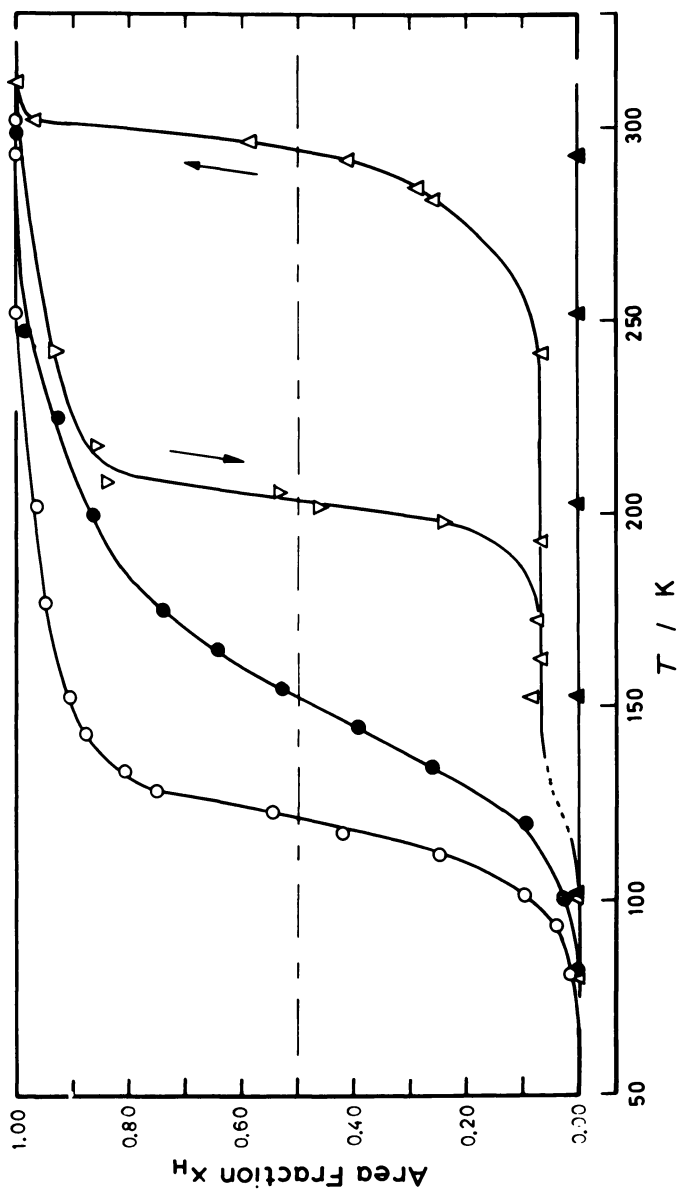


Figure 24. Temperature dependence of the area fraction of the iron(II) high-spin doublet in the Mössbauer spectra of $[\text{Fe}(\text{2-pic})_3]\text{Cl}_2 \cdot \text{Sol}$ with Sol = (O) $\text{C}_2\text{H}_5\text{OH}$; (●) CH_3OH ; (Δ) H_2O in heating mode; (▽) H_2O in cooling mode; and (▲) $2\text{H}_2\text{O}$ (40).

the three solvates are definitely different, and from this point of view the different magnetic behavior (see Figure 24) should not be surprising at all. The structure of the monohydrate is not known yet.

The geometry of the $[\text{Fe}(\text{2-pic})_3]^{2+}$ cationic complex was the same in the ethanolate (30, 32, 70) and the methanolate (31, 32), namely, meridional (C_{2v}), whereas that in the dihydrate was facial with approximately threefold symmetry (31, 32).

There are also major differences in the hydrogen-bond formation as revealed by the crystal structure determinations. Mikami et al. (30) state that in the ethanolate, all the amino nitrogen atoms of the $[\text{Fe}(\text{2-pic})_3]^{2+}$ complexes are linked to Cl^- ions by $\text{N-H} \dots \text{Cl}$ hydrogen bonds, and that the ethanol molecule is hydrogen bonded to a Cl^- ion by a $\text{Cl} \dots \text{H-O}$ bond. Katz and Strouse (32) have confirmed this kind of hydrogen-bond network in the ethanolate and also in the methanolate. Greenaway and Sinn reported (31) that, in the dihydrate, hydrogen bonds are formed between the $[\text{Fe}(\text{2-pic})_3]^{2+}$ complex and the water molecules, presumably facilitated by the facial geometry of the cationic complex having all three amino nitrogen atoms on one side of the ion. This kind of hydrogen bonding (solvent-to-cation) is absent in the methanolate and the ethanolate.

At any rate, from the different structures of the solvates of $[\text{Fe}(\text{2-pic})_3]\text{Cl}_2$, it must be inferred that the dispersion relations of the relevant lattice vibrational modes are also markedly different, and this may well be responsible for the different magnetic behavior.

The influence of crystal solvent molecules on the spin transition characteristics is also known from other spin crossover systems of iron(II) (71–80) and iron(III) (81–86).

Deuterium Isotope Effect on the Spin Crossover Behavior in $[\text{Fe}(\text{2-pic})_3]\text{Cl}_2 \cdot \text{Sol}$ (Sol = $\text{C}_2\text{H}_5\text{OD}$, CH_3OD). We have seen in the last section that replacing the whole crystal solvent molecule changes the crystal structure of the solvates $[\text{Fe}(\text{2-pic})_3]\text{Cl}_2 \cdot \text{Sol}$ (30–32, 70), which most likely causes the pronounced differences in the spin crossover characteristics as revealed by the Mössbauer studies (40). To alter the spin crossover system less drastically, we prepared the solvates $[\text{Fe}(\text{2-pic})_3]\text{Cl}_2 \cdot \text{C}_2\text{H}_5\text{OD}$ and $[\text{Fe}(\text{2-pic})_3]\text{Cl}_2 \cdot \text{CH}_3\text{OD}$, and measured their Mössbauer spectra as a function of temperature (48). The deuterium isotope effect was not restricted to the OH/OD group of the alcohol molecules because of unavoidable partial isotope exchange with the amino groups of the 2-pic ligand during the preparation. It is believed that the crystal structure does not change on going from the hydrogenated to the deuterated solvate. However, there should be a change in the dispersion relations of the phonon modes due to the alteration of the reduced mass,

and it was of interest to see how this rather mild modification of the system would affect the spin crossover behavior.

The Mössbauer spectra of the deuterated system showing again the well-resolved spectra of the coexisting high- and low-spin states are very similar to those of the nondeuterated ethanolate and methanolate, respectively (40, 48). The isomer shift and quadrupole splitting of the high- and low-spin states, respectively, also agree well with the corresponding parameters of the hydrogenated systems. A distinct difference, however, appears in the temperature dependence of the area fraction x_H of the high-spin state, as shown in Figure 25. The spin transition is complete in both deuterated solvates as in the nondeuterated ones, and the shape of the spin conversion curve does not seem to be affected. The spin transition temperature T_c is shifted upwards by 14–15 K in both pairs of solvates, indicating that the relative stability of the low-spin state increases on deuteration.

This H/D isotope effect may be understood qualitatively by looking at the expected change of the energy difference $\Delta E = E^{\circ}_{HS} - E^{\circ}_{LS}$ between the zero-point vibronic levels of the two spin states in a simple harmonic approximation as depicted in Figure 26,

$$\begin{aligned} \Delta E &= E^{\circ}_{HS} - E^{\circ}_{LS} \\ &= \epsilon(^5T_2) + \frac{1}{2} hc\tilde{\nu}^{\circ}_{HS} - \epsilon(^1A_1) - \frac{1}{2} hc\tilde{\nu}^{\circ}_{LS} \end{aligned} \quad (5)$$

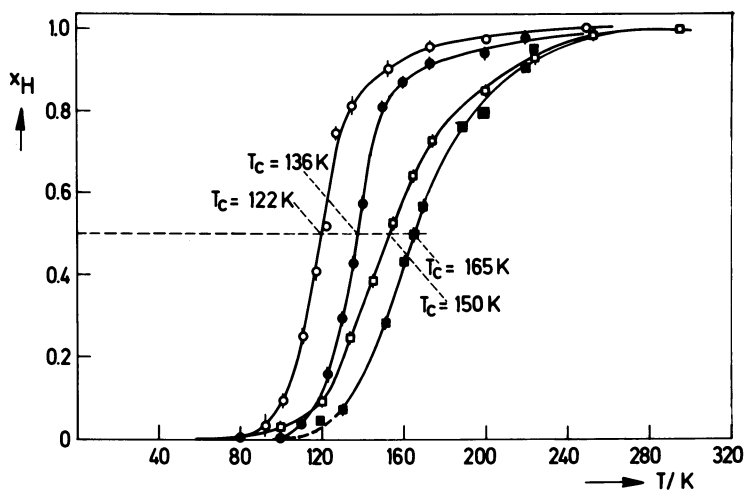


Figure 25. Temperature dependence of the area fraction x_H of the iron(II) high-spin doublet in the Mössbauer spectra of hydrogenated and deuterated solvates of $[Fe(2-pic)_3]Cl_2 \cdot Sol$ with $Sol = (\circ) C_2H_5OH$; $(\bullet) C_2H_5OD$; $(\square) CH_3OH$; and $(\blacksquare) CH_3OD$ (48).

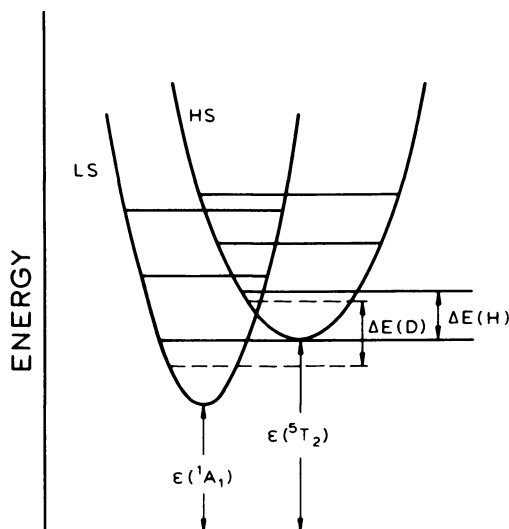


Figure 26. Schematic vibronic energy level diagram for a d^6 ion in the low-spin state ${}^1A_1(O_h)$ and the high-spin state ${}^5T_2(O_h)$, respectively. The meaning of the symbols is given in the text.

for one representative out of the 15 normal modes of vibration. (To understand the tendency of the H/D isotope effect, it suffices to consider the effect of deuteration on just one normal mode of vibration). The $\epsilon({}^5T_2)$ and $\epsilon({}^1A_1)$ terms refer to the electronic energies of the high- and low-spin states, respectively; the $\tilde{\nu}_{HS}^{\circ}$ and $\tilde{\nu}_{LS}^{\circ}$ terms denote the wave numbers of the zero-point vibrations of one representative mode in the two spin states. With $\tilde{\nu}^{\circ} = (1/2\pi c)\sqrt{k/\mu}$, where k is the force constant and μ the reduced mass, and taking $\mu_{HS} = \mu_{LS} = \mu$, we obtain from Equation 5 for a hydrogenated (H) solvate

$$\Delta E(H) = \Delta\epsilon + \frac{1}{2} h \sqrt{1/\mu_H} (\sqrt{k_{HS}} - \sqrt{k_{LS}}) \quad (6)$$

where $\Delta\epsilon$ stands for the differences in the electronic energies. Assuming no change in the symmetry and that $\Delta\epsilon$ remains constant on deuteration, we find an analogous expression for the deuterated solvate. The difference in ΔE between the deuterated (D) and the hydrogenated solvate is then

$$\begin{aligned} \delta(\Delta E) &= \Delta E(D) - \Delta E(H) \\ &= \frac{1}{2} h (\sqrt{1/\mu_D} - \sqrt{1/\mu_H}) (\sqrt{k_{HS}} - \sqrt{k_{LS}}) \end{aligned} \quad (7)$$

As $1/\mu_D < 1/\mu_H$ and $k_{HS} < k_{LS}$, which is well known from vibrational spectroscopy, $\delta(\Delta E)$ turns out to be positive, implying that the relative stability of the low-spin state increases, and thus shifting the transition temperature T_c upward upon deuteration, as has indeed been observed (see Figure 25).

Although the effect of deuteration on the spin transition behavior is significant, we are not, at the present time, in the position to decide whether the isotope effect influences primarily the relative population of the three orientational sites occupied by the solvent molecule (30), or whether the change in the reduced mass (on both the OH and the NH₂ groups) and thereby the change in the lattice vibrational modes, which are actively involved in the cooperative interaction, is the more effective influence on the spin transition behavior. More experiments are underway in our laboratory to clarify this.

Influence of the Preparation Method

It has been known for quite some time that the spin transition characteristics may be influenced by the sample preparation method (53, 55, 75, 87, 88).

One of the spin crossover systems showing this kind of dependence is [Fe(phen)₂(NCS)₂]. Although the spin transition in this compound has been well documented (35) and studied extensively by Mössbauer (53, 54), magnetic susceptibility (53, 54, 55), IR (20, 53, 56), FIR (7, 8, 21, 22, 57), UV/vis (53), NMR (54), heat capacity (7, 8), and x-ray (35, 53) techniques, we felt it necessary to reinvestigate this system since the correlation between the results from various techniques has not always been very satisfactory. In particular, the residual paramagnetism in this system was found to depend strongly on the method of preparation (53–55), although all the techniques, except for magnetic susceptibility, could not reveal any apparent differences between the samples prepared by different methods. For our reinvestigations by means of Mössbauer spectroscopy (36), we prepared the samples employing a precipitation method and an extraction method, both described in Ref. (36); in the following the different samples are referred to as Sample A (precipitated) and Sample B (extracted). The two samples differ in crystal size and quality. The extraction method yields the better-developed crystals, which are about five times larger than the more finely dispersed material obtained by the precipitation method.

Mössbauer spectra were recorded at 20 different temperatures for Sample A, and at 14 different temperatures for Sample B, with particular emphasis near the transition region. The spectra show clearly the coexistence of the high- and low-spin states of iron(II), with strongly temperature-dependent intensities, as has been observed previously by

other authors (54). However, the present studies have revealed major differences between Samples A and B.

Two representative Mössbauer spectra, one of each of Samples A and B, recorded at 4.2 K are displayed in Figure 27. No evidence for residual paramagnetism was found in Sample B, contrary to Sample A where it amounts to approximately 12%. It should be noted that in all previous studies on $[\text{Fe}(\text{phen})_2(\text{NCS})_2]$, the fraction of residual paramagnetism was established from magnetic susceptibility measurements alone, failing detection in all other techniques such as Mössbauer spectroscopy, IR, etc.

Figure 28 shows the temperature dependence of the area fraction of the high-spin quadrupole doublet of Samples A and B. The spin transition in Sample B is much sharper than in Sample A. The transition temperature T_c is nearly the same in both samples; it differs by 3–4 K. These observations from Mössbauer spectroscopy are in accordance with the magnetic susceptibility measurements on the same samples.

The temperature dependence of the quadrupole splitting, the linewidth and area fraction of the high-spin quadrupole doublet, and the temperature dependence of the magnetic moment of Sample A are plotted in Figure 29. A marked change in the Mössbauer linewidth and a pronounced irregularity in the quadrupole splitting of the high-spin molecules occur in the critical temperature region. Such changes in the linewidths and quadrupole splittings have been reported for the first time in a spin crossover system. This could not be observed in Sample B, since the spin transition is so sharp that practically no high-spin species are present below T_c . The unusual temperature dependence of the quadrupole splitting of the high-spin state near T_c and the sudden increase of the high-spin resonance linewidth by a factor of about two suggest that some kind of reorganization of the lattice sites accompanies the spin crossover.

The different spin crossover characteristics in Samples A and B also manifest themselves in a differential thermal analysis (DTA) plot (see Figure 30).

Structural Change Accompanying Spin Crossover

The question whether a structural change, beyond the known change in metal–ligand bond length by about 0.1–0.2 Å, accompanies the spin phase change has been raised often, particularly in systems with abrupt spin transitions such as $[\text{Fe}(\text{phen})_2(\text{NCS})_2]$. Temperature-dependent x-ray diffraction measurements on single crystals above and below T_c could give the answer. Unfortunately, only on a few spin crossover systems have such measurements been done so far (27, 30, 32, 89).

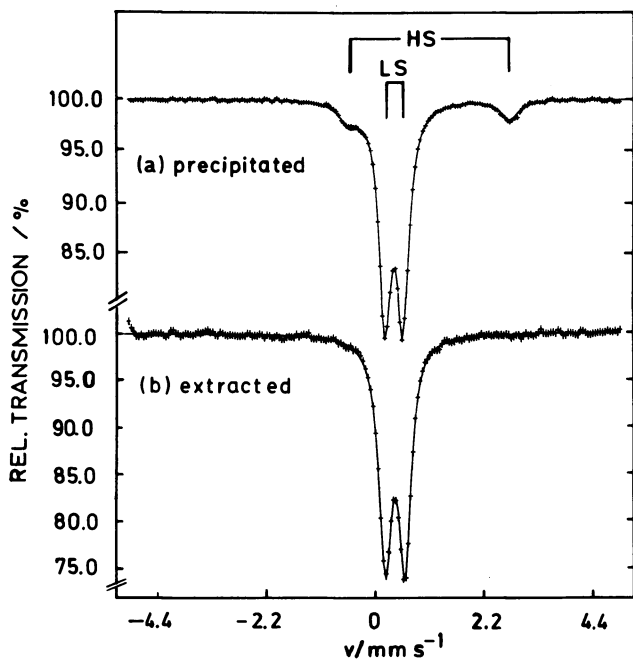


Figure 27. The ^{57}Fe Mössbauer spectra of $[\text{Fe}(\text{phen})_2(\text{NCS})_2]$ at 4.2 K: (a) Sample A (precipitated), (b) Sample B (extracted) (36).

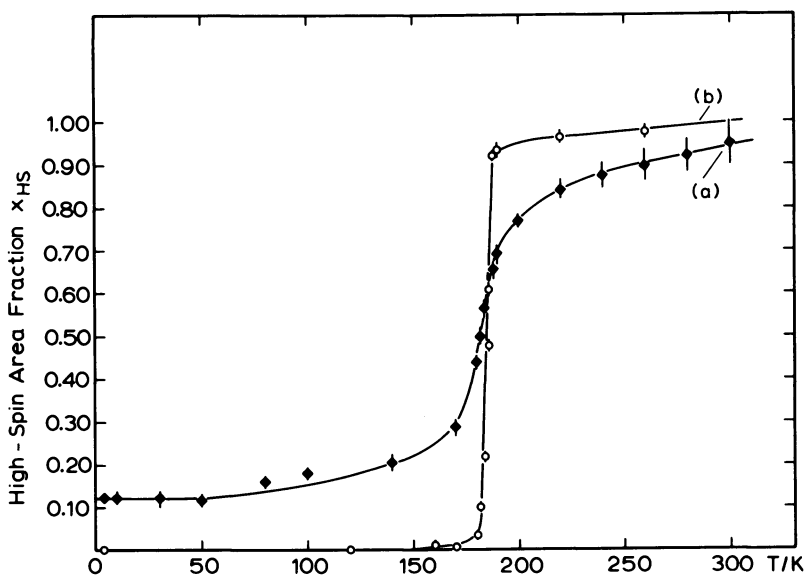


Figure 28. High-spin fraction x_{HS} from the Mössbauer spectra of $[\text{Fe}(\text{phen})_2(\text{NCS})_2]$ as a function of temperature: (a) Sample A (precipitated), (b) Sample B (extracted) (36).

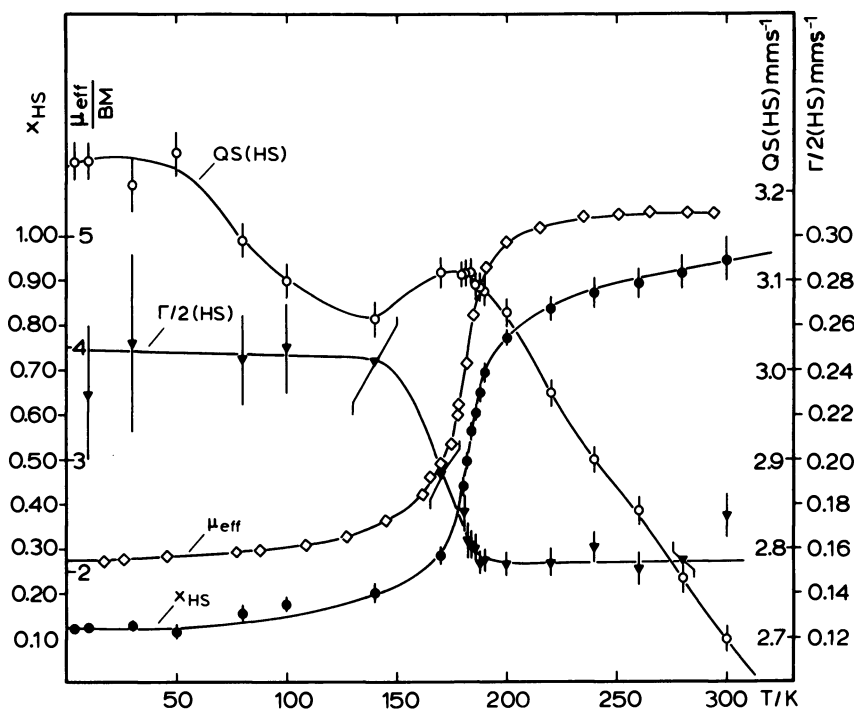


Figure 29. Quadrupole splitting (QS, \circ), linewidth ($\Gamma/2$, \blacktriangledown), area fraction (x_{HS} , \bullet), and effective magnetic moment (μ_{eff} , \diamond) of the high-spin state in $[\text{Fe}(\text{phen})_2(\text{NCS})_2]$, Sample A (precipitated) as a function of temperature (36).

König and Watson (89) investigated the crystal structures of the "Polymorph II" of $[\text{Fe}(\text{bipy})_2(\text{NCS})_2]$ (bipy = 2,2'-dipyridyl) at approximately 295 and 100 K, and found the same space group, $Pcnb$ (D_{2h}^{14}), at both temperatures. The spin transition behavior in this system is distinctly less abrupt than in the Polymorphs I and III of the same system (87).

Leipoldt and Coppens (27) studied the crystal structure of tris(*N,N*-diethylthiocarbamato)iron(III), which exhibits ${}^2T_2(O_h) \rightleftharpoons {}^6A_1(O_h)$ spin crossover with a very gradual spin transition (24) at 297 and 79 K. The space group was found to change on cooling from $P2_1/c$ to $C2/n$.

Mikami et al. (30) determined the crystal structures of $[\text{Fe}(2\text{-pic})_3]\text{Cl}_2 \cdot \text{C}_2\text{H}_5\text{OH}$ at 298, 150, and 90 K and found that the crystals are monoclinic, $P2_1/c$, in the two spin states. Besides the very pronounced changes in the iron–nitrogen bond distance (on the average 2.195 Å for the high-spin state, 2.013 Å for the low-spin state), they observed an orientational disorder of the ethanol molecule with a strongly temperature-dependent relative population of the three orientational sites it occupied. Mikami et al. suggested that this most probably triggers the spin transition in $[\text{Fe}(2\text{-pic})_3]\text{Cl}_2 \cdot \text{C}_2\text{H}_5\text{OH}$.

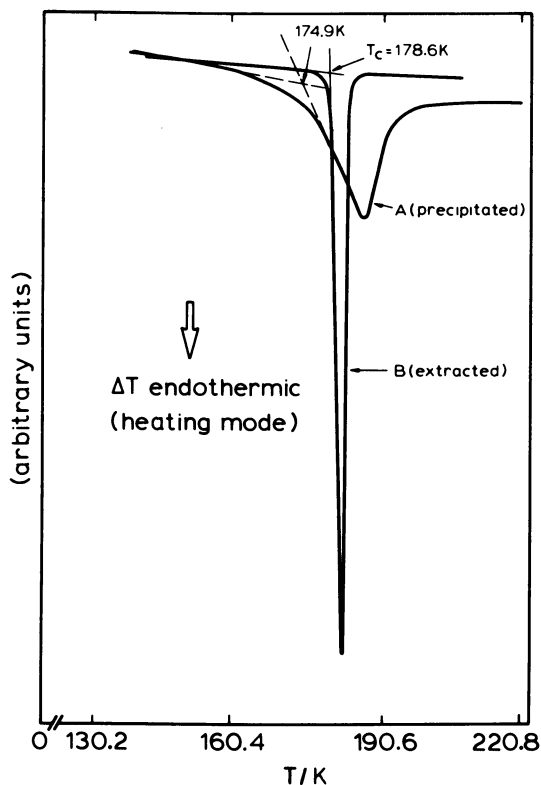


Figure 30. The DTA curves for Sample A (precipitated) and Sample B (extracted) of $[\text{Fe}(\text{phen})_2(\text{NCS})_2]$. (We thank H. G. von Schnering, Stuttgart, and M. Sorai, Osaka, who measured these curves.)

The irregularity in the temperature dependence of the quadrupole splitting as well as the enormous change in the linewidths of the high-spin quadrupole doublet observed in the Mössbauer spectra of $[\text{Fe}(\text{phen})_2(\text{NCS})_2]$, Sample A (precipitated), near T_c (36) appear to indicate a structural change going along with the spin crossover in this compound. All the previous x-ray investigations (Debye-Scherrer photographs) at room temperature and at low temperatures failed to detect any structural phase changes in $[\text{Fe}(\text{phen})_2(\text{NCS})_2]$ (20, 53). Recently we performed temperature-dependent x-ray diffractometry measurements between 80 and 300 K on Sample A (precipitated) and Sample B (extracted) of $[\text{Fe}(\text{phen})_2(\text{NCS})_2]$ and found indications for a structural change on passing through T_c (36). Figure 31 shows a series of x-ray peak profiles obtained with Sample B in the transition region ($T_c \approx 175$ K). In both Samples A and B, two new peaks appear on cooling, one around the Bragg angle $2\theta \approx 20.5^\circ$, and another as a shoulder on the

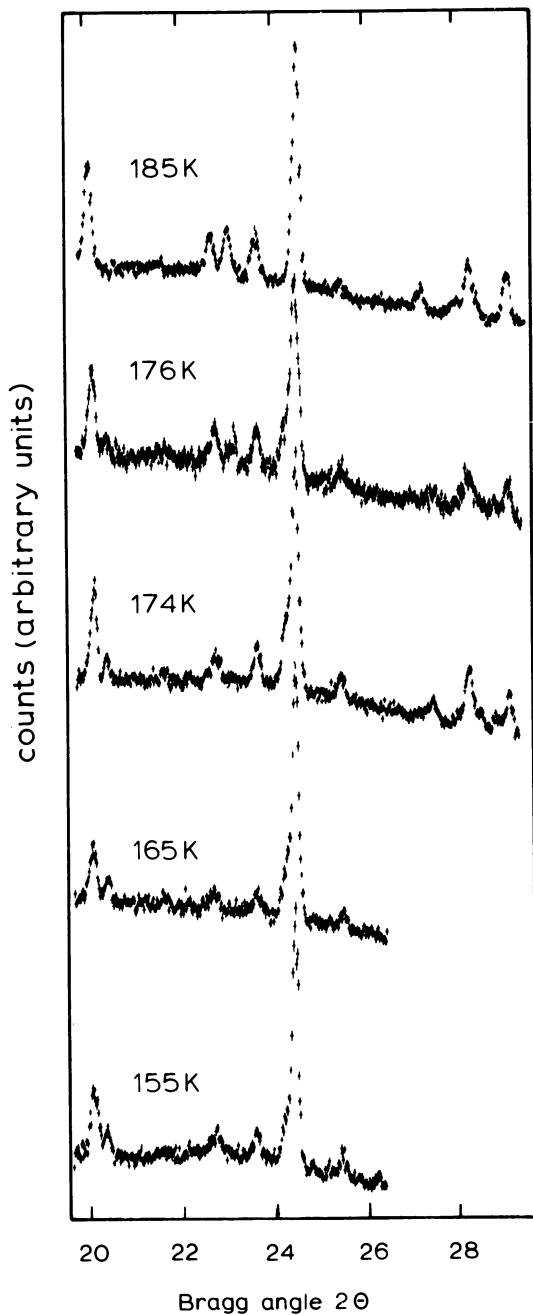


Figure 31. Peak profiles of x-ray powder diffraction of $[\text{Fe}(\text{phen})_2(\text{NCS})_2]$ Sample B (extracted), as a function of temperature in the transition region (36)

very intense 24° peak. Simultaneously, one peak of the group of three peaks around 22° – 24° disappears below T_c . The peak profiles in the case of Sample A are broader than in the case of Sample B, which is most probably due to the fact that Sample A is more finely dispersed and of lower crystal quality than Sample B. The overall features of the x-ray diffractometry spectra of the high-temperature (high-spin) and low-temperature (low-spin) phases are not too different, which implies that the structural characteristics of the two phases are quite similar. Nevertheless, in view of the marked changes in the Mössbauer linewidth and the quadrupole splitting of the high-spin phase near T_c , together with the differences in the x-ray diffractometry pattern between the high- and low-temperature phases, some kind of structural reorganization, beyond the change in iron–ligand bond length induced by the spin transition, can no longer be excluded. We believe that an orientational disorder-order transition, possibly with the NCS groups preferring certain rotational sites, may be an effective trigger for the spin transition in

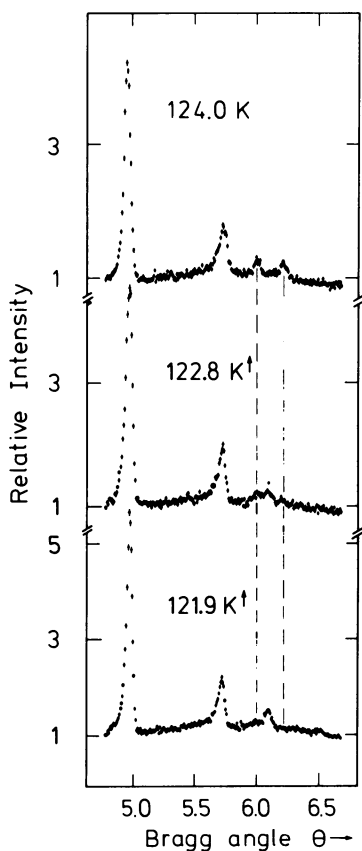


Figure 32. Peak profiles of x-ray powder diffraction on $[\text{Fe}(4,7\text{-(CH}_3)_2\text{phen)}_2(\text{NCS})_2]$ in the temperature region of the spin transition ($T_c = 122.9 \text{ K}$) (66)

Chemical Physics Letters

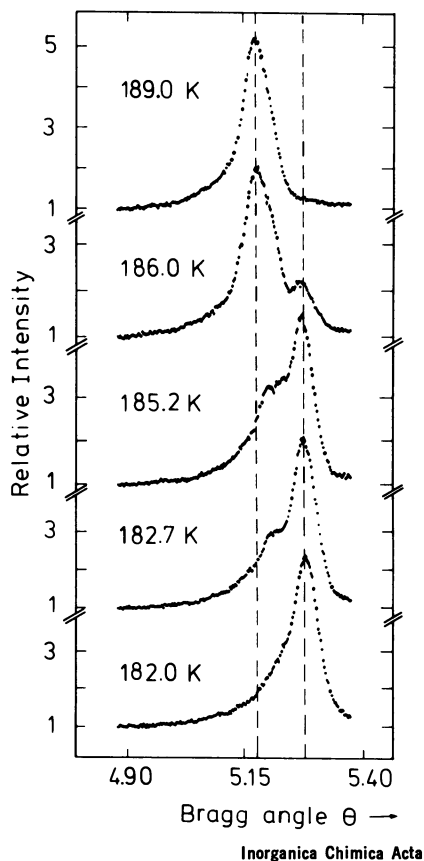
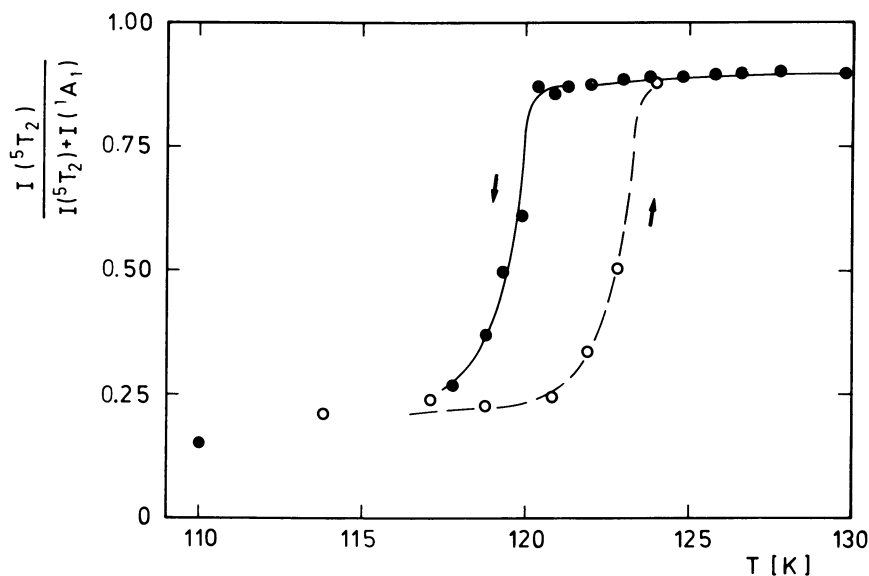


Figure 33. Peak profiles of x-ray powder diffraction on $[\text{Fe}(\text{bt})_2(\text{NCS})_2]$ in the temperature region of the spin transition (39)

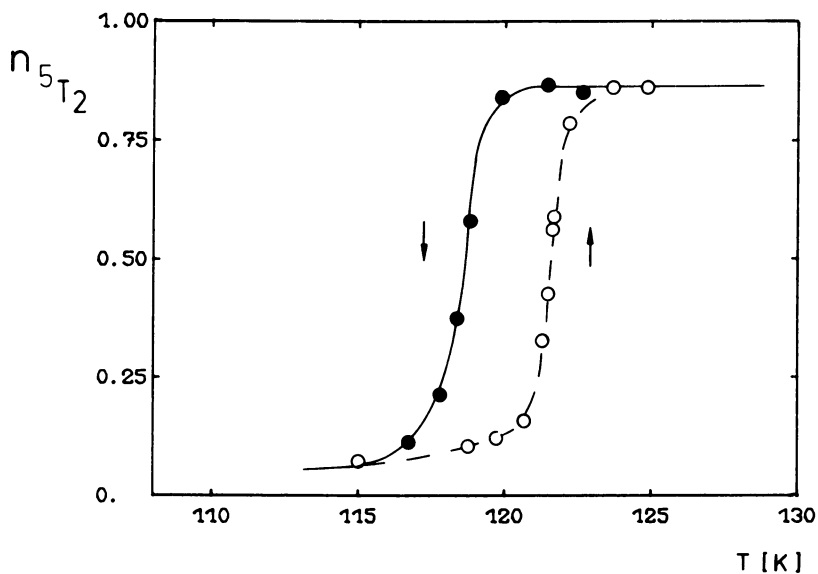
$[\text{Fe}(\text{phen})_2(\text{NCS})_2]$, similar to the suggestion of Mikami et al. (30) for $[\text{Fe}(2\text{-pic})_3]\text{Cl}_2 \cdot \text{C}_2\text{H}_5\text{OH}$. A single-crystal x-ray study is badly needed to clarify this.

Very fine variable-temperature x-ray diffraction work in connection with Mössbauer spectroscopy on the polycrystalline spin crossover systems $[\text{Fe}(4,7\text{-(CH}_3)_2\text{-phen})_2(\text{NCS})_2]$ and $[\text{Fe}(\text{bt})_2(\text{NCS})_2]$ ($\text{bt} = 2,2'\text{-bi-2-thiazoline}$) has been published recently by König et al. (39, 66). Distinct and different x-ray peak profiles were found for the high- and low-spin phases in both systems on passing through T_c , indicating that a crystallographic phase change is associated with the spin transformation (see Figures 32 and 33). The intensities of the x-ray peaks of $[\text{Fe}(4,7\text{-(CH}_3)_2\text{-phen})_2(\text{NCS})_2]$ show the same temperature dependence and the same hysteresis behavior as the fractions of the high- and low-spin species determined from the Mössbauer spectra (see Figures 34 and 35). Similar observations were made on the $[\text{Fe}(\text{bt})_2(\text{NCS})_2]$ system (39). This is clear evidence for a simultaneous change of the electronic spin state and the crystallographic properties.



Chemical Physics Letters

Figure 34. Temperature dependence of the relative intensity of the x-ray diffraction lines for the high-spin state in $[\text{Fe}(4,7\text{-(CH}_3)_2(\text{phen})_2\text{(NCS)}_2)]$ near T_c (66)



Chemical Physics Letters

Figure 35. Temperature dependence of the high-spin fraction in $[\text{Fe}(4,7\text{-(CH}_3)_2\text{(NCS)}_2)]$ evaluated from the Mössbauer spectra near T_c (66)

Acknowledgments

I wish to express my sincere thanks to my students and research associates K. Bode, J. Ensling, J. Fleisch, P. Ganguli, K. M. Hasselbach, H. Köppen, R. Link, E. W. Müller, I. Sanner, M. Sorai, H. Spiering, and H. G. Steinhäuser, who have collaborated with me on spin crossover problems with great enthusiasm. Financial support by the Deutsche Forschungsgemeinschaft, the Fonds der Chemischen Industrie, and the Alexander von Humboldt Stiftung is gratefully acknowledged.

Glossary of Symbols

HS	High-spin ground state of the central metal ion, ${}^5T_2(O_h)$ in case of an iron(II) complex molecule in the approximation of O_h symmetry
LS	Low-spin ground state of the central metal ion, ${}^1A_1(O_h)$ in case of an iron(II) complex molecule in the approximation of O_h symmetry
G	Gibbs free energy
k_B	Boltzmann factor
H	Enthalpy
S	Entropy
R	Gas constant
T_c	Transition temperature, formally defined as the temperature of 50% spin conversion
$x_H(x_{HS})$	Fraction of complex molecules in the high-spin ground state, taken here as approximately equal to the area fraction of the high-spin quadrupole doublet of the Mössbauer spectra
RP	Residual paramagnetism (residual fraction of high-spin molecules at low temperatures)
RD	Residual diamagnetism (residual fraction of low-spin molecules at high temperatures)
x	Iron concentration of mixed crystals
n	Number of complex molecules of like spin state in a domain
K	Equilibrium constant
h	Planck's constant
c	Velocity of light
ϵ	Energy difference between ${}^5T_2(O_h)$ and ${}^1A_1(O_h)$ states
δ_{tet}	Tetragonal distortion parameter
λ_o	Free ion spin orbit coupling constant
R	Sternheimer shielding factor
η	Asymmetry parameter
V_{CF}	Crystal field potential
k	Vibrational force constant
μ	Reduced mass

Literature Cited

1. Barefield, E. K.; Busch, D. H.; Nelson, S. M. *Quart. Rev.* 1968, 22, 457.
2. Martin, R. L.; White, A. H. "Transition Metal Chemistry"; Carlin, R. L., Ed.; Dekker: New York, 1968; Vol. 4, p. 113.
3. Sacconi, L. "Proceedings of XIIIth I.C.C.C., Cracow/Zakopane (Poland) 1970"; Butterworths: London, 1971.
4. König, E. *Ber. Bunsenges. Phys. Chem.* 1972, 76, 975.
5. Goodwin, H. A. *Coord. Chem. Rev.* 1976, 18, 293.
6. Gütlich, P. *J. Phys. (Paris)* 1979, 40(3), Colloque C2, C2-378.
7. Sorai, M.; Seki, S. *J. Phys. Chem. Solids* 1974, 35, 555.
8. Sorai, M.; Seki, S. *J. Phys. Soc. Jpn.* 1972, 33, 575.
9. Ewald, A. H.; Martin, R. L.; Ross, I. G.; White, A. H. *Proc. R. Soc., London, Ser. A* 1964, 280, 235.
10. Ho, R. K. Y.; Livingstone, S. E. *Chem. Commun.* 1968, 217.
11. Cox, M.; Darken, J.; Fitzsimmons, B. W.; Smith, A. W.; Larkworthy, L. F.; Rogers, K. A. *Chem. Commun.* 1970, 105.
12. Cox, M.; Darken, J.; Fitzsimmons, B. W.; Smith, A. W.; Larkworthy, L. F.; Rogers, K. A. *J. Chem. Soc., Dalton Trans.* 1973, 1192.
13. Dose, E. V.; Murphy, K. M. M.; Wilson, L. J. *Inorg. Chem.* 1976, 15, 2622.
14. Kunze, K. R.; Perry, D. L.; Wilson, L. J. *Inorg. Chem.* 1977, 16, 594.
15. Morassi, R.; Bertini, I.; Sacconi, L. *Coord. Chem. Rev.* 1973, 11, 343.
16. Ammeter, J. *J. Am. Chem. Soc.* 1974, 96, 7833.
17. El Murr, N.; Chaloyard, A.; Kläui, W. *Inorg. Chem.* 1979, 18, 1010.
18. Gütlich, P.; Kläui, W.; McGarvey, B. R. *Inorg. Chem.* 1980, 19, 3704.
19. König, E.; Ritter, G. "Mössbauer Effect Methodology"; Gruverman, I. J.; Seidel, C. W.; Dieterly, D. K., Eds.; Plenum: New York, 1974; Vol. 9, p. 3.
20. Baker, W. A., Jr.; Long, G. J. *Chem. Commun.* 1965, 368.
21. Takemoto, J. H.; Hutchinson, B. *Inorg. Nucl. Chem. Lett.* 1972, 8, 769.
22. Takemoto, J. H.; Hutchinson, B. *Inorg. Chem.* 1973, 12, 705.
23. Hall, G. R.; Hendrickson, D. N. *Inorg. Chem.* 1976, 15, 607.
24. Ewald, A. H.; Martin, R. L.; Sinn, E.; White, A. H. *Inorg. Chem.* 1969, 8, 1837.
25. Tweedle, M. F.; Wilson, L. J. *J. Am. Chem. Soc.* 1976, 98, 4824.
26. Tshipis, C. A.; Hadjikostas, C. C.; Manoussakis, G. E. *Inorg. Chim. Acta* 1977, 23, 163.
27. Leipoldt, J. G.; Coppens, P. *Inorg. Chem.* 1973, 12, 2269.
28. Cukauskas, E. J.; Deaver, B. S., Jr.; Sinn, E. *Inorg. Nucl. Chem. Lett.* 1977, 13, 283.
29. Albertsson, J.; Oskarsson, A. *Acta Crystallogr., Sect. B* 1977, 33, 1871.
30. Mikami, M.; Konno, M.; Saito, Y. *Chem. Phys. Lett.* 1979, 63, 566.
31. Greenaway, A. M.; Sinn, E. *J. Am. Chem. Soc.* 1978, 100, 8080.
32. Katz, B. A.; Strouse, C. E. *J. Am. Chem. Soc.* 1979, 101, 6214.
33. Dose, E. V.; Hoselton, M. A.; Sutin, N.; Tweedle, M. F.; Wilson, L. J. *J. Am. Chem. Soc.* 1978, 100, 1141.
34. Binstead, R. A.; Beattie, J. K.; Dose, E. V.; Tweedle, M. F.; Wilson, L. J. *J. Am. Chem. Soc.* 1978, 100, 5609.
35. Baker, W. A., Jr.; Bobonich, H. M. *Inorg. Chem.* 1964, 3, 1184.
36. Ganguli, P.; Gütlich, P.; Irlner, W.; Müller, E. W. *J. Chem. Soc., Dalton, Trans.* 1981, 441.
37. Goodwin, H. A.; Sylva, R. N. *Aust. J. Chem.* 1968, 21, 83.
38. Fleisch, J.; Gütlich, P.; Hasselbach, K. M.; Müller, E. W. *Inorg. Chem.* 1976, 15, 958.
39. König, E.; Ritter, G.; Irlner, W.; Nelson, S. M. *Inorg. Chim. Acta* 1979, 37, 169.

40. Sorai, M.; Ensling, J.; Hasselbach, K. M.; Gütllich, P. *Chem. Phys.* **1977**, *20*, 197.
41. Sorai, M.; Ensling, J.; Gütllich, P. *Chem. Phys.* **1976**, *18*, 199.
42. Gütllich, P.; Link, R.; Steinhäuser, H. G. *Inorg. Chem.* **1978**, *17*, 2509.
43. Gütllich, P.; Köppen, H.; Link, R.; Steinhäuser, H. G. *J. Chem. Phys.* **1979**, *70*, 3977.
44. Gütllich, P.; Köppen, H.; Link, R.; Steinhäuser, H. G., unpublished data.
45. Gütllich, P.; Köppen, H.; Sanner, I.; Spiering, H., unpublished data.
46. Bode, K.; Gütllich, P.; Köppen, H. *Inorg. Chim. Acta* **1980**, *42*, 281.
47. Ganguli, P.; Gütllich, P., unpublished data.
48. Gütllich, P.; Köppen, H.; Steinhäuser, H. G. *Chem. Phys. Lett.* **1980**, *74*, 475.
49. Renovitch, G. A.; Baker, W. A., Jr. *J. Am. Chem. Soc.* **1967**, *89*, 6377.
50. Fleisch, J.; Gütllich, P.; Hasselbach, K. M. *Inorg. Chem.* **1977**, *16*, 1979.
51. Ingalls, R. *Phys. Rev.* **1964**, *133*, A 787.
52. Sanner, I. Diplomarbeit (Thesis), Fachbereich Chemie, Johannes Gutenberg-Universität, D-6500 Mainz, 1979.
53. König, E.; Madeja, K. *Inorg. Chem.* **1967**, *6*, 48.
54. Dézsi, I.; Molnár, B.; Tarnoczi, T.; Tompa, K. *J. Inorg. Nucl. Chem.* **1967**, *29*, 2486.
55. Casey, A. T.; Isaac, F. *Aust. J. Chem.* **1967**, *20*, 2765.
56. König, E.; Madeja, K. *Spectrochim. Acta* **1967**, *23* A, 45.
57. Ferraro, J. R.; Takemoto, J. *Appl. Spec.* **1974**, *28*, 66.
58. Maddock, A. G.; Schleiffer, J. J. *J. Chem. Soc., Dalton Trans.* **1977**, 617.
59. Ganguli, P.; Gütllich, P. *J. Phys. (Paris), Colloq.* **1980**, *41*, C1-313.
60. Bargeron, C. B.; Avinor, M.; Drickamer, H. G. *Inorg. Chem.* **1971**, *10*, 1338.
61. Cukauskas, E. J.; Deaver, B. S., Jr.; Sinn, E. *J. Chem. Phys.* **1977**, *67*, 1257.
62. Orgel, L. E. "Report of the 10th Solvay Conf. in Chemistry," Brussels, 1956, p. 289.
63. Martin, R. L.; White, A. H.; "Transition Metal Chemistry"; Carlin, R. L., Ed.; Dekker: New York, 1968; Vol. 4, p. 127.
64. Shannon, R. D.; Prewitt, C. T. *Acta Crystallogr.* **1969**, *B* *25*, 925.
65. König, E.; Ritter, G. *Solid State Commun.* **1976**, *18*, 279.
66. König, E.; Ritter, G.; Irlner, W. *Chem. Phys. Lett.* **1979**, *66*, 336.
67. Bradley, G.; McKee, V.; Nelson, S. M.; Nelson, J. *J. Chem. Soc. (Dalton)* **1978**, 522.
68. Ritter, G.; König, E.; Irlner, W.; Goodwin, H. A. *Inorg. Chem.* **1978**, *17*, 224.
69. Irlner, W.; Ritter, G.; König, E.; Goodwin, H. A.; Nelson, S. M. *Solid State Commun.* **1979**, *29*, 39.
70. Greenaway, A. M.; O'Connor, C. J.; Schrock, A.; Sinn, E. *Inorg. Chem.* **1979**, *18*, 2692.
71. Sylva, R. N.; Goodwin, H. A. *Aust. J. Chem.* **1967**, *20*, 479.
72. *Ibid.*, **1968**, *21*, 1081.
73. Dossier, R. J.; Eilbeck, W. J.; Underhill, A. E.; Edwards, P. R.; Johnson, C. E. *J. Chem. Soc. (A)* **1969**, 810.
74. Cunningham, A. J.; Fergusson, J. E.; Powell, H. K. J.; Sinn, E.; Wong, H. *J. Chem. Soc., Dalton Trans.* **1972**, 2155.
75. König, E.; Ritter, G.; Goodwin, H. A. *Chem. Phys.* **1974**, *5*, 211.
76. Sams, J. R.; Tsin, T. B. *Inorg. Chem.* **1976**, *15*, 1544.
77. Sams, J. R.; Tsin, T. B. *J. Chem. Soc., Dalton Trans.* **1976**, 488.
78. König, E.; Ritter, G.; Goodwin, H. A. *Chem. Phys. Lett.* **1976**, *44*, 100.
79. Baker, A. T.; Goodwin, H. A. *Aust. J. Chem.* **1977**, *30*, 771.
80. Reeder, K. A.; Dose, E. V.; Wilson, L. J. *Inorg. Chem.* **1978**, *17*, 1071.
81. Sinn, E. *Inorg. Chem.* **1976**, *15*, 369.

82. Butcher, R. J.; Sinn, E. *J. Am. Chem. Soc.* **1976**, *98*, 2440.
83. *Ibid.*, 5159.
84. Butcher, R. J.; Ferraro, J. R.; Sinn, E. *J. Chem. Soc., Dalton Trans.* **1976**, 910.
85. Cukauskas, E. J.; Deaver, B. S., Jr.; Sinn, E. *Inorg. Nucl. Chem. Lett.* **1977**, *13*, 283.
86. Ganguli, P.; Marathe, V. R. *Inorg. Chem.* **1978**, *17*, 543.
87. König, E.; Madeja, K.; Watson, K. J. *J. Am. Chem. Soc.* **1968**, *90*, 1146.
88. Goodgame, D. M. L.; Machado, A.A.S.C. *Chem. Commun.* **1969**, 1420.
89. König, E.; Watson, K. J. *Chem. Phys. Lett.* **1970**, *6*, 457.

RECEIVED June 27, 1980.

A High-Pressure Mössbauer Effect Study of the Spin State in Bis[hydrotris(3,5-dimethyl-1-pyrazolyl)borate]iron(II)

GARY J. LONG and LAURIE W. BECKER

Department of Chemistry, University of Missouri—Rolla, Rolla, MO 65401 and the Nuclear Physics Division, Atomic Energy Research Establishment, Harwell, Didcot, Oxfordshire, England

BENNETT B. HUTCHINSON

Department of Chemistry, Abilene Christian University, Abilene, TX 79699

The opposed diamond anvil cell technique provides a fast and convenient means for measuring the Mössbauer spectrum of a material at pressures up to approximately 100 kbar. The major disadvantage of this technique is the non-hydrostatic pressure that results. The Mössbauer spectrum of the title compound obtained at room temperature, and at various pressures up to 44 kbar, indicates that this pseudo-octahedral iron(II) complex undergoes a reversible pressure-induced spin-state transformation from the $^5T_{2g}$ high-spin state ($\Delta E_Q = 3.57$ mm/s, $\delta = 1.00$ mm/s) at ambient pressure to the $^1A_{1g}$ low-spin state ($\Delta E_Q = 0.28$ mm/s, $\delta = 0.39$ mm/s) at 44 kbar. An analogous Mössbauer effect study of bis[hydrotris(1-pyrazolyl)borate]iron(II) indicates that it is low-spin ($\Delta E_Q = 0.19$ mm/s, $\delta = 0.40$ mm/s) at ambient pressure and that it exhibits an approximate 15% conversion to the high-spin state ($\Delta E_Q = 3.34$ mm/s, $\delta = 0.90$ mm/s) at 45 kbar.

Several papers have described very sophisticated and complex methods for obtaining the Mössbauer effect spectrum of a material at pressures up to 100 kbar (1-6). Although these devices produce hydrostatic pressures, they are often very expensive, cumbersome, and difficult to

0065-2393/81/0194-0453\$05.00/0

© 1981 American Chemical Society

calibrate and operate. In some instances they provide a poor geometry for the Mössbauer experiment. These problems are often compounded when working with the relatively low-energy 14.4-keV gamma ray used in iron Mössbauer effect studies. Many of these problems may be overcome by using the opposed diamond anvil cell technique (7, 8).

This chapter discusses some of the advantages and disadvantages of the opposed diamond anvil cell as applied to ^{57}Fe Mössbauer effect studies and reports results on the spin-state transformation resulting at high pressure in the title compound $\text{Fe}[\text{HB}(3,5\text{-Me}_2\text{pz}_3)_2]$ and in $\text{Fe}[\text{HB}(\text{pz})_3]_2$.

Diamond Anvil Cell Technique

A schematic of the opposed diamond anvil cell and its integration into a Mössbauer spectrometer is illustrated in Figure 1.

Probably the greatest advantage of the opposed diamond anvil cell technique in Mössbauer effect studies is its operating convenience and

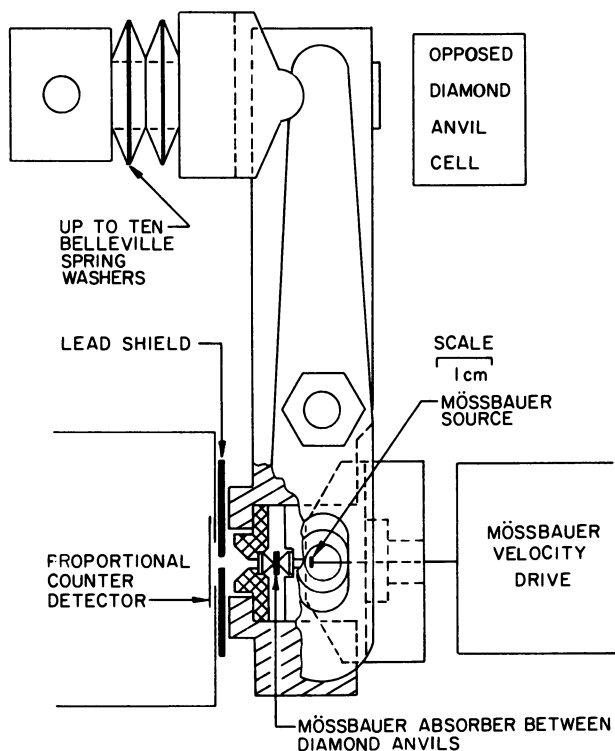


Figure 1. *Schematic of the opposed diamond anvil cell as it is used in the Mössbauer experiment*

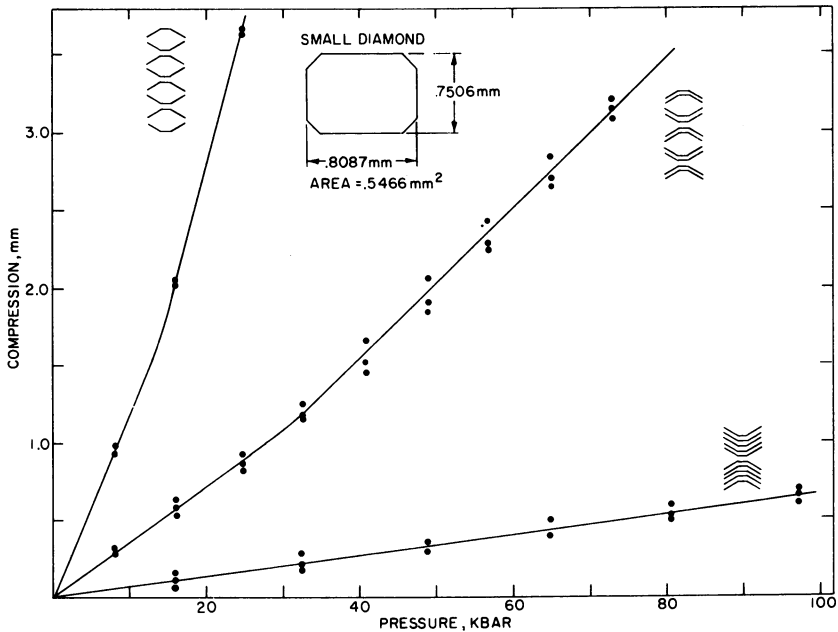


Figure 2. The diamond anvil cell pressure calibration obtained for the three Belleville spring washer configurations shown. The area of the small diamond is shown also.

small attenuation of even low-energy gamma rays. In a typical room-temperature experiment, the absorber under study may be loaded into the diamond anvil cell, pressure applied, the pressure determined, and the cell aligned in the Mössbauer spectrometer in a period of approximately 15 min. A change in the pressure may be accomplished in about 5 min. The low mass absorption coefficient of carbon is particularly advantageous for work with the 14.4-keV iron gamma ray. If it is assumed that the total diamond path length in the cell is 2 mm and that the mass absorption coefficient for carbon at 14.4 keV is $0.66 \text{ cm}^2/\text{g}$, then the diamond attenuation of the gamma ray is only about 35%. The geometry of the diamond anvil cell is also good in that the distance from the source to the detector window may be less than 2 cm (see Figure 1). Other advantages include a variety of pressure ranges available either by changing the configuration of the Belleville spring washers (see Figure 2) or by using larger- or smaller-area diamonds. A variety of calibration techniques (8), including the in situ use of the ruby R-line fluorescence technique (9,10), are available. Gasketing techniques (8,11) may be used to help overcome the nonhydrostatic pressures resulting in this technique (see following material) and apparently will allow the extension of this technique to about 500 kbar (12). The diamond anvil cell also

permits the consecutive study of the infrared (8, 13), optical (14), and x-ray powder diffraction pattern (12) of a compound under identical conditions in the same pressure cell. Finally, a major advantage of the diamond anvil cell is its relatively low cost. The cell and its diamonds currently can be obtained for about \$5,000.

Unfortunately, there are some disadvantages in the use of the diamond anvil cell. Probably most important is the nonhydrostatic pressures that are produced by the nongasketed diamond anvil cell (15, 16). As a result "edge effects" are difficult to eliminate. However, the pressure gradient is often smaller than expected because of self-gasketing resulting from the internal friction of the sample under high pressure (16). This internal friction can also prevent the immediate relaxation of the sample upon release of the pressure. Hence it may be difficult to study the reversibility of a pressure-induced change. This nonhydrostatic pressure can lead to calibration problems in determining the best average pressure experienced by the sample. Unfortunately, the nonhydrostatic pressure prevents the study of single crystals. The small cross-sectional area of the diamonds (see Figure 2) requires the use of a small area source (with the associated linewidth broadening) and relatively long counting times. The long counting times may be overcome by using ^{57}Fe -enriched samples. In fact, it is almost essential that ^{57}Fe -enriched samples be used for materials with a low iron content, a serious disadvantage in some cases. In addition, it is quite difficult to use the cell at temperatures below about 100 K because of its size.

Experimental

The results reported herein were obtained by using an opposed diamond anvil cell placed in a Mössbauer spectrometer in the configuration shown in Figure 1. The source-to-detector distance was about 2 cm. Pressure calibration was accomplished by measuring the Belleville spring compression as a function of applied force on a Dillon force gauge. The area of the smaller diamond (Figure 2) was determined by microscopic methods. The geometry of the diamond anvil cell was then used to calculate the pressure between the diamonds for a given spring compression and for the different Belleville spring washer configurations. The results of this calibration for three washer configurations are shown in Figure 2. This calibration was then checked with HgI_2 which exhibits a phase change at 13 kbar (8). In operation, the spring compression was measured with a metric micrometer, and the center configuration in Figure 2 was used for the Belleville washers.

A constant-acceleration Harwell Mössbauer spectrometer and Harwell gas proportional counter were used in this work. The spectrometer was calibrated with room-temperature natural α -iron foil and utilized a room-temperature rhodium matrix ^{57}Co source with an area of about 1.5 mm^2 and a nominal activity of 30 millicuries during the course of this

work. This small area source, obtained from the Radiochemical Centre, Amersham, England, exhibited a linewidth of 0.31 mm/s. The typical count rate at the detector was 5000 counts/s and about 24 h were required to accumulate each spectrum. The resulting spectra were evaluated using standard statistical methods, and the resulting parameters are accurate to about ± 0.02 mm/s.

Both of the compounds studied in this chapter were prepared by modifying a previously published method (17). The modifications included recrystallization from toluene and subsequent drying for about 10 h at 100°C in a vacuum. In addition, the compounds were prepared on a small scale and used about 90%-enriched ^{57}Fe obtained from Oak Ridge National Laboratory.

Results and Discussion

The iron(II) complexes formed with the various pyrazolylborate ligands (18) form an interesting system to study at high pressure. $\text{Fe}[\text{HB}(\text{pz})_3]_2$ is known to exhibit a high-spin-low-spin equilibrium in chloroform solution and to be low-spin in the solid state at room temperature (19, 20). We reported recently (21) that this compound undergoes a transition to the high-spin state at about 390 K. Hence, this compound, which is already low-spin at room temperature, would be expected to remain low-spin when pressure is applied. In contrast, the substituted pyrazolylborate compound $\text{Fe}[\text{HB}(3,5\text{-Me}_2\text{pz})_3]_2$ is known (20) to be high-spin at room temperature, to undergo a spin-state interconversion between 245 and 194 K, and to be low-spin at 147 K and below. A recent x-ray structural study of both compounds (22) revealed average iron-nitrogen bond lengths of 2.172(22) Å in $\text{Fe}[\text{HB}(3,5\text{-Me}_2\text{pz})_3]_2$ and 1.973(7) Å in $\text{Fe}[\text{HB}(\text{pz})_3]_2$. Hence, although both compounds possess virtual D_{3d} solid-state symmetry, the high-spin complex has an average iron-nitrogen bond distance that is about 0.20 Å longer than the low-spin complex. Thus, $\text{Fe}[\text{HB}(3,5\text{-Me}_2\text{pz})_3]_2$ is an excellent candidate for a transformation from the high-spin state to the low-spin state at high pressure.

The Mössbauer effect spectra of $\text{Fe}[\text{HB}(3,5\text{-Me}_2\text{pz})_3]_2$ obtained at room temperature and at ambient, 9, and 44 kbar pressure are illustrated in Figure 3. Mössbauer spectral parameters obtained both before and after applying the maximum pressure are presented in Table I. The ambient pressure spectrum is clearly that expected of a high-spin pseudo-octahedral iron(II) complex. However, there are some small differences in the parameters reported in Table I and those presented earlier by Jesson et al. (20). These differences apparently are related to the method of preparation (23). With increasing pressure a low-spin component appears at about 0.4 mm/s with increasing area relative to that of the high-spin component. At 44 kbar the spectrum exhibited 83% low-spin

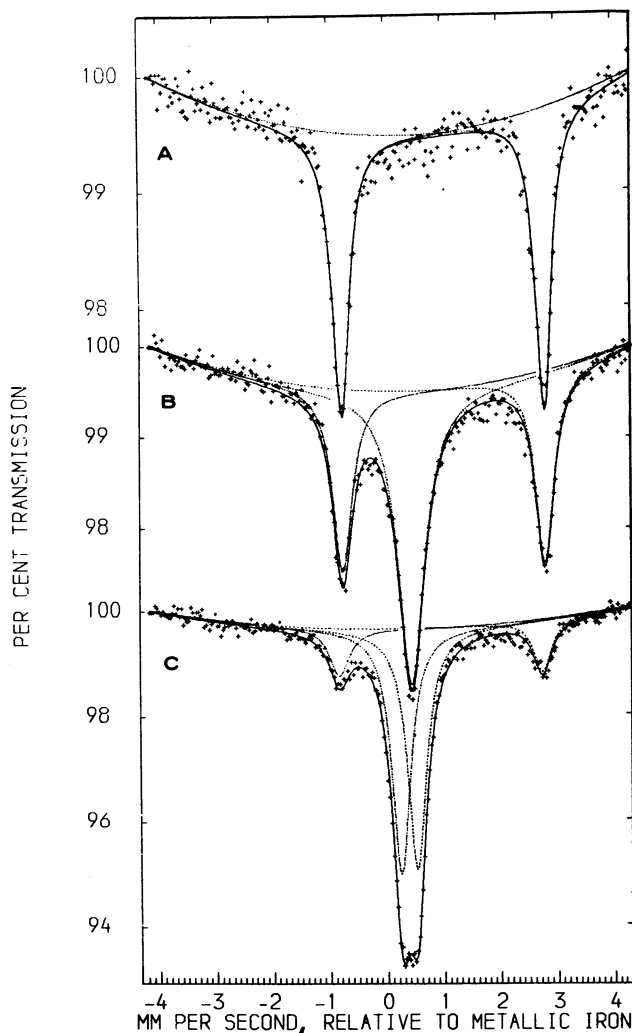


Figure 3. Mössbauer effect spectra of $\text{Fe}[\text{HB}(3,5\text{-Me}_2\text{pz})_3]_2$ obtained at room temperature and at (A) ambient pressure, (B) 9 kbar, and (C) 44 kbar in a diamond anvil cell

iron(II) and 17% high-spin iron(II). The residual high-spin iron(II) present at 44 kbar probably results from edge effects present in the ungasketed cell. Experiments in a gasketed cell are currently under way to evaluate this possibility. The spin-state transition is essentially reversible in that the release of the pressure resulted in a greater than 96% return to the high-spin state. The isomer shift of the high-spin component remained essentially constant during the entire experiment. In contrast,

the quadrupole interaction slowly decreased during the course of the entire experiment, a result for which we have no explanation at this time. The parameters for the low-spin component observed at 9 kbar and above are typical of those found in low-spin pseudooctahedral iron(II) complexes and resemble those observed in $\text{Fe}[\text{HB}(\text{pz})_3]_2$ at room temperature (see Table I) and at lower temperatures (20, 21).

Apparently the ligand field potential present at room temperature in high-spin, $^5\text{T}_{2g}$, $\text{Fe}[\text{HB}(3,5\text{-Me}_2\text{pz})_3]_2$ is very close to the mean pairing energy required for the formation of the low-spin $^1\text{A}_{1g}$ state. Thus, the application of pressure must initially increase the ligand field potential of the high-spin state enough to allow the thermal population of both states at room temperature, and eventually enough so that only the low-spin state is occupied. Similar results have been reported for related compounds close to the spin-crossover crystal field potential (24–28). This compound thus belongs to Class 3A in the behavior-class scheme proposed by Ferraro and Long for pressure-induced solid-state transformations (29).

The Mössbauer effect spectra of $\text{Fe}[\text{HB}(\text{pz})_3]_2$ obtained at room temperature and ambient and 45 kbar pressure are illustrated in Figure 4. The spectral parameters are presented in Table I. In this instance, we would have expected little if any change in the spectrum with increasing pressure because $\text{Fe}[\text{HB}(\text{pz})_3]_2$ is already low-spin at room temperature as is evidenced by its Mössbauer spectral parameters (Table I) and by its magnetic and infrared properties (21). It is thus surprising to observe the presence of 15% of a second, presumably high-spin component at 45 kbar (Figure 4B). The formation of this component is completely reversible; the Mössbauer spectrum obtained after release of the pressure is identical to Figure 4A. The Mössbauer parameters for this component ($\Delta E_Q = 3.34$ mm/s, $\delta = 0.90$ mm/s) indicate the high-spin $^5\text{T}_{2g}$ state in divalent iron. For comparison, at 423 K and ambient pressure, this compound exhibits a high-spin Mössbauer spectrum with $\Delta E_Q = 2.77$ mm/s, $\delta = 0.81$ mm/s, and a magnetic moment of about $5\mu_B$ (21). The appearance of this presumably high-spin component is surprising, but not totally unexpected. Drickamer and co-workers (25–28) observed a similar phenomenon at pressures of 50 kbar and above in several divalent iron compounds that are low-spin at room temperature and ambient pressure. For instance, in one of several examples (25) the low-spin complex $\text{Fe}(\text{phenanthroline})_3\text{Cl}_2 \cdot 7\text{H}_2\text{O}$ is converted to the extent of about 15% to a high-spin component with $\Delta E_Q = 2.62$ mm/s and $\delta = 1.00$ mm/s at 50 kbar. Optical spectroscopy also supported the formation of this component at high pressures. Drickamer and co-workers (30) propose that the high-spin form results at high pressure in their imine complexes

Table I. High-Pressure

Compound	P (kbar)	High-Spin Component			
		ΔE_Q	δ	Γ_{ave}	% A
Fe[HB(pz) ₃] ₂	0				
	45	3.34	0.90	0.72	15
	0 ^b				
Fe[HB(3,5-Me ₂ pz) ₃] ₂	0	3.57	1.00	0.35	> 98
	9	3.57	1.00	0.40	48
	19	3.56	1.00	0.38	26
	44	3.56	0.96	0.40	17
	20 ^b	3.54	0.99	0.56	23
	9 ^b	3.52	1.00	0.44	39
	0 ^b	3.50	0.99	0.42	> 96

* All data in mm/s relative to natural α -iron foil and measured at ambient (about 298 K) temperature.

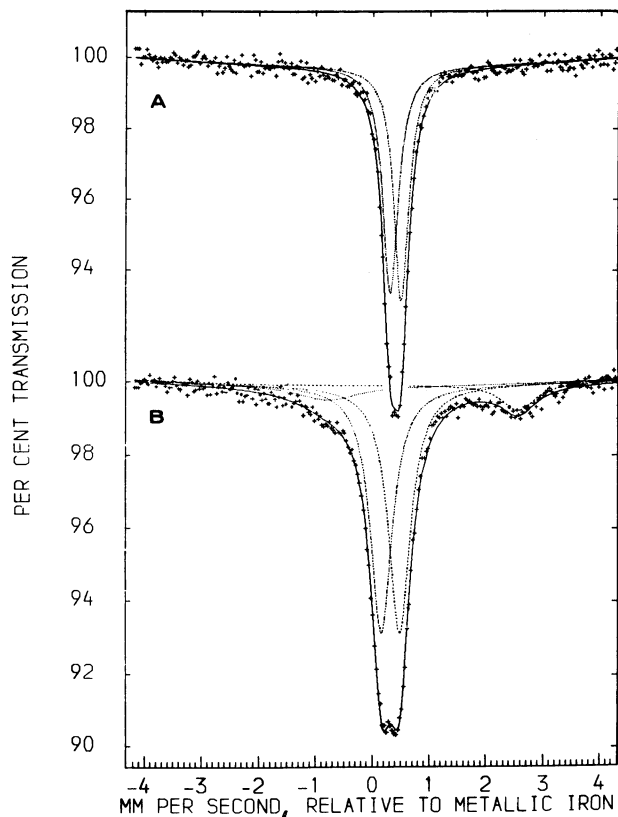


Figure 4. Mössbauer effect spectra of Fe[HB(pz)₃]₂ obtained at room temperature and at (A) ambient pressure, and (B) 45 kbar in a diamond anvil cell

Mössbauer Effect Results^a

<i>Low-Spin Component</i>				
ΔE_Q	δ	Γ_{ave}	% A	χ^2
0.19	0.40	0.32	100	1.18
0.32	0.33	0.46	85	1.25
0.19	0.40	0.30	100	1.00
			< 2	1.16
0.00	0.58	0.56	52	1.32
0.21	0.42	0.38	74	1.25
0.28	0.39	0.40	83	1.35
0.24	0.41	0.37	76	1.10
0.15	0.44	0.46	61	0.90
			< 4	0.94

^a Measured after the application of the maximum pressure.

because of a thermal occupation of a π -antibonding state which is stabilized at high pressure and thus yields a reduction in the crystal field potential at high pressure. It would be interesting to find a similar situation in this pyrazolylborate complex. Unfortunately, it appears that much additional work will be required to support either this model or to develop a better explanation.

Acknowledgment

The author would like to thank G. Longworth, T. E. Cranshaw, D. M. Adams, J. R. Ferraro, and L.J. Basile for their encouragement and many helpful discussions during the course of this work.

Literature Cited

1. Debrunner, P.; Vaughan, R. W.; Champion, A. R.; Cohen, J.; Magzis, J.; Drickamer, H. G. *Rev. Sci. Instrum.* **1966**, *37*, 1310.
2. Schilling, J. S.; Klein, U. F.; Holzapfel, W. B. *Rev. Sci. Instrum.* **1974**, *45*, 1353.
3. Holzapfel, W. B. *Crit. Rev. Solid State Sci.* **1975**, *5*, 89.
4. Liu, C. M.; Ingalls, R. *Rev. Sci. Instrum.* **1978**, *49*, 1680.
5. Ingalls, R. *J. Phys. (Paris), Colloq. C2* **1979**, *40*, 174.
6. Holzapfel, W. B. In "High Pressure Chemistry"; Kelm, H., Ed.; D. Reidel: Dordrecht, Holland, 1978; p. 159.
7. Heydemann, P. L. M. In "High Pressure Chemistry"; Kelm, H., Ed.; D. Reidel: Dordrecht, Holland, 1978; p. 1.
8. Ferraro, J. R.; Basile, L. J. *Appl. Spectrosc.* **1974**, *6*, 505.
9. Adams, D. M.; Appleby, R.; Sharma, S. K. *J. Phys. E* **1976**, *9*, 1140.
10. Adams, D. M.; Payne, S. J.; Martin, K. *Appl. Spectrosc.* **1973**, *5*, 377.
11. Ferraro, J. R.; Quattrochi, A. *Appl. Spectrosc.* **1971**, *25*, 102.
12. Piermarini, G. J.; Block, S. *Rev. Sci. Instrum.* **1975**, *46*, 973.
13. Ferraro, J. R.; Basile, L. J. *Am. Lab.* **1979**, *11*, 31.

14. Long, G. J.; Miles, G.; Ferraro, J. R. *Appl. Spectrosc.* 1974, 28, 377.
15. Lippincott, E. R.; Duecker, H. C. *Science* 1964, 144, 1119.
16. Sung, C.; Goetze, C.; Mao, H. *Rev. Sci. Instrum.* 1977, 48, 1386.
17. Trofimenko, S. *J. Am. Chem. Soc.* 1967, 89, 3170.
18. Trofimenko, S. *Acc. Chem. Res.* 1971, 4, 17.
19. Jesson, J. P.; Trofimenko, S.; Eaton, D. R. *J. Am. Chem. Soc.* 1967, 89, 3158.
20. Jesson, J. P.; Weiher, J. F.; Trofimenko, S. *J. Chem. Phys.* 1968, 48, 2058.
21. Hutchinson, B. B.; Daniels, L.; Henderson, E.; Neill, P.; Long, G. J.; Becker, L. W. *J. C. S. Chem. Comm.* 1979, 1003.
22. Oliver, J. D.; Mullica, D. F.; Hutchinson, B. B.; Milligan, W. O. *Inorg. Chem.* 1980, 19, 165.
23. Long, G. J.; Hutchinson, B. B., unpublished data.
24. Ferraro, J. R.; Takemoto, J. *J. Appl. Spectrosc.* 1974, 28, 66.
25. Fisher, D. C.; Drickamer, H. G. *J. Chem. Phys.* 1971, 54, 4825.
26. Grenoble, D. C.; Drickamer, H. G. *J. Chem. Phys.* 1971, 55, 1624.
27. Bargeron, C. B.; Drickamer, H. G. *J. Chem. Phys.* 1971, 55, 3471.
28. Frank, C. W.; Drickamer, H. G. *J. Chem. Phys.* 1972, 56, 3551.
29. Ferraro, J. R.; Long, G. J. *Acc. Chem. Res.* 1975, 8, 171.
30. Drickamer, H. G.; Frank, C. W. "Electronic Transitions and the High-Pressure Chemistry and Physics of Solids"; Chapman and Hall: London, 1973; p. 131.

RECEIVED June 27, 1980.

Relaxation Effects Associated with Magnetic Phase Transitions

G. R. HOY

Physics Department, Old Dominion University, Norfolk, VA 23508

M. R. CORSON

Physics Department, Bowdoin College, Brunswick, ME 04011

Mössbauer spectra of substances that magnetically order often show a central peak with prominent wings in the region of the ordering temperature. We show that such spectra can arise from the critical slowing down of the Mössbauer ion's spin fluctuation rate. Using a dynamic model, detailed calculations are presented for Kramers ($S = 1/2$) and non-Kramers ($S = 1$) salts. The spin Hamiltonian parameters, the reduced magnetization, the form and strength of the hyperfine interaction, and the spin fluctuation rate can be determined. Our results showing the critical slowing down of spin fluctuations in K_2FeO_4 are presented. We also give a qualitative discussion of how these microscopic results for the spin dynamics may fit into the framework of critical fluctuations.

In the region of magnetic phase transitions, so-called anomalous Mössbauer spectra are often observed (1), consisting of small broadened peaks on the wings of a large central peak. Such spectra are not characteristic of single-valued, static hyperfine fields. Because of the difficulty in theoretically fitting such spectra, these strange features are commonly attributed to effects arising from sample temperature inhomogeneities, a distribution of Curie or Néel temperatures in the sample, or critical superparamagnetism. While these may be the correct interpretation in some individual cases, these anomalous spectra have been observed in many nonmetallic systems investigated by many different researchers. Hence, it seems reasonable to search for an underlying

0065-2393/81/0194-0463\$05.00/0

© 1981 American Chemical Society

physical reason for their occurrence. In addition to providing a qualitative interpretation of these spectra, we also propose to formulate the problem in such a manner that some quantitative progress can be made in understanding such phenomena.

Very powerful and general theoretical techniques for calculating Mössbauer effect line shapes in the presence of relaxation now exist (2–20). By particularizing this general theory, it is possible to formulate the problem in such a way that many interesting physical parameters can be determined using Mössbauer spectroscopy. In particular, one can observe (21) and also clarify the meaning of the “critical slowing down” of an ion’s spin fluctuation rate near the critical temperature. Furthermore, it may be possible to begin to connect the results of these microscopic Mössbauer measurements with the usual critical phenomena picture consisting of clusters of correlated atomic spins.

Formulation of the Problem

It is common in Mössbauer spectroscopy to consider the Mössbauer nucleus to be in an “effective magnetic field” produced by the electrons in the ion. In general it is not true that one can treat the problem in this way. A more general type of interaction would be a hyperfine term conventionally written $\vec{I} \cdot \vec{A} \cdot \vec{S}$. If the hyperfine interaction tensor contains only an A_{zz} component, then the hyperfine interaction can be written $A_{zz}S_zI_z$, which clearly gives the effective magnetic field result.

The electrons that interact with the nucleus are moving in a complicated fashion. In addition, the ions can interact with each other and/or with the lattice vibrations of the solid. Under certain conditions these dynamic effects can be observed, and the correct interpretation of these effects contains remarkably detailed information. Because of the difficulty in visualizing the most general formulation of the time-dependent problem, it is very useful to gain some physical insight by considering a less general case. To do this, consider a ^{57}Fe ion having no orbital angular momentum, and total ionic spin $S = 1/2$. In the absence of a real or effective magnetic field, this Kramers ion will have a doubly degenerate ground state independent of the degree of asymmetry of the crystalline environment (Kramers Theorem). Assume, for simplicity, that the $\vec{I} \cdot \vec{A} \cdot \vec{S}$ hyperfine interaction can be represented by the effective magnetic field approximation. Under these conditions the ^{57}Fe nucleus is in an effective magnetic field equal to $-H$ or H when $S_z = 1/2$ and $-1/2$, respectively. If the spin system magnetically orders below some critical temperature, the ground-state degeneracy is removed and the $|S = 1/2, S_z = 1/2\rangle$ and $|1/2, -1/2\rangle$ eigenstates become unequally populated. If the ion undergoes transitions between these eigenstates because of some relaxation mechanism in the solid, we must determine the effective magnetic field at the nucleus.

Consider the cases of slow, fast, and intermediate relaxation shown in Figure 1. By the time-energy uncertainty principle, the time required for a nucleus to "measure" an effective magnetic field is approximately the Larmor period of the nucleus in that field, which for ^{57}Fe is typically 10^{-9} s. If the ionic spin fluctuation rate is slow, and an ion spends many Larmor periods in each eigenstate, then a Mössbauer nucleus experiences a magnetic field $-H$ or $+H$ depending on the state of the atom containing the nucleus. In this case, the Mössbauer spectrum is the Boltzmann-weighted sum of two spectra characteristic of these two fields. Since $-H$ and $+H$ produce the same Mössbauer pattern, the resulting spectrum is as shown in the upper curve in Figure 1.

If the ionic spin fluctuation rate is fast compared to the Larmor frequency, then the nucleus cannot respond to the individual fields H and $-H$, and all nuclei experience the same, single-valued effective magnetic field which is the Boltzmann-weighted average of these two

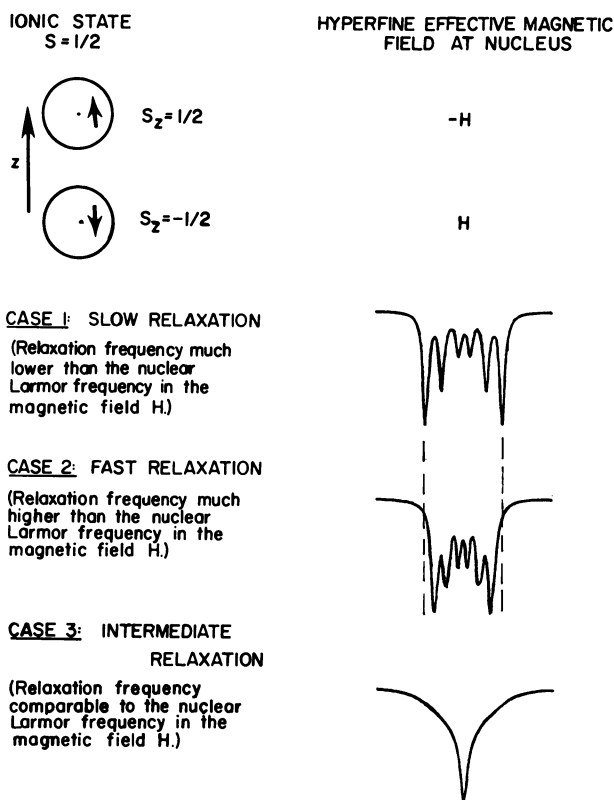


Figure 1. Calculated Mössbauer transmission spectra, including the effects of relaxation, for an $S = 1/2$ Kramers ion having eigenstates $|S, M_s\rangle$ of $|1/2, 1/2\rangle$ and $|1/2, -1/2\rangle$. In these spectra, the hyperfine interaction is assumed to be an effective magnetic field.

values. For a system with some magnetic order, a possible spectrum is shown as the middle curve in Figure 1. Note that the overall width of the fast relaxation spectrum is less than that of the slow relaxation spectrum.

If the ionic spin fluctuation rate is comparable to the nuclear Larmor frequency, then the effective magnetic field experienced by the nucleus is not well defined. This gives rise to a "relaxation -broadened" spectrum. The lowest curve in Figure 1 shows such an example for a system having zero magnetic order.

Next consider a ^{57}Fe ion with no orbital angular momentum, total ionic spin $S = 1$, and nondegenerate ionic eigenstates $S_z = 1, 0$, and -1 . Again assume the effective magnetic field approximation for the hyperfine interaction. This effective magnetic field takes on the values $-H$, 0 , and $+H$ when $S_z = 1, 0$, and -1 , respectively. In the presence of relaxation effects, we must again determine the resulting Mössbauer spectra. Figure 2 shows results similar to those in Figure 1 for this non-Kramers ion. There are several important differences between these two sets of results. The ionic state $|S = 1, S_z = 0\rangle$ does not produce a magnetic field at the nucleus. Thus, in the slow relaxation limit this state produces a single peak at the center of the pattern as shown in the upper curve in Figure 2. The two missing peaks of the accompanying six-line pattern from states $|1, 1\rangle$ and $|1, -1\rangle$ are hidden by the central peak.

In the fast relaxation limit, as in the middle curve of Figure 2, all nuclei experience the same single-valued effective magnetic field which is the Boltzmann-weighted average of the three values $-H$, 0 , and $+H$. The meaning of this is that the three fields $-H$, 0 , and $+H$ have lost their individual identities. As a consequence, the central peak in the slow relaxation spectrum of Figure 2 attributable to the magnetic field of 0 is completely absent in this fast relaxation limit.

A more complete analysis applicable to Mössbauer experimental results including time-dependent effects recently has been formulated in a very useful and general way (12), and this method is used in the development presented here. The details of the formulation can be found in the original reference, so we will only give a summary.

We will assume that the ^{57}Fe nucleus is coupled to its atomic electrons through the hyperfine interaction, and that in the ionic system some random process induces transitions between the eigenstates of the ion. This "relaxation" process is assumed to be stationary Markoffian, so that it is possible to obtain closed-form mathematical expressions for the resulting line shape using the so-called super operator formalism. The essential result for the line shape as a function of emitted energy $\hbar\omega$ is (12),

$$F(\omega) = \sum_{\mu, \nu, \mu', \nu'} b_{\nu} \langle \nu | A^+ | \mu \rangle \langle \mu \nu | u(p) | \mu' \nu' \rangle \langle \mu' | A | \nu' \rangle \quad (1)$$

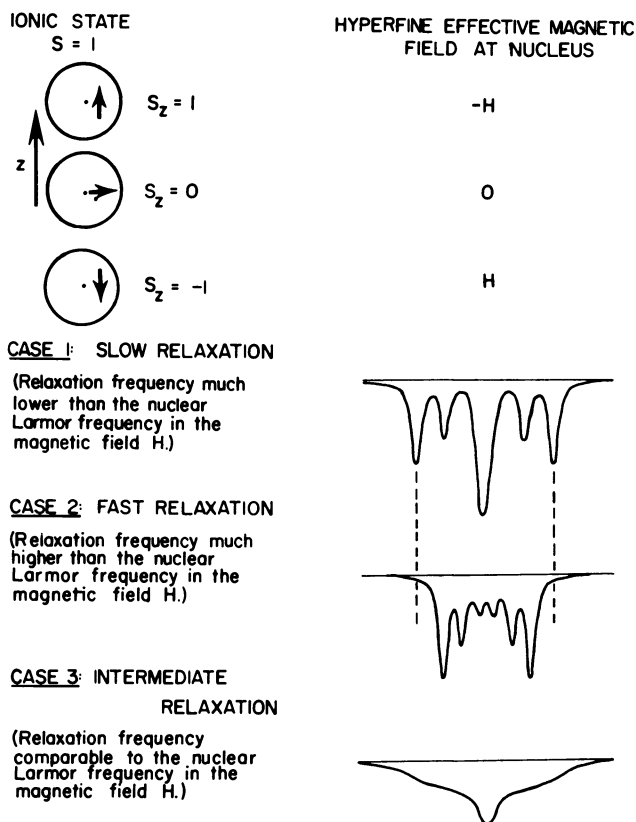


Figure 2. Calculated Mössbauer transmission spectra, including the effects of relaxation, for an $S = 1$ non-Kramers ion having eigenstates $|S, M_s\rangle$ of $|1, 1\rangle$, $|1, 0\rangle$ and $|1, -1\rangle$. In these spectra, the hyperfine interaction is assumed to be an effective magnetic field.

where b_ν is the occupation probability of the initial state $|\nu\rangle$, $p = \frac{1}{2} \Gamma - i\hbar\omega$, A is the operator for emission (or absorption) of radiation, and $u(p) = (p - W - iH_o^*)^{-1}$. The matrix elements of A are essentially Clebsch-Gordan coefficients times vector spherical harmonics. The matrix elements of $u(p)$ are calculated by inverting the super matrix whose dimensionality is $(2S + 1)^2(2I_1 + 1)(2I_0 + 1)$, where S is the (effective) ionic spin and I_1 and I_0 are the spins of the excited and ground nuclear levels. The matrix elements of the super Hamiltonian H_o^* are given by (12),

$$(\mu\nu|H_o^*|\mu'\nu') = \delta_{\nu\nu'} \langle \mu|H_o|\mu'\rangle - \delta_{\mu\mu'} \langle \nu'|H_o|\nu\rangle \quad (2)$$

The matrix elements of the super relaxation matrix W will be given later. In our calculation we do not actually compute the needed inverse for every value of ω , but use a method (13, 17) that allows the computer calculation to be done more rapidly.

In our approach, we write the Hamiltonian \mathcal{H} in the following form:

$$\mathcal{H} = H_{\text{cf}} + H_{\text{mf}} + H_{\text{hyper}} + H_{\text{n}} + H_{\text{relax}}(t) \quad (3)$$

where

$$H_{\text{cf}} = D \left[S_z^2 - \frac{1}{3} S(S+1) \right] + E (S_x^2 - S_y^2)$$

$$H_{\text{mf}} = \gamma \sigma S_z$$

$$H_{\text{hyper}} = A_z I_z S_z + A_x I_x S_x + A_y I_y S_y$$

$$H_{\text{n}} = \frac{e^2 q Q}{4I(2I-1)} \left[3I_z^2 - I(I+1) + \frac{\eta}{2} (I_x^2 + I_y^2) \right]$$

Thus H_{cf} represents the effect of the crystalline field on the ion in the spin Hamiltonian approximation, and H_{mf} arises from magnetic ordering in the Weiss molecular field model. We are allowing for the possibility of ferromagnetic or some other type of magnetic ordering of the ionic moments. H_{hyper} represents the hyperfine interaction between the nucleus and the electrons in the ion. This term is treated fully quantum mechanically in the calculation. H_{n} is the usual quadrupole interaction between the nucleus and any existing electric field gradients. Because we are primarily interested in magnetic effects we will set $H_{\text{n}} = 0$ in this discussion. $H_{\text{relax}}(t)$ is the term that causes the ionic system to flip from one of its states to another as the result of interactions with its neighbor. This term is not written explicitly, but its effect is incorporated into the calculation by including the relaxation super matrix W .

The first two terms of Equation 3 represent the ionic Hamiltonian,

$$H_{\text{ion}} = D \left[S_z^2 - \frac{1}{3} S(S+1) \right] + E (S_x^2 - S_y^2) + \gamma \sigma S_z \quad (4)$$

where D and E are the spin Hamiltonian parameters, σ is the reduced magnetization of the ionic spin system in the mean field approximation, and S is the spin of the ion. Thus H_0 (see Equation 2) can be written,

$$H_0 = H_{\text{ion}} + H_{\text{hyper}} \quad (5)$$

The relaxation process associated with $H(t)$ is taken to consist of an interaction that causes the ion to evolve in time according to a stationary Markoffian chain through its ionic energy levels E_i and its corresponding eigenstates ψ_i . E_i and ψ_i are determined by obtaining the eigenvalues and eigenvectors of the ionic Hamiltonian H_{ion} . In our case, because we are primarily interested in the low-temperature region, we have taken the relaxation mechanism to arise from the "flip-flop" part of the dipole-

dipole interaction. We expect this energy-conserving spin-spin interaction to be the dominant mechanism at low temperatures. (This is not completely correct for an $S = 1/2$, doubly degenerate system, which, in addition to the Clouser-Blume theory is discussed by Dattagupta (22). At high temperatures, the large number of phonons is expected to cause spin-lattice relaxation to dominate.)

Assuming that the ionic system is initially in state ψ_i , the transition probability for the ion to flip from state ψ_i to state ψ_j is given by

$$\Omega_{ij} = \Omega | \langle \psi_i \psi_j | S_{+i} S_{-j} + S_{-i} S_{+j} | \psi_i \psi_j \rangle |^2 \times \exp(-E_j/kT) / \sum_i \exp(-E_i/kT) \quad (6)$$

where Ω is the relaxation rate parameter, S_+ and S_- are the usual raising and lowering operators, respectively, and the normalized Boltzmann factor determines the probability of finding a neighbor with which to undergo a spin flip. It is important to realize that at sufficiently low temperatures in a magnetically ordered sample, the transition probabilities for flipping cannot occur simply because the number of neighbors with which to exchange spin has been reduced to zero for the unfavored spin orientation.

An important step of this calculation is the construction of the so-called super or Liouville Hamiltonian. This particular construction is interesting because the eigenvalues of the resulting super matrix give the actual energies of all possible radiations of the system. In addition, from a theoretical point of view, the introduction of this type of operator results in simplifying the commutation relations needed to solve the time-dependent problem. The super Hamiltonian matrix is defined by

$$(\psi_i m_g \psi_j m_e | H_o^* | \psi_i' m_g' \psi_j' m_e') = \langle \psi_i m_g | H_o | \psi_i' m_g' \rangle \delta_{\psi_j, \psi_j'} \delta_{m_e, m_e'} - \langle \psi_j' m_e' | H_o | \psi_j m_e \rangle \delta_{\psi_i, \psi_i'} \delta_{m_g, m_g'}$$

where m_g and m_e refer to the nuclear ground and excited states, respectively.

The relaxation super matrix W is defined as (12),

$$(\psi_i m_g \psi_j m_e | W | \psi_i' m_g' \psi_j' m_e').$$

To simplify the notation let $\psi_i = \mu$ and $\psi_j = \nu$. Then, the matrix elements of W are given by,

$$(\mu m_g \nu m_e | W | \mu' m_g' \nu' m_e') = [\delta_{\mu\nu} \delta_{\mu'\nu'} \Omega_{\mu\mu'} + \delta_{\mu\mu'} \delta_{\nu\nu'} (1 - \delta_{\mu\nu}) (\Omega_{\mu\mu} + \Omega_{\nu\nu})] \delta_{m_g m_g'} \delta_{m_e m_e'} \quad (7)$$

where $\Omega_{\mu\mu'}$ is defined in Equation 6.

When constructing the relaxation operator super matrix W , it is important to know a relationship involving the diagonal elements, namely,

$$(i | W | i) = - \sum_{j \neq i} (i | W | j),$$

where this relationship follows from the concept of detailed balance.

Consideration of Various Cases

In this section we present model calculations showing theoretical ^{57}Fe Mössbauer spectra as the following parameters are varied: the spin Hamiltonian parameters D and E , the reduced magnetization σ , the form and strength of the hyperfine interaction A_x, A_y, A_z , ($A_x = A_{xx}$, etc.), the ionic spin S , and relaxation rate parameter Ω . We consider three possible cases of the crystalline field—the highly symmetrical one in which $D = E = 0$, the axially symmetric crystalline field where $D \neq 0$, and $E = 0$, and finally, the rhombic crystalline field where $D \neq 0$ and $E \neq 0$. We assume that the ionic system follows a Weiss magnetization curve as it magnetically orders when the temperature is lowered below the transition temperature. We include two forms for the hyperfine interaction, namely, the effective field case $A_x = A_y = 0$ and $A_z \neq 0$, and the isotropic hyperfine interaction $A_x = A_y = A_z \neq 0$. We also consider two cases for the ionic spin—the $S = 1/2$ Kramers system and the $S = 1$ non-Kramers ion. A similar calculation for $S = 3/2$ has been considered previously (23). However, in that case, the off-diagonal elements of the electron nuclear magnetic hyperfine interaction were neglected.

In our calculations all the parameters D , E , A_x , A_y , A_z , and Ω are expressed in energy units such that the number eight corresponds to a typical iron Mössbauer experimental linewidth of 0.30 mm/s. For energy conversion purposes note that *one* of our units equals: 3.75×10^{-2} mm/s, 1.8×10^{-9} eV, 2.09×10^{-5} K, 2.89×10^{-21} erg, or 1.46×10^{-5} cm $^{-1}$.

$S = 1/2$ Kramers System. For this case the spin Hamiltonian parameters D and E have no effect, as can be seen from the form of H_{cf} . In Figure 3 we consider the Kramers ion system with $S = 1/2$. The first column shows the calculated Mössbauer spectra when the ionic system follows a Weiss molecular field magnetization curve as the temperature is lowered, and the ionic relaxation rate Ω is held constant at a fairly large value (here large means compared to the value of the hyperfine interaction coupling constant as discussed in the previous section). The second column shows the spectra for the case of a constant small value of reduced magnetization σ , but with the relaxation rate Ω decreasing by several orders of magnitude. The third column is similar to the second but the system is assumed to be above its magnetic transition temperature

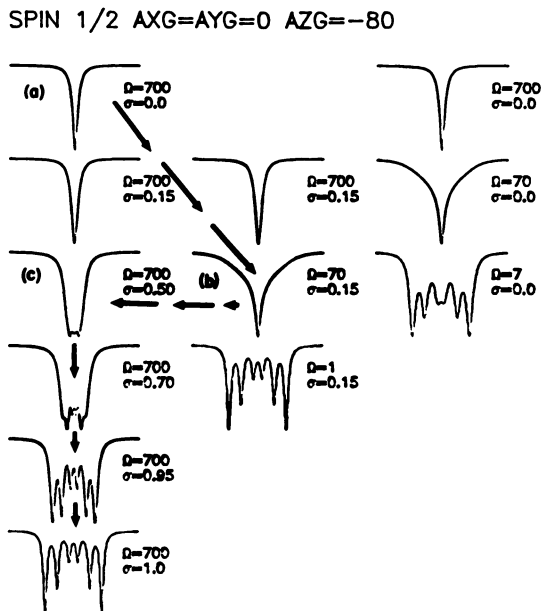


Figure 3. Calculated Mössbauer spectra, including the effects of relaxation, for an $S = \frac{1}{2}$ Kramers ion. The hyperfine interaction is assumed to be an effective magnetic field.

and thus has a zero value of reduced magnetization σ . The dashed-arrow path connecting the Spectra *a* to *b* to *c* and then down Column 1 shows a possible sequence of spectra if there is a “critical slowing down” of the ion’s spin fluctuation rate in the transition region as the temperature is lowered.

Figure 4 shows the same calculations as in Figure 3 except that in Figure 4, the hyperfine interaction is taken to be isotropic. There are two important new features shown in this figure. First, notice the two upper curves in Column 1. The pattern actually narrows as the temperature is lowered below the transition temperature. The reason for this is explained by the second important feature, seen in Column 3, which shows the spectra resulting from the isotropic hyperfine interaction when $\sigma = 0$, as the relaxation rate Ω is decreased. The important point is that for a small value of the relaxation rate parameter Ω , the isotropic hyperfine interaction produces a spectrum in which the total peak spacing is greater than the fully split effective magnetic field spectrum shown at the bottom of Column 1. This means that even for a relatively large value for the relaxation rate parameter Ω as shown in the first patterns in Columns 1 and 3, the spectrum is not “motionally narrowed” to its minimum value.

SPIN 1/2 AXG=AYG=AZG=-80

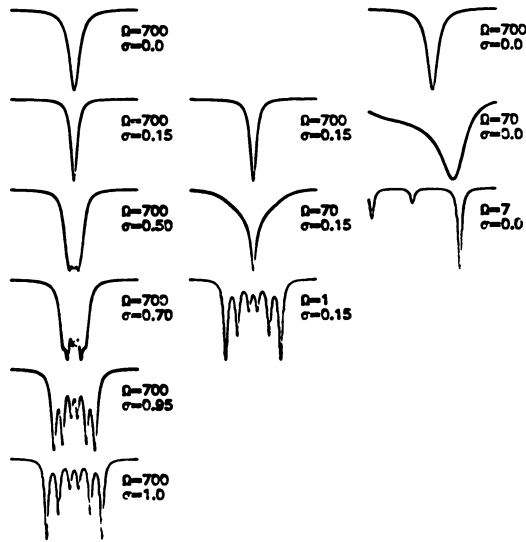


Figure 4. Calculated Mössbauer spectra, including the effects of relaxation, for an $S = \frac{1}{2}$ Kramers ion. The hyperfine interaction is taken to be isotropic.

SPIN 1 D=0 E=0 AXG=AYG=0 AZG=-44

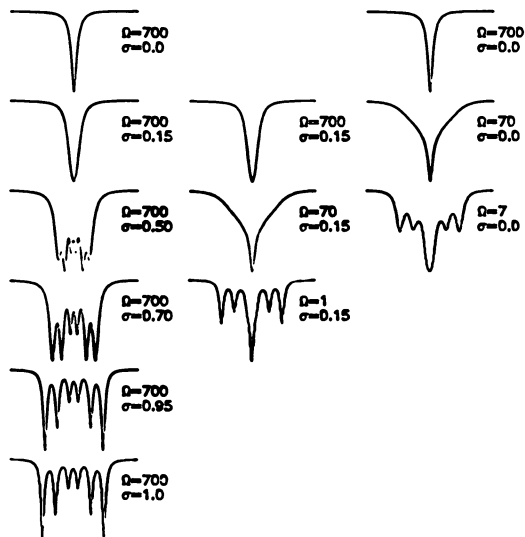


Figure 5. Calculated Mössbauer spectra, including the effects of relaxation for an $S = 1$ Kramers ion in a highly symmetric crystalline field. The hyperfine interaction is assumed to be an effective magnetic field.

Notice, by comparing Columns 2 and 3, that it takes only a very small value of reduced magnetization σ to "quench" the isotropic interaction into the effective field approximation. Even with a small value of reduced magnetization, the size of the mean-field magnetization term in the total Hamiltonian is such that the terms off the diagonal coming from A_x and A_y are very small compared to the terms along the diagonal, and hence have little effect.

S = 1 Non-Kramers System. For this case the spin Hamiltonian parameters D and E affect the spectra greatly. If $D > 0$ and $E = 0$, the ionic eigenstate $|S = 1, M_s = 0\rangle$ has the lowest energy, and the states $|1, 1\rangle$ and $|1, -1\rangle$ are degenerate. If $D < 0$ and $E = 0$ the ionic energy level diagram is just inverted, and if $D \neq 0$ and $E \neq 0$ the three ionic energy levels are nondegenerate.

Figure 5 shows the results for a non-Kramers ion system ($S = 1$) in a highly symmetric crystalline field (i.e., $D = E = 0$) using the effective-field hyperfine interaction ($A_x = A_y = 0, A_z \neq 0$). These results look very similar to those of Figure 3 except for one important difference. Notice that in the slow relaxation limit, there is a large central peak. As discussed in a previous section, this results from the ionic eigenstate $|S, M_s\rangle |1, 0\rangle$ which possesses no magnetic moment.

Figure 6 is similar to Figure 4, and in Column 3 specifically shows the effect of an isotropic hyperfine interaction for this case of a non-

SPIN 1 $D=0$ $E=0$ $A_x=A_y=A_z=-44$

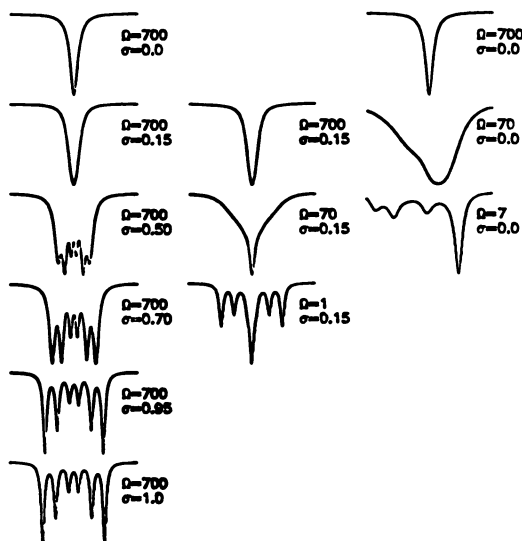


Figure 6. Calculated Mössbauer spectra, including the effects of relaxation, for an $S = 1$ Kramers ion in a highly symmetric crystalline field. The hyperfine interaction is taken to be isotropic.

Kramers system. Notice also in Column 2 that in the slow relaxation limit when $\sigma \neq 0$, there is again a large central peak in the spectrum.

In Figure 7, the $S = 1$ ion is in an axially symmetric crystalline field (i.e., $D \neq 0$, $E = 0$). Even though the hyperfine interaction is taken to be isotropic, the presence of the D term produces spectra that are identical to the effective field result specifically calculated in Figure 8. The reason that Figure 7 gives the same results as Figure 8 is that the presence of the D term in the Hamiltonian produces large values down the diagonal of the Hamiltonian matrix, and thus the off-diagonal elements arising from the A_x and A_y terms are negligible.

Figure 9 shows the result for an $S = 1$ ion in a rhombic crystalline field (i.e., $D \neq 0$, $E \neq 0$). The effective-field hyperfine interaction also has been assumed. Perhaps the only surprising result is contained in Column 3. Notice that above the transition temperature, when the reduced magnetization $\sigma = 0$, there is no effective magnetic field at the nucleus independent of the value of the relaxation rate Ω . This result is attributable to the fact that for the non-Kramers $S = 1$ ion in a rhombic crystalline field, the ionic energy levels are nondegenerate. In general these eigenstates can be written using the $|S, M_s\rangle$ notation as,

$$\begin{aligned}\psi_1 &= a_1|1,1\rangle + a_2|1,-1\rangle \\ \psi_2 &= b_1|1,1\rangle + b_2|1,-1\rangle \\ \psi_3 &= |1,0\rangle\end{aligned}$$

When the reduced magnetization σ is equal to zero, the magnitude of the coefficients a_1 , a_2 , b_1 , and b_2 are all equal, that is to say, each of the states ψ_1 and ψ_2 contain equal amounts of "circulation" up and "circulation" down. Thus, none of these states produces an effective magnetic field at the nucleus. This result is sometimes known as Van Vleck's theorem. However, if the reduced magnetization takes on a finite value, the magnitudes of the coefficients a_1 and a_2 are not equal (and likewise for the coefficients b_1 and b_2). Thus, under these circumstances the ionic states ψ_1 and ψ_2 produce an effective magnetic field at the nucleus, and a split hyperfine pattern can exist.

Further Results and Speculations

Our calculations, although rather complicated, still only treat the individual ion in a magnetic mean-field approximation. How then can this type of calculation be used to get any information about critical fluctuations, since they are, by their nature, associated with long-range correlations? In our model we expect that the relaxation rate parameter Ω would be constant over a small range of cryogenic temperatures,

SPIN 1 D=7524 E=0 AXG=AYG=AZG=-44

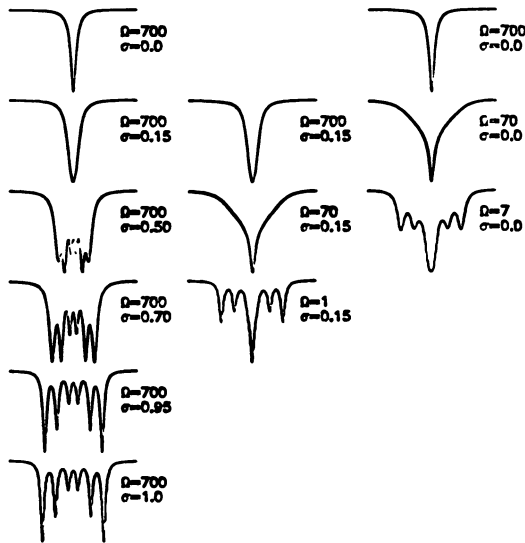


Figure 7. Calculated Mössbauer spectra, including the effects of relaxation, for an $S = 1$ Kramers ion in an axially symmetric crystalline field. The hyperfine interaction is taken to be isotropic.

SPIN 1 D=7524 E=0 AXG=AYG=0 AZG=-44

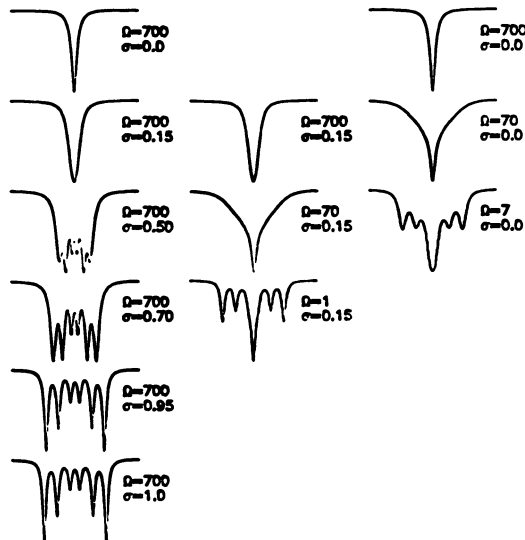


Figure 8. Calculated Mössbauer spectra, including the effects of relaxation, for an $S = 1$ Kramers ion in an axially symmetric crystalline field. The hyperfine interaction is assumed to be an effective magnetic field.

SPIN 1 D=7524 E=1368 AXG=AYG=0 AZG=-44

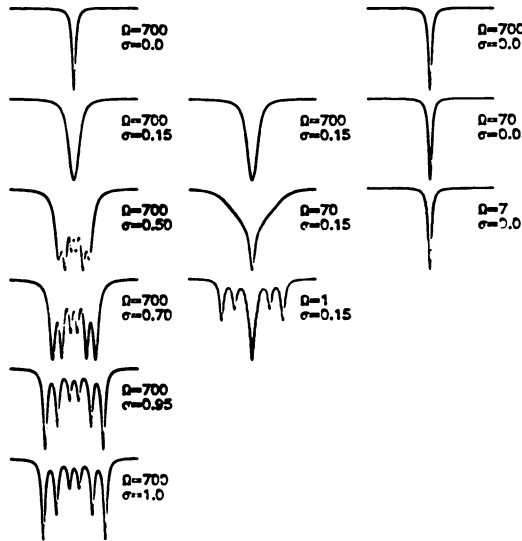


Figure 9. Calculated Mössbauer spectra, including the effects of relaxation, for an $S=1$ Kramers ion in a rhombic crystalline field. The hyperfine interaction is assumed to be an effective magnetic field.

because Boltzmann-factor effects are explicitly included in the calculation. However, near a critical point, as a consequence of critical fluctuations, the sample consists of clusters of ionic spins in which the orientations of the spins are much more highly correlated than would be the case in the absence of these critical fluctuations. Under such conditions the spin system consists of highly correlated spins. The likelihood that an ion, containing a Mössbauer nucleus, will find a neighbor spin with which to exchange spin orientations should be less than that given by the normalized Boltzmann factor in Equation 6. This then would result in our needing a smaller value of the relaxation rate parameter Ω than would be expected if these correlated clusters did not exist. Therefore, the existence of critical fluctuations would appear by requiring a sharp reduction in the relaxation rate parameter Ω in order to fit the experimental spectra in this temperature range.

Using these model spectra, it is possible to observe the critical slowing down of an ion's spin fluctuations by means of Mössbauer spectroscopy, and to determine crystal field, magnetization, and relaxation information using the relevant theoretical analysis. In Figure 10 we present our earlier work using a sample of K_2FeO_4 (24). The determined values of the parameters for this case are $S = 1$, and in our units $D =$

7524.1, $E = 1368.0$, and an isotropic magnetic hyperfine coupling constant for the nuclear ground state $A_g = -44.67$. The calibration was 0.03766 mm/s/channel. The values of D and E correspond to the published values (25) of 0.11 cm^{-1} and 0.02 cm^{-1} , respectively. The dots in Figure 10 show the experimental data and the lines show the theoretical fits. The overall features of the experimental spectra are fitted rather well. To obtain such fits, the relaxation rate parameter was required to be $\Omega = 700$ for all spectra outside of the critical region, and $\Omega = 1$ at 3.6 K.

To fit precisely our experimental Mössbauer spectra of K_2FeO_4 in the temperature range from 3.75 K to 3.56 K (the results are not shown here), it was necessary to superimpose spectra having several values of reduced magnetization σ , and for some spectra, two values of relaxation rate Ω . In addition to the critical slowing down of the ionic spin fluctuations in this region, the microscopic picture that seems to be emerging is that just above the critical temperature, K_2FeO_4 is effectively composed of paramagnetic regions, with $\sigma = 0$, and also of clusters of spins having a range of small values of reduced magnetization σ , for example, $\sigma = 0.002, 0.004, 0.006$ (26). The individual ions in these spin clusters are fluctuating slowly, $\Omega = 1.0$ on our scale, and the $\sigma = 0$ paramagnetic

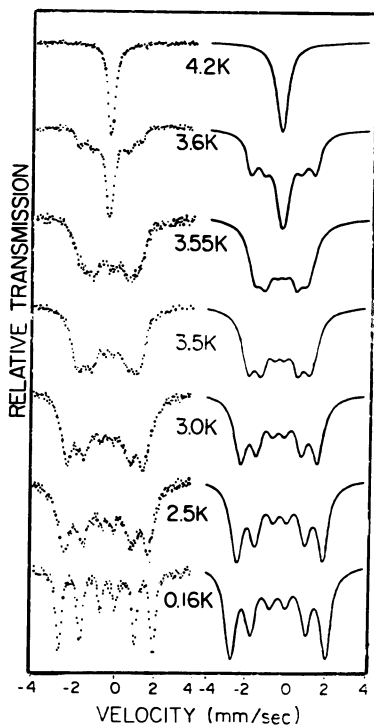


Figure 10. Our experimental transmission spectra of polycrystalline K_2FeO_4 from 4.2 K to 0.16 K are shown as dots. The solid curves show our calculated spectra based on the theory of Clauser and Blume. These curves include the effects of relaxation, but not the effects of spin clusters (24).

regions are presumed to be fluctuating rapidly. Note, however, for systems with $S = 1$ having nondegenerate ionic levels, the spectra are independent of Ω for $\sigma = 0$ (see Figure 9, Column 3). As the temperature is lowered into the critical region, the spectra attributable to these slowly relaxing cluster regions begin to appear as wings on the large paramagnetic central peak. As the temperature is lowered further, the relative amount of paramagnetic to slightly ordered components decreases until at 3.6 K the paramagnetic component completely disappears. At lower temperatures, instead of a paramagnetic component, one obtains an ordered component that has a significant value of reduced magnetization σ , for example, $\sigma = 0.4$, which is relaxing at a relaxation rate of $\Omega = 700$. This relaxation rate is the same as the observed value outside the critical region. In the critical region, the relationship of the reduced magnetization measured by Mössbauer spectroscopy to that obtained from bulk measurements is unclear.

As the temperature is lowered still further, the ordered component increases at the expense of the slowly relaxing clusters until finally, only the normally ordered component exists in the spectrum. It is hoped that with this interpretation it will be possible in the future to establish a clear relationship between measurements of this type and the extensive work done on critical phenomena (27). Furthermore, it may be possible by future analysis to obtain quantitative information about the spin correlation functions by interpreting the needed reduction in the relaxation rate parameter Ω in the critical region. This then begins to form a bridge between microscopic Mössbauer measurements and the critical phenomenon approach.

Acknowledgments

We would like to thank Rolfe Herber for the K_2FeO_4 samples and Peter Reynolds, Sidney Redner, and George Kirczenow for theoretical discussions. Steven Millman and Marcia Bartusiak helped greatly in the numerical work.

Literature Cited

1. Levinson, L. M.; Luban, M.; Shtrikman, S. *Phys. Rev.* **1969**, *177*, 864.
2. Abragam, A. "The Principles of Nuclear Magnetism"; Oxford University Press: London, 1961; pp. 424-477.
3. Afanas'ev, A. M.; Kagan, Yu. *Zh. Eksp. Teor. Fiz.* **1963**, *45*, 1660.
4. Afanas'ev, A. M.; Kogan, Yu. *Sov. Phys.-Jexp* **1964**, *18*, 1139.
5. Blume, M. *Phys. Rev. Lett.* **1965**, *14*, 96.
6. van der Woude, F.; Dekker, A. J. *Phys. Stat. Sol.* **1965**, *9*, 775.
7. Wickman, H. H.; Klein, M. P.; Shirley, D. A. *Phys. Rev.* **1966**, *152*, 345.
8. Gabriel, H. *Phys. Stat. Sol.* **1967**, *23*, 195.
9. Gabriel, H.; Basse, J.; Rander, K. *Phys. Stat. Sol.* **1968**, *27*, 301.

10. Blume, M. *Phys. Rev.* **1968**, *174*, 351.
11. Schwegler, H. *Phys. Stat. Sol.* **1970**, *41*, 353.
12. Clauser, M. J.; Blume, M. *Phys. Rev.* **1971**, *B3*, 583.
13. Clauser, M. J. *Phys. Rev.* **1971**, *B3*, 3748.
14. Schwegler, H. *Fortschr. Phys.* **1972**, *20*, 251.
15. Afanas'ev, A. M.; Gorobchenko, V. D. *Zh. Eksp. Teor. Fiz.* **1974**, *66*, 1406.
16. Afanas'ev, A. M.; Gorobchenko, V. D. *Sov. Phys.-Jetcp* **1974**, *39*, 690.
17. Shenoy, G. K.; Dunlap, B. D. *Phys. Rev.* **1976**, *B13*, 1353.
18. Hartmann-Boutron, F. *J. Phys. (Paris)* **1976**, *37*, 537.
19. Dattagupta, S. *Phys. Rev.* **1977**, *B16*, 158.
20. Dattagupta, S.; Shenoy, G. K.; Dunlap, B. D.; Asch, L. *Phys. Rev.* **1977**, *B16*, 3893.
21. Wickman, H. H.; Wagner, C. F. *J. Chem. Phys.* **1969**, *51*, 435.
22. Dattagupta, S. *Phys. Rev.* **1975**, *B12*, 3584.
23. Grow, J. M.; Robbins, G. L.; Wickman, H. H.; *J. Chem. Phys.* **1977**, *67*, 5282.
24. Hoy, G. R.; Corson, M. R. *J. Mag. Mag. Mat.* **1980**, *15-18*, 627.
25. Carrington, A.; Ingram, D. J. E.; Lott, K. A. K.; Schonland, D. S.; Symons, M. C. R. *Proc. Roy. Soc. (London)* **1960**, *A254*, 101.
26. Hoy, G. R.; Corson, M. R. *Bull. Am. Phys. Soc.* **1980**, *25*, 272.
27. Shenoy, G. K.; Dunlap, B. D.; Dattagupta, S.; Asch, L. *Phys. Rev. Lett.* **1976**, *37*, 539.

RECEIVED June 27, 1980.

Tantalum-181 Mössbauer Studies of the Alkali Tantalates

Ferroelectric Phase Transition in LiTaO_3

G. WORTMANN, M. LÖHNERT, and G. KAINDL

Institut für Atom- und Festkörperphysik, Freie Universität Berlin,
D-1000 Berlin 33, West Germany

The application of the high-resolution 6.2-keV Mössbauer resonance of ^{181}Ta to the study of alkali tantalates MTaO_3 ($M = \text{Li, Na, K}$) is reviewed. Emphasis is placed on a recent study of the ferroelectric phase transition in LiTaO_3 . In this case, a dramatic variation of the electric field gradient tensor with temperature is observed, which is closely related to the ferroelectric displacement. The Mössbauer results are compared with electric field gradient data of ^7Li and ^{93}Nb in LiNbO_3 and LiTaO_3 .

The 6.2-keV gamma transition of ^{181}Ta belongs to the few Mössbauer resonances with lifetimes τ in the microsecond region. The high resolving power of these resonances is based mainly on the relative size of the hyperfine interaction energy, as compared to the minimal linewidth $W_0 = 2 \cdot \hbar/\tau$, or, what is more relevant from an experimental point of view, to the actually observed linewidth W (1, 2). For ^{181}Ta , the lifetime of the 6.2-keV level ($\tau = 9.8 \mu\text{s}$) corresponds to $W_0 = 1.34 \cdot 10^{-10}$ eV, or $6.5 \mu\text{m/s}$ in velocity units. Although the best experimental linewidth observed so far, $W = 53(1) \mu\text{m/s}$ (3), is roughly one order of magnitude larger than W_0 , the ^{181}Ta resonance has made possible a variety of new applications in the field of solid-state physics (1, 2, 4, 5). When compared with other narrow-line Mössbauer resonances, namely those in ^{67}Zn (93 keV; $\tau = 13.5 \mu\text{s}$) (6, 7) and in ^{73}Ge (13.3 keV; $\tau = 6.2 \mu\text{s}$) (8, 9), two factors may be mentioned in favor of the ^{181}Ta resonance: (1) The relevant nuclear parameters are extremely large, giving rise to large hyperfine interaction energies. This is demonstrated by the presently

observed range of isomer shifts (110 mm/s) which is about 2000 times the value of W just given (2). The ^{181}Ta resonance is relatively easy to handle mainly because of the low gamma energy. It allows measurements at room temperature (or even up to the melting point of the refractory metals (10)), and in most cases only a standard Mössbauer spectrometer is needed. A proportional counter can be used for the detection of the gamma rays, and the source activity ^{181}W has a convenient half-life of 140 days.

There are, however, some tantalizing aspects of this resonance, a fact which is underlined by the small number of chemical applications. Apart from a large number of d -metal systems, the resonance has been observed so far only in the alkali tantalates MTaO_3 ($M = \text{K, Na, Li}$), in TaC , and in the tantalum chalcogenides (1, 2, 11, 12). The first two sections of this chapter deal with special experimental requirements for ^{181}Ta spectroscopy and some characteristics involved in the analysis of ^{181}Ta spectra. Then we report experimental results and chemical information obtained from ^{181}Ta spectroscopy of the tantalates. In the last section, emphasis is put on a recent study of the ferroelectric phase transition in LiTaO_3 and on a discussion of electric field gradients observed at ^7Li , ^{93}Nb , and ^{181}Ta in the niobates and tantalates.

Experimental

As mentioned already, the 6.2-keV resonance of ^{181}Ta can be studied with standard Mössbauer techniques. Since the ratio of line shift to linewidth can be large, special attention must be devoted to the stability and accuracy of the velocity drive. This requirement is met most easily by using an electro-mechanical drive system with a sinusoidally moved source. All spectra shown here were taken in this way. It should be mentioned, however, that for ^{181}Ta spectroscopy (due to large line shift-to-linewidth ratios) a region-of-interest spectrometer, which scans only the velocity region around the resonance, can be very useful. Such a spectrometer has been used in a recent temperature study on NaTaO_3 (11). It should be mentioned that commercially available region-of-interest spectrometers, in most cases, do not meet the requirements for ^{181}Ta spectroscopy.

When sweeping the whole velocity range, the data acquisition system should have an increased number of channels (1024 or more), since sometimes the information is contained only in a few channels (see, for example, the spectrum of LiTaO_3 in Figure 2). In addition, small solid angles ought to be used to prevent excessive geometrical broadening.

One of the main difficulties with ^{181}Ta spectroscopy is the preparation of strong sources with good single-line performance. For absorber experiments as reported here, the conditions are met by diffusing ^{181}W activity into high-purity single crystals of tungsten under ultra-high vacuum conditions (1, 2, 3). Considerable efforts have to be made to get ^{181}W of the highest possible specific activity. One way is to irradiate 90%-enriched ^{180}W (natural abundance 0.5%) in the highest available thermal neutron fluxes (10^{15} n/cm² s) for periods up to several months. Alternatively, carrier-free ^{181}W activity can be obtained by

bombarding tantalum with deuterons ($^{181}\text{Ta}(d, 2n) ^{181}\text{W}$) and by performing a radiochemical separation of ^{181}W from the tantalum target (3). When the radiochemical work can be done in one's own laboratory, the use of cyclotron-produced ^{181}W activity is preferable to neutron activation.

Standard single-line tantalum metal absorbers are prepared from high-purity tantalum foils (13). The ultra-high vacuum annealing and outgassing procedure at temperatures up to 2300°C has been described by Sauer (14). The main problem is that one has to handle very thin foils of 2–5 μm thickness. The preparation of absorbers of (polycrystalline) tantalum compounds with homogeneous thickness is also quite delicate. A method used is to sediment the finely milled powders in a polystyrene–benzene solution on thin Mylar foils (for room temperature experiments). The absorbers for the high-temperature studies reviewed here were prepared by sedimentation of 5 mg/cm^2 LiTaO_3 from a benzene suspension on 0.1-mm thick beryllium discs.

Tantalum-181 spectroscopy has to cope with a relatively low flux of the 6.2-keV gamma rays. This is primarily attributable to the high conversion coefficient ($\alpha = 45$), the low gamma-ray energy (which limits the source thickness), and the long lifetime of the ^{181}W activity. Furthermore, the detection of the 6.2-keV gamma rays is accompanied by serious background problems since they lie on the low-energy side of rather intense *L*-x-ray lines (15). Using an Ar–Kr/ CO_2 proportional counter (16), the peak-to-background ratio for the 6.2-keV line is about 1:2 with a 5 mg/cm^2 tantalum absorber. In some cases, especially at low count rates, an intrinsic germanium detector with good energy resolution can be superior to a proportional counter (15).

For low-temperature experiments, standard Mössbauer cryostats can be used. Special care, however, must be taken to avoid mechanical vibrations (i.e., originating from the boiling cryogenic liquids) which would destroy the resonance. A considerable loss (up to 60%) of the gamma flux occurs in the windows of the cryostat, even when rather thin Mylar (50 μm) or beryllium (0.2 mm) windows are used. The same holds for the high-temperature experiments with a Mössbauer oven (17), since the radiation has to pass through a considerable number of beryllium windows.

Hyperfine Structure of ^{181}Ta Gamma-Resonance Spectra

The nuclear parameters of the 6.2-keV resonance of ^{181}Ta are summarized in Table I. Due to the large magnitudes of the nuclear moments of both nuclear states and the high spin quantum numbers, $I_e = 9/2$ and $I_g = 7/2$, widely split and rather complex hyperfine spectra are obtained in the presence of relatively small magnetic hyperfine fields or electric field gradients (1, 2, 18, 19). Single-line spectra can be expected only for perfect cubic symmetry around the emitting and absorbing nuclei. Distortions of the source or absorber matrix by lattice imperfections—introduced, for example, by cold working (14), by residual amounts of interstitial impurity atoms (e.g., O_2 , N_2 , or H_2 in tantalum) (5, 14), or by substitutional tantalum atoms in the tungsten source matrix (3)—lead to excessive line broadening via small quadrupole interactions and/or fluctuations in the isomer shift.

**Table I. Nuclear Parameters of the 6.2-keV
Gamma Resonance of $^{181}\text{Ta}^a$**

$\frac{7^+}{2}$ Ground state	$\mu = 2.35 \pm 0.01$ n.m.
	$Q = 3.5 \pm 0.2$ b
$\frac{9^-}{2}$ Excited state	$\tau = 9.8 \pm 0.6$ s
	$\mu = 5.35 \pm 0.09$ n.m.
	$Q = 4.0 \pm 0.3$ b
E1 Transition	$W_0 = 0.0065$ mm/s
	$\Delta \langle r^2 \rangle = -5 \times 10^{-2}$ fm ²
Moment ratios	$g(9/2)/g(7/2) = 1.77 \pm 0.02$
	$Q(9/2)/Q(7/2) = 1.133 \pm 0.010$

^a See Refs. 1, 2, 18, 19, 40, 41.

Since this chapter deals with nonmagnetic tantalum compounds, we will concentrate on quadrupolar hyperfine splittings only. Due to the nuclear spin quantum numbers, polycrystalline ^{181}Ta spectra yield the magnitude *and* the sign of V_{zz} (the main component of the electric field gradient tensor), as well as the asymmetry parameter $\eta = (V_{xx} - V_{yy})/V_{zz}$, which has a nonvanishing value ($0 \leq \eta \leq 1$) in the case of non-axial point symmetry at the tantalum atoms. In Figure 1, computer-simulated ^{181}Ta spectra are shown for various values of η . The best experimental example for a quadrupole-split ^{181}Ta spectrum with $\eta = 0$ is still the $^{181}\text{TaRe}$ system (1, 2), whereas the first analysis of a quadrupole spectrum with $\eta \neq 0$ was recently performed in the case of NaTaO_3 (see Ref. 8 and Figure 2 of this work).

Due to the E1 multipolarity of the 6.2-keV transition, the absorption lines exhibit a characteristic asymmetry, which originates from an interference between photoelectric absorption and Mössbauer absorption followed by internal conversion. This interference effect leads to absorption spectra that can be described by dispersion-modified Lorentzian lines of the form

$$N(\nu) = N(\infty) - \sum A_i (1 - 2\xi X_i)/(1 + X_i^2)$$

with $X_i = 2(\nu - \nu_i)/W$.

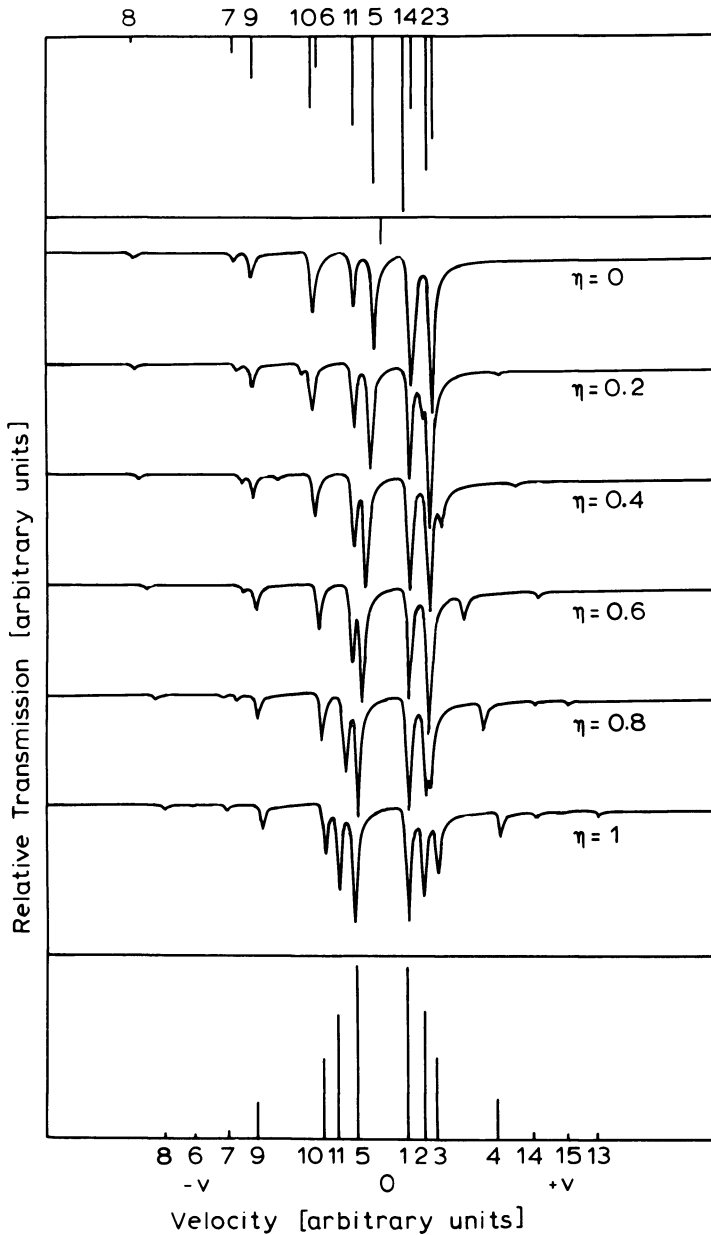


Figure 1. Computer-simulated ^{181}Ta quadrupole-split spectra as a function of the asymmetry parameter η .

The bar diagrams at the top (for $\eta = 0$) and at the bottom (for $\eta = 1$) represent the positions and relative intensities of the various transitions between the excited state ($I_e = 9/2$) and the ground state ($I_g = 7/2$). The respective sub-quantum numbers for $\eta = 0$ may be found in Refs. 1 and 2.

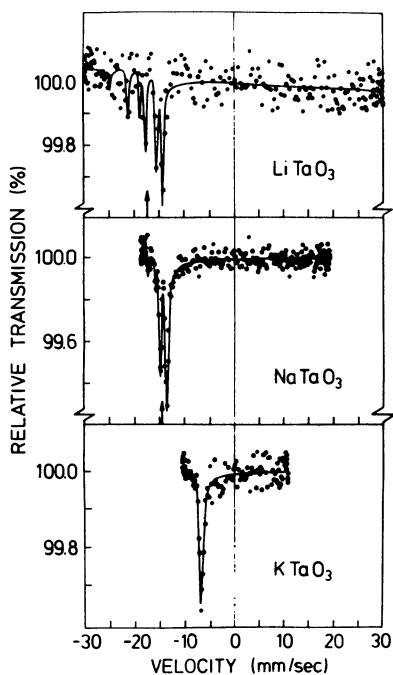


Figure 2. The ^{181}Ta Mössbauer absorption spectra of the alkali tantalates at room temperature (11, 27).

The centers of the quadrupole-split spectra are indicated by arrows. The LiTaO_3 spectrum is fitted with a correction for slanting background.

Here $N(v)$ is the transmitted intensity at a relative velocity v , v_i is the position of the i th line, W is the full linewidth at half maximum, and A_i is the amplitude of the i th line. The parameter ξ determines the relative magnitude of the dispersion term. Its magnitude varies, depending on the absorber thickness, around $2\xi = -0.30$ (18, 19, 20). The energies and relative intensities of the 19 possible lines of a ^{181}Ta quadrupole-split spectrum have been calculated as a function of η and were included in the fitting routine by using a tabulated expansion series (21). In this way, the quadrupole-split spectra shown in this work were normally fitted with six parameters: background rate $N(\infty)$, half-width W , an amplitude factor, the isomer shift S , V_{zz} , and η . In some cases with unresolved hyperfine splittings, W is fixed to a value observed in resolved spectra.

Tantalum-181 Mössbauer Spectroscopy of the Alkali Tantalates *LiTaO_3 , NaTaO_3 , KTaO_3*

The crystal structure and ferroelectric properties of the tantalates MTaO_3 ($M = \text{Li}, \text{Na}, \text{K}$) are rather different (22, 23). KTaO_3 has the cubic perovskite structure (like BaTiO_3), but does not order ferroelectrically. However, it has a large electric polarizability indicating that it is close to the ferroelectric state (by means of uniaxial pressure, for instance, ferroelectric ordering can be introduced in KTaO_3). NaTaO_3

has an orthorhombic unit cell at room temperature, which can be considered as a slightly distorted perovskite structure. With increasing temperature, it undergoes a series of structural phase transitions, ending with the cubic perovskite structure at 630°C. Although it has been reported as antiferroelectric in the older literature, it is nowadays classified as quasiferroelectric, since it does not possess a permanent electric dipole moment. LiTaO_3 has trigonal symmetry and, for convenience, is described by a hexagonal unit cell (see Figure 3). LiTaO_3 is ferroelectric with an exceptionally high Curie temperature ($T = 910$ K). Besides the isostructural LiNbO_3 it is a prototype for a displacive ferroelectric. Its structure and the atomic positions within the unit cell have been investigated thoroughly below and above T_C by x-ray and neutron scattering techniques (24, 25).

Tantalum-181 Mössbauer spectra have been observed for the tantalates in the early days of this resonance (1, 2, 26). For KTaO_3 , a single, but rather broad resonance line (1, 2) was observed (to detect a resonance effect at all is quite a success in ^{181}Ta spectroscopy). In the cases of NaTaO_3 and LiTaO_3 , partially split resonance patterns centered around isomer shifts of -15 mm/s were observed (26). Recently, NaTaO_3 and LiTaO_3 were reinvestigated more thoroughly (11). In this study the resolution could be improved considerably because of better experimental linewidths, and consequently, much larger resonance effects were observed. In the case of orthorhombic NaTaO_3 , in particular, it

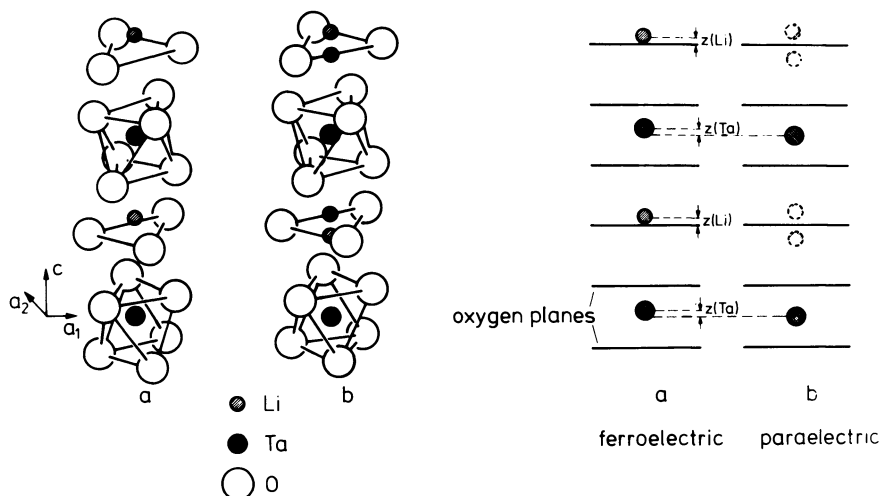


Figure 3. Stereographic and schematic presentation of the hexagonal LiTaO_3 structure in the (a) ferroelectric and (b) paraelectric phase.

The ferroelectric displacements $z(\text{Ta})$ and $z(\text{Li})$ of the metal atoms with respect to the oxygen planes closely follow the electric polarization of LiTaO_3 (for details see Refs. 24 and 25). In the paraelectric phase the lithium atoms are thought to be randomly distributed on both sides of their oxygen plane.

was possible for the first time to achieve sufficient resolution for extracting a value of the asymmetry parameter η from the quadrupole-split spectrum (11). In addition, the temperature dependence of isomer shift and quadrupole interaction were studied in NaTaO_3 between 77 K and 700 K (11, 27). Figure 2 shows ^{181}Ta spectra of KTaO_3 , NaTaO_3 , and LiTaO_3 taken at room temperature.

The ^{181}Ta Mössbauer studies of LiTaO_3 (30) were performed in view of the ferroelectric and nonlinear optical properties of this compound. LiTaO_3 is isostructural with the well-known LiNbO_3 ($T_C = 1470$ K). Both compounds have experienced wide applications in laser spectroscopy and as optical storage media. With ^{181}Ta as the probe atom, LiTaO_3 offers Mössbauer studies of a ferroelectric phase transition in a pure system. Most of the previous Mössbauer studies of ferroelectric phase transitions suffered because they were performed on substitutional Mössbauer impurity atoms (28), since most ferroelectrics do not contain suitable Mössbauer elements. In addition, their relatively poor resolving power for quadrupole interactions prevented studies with similar resolution as performed, for instance, on magnetic phase transitions.

In the beginning of the ^{181}Ta Mössbauer work with LiTaO_3 reviewed here (30), a puzzling effect was observed. In spite of the fact that the space group of trigonal LiTaO_3 was determined as C_{3v}^6 (24, 25), implying a three-fold point symmetry at the tantalum atoms, the electric field gradient at the ^{181}Ta nucleus, as obtained from the fit of the resonance spectra, was found not to be axially symmetric. At room temperature, all ^{181}Ta spectra taken from various absorbers yield a coupling constant $e^2qQ(7/2) = (9.80 \pm 0.04) \cdot 10^{-7}$ eV and an asymmetry parameter $\eta = 0.09 \pm 0.03$. (These spectra can be fitted quite well with an axially symmetric electric field gradient, as done in Ref. 11; inclusion of the asymmetry parameter η , however, improves the fit of the less intense lines). These results are in excellent agreement with a recent ^{181}Ta nuclear quadrupole resonance study of LiTaO_3 at room temperature and below. The observation of $\eta \neq 0$ implies that the trifold symmetry of the oxygen octahedron (with respect to the tantalum atom) is somewhat lowered by a small distortion, which may occur in addition to the well-known ferroelectric displacement along the c -axis. Such a distortion must be rather small, since it has not been detected in rather extensive x-ray and neutron diffraction studies. It should be noted also that an asymmetry parameter of $\eta = 0.02$ has been reported in LiNbO_3 on the niobium site from a ^{93}Nb study (46). We want to emphasize that this is an important piece of information for a full understanding of a variety of experimental data, especially those obtained by Raman spectroscopy (31).

A discussion of the ^{181}Ta isomer shifts in the (nominally pentavalent) tantalates is hampered by the fact that there are at present no isomer

Table II. Compilation of ^{181}Ta Mössbauer Data on Several Tantalum Compounds, Obtained at Room Temperature

Compound	W^a (mm/s)	S^b (mm/s)	$e^2qQ(7/2)^c$ (10^{-7} eV)	η^d	Ref.
LiTaO_3	0.40 (2)	-17.95 (3)	+9.50 (4)	0.09 (3)	30
NaTaO_3	0.42 (2)	-15.50 (3)	+3.67 (4)	0.47 (2)	11
KTaO_3	0.97 (8)	-7.81 (7)	—	—	1, 2, 11
2 H-TaSe ₂	0.70 (7)	+80.40 (5)	-49.76 (25)	0	12
TaC	2.4 (4)	+70.8 (5)	—	—	1, 2

^a W = experimental linewidth (FWHM).

^b S = isomer shift relative to tantalum metal.

^c $e^2qQ(7/2)$ = quadrupole interaction energy.

^d η = asymmetry parameter.

shift data available for other (nonmetallic) tantalum compounds with different valence states. The (nominally tetravalent) tantalum dichalcogenides (12) and TaC (1, 2) have metallic properties with band electrons of predominantly d character (32, 33). As shown in Table II, there is a large difference in the isomer shift S between Ta^{4+} and Ta^{5+} compounds: $\Delta S \cong 90$ mm/s indicates that $\rho(0)$, the s electron density at the ^{181}Ta nucleus, is considerably smaller in TaSe_2 and in TaC than in the tantalates. This can be explained by a higher shielding effect in the Ta^{4+} compounds through the larger number of localized tantalum d electrons (1, 2). The shielding potential of tantalum electrons in the rather localized d band of TaC and TaSe_2 is considered to be similar to that of tantalum d electrons in covalent bonds, which are, as shown in the following, characteristic for the tantalates. The difference in S between tantalum metal (where the tantalum atom is nominally pentavalent) and metallic TaC or TaSe_2 can be accounted for by the larger number of s -like conduction electrons in tantalum metal (34). The relatively small difference in S between the tantalates and tantalum metal, however, points to a highly covalent character of the Ta—O bonds, a fact well known from other properties of the tantalates and niobates and closely related to the occurrence of ferroelectricity (35). For example, theoretical calculations (36) of the ferroelectric properties of LiTaO_3 yield an effective charge of +0.8 on the tantalum atom (instead of +5, as expected for a purely ionic Ta^{5+} compound). Similarly, as will be shown in another section, the electric field gradient at the tantalum site in LiTaO_3 can be explained only by an effective charge considerably smaller than +5.

Within the tantalates, $\rho(0)$ decreases from LiTaO_3 to NaTaO_3 and further to KTaO_3 . This behavior can be accounted for by an increase of the Ta—O bond length and by a decrease in covalency when going from LiTaO_3 to KTaO_3 .

Study of the Ferroelectric Phase Transition in LiTaO₃

As mentioned previously, LiTaO₃ offers the opportunity to study a "pure" ferroelectric in its ferroelectric and paraelectric phase by Mössbauer spectroscopy. Most of the experiments at temperatures up to 1040 K ($T_C = 910$ K) were performed in an absorber oven (17), which could be evacuated to pressures below 10^{-5} mbar. The temperature was controlled to within ± 2 K. After a series of high-temperature measurements, control spectra taken at 300 K showed that the LiTaO₃ absorber did not deteriorate during heating. Depending on the strength of the ¹⁸¹W(W) source, the time for taking one spectrum ranged from 5 to 20 days.

Figure 4 shows ¹⁸¹Ta spectra of LiTaO₃ at various temperatures, which reveal a dramatic temperature dependence of the electric quadrupole interaction. With increasing temperature this interaction decreases rapidly, and virtually vanishes around 800 K. It then starts to increase again with opposite sign. The results of least-squares fits of the isomer shift S , the electric field gradient V_{zz} , and the asymmetry parameter η are given in Figure 5. V_{zz} was calculated from the quadrupole coupling constant eQV_{zz} by taking $Q(7/2) = 3.5$ barn (37) and $Q(9/2)/Q(7/2) = 1.133$ (1, 2). The potential of the ¹⁸¹Ta resonance for high-resolution hyperfine interaction studies is obvious from Figures 4 and 5. Only the asymmetry parameter η shows rather large error bars between 600 K and 900 K, where the quadrupole-split spectra are resolved only partially. Above the ferroelectric phase transition, η is found to be zero within statistical accuracy. It should be noted that around the zero-crossing of the quadrupole interaction at 800 K, the V_{zz} component of the electric field gradient tensor actually changes its definition. Because of the nonaxial interaction, one of the principal axes of the electric field gradient tensor can vanish, yielding $\eta = 1$. At temperatures well above and well below 800 K, however, the V_{zz} component of the electric field gradient tensor virtually coincides with the c -axis of the hexagonal unit cell (because of the rather small value of η). This has been verified by other experiments in LiTaO₃ and LiNbO₃ (38, 39, 46). The vanishing of V_{zz} and the maximum of η in Figure 5 are not correlated with the ferroelectric phase transition, which actually occurs at a considerably higher temperature. They can be explained, as will be shown later, by the mutual cancellation of two contributions of opposite sign to the electric field gradient.

The only obvious correlation of the data of Figure 5 with the ferroelectric phase transition at T_C is, besides the virtual vanishing of η , the change in the slope of $V_{zz}(T)$ around T_C . The isomer shift S shows

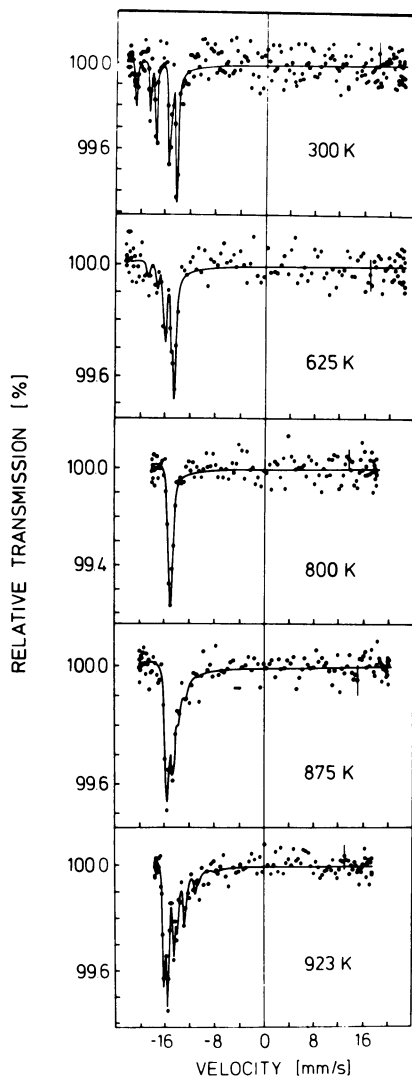


Figure 4. The ^{181}Ta absorption spectra of LiTaO_3 at various temperatures (30).

Note that only the lowest spectrum is taken in the paraelectric phase. The zero-crossing and sign reversal of the electric quadrupole interaction at 800 K occur well below the ferroelectric transition temperature of 910 K.

no change in its slope when going through T_C , indicating that the phase transition is second order.

Before discussing the more dramatic results of the electric quadrupole interaction, a few comments on the temperature dependence of the isomer shift S_{IS} will be made. As originally reported for ^{181}Ta in d -transition metals (4), the temperature-induced variation of the position S of the ^{181}Ta resonance line is governed by changes in the electron density at the nucleus and not by the second-order Doppler effect S_{SOD}

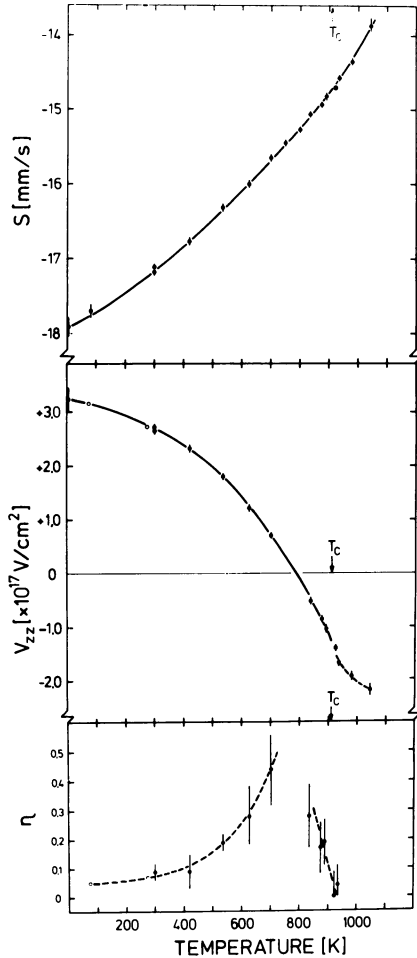


Figure 5. Temperature variation of the ^{181}Ta isomer shift S , the electric field gradient V_{zz} , and the asymmetry parameter η at ^{181}Ta in LiTaO_3 . The ferroelectric transition temperature T_c is marked by arrows. ((●) from the Mössbauer study; (○) from a NQR study (29)).

(as with all other gamma resonances: $S = S_{\text{IS}} + S_{\text{SOD}}$). The second-order Doppler shift S_{SOD} contributes very little to the observed variation of S . For a more detailed discussion we refer to Refs. 4, 40, 41. In the high-temperature limit, S_{SOD} is given for a Debye solid by $-3k/Mc$ in velocity units, which amounts to $-2.3 \cdot 10^{-4}$ mm/s per degree for the ^{181}Ta resonance. This contribution is of opposite sign and one order of magnitude smaller than the observed shift in LiTaO_3 , $(\delta S/\delta T)_P = 35 \cdot 10^{-4}$ mm/s per degree (this value is obtained by assuming, for simplicity, a linear variation of S between 300 K and 700 K). In KTaO_3 and NaTaO_3 , similar values of $(\delta S/\delta T)_P$ were observed (11), indicating that the temperature variation of S (and, accordingly, of $\rho(o)$) is very similar in the tantalates and not directly connected with the ferroelectric transition of LiTaO_3 . A discussion of $(\delta S/\delta T)_P$ in terms of an implicit variation of

S_{IS} (resulting from the thermal expansion of the lattice) and an explicit variation of S_{IS} (resulting from temperature-induced changes of the electronic structure at constant volume) must await high-pressure studies of the tantalates, which would yield the volume dependence of S_{IS} . It should be mentioned that the ^{181}Ta isomer shift exhibits a strong explicit temperature dependence in metallic systems (4, 40, 41). A similar behavior is also expected in tantalum compounds.

To clarify the origin of the striking temperature-induced variation of the electric quadrupole interaction in LiTaO_3 , electric field gradient calculations were performed (43) by using the point-charge model of de Wette (42). Similar calculations previously were applied (44–47) to explain ^7Li and ^{93}Nb NMR data of LiNbO_3 and LiTaO_3 . Details of these calculations are given elsewhere (43). It is well known that the point-charge model is by no means a suitable tool to calculate absolute values of electric field gradient in covalent compounds. In many cases, however, this model can be used successfully to calculate the sign and relative change of the electric field gradient in a system where only few parameters vary. LiTaO_3 with its ferroelectric phase transition and its well-known interatomic displacements (24, 25) offers an exceptional case for electric field gradient calculations, since the experimental ^{181}Ta data (with the known sign and the zero-crossing of the electric field gradient) provide an unambiguous proof of the model calculations.

The results of the electric field gradient calculations for ^{181}Ta in LiTaO_3 in the temperature range between 295 K and 940 K are shown in Figure 6. The effective charges used were taken from Ref. 45, and a Sternheimer antishielding factor of $(1 - \gamma^\infty) = 60$ was used (48). It is obvious from Figure 6 that the calculated electric field gradient has the right sign and follows the experimental data rather closely in its relative variations; in particular, the zero-crossing at 800 K is reproduced by the calculations. To elucidate the effect of $z(\text{Ta})$, which is the ferroelectric displacement of the oxygen atoms with respect to the tantalum atom (see Figure 3b), further calculations were performed. Figure 6 contains two more thin-dashed curves that were calculated with the following two assumptions: (1) $z(\text{Ta}) = 0$ over the entire temperature range and normal lattice expansion with temperature, and (2) the unit cell does not exhibit thermal expansion, but $z(\text{Ta})$ varies in a normal way with temperature.

The synopsis of these calculations together with the experimental data lead to the following conclusions (30, 43). There are two main contributions to the electric field gradient at ^{181}Ta in LiTaO_3 : (1) the hexagonal lattice produces a negative electric field gradient, the magnitude of which decreases slowly with increasing temperature due to the lattice expansion. (2) The ferroelectric displacement $z(\text{Ta})$ produces a positive electric field gradient, which is about twice as large and of

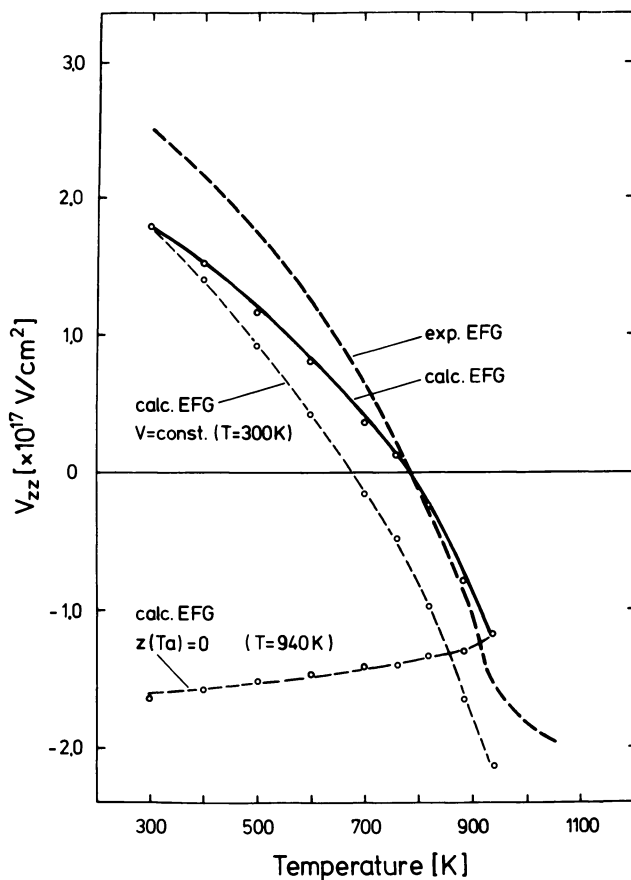


Figure 6. Comparison of calculated and experimentally observed electric field gradients at ^{181}Ta in LiTaO_3 .

The effective charges used in this calculation were taken from Ref. 45; (○) represents calculated results. The additional two (---) lines show electric field gradients calculated with the assumption that (1) the ferroelectric displacement $z(\text{Ta})$ and $z(\text{Li})$ is zero over the entire temperature range and that (2) no volume expansion takes place (for details see text and Figure 3).

opposite sign as contribution (1). The magnitude of this positive contribution follows the ferroelectric displacement (and, with that, the ferroelectric polarization). At 800 K, because of the characteristic temperature dependence of $z(\text{Ta})$, contributions (1) and (2) cancel. Above T_C , contribution (2) should vanish. The slope of the experimental electric field gradient T_C , however,, indicates that there are also other contributions to the electric field gradient. A ferroelectric phase transition is thought to be triggered by anisotropic lattice vibrations (49). Such "soft modes" along the hexagonal c -axis could produce a "dynamical" contribution to the electric field gradient (50), which would have the same origin and sign as contribution (2). A more detailed discussion of a dynamical contribution to the electric field gradient in LiTaO_3 has to wait for more experimental data above T_C .

With respect to the ^7Li and ^{93}Nb NMR studies performed on LiNbO_3 , LiTaO_3 , and $\text{LiNb}_{1-x}\text{Ta}_x\text{O}_3$ (44–47, 50), the ^{181}Ta data are of special importance. They allow a comparison of measured and calculated electric field gradients in two isostructural and chemically very similar systems on two different lattice sites. It can be concluded, for instance, that the electric field gradients at niobium and lithium are positive at room temperature. Furthermore, the temperature dependence of the electric field gradient at ^{93}Nb in LiNbO_3 observed between 20 K and 820 K (38, 46) has to be discussed relative to the ^{181}Ta data in LiTaO_3 . We have performed point-charge calculations for the electric field gradients at ^7Li and ^{93}Nb with the same formalism used for the ^{181}Ta data. Details are given in Ref. 43. Again, absolute values of the electric field gradients are not to be expected, especially in view of the uncertainty involved in the Sternheimer factors and in the electric quadrupole moments (51).

Figure 7 summarizes the results of point-charge calculations of the electric field gradients for ^7Li , ^{93}Nb , and ^{181}Ta in LiNbO_3 and LiTaO_3 (43). The calculated electric field gradients are plotted as a function of the effective charge at the niobium/tantalum atoms. The dotted lines show the effective charges that correspond to the observed electric field gradients. Their values lie between +1.5 and +2.5. The overall consistency of the experimental and calculated electric field gradients is surprisingly good, especially with respect to the limitations of the point-charge model and the uncertainties involved in the $(1 - \gamma^\infty)$ and Q values. The ^{93}Nb and ^{181}Ta data clearly reflect the high covalency of the Nb—O and Ta—O bonds, respectively, with the latter being slightly more covalent, in agreement with other arguments (36, 45). The success of the simple point-charge model in the present calculations lies, in our opinion, in the fact that the niobium/tantalum atoms have a nearest-neighbor oxygen shell with a high (sixfold) coordination and similar bonds. In conclusion, we hope that the experimental electric field

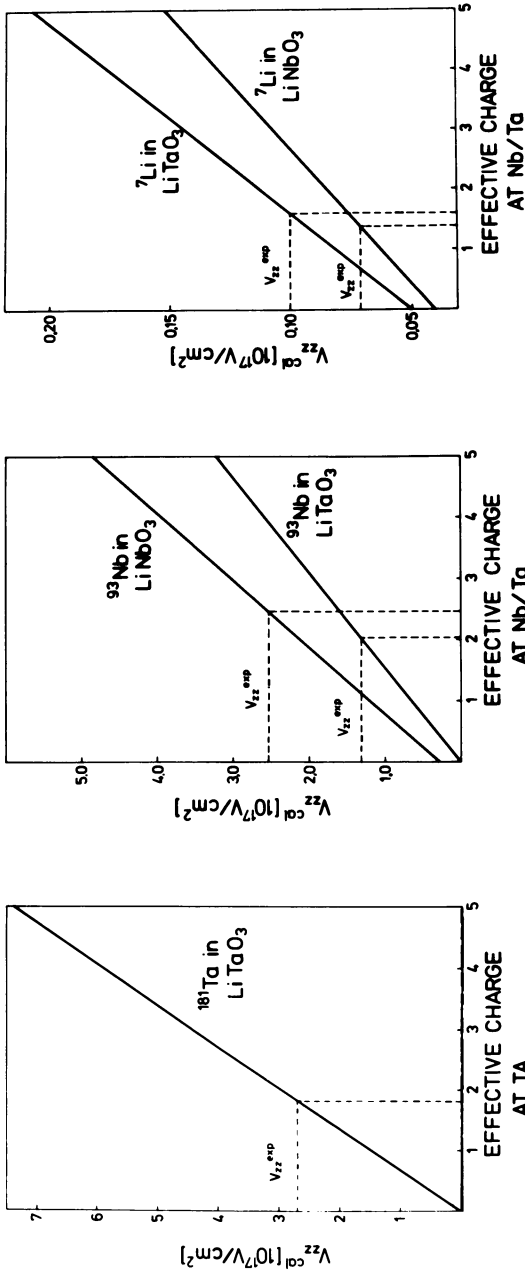


Figure 7. Comparison of calculated electric field gradients at ^{181}Ta , ^{93}Nb , and ^7Li in LiTaO_3 and LiNbO_3 .

The calculated electric field gradient values (at room temperature) are plotted vs. the effective charges at the niobium/tantalum atoms. (---) indicates those effective charges where V_{zz}^{cal} is equal to V_{zz}^{exp} (the ^7Li and ^{93}Nb data are taken from Refs. 44-47).

gradient data now available in LiNbO_3 and LiTaO_3 will stimulate more sophisticated electric field gradient calculations (52, 53) that may yield physically and chemically more detailed information about the electronic structure of these compounds. Our point-charge model calculations, however, have already shown the major contributions to the electric field gradients in LiNbO_3 and LiTaO_3 .

Acknowledgments

This work was supported by the Sonderforschungsbereich 161 of the Deutsche Forschungsgemeinschaft. The constant technical assistance of D. Sobanski is gratefully acknowledged.

Literature Cited

1. Kaindl, G.; Salomon, D.; Wortmann, G. *Phys. Rev.* 1973, *B8*, 1912.
2. Kaindl, G.; Salomon, D.; Wortmann, G. *Phys. Rev. Lett.* 1972, *28*, 952.
3. Dornow, V. A.; Binder, J.; Heidemann, A.; Kalvius, G. M.; Wortmann, G. *Nucl. Instrum. Methods* 1979, *163*, 491.
4. Kaindl, G.; Salomon, D. *Phys. Rev. Lett.* 1973, *30*, 579.
5. Heidemann, A.; Kaindl, G.; Salomon, D.; Wipf, H.; Wortmann, G. *Phys. Rev. Lett.* 1976, *36*, 213.
6. de Waard, H.; Perlow, G. J. *Phys. Rev. Lett.* 1970, *24*, 566.
7. Forster, A.; Potzel, W.; Kalvius, G. M. *Z. Phys.* 1980, *B37*, 209.
8. Raghaven, R. S.; Pfeiffer, L. *Phys. Rev. Lett.* 1974, *32*, 512.
9. Pfeiffer, L.; Kovacs, T. *Bull. Am. Phys. Soc.* 1980, *25*, 549.
10. West, P. J.; Salomon, D. *J. Physique* 1979, *40*, C2-616.
11. Wortmann, G.; Trollmann, G.; Heidemann, A.; Kalvius, G. M. *Hyperfine Interact.* 1978, *4*, 610.
12. Pfeiffer, L.; Eibschütz, M.; Salomon, D. *Hyperfine Interact.* 1978, *4*, 803.
13. Materials Research Corp., Orangeburg, NY 10692; Goodfellow Metals Ltd., Cambridge CB4 4DJ, U.K.
14. Sauer, Ch. *Z. Phys.* 1969, *222*, 439.
15. Pfeiffer, L. *Nucl. Instr. Methods* 1977, *140*, 57.
16. Reuter-Stokes, Cleveland, OH 44128.
17. RICOR, En-Harod, Israel.
18. Sauer, Ch.; Matthias, E.; Mössbauer, R. L. *Phys. Rev. Lett.* 1968, *21*, 961.
19. Kaindl, G.; Salomon, D. *Phys. Lett.* 1970, *B32*, 364.
20. Salomon, D.; West, P. J.; Weyer, G. *Hyperfine Interact.* 1977, *5*, 61.
21. Shenoy, G. K.; Dunlap, B. D. *Nucl. Instr. Methods* 1969, *71*, 285.
22. Landolt-Börnstein New Series III/3: "Ferro- and Antiferroelectric Substances"; Springer Verlag: Berlin, 1969; Vol. 3, No. 3.
23. Landolt-Börnstein "Oxides"; Springer Verlag: Berlin, 1969; Vol. 3, No. 9.
24. Abrahams, S. C.; Bernstein, J. L. *J. Phys. Chem. Solids* 1967, *28*, 1685.
25. Abrahams, S. C.; Buchler, E.; Hamilton, W. C.; Laplace, S. J. *J. Phys. Chem. Solids* 1973, *34*, 521.
26. Kaindl, G.; Salomon, D. *Bull. Am. Phys. Soc.* 1972, *17*, 681.
27. Trollmann, G., unpublished data.
28. Wildner, W.; Gonser, U.; Schmidt, H.; Albers, J.; Date, S. K. *Ferroelectrics* 1980, *23*, 193.
29. Zhukov, A. P.; Soboleva, L. V.; Belyaev, L. M.; Volkov, A. F. *Ferroelectrics* 1978, *21*, 601.
30. Löhnert, M.; Wortmann, G.; Kaindl, G.; Salomon, D., unpublished data.

31. Penna, A. F.; Chaves, A.; Andrade, P. da R.; Porto, S. P. S. *Phys. Rev.* **1976**, *B13*, 4907.
32. Wilson, J. A.; DiSalvo, F. J.; Mahajan, S. *Adv. Phys.* **1975**, *24*, 117.
33. Schwarz, K. *J. Phys.* **1977**, *C10*, 195.
34. Boyer, L. L.; Papaconstantopoulos, D. A.; Klein, B. M. *Phys. Rev.* **1977**, *B15*, 3685.
35. Michel-Calendini, F. M.; Chermette, H.; Weber, J. *J. Phys.* **1980**, *C13*, 1427.
36. Lines, M. E. *Phys. Rev.* **1970**, *B2*, 698.
37. deWit, S. A.; Backenstoss, G.; Daum, C.; Sens, J. C.; Acker, H. L. *Nucl. Phys.* **1967**, *87*, 657.
38. Fujara, F.; Stöckmann, H.-J.; Ackermann, H.; Buttler, W.; Dörr, K.; Grupp, H.; Heitjans, P.; Kiese, G.; Körblein, A. *Z. Phys.* **1979**, *B37*, 151.
39. Keune, W.; Date, S. K.; Dézsi, I.; Conser, U. *J. Appl. Phys.* **1975**, *46*, 3914.
40. Kaindl, G.; Salomon, D.; Wortmann, G. *Mössbauer Eff. Methodol.* **1973**, *8*, 211.
41. Kaindl, G.; Salomon, D.; Wortmann, G. In "Mössbauer Isomer Shifts"; Shenoy, G. K.; Wagner, F. E., Eds.; North Holland: N.Y., 1978; p. 563.
42. de Wette, F. W. *Phys. Rev.* **1961**, *123*, 103.
43. Löhnert, M.; Wortmann, G.; Kaindl, G., unpublished data.
44. Peterson, G. E.; Bridenbaugh, P. M.; Green, P. *J. Chem. Phys.* **1967**, *46*, 4009.
45. Peterson, G. E.; Bridenbaugh, P. M. *Phys. Rev.* **1968**, *48*, 3402.
46. Schempp, E.; Peterson, G. E.; Carruthers, J. R. *J. Chem. Phys.* **1970**, *53*, 306.
47. Peterson, G. E.; Carruthers, J. R.; Carnevale, A. *J. Chem. Phys.* **1970**, *53*, 2436.
48. Feiock, F. D.; Johnson, W. R. *Phys. Rev.* **1969**, *187*, 39.
49. Cochran, W. *Adv. Phys.* **1960**, *9*, 387.
50. Halstead, T. K. *J. Chem. Phys.* **1970**, *53*, 3427.
51. Büttgenbach, S.; Dicke, R. *Z. Phys.* **1975**, *A275*, 197.
52. Reschke, R.; Trautwein, A.; Harris, F. E.; Date, S. K. *J. Magn. Magnet. Mat.* **1979**, *12*, 176.
53. Trautwein, E. See Chapter 1 in this book.

RECEIVED August 14, 1980.

Hydrogen Storage Materials

G. K. SHENOY, B. D. DUNLAP, P. J. VICCARO, and D. NIARCHOS

Argonne National Laboratory, Argonne, IL 60439

Many intermetallic compounds of d- and f-shell elements reversibly absorb large amounts of hydrogen to form ternary hydrides at easily accessible temperatures (0°–100°C) and pressures (.01–1000 Torr). Such ternary hydrides have been considered for use in a number of energy conversion applications. In this work we review the application of Mössbauer spectroscopy to understand various physical and chemical properties of ternary hydrides. This microscopic technique helps elucidate properties such as the chemical nature of hydrogen and its location, the formation and stability of various structural phases, and the influence of hydrogen absorption on the electronic and magnetic properties of the host lattice. We also present results on the role of the surface in the mechanism of hydrogen absorption by the intermetallic alloy using Mössbauer conversion electron spectroscopy.

The study of hydrogen in metals has been a subject of scientific interest for many years and has been approached by essentially all the tools, both experimental and theoretical, available to materials research. Until recently, most of this work has dealt with binary metallic hydrides, that is, phases consisting of hydrogen in simple metals (1, 2). Recently there has been a great deal of interest in ternary hydrides—phases consisting of hydrogen in intermetallic compounds. The ternary hydrides not only have many interesting physical properties, but also have potential for energy applications. In many cases, the intermetallic compounds reversibly absorb hydrogen with a hydrogen density that is comparable to that in binary hydrides, and often in excess of that in liquid hydrogen. However, in contrast to many binary hydrides, the hydrogen equilibrium pressure for the hydride phases is often in the neighborhood of 1 atm or more, even at room temperature. Consequently, easily attained variations

0065-2393/81/0194-0501\$05.25/0

© 1981 American Chemical Society

in the hydrogen pressure can be used to form the phase (i.e., store the hydrogen) and then remove it from the material as well. The absorption and desorption processes proceed reversibly and rapidly. As a result, these materials often have been called "hydrogen storage materials."

To introduce the reader to the kind of materials involved, Table I presents a short list of hydrogen storage materials. As one can see, a wide variety of intermetallic structure types are known to absorb hydrogen and form stable phases. Typically one obtains phases having approximately one hydrogen atom per metal atom in the intermetallic compound.

A number of potential applications of such materials have been proposed and demonstrated (3, 4). For example, because of the high hydrogen content and ease of absorption and desorption, a simple hydrogen compressor can be built. The storage materials can be used in a hydrogen fuel tank of an automobile. The fact that the hydrogen absorption process is exothermic can be utilized in heat pumps (5). In one instance, an entire home with appliances and cars has been converted to be operated with hydrogen as the sole fuel (6).

At present, the use of intermetallic hydrides for practical devices is still in its infancy, although developmental work is under way. A clear limitation is that the basic properties of such hydrides are not sufficiently well understood to allow one to engineer materials that will be the most efficient for specific applications. Although a large number of hydrides now have been investigated, currently there are only crude thumb rules for systematically understanding the results. Thus, for example, the fact that a more stable hydride can be obtained from a less stable intermetallic compound is expressed in the so called "rule of reversed stability" (7). Although the rule has a certain validity, many exceptions have frequently been noted (8). Another such observation regards the relationship

Table I. Typical Ternary Hydrides

	<i>Structure Type</i>	<i>Intermetallic Compound</i>	<i>Hydride</i>	<i>x</i>
<i>AB</i>	CsCl	FeTi	FeTiH _x	1.0, 1.9
<i>A₂B</i>	Ti ₂ Ni	Hf ₂ Fe	Hf ₂ FeH _x	3.5
<i>AB₂</i>	Cubic	ErFe ₂	ErFe ₂ H _x	2.0, 3.6, 4.1
	Laves (C15)	DyFe ₂	DyFe ₂ H _x	2.0, 3.6, 4.1, 4.5
<i>AB₂</i>	Hexagonal	ErMn ₂	ErMn ₂ H _x	4.0, 4.6
	Laves (C14)	ScFe ₂	ScFe ₂ H _x	2.0, 3.1
<i>AB₃</i>	PuNi ₃	REFe ₃	REFe ₃ H _x	1.7, 2.5, 4.3
		RECo ₃	RECo ₃ H _x	
(<i>RE</i> = Nd, Gd, Dy, Er)				
<i>AB₅</i>	CaCu ₅	LaNi ₅	LaNi ₅ H _x	6.0

between cell volume (or available interstitial volume) and the heat of formation, or equilibrium pressure of a given hydride phase (5, 9), for compounds with the same structure. Indeed, many such rules have been suggested (10).

Much of the current research on intermetallic hydrides consists of measuring the physical and chemical properties of many systems and attempting to find ways in which their properties can be discussed systematically. From the point of view of applications, the relevant properties to be measured are the hydride phase diagrams, the equilibrium pressures of various phases, the total storage capacity, and the stability of the intermetallic to the kinetics of hydride formation and decomposition. Such data are obtained from thermodynamic measurements on bulk samples. From a standpoint of deriving basic understanding, one also demands information such as the location of hydrogen in the various phases, the hydrogen mobility, and the effect of hydrogen on the mechanical, thermal, electronic, and magnetic properties. In this regard, microscopic measurements are very useful and Mössbauer spectroscopy can supplement the information derived from other tools.

In this review we will first briefly discuss the way in which hydrogen-intermetallic compound phase diagrams are measured. Then we will survey the published literature for hydride phases formed in various structure types and the application of Mössbauer spectroscopy to some of those systems. Finally, we will single out two important investigations where the Mössbauer effect measurements have contributed directly: degradation of hydrogen absorbing capacity by repeated absorption-desorption cycling, and the mechanism for the absorption of hydrogen by the intermetallics.

Phase Diagram Measurements

The most important measurements in bulk properties are those determining the phases that are formed. Such measurements are of special importance in any detailed investigation since they provide the parameters determining the unique phase of a given hydride. In addition, one can deduce the fundamental thermodynamic information such as the heat and entropy of hydride formation for the various phases.

Such measurements are straightforward, in principle. A block diagram of an appropriate apparatus is shown in Figure 1, consisting primarily of a standard volume, a reactor vessel containing the sample, and an accurate pressure gauge. With this the equilibrium pressures for various compositions of hydrogen in the sample can be measured, constituting an isotherm. Figure 2 shows an 80°C isotherm for the NdCo₃-H system (11). The initial increase in pressure at low concentrations, x , corresponds to the formation of a solid solution of hydrogen in NdCo₃.

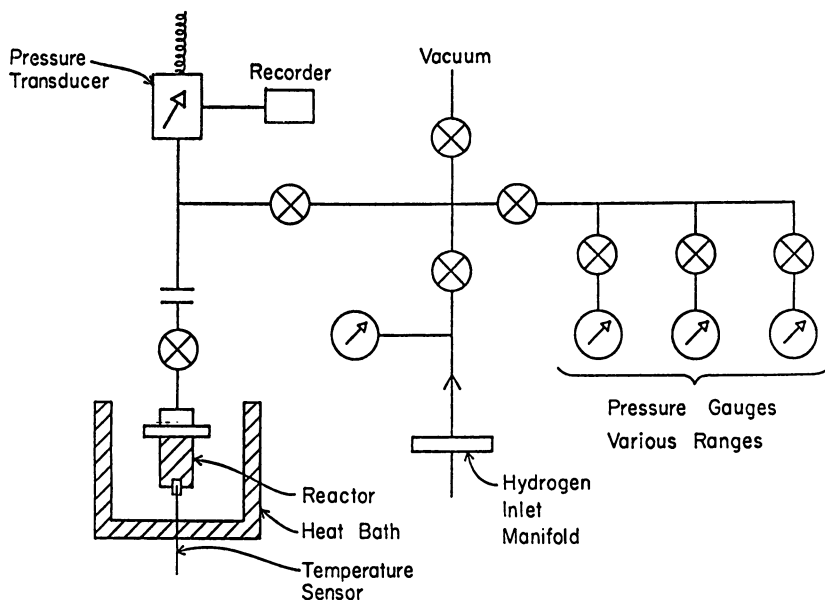


Figure 1. Schematic of a setup for hydriding materials. The temperature of the reactor can be set to any value between 77 and 900 K. The pressure gauges cover the range from 10^{-3} Torr to 150 atm. The volume of each part of the apparatus is known.

Around $x \simeq 0.2$, the isotherm shows a plateau indicating the presence of two phases. Finally, the formation of NdCo_3H_2 is completed at $x = 2.0$. At higher pressures and values of x , a second hydride phase (NdCo_3H_4) is formed similarly. It should be pointed out that one can measure isotherms during either absorption or desorption of hydrogen. Between such measurements one often observes hysteresis, with the equilibrium pressure for the desorption process being lower than that for the absorption process. The origin of such hysteresis effects is not well understood (12).

The dissociation pressure for a specific hydride phase is the pressure at which the plateau for that phase is formed. If the hydrogen partial pressure is lowered below this value, the phase will decompose with rapid evolution of hydrogen gas. Once the isotherm is well established, any desired hydride phase can be formed through some careful bookkeeping. However, once the desired phase is formed and the sample is extracted from the reactor for other physical measurements, the hydride may decompose depending on the isotherm characteristics. Procedures are known for poisoning the surface of the material in order to impede such a loss of hydrogen from the sample (13). In spite of such procedures, measuring the hydrogen content by both gravimetric and volumetric

procedures on samples extracted from the reaction vessel is rather important if the material is to be considered well characterized. Only well-defined samples are suitable for other physical measurements. It also should be emphasized that the preparation of hydrides without prior knowledge of the phase diagram (or isotherms) frequently will result in an ill-defined, possibly multiphase sample.

From the temperature dependence of the plateau pressures one can obtain fundamental thermodynamic information. In most cases the so called van Hoft law is valid (1, 2):

$$\ln p = \frac{1}{RT} [\Delta H - T\Delta S]$$

where p is the plateau pressure for the phase in question and ΔH and ΔS represent the enthalpy and entropy of formation for that hydride phase, respectively. Since the formation of metal hydrides is usually exothermic, ΔH is negative and the plateau pressure increases with temperature.

Compounds of the Form ABH_x

Most of the known hydrides made from equiatomic binary intermetallics are listed in Table II. Where known, the structure of the starting compound as well as of the metal atoms in the hydride phase

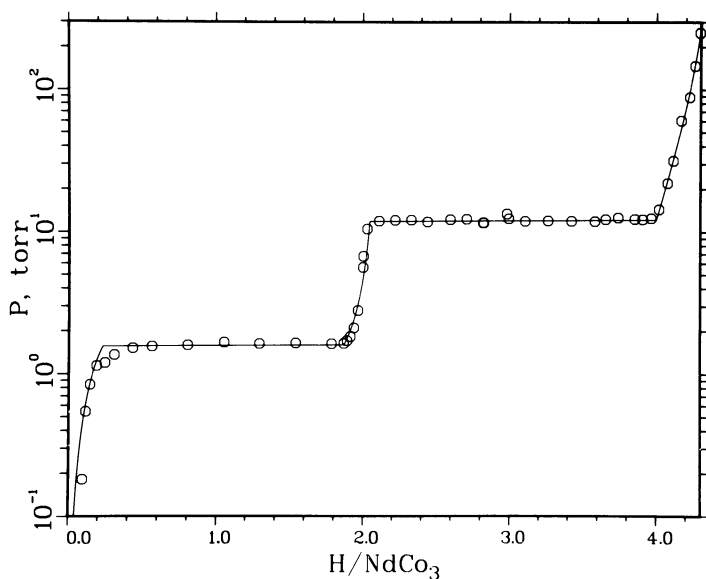


Figure 2. Pressure-composition isotherm for the $\text{NdCo}_3\text{-H}$ system at 80°C

Table II. Typical Hydrides of AB Compounds

<i>Compound</i>	<i>Compound Structure</i>	<i>Concentration H Atoms/ Formula Unit</i>	<i>Hydride Structure</i>	<i>References</i>
FeTi	CsCl	1.1, 1.9	o.r.	14
CuTi	CuTi	0.97	CuTi	15
LaNi	CrB	2.6	? ^a	16
		3.6	?	17
HfCo	CsCl	3.2	CrB	18
HfNi	CrB	1.0, 2.6	CrB	18, 19
ThCo	CrB	3.6-4.2	?	20
ThNi	ThNi	3.6	?	20
ZrCo	CsCl	2.5	CrB	18, 21
ZrNi	CrB	2.5	CrB	18, 22
Ti(Fe _{1-x} Co _x)	CsCl	1.0, 2.0	—	23

^a In this material, a decomposition to LaH_{2.6} + Ni is suspected.

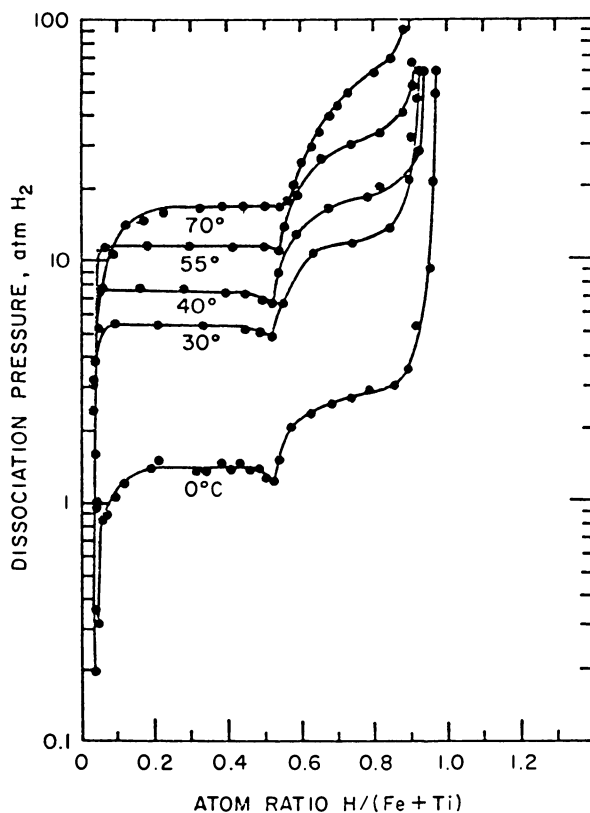
are shown. The structure determination of hydrides using x-ray diffraction was reported in most cases. The location of hydrogen has been investigated in detail only in the case of FeTi hydrides using neutron diffraction (24, 25). Some caution should be exercised in investigating hydrides without a structure study. Often the hydrides of binary alloys decompose into elemental hydrides, especially at elevated temperatures. For example, it is suspected that LaNiH_{2.6} is actually a mixture of LaH_{2.6} and Ni (16) since the lanthanum hydrides are far more stable than the intermetallic hydride.

By far the most studied compounds in this class of materials are FeTi and its hydrides. This is one of the most important materials for practical applications, judged from the isotherm characteristics (Figure 3), chemical stability towards hydrogen cycling, cost, etc. From the isotherm one can clearly identify two phases. While FeTi is cubic, FeTiH_{1.1} (β -phase) and FeTiH_{1.9} (γ -phase) are orthorhombic (14, 24, 25).

Mössbauer spectra of FeTi show a single resonance line, as expected from the structure. The addition of hydrogen causes a large change in the isomer shift: the β -phase is shifted by 0.18 mm/s and the γ -phase is shifted by 0.42 mm/s, both relative to the FeTi alloy. This implies a decrease in the electron density at the iron nucleus as a result of hydrogen absorption. The isomer shift differences, along with the quadrupole interaction present in the orthorhombic hydrides, have made the ⁵⁷Fe resonance useful for phase analysis studies (24, 26). This is illustrated in Figure 4 where the spectrum of an inhomogeneous FeTi hydride is shown. The analysis yields the subcomponents resulting from various hydride phases.

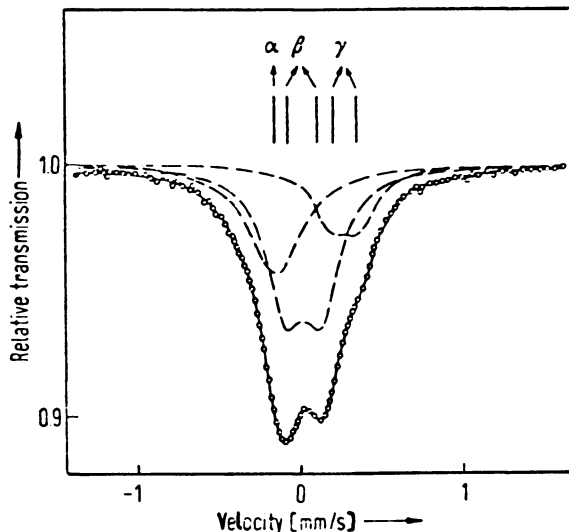
FeTi itself is magnetically interesting because it is a Pauli paramagnet with no magnetic moment on iron. The addition of hydrogen to a material frequently can cause dramatic changes in the electronic structure and hence in the magnetic properties (27). However, the hydrides of FeTi remain Pauli paramagnetic. In Figure 5 we present ^{57}Fe spectra of FeTi and FeTiH_{1.9} at 4.2 K, both with and without an external field of 75 kOe. The observed fields of the ^{57}Fe from the Zeeman split spectra of FeTi and FeTiH_{1.9} are the same as the applied field, showing the absence of magnetic moment on the iron atom.

By forming the pseudo-binary compounds Ti(Fe_{1-x}Co_x), magnetic ordering can be induced. The hydrides of these compounds have been investigated by Mössbauer spectroscopy (23) and show that the Curie temperature and magnetic moment of iron increase in the α -phase.



Inorganic Chemistry

Figure 3. Pressure-composition isotherms at various temperatures for FeTi-H (67)



Zeitschrift fuer Physikalische Chemie

Figure 4. Mössbauer spectrum of inhomogeneous FeTi hydrides showing the subspectra resulting from various hydride phases (24)

It should be noted that repeated absorption and desorption of hydrogen in FeTi results in a finite magnetization of the material. However, this is specifically a surface effect, and will be discussed in detail in the section on hydrogen absorption mechanisms.

Compounds of the Form A_2BH_x

A number of hydrides of A_2B type intermetallic compounds have been made (Table III). Among these, Mg_2Ni has been cited frequently in regard to its hydride applications. Most of the remaining compounds form their hydrides with decomposition pressures well below 10^{-5} Torr.

Hf_2Fe and Hf_2FeH_3 have been studied by ^{57}Fe Mössbauer spectroscopy and magnetization measurements (29). While no magnetic moment is present in Hf_2Fe , the hydride has a magnetic moment of $0.9 \mu_B/Fe$ atom and a ferromagnetic Curie temperature of 73 K. The isomer shift for Hf_2FeH_3 is $+0.40$ mm/s relative to Hf_2Fe , and this change is comparable to that observed on hydriding FeTi.

Compounds of the Form AB_2H_x

All of the compounds of the form AB_2 that have been investigated have a Laves phase structure, either cubic ($MgCu_2$ -type) or hexagonal ($MgZn_2$ -type). Detailed phase diagrams are available for only a few of

these. For the RFe_2H_x systems ($R = Er, Y$), complicated isotherms are obtained that show several phases, up to a maximum concentration of $x = 4.1$ (30). The hexagonal $ErMn_2$ shows a higher concentration phase at $x = 4.6$ (32). For $EuRh_2$, a hydride phase at $x = 5.5$ has been reported, although isotherms have not been measured (37). In general, the hydrogen atom-to-metal atom ratio (H/M) of approximately 1.5 is among the highest available, although low equilibrium pressures make them less convenient to use.

Mössbauer spectroscopy has been used to investigate a number of these materials. In early work, x-ray measurements on some of the

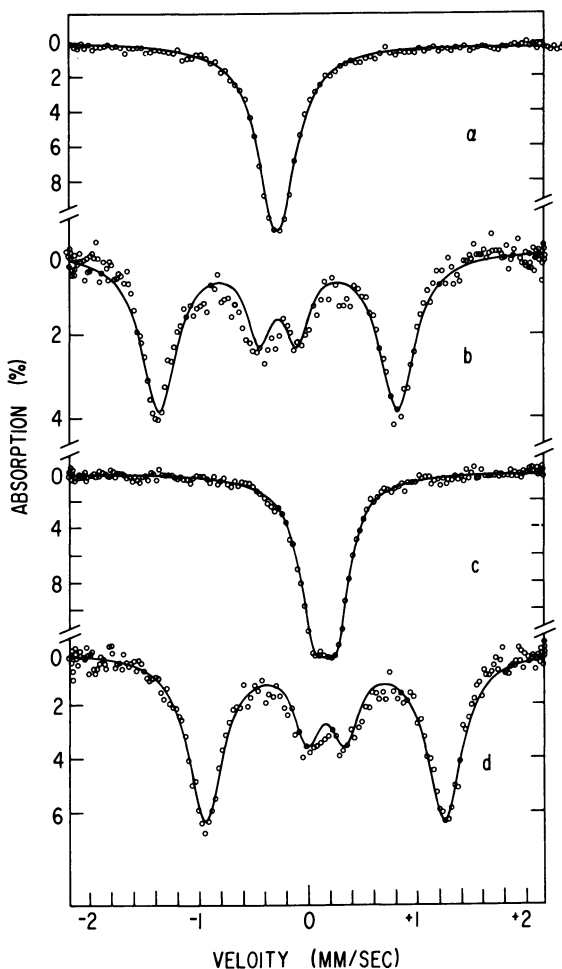


Figure 5. Spectra of $FeTiH_x$ at 4.2 K with and without external magnetic field: (a) $x = 0, H = 0$; (b) $x = 0, H = 75$ kOe; (c) $x = 1.9, H = 0$; (d) $x = 1.9, H = 75$ kOe

Table III. Typical Hydrides of A_2B Compounds

<i>Compound</i>	<i>Compound Structure</i>	<i>Concentration H Atoms/ Formula Unit</i>	<i>Hydride Structure</i>	<i>Reference</i>
Mg_2Ni		4		28
Ti_2Cu		2.58, 2.74	*	15
Hf_2T ($T = Fe, Mn$)	Ti_2Ni	3	Ti_2Ni	18
Hf_2Co	Ti_2Ni	3.6	Ti_2Ni	18
Hf_2Zn	Ti_2Ni	2.04	Ti_2Ni	18
Hf_2Cu	$MoSi_2$	2.9	o.r.	18
Hf_2Ni	$CuAl_2$	3.1	$CuAl_2$	18
Zr_2T ($T = Co, Ni$)	$CuAl_2$	4.5	6 ^b	18

* Decomposition to $TiH_2 + Cu$ is suspected.

^b Zr_2T compounds decompose to $ZrTH_{2.5} + ZrH_2$ when hydrided.

hydrides indicated that an amorphous compound had been formed. However, this appears to result from preparing materials under high hydrogen pressure (~ 150 atm) (33). In that case, the heating associated with a very rapid exothermic reaction, coupled with the large volume changes, results in a material having a great deal of internal strain and perhaps short-range disorder. Preparation procedures with pressures of a few atmospheres result in well-defined compounds (Table IV).

Much effort has gone into studies of magnetic properties of these materials, particularly for the RFe_2 compounds where both rare-earth

Table IV. Typical Hydrides of AB_2 Compounds

<i>Compound</i>	<i>Structure</i>	<i>Concentration H Atoms/ Formula Unit</i>	<i>Structure</i>	<i>Reference</i>
RFe_2 ($R = Y, Dy, Er$)	$MgCu_2$	2, 3.5	$MgCu_2$	30, 31
		4.1	o.r.	30, 31
$ErMn_2$	$MgZn_2$	4.0, 4.6	$MgZn_2$	32
DyT_2	$MgCu_2$	2.0, 3.4	$MgCu_2$	33
($T = Co, Mn, Ni, Fe$)		> 4	?	33
$LaNi_2$	$MgCu_2$	4.1–4.5	*	34, 35
$GdNi_2$	$MgCu_2$	4.35	?	36
$EuRh_2$	$MgCu_2$	5.5	$MgCu_2$	37
$ZrMn_2$	$MgZn_2$	3	$MgZn_2$	38
ZrV_2	$MgCu_2$	4.5	$MgCu_2$	39
$TiCr_{1.8}$	$MgCu_2$	2.4, 3.4	o.r.	40
$CaNi_2$	$MgCu_2$	3.44	$MgCu_2$	41
$ScFe_2$	$MgZn_2$	2	$MgZn_2$	42
RT_2	$MgCu_2$	3.2–4.9	?	43
($R = Gd, La; T = Rh, Ru$)				

* Decomposes to LaH_3 above $100^\circ C$.

and iron Mössbauer spectroscopy can be used (44, 45, 46). The intermetallics themselves have been the subjects of many investigations in the past. These are ferrimagnetic materials, with the iron and rare-earth magnetic sublattices being oppositely directed. The magnetic transition temperatures T_c in the neighborhood of 600 K are determined predominantly by Fe-Fe exchange, with the R-Fe exchange being much weaker, and the R-R exchange essentially negligible. The hydrides ErFe_2H_x show a general decrease in T_c as a function of x up to $x \sim 3.5$, indicating a weakening of the Fe-Fe exchange interaction. In Figure 6 we present the ^{57}Fe Mössbauer spectra of these hydrides. In this concentration range, the ^{57}Fe hyperfine fields indicate a small increase in the iron magnetic

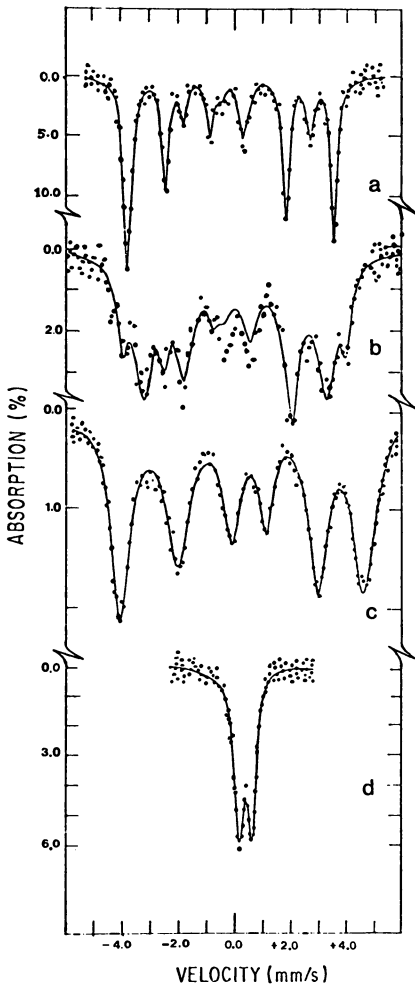


Figure 6. ^{57}Fe Mössbauer spectra of various ErFe_2H_x at 4.2 K: (a) $x = 0$; (b) $x = 2$; (c) $x = 3.5$; (d) $x = 4.1$ (44)

Journal of Applied Physics

moment from about 1.3 to about 1.7 μ_B . At the same time, an increase in the isomer shift of approximately 0.15 mm/s with respect to the unhydrided material is observed. All of these results arise from the combined effects of a rather large lattice expansion ($\Delta V/V \approx 15\%$ for RFe_2H_2) plus changes in the electronic structure attributable to the addition of hydrogen; however, no detailed understanding is yet available (19).

In the cases just discussed, the crystal structure of the hydrides consists of an expanded version of the starting compounds. However, in $ErFe_2H_{4.1}$, a rhombohedral distortion occurs. Commensurate with this, there is a severe reduction in the iron magnetic moment and a correspondent reduction in T_c to about 2 K. Mössbauer spectra taken at low temperatures and in external fields show that the magnetic moment on the iron atom is about 0.2 μ_B .

The rare-earth site in RFe_2H_x has been studied by ^{161}Dy and ^{166}Er spectroscopy (33, 45, 46). In the starting materials, hyperfine fields are observed to be somewhat larger than those of the free-ion, arising from the fact that $R-Fe$ exchange fields are larger than crystalline electric fields in the material, coupled with some contribution to the hyperfine field from conduction electron polarization. When hydrogen is added there is a decrease in the hyperfine field, a more pronounced temperature dependence, and an appearance of line-broadening effects from a decreased electronic relaxation time. All of these results indicate a decrease in the $R-Fe$ exchange interaction as hydrogen is added.

Very similar results to those just described have been obtained from neutron diffraction data (47). Additionally, the average magnetization on the erbium atom as determined by neutron diffraction in $ErFe_2H_2$ is found to be substantially smaller than the local erbium moment determined by the Mössbauer data. This indicates clearly that the simple ferrimagnetic spin ordering present in $ErFe_2$ is not present in the hydride. The most likely explanation of this is that some directional disorder of the erbium moments about the easy axis of magnetization exists (47). Such an effect is found in amorphous RFe_2 materials (48), where local defects in the material cause random variations in the local anisotropies, resulting in the fanning of the moments in a variety of directions around the average easy axis. In the present case, a similar effect occurs because of the local strains arising from the hydrogen atoms that randomly occupy a large number of available sites.

The changes in isomer shift on hydriding at both the rare-earth as well as the iron sites in all of the AB_2 compounds investigated show a decrease in the electron density at those sites. This can be understood qualitatively by assuming the hydrogen atoms to be electron acceptors forming an anion in the lattice. This idea applies to numerous rare-earth metal hydrides that have been investigated, but as pointed out earlier,

Table V. Valence State of Europium in Some AB_2 Compounds

Compound	Cell Volume (\AA^3)	A-B Separation (\AA)	Valence State
Eu:SmFe ₂	405.0	3.07	Eu ³⁺
EuRh ₂	427.1	3.12	Eu ²⁺ \longleftrightarrow Eu ³⁺
EuPt ₂	462.1	3.21	Eu ²⁺
EuAl ₂	533.4	3.36	Eu ²⁺
EuRh ₂ H _x	578.0	3.45	Eu ²⁺

the lattice size increase on hydriding also should decrease the electron density at both sites as observed. The influence of size change on the isomer shift of europium in EuRh₂H_x is rather apparent (37). It is well known that the europium can be either trivalent ($4f^6$) or divalent ($4f^7$) depending on the space available for the ion, the trivalent ion being about 10% smaller than the divalent ion. In EuRh₂, the europium shows ambivalence, a result expected on the basis of lattice size alone (Table V). On hydriding we expect the formation of a divalent state as observed in EuRh₂H_x (37) because of the increase in the lattice volume.

An interesting observation also has been made concerning ¹⁶¹Dy isomer shifts in the hydrides of DyT₂ ($T = \text{Mn, Fe, Co, Ni}$) (33). Initial hydriding of the materials to DyT₂H₂ causes a large change (~ -2 mm/s) in the isomer shift relative to the starting material, after which little change occurs up to DyT₂H₄. The resultant value for the isomer shift is very similar to that seen in DyH₂ and DyH₃, presumably showing the importance of the rare-earth-hydrogen bond in these materials.

The only Laves phase materials studied by Mössbauer spectroscopy that do not contain a rare-earth element are ScFe₂H_x (42, 51) and YFe₂H_x (49, 50). Again in these cases, a change in the ⁵⁷Fe isomer shift comparable with that in the RFe₂ series is observed in hydriding. Also, for ScFe₂H_x, a large increase in the hyperfine field of approximately 60% is observed for $x = 3.2$ compared to that measured in ScFe₂.

Hydrides have been reported for a number of AB₃ compounds, all of which have the PuNi₃ structure (see Table VI). Mössbauer data have been obtained for ErFe₃H_x (55) and DyFe₃H_x (56) using the ⁵⁷Fe resonance along with that of ¹⁶⁶Er or ¹⁶¹Dy. In this structure, the A atoms occupy two crystallographically inequivalent sites while the B atoms occupy five inequivalent sites.

In the starting materials (ErFe₃ or DyFe₃), a single hyperfine field for the rare-earth ion is seen. This field is near the free-ion value, and arises from the fact that the large exchange fields present dominate the crystal field interactions in both sites. As the hydrogen concentration is increased, the hyperfine field decreases rapidly, with the two sites becoming distinguishable. The overall decrease probably arises from a

Table VI. Typical Hydrides of AB_3 Compounds

Compound	Compound Structure	H Atoms/ Formula Unit	Structure	Reference
RFe_3	$PuNi_3$	3.1 (Gd), 4.2 (Tb), 3.0 (Dy) 3.6 (Ho), 2.7 (Er)	$PuNi_3$	52
$(R = Gd, Dy, Ho, Tb, Er)$				
$RCO_3 (R = Nd, Gd)$	$PuNi_3$	2.4	$PuNi_3$	52, 53
$DyCo_3$	$PuNi_3$	1, 1.8, ~ 3.5	$PuNi_3$	52, 53
$ErCo_3$	$PuNi_3$	1.17, 1.67, 3.67	$PuNi_3$	52, 53
YNi_3	$PuNi_3$	4	$PuNi_3$	54
$LaNi_3$	$PuNi_3$	2.8	?	16
		5	?	17
$CeNi_3$	$PuNi_3$	4.1	?	41
$CaNi_3$	$PuNi_3$	4.1	$PuNi_3$	41

decrease in the ratio of exchange-field to crystal-field energies, attributable to a weakening of the R -Fe exchange. This explanation, similar to that used in RFe_2 hydrides, is supported by the observation that the spin compensation temperature (i.e., the temperature at which the R and iron sublattice magnetizations cancel) decreases with increasing hydrogen content. The fact that the hyperfine fields at the two sites decrease at different rates as a function of hydrogen concentration undoubtedly is related to the way in which the various available interstitial sites are being occupied in the material. However, no detailed structural studies to determine the hydrogen positions are yet available.

Because of the five inequivalent iron positions, the ^{57}Fe spectra are very complicated, even in the starting materials (57, 58). In the hydrides, a realistic analysis of all sites has not been possible. However, the overall trend is similar to that of RFe_2 , namely, a small increase in the iron hyperfine field as the hydrogen concentration increases.

In $DyFe_3H_x$, the ^{161}Dy isomer again shows a behavior like that discussed previously for DyT_2H_x . Upon hydriding, a change in the isomer shift of about -2.0 mm/s is observed, relative to $DyFe_3$. The final value is near that of the elemental hydrides, again indicating a pronounced rare-earth-hydrogen bond.

Compounds of the Form AB_5H_x

Hydride forming compounds of the form AB_5 all have the $CaCu_5$ structure (Table VII). These are among the most discussed materials, with $LaNi_5H_6$ being one of the first hydrogen-storage compounds. However, Mössbauer spectroscopy has been used very little to investigate these materials. Samples of $Gd_{0.1}La_{0.9}Ni_5H_x$ ($x \leq 6.7$) and $Gd_{0.1}La_{0.9}Co_5H_x$ ($x \leq 4.2$) have been considered using the ^{155}Gd resonance (66). The

electric field gradient is found to decrease as a function of increasing hydrogen concentration for both cases, while the magnetic hyperfine field in $\text{Gd}_{0.1}\text{La}_{0.9}\text{Co}_5\text{H}_x$ first increases up to $x = 3.2$, then decreases again. These spectra can be used for a phase analysis of the materials. The isomer shifts show a small increase, but again finally achieve a value very near that of the elemental hydrides.

Investigations also have been performed using the ^{151}Eu resonance in EuNi_5 and europium doped LaNi_5 . These will be discussed later with reference to the long-term stability of such materials under repeated absorption-desorption cycles.

Role of Surface Layers in Hydrogen Absorption Mechanism

The previous discussions in this chapter have pointed out the changes occurring in the lattice and electronic structures of various intermetallic compounds on hydrogen absorption. The understanding of the behavior of hydrides clearly demonstrates that the hydrogen is residing in well-defined positions in the lattice after having dissociated from its molecular form prior to its entry in the lattice. Thus, the kinetics of dissociation and subsequent absorption are two aspects that we have not yet addressed.

Most intermetallic compounds (and most rare-earth metals) disintegrate into very fine particles of about $10\text{--}40\ \mu$ on hydrogen absorption, thus producing a large specific surface area (typically $0.3\ \text{m}^2/\text{g}$). Along with the generation of ever-larger surface area on repeated absorption-desorption cycles, the hydrogen is absorbed and desorbed easily.

More important is the fact that the absorption-desorption mechanism itself is a two-stage process. Firstly, in the absorption process the hydrogen molecules from the gas phase have to break into atoms. Secondly, these atoms have to enter the lattice. In the desorption process we expect the atoms to combine again into molecules at the surface of the compound. Clearly, the surface has to play a major role.

Table VII. Typical Hydrides of AB_5 Compounds

<i>Compound</i>	<i>Compound Structure</i>	<i>Concentration H Atoms/ Formula Unit</i>	<i>Hydride Structure</i>	<i>Reference</i>
LaNi_5	CaCu_5	6	CaCu_5	59
LaCo_5	CaCu_5	3.35, 4.2	o.r.	60
		6, 9	?	61
NdCo_5	CaCu_5	2.8	o.r.	60
YCo_5	CaCu_5	3	?	62
ThFe_5	CaCu_5	~ 1	?	63
CaNi_5	CaCu_5	$\sim 1, 4$?	64
		4.5, 5.7	CaCu_5	41
$\text{LaNi}_{5-x}\text{Al}_x$	CaCu_5	4, 5	CaCu_5	65

The energy involved in breaking the hydrogen molecule into atoms is about 4 eV and is expected to occur at the surface through its catalytic activity. It is hence interesting to investigate the nature of the surface of hydrogen-absorbing intermetallic compounds. The absorption-desorption kinetics in various materials are not identical. Thus it is rather difficult to realize hydrogen absorption by a virgin sample of FeTi. Repeated heat treatments (14) are essential in order to activate the hydrogen absorption process. On the other hand, YFe_2 , $ErFe_2$, etc. readily absorb hydrogen with no special treatment required. Indeed, these differences in absorption kinetics are fundamental in nature.

As pointed out earlier, FeTi forms various metal hydrides. A combination of Auger spectroscopy and x-ray photoelectron spectroscopy (XPS) measurements have been used to examine the surface of FeTi subjected to numerous absorption-desorption cycles (67, 68, 69). Those results suggest a disproportionation of the surface of FeTi into iron-rich and titanium-rich overlayers that occurs when FeTi is subjected to many absorption-desorption cycles. In Figure 7 we present a representation of such a surface.

It was pointed out earlier that FeTi, when subjected to many absorption-desorption cycles, shows an increase in the bulk magnetization, although the virgin FeTi is a Pauli paramagnetic (70, 71). Mössbauer conversion electron spectroscopy of the surface of such a material shows a six-line hyperfine pattern in addition to a line from nonmagnetic iron (Figure 8). This has been interpreted in terms of the previously discussed picture of the surface (72, 73). The iron-rich overlayers observed in the Auger measurements behave like magnetically ordered (or superparamagnetic) iron and produce the six-line pattern with a characteristic field of 330 ± 30 kG, which is equal to the value measured for iron metal at room temperature. These surface iron atoms carry $2.2 \mu_B$ and reside in a layer of about 200 Å thickness, and they contribute to the observed

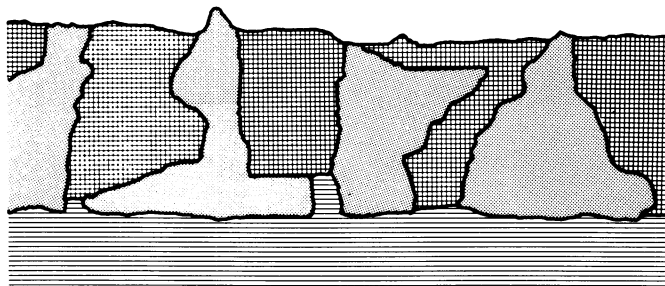

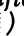
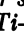
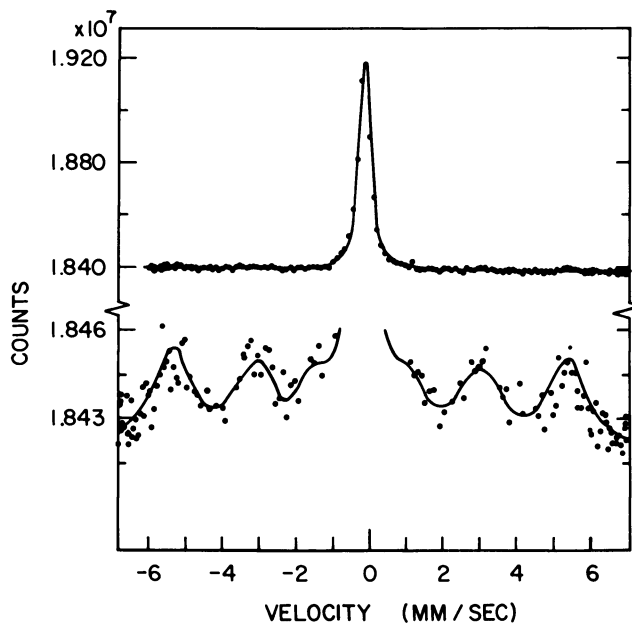


Figure 7. Schematic model of the surface layer of FeTi after subjecting it to many hydrogen absorption-desorption cycles (() Ti-rich containing Ti oxide; () Fe-rich; () FeTi)



Journal of Less-Common Metals

Figure 8. Conversion electron spectrum of FeTi after 51 absorption-desorption cycles showing the presence of magnetic surface layer (72)

increase in the bulk magnetization of the recycled FeTi. The central unsplit line results from electrons sampling deeper in the material made up of FeTi.

These studies offer support to the interpretation that the iron-rich layer (Figure 7) may act as a catalytically active surface responsible for dissociating the hydrogen molecule in the hydrogen absorption process. The ideas presented here are perhaps applicable to most of the hydrogen-absorbing materials, and also have been demonstrated with LaNi₅ (74).

Chemical Degradation Studies

The various applications of hydrogen storage materials mentioned in the introduction demand that the material be stable against numerous hydrogen absorption-desorption cycles. Already we have cast certain doubts about this by pointing out that some of the materials dissociate into component metallic hydrides. FeTi has been subjected to over 17,000 absorption-desorption cycles and its integrity has been maintained. LaNi₅, the other promising material for applications, degrades with a number of absorption-desorption cycles, and the most direct evidence for this came from the Mössbauer investigations (75).

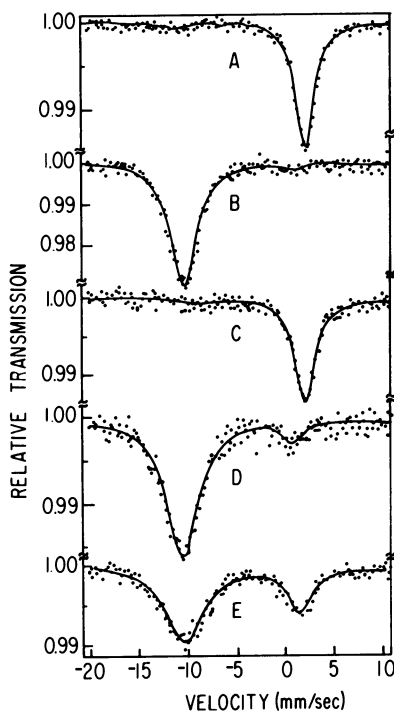


Figure 9. Mössbauer spectra with ^{151}Eu resonance of $(\text{La}_{0.9}\text{Eu}_{0.1})\text{Ni}_{4.6}\text{Mn}_{0.4}$: (A) starting material showing trivalent Eu; (B) hydrided material showing divalent Eu; (C) dehydrided after 10 absorption-desorption cycles; (D) hydrided after 1500 absorption-desorption cycles; (E) dehydrided after 1500 absorption-desorption cycles. The divalent Eu in (E) is from permanent Eu hydride (75).

Journal of Less-Common Metals

The LaNi_5 lattice was probed by substituting lanthanum with europium atoms. Europium exhibits a trivalent state ($4f^6$) in LaNi_5 , and on hydrogen absorption becomes divalent ($4f^7$). These two charge states can be distinguished easily in the Mössbauer spectra because of the large difference (five times the linewidth) in the isomer shift of the two charge states (Figure 9). On removal of hydrogen from LaNi_5 the trivalent state of europium is fully recovered. Thus the oxidation state of europium in LaNi_5 can be used as a probe of the ability to recycle the material. After approximately 1500 cycles one observes that the trivalent state is still present. Along with such a behavior one notices that the total hydrogen storage capacity of LaNi_5 also has degraded. It is argued that the degradation occurs with the formation of rare-earth metal hydride and precipitation of nickel metal. The divalent europium resonance in the 1500-times recycled material then represents europium metal hydride. Thus Mössbauer effect studies can provide quantitative information on the degradation of the material.

Acknowledgments

We would like to thank H. Kierstead, A. T. Aldred, D. Westlake, and R. L. Cohen for many valuable discussions. This work was supported by the U.S. Department of Energy.

Literature Cited

1. Mueller, W. M.; Blackledge, J. P.; Libowitz, G. G., Eds. "Metal Hydrides"; Academic: New York, 1968.
2. Alefeld, G.; Voelkl, J., Eds. "Hydrogen in Metals"; Springer: New York, 1978.
3. Van Mal, H. H. *Philips Res. Rept. Suppl.* 1976, (1).
4. Reilly, J. J.; Sandrock, G. D. *Sci. Am.* 1980, 241, 118.
5. Gruen, D. M.; Mendelsohn, M. H.; Dwight, A. E. *Adv. Chem. Ser.* 1977, 167, 312.
6. Billings, R. E. In "Hydrogen Energy System," Veziraglu, T. N.; Seifritz, W., Eds.; Pergamon: New York, 1978; Vol. 4, p. 1709.
7. van Maal, H. H.; Buschow, K. H. J.; Miedema, A. R. *J. Less-Common Met.* 1974, 35, 65.
8. Libowitz, G. G.; Blank, Z. In "Solid State Chemistry of Energy Conversion and Storage," Goodenough, J. B.; Whittingham, M. S., Eds.; *Adv. Chem. Ser.* 1977, 163, 271.
9. Lundin, C. E.; Lynch, F. E.; McGee, C. B. *J. Less-Common Met.* 1977, 56, 19.
10. Lundin, C. E. *J. Phys. (Paris)* 1979, 40, C5-286.
11. Kierstead, H. A., *J. Less-Common Met.* 1981, 78, 29.
12. Lundin, C. E.; Lynch, E. F. In "Hydrides for Energy Storage," Andresen, A. F.; Maeland, A. J., Eds.; Pergamon: New York, 1978; p. 395.
13. Gualtieri, D. M.; Narasimham, K. S. V. L.; Takeshita, T. *J. Appl. Phys.* 1976, 47, 3432.
14. Reilly, J. J.; Wiswall, R. H. *Inorg. Chem.* 1974, 13, 218.
15. Maeland, A. J. In "Hydrides for Energy Storage," Andresen, A. F.; Maeland, A. J., Eds.; Pergamon: New York, 1978; p. 447.
16. Maeland, A. J.; Andresen, A. F.; Videm, K. *J. Less-Common Met.* 1976, 45, 347.
17. Oesterreicher, H.; Clinton, J.; Bittner, H. *Mat. Res. Bull.* 1976, 11, 1241.
18. van Essen, R. M.; Buschow, K. H. J. *J. Less-Common Met.* 1979, 64, 277.
19. Buschow, K. H. J.; de Chatel, P. F. *Pure Appl. Chem.* 1979, 52, 135.
20. Buschow, K. H. J.; van Mal, H. H.; Miedema, A. R. *J. Less-Common Met.* 1975, 42, 163.
21. Irvine, S. J. C.; Harris, I. R. In "Hydrides for Energy Storage," Andresen, A. F.; Maeland, A. J., Eds.; Pergamon: New York, 1978; p. 431.
22. Libowitz, G. G.; Hayes, H. T.; Gibb, T. R. P. *J. Phys. Chem.* 1958, 62, 76.
23. Hilscher, G.; Wiesinger, G.; Lebsanft, E. *J. Magn. Magn. Mater.* 1980, 15-18, 1273.
24. Schäfer, W.; Lebsanft, E.; Bläsius, A. *Z. Phys. Chem. N.F.* 1979, 115, 201.
25. Thompson, P.; Reidinger, F.; Reilly, J. J.; Corliss, L. M.; Hastings, J. M. *J. Phys. F* 1980, 10, L57.
26. Swartzendruber, L. J.; Bennett, L. H.; Watson, R. E. *J. Phys. F* 1976, 6, L331.
27. Wallace, W. E. *Z. Phys. Chem.* 1979, 115, 395.
28. Reilly, J. J.; Wiswall, R. H., Jr. *Inorg. Chem.* 1976, 7, 2254.
29. Buschow, K. H. J.; van Diepen, A. M. *Sol. State Comm.* 1979, 31, 469.
30. Kierstead, H. A.; Viccaro, P. J.; Shenoy, G. K.; Dunlap, B. D. *J. Less-Common Met.* 1979, 66, 219.
31. Kierstead, H. A. *J. Less-Common Met.*, 1980, 70, 199.
32. Viccaro, P. J.; Shenoy, G. K.; Niarchos, D.; Dunlap, B. D. *J. Less-Common Met.* 1980, 73, 265.
33. Cohen, R. L.; West, K. W.; Oliver, F.; Buschow, K. H. J. *Phys. Rev. B* 1980, 21, 941.
34. Maeland, A. J.; Andresen, A. F.; Videm, K. *J. Less-Common Met.* 1976, 45, 347.
35. Oesterreicher, H.; Clinton, J.; Bittner, H. *Mat. Res. Bull.* 1976, 11, 1241.
36. Malik, S. K.; Wallace, W. E. *Sol. State Comm.* 1977, 24, 417.

37. Buschow, K. H. J.; Cohen, R. L.; West, K. W. *J. Appl. Phys.* 1978, 48, 5289.
38. Didisheim, J. J.; Yvon, K.; Shaltiel, D. *Sol. State Comm.* 1979, 31, 47.
39. Didisheim, J. J.; Yvon, K.; Shaltiel, D. *Sol. State Comm.* 1979, 32, 1087.
40. Johnson, J. R.; Reilly, J. J. *Inorg. Chem.* 1978, 17, 3013.
41. Oesterreicher, H.; Ensslen, K.; Kerlin, A.; Bucher, E. *Mat. Res. Bull.* 1980, 15, 275.
42. Smit, P. H.; Buschow, K. H. J. *Phys. Rev. B* 1980, 21, 3839.
43. Jacob, I.; Shaltiel, D. *J. Less-Common Met.* 1978, 65, 117.
44. Dunlap, B. D.; Shenoy, G. K.; Friedt, J. M.; Viccaro, P. J.; Niarchos, D.; Kierstead, H.; Aldred, A. T.; Westlake, D. G. *J. Appl. Phys.* 1979, 50, 7862.
45. Viccaro, P. J.; Shenoy, G. K.; Dunlap, B. D.; Westlake, D. G.; Miller, J. F. *J. Phys. (Paris)* 1979, 40, C2-198.
46. Viccaro, P. J.; Friedt, J. M.; Niarchos, D.; Dunlap, B. D.; Shenoy, G. K.; Aldred, A. T.; Westlake, D. G. *J. Appl. Phys.* 1979, 50, 2051.
47. Rhyne, J. J.; Fish, G. E.; Sankar, S. G.; Wallace, W. G. *J. Phys. (Paris)* 1979, 40, C5-209.
48. Rhyne, J. J.; Schelling, J. H.; Koon, N. C. *Phys. Rev. B* 1974, 10, 4672.
49. Buschow, K. H. J.; van Diepen, A. M. *Solid State Comm.* 1976, 19, 79.
50. Viccaro, P. J.; Shenoy, G. K.; Dunlap, B. D.; Niarchos, D.; Aldred, A. T., to be published.
51. Niarchos, D.; Viccaro, P. J.; Shenoy, G. K.; Dunlap, B. D.; Aldred, A. T. *Proc. Int. Conf. Hyperfine Inter., 5th, Berlin, 1980.*
52. Beckman, C. A.; Goudy, A.; Takeshita, T.; Wallace, W. E.; Craig, R. S. *Inorg. Chem.* 1976, 15, 2184.
53. Kierstead, H. A., *J. Less-Common Met.* 1981, 78, 29.
54. Buschow, K. H. J.; van Essen, R. M. *Solid State Comm.* 1979, 32, 1241.
55. Niarchos, D.; Viccaro, P. J.; Dunlap, B. D.; Shenoy, G. K. *J. Appl. Phys.* 1979, 50, 7690.
56. Niarchos, D.; Viccaro, P. J.; Dunlap, B. D.; Shenoy, G. K.; Aldred, A. T. *J. Less-Common Met.* 1980, 73, 283.
57. Arif, S. K.; Bunbury, D. St. P.; Bowden, G. J.; Day, R. K. *J. Phys. F* 1975, 5, 1048.
58. van der Kraan, A. M.; van der Velden, J. N. J.; van Apeldoorn, H. F.; Gubbens, P. C. M.; Buschow, K. H. J. *Phys. Stat. Sol. (a)* 1976, 35, 137.
59. van Mal, H. H.; Buschow, K. H. J.; Miedema, A. R. *J. Less-Common Met.* 1974, 35, 65.
60. Kuijpers, F. A.; Loopstra, B. O. *J. Phys. Chem. Solids* 1974, 35, 301.
61. Steward, S. A.; Lakner, J. F.; Uribe, F. In "Solid State Chemistry of Energy Conversion and Storage," *Adv. Chem. Ser.* 1977, 163, 284.
62. Takeshita, T.; Wallace, W. E.; Craig, R. S. *Inorg. Chem.* 1974, 13, 2282.
63. Buschow, K. H. J.; van Maal, H. H.; Miedema, A. R. *J. Less-Common Met.* 1975, 42, 163.
64. Shinar, J.; Shaltiel, D.; Davidov, D.; Grayevsky, A. *J. Less-Common Met.* 1978, 60, 209.
65. Mendelsohn, M. H.; Gruen, D. M.; Dwight, A. E. *J. Less-Common Met.* 1979, 63, 193.
66. Bauminger, E. R.; Davidov, D.; Felner, I.; Nowik, I.; Ofer, S.; Shaltiel, D. *Physica* 1977, 86-88B, 201.
67. Reilly, J. J.; Wiswall, R. H. Jr. *Inorg. Chem.* 1974, 13, 218.
68. Sandrock, G. D. "BNL Report," 1976, 352410S.
69. Busch, G.; Schlapbach, L.; Stucki, F.; Fischer, P.; Andresen, A. F. *Int. J. Hydrogen Energy* 1979, 4, 29.
70. Sandrock, G. D.; Trozz, C. J. "BNL Report," 1977, 352410S.
71. Hempelmann, R.; Wicke, E. *Ber. Bunsenges. Phys. Chem.* 1977, 8, 425.

72. Shenoy, G. K.; Niarchos, D.; Viccaro, P. J.; Dunlap, B. D.; Aldred, A. T.; Sandrock, G. D. *J. Less-Common Met.* **1980**, *73*, 171.
73. Bläsius, A.; Gonser, V. *J. Appl. Phys.* **1980**, *22*, 331.
74. Wallace, W. E.; Karlicek, R. F., Jr.; Imamura, H. *J. Phys. Chem.* **1979**, *83*, 1708.
75. Cohen, R. L.; West, K. W.; Wernick, J. H. *J. Less-Common Met.*, **1980**, *73*, 273.

RECEIVED July 22, 1980.

Mössbauer Studies of Battery Materials

M. EIBSCHÜTZ

Bell Laboratories, Murray Hill, NJ 07974

The application of Mössbauer spectroscopy to the study of high energy density secondary (rechargeable) battery materials is reviewed. The ^{57}Fe Mössbauer effect was used to study the electrochemical reaction associated with the insertion of a metal "guest" species (lithium) in a chalcogenide "host" lattice (VS_2 or TaS_2) at the cathode of a battery. The Mössbauer effect gives us valuable information about the guest-host interaction and the change in the electronic properties of the host matrix. The changes of the microscopic properties of the hosts involved in the mechanism of the electrochemical reaction at the cathode as a function of the state of charge of the battery are examined and discussed.

As part of an increased effort to develop more efficient methods of utilization of our energy resources, the study of new types of secondary rechargeable batteries as power sources has intensified. Through a better understanding and improvement of established battery systems, the range of applications can be increased, for example, in electric vehicle propulsion, off-peak electric storage, solar and wind energy storage, and powered electric energy generators, as reviewed by Cairns and Shimotake (1). There are many types of batteries under development, but in this chapter we limit our discussion to lithium intercalation compounds of the transition-metal layer dichalcogenides. The major impetus of the dichalcogenides is that they exhibit high electrochemical activity, high energy density, and reversibility as cathodes in alkali metal cells (2, 3, 4).

We used the ^{57}Fe Mössbauer effect to study the electrochemical reaction at the cathode for a better understanding of the mechanism of cathodic reduction. The Mössbauer effect will give us information about the electronic spin configuration of iron substituted in this high energy density battery cathode material $\text{Li}_x\text{Fe}_y\text{V}_{1-y}\text{S}_2$ ($0 \leq x \leq 1$; $0 \leq y \leq 1/2$)

0065-2393/81/0194-0523\$05.00/0

© 1981 American Chemical Society

and $\text{Li}_x\text{Fe}_{0.05}\text{Ta}_{0.95}\text{S}_2$ ($0 \leq x \leq 1$). It also gives information about the guest–host interaction, and the change in the electronic and magnetic properties of the host matrix.

Structure and Properties

The layer transition-metal dichalcogenides have the chemical formula MX_2 , where $X = \text{S}, \text{Se}, \text{or Te}$, and M can be a transition metal from Group IVB, VB, or VIB (5). Here we will discuss primarily $M = \text{V}$ or Ta and $X = \text{S}$. The structure of the compounds consists of three atom-sheet-thick “sandwiches.” The top and bottom sheets of the sandwich are comprised of closed-packed chalcogenide (S) atoms while the middle sheet is comprised of metal atoms (M). The bonding within a sandwich is strong; however, between the sandwiches it is very weak and usually labeled a van der Waals bonding. Consequently, the sandwiches possess a two-dimensional layered structure that is reflected in pronounced anisotropies of their physical properties. In a given sandwich (or slab) the metal atom may be either octahedrally coordinated or trigonal-prismatically coordinated by the chalcogen atoms. The layers can be stacked one on top of another in a regular way building the crystal. Since the interslab forces are so weak and two metal coordinations are possible, many of the layer compounds exist in several polytypes. These polytypes differ from each other in stacking arrangements of the layers, and in the metal coordination within a given layer. We will concern ourselves primarily with the simplest polymorph, the polytype 1T, which has one sandwich per unit cell, has all M atoms octahedrally coordinated, and has overall trigonal symmetry. The 1T polytype has the CdI_2 structure and is shown in Figure 1.

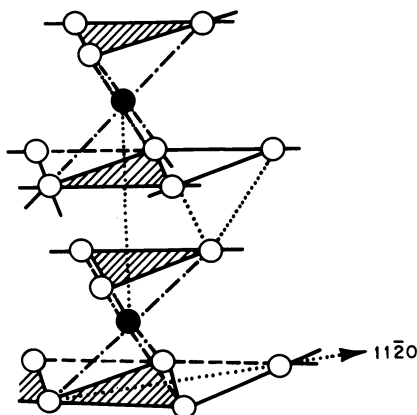


Figure 1. Structure of 1T- VS_2 ,
((●) V; (O) S)

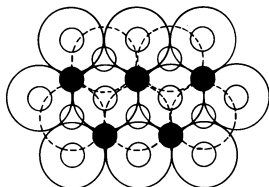


Figure 2. Sites available for lithium between chalcogen layers in 1T polytype ((●) octahedral hole; (○) tetrahedral hole)

The electron configurations of the Group VB compounds are d^1 , and the materials are electronically conductive. The anomalous physical properties of these chalcogenide compounds as observed in the magnetic susceptibility data, and any other physical properties, are attributable to the charge-density wave instabilities (6). The MS_2 compounds have the ability to exist in high oxidation states and to form intercalation compounds with alkali metals. In this chapter we limit our discussion to lithium-intercalated MS_2 compounds.

Intercalation

The electrochemical reaction at the cathode involves a host lattice (MS_2) in which a guest (lithium) is inserted, with the product maintaining the basic structural features of the host. The intercalation reaction $xLi + MS_2 = Li_xMS_2$ ($x = 0$ to 1) must be reversible through appropriate thermal or chemical treatment. Since this reaction is of a redox type, the reversibility of the intercalation reaction may serve as the basis of an anode/cathode couple for a secondary battery. The other basic requirements for solid-state cathode materials have been proposed by a number of authors (4, 7, 8) and we shall not discuss them here. The van der Waals gap between the layers of MS_2 compounds provides sufficient vacant sites to allow a wide composition range of intercalated lithium, up to one lithium per metal ion, and also provides a pathway to facilitate lithium diffusion (2, 4). The sites available for Li^+ in the 1T- MS_2 structure in the van der Waals gap are octahedral and tetrahedral: one vacancy per M octahedral sites and two per M tetrahedral sites. The empty sites are illustrated in Figure 2 together with the two chalcogenide layers across the van der Waals gap. Neutron diffraction results indicate that lithium ions occupy octahedral sites (one per transition metal) in $LiVS_2$ and $LiCrS_2$ (9). Lithium can diffuse between octahedral sites only by passing through one of the tetrahedral sites surrounding the octahedral sites.

The Li_xMS_2 may form at single ternary phase or be multiphase as a function of lithium content. One such electrochemical system is Li_xTiS_2 ($0 \leq x \leq 1$), which is a single nonstoichiometric phase for all x and is readily reversible (10, 11). The reversibility is optimized when no

chemical bonds are broken during discharge, that is, when ternary phases are formed by an intercalation reaction and a broad range of non-stoichiometry exists. Most of the other layer compounds exhibit some structural changes of the host or phase disproportionation for some lithium stoichiometries. The room-temperature electrochemical reversibility of the $\text{VS}_2\text{-LiVS}_2$ couple is impaired by slight structural distortions at intermediate lithium concentrations (12). The reversibility of the Li_xVS_2 cathode is greatly improved when some of the vanadium is replaced by iron (13). The improved reversibility is attributable to the suppression of the distorted intermediate phases in the region $0.3 \leq x \leq 0.5$ (13, 14).

Magnetic susceptibility data (14) have shown that the iron atoms do not have a magnetic moment in the delithiated samples, but paramagnetic moments appear in fully lithiated compounds. When $x = 0$ (no lithium) the iron is divalent with low spin state ($S = 0$), and no paramagnetic moments are observed on the vanadium atoms. For fully lithiated samples the iron remains divalent, but local moments appear. At high iron concentration the magnetic state of the material is complicated.

Experimental

Sample Preparation. The lithiated materials $\text{LiFe}_y\text{V}_{1-y}\text{S}_2$ were prepared (12) by reacting stoichiometric quantities of Li_2CO_3 , $(1-y)\text{V}_2\text{O}_5$, and $y\text{Fe}_2\text{O}_3$ at 650°C in a flow of H_2S for 24 h, followed by grinding and refring in H_2S for another 24 h. The lithium ions were removed by an oxidative deionization reaction with iodine in acetonitrile (12).

The $1\text{T-Fe}_y\text{Ta}_{1-y}\text{S}_2$ was prepared from stoichiometric mixtures of tantalum, iron, and sulfur sealed in a small quartz tube under vacuum (10 mTorr or less) and reacted initially for several days at 800°C . After this initial reaction, the samples were opened, ground, pressed into pellets at 50,000 psi, and resealed in the quartz tube with enough excess sulfur to give approximately 1–2 atm vapor pressure at 900°C . These samples were reheated to 950°C for 7 days, so that diffusion of the cations could occur producing essentially homogeneous pellets, and later were quenched into cold water from 750°C . The lithiated compound $\text{Li}_x\text{Fe}_{0.05}\text{Ta}_{0.95}\text{S}_2$ was prepared by reacting *n*-butyl lithium with 1T material. The maximum amount of lithium incorporated in the sample studied was $x = 0.86$.

Results and Discussions

The $\text{VS}_2\text{-LiVS}_2$ Cathode. The ^{57}Fe Mössbauer spectra were obtained in a standard transmission geometry with a conventional constant-acceleration spectrometer using a ^{57}Co in palladium source. Powder absorbers for Mössbauer effect measurements were made in a dry argon atmosphere by mixing the material with boron nitride powder. Figure 3

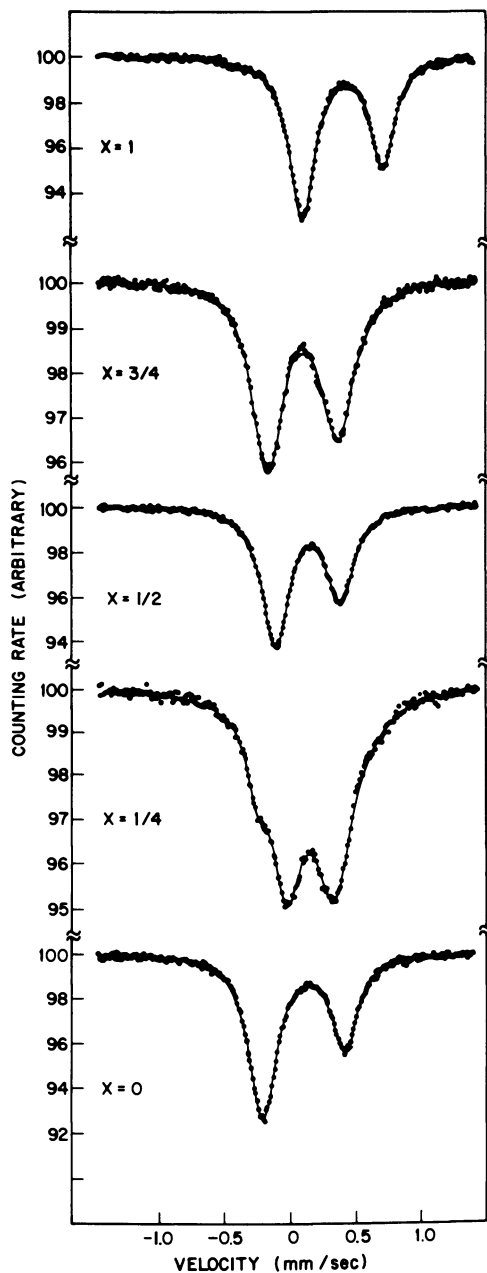


Figure 3. Room-temperature ^{57}Fe Mössbauer absorption spectra of $\text{Li}_2\text{Fe}_{0.1}\text{V}_{0.9}\text{S}_2$ for $x = 0$ to 1. The solid line represents the sum of two (four for $x = 1/4$) Lorentzian least-squares fit to the data.

shows the Mössbauer effect spectra of $\text{Li}_x\text{Fe}_{0.1}\text{V}_{0.9}\text{S}_2$ as a function of lithium concentration (from $x = 0$ to 1). The spectrum shows two resonance lines (except $x = 1/4$) attributable to the electric field gradient at the iron nucleus. The asymmetry in the line intensities of the spectrum results from nonrandom orientation of small, single-crystal platelets in a powder sample. The spectra were analyzed by fitting to a sum of two Lorentzian curves of independent position, width and dip. The iron quadrupole splitting is about the same for $x = 0$ or 1; $e^2qQ/2 = -0.626 \pm 0.005$ mm/s for $x = 0$ and -0.614 ± 0.005 mm/s for $x = 1$. The negative sign of the quadrupole splitting was inferred from the asymmetry of the Mössbauer effect line intensities. The Mössbauer effect spectrum for $x = 1/4$ shows four resonances attributable to the monoclinic distortion of the compound. This indicates the existence of more than one crystallographic site for vanadium and explains the electrochemical sluggishness of the battery. The spectra for $\text{Li}_x\text{Fe}_{1/4}\text{V}_{3/4}\text{S}_2$ and $\text{Li}_x\text{Fe}_{1/3}\text{V}_{2/3}\text{S}_2$ as a function of lithium concentration (from $x = 0$ to 1) are given in Figures 4 and 5, respectively.

The isomer shift is the shift in the nuclear transition energy reflecting a perturbation of the nuclear energy levels resulting from the electrostatic interactions between the nucleus and its electronic environment. It is a measure of the s electronic charge density at the nucleus and is affected by the valence state of the atom. The isomer shift values for $\text{Li}_x\text{Fe}_{0.1}\text{V}_{0.9}\text{S}_2$ (with $x = 0$ and $x = 1$) are given in Table I at 4.2 and 296 K. The value of 0.402 mm/s for the isomer shift at 4.2 K for $x = 0$ indicates that iron is Fe^{2+} in the low-spin state, which is in agreement with the susceptibility results. This value is about 0.23 mm/s smaller than the isomer shift for $1\text{T-Fe}_{0.1}\text{Ta}_{0.9}\text{S}_2$, where Fe^{2+} is also low-spin at low temperature. This difference is related to the change in the electronic configuration of the hosts from V^{4+} ($3d^1$) and Ta^{4+} ($5d^1$) (15). The values of 0.730 mm/s for the isomer shift at 4.2 K for $x = 1$ indicates that the iron is Fe^{2+} in the high-spin state ($S = 2$). This value of the isomer shift is 0.22 mm/s smaller than that for $\text{Fe}_{1/3}\text{TaS}_2$ intercalated (16) high-spin Fe^{2+} (isomer shift = 0.95 mm/s), but is in agreement with other sulfide compounds containing iron in the high-spin state (17, 18). Since the difference in the isomer shift between low- and high-spin iron in the tantalum compounds (19) is the same as that observed here at $x = 0$ and $x = 1$, it is very likely that the iron is high-spin at $x = 1$. The magnetic moments obtained from magnetic susceptibility data are somewhat smaller than the $4.9 \mu_B$ expected for high-spin Fe^{2+} . At present there are some difficulties in understanding the origin of this smaller moment. Future experiments will address this question.

The Mössbauer effect spectra in $\text{Li}_x\text{Fe}_{1/4}\text{V}_{3/4}\text{S}_2$ show two resonance lines for $x = 0, 1/4$, and $1/2$ (see Figure 4). For $x = 3/4$ the spectrum

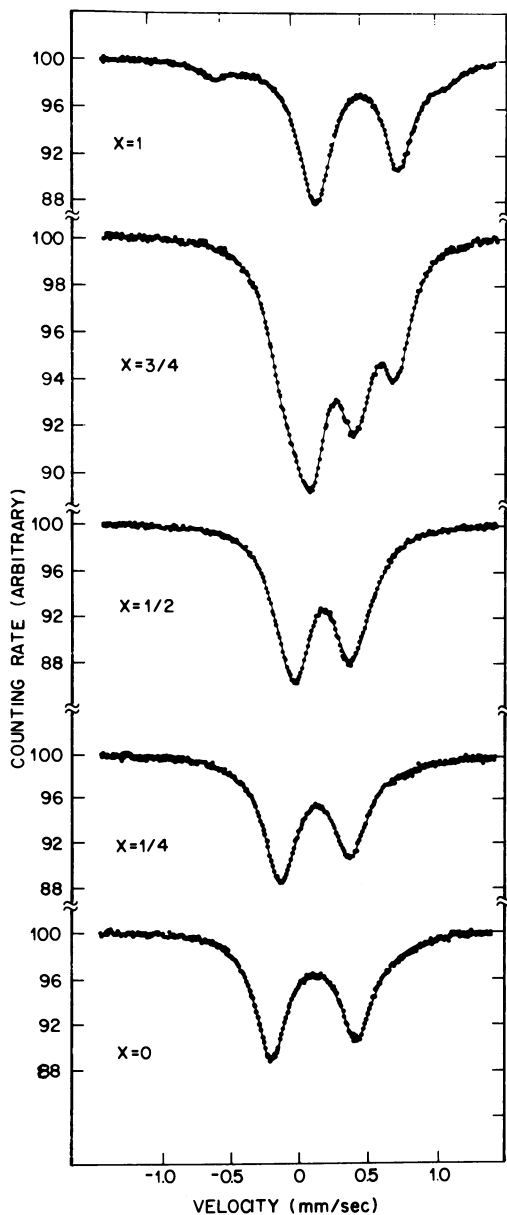


Figure 4. Room-temperature ^{57}Fe Mössbauer absorption spectra of $\text{Li}_x\text{Fe}_{1/4}\text{V}_{3/4}\text{S}_2$ for $x=0$ to 1 (20)

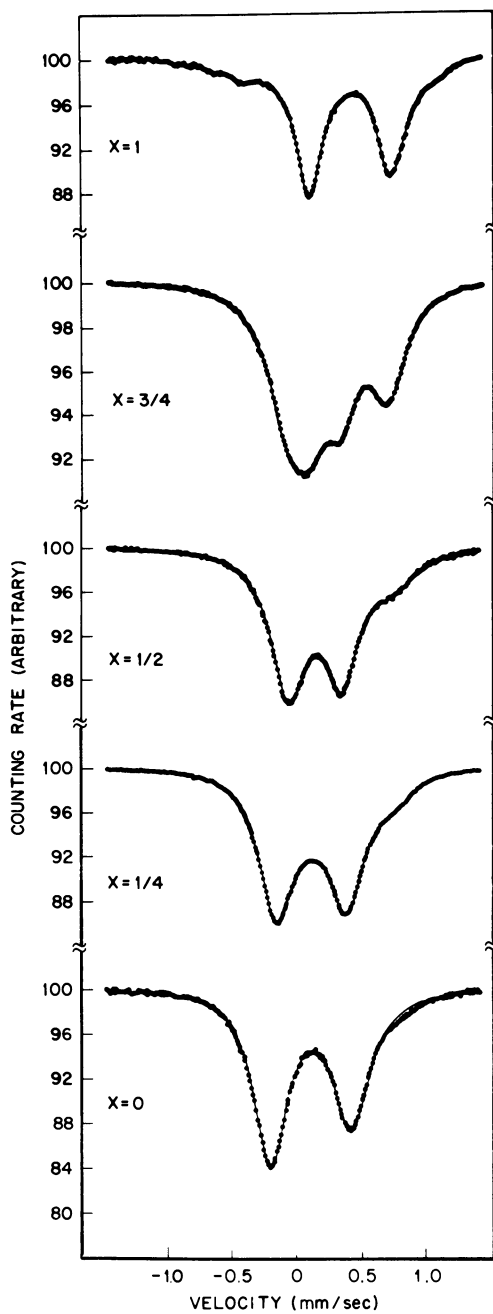


Figure 5. Room-temperature ^{57}Fe Mössbauer absorption spectra of $\text{Li}_x\text{Fe}_{1/3}\text{V}_{2/3}\text{S}_2$ for $x=0$ to 1.

Table I. Mössbauer Parameters for $\text{Li}_x\text{Fe}_{0.1}\text{V}_{0.9}\text{S}_2$ Compounds (20)

<i>Compounds</i>	<i>T</i> (K)	<i>Isomer Shift</i> ^{a, b} (mm/s)	$ e^2qQ/2 ^b$
$\text{Fe}_{0.1}\text{V}_{0.9}\text{S}_2$	4.2	0.403	0.759
$\text{Fe}_{0.1}\text{V}_{0.9}\text{S}_2$	296	0.297	0.626
$\text{LiFe}_{0.1}\text{V}_{0.9}\text{S}_2$	4.2	0.730	0.678
$\text{LiFe}_{0.1}\text{V}_{0.9}\text{S}_2$	296	0.592	0.614

^a Isomer shift with respect to iron metal.

^b The standard deviation for the isomer shift and quadrupole splitting is ± 0.005 mm/s.

Physica

is different. For $x = 1$ the spectrum shows mainly two resonance lines with an additional splitting on the wings of the spectrum. This occurs at higher iron concentrations and therefore may result from local iron clustering within the layers. There is very little difference between the Mössbauer effect spectrum for $\text{Fe}_{0.1}\text{V}_{0.9}\text{S}_2$ and $\text{Fe}_{1/4}\text{V}_{3/4}\text{S}_2$; both spectra give about the same isomer shift. Therefore, the change in iron concentration from 0.1 to 0.25 in VS_2 does not change the valence state of iron or the electronic nature of the material. At low lithium concentration ($x < 1/2$) the Mössbauer effect spectra shift slightly, and both the quadrupole splitting and the isomer shift change slightly. The isomer shift results are given in Figure 6. The value of the isomer shift for $\text{LiFe}_{1/4}\text{V}_{3/4}\text{S}_2$ is the same as that for $\text{LiFe}_{0.1}\text{V}_{0.9}\text{S}_2$, indicating that increasing iron from $y = 0.1$ to 0.25 does not change the state of iron in the fully lithiated material. The spectrum for $x = 0.75$ is different from any other spectrum. It contains lines from the spectrum with $x = 0.5$ and lines from the spectrum with $x = 1$. This indicates that for $x = 0.75$ we have a two-phase structure, or chemically distinct iron atoms in a continuous nonstoichiometric phase. This could be attributable to the existence of a first-order phase transition, for example, metal to semiconductor or low-spin to high-spin Fe^{2+} (20). The effect of this transition on the electrochemical cell will be discussed elsewhere.

The Mössbauer effect spectra in $\text{Li}_x\text{Fe}_{1/3}\text{V}_{2/3}\text{S}_2$ are very similar to those of $\text{Li}_x\text{Fe}_{1/4}\text{V}_{3/4}\text{S}_2$. For $x = 0$ only two resonance lines have been observed, while for $x = 1/4, 1/2,$ and $3/4$, an additional peak appears around 0.70 mm/s, and the peak around -0.13 mm/s broadens. As the lithium concentration increases from 0 to 1, the peak around 0.70 mm/s increases in intensity, indicating an increase in the iron concentration in the high-spin state. The spectrum of the fully lithiated sample ($x = 1$) has mainly two resonance lines, and is very similar to that of $\text{LiFe}_{1/4}\text{V}_{3/4}\text{S}_2$. The isomer shift for $x = 0$ is almost identical to the value for $y = 0.1$ or $1/4$. Therefore, the change in iron concentration up to $1/3$ in VS_2 does not affect the valence state of iron. The isomer shifts as a

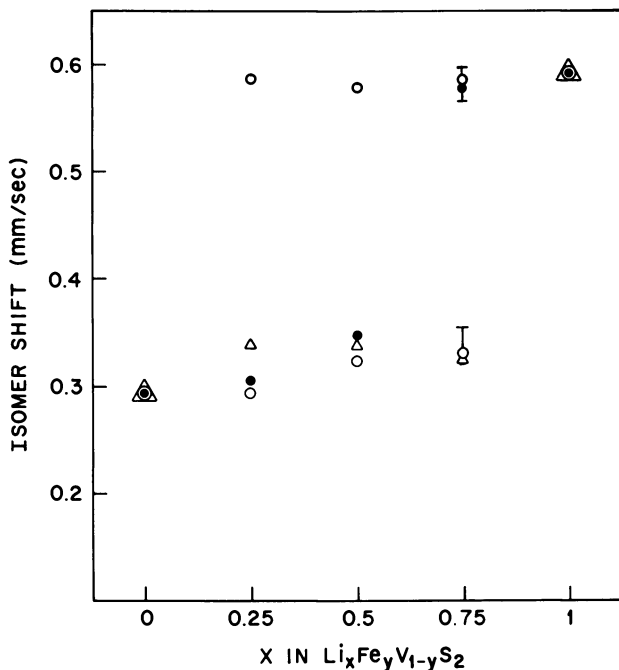


Figure 6. Isomer shift of the Mössbauer absorption gamma ray of ^{57}Fe in $\text{Li}_x\text{Fe}_y\text{S}_2\text{V}_{1-y}\text{S}_2$ for $x = 0$ to 1 and $y = 0$ to $1/3$ expressed relative to metallic iron at 296 K ((Δ) $y = 0.1$; (\bullet) $y = 1/4$; (\circ) $y = 1/3$)

function of lithium concentration, given in Figure 6, show that the values for $y = 1/3$ are similar to those for $y = 1/4$. These results indicate that the iron in $\text{Li}_x\text{Fe}_{1/3}\text{V}_{2/3}\text{S}_2$ could exist in two forms, Fe^{2+} low-spin state and Fe^{2+} high-spin state. When $x = 1/4$ and $y = 1/3$ we have about 10% iron in the high-spin state, which increases gradually as x increases from 0 to 1.

The quadrupole coupling is the result of the interaction of the nuclear quadrupole moment Q with the gradient of the electric field attributable to other charges in the crystal. The nuclear quadrupole moment reflects the deviation of the nucleus from spherical symmetry. The presence of a nonzero field gradient at the nucleus is determined primarily by the symmetry of the distribution of the electrons about the nucleus, which in turn depends on the symmetry of the bonding about the atom in question. The Mössbauer effect gives us information about site symmetries and field gradients within a crystal.

The quadrupole splitting as a function of lithium and iron concentration is given in Figure 7. The main information is that for $x = 0$ or 1, quadrupole splitting is independent of y and has a value of 0.62 ± 0.1

mm/s; at different lithium concentrations the quadrupole splitting depends on y . There is a minimum around $x = 0.6$ with the quadrupole splitting ≈ 0.41 mm/s for Fe^{2+} in the low-spin state. The quadrupole splitting for Fe^{2+} in the high-spin state is almost independent of the lithium concentration. These results correlate well with the observed shallow maximum at $x = 0.4-0.5$ in the c/a lattice parameter ratio (12).

The TaS_2 - LiTaS_2 Cathode. The $1\text{T-Fe}_y\text{Ta}_{1-y}\text{S}_2$ is a layered compound with the CdI_2 structure (19, 21), and for $y \rightarrow 0$, has a metallic character that supports both incommensurate and commensurate charge density wave instabilities (6, 22). Iron is essentially randomly distributed on octahedrally coordinated tantalum sites, and no evidence of iron ordering is seen for $y < 1/3$. Doping rapidly destroys the commensurate charge density wave, but the incommensurate wave is present to $y \sim 0.1$, as evidenced by the existence of sharp satellite diffraction peaks. For $y > 0.1$ the peaks become diffuse. Electrical resistivity increases rapidly, both with increasing x and decreasing temperature.

The magnetic susceptibility and Mössbauer isomer shift (21) in $1\text{T-Fe}_y\text{Ta}_{1-y}\text{S}_2$ ($y \leq 1/3$) demonstrated the presence of a dynamic low-spin-high-spin transition of Fe^{2+} with increasing T . It was established that the iron was present solely as Fe^{2+} , that its magnetic electrons were localized, and that the low-spin-high-spin energy gap was modulated significantly as a function of T by a restrictive interaction with the local lattice environment. As a result of this interaction, the mean displacement coordinate of local ion motion is modulated in a distinctive manner as a thermal population of high-spin levels takes place. Fig-

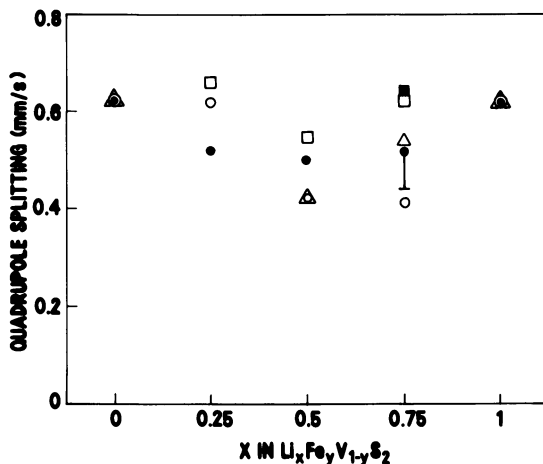


Figure 7. Quadrupole splitting in $\text{Li}_x\text{Fe}_y\text{V}_{1-y}\text{S}_2$ for $x = 0$ to 1 and $y = 0$ to $1/3$ ((Δ) $y = 0.1$; (\bullet, \blacksquare) $y = 1/4$; (\circ, \square) $y = 1/3$)

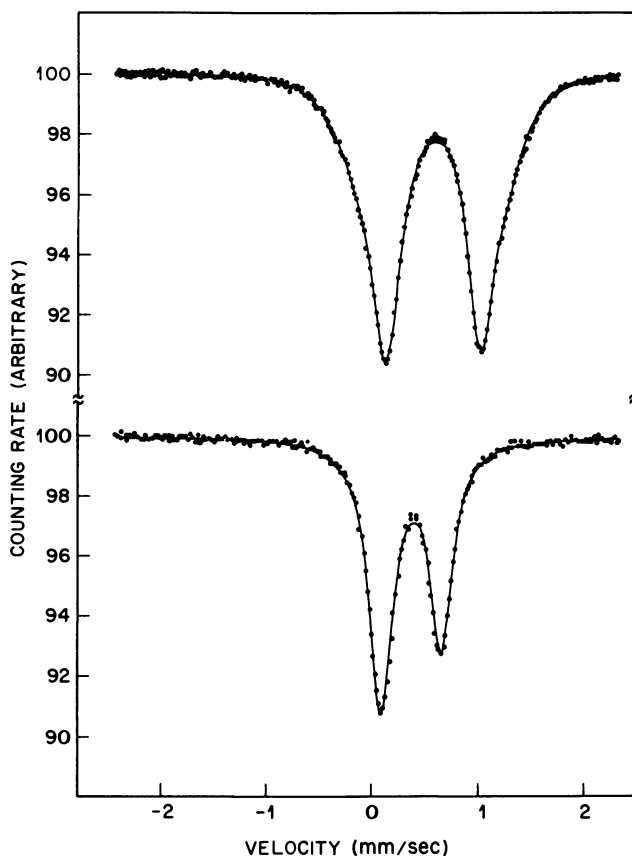


Figure 8. Room-temperature ^{57}Fe Mössbauer absorption spectra of $\text{Li}_{0.86}\text{Fe}_{0.05}\text{Ta}_{0.95}\text{S}_2$ (top) and $\text{Fe}_{0.05}\text{Ta}_{0.95}\text{S}_2$ (bottom)

Figure 8 shows the Mössbauer effect spectra of $1\text{T-Fe}_{0.05}\text{Ta}_{0.95}\text{S}_2$ and $\text{Li}_{0.86}\text{Fe}_{0.05}\text{Ta}_{0.95}\text{S}_2$. The spectrum for $x=0$ shows two resonance lines similar to iron-substituted VS_2 . At room temperature $|1/2 e^2qQ| = 0.56 \pm 0.01$ mm/s and the isomer shift $= 0.56 \pm 0.01$ mm/s, which corresponds to Fe^{2+} in an intermediate state. The iron atoms fluctuate between the low- and high-spin state faster than the inverse of the spectral splittings involved (10^{-7} s). In $1\text{T-Fe}_y\text{Ta}_{1-y}\text{S}_2$ ($y \leq 1/3$), each iron atom must rapidly change its electronic state so that the Mössbauer spectrum is time averaged and only one set of resonance lines is seen. Details of the dynamic low-spin-high-spin Fe^{2+} in $1\text{T-Fe}_y\text{Ta}_{1-y}\text{S}_2$ ($0 < y \leq 1/3$) are given elsewhere (19). The Mössbauer effect spectrum of $\text{Li}_{0.86}\text{Fe}_{0.05}\text{Ta}_{0.95}\text{S}_2$, which is different from the spectrum without lithium, shows two sets of quadrupole splitting resonance lines. The two main

resonance lines that correspond to one quadrupole splitting account for about 80% of the spectrum area. The quadrupole splittings (QS) and isomer shifts (IS) are: $QS(1) = 0.90 \pm 0.01$ mm/s, $QS(2) = 1.42 \pm 0.01$ mm/s, $IS(1) = 0.77$ mm/s, and $IS(2) = 0.75 \pm 0.01$ mm/s. The two different types of iron correspond to Fe^{2+} in the high-spin state. The isomer shift value of 0.77 mm/s is in agreement with the value predicted for Fe^{2+} in the high-spin state (19). The slightly smaller value for the isomer shift of 0.75 mm/s probably results from the absence of some lithium, since the maximum amount of lithium in the sample is $x = 0.86$. For $x = 0.5$ the spectrum is slightly more complex because of the dynamic low-spin-high-spin states in the compound. The spectrum essentially shows two sets of resonance lines with some iron in the low-spin and some in the high-spin state. For a better understanding of the cathodic reaction in $Li_xFe_yTa_{1-y}S_2$, more spectra as a function of x are necessary and are in the process of being obtained. These isomer shift results reflect a change in the electronic structure of the host from Ta^{4+} ($5d^1$) to Ta^{3+} ($5d^2$), and an increase in ionicity as the lithium content increases from 0 to 1. They also reflect the valence change of iron and indirectly that of tantalum as a function of the state of charge of the battery.

The $KFeS_2$ – $LiKFeS_2$ Cathode. Jacobson, Whittingam, and Rich (23) have shown that M_yFeS_2 compounds ($M = K, Rb, Cs$ for $y = 1$, and $M = Sr, Ba$ for $y = 1/2$) are electrochemically active, reversible cathode materials in a nonaqueous lithium electrochemical cell. The reactions of these compounds with lithium are more complex than those observed for the MS_2 systems described previously. The Li_xKFeS_2 ($0 \leq x \leq 1$) system has been studied in situ by Jacobson and McCandlish using the Mössbauer effect, and their results will be summarized (24). The structure of $KFeS_2$ is monoclinic and consists of infinite chains of edge-shared FeS_4 tetrahedra. K^+ ions occupy interchain sites, but vacant sites are available for lithium incorporation. The corresponding reduction at the cathode is from Fe^{3+} to Fe^{2+} . The reaction is not a simple intercalation reaction as in Li_xMS_2 dichalcogenides: it is more complex and involves a change of $KFeS_2$ to structurally different phases. The Mössbauer effect spectrum of Li_xKFeS_2 for $x = 0$ consists of a quadrupole split doublet (25). When $0 < x < 1$ the spectra are complex; for example, when $x = 0.5$ the spectrum was analyzed with four quadrupole doublets (24). The appearance of new iron sites at intermediate composition was associated either with chemically distinct iron atoms in a continuous, nonstoichiometric-phase Li_xKFeS_2 , or with the presence of distinct structural phases of Li_xKFeS_2 with slightly different compositions. The electrochemical reaction suggested at the cathode (23) has been confirmed by the Mössbauer effect data (24).

Conclusions

The overview discussed here shows that the Mössbauer effect is a powerful tool in the study of high energy density secondary battery materials. It can be applied successfully to obtain information about the electrochemical reaction at the cathode, guest–host interactions, structural changes, symmetry of the environment, and the change in electronic and magnetic properties of the host matrix. The Mössbauer effect isomer shift results for $\text{Li}_x\text{Fe}_y\text{V}_{1-y}\text{S}_2$ ($0 \leq x \leq 1$; $0 \leq y \leq 1/3$) show that the valence state of iron, and indirectly that of vanadium, changes as a function of the state of charge of the battery. These results reflect a change in the electronic structure of the host from V^{4+} ($3d^1$) to V^{3+} ($3d^2$) and an increase in ionicity as the lithium content increases from 0 to 1. The Mössbauer effect results indicate that the iron is divalent Fe^{2+} and changes from low-spin to high-spin at a certain concentration of lithium. Iron does not participate in the electrochemical reaction, but reflects the change in the electronic structure of the host.

Acknowledgment

The valuable contributions of my colleagues D. W. Murphy and F. J. DiSalvo, who are an integral part of this research program, are gratefully acknowledged.

Literature Cited

1. Cairns, E. J.; Shimotake, H. *Science* **1969**, *164*, 1347.
2. Whittingham, M. S. *Science* **1976**, *192*, 1126.
3. Murphy, D. W.; Trumbore, F. A. *J. Cryst. Growth* **1977**, *39*, 185.
4. Whittingham, M. S. *Progr. Solid State Chem.* **1978**, *12*, 1.
5. Wilson, J. A.; Yoffe, A. D. *Adv. Phys.* **1969**, *18*, 193.
6. Wilson, J. A.; DiSalvo, F. J.; Mahajan, S. *Adv. Phys.* **1975**, *24*, 117.
7. Steele, B. C. H., Ed. In "Fast Ion Transport in Solids"; North-Holland: Amsterdam, 1973; pp. 645-652.
8. Heyne, L. In "Fast Ion Transport in Solids; North-Holland: Amsterdam, 1973; pp. 123-139.
9. van Laar, B.; Ijdo, D. V. W. *J. Solid State Chem.* **1974**, *3*, 590.
10. Bichon, J.; Danot, M.; Rouxel, J. *Comp. Rend. C* **1973**, *276*, 1283.
11. Whittingham, M. S. *J. Electrochem. Soc.* **1976**, *123*, 313.
12. Murphy, D. W.; DiSalvo, F. J.; Cros, C.; Waszczak, J. V. *Inorg. Chem.* **1977**, *16*, 3027.
13. Murphy, D. W.; Carides, J. N.; Di Salvo, F. J.; Cros, C.; Waszczak, J. V. *Mat. Res. Bull.* **1977**, *12*, 825.
14. DiSalvo, F. J.; Eibschütz, M.; Cros, C.; Murphy, D. W.; Waszczak, J. V. *Phys. Rev. B* **1979**, *19*, 3441.
15. Eibschütz, M.; DiSalvo, F. J. *Phys. Rev. Lett.* **1976**, *36*, 104.
16. Eibschütz, M.; DiSalvo, F. J.; Hull, G. W.; Mahajan, S. *Appl. Phys. Lett.* **1976**, *27*, 464.
17. Eibschütz, M.; Hermon, E.; Shtrikman, S. *J. Phys. Chem. Solids* **1967**, *28*, 1963.

18. Oka, Y.; Kosuge, K.; Kachi, S. *Mat. Res. Bull.* **1977**, *12*, 1117.
19. Eibschütz, M.; Lines, M. E.; DiSalvo, F. J. *Phys. Rev. B* **1977**, *15*, 103.
20. Eibschütz, M.; Murphy, D. W.; DiSalvo, F. J. *Physica B* **1980**, *99*, 145.
21. Fleming, R. M.; Coleman, R. V. *Phys. Rev. Lett.* **1975**, *34*, 1975.
22. DiSalvo, F. J.; Wilson, J. A.; Bagley, B. G.; Waszczak, J. V. *Phys. Rev. B* **1975**, *12*, 464.
23. Jacobson, A. J.; Whittingham, M. S.; Rich, S. M. *J. Electrochem. Soc.* **1979**, *126*, 887.
24. Jacobson, A. J.; McCandlish, L. E. *J. Solid State Chem.* **1979**, *29*, 355.
25. Taft, C. A.; Raj, D.; Danon, J. *J. Phys. Chem. Solids* **1975**, *36*, 283.

RECEIVED July 22, 1980.

Mössbauer Studies of Colloidal Catalyst Solutions Used in Metallization of Plastics

R. L. COHEN

Bell Laboratories, Murray Hill, NJ 07974

The electronics industry uses a colloidal catalyst containing tin and palladium to make printed wiring boards and flexible circuits. This chapter reviews an extensive series of reports in which the chemistry of formation and stabilization of the colloid, and its interactions with the surface being treated, were elucidated. These studies were carried out mainly by Mössbauer spectroscopy of the ^{119}Sn , with additional information being gained from centrifugation and Rutherford backscattering analyses. Definition of the chemical processes occurring has allowed an improved procedure to be invented.

Most scientists are by this time familiar with the use of Mössbauer spectroscopy to study hyperfine interactions in solids, with the ultimate goals being the improved understanding of magnetism and electronic bonding in solids. Most of these experiments are carried out on relatively pure and carefully prepared samples. In recent years Mössbauer spectroscopy has become more widely used for "materials science" research, and also for studies of intermediate products in manufacturing processes. This volume contains a number of discussions of research in these areas, with special vigor demonstrated in studies of steels and coal. A characteristic of most of these studies is that the materials involved are usually *not* the pure, homogeneous, single-phase samples used in the basic research measurements. In fact, this complexity or heterogeneity is frequently the basis of the technologically interesting properties.

For such materials the following features of Mössbauer spectroscopy make it a particularly useful tool:

1. Since the resonance absorption is a purely nuclear process, its existence is inherently independent of the properties of the host (e.g., symmetry, metallic character), which sometimes interfere with the use of other resonance techniques.

0065-2393/81/0194-0539\$05.00/0

© 1981 American Chemical Society

2. The nuclear energy level perturbations observable using the Mössbauer effect arise only from the first few nearest-neighbor shells of an ion. Thus, short-range order, over as little as 10–15 Å, is adequate to provide sharp Mössbauer spectra. Glassy materials, disordered alloys, and very finely divided samples can all produce well-defined spectra.
3. Sample preparation is usually very simple—single crystals normally are not necessary, and no special polishing or surface treatment is required. Powder samples can be utilized readily.
4. The existence of chemically, crystallographically, or magnetically inequivalent sites is generally revealed by the appearance of distinct components, arising from the different sites, in the Mössbauer spectrum.
5. Although the technique is in principle limited to studying nuclei in solids, it is possible to investigate dissolved molecules and complexes by freezing the solutions and making measurements on the resulting solid.
6. It is possible to incorporate the radioactive source atoms in the material to be studied and thus combine the advantages of radioactive tracer experiments with those of the Mössbauer technique. Samples containing as few as approximately 10^{12} probe atoms thus can be studied.
7. Since nuclear energy levels in the range involved here are so narrow and sharply defined, gamma rays from any nucleus (e.g., ^{57}Fe) can be reabsorbed only by nuclei of the same type, since any other isotope will have absorption energies (corresponding to excited states) in a different energy region. Thus, experiments are absolutely specific to the particular isotope involved, and no cross-interference from other isotopes or elements ever arises.
8. The dependence of the recoil-free fraction on the properties of the host lattice allows investigation of the Debye temperature and anharmonic binding forces via the temperature dependence of the resonance intensity.

The significance of some of these points is clear in the following discussion, which reviews extensive research on colloidal catalysts used in the electronics industry. So far as we are aware, the papers cited here are the only Mössbauer spectroscopy measurements in this field, and (except for one brief subsequent paper that served to confirm the results of the Mössbauer measurements) are the only published studies of these materials.

Colloidal Catalyst Systems

A few years ago, we learned that the entire electronics industry was making printed wiring boards (the insulating panels with copper conductor patterns, on which integrated circuits and components are

mounted) using a process called "sensitization and electroless plating." With this process, it is possible to put an adherent coating of metal on plastic. The metal can be deposited on "through-holes" to connect conductors on different sides of the panel, or can be used to build up the entire pattern. The same process also is used widely in automobile and appliance factories to metallize plastic trim parts. The process as seen by the plant manager contained basically three steps: sensitization, acceleration, and electroless plating, as shown in Figure 1. The last step, electroless plating, was relatively well understood: The solution consisted (typically) of copper ions, a complexing agent (EDTA), a reducing agent (formaldehyde), and a strongly alkaline aqueous electrolyte (KOH). The reducing agent concentration was adjusted to make the solution metastable to the reduction of copper ions to copper metal. Then the introduction of a catalytic surface (e.g., copper metal) leads to the deposition of metallic copper on the surface. The untreated plastic surface will not initiate copper deposition. The purpose of the sensitizing step was then, presumably, to load the plastic surface to be metallized with catalytic material. The purpose of the acceleration step was not at all clear, but it made the initial copper deposition occur much more rapidly (hence the name).

This process came into commercial use in about 1962, and by 1972 when we started this research, it was being used to manufacture hundreds of millions of dollars of product each year. No research article discussing the action of the sensitizer and accelerator baths had ever been published. A number of patents covering composition of the baths had been issued, but they were in severe conflict in the microscopic models they presented for the chemical reactions occurring. The common elements among these descriptions were that the sensitizers were made using SnCl_2 , PdCl_2 , and HCl , and that the accelerator contained fluoboric acid or some other strong acid or alkali. The proposed model which looked the best (1) was that the Sn^{2+} reduced the Pd^{2+} ions to the metallic state,

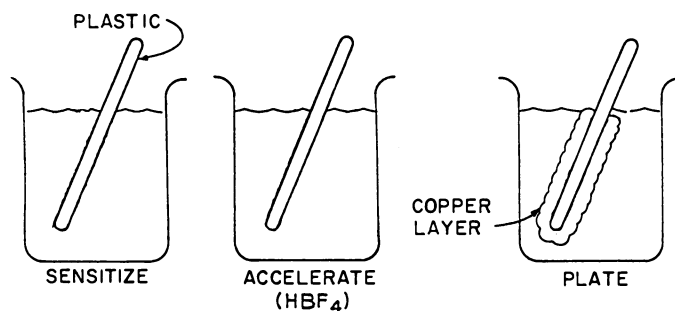


Figure 1. Basic steps in metallizing plastics by electroless plating. Rinses have been omitted.

forming a colloidal palladium catalyst that was adsorbed on the plastic surface. Arguments presented against this model, and in favor of a tin-palladium complex model, were that the sensitizer solution did not scatter light (no Tyndall effect) and that it could not be separated centrifugally.

We set out to trace the chemical processes occurring in making the sensitizer solution. Although the reactions took place in a liquid phase, it was possible to study them via Mössbauer spectroscopy of the ^{119}Sn , if the solutions were frozen rapidly so as to retain the tin ions complexed as they were in the liquid. (It is not obvious that this is possible—one must look for a system that freezes into a “glassy” state, remaining a single phase, rather than phase separating into hydrated salts and a frozen pure electrolyte (2).) In this sensitizer work, we found that the $\text{HCl-H}_2\text{O}$ electrolyte was itself a good glass-forming system, and did not need glass-forming additives. We started out with a solution of Sn^{2+} in HCl , and then added the Pd^{2+} ions, also in HCl . We took samples of the solutions at various times after the initial mixing, and froze those samples to 78 K to stop the reaction and to solidify the solutions for the Mössbauer study. Figure 2 shows the results of the experiments (3). The tin is initially present as chlorine-complexed Sn^{2+} (Figure 2A). Immediately upon the addition of the palladium solution, the spectrum of the tin changes to that of Figure 2B. Obviously, the tin has somehow combined with the palladium ions. The isomer shift and large quadrupole splitting of the tin lines are consistent with those expected for a π -bonding complex. The tin solution has changed from being essentially colorless to an intense red-brown. After a few minutes, the solution color changes further, toward a grayish or greenish brown. The Mössbauer spectrum shows that the lines of the initial tin-palladium complex disappear, and are replaced by three new lines (Figure 2C). Initially, only one of these lines can be explained readily—the line at 0.5 mm/s (which arises from chlorine-complexed Sn^{4+}), which has apparently been returned to the electrolyte as the end product of a redox reaction which has reduced the palladium ions. The origin of the other two lines can be determined from a combination of oxidative coagulation, which is irreversible, and very intense centrifugation, which is able to concentrate the colloidal particles without coagulation. Earlier reports that the material could not be separated centrifugally did not anticipate the extraordinarily fine particle size attained in this colloidal system—accelerations of 100,000 G for 24 h are required. Figure 2D shows the spectrum of the centrifugally separated particles. The centrifugal separation makes it clear that the tin is present in the electrolyte, as dissolved chlorine-complexed Sn^{4+} , and in two forms in the centrifuged particles—one with a line near 1.6 mm/s, the other with a line near 3 mm/s. If an uncentrifuged suspension of the particles is oxidized by exposure to air, the line near 3 mm/s decreases in intensity, the line at 1.6 mm/s stays at the

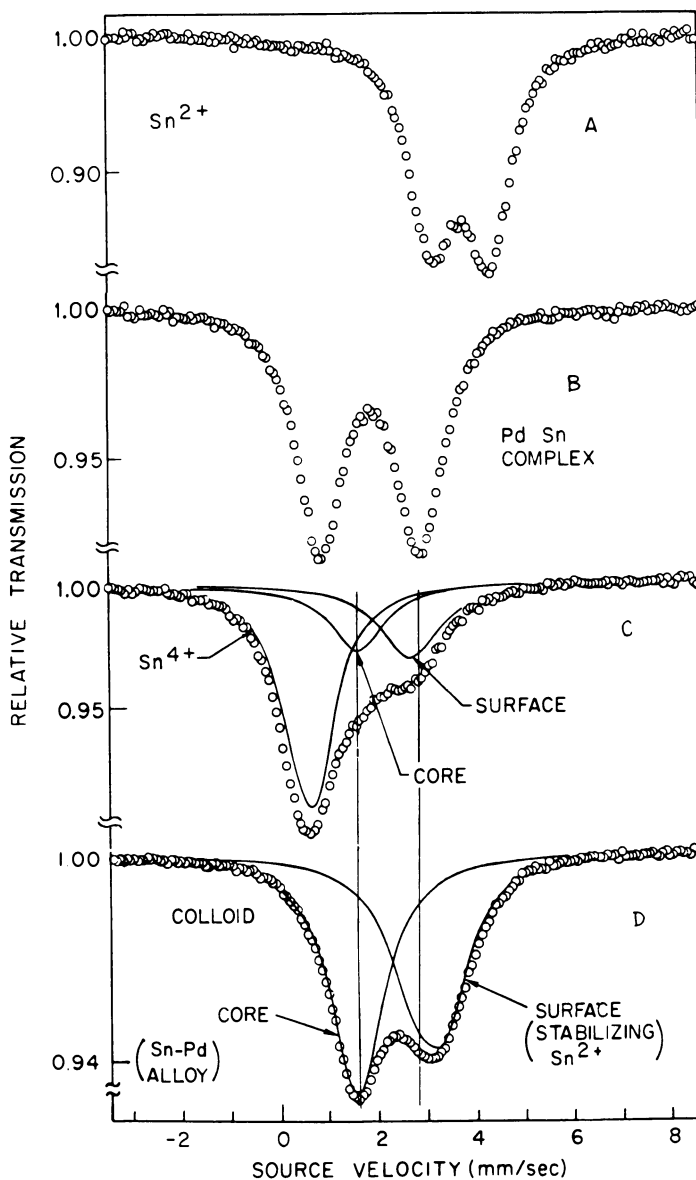
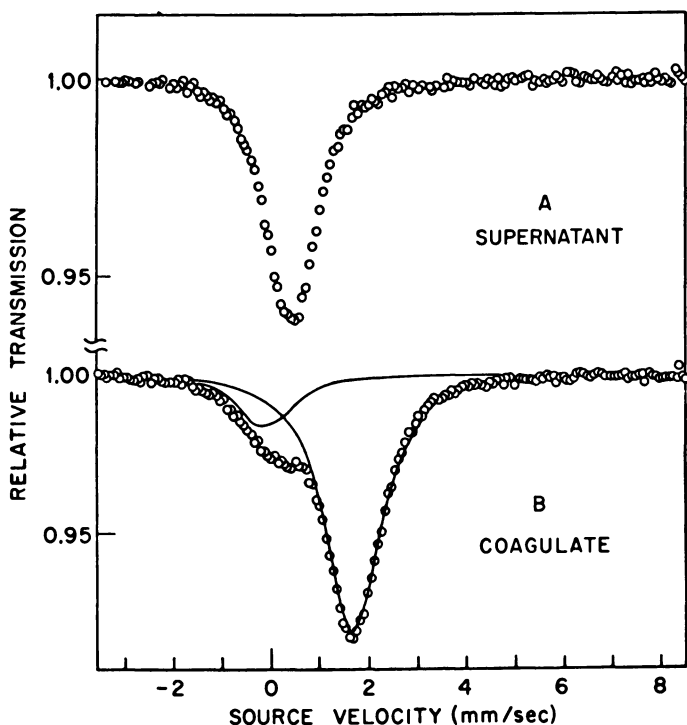


Figure 2. ^{119}Sn Mössbauer spectra tracing the chemical reactions in the successive steps of manufacture of the palladium-tin colloidal catalyst system (3, 4). Spectra taken in frozen solutions.



Journal of the Electrochemical Society

Figure 3. Spectra of oxidatively coagulated colloidal catalysts: (A) chlorine-complexed Sn^{4+} ; (B) palladium-tin alloy (3)

same intensity, and additional Sn^{4+} appears. Suddenly, just as the line at 3 mm/s disappears, the particles coagulate, and the suspension changes from a dark liquid to a colorless liquid with a small amount of spongy black material at the bottom of the tube. The coagulate now shows only the 1.6-mm/s line (Figure 3B) and the solution only Sn^{4+} (Figure 3A). Clearly, the tin species that produced the line at 3 mm/s was acting as the colloid stabilizer, preventing the coagulation. The precipitate, its spectrum unchanged from that when it was suspended, can be identified by both Mössbauer spectroscopy and x-ray diffraction as an alloy of about $\text{Sn}_{0.15}\text{Pd}_{0.85}$. One can now reconstruct the colloid formation process: The tin and palladium combine initially to form a polynuclear complex, which is unstable. This decomposes via a redox reaction, producing metallic palladium, and returning Sn^{4+} to the electrolyte. Some amount of tin is reduced also and is included in the metallic palladium to make the palladium-tin alloy.

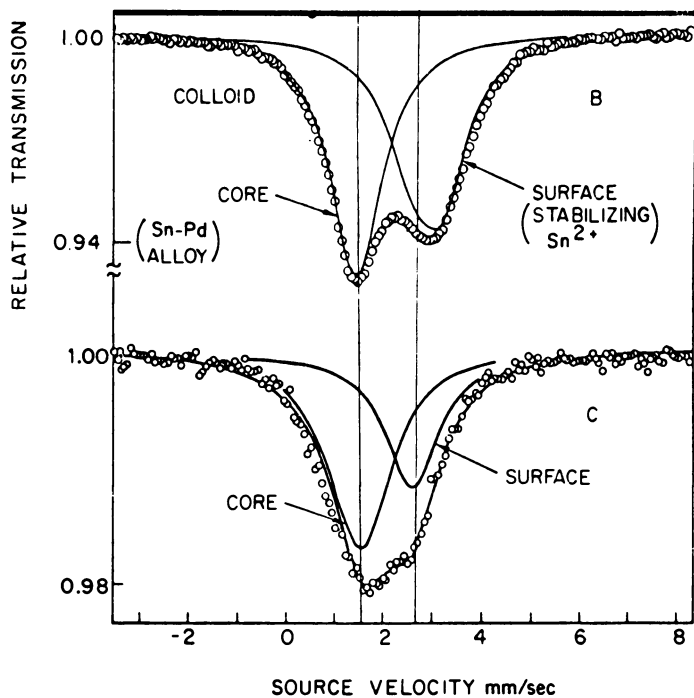
The role of the divalent tin as a stabilizer now can be examined. Both in the commercial catalyst preparation and in our initial experiments, we used an amount of Sn^{2+} substantially in excess of that needed

to reduce the palladium from Pd^{2+} to Pd^0 (metallic). If the molar ratio of $\text{Sn}^{2+}/\text{Pd}^{2+}$ in the initial solution is less than 1.5, no stable colloid is formed—the palladium ions are indeed reduced, but they coagulate and form a precipitate immediately. This again emphasizes the role of the Sn^{2+} as a stabilizing species. Since the Sn^{2+} would be present in the solution as SnCl_3^- complexes, and since these complexes are known to form strong tin–palladium bonds, one could even guess that the stabilizing mechanism was that the SnCl_3^- complexes were adsorbed onto the palladium–tin alloy particles until the surface was covered with a monolayer of complexes. If there were not enough Sn^{2+} to coat the surface, the particles would coagulate. If there were some Sn^{2+} present, one could imagine that the palladium particles would agglomerate until the surface had decreased to match the amount of Sn^{2+} available, at which point the growth would stop. This immediately suggests that the colloid particle size could be controlled by adjusting the amount of available Sn^{2+} , and that turns out to be the case.

We made colloids using ratios of $\text{Sn}/\text{Pd} = 3$, and $\text{Sn}/\text{Pd} = \sim 2.5$. From the sedimentation rate in centrifugation, the latter solution was in fact determined to contain a larger particle size distribution of the palladium alloy particles. We also studied the Mössbauer spectra of the centrifugally separated particles, and obtained the results shown in Figures 4B ($\text{Sn}/\text{Pd} = 3$) and 4C ($\text{Sn}/\text{Pd} = \sim 2.5$). The spectra of the two sets of particles look similar, but the Sn^{2+} stabilizing line is relatively weaker in the sample with the larger particle size, as would be expected, since the particle surface/volume ratio is smaller.

We also can verify this model quantitatively. Sedimentation rate data yield a mean size of about 30 Å diameter for the particles in Figure 4B. If the alloy cores contain approximately 15 at. % Sn, each particle would contain about 100 tin atoms. If the SnCl_3^- complexes each cover an area of about 16 \AA^2 (4), about 200 complexes would be required for monolayer coverage of the particle. The spectrum shows roughly equal intensities for the two components, which is pretty good agreement considering that the f value is not known for the stabilizing complex. Thus, the somewhat speculative nature of the proposed model has been borne out both by the prediction of particle size dependence on tin concentration, and by the quantitative determination that the amount of the adsorbed tin complex corresponds roughly to monolayer coverage. We also verified that the colloidal materials we were preparing were similar to those in the commercial (proprietary) sensitizer systems by centrifuging the latter and observing that the spectra of those particles were similar to those of the model systems we had examined.

It is worthwhile to point out that the Mössbauer technique was particularly useful in these experiments because it gave us well-defined spectra even from monolayers and very small particles, and allowed



Chemical Physics Letters

Figure 4. Spectra of centrifugally separated particles from colloidal catalysts with different surface/volume ratios (4)

determination of the valence state of the tin. The ability to monitor reactions proceeding in the solution via the frozen-solution technique also was vital. This approach has been used only in a few chemistry studies to date, and probably could be applied more widely.

After this success in discovering the composition of the catalyst solutions, we turned to studying the acceleration step. Since we had established that the sensitizer contained palladium alloy particles, and since palladium is an excellent catalyst, it seemed obvious that the plastic surface was adsorbing palladium particles, and that those were the catalytic sites in the copper plating bath. But what was the role of the accelerator?

We undertook a new series of experiments in which the Mössbauer technique (to tell us about the tin chemistry) was combined with Ruthenium backscattering (5) to tell us about the elemental composition of layers on the surface at various points in the process. Cleaved graphite was used as a substrate in these experiments, both for its convenience and simple surface chemistry. A more complete picture of the production process is given in Figure 5, which also shows the conclusions of

the research (6). The backscatter spectrum (Figure 6) shows that after the accelerator step, most of the tin has been removed, but the amount of palladium has remained roughly the same. Both the backscatter and Mössbauer spectra have been normalized so that the presence of a particular element or phase is proportional to the height of the corresponding peak in the spectrum. Thus, we can see from the backscatter spectrum that the main role of the accelerator step is to remove tin from the surface—the palladium concentration is unchanged. The backscatter spectrum after the sensitization and rinse step shows that far more tin is on the surface than we would have expected from the model above—the palladium–tin alloy cores contained only about 15% tin, and even if the surface passivating layer were retained when the colloidal par-

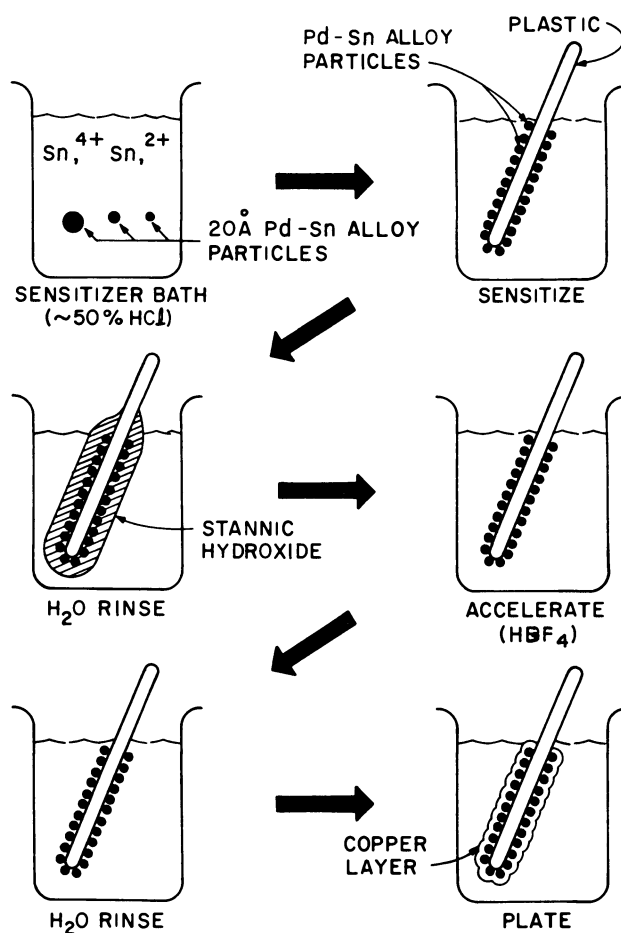


Figure 5. Schematic of surface chemistry processes occurring in sensitization and acceleration steps

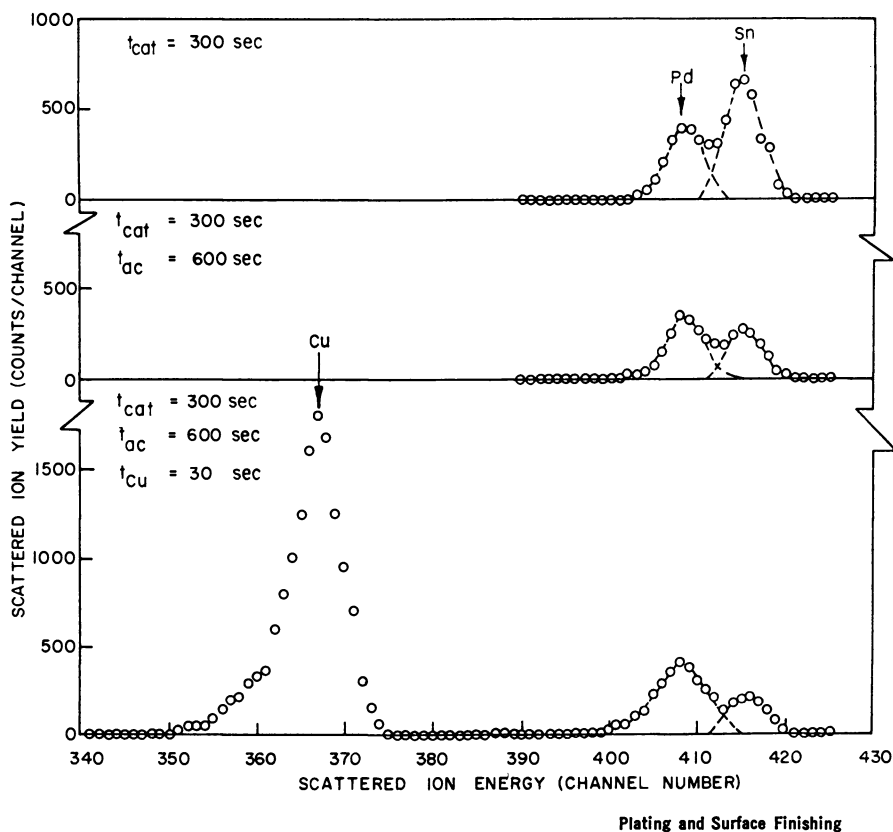


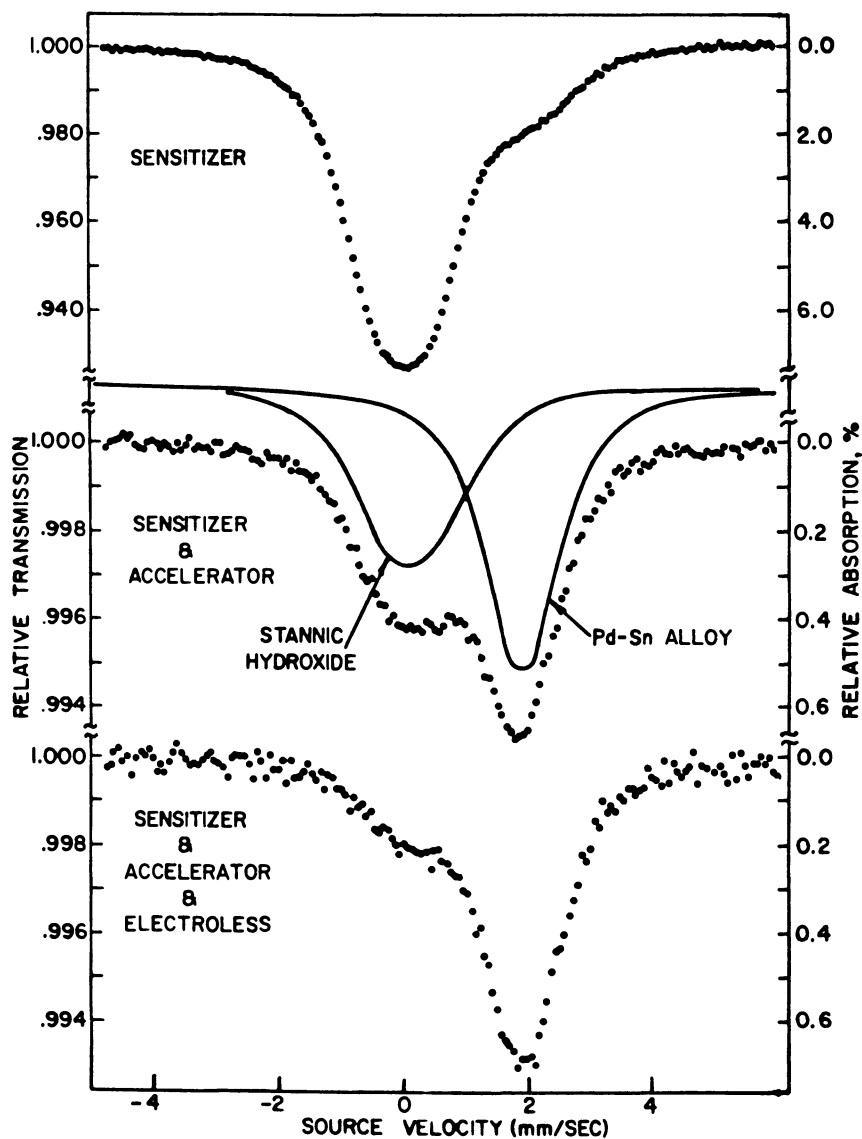
Figure 6. Rutherford backscatter spectra of surfaces after sensitization, acceleration, and short electroless plating treatments (7)

ticles were adsorbed, the surface layer should have 2–3 times as much palladium as tin. In fact, the surface layer has about half as much palladium as tin.

The Mössbauer spectra show that this extra tin is present as Sn^{4+} , shown by the strong absorption line at zero velocity. In fact, after the sensitization step, the tin line from the palladium–tin alloy is almost invisible on the shoulder of the line from Sn^{4+} . The accelerator solution removes most of the Sn^{4+} (middle spectrum in Figure 7, note change in scale), and leaves the tin in the palladium–tin alloy as the dominant species. Where did the extra tin come from?

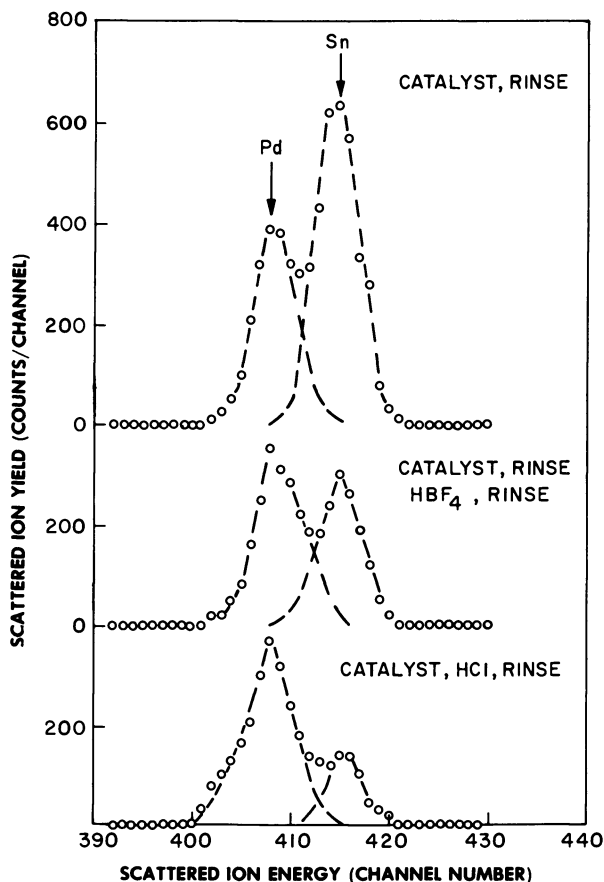
The key to understanding these phenomena is the realization that the sensitizer bath contains a large amount of dissolved Sn^{4+} . This comes from impurities in the SnCl_2 used to make the sensitizer, the redox reaction by which the palladium is reduced, and air oxidation of dissolved Sn^{2+} during use of the bath. The Sn^{4+} is dissolved stably in the

strong HCl electrolyte, being complexed with chlorine ions. In the water rinse after the sensitization step, however, the Sn^{4+} is hydrolyzed and immediately precipitated as stannic hydroxide. The amount of stannic hydroxide formed in the rinse step is enough to form a layer about 100–200 Å thick. This apparently acts as a passivating layer covering



Plating and Surface Finishing

Figure 7. Mössbauer spectra of surfaces at successive stages in process sequence, as in Figure 6 (7)



Plating and Surface Finishing

Figure 8. Rutherford backscatter spectra showing relative palladium and tin concentrations on sensitized surfaces (top) with no acceleration, (middle) after standard acceleration treatment, and (bottom) new sequence using HCl rinse (8)

the palladium-tin particles, and the role of the accelerator step is to remove this stannic hydroxide layer, exposing the adsorbed particles so that they can catalyze deposition of copper from the electroless solution. Thus, the purpose of the acceleration step is to remove a material that was only inadvertently deposited on the surface.

With this microscopic understanding of the chemistry, it is possible to redesign the process to eliminate the acceleration step (7, 8). We expected that if the sensitizer solution were washed off the surface with HCl instead of water, the hydrolysis of the Sn^{4+} and stannic hydroxide precipitation would not occur. (A water rinse after the HCl is still necessary to prevent carryover of HCl into the alkaline electroless solu-

tion.) Figure 8 shows that this approach is very successful—the residual tin remaining after the HCl rinse is even lower than that achieved by the acceleration step. The atomic ratio of Pd/Sn is in fact about 4, approximately what would have been expected from the colloid model just discussed. Surfaces produced using the HCl rinse are more effective catalysts for the deposition of copper from the plating solution than those made by the standard process. Additionally, the HCl is far cheaper and less toxic than the fluoboric acid usually used in the acceleration step.

It is worth emphasizing that this advance was a direct consequence of the microscopic understanding of the process, obtained through the research described here. Over the ten years that the process had been in commercial use, a wide variety of materials and process were used for acceleration, and many patents were issued—but no one thought of the simple expedient of the HCl rinse, because no one knew what was happening on the surface.

Conclusions

I have discussed an application of Mössbauer spectroscopy to materials science problems. Materials used in the real world, and processes used to manufacture them, are in many cases very poorly understood. Studying these materials can be very difficult, because of their complexity and (in many cases) poorly controlled origin. But many poorly understood phenomena are susceptible to attack with new tools and knowledge. In some cases, as exemplified by the colloid studies cited here, the applied-science study may become the gateway to interesting new areas of basic science research.

Literature Cited

1. Shipley, Jr., C. R. U.S. Patent 3 011 920, 1961.
2. Cohen, R. L.; West, K. W. *Chem. Phys. Lett.* **1972**, *13*, 482.
3. Cohen, R. L.; West, K. W. *J. Electrochem. Soc.* **1973**, *120*, 502.
4. Cohen, R. L.; West, K. W. *Chem. Phys. Lett* **1972**, *16*, 128.
5. Chu, W.-K.; Mayer, J. W.; Nicolet, M. A. "Backscattering Spectrometry"; Academic: New York, 1978.
6. Cohen, R. L.; Meek, R. L. *J. Coll. Int. Sci.* **1976**, *55*, 156.
7. Cohen, R. L.; Meek, R. L. *Plating and Surface Finishing* **1976**, (5), 52.
8. Cohen, R. L.; Meek, R. L. *Plating and Surface Finishing* **1976**, (6), 47.

RECEIVED July 22, 1980.

Characterization of Mixed-Metal Catalysts by Iron-57 and Ruthenium-99 Mössbauer Spectroscopy

M. L. GOOD¹, M. D. PATIL, J. T. DONNER, and C. P. MADHUSUDAHAN²

Division of Engineering Research, Louisiana State University,
Baton Rouge, LA 70803

Iron-57 and ⁹⁹Ru Mössbauer spectroscopy have been used to assess the chemical composition of an iron-ruthenium bimetallic catalyst system as a function of preparation and treatment. Supplementary data from ESCA spectroscopy and x-ray powder diffraction made it possible to completely characterize the material from the initial salt mixture through a hydrogen reduction and a subsequent calcination step. RuCl₃ · xH₂O and FeSO₄ · xH₂O were mixed in a 1:2 mole ratio in the solid state, slurried with a small amount of water, and evaporated to dryness. The product contained a mixture of iron(II) and iron(III) salts and some anhydrous RuCl₃. This material was reduced under flowing H₂ at 400°C for 4 h. Surprisingly, the "reduced" product contained ruthenium metal, RuO₂, bulk γ-Fe₂O₃ (some FeS), and a fraction of small-particle paramagnetic γ-Fe₂O₃. After calcination the product was unchanged except for the loss of the FeS and an increase in the average particle size. The study indicates the special application of ⁹⁹Ru Mössbauer spectroscopy to such solid-state problems and the extra versatility gained by "double Mössbauer labeling."

The complete physical and chemical description of heterogeneous metallic catalysts and the relationship between their properties and their catalytic activity has become the goal of numerous groups of investi-

¹ Current address: Universal Oral Products, Inc., Des Plaines, IL 60016.

² Current address: Englehard Industries Division, Menlo Park, Edison, NJ 08817.

gators. The overall theme of their work is to understand better the interrelationships among electronic structures, physical characteristics, and catalytic activity so that more effective catalysts can be designed rather than discovered. Since most heterogeneous catalyst systems are complex solid-state mixtures of metal and support, the complete description in both chemical and physical terms is very difficult, if not impossible to achieve. However, during the past decade new physical tools have become available to probe these materials, and our detailed knowledge of their molecular and solid-state structures is improving at a rapid rate. Electron microscopy has become a routine tool (joining the long available x-ray diffraction techniques) for accessing the physical state of heterogeneous catalysts, and the improvement in resolution down to a few angstroms has made it possible to "see" even small clusters of metal atoms highly dispersed on a support material (1, 2). New and improved spectroscopic techniques, particularly ESCA, Auger, and magnetic resonance methods, are now used routinely for probing the electronic properties and elemental composition of the surface and bulk of supported and mixed-metal catalysts (3, 4, 5). A relatively recent addition to this arsenal of physical methods is Mössbauer spectroscopy, which can provide unique information in special cases involving a metal having a nucleus that is Mössbauer active. The utility of this method has progressed to the point where Mössbauer spectroscopy is included in any general discussion of spectroscopic methods for evaluating heterogeneous catalyst systems (6). In those cases where it is applicable, this technique has several advantages for heterogeneous catalyst characterization. It is basically a solid-state measurement which in the transmission mode can penetrate solid substrates that are opaque to energies in the optical or vibrational spectral ranges, and in the backscatter mode can provide information about surface species. The method provides chemical speciation information through "fingerprint" spectra, and structural and particle size information by analysis of quadrupole splitting parameters and magnetic spectra. Used in conjunction with other methods such as ESCA, x-ray, and electron diffraction, Mössbauer spectroscopy can provide definitive chemical and physical parameters for heterogeneous catalyst systems, both supported and unsupported. Particularly significant measurements can be made in those few cases where mixed-metal catalysts contain more than one Mössbauer-active nuclide. This chapter reports the results of such a case where an unsupported catalyst system of iron and ruthenium was characterized as a function of catalyst treatment.

Bimetallic Catalyst Systems—The Special Case of Ruthenium—Iron

Until quite recently, most bimetallic or alloy catalysts have been bulk materials with low surface areas, usually formulated as pressed

powders, wires, or foils. However, the ever increasing need for more efficient and more selective catalysts has stimulated a number of studies of bimetallic materials of high surface area dispersed on a variety of supports. Mössbauer spectroscopy has been especially effective in determining the chemical states of these dispersed materials where other techniques provide only limited information. Illustrative examples are the platinum-iron alloys on graphite (7); the palladium-iron alloys on alumina (8, 9); the ruthenium-iron alloys on silica (10); and the nickel-iron alloys on silica (11, 12, 13). In each case, only iron Mössbauer spectroscopy was carried out, and the chemical state of the second metal was inferred from the iron data or determined by other, usually less definitive, methods. The Mössbauer data provided additional information of catalytic significance by exhibiting superparamagnetic spectra associated with the very small particles dispersed on the supports. An analysis of this feature of the various spectra allowed the determination of the particle sizes of the active catalyst materials. The success of these studies, and particularly the information obtained from just the iron Mössbauer spectra for the ruthenium-iron system, suggested that similar studies where both metals were susceptible to Mössbauer spectral analysis might be quite productive and indeed, might have the potential to eliminate certain ambiguities left by the fact that so far only the iron in the bimetallic mixtures has been studied.

Several classic studies using other Mössbauer-active nuclei to study alloys have been reported, although in general these have been directed toward understanding the electronic effects in pure metallic alloys instead of following the chemical and physical changes that occur during the preparation and manipulation of catalyst materials. The electronic and magnetic properties of the high-pressure hexagonal phase of iron (ϵ -phase) have been probed by alloying iron with ruthenium and osmium, and observing the iron Mössbauer spectra (14, 15, 16). Similar studies to observe internal hyperfine fields and alloy electronic structures have been carried out on iron-rhodium alloys (17, 18) and other ferromagnetic alloys (19, 20). A few systems have been investigated by probing with other Mössbauer nuclei. Iron-platinum alloys have been studied both in transmission and backscatter experiments using the 99-keV transition in ^{195}Pt (21, 22, 23). The results of these studies have provided the necessary data for constructing and evaluating theoretical models of the electronic structure of these alloys at the atomic level, and have allowed the deduction of the mechanism of transferred hyperfine fields in these materials. One similar study has been reported using the 73-keV Mössbauer line in ^{193}Ir for observing the hyperfine field in iron-platinum-iridium alloys (24). These reports indicate the potential utility of the Mössbauer effect in probing the chemistry, magnetic properties, and particle structure of "double-labeled" bimetallic systems.

The proven utility of the ^{99}Ru Mössbauer probe for assessing the complex chemistry of a variety of ruthenium compounds (25) and for describing the chemical transformations that accompany various treatments of ruthenium species on catalytic supports (26–29) would indicate that it may be a nuclide of choice for examining bimetallic catalysts in general. This is quite fortuitous since both iron and ruthenium are known to be effective Fischer–Tropsch catalysts (30), and their bimetallic systems exhibit interesting selectivity in hydrocarbon production from CO/H_2 (10, 31) and in nitrogen fixation (32). Thus we have begun a systematic study of iron–ruthenium bimetallic catalyst systems, both supported and unsupported. This chapter represents the first complete study of an unsupported system where both ^{57}Fe and ^{99}Ru Mössbauer spectroscopy have been applied to the same samples. Supplementary information from ESCA spectroscopy and x-ray diffraction has made it possible to define completely the solid-state reactions that accompany the physical and chemical treatment of the bimetallic materials. Preliminary results of a similar study on the bimetallic system on a zeolite support have been reported separately (33).

Details of the Acquisition and Interpretation of ^{99}Ru Mössbauer Spectra

The experimental conditions necessary for the collection of good-quality ^{57}Fe Mössbauer data and methods for their subsequent interpretation are now well known and easily accessible in the primary and secondary literature. Thus no detailed background material on this technique will be presented. However, similar information for the ^{99}Ru system is not readily available, and a substantial outline of the problem will be presented here for the readers' convenience. A review of ^{99}Ru and ^{101}Ru Mössbauer spectroscopy through 1973 is available, and is recommended reading for the serious experimentalist (25).

The 90-keV Mössbauer transition in ^{99}Ru was first discovered by Kistner and co-workers who reported the spectrum for a metal absorber at 85 K (34). These workers observed a single-line resonance of 0.37-mm/s linewidth with a calculated lifetime for the 90-keV level of 8×10^{-9} s as a lower limit. This value compared favorably with the well-known value for the 14-keV Mössbauer level in ^{57}Fe . Subsequent work using the delayed-coincidence method produced a lifetime value of $(20 \pm 1) \times 10^{-9}$ s (35). Further experiments at liquid-helium temperature (both source and absorber) provided detailed information about the nuclear parameters of the Mössbauer transition (36, 37). An iron–ruthenium alloy exhibited a well-resolved, 18-line, magnetic hyperfine spectrum that was uniquely fit by a model assuming a mixed dipole–

quadrupole (M1-E2) transition from $I = 3/2$ to $I = 5/2$. Further analysis produced a value of -0.19 ± 0.05 for the magnetic g -factor (g_1) of the 90-keV state and a value of 2.7 ± 0.6 for the E2/M1 mixing ratio δ^2 , with the assignment of a negative sign to the mixing parameter δ . A close examination of the quadrupole-split spectra of ruthenocene $[\text{Ru}(\text{C}_5\text{H}_5)_2]$ and ruthenium dioxide (RuO_2) indicated that the observed doublet was a consequence of the dominance of the nuclear quadrupole moment of the excited $3/2$ state, with a value of $Q_1/Q_0 \geq 3$. These early studies by Kistner and co-workers provided the necessary nuclear parameters and the verification of large chemical isomer shifts for non-metallic absorbers that led to the exploitation of ^{99}Ru Mössbauer spectra to elucidate the complex chemistry of ruthenium systems. Thus both unique compounds and various mixtures of chemical interest can be addressed.

Experimentally, good-quality ^{99}Ru Mössbauer spectra are difficult and expensive to obtain. The 16-day ^{99}Rh precursor of the excited state of ^{99}Ru was first produced by 10-MeV proton bombardment of metallic ruthenium in the cyclotron. Sources can be prepared from natural ruthenium (12.7% ^{99}Ru) or from metal enriched with ^{99}Ru (>98% ^{99}Ru). The natural metal sources are only usable between two and six weeks after bombardment because of short- and long-lived ^{101}Rh contaminants. High specific activity sources having longer useful lives can be prepared from an enriched target by chemically separating the resulting ^{99}Rh and co-precipitating it with a small amount of natural ruthenium metal (36, 37). Where ruthenium metal serves as the host lattice, single resonance linewidths close to the natural linewidth have been achieved, although the metal has a hexagonal crystal structure. The actual preparation of the source is somewhat of an art rather than a science, and quality has been a variable from source to source, even from the same vendor. In every case, the high-energy (90-keV) Mössbauer transition and the low Debye-Waller factors for most ruthenium compounds (as compared to ruthenium metal) have made it necessary to obtain ^{99}Ru Mössbauer spectra at low temperatures, preferably having both the source and absorber cooled to 4.2 K. The lifetime of the excited state of ^{99}Ru and the magnitude of the chemical isomer shifts are comparable to those of ^{57}Fe , thus making it possible to utilize ^{57}Fe instrumentation without modification, except for the gamma detector which must be optimized for the higher energy 90-keV x-ray. Most workers have used large glass or metal liquid-helium Dewars, where the spectrometer velocity drive motor is mounted vertically on top of the Dewar and attached to the source via a long drive rod extending into the liquid-helium bath (36-39). For most reported spectra, a NaI (Tl) scintillation detector has been used (a 3-mm thick crystal is optimal) to assay the

90-keV gamma rays, although a germanium–lithium drifted detector can provide improved resolution (26). Velocity calibration is provided in the usual way, either using an ^{57}Fe source and pure iron foil absorbers or using laser interferometry for absolute velocity measurements (40). All isomer shift values have been reported with respect to metallic ruthenium, although this material is subject to some unresolved quadrupole splitting. Cohen and Kalvius (41) and the National Research Council Ad Hoc Panel on Mössbauer Data (42) have recommended the use of $\text{K}_4[\text{Ru}(\text{CN})_6] \cdot 3\text{H}_2\text{O}$ as an isomer shift standard. This cyanide complex has the advantage of a symmetric ruthenium site that provides a single, narrow line just slightly broader than the natural linewidth; however, it suffers from a low recoil-free fraction that requires long run times to provide data with suitable statistics. Typical ^{99}Ru Mössbauer spectra are of overall poorer quality than analogous ^{57}Fe spectra because of the smaller recoil-free fraction and the need for large samples (i.e., 50–100 mg of ruthenium per cm^2 are typically required for adequate signal-to-noise ratios in the observed spectrum).

The relatively large isomer shifts compared to the observed linewidths reported for ^{99}Ru Mössbauer spectra implied that the technique should have significant potential for providing chemical information about ruthenium systems. This was an exciting prospect in view of the complex chemistry of ruthenium, an element which exhibits formal oxidation states from zero to positive eight in a large variety of compounds and which has a tendency to form multinuclear complexes with mixed-metal oxidation states, metal–metal bonds, and bridging ligands. The mechanisms of complex ruthenium reactions and the structure of ruthenium complexes have taxed the skills and insight of numerous ruthenium chemists since the early experiments on the material in the latter part of the last century. Thus there was an already established clientele for the application of ^{99}Ru Mössbauer spectroscopy to chemical problems. Kistner and co-workers (36, 37) provided the first correlation of ^{99}Ru Mössbauer parameters with chemical bonding by relating the doublet splitting in RuO_2 and ruthenocene to the sign and magnitude of the electric field gradient at the ruthenium nucleus in these two compounds. The doublet spectrum reported for these compounds is typical for ruthenium spectra of systems expected to have quadrupole interaction in the absence of magnetic hyperfine interactions. Each component of the doublet consists of an unresolved triplet which is a consequence of the $I = 3/2 \rightarrow I = 5/2$ transition, where the large $Q_{3/2}/Q_{5/2}$ allows the simple quadrupole splitting of the excited $I = 3/2$ state to predominate. For spectra of this type, the isomer shift usually is reported as the center of the doublet, and the doublet splitting is referred to as ΔE_Q . This simple

extraction of Mössbauer parameters is over-simplified for very precise values (43, 44, 45), but is quite practical for routine chemical analysis and fingerprinting of particular ruthenium species.

Isomer shift trends in several series of ruthenium compounds have been reported. The first extensive study by Wagner, Mössbauer, and co-workers (46) indicated that a monotonic increase in isomer shift occurred with increasing oxidation number. This indicated a positive nuclear factor ($\Delta R^2/R$) for ^{99}Ru based on the assumption that the *s*-electron density at the ruthenium nucleus increased as the *d*-electron shielding was reduced with increasing oxidation states. This assumption was further substantiated by Clausen, Prados, and Good (38) who calculated the total charge density at the ruthenium nucleus using restricted Hartree-Fock wave functions of the *s*-electron density at the nucleus for specific oxidation states. Both of these studies identified more subtle chemical effects by observing that the electron delocalization effected by certain ligands such as nitrosyl (NO^+) could be semi-quantitatively described by comparing isomer shifts within a homologous series of compounds. This concept has been exploited further by relating the isomer shifts in a series of ruthenium(II) pentaamines ($[\text{Ru}(\text{NH}_3)_5X]^{2n}$ where $X = \text{NO}^+$, CO , SO_2 , N_2 , pyrazine, CH_3CN , $\text{C}_6\text{H}_5\text{CN}$, pyridine, and NH_3) to the relative σ - and π -bonding capabilities of the sixth ligand (47). The utility of the ^{99}Ru Mössbauer parameters for describing chemical bonding and structure in simple ruthenium complexes can best be illustrated by examining the values obtained for a series of ruthenium(II)-cyanide complexes (48). These parameters are: (1) $\text{K}_4[\text{Ru}(\text{CN})_6]$; IS = -0.25 mm/s; $\Delta E_Q = 0.0$ mm/s; (2) $\text{K}_2[\text{Ru}(\text{CN})_5\text{NO}] \cdot 2\text{H}_2\text{O}$; IS = $+0.03$ mm/s; $\Delta E_Q = 0.49$ mm/s; and (3) $\text{K}_4[\text{Ru}(\text{CN})_5\text{NO}_2] \cdot 2\text{H}_2\text{O}$; IS = -0.40 mm/s; $\Delta E_Q = 0.35$ mm/s. First, the isomer shift for the hexacyano complex is significantly larger than the comparable value for the ruthenium(II)-hexamine (46, 47, 49), -0.25 vs. -0.92 mm/s, indicating the effective delocalization of two *d*-electrons from the t_{2g}^6 level of ruthenium(II) into the cyanide orbitals. Note that the isomer shifts decrease in the order of ligand substitution as $\text{NO}^+ > \text{CN}^- > \text{NO}_2^-$, and the quadrupole splitting is greater for NO^+ than for NO_2^- . The large increase in isomer shift for NO^+ (from -0.25 to $+0.03$ mm/s) results from the large, extra π -delocalization of *d*-electrons from the t_{2g}^6 configuration into the π^* orbital of NO^+ . The decrease of the isomer shift in the NO_2^- case (from -0.25 to -0.40 mm/s) is attributable to the fact that NO_2^- is a poor π -delocalizing ligand as compared to CN^- . The ΔE_Q values indicate the symmetry of the electric field gradient about the ruthenium nucleus in each case, that is, $\Delta E_Q = 0.0$ for the symmetric electronic configuration in $\text{Ru}(\text{CN})_6^{4-}$; and ΔE_Q for $[\text{Ru}(\text{CN})_5\text{NO}]^{2+} >$

ΔE_Q for $[\text{Ru}(\text{CN})_5\text{NO}_2]^{4+}$ because of larger distortion caused by greater delocalization in the Ru—NO bond as compared to the Ru—NO₂ entity. This type of analysis has now been applied to many simple ruthenium complexes and to some binuclear systems (50, 51). The success of the ⁹⁹Ru spectral parameters in elucidating such chemical bonding problems has led to the use of the technique to define chemical species involved in solid-state catalysts, as mentioned earlier in this chapter. The problem outlined here is yet another instance of the unique contribution to be made by Mössbauer spectroscopy to the understanding of ruthenium chemistry, both in complex molecular systems and in catalytic materials.

Experimental

Materials. Ferrous sulfate (hydrated) was purchased from Fischer Scientific Co. and ruthenium trichloride trihydrate from Engelhard Industries. Hydrogen gas was obtained from Matheson (grade = 99.9%). All materials were used without subsequent purification.

Preparation of the Catalyst Material. Ruthenium trichloride trihydrate and ferrous sulfate (hydrated) were mixed in a 1:2 mole ratio in the solid state. A few drops of sulfuric acid and a few grains of ascorbic acid (to maintain the ferrous state by oxidation retardation) were added to the mixture. A minimum amount of distilled water was added to prepare a reasonable slurry, and the ingredients were thoroughly mixed. The mixture was heated in a porcelain dish on a steam bath for 2 h with constant stirring. The residue was filtered, washed with water, and dried in a vacuum desiccator at a pressure of approximately 10⁻³ torr for 5 h. A small sample of the resulting material was removed for analysis and designated Fe—Ru (initial).

The remainder of the Fe—Ru (initial) material was placed in a porcelain boat and reduced in flowing hydrogen at 400°C for 4 h. During reduction, copious amounts of white fumes were evolved. The reduced sample was cooled to room temperature in a stream of hydrogen. Again a small sample was removed for analysis. This reduced residue was designated Fe—Ru (reduced).

The larger portion of the Fe—Ru (reduced) sample was exposed to air at room temperature for 24 h. A small sample was removed for analysis and designated as Fe—Ru (exposed). The remainder of the material was heated to 400°C in air for 4 h. The sample was cooled slowly to room temperature and designated as Fe—Ru (calcined).

Physical Methods. The ruthenium and iron Mössbauer spectra were obtained with an Austin Science Associates Mössbauer spectrometer operating in the constant-acceleration mode. Calibration of the spectrometer was accomplished by laser interferometry using the Austin Science Associates ruby laser system (38, 40). Isomer shifts for ruthenium were referenced to the single-line resonance of pure (99.9%) ruthenium metal powder. An NBS-certified iron foil was used for the reference standard for the iron isomer shift.

The physical arrangement of the Mössbauer spectrometer and the Kontes/Martin glass liquid-helium Dewar for studying ruthenium catalyst samples has been described previously (26). Sample and absorber were immersed in the liquid helium at 4.2 K. For the results reported here, a scintillation detector with a 3-mm thick Harshaw NaI (T1) crystal was used. The ruthenium source

was approximately 8 mCi of 16-day ^{99}Rh contained in a host lattice of ruthenium metal. The source was prepared by the New England Nuclear Corp. of Boston, MA by separating the ^{99}Rh activity from an enriched ^{99}Ru target that had been proton bombarded in the Oak Ridge National Laboratory cyclotron. The ^{99}Rh activity was subsequently coprecipitated with 8 mg of natural ruthenium metal and annealed at 1000°C in hydrogen for 20 min. The source, as received, exhibited a linewidth of 0.22–0.25 mm/s for a natural ruthenium metal absorber.

The iron Mössbauer data were collected with the source at room temperature and the absorber at liquid-nitrogen (77 K) temperature. Corrections for second-order Doppler shifts were not made. The source was 54.3 mCi of ^{57}Co in a host lattice of rhodium metal purchased from the Spire Corp., Bedford, MA. This source exhibited a linewidth of 0.28 mm/s for a $\text{K}_4\text{Fe}(\text{CN})_6 \cdot 3\text{H}_2\text{O}$ absorber. Data reduction for both the iron and ruthenium spectra was carried out by a conventional least-squares Lorentzian line shape program on a DEC PDP-10 or Perkin-Elmer Interdata 8/32 computer.

The x-ray photoelectron spectra were taken on a PHI-548 ESCA/AES spectrometer. Powder samples were pressed onto a pure indium foil, and spectra were scanned with the neutralizer (zero kinetic energy electrons) on. The samples were sputtered with argon ions, and the indium peaks were used as internal reference standards for the assignment of sample binding energies.

X-ray powder diffraction spectra were taken on a Phillips' diffractometer equipped with an XRG-3000 x-ray generator and an APD-3500 data controller and processor. The scan rate was $2^\circ/\text{min}$.

Average surface areas for the catalyst particles in the power samples were determined using the gas-adsorption method. A continuous gas flow on a Perkin-Elmer Shell Model 212D spectrometer was used. Measurements were made in triplicate for each sample and the BET equation was used for the average surface area calculation (52).

Results and Discussion

The intent of this study was to evaluate our ability to characterize in detail the chemical (and physical) transformations that accompany the various preparative steps in formulating a bulk bimetallic catalyst. The choice of the particular starting materials was somewhat arbitrary, other than the fact that we wanted to investigate a defined iron–ruthenium system. The rationale for the particular metal salts used was based on our previous experience with $\text{RuCl}_3 \cdot x\text{H}_2\text{O}$ on alumina and silica supports (26), and the fact that oxidation–reduction reactions of $\text{FeSO}_4 \cdot x\text{H}_2\text{O}$ on zeolites had been investigated extensively by other workers (53). It has been recognized that the anions associated with the metal in the initial mix can influence the final products (54), and future studies are planned where the chemical transformations are monitored as a function of initial anion(s) present. The actual treatment procedures were chosen to correspond to those used previously in our laboratory for the oxidation–reduction of supported ruthenium catalysts on alumina, silica, and zeolites (26, 28). Products at each stage of treatment were characterized as fully as possible, as outlined later. Ruthenium-99 and

^{57}Fe Mössbauer spectra were obtained for each sample, and the results are given in Tables I and II and Figures 1–5. ESCA spectra for all samples, both as removed from the reaction sequence and after extensive sputtering with argon ions (to probe the bulk properties of the materials), are shown in Figure 6 and 7. X-ray diffraction patterns for the individual samples are displayed in Figure 8.

Fe–Ru (Initial). The Mössbauer data for this sample indicates that it contains a mixture of iron(III) and iron(II) and a ruthenium entity with an isomer shift of -0.61 mm/s and a ΔE_Q value of 0.69 mm/s.

Table I. Iron-57 Mössbauer Parameters of Iron–Ruthenium Bimetallic Catalysts

Sample ^a	Absorption Lines ^b	Comments ^c
Fe–Ru (initial)	Peak 1 2.63 ± 0.01	Fe^{2+} IS = 1.32 ± 0.01 ; $\Delta E_Q = 2.63 \pm 0.01$
	Peak 2 0.97 ± 0.01	
	Peak 3 0.00 ± 0.01	Fe^{3+} IS = 0.49 ± 0.01 ; $\Delta E_Q = 0.97 \pm 0.01$
Fe–Ru (reduced)	Peak 1 8.39 ± 0.02	$\gamma\text{-Fe}_2\text{O}_3$ (magnetic) IS = 0.07 ± 0.02 ; HI = 522 kG
	Peak 2 4.85 ± 0.02	
	Peak 3 2.56 ± 0.03	FeS (magnetic) IS = 0.50 ± 0.02 ; HI = 281 kG
	Peak 4 1.32 ± 0.02	
	Peak 5 0.49 ± 0.02	
	Peak 6 -0.27 ± 0.02	$\gamma\text{-Fe}_2\text{O}_3$ (supermagnetic) IS = 0.11 ± 0.02 ; $\Delta E_Q = 0.76 \pm 0.02$
	Peak 7 -1.22 ± 0.02	
	Peak 8 -2.60 ± 0.03	
	Peak 9 -3.92 ± 0.03	
	Peak 10 -4.71 ± 0.02	
	Peak 11 -8.22 ± 0.02	
Fe–Ru (calcined)	Peak 1 8.49 ± 0.02	$\gamma\text{-Fe}_2\text{O}_3$ (magnetic) IS = 0.09 ± 0.02 ; HI = 525 kG
	Peak 2 4.89 ± 0.02	
	Peak 3 1.37 ± 0.05	$\gamma\text{-Fe}_2\text{O}_3$ (supermagnetic) IS = 0.16 ± 0.02 ; $\Delta E_Q = 0.57 \pm 0.02$
	Peak 4 0.45 ± 0.02	
	Peak 5 -0.12 ± 0.02	
	Peak 6 -1.24 ± 0.03	
	Peak 7 -4.70 ± 0.02	
	Peak 8 -8.30 ± 0.02	

^a See text for preparative conditions.

^b Error estimates are from computer least-squares fits to Lorentzian lines. Precision (reproducibility) from two mirror-image spectra is ± 0.04 mm/s.

^c IS = Isomer shift in mm/s; ΔE_Q = quadrupole splitting in mm/s; HI = internal field in kG calculated from Mössbauer magnetic splitting.

Table II. Ruthenium-99 Mössbauer Parameters of Iron–Ruthenium Bimetallic Catalysts

<i>Sample</i> ^a	<i>Isomer Shift</i> ^b (mm/s)	<i>Linewidth</i> (mm/s)	
Fe–Ru (initial)	Peak 1	-0.27 ± 0.01	0.38 ± 0.01
	Peak 2	-0.96 ± 0.01	0.38 ± 0.01
Fe–Ru (reduced)	Peak 1	0.01 ± 0.01	0.21 ± 0.01
	Peak 2	-0.48 ± 0.01	0.39 ± 0.02
Fe–Ru (exposed)	Peak 1	0.01 ± 0.01	0.22 ± 0.01
	Peak 2	-0.49 ± 0.01	0.36 ± 0.02
Fe–Ru (calcined)	Peak 1	-0.02 ± 0.01	0.24 ± 0.01
	Peak 2	-0.48 ± 0.01	0.39 ± 0.02
Ru (metal)		0.00 ± 0.00	0.21 ± 0.01
RuO ₂	Peak 1	0.02 ± 0.01	0.38 ± 0.01
	Peak 2	-0.49 ± 0.01	0.38 ± 0.01
β -RuCl ₃		-0.67 ± 0.05	0.35 ± 0.05 $\Delta E_Q = 0.79 \pm 0.05$

^a See text for preparative conditions.

^b Error estimates are from computer least-squares fits to Lorentzian lines. Precision (reproducibility) from two mirror-image spectra is ± 0.04 mm/s.

An alternative assignment for the ruthenium spectrum would be two ruthenium species, both with no quadrupole splitting and an isomer shift of -0.27 and -0.96 mm/s, respectively. The ESCA spectra of the sample indicate that both chloride and sulfate are present in the surface and bulk of the sample. Thus the ruthenium entity(ies) present could be a ruthenium(III)–chloride compound or a mixture of the hexahalide complexes of ruthenium(II) and ruthenium(IV). The isomer shift value(s) are compatible with either of these two possibilities (25). However, the material is insoluble in water and alcohol, which is characteristic of the insoluble, anhydrous trihalides such as α -RuCl₃. We do not have Mössbauer parameters for α -RuCl₃ for comparison, but the values for β -RuCl₃ are shown in Table II and in Figure 2. The x-ray diffraction pattern shown in Figure 8 is inconclusive for Fe–Ru (initial) since no definitive assignments could be made. Thus, the most probable chemical composition of the dried Fe–Ru (initial) sample is a mixture of iron(II) and iron(III) salts, probably mixed chlorides and sulfates, and an anhydrous RuCl₃ species.

Fe–Ru (Reduced). The chemical character of the sample changed drastically after the Fe–Ru (initial) was reduced in hydrogen at 400°C, as is indicated in the Mössbauer and ESCA spectra. A first trial for the data analysis of the ⁵⁷Fe Mössbauer spectra fit the data to eight lines as shown in Figure 3. However, the fit was not particularly good and other

small unresolved peaks are clearly visible. A rerun of these data resolved the spectrum into 11 lines with the peak positions listed in Table I. The data could be sorted into two six-line magnetic spectra and a paramagnetic doublet. The lower intensity six-line doublet with an internal field of 281 kG is most probably FeS (56, 57). This assignment is substantiated by the ESCA data which exhibit two sulfur peaks on the surface of the reduced sample, one which can be assigned to sulfate and the other to sulfide (58). After sputtering only the sulfide peak remains, indicating the presence of a sulfide in the bulk.

The more intense six-line spectrum was first thought to be α -Fe₂O₃ with the center doublet representing a fraction of small particles that are paramagnetic (11, 56). No configuration could be obtained from the x-ray diffraction data since they contained only a small number of resonance peaks, indicating very small particle sizes. Gas absorption measurements confirmed this fact by showing that the average particle size was about 300 Å or less as calculated from the surface area of 18.6 m²/g. However, the x-ray diffraction pattern for the calcined samples, as discussed later, indicated the presence of γ -Fe₂O₃ rather than α -Fe₂O₃.

The ⁹⁹Ru Mössbauer spectrum for the reduced sample was particularly interesting in that the ruthenium salt in the initial sample did not reduce all the way to ruthenium metal as had been observed previously for ruthenium trichloride supported on silica and alumina or a ruthenium cation exchanged onto a Y-type zeolite (26, 28). The ruthenium spectrum could be analyzed as two signals, one rather intense peak at approximately zero velocity (as compared to a ruthenium metal standard) and

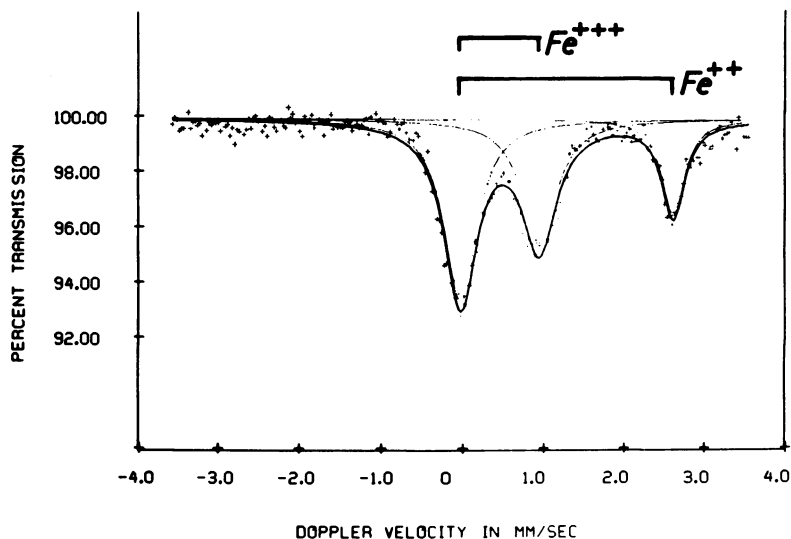


Figure 1. Iron-57 Mössbauer spectrum of Fe-Ru (initial)

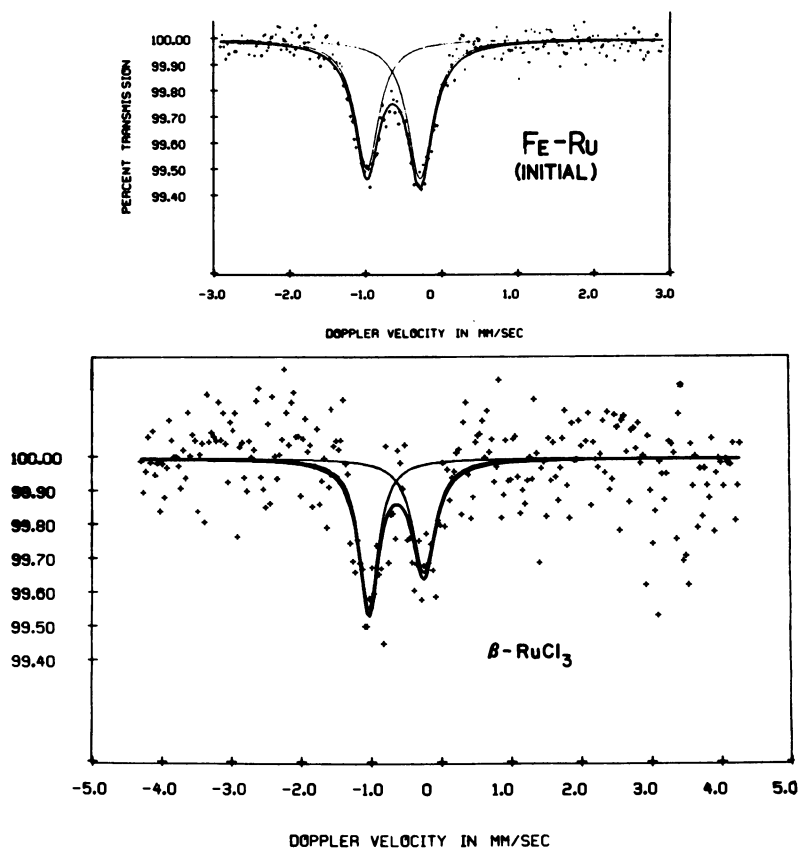


Figure 2. Ruthenium-99 Mössbauer spectrum of Fe-Ru (initial)

a doublet with parameters characteristic of RuO_2 . Note that one half of the RuO_2 doublet is buried in the more intense metal peak. Thus it appears that the chemical composition of the reduced sample is bulk $\gamma\text{-Fe}_2\text{O}_3$, small-particle paramagnetic $\gamma\text{-Fe}_2\text{O}_3$, FeS (small component), ruthenium metal, and RuO_2 . This assignment is further corroborated by the Mössbauer and x-ray data cited later for the calcined sample.

Fe-Ru (Exposed). Previous work on reduced ruthenium metal dispersed on a zeolite support indicated that the material was quite reactive and changed chemical composition on exposure to air, even at room temperature (28). To test the reactivity of the mixed-metal system, the Fe-Ru (reduced) sample was exposed to air at room temperature. The Mössbauer and ESCA spectra indicated that the sample composition did not change from that reported earlier for the reduced sample. Again this behavior is quite different from that observed for ruthenium alone on a support system.

Fe-Ru (Calcined). The ^{57}Fe and ^{99}Ru Mössbauer parameters for the calcined sample are given in the Tables and in Figures 3 and 5. The main differences between these spectra and those for the reduced sample are the absence of the FeS pattern and the more clearly resolved peaks for $\gamma\text{-Fe}_2\text{O}_3$. Note that the paramagnetic fraction of the iron oxide remains. The treatment with oxygen apparently transforms any FeS to $\gamma\text{-Fe}_2\text{O}_3$ and produces particles of larger sizes. The average surface area of the Fe-Ru (calcined) particles was reduced to $6\text{ m}^2/\text{g}$, which corresponds to an average particle size of 900 Å. The ESCA spectra substan-

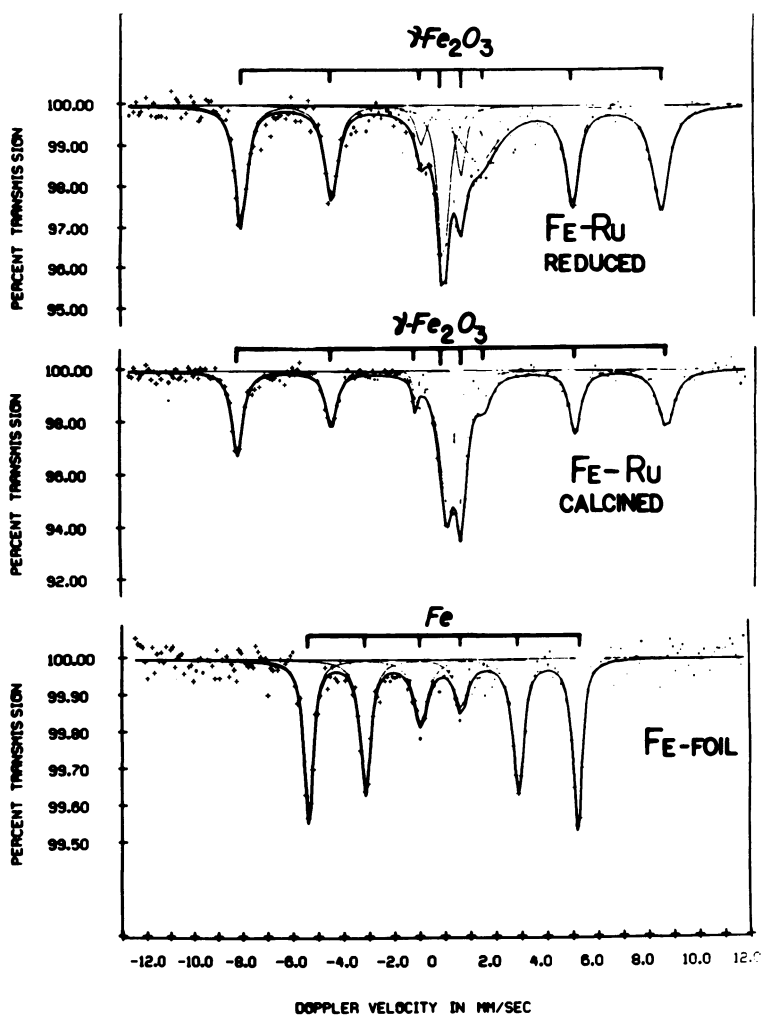


Figure 3. Iron-57 Mössbauer spectra for Fe-Ru (reduced) and Fe-Ru (calcined). (Spectrum for iron foil is shown for comparison.)

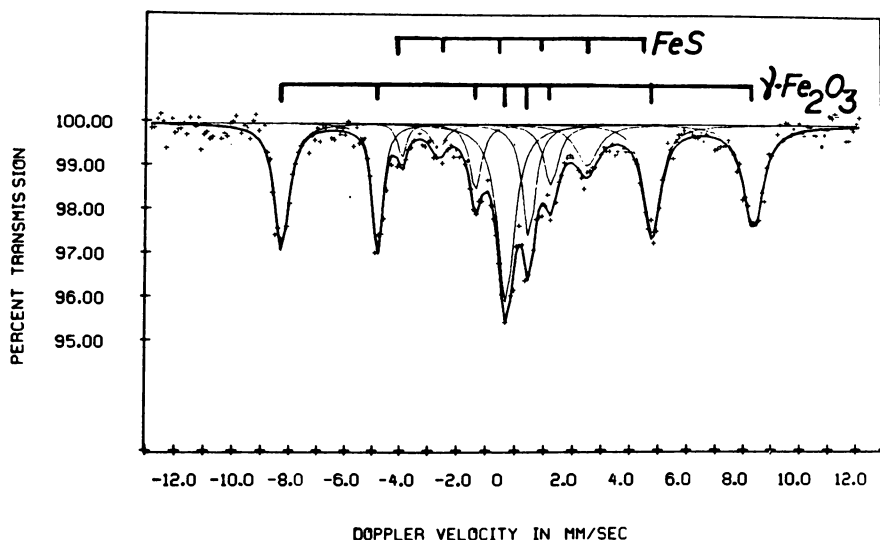


Figure 4. Iron-57 Mössbauer spectrum of Fe-Ru (reduced) rerun with 11 resolved lines. (Note that most of the magnetically split spectrum for FeS can be resolved although it is a minor component of the total spectrum.)

tiated the loss of FeS since the sputtered samples in Figure 7 show no sulfide peaks in the bulk sample.

It is interesting that the ^{99}Ru Mössbauer spectra are unchanged by the calcination. The spectra still can be assigned to a mixture of ruthenium metal and RuO_2 . These assignments of the chemical species of the bimetallic material are enhanced by the observed x-ray diffraction powder patterns. Since the average particle sizes were increased, the powder pattern is now clearly assignable as shown in Figure 8. Peaks corresponding to ruthenium metal, RuO_2 , and $\gamma\text{-Fe}_2\text{O}_3$ are clearly visible. The assignment of $\gamma\text{-Fe}_2\text{O}_3$ is particularly significant since the Mössbauer parameters could have been assigned to the more common $\alpha\text{-Fe}_2\text{O}_3$ (56). However, the x-ray peaks could not be fit to those reported for $\alpha\text{-Fe}_2\text{O}_3$ but did correspond well to those reported for $\gamma\text{-Fe}_2\text{O}_3$ (59).

Summary

The data outlined in this chapter clearly indicate the utility of Mössbauer spectroscopy as a probe for assessing the chemical composition of solid-state catalyst materials and for following their solid-state reactions. The ability to "double label" a bimetallic system is particularly effective. The advantage of supplementary data such as ESCA spectra and x-ray

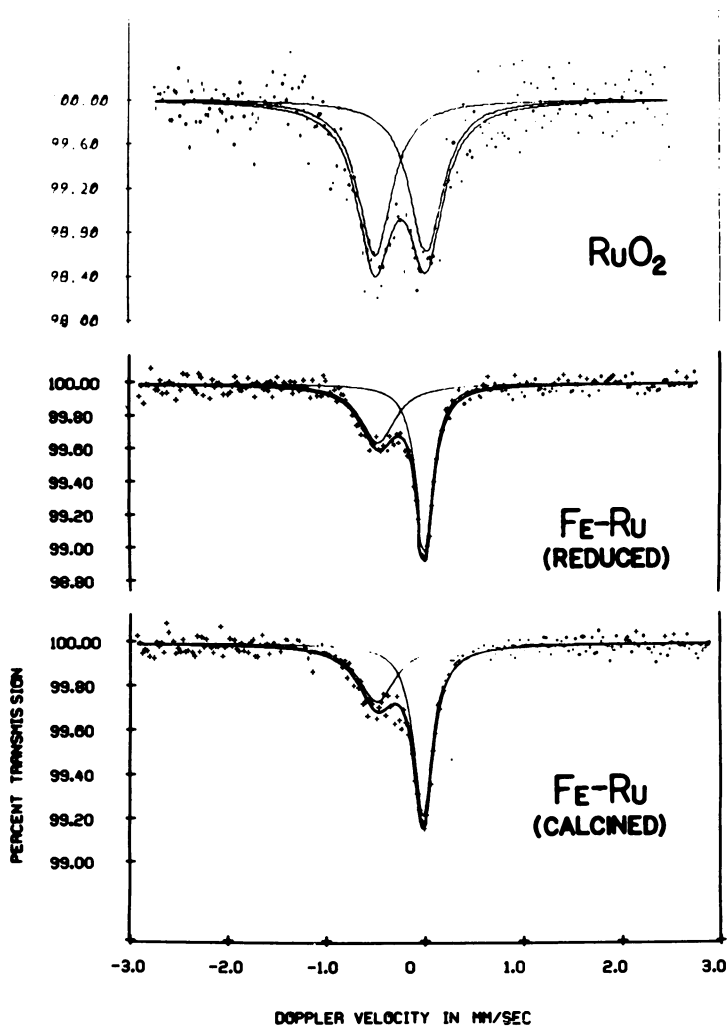


Figure 5. Ruthenium-99 Mössbauer spectra for Fe-Ru (reduced) and Fe-Ru (calcined). (Spectrum for pure RuO_2 is shown for comparison.)

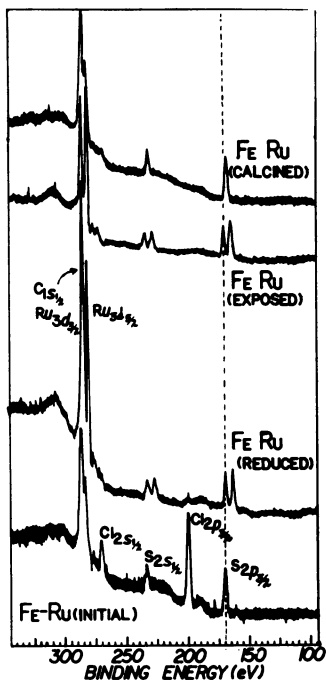


Figure 6. ESCA spectra for Fe-Ru samples as a function of treatment

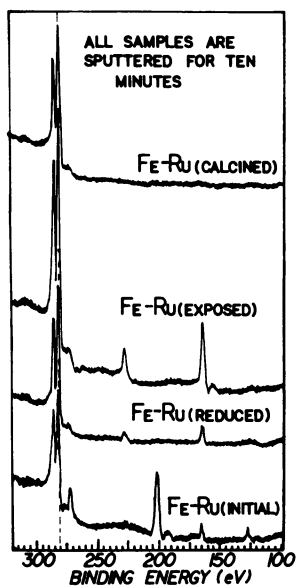


Figure 7. ESCA spectra for Fe-Ru samples as a function of treatment. (Samples were first sputtered with argon ions for 10 min to remove surface contamination.)

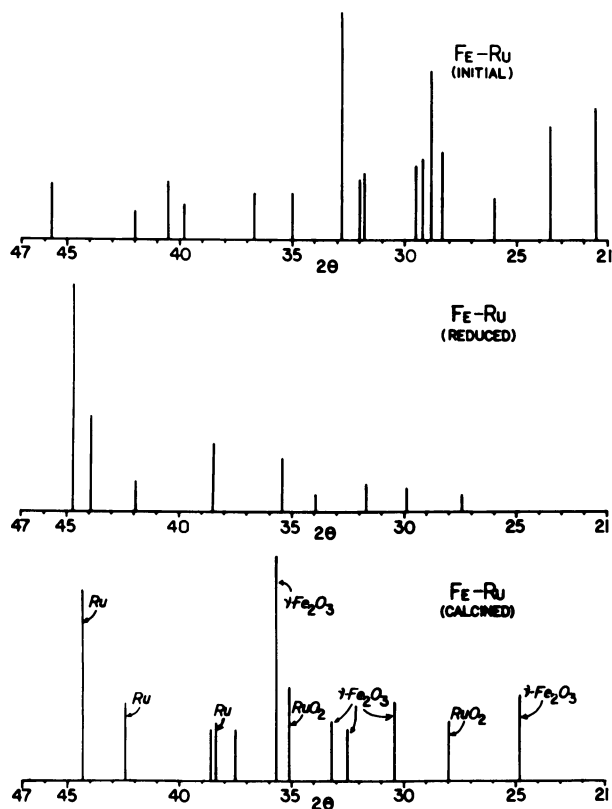
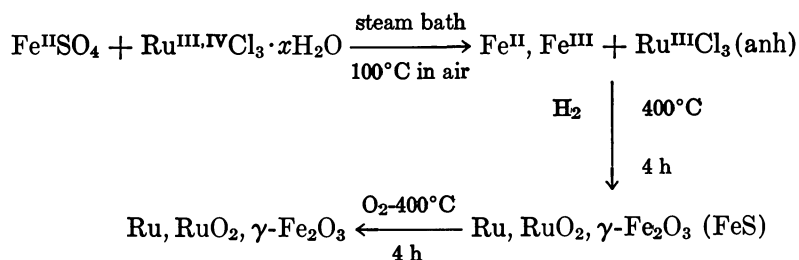


Figure 8. X-ray powder patterns for the Fe-Ru samples as a function of treatment

diffraction parameters in providing complementary details for the complete characterization of such solid-state systems also has been demonstrated.

The actual chemical nature of this particular iron-ruthenium bimetallic system is most interesting in light of previously reported information for related systems. The overall reaction scheme can be summarized as follows:



There is no evidence for the formation of an iron–ruthenium alloy during the reduction step as has been reported for other samples that have been prepared from mixed iron–ruthenium metals at elevated temperatures (14, 15, 16) or from the reduction of mixed-metal salts (10, 31, 32). Also, there is no evidence of reduction of iron to the metallic state although some ruthenium is reduced to the metal. The reduction step could include a disproportionation reaction of the ruthenium(III) species to form ruthenium(0) and ruthenium(IV) with the concurrent oxidation of the iron(II) species to Fe_2O_3 . The determination of the mechanism of this particular solid-state reaction presents quite a challenge. In an effort to understand the detailed chemistry, future work is planned in evaluating the role of the anions used, the determination of reduction products formed at temperatures above 400°C , the effect of other procedures such as hydrazine reduction, and the properties of single-metal salt systems.

Acknowledgments

The authors acknowledge the substantial support received for this work from the National Science Foundation (NSF) Grant No. CHE 76-17434 and Grant No. CHE-7912999. The ESCA/Auger spectrometer was purchased primarily with NSF funds provided as a supplement to NSF Grant No. CHE 76-17434.

Literature Cited

1. Prestridge, E. G.; Via, G. H.; Sinfelt, J. H. *J. Catal.* **1977**, *50*, 115.
2. Raghavan, M. *Norelco Rep.* **1979**, *26*, 7.
3. Nakamura, M.; Wise, H. *Proc. Int. Congr. Catal.*, *6th*, 1976, *2*, 881.
4. Pedersen, L. A.; Lunsford, J. H. *J. Catal.* **1980**, *61*, 39.
5. Aika, K.; Lunsford, J. H. *J. Phys. Chem.* **1977**, *81*, 1393.
6. Delgass, W. N.; Haller, G. L.; Kellerman, R.; Lunsford, J. H. "Spectroscopy in Heterogeneous Catalysis"; Academic: New York, 1979; p. 132.
7. Bartholomew, C. H.; Boudart, M. *J. Catal.* **1973**, *29*, 278.
8. Garten, R. L.; Ollis, D. F. *J. Catal.* **1974**, *35*, 232.
9. Garten, R. L. *J. Catal.* **1976**, *43*, 18.
10. Vannice, M. A.; Lam, Y. L.; Garten, R. L. *Am. Chem. Soc. Div. Petrol. Chem. Prepr.* **1978**, *23*, 495.
11. Raupp, G. B.; Delgass, W. N. *J. Catal.* **1979**, *58*, 337.
12. Raupp, G. B.; Delgass, W. N. *J. Catal.* **1979**, *58*, 348.
13. Raupp, G. B.; Delgass, W. N. *J. Catal.* **1979**, *58*, 361.
14. Ohno, H.; Mekata, M.; Takaki, H. *J. Phys. Soc. Jpn.* **1968**, *25*, 283.
15. Williams, J. M.; Pearson, D. I. C. *J. Phys. (Paris)* **1976**, *37*, 401.
16. Pearson, D. I. C.; Williams, J. M. *Physica* **1977**, *86–88B*, 279.
17. Shirane, G.; Chen, C. W.; Flinn, P. A.; Nathans, R. *J. Appl. Phys.* **1973**, *34*, 1044.
18. Shirane, G.; Chen, C. W.; Flinn, P. A.; Nathans, R. *Phys. Rev.* **1963**, *131*, 183.
19. Johnson, C. E.; Ridout, M. S.; Cranshaw, T. E.; Madsen, P. E. *Phys. Rev. Lett.* **1961**, *6*, 450.
20. Vincze, I.; Campbell, I. A. *J. Phys. F.* **1973**, *3*, 647.
21. Atac, M.; Debrunner, P.; Frauenfelder, H. *Phys. Lett.* **1966**, *21*, 699.
22. Agresti, D.; Kankeleit, E.; Persson, B. *Phys. Rev.* **1967**, *155*, 1339.

23. Buyrn, A.; Grodzins, L.; Blum, N. A.; Wulff, J. *Phys. Rev.* **1969**, *163*, 286.
24. Kanashiro, M.; Nishi, M.; Kunitomi, N.; Sakai, H. *J. Phys. Soc. Jpn.* **1975**, *38*, 897.
25. Good, M. L. "Mössbauer Effect Data Index"; Stevens, J., Stevens, V., Eds.; EFC/Plenum: New York, 1972; p. 51.
26. Clausen, C. A., III; Good, M. L. *J. Catal.* **1975**, *38*, 92.
27. Clausen, C. A., III; Good, M. L. *J. Catal.* **1977**, *46*, 58.
28. Clausen, C. A., III; Good, M. L. *Inorg. Chem.* **1977**, *16*, 816.
29. Madhusudhan, C. P.; Patil, M. D.; Good, M. L. *Inorg. Chem.* **1979**, *18*, 2384.
30. Vannice, M. A. *J. Catal.* **1975**, *37*, 449.
31. Ott, G. L.; Fleisch, T.; Delgass, W. N. *J. Catal.* **1979**, *60*, 394.
32. Urabe, K.; Ozaki, A. *J. Catal.* **1978**, *52*, 542.
33. Good, M. L.; Akbarnejad, M.; Donner, J. T. *Am. Chem. Soc. Div. Petrol. Chem. Prepr.* (San Francisco, Sept., 1980).
34. Kistner, O. C.; Monaro, S.; Segnam, R. *Phys. Lett.* **1963**, *5*, 299.
35. Kistner, O. C.; Monaro, A.; Schwarzschild, A. *Phys. Rev.* **1965**, *137*, 1323.
36. Kistner, O. C. *Phys. Rev.* **1966**, *144*, 1022.
37. Kistner, O. C. *Mössbauer Eff. Methodol.* **1967**, *3*, 217.
38. Clausen, C. A., III; Prados, R. A.; Good, M. L. *Mössbauer Eff. Methodol.* **1971**, *6*, 31.
39. Kaindl, G.; Maier, M. R.; Schaller, A.; Wagner, F. *Nucl. Instrum. Methods* **1968**, *66*, 277.
40. Cosgrove, J. G.; Collins, R. L. *Nucl. Instrum. Methods* **1971**, *95*, 269.
41. Cohen, R. L.; Kalvius, G. M. *Nucl. Instrum. Methods* **1970**, *86*, 209.
42. Stevens, J.; Stevens, V., Eds. "Mössbauer Effect Data Index—1971"; IFC/Plenum: New York, 1972; p. 19.
43. Greatrex, R.; Greenwood, N. N.; Kaspi, P. *J. Chem. Soc.* **1971**, *A*, 1873.
44. Foyt, D. C.; Siddall, T. H., III; Alexander, C. J.; Good, M. L. *Inorg. Chem.* **1974**, *13*, 1793.
45. Foyt, D. C.; Cosgrove, J. G.; Collins, R. L.; Good, M. L. *J. Inorg. Nucl. Chem.* **1975**, *37*, 1913.
46. Kaindl, G.; Potzel, W.; Wagner, F.; Zahn, U.; Mössbauer, R. L. *Z. Phys.* **1969**, *226*, 103.
47. Prados, R. A.; Clausen, C. A., III; Good, M. L. *J. Coord. Chem.* **1973**, *2*, 201.
48. Clausen, C. A., III; Prados, R. A.; Good, M. L. *J. Am. Chem. Soc.* **1970**, *92*, 7482.
49. Potzel, W.; Wagner, F. E.; Zahan, U.; Mössbauer, R. L.; Danon, J. *Z. Phys.* **1970**, *240*, 306.
50. Clausen, C. A., III; Prados, R. A.; Good, M. L. *Inorg. Nucl. Chem. Lett.* **1971**, *7*, 485.
51. Creutz, C.; Good, M. L.; Chandra, S. *Inorg. Nucl. Chem. Lett.* **1973**, *9*, 171.
52. Dalla-Bett, R. A. *J. Catal.* **1974**, *34*, 57.
53. Dickson, B. L.; Rees, L. C. *J. Chem. Soc., Faraday Trans.* **1974**, *70*, 2038.
54. Moss, R. L. "Experimental Methods in Catalytic Research"; Anderson, R. B.; Dawson, P. T., Eds.: Academic: New York, 1976; Vol. 2, p. 43.
55. Clausen, C. A., III; Prados, R. A.; Good, M. L. *Chem. Phys. Lett.* **1971**, *8*, 565.
56. Greenwood, N. N.; Gibb, T. C. "Mössbauer Spectroscopy"; Chapman and Hall, Ltd.: London, 1971; p. 239–296.
57. Sprengel-Segal, E. L.; Houna, S. S. *Mössbauer Effect Methodol.* **1966**, *2*, 113.
58. Lindberg, B. J.; Hamrin, K.; Johansson, G.; Gelius, U.; Fahlman, A.; Nordling, C.; Siegbahn, K. *Physica Scripta* **1970**, *1*, 28C.
59. "X-ray Powder Data File"; ASTM: Philadelphia, 1962; No. 13-458.

RECEIVED July 22, 1980.

Mössbauer and Magnetic Studies of Bifunctional Medium-Pore Zeolite-Iron Catalysts Used in Synthesis Gas Conversion

CARY LO—Physics Department, Pennsylvania State University, University Park, PA 16802

K. R. P. M. RAO¹ and L. N. MULAY²—Department of Materials Science and Engineering, 136 Materials Research Laboratory, Pennsylvania State University, University Park, PA 16802

V. U. S. RAO, R. T. OBERMYER³, and R. J. GORMLEY—Pittsburgh Energy Technology Center, U.S. Department of Energy, P.O. Box 10940, Pittsburgh, PA 15236

Medium-pore (diameter ~ 6 Å) zeolites such as ZSM-5 and Silicalite impregnated with Group VIII metals provide selective catalytic pathways for the conversion of coal-derived synthesis gas to gasoline or olefins. Mössbauer and magnetic studies on these catalysts containing iron or iron plus cobalt are reported. The zeolites were impregnated with metal nitrate solutions, reduced, and carbided to yield the active catalyst. The freshly impregnated samples showed Fe³⁺ type spectra. The ZSM-5 (14.7% Fe) and Silicalite (13.6% Fe) samples exposed to H₂ (450°C) showed an approximate 85% reduction to the metallic state. The carbided ZSM-5 (14.7% Fe) revealed a spectrum of Hagg carbide (Fe₅C₂), an active component of the catalyst. The used catalysts showed mixtures of Hagg carbide (Fe₅C₂) and cementite (Fe₃C). It is suggested that the selectivity of ZSM-5 (5.6% Fe, 4.5% Co) resulted from iron-cobalt alloy formation.

¹ Current address: Bhabha Atomic Research Center, Trombay, Bombay, India.

² Address inquiries to this author.

³ Current address: Physics Department, Pennsylvania State University, McKeesport, PA 15132.

The interest of Mulay's group (Penn State University) in this challenging area of catalysis research stemmed from his earlier basic research (1-4) on superparamagnetic dispersions of $\alpha\text{-Fe}_2\text{O}_3$. This dispersion was obtained by a novel technique, which consisted of introducing vapors of $\text{Fe}(\text{CO})_5$ [maximum dimension $\sim 9 \text{ \AA}$] into the cage structure of Linde-13X zeolite, via its aperture of about 10 \AA . The superparamagnetism of the dispersions was elucidated by magnetization measurements as a function of the field (H) and temperature (T) as well as by ^{57}Fe Mössbauer spectroscopy. The technological interest of V. U. S. Rao's group (Pittsburgh Energy Technology Center) centered around making relatively more efficient zeolite-Silicalite-based catalysts for synthesis gas conversion. The overlapping of the interests of these two research groups has led to a fruitful collaboration, which exemplifies interdisciplinary as well as interorganizational efforts between a federal and a university laboratory.

The catalytic conversion of coal-derived synthesis gas ($\text{CO} + \text{H}_2$) to gasoline-range hydrocarbons and olefins using bifunctional zeolite catalysts (5-7) is of much interest today. The medium-pore (diameter $\sim 6 \text{ \AA}$) zeolite ZSM-5 in combination with iron (5, 6) or with iron-cobalt (7) was shown to yield a high fraction of aromatics in the product, resulting in a favorable octane number (> 80). It was indicated (7) that the bimetallic iron-cobalt on ZSM-5 could alter the product selectivity, mainly in reducing the shift conversion of $\text{CO} + \text{H}_2\text{O}$ to CO_2 from the high shift yields of iron on ZSM-5. The aromatics in the product decreased by the addition of cobalt to the zeolite (7).

In contrast to ZSM-5, Silicalite lacks aluminum, although the two appear to possess similar crystal structures (8, 9). They crystallize with the orthorhombic space group Pnma or $\text{Pn}2_1a$ with $a = 20.1 \text{ \AA}$; $b = 19.9 \text{ \AA}$; $c = 13.4 \text{ \AA}$. The framework structure consists of five-membered rings of $\text{Si}(\text{Al})\text{-O}$ tetrahedra. The pore structure (Figure 1) consists of inter-

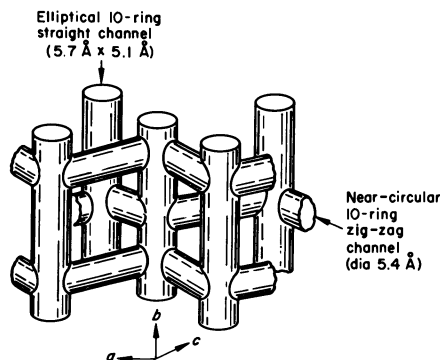


Figure 1. Possible model of the pore structure of ZSM-5 and Silicalite

Table I. Comparison of ZSM-5 and Silicalite

	ZSM-5	Silicalite
<i>Composition</i>	$\text{Na}_x(\text{AlO}_2)_x(\text{SiO}_2)_{100-x}$ $x = 1 \text{ to } 25$	SiO_2 $x = 0$
<i>Ion Exchange properties</i>	$\left[\begin{array}{c} \text{Present} \\ \text{EXCH} \quad \text{Calcine} \\ \text{Na}^+ \longrightarrow \text{NH}_4^+ \longrightarrow \text{H}^+ \end{array} \right]$	Absent
<i>Crystal Structure</i>	Orthorhombic $a = 20.1 \text{ \AA}$ $b = 19.9 \text{ \AA}$ $c = 13.3 \text{ \AA}$	Orthorhombic $a = 20.06 \text{ \AA}$ $b = 19.80 \text{ \AA}$ $c = 13.36 \text{ \AA}$
<i>Pore Structure</i>	Straight channels along b -axis. Zig-zag along a -axis. Pore diameter = 6 \AA .	Same as ZSM-5
<i>Sorption of H_2O</i>	Low for high silicon content	Low
<i>Thermal Stability</i>	Increases with silicon content	High

secting channels defined by ten rings of oxygen atoms. The elliptical straight channels of cross section $5.7 \text{ \AA} \times 5.1 \text{ \AA}$ along the b -axis and the circular zigzag channels of diameter 5.4 \AA interconnect the straight channels.

While the silicon/aluminum ratio in ZSM-5 can be varied from 3 to over 100, Silicalite has essentially no aluminum. Hence it appears that Silicalite is the limiting form of ZSM-5 when the aluminum concentration is vanishingly small. A comparison of the properties of ZSM-5 and Silicalite is shown in Table I.

Owing to the absence of cations that can be exchanged with protons, Silicalite has no acidity, while HZSM-5 is a highly acidic zeolite. Recent investigations (7) have shown that the difference in selectivity for synthesis gas conversion by ZSM-5 (iron) and Silicalite (iron) catalysts results from the previously mentioned difference in acidity. The main influence was on the production of aromatics and olefins; the former were dominant with the acidic ZSM-5 (iron) catalyst and the latter with the nonacidic Silicalite (iron) catalyst.

Mössbauer and magnetic investigations, described in this chapter, were conducted to determine the state of iron and iron-cobalt in the zeolite catalyst at different stages of catalyst preparation and use. Among the several aims of the investigation were the determination of:

1. the valence state of the transition metal in the freshly impregnated state;
2. the extent of reduction on exposure to H_2 ;
3. the active catalytic species after carburizing with synthesis gas;

4. the species present in the used catalyst; and
5. in the case of iron-cobalt, the possible formation of bi-metallic or alloy clusters and their influence on the selectivity of the catalyst.

Experimental

Preparation of Samples. ZSM-5 and Silicalite were prepared using methods described in the literature (10, 11). X-ray powder diffraction patterns revealed no phases other than ZSM-5 or Silicalite. The metal component was introduced by gradually adding the metal nitrate solution to the zeolite until incipient wetness was reached. The impregnation with the metal (Fe or Fe + Co) nitrate solution was carried out for 1 h under vacuum to enable the nitrate solution to enter the pore of the zeolite. The material is dried initially with constant stirring over a boiling water bath, and further dried in air at 110°C for 12 h. The amount of iron and cobalt in the samples was determined by standard wet chemical techniques and atomic absorption.

The zeolite impregnated with iron or iron plus cobalt was reduced in flowing H₂ at 450°C for 24 h. It was then carbided in flowing synthesis gas at 250°C for 24 h to yield the active catalyst. The catalysts were tested (7) for synthesis gas conversion in both a fixed-bed microreactor and a Berty (continuous-flow stirred-tank) reactor. For catalytic testing, these steps on the metal-impregnated zeolite were all carried out in the reactor. For Mössbauer studies, all the samples except the used catalysts were prepared separately under the conditions just described. In the ensuing discussion such samples will be described variously as (a) freshly impregnated, (b) reduced, (c) carbided, and (d) used catalysts. The last mentioned was taken from the reactor after its use for periods lasting from one to three weeks under synthesis gas under temperatures ranging from 280° to 320°C. X-ray diffraction studies were carried out on the samples after steps (a) and (d).

Characterization Techniques. The apparatus used for Mössbauer spectroscopy and magnetic measurements is described separately under the corresponding sections.

Results and Discussion

Mössbauer Studies. The Mössbauer spectra of catalysts listed in Table II were recorded utilizing a conventional constant-acceleration spectrometer made by Nuclear Science and Engineering Corporation and Nuclear Data ND-100 multichannel analyzer in MCS mode. The spectra were calibrated with a standard NBS iron foil. The parabolic background observed in the spectra arose from the geometry of the Mössbauer setup. A least-squares program fitting, in progress, has justified our interpretations. The spectra were recorded at room temperature using an 80-mCi ⁵⁷Co in Rh matrix. The spectra were analyzed, in general, on the basis of the studies on carbides by Raupp and Delgass (12).

The Mössbauer spectra of the different catalysts were recorded at various stages; namely, (a) after impregnation with Fe(NO₃)₃; (b) on reduction in H₂ at 450°C for 24 h; (c) on carbiding in 1:1 H₂/CO syn-

thesis gas at 250°C for 24 h; and (d) finally after utilization of the catalyst in the conversion of the synthesis gas to gasoline-range hydrocarbons. The spectra have revealed the existence of various phases, formed at different stages, and have given clues to the nature of the active component(s) responsible for the efficient conversion of synthesis gas into gasoline.

The spectrum of a fresh catalyst, in general, consisted of a doublet with an isomer shift of about +0.35 mm/s and a quadrupole splitting of about 0.75 mm/s, which indicate that the valence state of iron in the starting material is Fe^{3+} . A typical spectrum for a fresh catalyst of Silicalite impregnated with 13.6% iron using $\text{Fe}(\text{NO}_3)_3$ is shown in Figure 2.

As discussed in a later section, the magnetization (M) vs. magnetic field (H) measurements on the fresh catalyst gave a magnetic moment of about $5.96 \mu_B$, which further confirmed that the iron ion is in a high-spin Fe^{3+} state. It should be noted that the magnitude of the quadrupole splitting and isomer shift significantly depend upon the nature of the support used and the size of the iron particles (13).

The spectrum of a reduced catalyst consisted of a six-line pattern corresponding mostly to iron metal, in addition to indicating the presence of a small quantity of an oxide, if the catalyst contained only iron, on

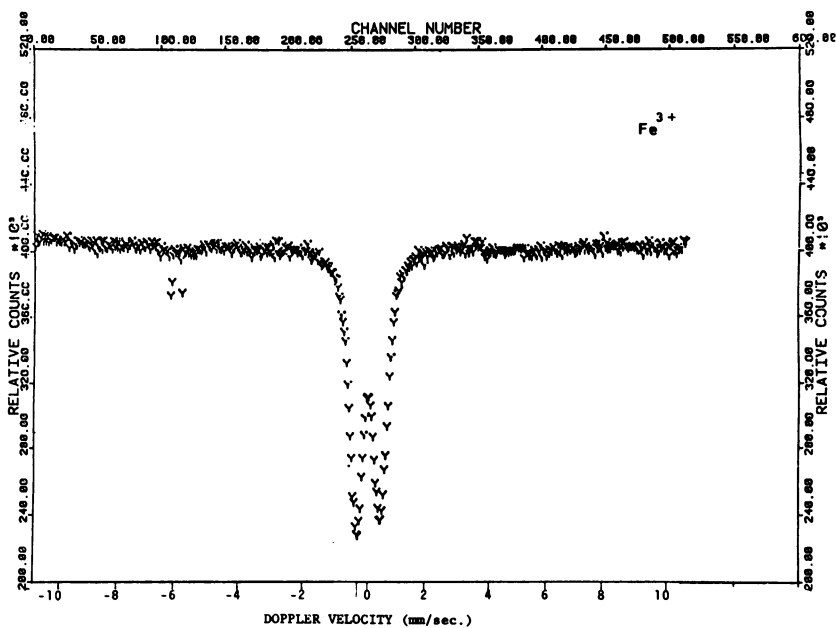


Figure 2. Mössbauer spectrum of Silicalite impregnated with 13.6% iron using $\text{Fe}(\text{NO}_3)_3$

Table II. Summary of Mössbauer

<i>Sample No.</i>	<i>Sample</i>	<i>State</i>
M1	ZSM-5 (14.7% Fe)	Reduced
M2	ZSM-5 (14.7% Fe)	Carbided
M3	ZSM-5 (14.7% Fe)	Used
M4	ZSM-5 (5.4% Fe + 1.3% Co)	Reduced
M5	ZSM-5 (5.4% Fe + 1.3% Co)	Carbided
M6	ZSM-5 (5.4% Fe + 4.5% Co)	Used
M7	Silicalite (13.6% Fe)	Fresh
M8	Silicalite (13.6% Fe)	Used
M9	Silicalite (4.4% Fe + 3% Co)	Reduced
M10	Silicalite (4.4% Fe + 3% Co)	Used

the one hand; whereas the spectrum of a catalyst consisting of both iron and cobalt clearly indicated the formation of an iron-cobalt alloy on reduction, on the other hand. The spectrum of reduced ZSM-5 containing 14.7% iron, shown in Figure 3A, essentially corresponds to that of metallic iron. However, there is a small amount of unreduced iron in the form of an oxide, probably α -Fe₂O₃. The reduction in this case is about 85%. This is also confirmed by the magnetization measurements, which indicated an approximate 15% lowering in the observed saturation magnetization of iron.

The spectrum of reduced ZSM-5 containing 5.4% iron and 1.3% cobalt, shown in Figure 3B, revealed a six-line pattern corresponding to an average internal magnetic field of about 340 kOe, and indicates the formation of an iron-cobalt alloy.

A typical spectrum of reduced Silicalite containing 4.4% iron and 3.0% cobalt is shown in Figure 4. The spectrum consists of a well-defined six-line pattern corresponding to an internal magnetic field of 345 ± 3 kOe, which is much larger than the 330-kOe field expected for metallic iron. Second, the isomer shift observed is 0.18 mm/s with respect to iron metal, which indicates that the electron density at the iron nucleus is smaller in the iron-cobalt alloy than in iron metal. This decrease in the electron density in the iron-cobalt alloy is consistent with the experimental results reported by Van der Woude and Sawatsky (14). The formation of an iron-cobalt alloy is supported further by the magnetization

Results of Various Catalysts*Remarks*

Iron metal and small amount of an oxide (α -Fe₂O₃)

Fe₅C₂ and Fe₃C

Fe₅C₂, Fe₃C, and Fe₃O₄

Fe₅C₂ has been relatively reduced as compared to that in Sample No. 2

Iron-cobalt alloy

Fe₅C₂, Fe₃C, and a strong doublet

Iron-cobalt alloy

Cobalt seems to have inhibited the formation of carbides.

Strong doublet corresponding to Fe³⁺

Fe₅C₂ and Fe₃C

Iron-cobalt alloy

Fe₅C₂, Fe₃C, and a strong doublet. Fe₅C₂ and Fe₃C are considerably small compared to those observed in Sample 8. Presence of cobalt seems to have inhibited the formation of carbides.

measurements on this catalyst, which indicated a magnetic moment intermediate between the moments corresponding to iron and cobalt.

The spectra of carbided catalysts consist of superposition of at least two apparent six-line patterns corresponding to at least two different iron-carbon phases. A typical spectrum of carbided ZSM-5 with 14.7% is shown in Figure 5A. This spectrum represents the presence of Hagg carbide (Fe₅C₂) and cementite (Fe₃C). The former has three inequivalent iron sites, whereas the latter has only one. The possibility of the presence of small quantities of less stable ϵ' and ϵ carbides (Fe_{2.2}C and Fe₂C) cannot be ruled out. A doublet due to Fe³⁺ was not apparent in Figure 5A; further low-temperature studies are in progress to discern any superparamagnetic behavior.

The spectrum of carbided ZSM-5 containing 5.4% iron and 1.3% cobalt, shown in Figure 5B, indicates the presence of both Fe₅C₂ and Fe₃C in addition to a strong doublet. Apparently fewer carbides have been formed in this catalyst than in those containing no cobalt; it appears that the presence of cobalt has somewhat inhibited the formation of carbides. The doublet may be attributable partly to superparamagnetic behavior. Similar spectra also have been observed in the case of Silicalite-based catalysts as well. Further low-temperature studies are under way to identify the nature of the doublet.

The spectra of used catalysts are in general very complicated and seem to consist of three or more magnetically split hyperfine spectra. A

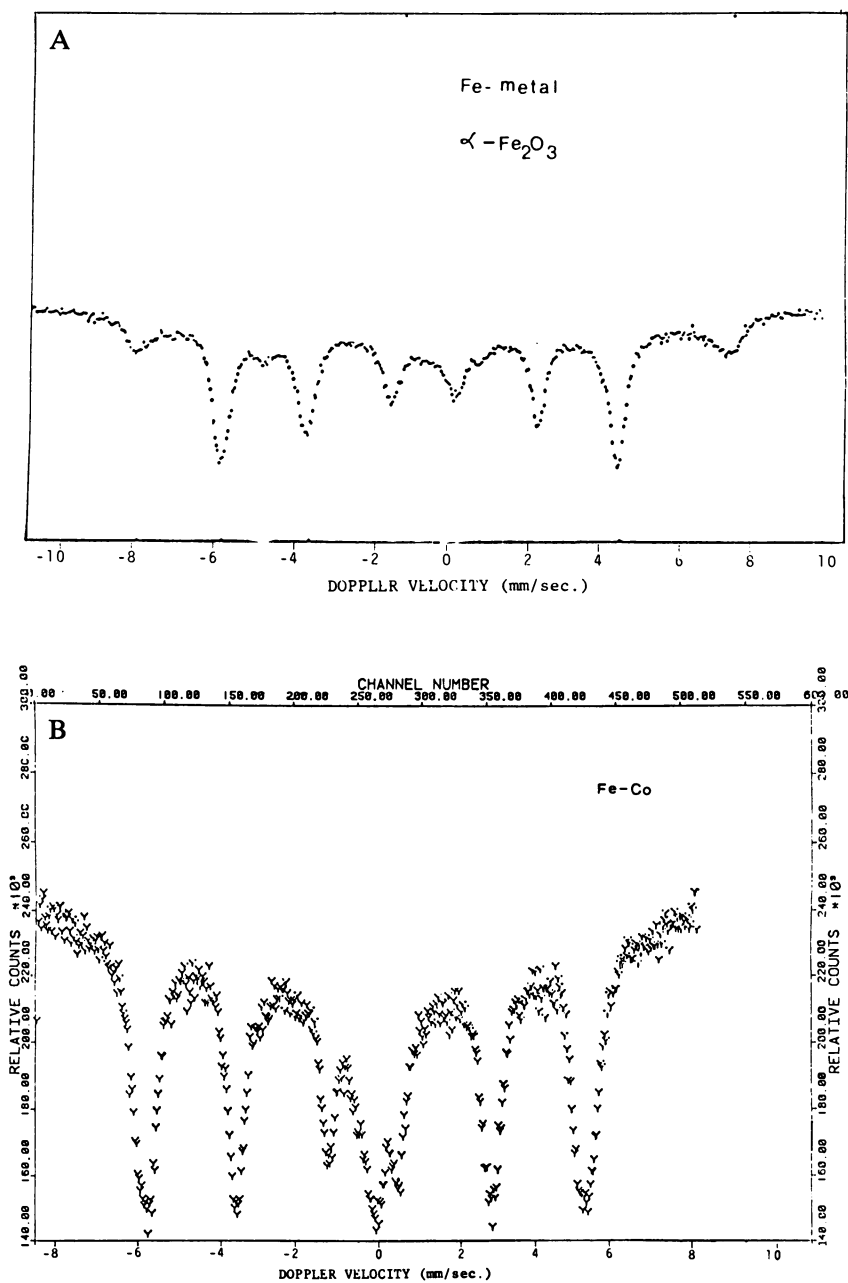


Figure 3. Mössbauer spectrum of reduced ZSM-5 (A) 14.7 Fe and (B) 5.4% Fe, 1.3% Co

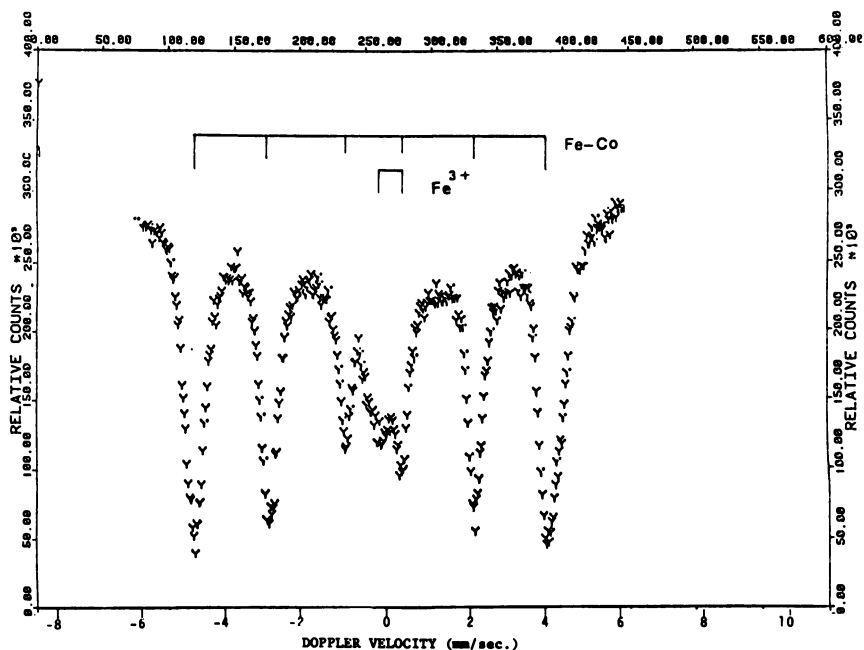


Figure 4. Mössbauer spectrum of reduced Silicalite (4.4% Fe, 3% Co)

typical spectrum of used ZSM-5 with 14.7% iron is shown in Figure 6. This spectrum can be explained in terms of the presence of Hagg carbide, cementite, and Fe_3O_4 . It is noteworthy that the cementite content has relatively increased at the expense of the Hagg carbide in the used catalyst as compared to that found in the carbided catalyst. (See the lines marked by arrows in Figure 5A and Figure 6.)

The spectrum of used ZSM-5 with 5.6% iron and 4.5% cobalt shown in Figure 7 consisted of a six-line pattern corresponding to an internal magnetic field of 344 ± 3 kOe and an isomer shift of $+0.15$ mm/s with respect to iron metal, and appears to indicate the formation of an iron-cobalt alloy. It is to be noted that the carbides, which were present in the case of used ZSM-5 containing only iron, are surprisingly absent in this case. Once again, the presence of a large amount of cobalt appears to inhibit the formation of carbides in these samples. The x-ray powder patterns showed the presence of a bcc iron-cobalt alloy phase in addition to the ZSM-5 phase.

The spectrum of used Silicalite containing 13.6% iron is shown in Figure 8. It consists of both Hagg carbide and cementite and is similar to that observed for ZSM-5 with 14.7% iron, except that this spectrum does not indicate the presence of any oxide. The spectrum of used Silicalite containing both 5% iron and 5% cobalt is shown in Figure 9.

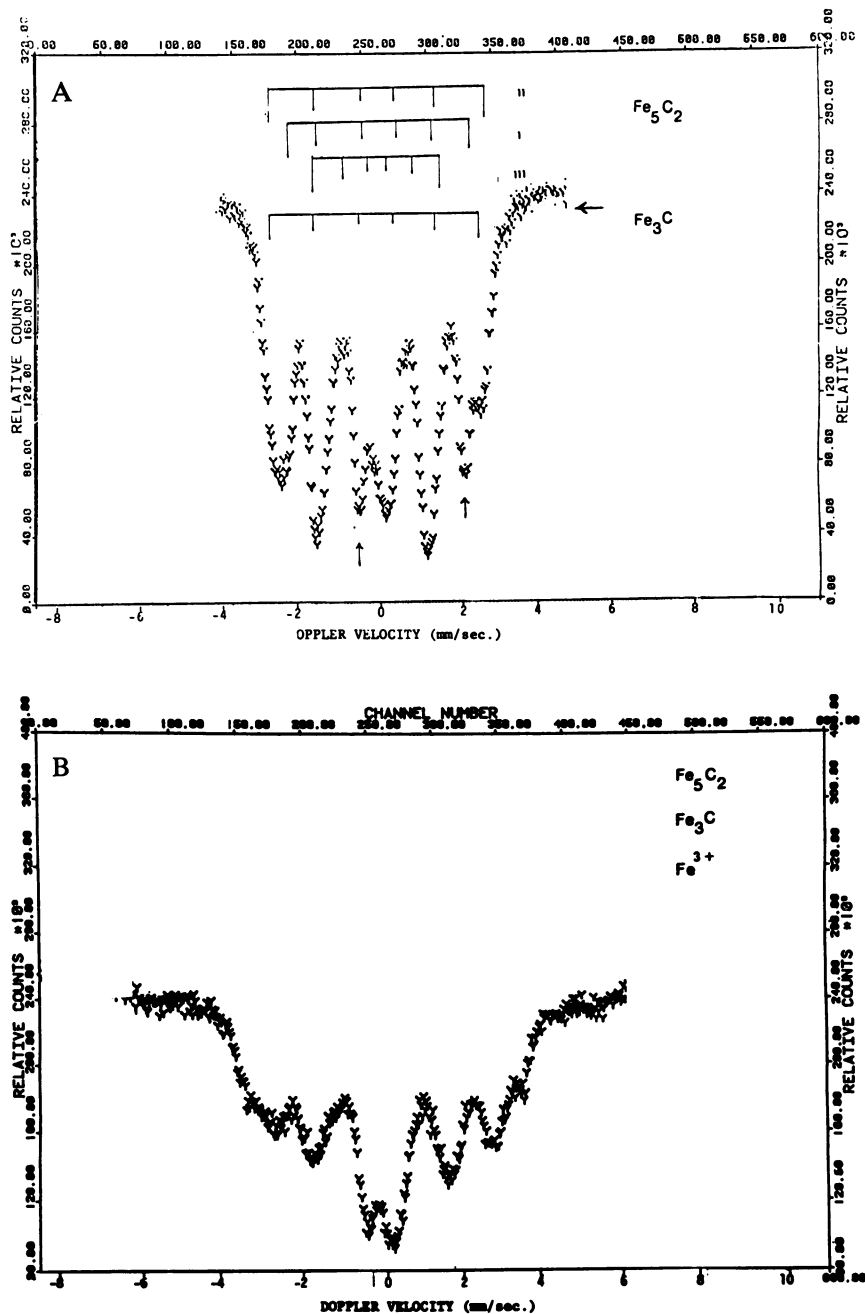


Figure 5. Mössbauer spectrum of carbided ZSM-5 (A) 14.7% Fe and (B) 5.4% Fe, 1.3% Co

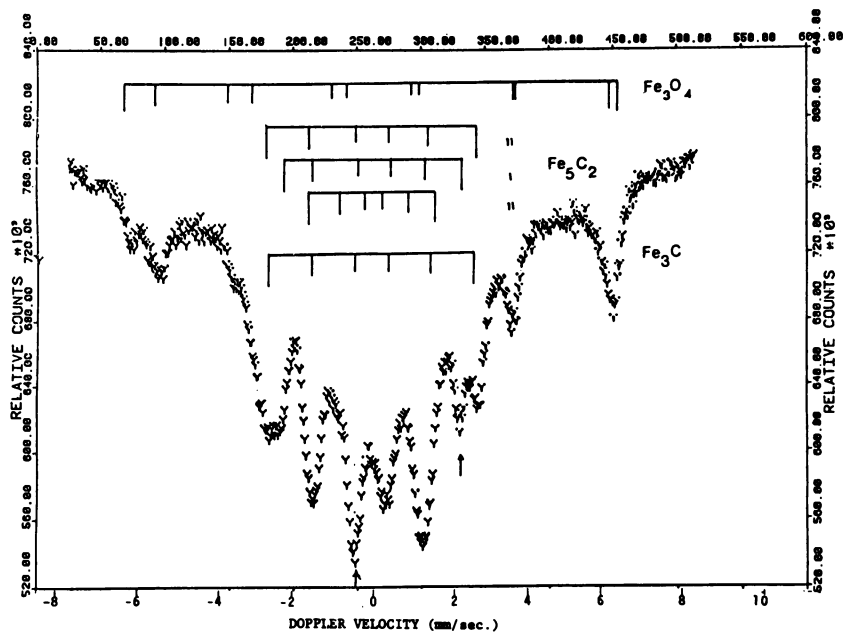


Figure 6. Mössbauer spectrum of used ZSM-5 (14.7% Fe)

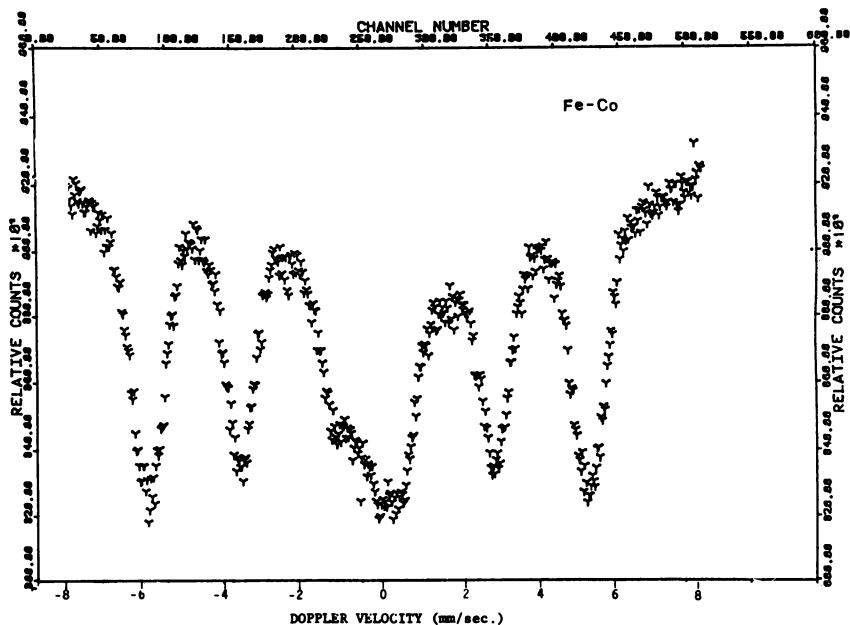


Figure 7. Mössbauer spectrum of used ZSM-5 (5.4% Fe, 4.5% Co)

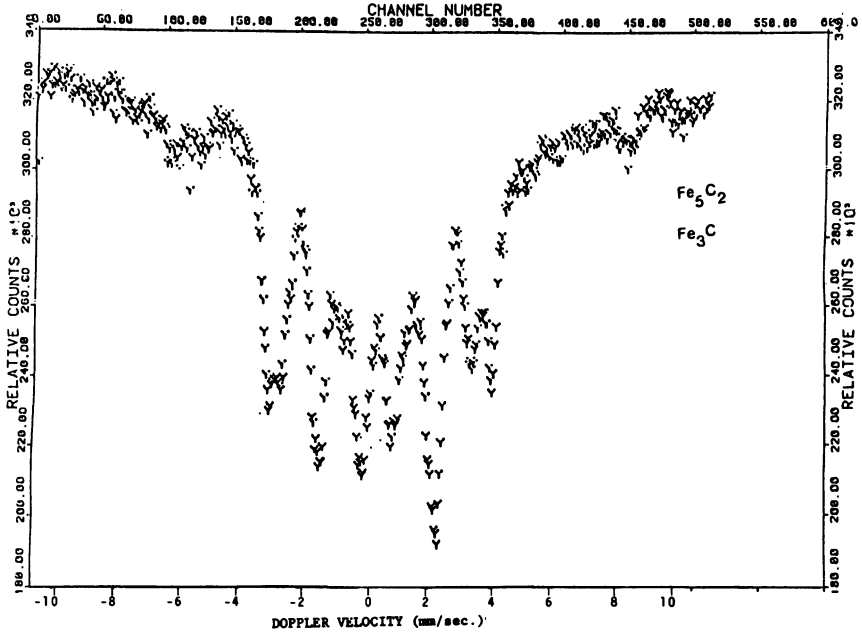


Figure 8. Mössbauer spectrum of used Silicalite (13.6% Fe)

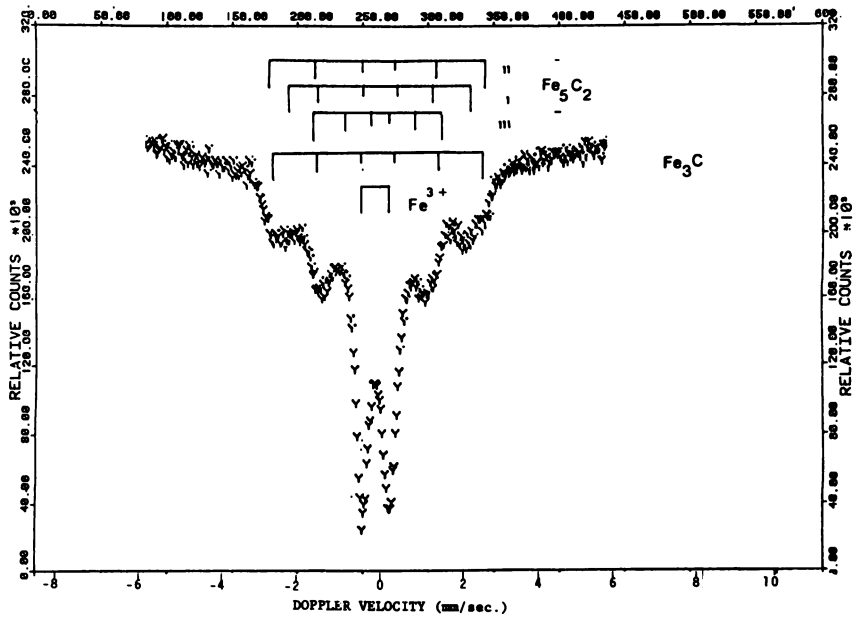


Figure 9. Mössbauer spectrum of used Silicalite (4.4% Fe, 3% Co)

This spectrum also contains Hagg carbide and cementite in addition to a strong doublet. However, the relative amounts of Hagg carbide and cementite present in this catalyst appear to be considerably less than those in the catalyst containing only iron. Thus, the presence of cobalt appears to hinder the formation of carbides in the Silicalite-based catalysts as well. Preliminary low-temperature studies have shown that the central doublet is partly a result of superparamagnetic behavior of a magnetic phase.

The stick diagrams on various Mössbauer spectra shown are the approximate line positions for Hagg (Fe_5C_2) and cementite (Fe_3C) phases and are drawn on the basis of Raupp and Delgass' results (12).

The observation that the carbided ZSM-5 containing only iron has relatively more Hagg carbide compared to cementite, and that the used catalyst has, in contrast, relatively more cementite than Hagg carbide, suggests that the Hagg carbide has been converted into cementite during the course of the reaction. Since synthesis gas conversion is exothermic, it is possible that local hot spots on the catalyst resulted in the conversion of the active Hagg carbide to the relatively inactive cementite phase. This could partly be the reason for the reduction in activity of these catalysts, amounting to about a 30% decrease over a period of 2-weeks exposure to synthesis gas at 280°C.

Magnetic Measurements. The magnetization and susceptibility measurements were performed using the Faraday technique (15, 16, 17) in the temperature range 78 to 1000 K and applied fields up to 20 kOe. A Cahn RH electrobalance was used for these measurements.

The freshly impregnated zeolites indicated the presence of Fe^{3+} species from an analysis of the paramagnetic susceptibility, which showed an effective moment of about 5.96 Bohr magnetons.

The magnetization studies on the reduced samples of ZSM-5 (14.7% Fe) and Silicalite (13.6% Fe) indicate that iron is in the metallic state with 86% and 85% reduction, respectively. The magnetization vs. temperature curves for ZSM-5 (11.1% Fe) are shown in Figure 10. The carbided sample of ZSM-5 (11.1% Fe) appears to be the high Curie point form (18) of the Hagg carbide with $T_C = 540$ K. The used sample of ZSM-5 (11.1% Fe) exhibited a magnetic transition with $T_C = 650$ K, which corresponds to the hcp phase of (Fe_2C). The magnetic transition of cementite (Fe_3C) was masked in the M vs. T curve shown in Figure 10 since T_C of Fe_3C is about 490 K, well below that of the hcp carbide. The hcp phase of Fe_2C is considered to be stable (18) below 470 K in an atmosphere of synthesis gas. Its presence in the used sample may indicate that it was formed while the catalyst was cooled after the reaction.

The magnetization data (Figure 11) on ZSM-5 (5.6% Fe, 4.5% Co) show that the reduced, carbided, and used samples have large magnetic moments (1.94, 2.04, and 2.61 μ_B per transition metal atom, respectively,

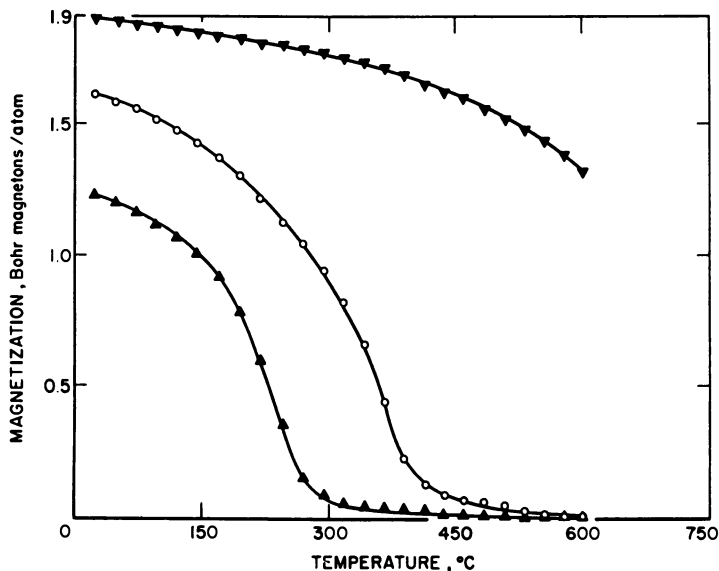


Figure 10. Magnetization (Bohr magnetons/iron atom) as a function of temperature for ZSM-5 (11.1% Fe) ($H = 6300$ gauss; (▼) reduced; (▲) carbided; (○) used)

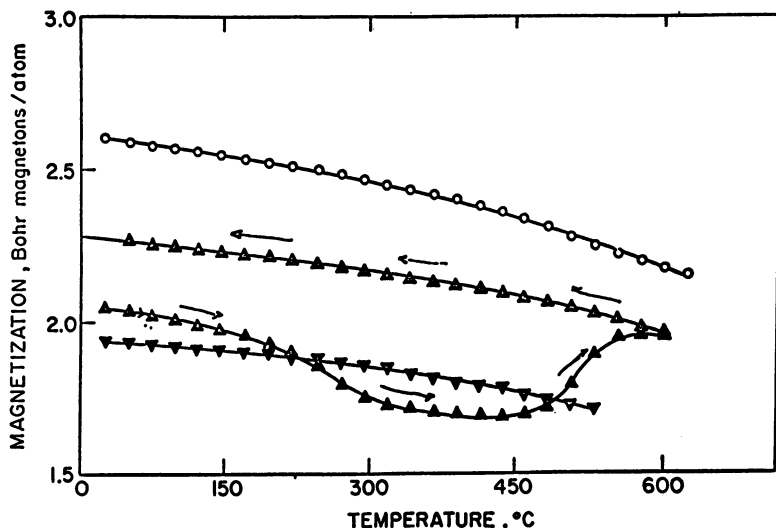


Figure 11. Magnetization as a function of temperature for ZSM-5 (5.6% Fe, 4.5% Co). The Bohr magneton number represents the weighted average of the two components present. ($H = 6300$ gauss; (▼) reduced; (▲) carbided; (○) used)

Table III. Product Compositions from the Catalysts ZSM-5 (11.1% Fe) and ZSM-5 (5.6% Fe, 4.5% Co) in a Berty Reactor, Showing the Influence of Cobalt Addition to the Catalyst^a

	<i>Catalyst</i>	
	ZSM-5 (11.1% Fe)	ZSM-5 (5.6% Fe, 4.5% Co)
Temperature	300	280
CO Conversion, %	68.2	37.8
H ₂ Conversion, %	38.7	41.3
Space Velocity	1500	1400
<i>Product Composition (%)</i>		
CO ₂	52.0	9.8
H ₂ O	19.4	51.8
CN _n + Oxygenates	28.6	38.4
<i>Hydrocarbon and Oxygenate Composition (%)</i>		
C ₁ -C ₄ hydrocarbons	83.1	74.3
C ₅ + and Oxygenates	16.9	25.7
<i>Composition of C₅+ and Oxygenates (%)</i>		
Aromatics	72	10
Olefins	3	46
Saturates	24	37
Oxygenates	1	7
% Gasoline range (BP < 204°C)	75	94
Research octane No.	96	81

^a Process condition: H₂/CO = 2, P = 21 bar.

at room temperature) and high Curie points (> 900°C), which cannot be accounted for on the basis of individual iron and cobalt particles. The magnetic data indicate the composition to be that of an iron-cobalt alloy (19), supporting the conclusions derived from the Mössbauer analysis. Hence, one can conclude that the difference in selectivity between ZSM-5 (11.1% Fe) and ZSM-5 (5.6% Fe, 4.5% Co) catalysts (see Table III) arises from the presence of bimetallic transition-metal clusters in the latter, with consequent changes in the average number of 3d electrons per transition metal atom. The *M* vs. *T* curve (Figure 11) of the carbided sample of ZSM-5 (5.6% Fe, 4.5% Co) indicated an irreversible formation of a second phase with a higher moment above a temperature of 450°C. This phase has not yet been identified.

Conclusions

A comparison of the spectra of carbided and used ZSM-5 with iron to those with both iron and cobalt, and their relative yields of aromatics (see Table III) in the conversion process, and an overall consideration

of all spectra and magnetic measurements indicate that: (a) the plausible active phase taking part in the conversion of the synthesis gas by iron-containing ZSM-5 and Silicalite is the Hagg carbide which is converted into cementite during the catalytic reaction; (b) the difference in selectivity between ZSM-5 (Fe) and ZSM-5 (Fe + Co) arises from alloy formation in the latter with changes in $3d$ electron concentration; and (c) the increase in cobalt concentration in ZSM-5 (Fe + Co) results in decreasing carbide formation. This suggests that the iron-cobalt alloy phase may itself be the active species in cobalt-rich catalyst compositions.

Acknowledgments

The authors are grateful to B. D. Blaustein, Manager, Process Sciences Division and to R. R. Schehl, Chief, Synthesis Gas Chemistry Branch at the Pittsburgh Energy Technology Center for many helpful discussions. This work was supported by DOE contract DE-AC-22-79PC1035.

Literature Cited

1. Collins, D. W.; Mulay, L. N. *IEEE Trans. Magn.* 1968, 4, 470.
2. Collins, D. W.; Dehn, J. T.; Mulay, L. N. In "Mössbauer Methodology"; Gruverman, I. J., Ed.; Plenum: New York, 1967; Vol. 3, p. 103.
3. Mulay, L. N. In "Mössbauer Methodology"; Gruverman, I. J., Ed.; Plenum: New York, 1967; Vol. 3, p. 79.
4. Mulay, L. N.; Collins, D. W.; Thompson, A. W.; Walker, P. L., Jr. *J. Organometal. Chem.* 1979, 178, 217-226.
5. Chang, C. D.; Lang, W. H.; Silvestri, A. J. *J. Catal.* 1979, 56, 268.
6. Caesar, P. D.; Brennan, J. A.; Garwood, W. E.; Circ, J. *J. Catal.* 1979, 56, 274.
7. Rao, V. U. S.; Gormley, R. J.; Schneider, L. C.; Obermyer, R. *Am. Chem. Soc., Div. Fuel Chem. Prepr.* (Houston, Mar., 1980) 25, 119.
8. Kokotailo, G. T.; Lawton, S. L.; Olson, D. H.; Meier, W. M. *Nature* 1978, 272, 437.
9. Flanigen, E. M.; Bennett, J. M.; Grose, R. W.; Cohen, J. P.; Patton, R. L.; Kirchner, R. M.; Smith, J. V. *Nature* 1978, 271, 512.
10. Argauer, R. J.; Landolt, G. R. U.S. Patent 3 702 886, 1972.
11. Grose, R. W.; Flanigen, E. M. U.S. Patent 4 061 724, 1977.
12. Raupp, G. B.; Delgass, W. N. *J. Catal.* 1979, 58, 348.
13. Gager, H. M.; Hobson, M. C., Jr. *Catal. Rev. Sci. Eng.* 1975, 11, 117.
14. Van der Woude, F.; Sawatsky, G. A. *Phys. Lett.* 1974, 12C, 335.
15. Mulay, L. N. "Magnetic Susceptibility"; Wiley-Interscience: New York, 1966.
16. Mulay, L. N. In "Methods of Physical Chemistry"; Weissberger, A.; Rossiter, B. W., Eds. Wiley-Interscience: New York, 1972.
17. Mulay, L. N.; Boudreaux, E. A., Eds. "Theory and Applications of Molecular Paramagnetism"; Wiley-Interscience: New York, 1976.
18. Sancier, K. M.; Isakson, W. E.; Wise, H. *Am. Chem. Soc., Div. Pet. Chem. Prepr.* (Anaheim, Mar., 1978) 23(2), 545.
19. Bozorth, R. M. "Ferromagnetism"; Van Nostrand: New York, 1951; pp. 190-209.

RECEIVED July 22, 1980.

Mössbauer Spectroscopic Investigations of Oxidation Catalysts

FRANK J. BERRY

Department of Chemistry, University of Birmingham, England

Catalytically active tin–antimony oxides of composition $\text{Sn}_{1-x}\text{Sb}_x\text{O}_2$ were investigated by ^{119}Sn and ^{121}Sb Mössbauer spectroscopy. Short period calcination of the coprecipitated materials at 600°C gives blue solids containing tin(IV), antimony(V), and antimony(III) in oxide environments. Heating for longer periods or at higher temperatures when $x > 0.20$ gives the segregation of an additional antimony oxide phase. When $x < 0.10$, antimony enters the tin(IV) oxide lattice as antimony(V), but no evidence is found for the formation of either tin(II) or antimony(III). A mechanism for charge compensation involving the delocalization of electrons into low-energy conduction bands is proposed. Mixed oxide catalysts are unaltered by the adsorption of acids or bases, whereas reaction of tin–antimony oxides with hydrogen or their use in the catalytic oxidation of olefins is accompanied by the reduction of antimony(V) to antimony(III). The Mössbauer parameters are related to the fundamental properties of the materials and their catalytic character.

The catalytic properties of mixed oxides have been known for many years, and several systems have been developed commercially for the selective oxidation and ammoxidation of olefins (1). Despite the industrial and economic significance of these materials, surprisingly few details of their physical and chemical properties have been established, and consequently there is a sparsity of data by which their fundamental properties may be related to their catalytic character.

Although the recent development of spectroscopic techniques has been of considerable importance in the elucidation of catalytic phenomena, the operating conditions of some of these techniques are far

from those of actual catalytic processes, and samples are frequently required in a specially prepared form. Mössbauer spectroscopy is, in principle, a technique that is most favorable for investigating catalytically active materials. The method is able to examine authentic catalysts under realistic conditions and is highly sensitive to chemical, structural, and magnetic changes. Additionally, the technique is able to sense these changes whether they occur on the surface of a bulk solid (2) or within supported, catalytically active small particles (3). Moreover, many inorganic mixed-oxide catalysts contain *p*- or *d*-block elements that are Mössbauer active and that are amenable to investigation by conventional transmission-mode Mössbauer spectroscopy.

Although the catalytic properties of tin–antimony oxides in the selective oxidation, oxidative dehydrogenation, and ammoxidation of hydrocarbons have provoked several investigations, there seems to be little unanimity as to the nature of the active sites and whether or not any changes in oxidation state and lattice structure accompany the adsorption and catalytic processes (1). The importance of Mössbauer spectroscopy to the study of this catalyst arises from the amenability of both tin and antimony to Mössbauer investigation and the ability of the technique to probe features of catalytic relevance such as the phase composition, the cationic oxidation states, the environments of the cations, the charge compensation mechanism, and the distortion of the host tin(IV) oxide lattice by the dopant antimony atoms. Although a few Mössbauer studies (4, 5, 6) of rutile-type materials have included tin–antimony oxides, the inconsistencies in data reflect the need for systematic investigations of materials of known compositions when prepared by well-defined methods under controlled conditions.

These catalytically active materials often have been prepared by coprecipitation techniques, and an initial study (7) has shown that conventional transmission-mode Mössbauer spectroscopy is a potentially powerful means by which such catalysts may be investigated. This work describes how ^{119}Sn and ^{121}Sb Mössbauer studies of catalytically active tin–antimony oxides have been used to investigate:

1. the formation of the catalyst by the dehydration of a gel and the relationship between the catalyst, its composition, and its pretreatment;
2. the physical and chemical properties of the catalyst that are amenable to investigation by Mössbauer spectroscopy;
3. the effect of adsorption on the catalyst and its use in catalytic reactions;
4. the correlation between the physical and chemical properties of the catalyst and the catalytic character of the material.

Experimental

Preparation of Samples. Tin-antimony oxides of the type $\text{Sn}_{1-x}\text{Sb}_x\text{O}_2$ ($x = 0.00-1.00$) were prepared by coprecipitation techniques from the simultaneous addition of anhydrous tin(IV) chloride and antimony(V) chloride to ammonium hydroxide solution. The filtered and washed white precipitates were dried at 120°C , ground to constant particle size, and heated at 600°C in air for 16 h. Some materials also were heated for longer periods and/or at higher temperatures in sealed tubes.

Samples of tin(IV) oxide, tin-antimony oxide, and tin-molybdenum oxide were treated by: (a) pyridine at 200°C or acetic acid at 150°C until a steady rate of adsorption and desorption was obtained; (b) a 10% hydrogen/90% nitrogen gas mixture at 480°C ; (c) a 5% butene/10% oxygen/85% nitrogen gas mixture at 400°C .

Mössbauer Spectroscopy. Tin-119 Mössbauer spectra were recorded at 77 K using a conventional constant-acceleration spectrometer with a $\text{Ca}^{119\text{m}}\text{SnO}_3$ source and samples containing 10 mg Sn/cm². The drive velocity was calibrated with a $^{57}\text{Co}/\text{Rh}$ source and iron foil. All the ^{119}Sn Mössbauer spectra were computer-fitted (8). Spectra of tin(IV) oxide were recorded at frequent intervals and used as a standard to which the chemical isomer shift data have been referred.

Antimony-121 Mössbauer spectra were recorded at 77 K with a constant-acceleration, 256-channel, microprocessor-controlled spectrometer (9) using a 1-mCi $\text{Ca}^{121\text{m}}\text{SnO}_3$ source. The samples containing 10 mg Sb/cm² were mixed with powdered polythene and compressed into 1.6-cm diameter discs of 0.3-cm thickness. All the ^{121}Sb Mössbauer spectra were least-squares fitted to two Lorentzian peaks to account for the possible presence of both antimony(V) and antimony(III) species. The data were subsequently fitted to two sets of eight lines as would be produced by quadrupole splitting in the 7/2 to 5/2 nuclear transition of ^{121}Sb . The asymmetry parameter η was taken as zero (10), and a ratio of 1.34 was adopted for the quadrupole moments of the excited and ground states (11).

Results and Discussion

Tin-Antimony Oxides. Calcination of the materials at temperatures of 600°C and above gave blue solids.

The ^{119}Sn Mössbauer data gave superior χ^2 values and linewidths closer to those of barium stannate when fitted to two lines. No statistically significant evidence of more complex spectra could be obtained. The ^{119}Sn Mössbauer parameters are given in Table I.

Only two samples gave ^{121}Sb Mössbauer data that showed an improvement in χ^2 and other Mössbauer parameters when fitted according to the quadrupole split model. The ^{121}Sb Mössbauer parameters are recorded in Table II and typical spectra are depicted in Figure 1.

THE THERMAL DECOMPOSITION OF TIN(IV)HYDROXIDE AND ANTIMONIC ACID. The gel formed by alkaline precipitation of aqueous tin(IV) chloride and allowed to dry at room temperature gives a single broad-line

Table I. ^{119}Sn Mössbauer Parameters of Tin–Antimony Oxides ($\text{Sn}_{1-x}\text{Sb}_x\text{O}_2$)

x	$\delta^a \pm 0.03$ (mms^{-1})	$\Delta \pm 0.03$ (mms^{-1})	Γ (mms^{-1})
0.000	0.00	0.56	1.06
0.005	0.00	0.60	0.97
0.01	0.07	0.66	1.10
0.02	0.05	0.66	1.12
0.03	0.05	0.67	1.11
0.04	0.08	0.68	0.97
0.05	0.08	0.67	0.96
0.06	0.10	0.69	1.28
0.073	0.11	0.68	1.09
0.08	0.11	0.67	1.13
0.175	0.13	0.73	0.99
0.28	0.13	0.75	1.13
0.52	0.12	0.74	1.19
0.83	0.08	0.75	0.91

^a δ relative to SnO_2 .

Table II. ^{121}Sb Mössbauer Parameters Antimony(V)

x	Treatment	δ^b (mms^{-1})	Γ (mms^{-1})
0.03	20 d/1000°C	8.228(116)	3.24(44)
0.10	16 h/600°C	8.240(60)	3.92(24)
0.10	14 d/600°C sealed tube	8.351(60)	3.16(30)
0.20	16 h/600°C	8.464(34)	3.55(14)
0.20	14 d/600°C sealed tube	8.440(52)	3.96(22)
0.40	16 h/600°C	8.384(56)	4.39(20)
0.40	14 d/600°C sealed tube	8.564(40)	3.93(16)
0.65	16 h/600°C	8.655(34)	3.94(14)
0.65	14 d/600°C sealed tube	8.704(32)	3.74(12)
0.65	16 h/900°C	8.860(54)	3.48(22)

^a The standard deviations are in units of the last decimal place and correspond to 95% confidence limits.

Mössbauer spectrum (12). Subsequent heating of this material produces intermediate dehydration species that give quadrupole split Mössbauer spectra that reflect an initial increase and subsequent decrease in asymmetry at the oxyhydroxytin nucleus, until at 600°C white tin(IV) oxide is produced. The oxide gives a small quadrupole split Mössbauer spectrum (Table I) that may be attributed to the slightly distorted arrangement of six oxygen atoms around the tin nucleus in a rutile-type structure (13).

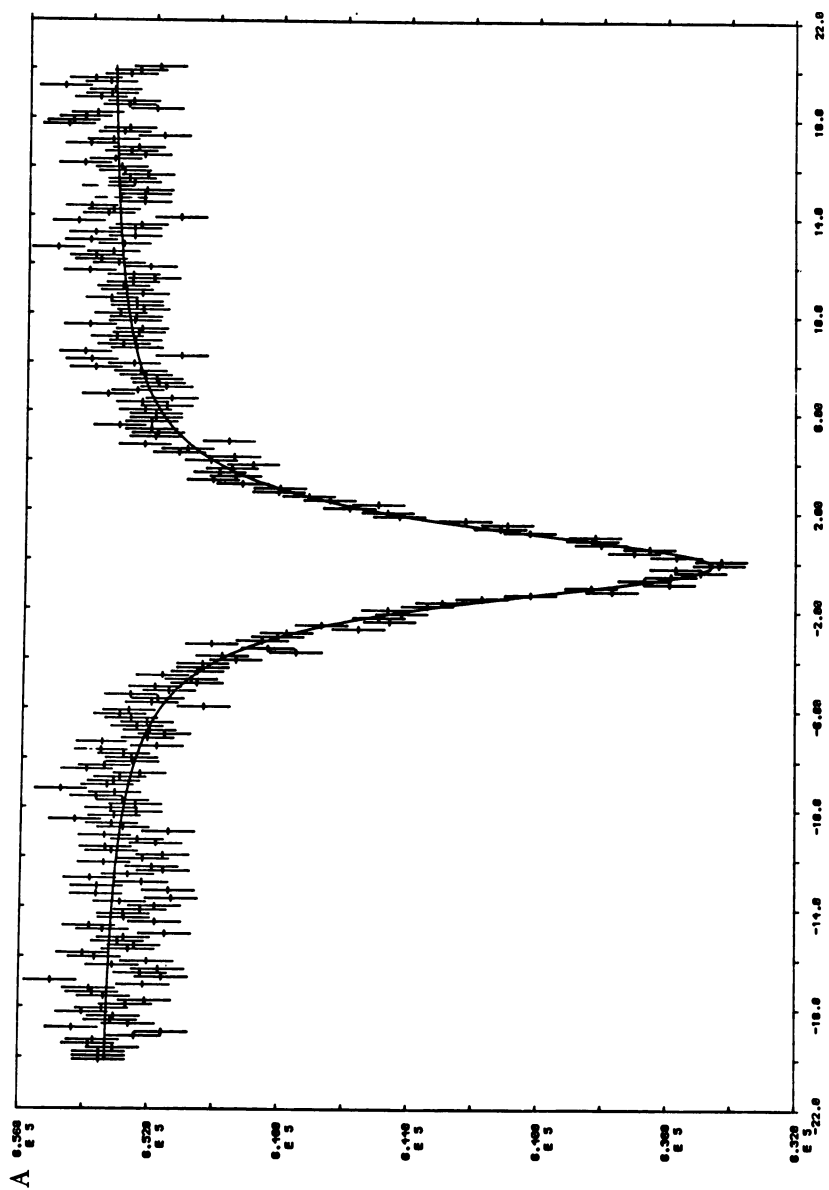
The pyrolysis of antimonous acid (14) shows that a compound with formula Sb_2O_5 cannot be reached without reduction of antimony(V) to antimony(III). The first product that forms between 650° and 850°C is Sb_6O_{13} which transforms at 935°C to β - Sb_2O_4 . These oxides contain both antimony(V) and antimony(III). Complete reduction to Sb_2O_3 is not achieved below 927°C.

Since the metal–oxygen distances in all these oxides are similar, it might reasonably be expected that the formation of mixed oxides by coprecipitation, especially in materials containing low concentrations of antimony, would involve the replacement of tin atoms in the tin(IV) oxide rutile-type lattice by antimony. Under such circumstances it also

of Tin–Antimony Oxides ($Sn_{1-x}Sb_xO_2$)^a

<i>Antimony(III)</i>		e^2qQ (mms^{-1})	<i>Area Ratio</i> <i>Sb(III):Sb(V)</i>
δ^b (mms^{-1})	Γ (mms^{-1})		
–4.50 (50)	5.17 (140)		0.14 (3)
–5.18 (54)	5.99 (140)		0.16 (3)
–5.38 (22)	4.80 (70)		0.15 (2)
–5.06 (76)	5.72 (76)		0.27 (2)
–5.76 (180)	2.62 (64)	14.1 (50)	0.21 (2)
–5.44 (10)	2.87 (34)	13.7 (3)	0.87 (5)

^a δ relative to InSb.



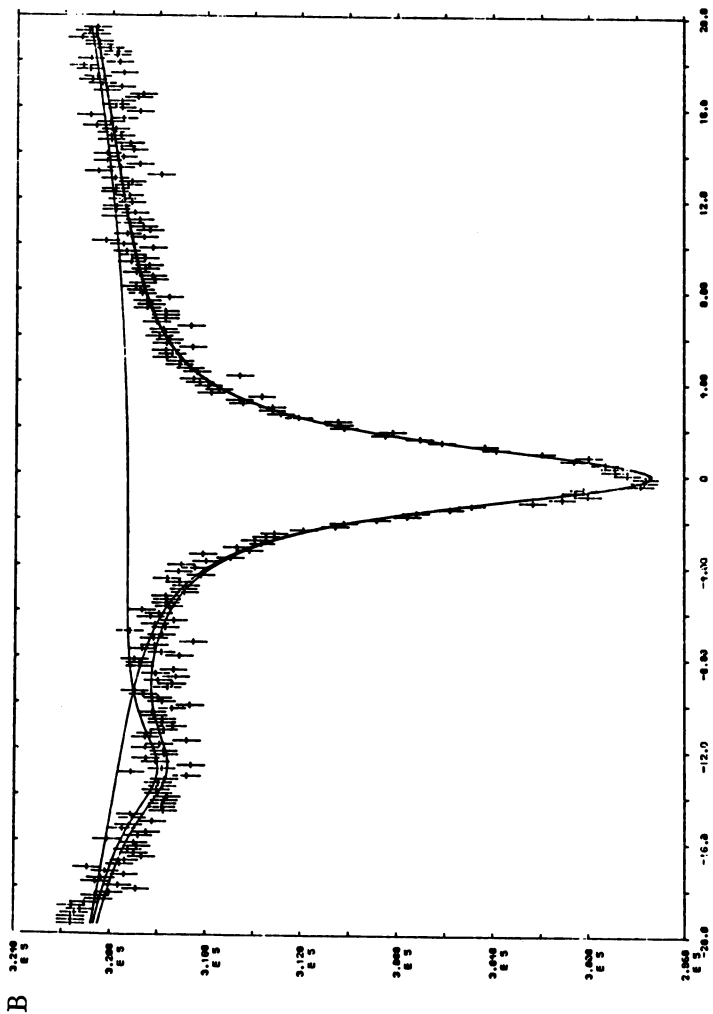


Figure 1. Antimony-121 Mössbauer spectra of $\text{Sn}_{0.80}\text{Sb}_{0.20}\text{O}_2$; (A) calcined for 14 days at 600°C in a sealed tube; (B) calcined for 16 h at 600°C

might be expected that charge balance would be achieved by one of two simple processes: (a) the replacement of three tin(IV) atoms by two antimony(V) and one tin(II); (b) the replacement of two tin(IV) atoms by one antimony(V) and one antimony(III).

TIN-119 MÖSSBAUER INVESTIGATIONS OF TIN-ANTIMONY OXIDES. A plot of ^{119}Sn Mössbauer chemical isomer shifts and quadrupole splittings as a function of antimony concentration (7) for the tin-antimony oxides heated at 600°C in air is given in Figure 2.

Both Mössbauer parameters clearly increase from those of tin(IV) oxide as the antimony concentration is increased to 10%. Since $\Delta R/R$ is positive for the ^{119}Sn transition (15, 16), the larger chemical isomer shifts represent increasing s electron density at the tin nucleus but remain characteristic of the tin(IV) species in oxide environments. It is significant that the Mössbauer spectra provide no evidence for the formation of tin(II), which separate experiments found to be easily recognizable when present in quantities above 2 mol %. The larger quadrupole splittings indicate increasing distortion of the environment about the tin nucleus with increasing antimony concentration.

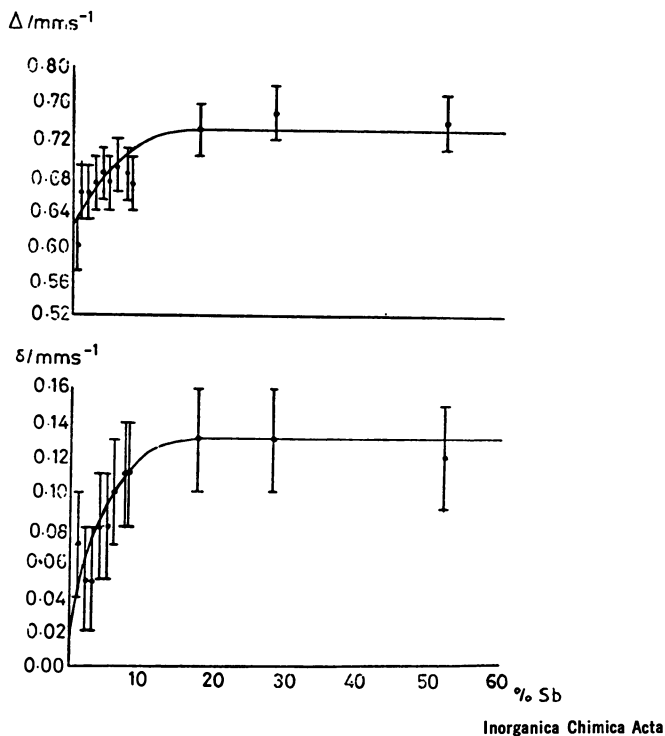


Figure 2. Tin-119 Mössbauer parameters as a function of antimony content (7)

It is clear that the character of the tin–antimony oxide changes when the antimony content exceeds about 10%, and it seems that up to this point the samples can be regarded as single phases in which antimony may enter the tin(IV) oxide rutile lattice. It is significant that the catalytic activity for the oxidation of propene to acrolein also increases over a similar range of antimony concentrations (17). The ^{119}Sn Mössbauer spectra clearly show that within this range charge balance cannot be achieved by replacing three tin(IV) units by two antimony(V) and one tin(II). The single more positive ^{119}Sn chemical isomer shifts suggest that if charge compensation does involve the reduction of tin atoms, then the extra electrons are delocalized in the tin-containing phase and are not localized on individual tin atoms. It is interesting to note that a model for the mixed tin–antimony oxide system involving conduction bands composed mainly of 5s orbitals has been suggested (18), and the low ^{119}Sn Mössbauer chemical isomer shift in CsSnBr_3 has been explained (19–22) in terms of delocalization of tin 5s electron density into a low-energy conduction band. The ^{119}Sn Mössbauer data are therefore compatible with a material in which charge balance in the interior of the solid is achieved by delocalization of electrons in a 5s conduction band.

It appears that when the mixed oxide contains a concentration of antimony in excess of 10%, a two-phase region begins in which the second phase does not contain any appreciable amount of tin.

ANTIMONY-121 MÖSSBAUER INVESTIGATIONS OF TIN–ANTIMONY OXIDES. The ^{121}Sb Mössbauer parameters of tin–antimony oxides are characteristic of antimony(V) and antimony(III) species in oxide environments. The chemical isomer shift data for antimony(V) resemble those recorded (23, 24) in other antimony compounds with rutile-type structure and which contain Sb(V)O_6 octahedral units.

The linewidths of the resonance peaks, especially those for materials calcined at 600°C for 16 h, are broader ($\Gamma > 3.55 \text{ mms}^{-1}$) than expected for thin, single-line absorbers. The failure of the antimony(V) data to show an improvement when fitted to eight lines, and the computation of similar values of quadrupole splitting for both positive and negative values of e^2qQ indicate that the peak is symmetric and that line broadening is not due to the occupation by antimony(V) of significantly distorted oxygen environments. The antimony(III) data for these materials ($\Gamma > 5.17 \text{ mms}^{-1}$) are also indicative of quadrupole interaction, but like the antimony(V) data are also resistant to fitting according to a quadrupole split model. Therefore, the broad spectral linewidths suggest that short-period calcination at 600°C produces dehydrated materials containing both antimony(V) and antimony(III) species in a heterogeneity of surroundings that differ only in the nature of the immediate oxygen environment.

The Mössbauer antimony(III):antimony(V) peak area ratio decreases with decreasing antimony concentration and thereby shows a diminishing antimony(III) presence in the mixed oxides.

Tin-Antimony Oxides in Which $x = 0.20-0.65$. Materials in which $x = 0.65$ give the largest antimony(III):antimony(V) peak area ratios, and the samples calcined either at 600°C for 14 days or 900°C for 16 h are the only pure mixed oxides to give a significant improvement in χ^2 when the antimony(III) data are fitted to eight lines. X-ray diffraction investigations (25) show that materials of similar Möss composition contain both a rutile and antimony oxide phase. The Mössbauer parameters of these samples resemble those of antimony oxides containing both antimony(III) and antimony(V) (14, 26) and suggest that the antimony oxide dominates any contribution from the rutile phase. The peak area ratio for the sample treated at higher temperature suggests that the additional phase is Sb_2O_4 while that formed by prolonged heating at 600°C is more characteristic of Sb_6O_{13} . It is interesting that the other sample containing 65% antimony and subjected to 16-h calcination at 600°C indexed as a single-phased rutile-type material and gave a Mössbauer spectrum more similar to that of Sb_6O_{13} than Sb_2O_4 .

Samples in which $x = 0.40$ were subjected to calcination treatments that gave (25) both a single-phased material with a rutile-type structure (600°C for 16 h) and a rutile-plus-antimony oxide two-phased material (600°C for 14 days). Both substances gave similar Mössbauer spectra that suggest the occupation by antimony of similar environments. The antimony(III):antimony(V) ratios are smaller than those observed in samples containing 65% antimony, indicating that any antimony oxide in these materials is insufficient to dominate the spectra.

Materials in which $x = 0.20$ are interesting since calcination at 600°C for both 16 h and 14 days produces single-phased samples with rutile-type structures (25). However, the Mössbauer parameters show that 16-h calcination produces both antimony(III) and antimony(V) species in a ratio similar to the material in which $x = 0.40$, whereas longer calcination gives a sample showing only an antimony(V) contribution.

The ^{119}Sn and ^{121}Sb Mössbauer parameters for materials containing between 20 and 65% antimony may be related to the preparative procedure. The white precipitate formed in alkaline media containing hydrated tin(IV) and antimony(V) dehydrates on heating at 600°C for 16 h and forms blue solids. The x-ray diffraction data (25) show these materials to be poorly crystalline, highly defective, rutile-type solids. The Mössbauer spectra reveal the presence of tin(IV), antimony(V), and antimony(III) species in oxygen environments, and are consistent with the dehydration process causing reduction of antimony(V) as is observed during the pyrolysis of antimonous acid (14) and the transformation of the

tin(IV) hydroxide gel to tin(IV) oxide. The coexistence of random arrays of such units in a noncrystalline solid are consistent with the description of these materials (25) as single-phased amorphous solids.

Despite the confusion in the literature (17, 27, 28) over materials in which tin and antimony are in roughly equal proportions, there is little evidence for compound formation below 900°C, and the Mössbauer data confirm that bulk equilibrium is difficult to establish by short-period calcination at low temperatures. Prolonged heating at 600°C or short-period calcination at higher temperatures gives the formation of a second phase which ¹²¹Sb Mössbauer spectroscopy shows to have characteristics of an antimony oxide containing both antimony (III) and antimony (V).

An interesting feature of tin-antimony oxides heated at 600°C is their blue color which resembles that observed in the alkali metal antimony halides and which has been attributed (29) to a Sb³⁺-Sb⁵⁺ charge-transfer process. The close coexistence of antimony(III) and antimony(V) in similar sites as shown by the Mössbauer data would be achieved easily in tin-antimony oxides with compositions just described and when heated to 600°C for 16 h. The apparent absence (30) of any dark blue solids for which a Sn²⁺-Sn⁴⁺ mechanism has been proposed would support such a Sb³⁺-Sb⁵⁺ charge-transfer process in tin-antimony oxides.

Tin-Antimony Oxides in Which $x < 0.20$. Like the ¹¹⁹Sn Mössbauer data, the ¹²¹Sb Mössbauer parameters for materials within this range of compositions are different from those of the other tin-antimony oxides. The materials show only an antimony(V) contribution to the spectrum and, when subjected to prolonged or high-temperature calcination, give linewidths that are smaller ($\Gamma < 3.24 \text{ mms}^{-1}$) than those reported for antimony compounds with a lead antimonate structure (23). Such Mössbauer parameters might be expected from single-phased, rutile-type materials in which the antimony(V) species occupies a unique site within an octahedral array of oxygen atoms.

Given that the metal-oxygen distances in SnO₂, Sb₆O₁₃, and Sb₂O₄ are all similar (13, 14), it might be expected that any replacement of tin atoms in the tin(IV) oxide rutile lattice by antimony would be most likely to occur during the calcination process in materials containing a low concentration of antimony. Although the upper limit of antimony solubility has been defined as high as 20% (28), the ¹¹⁹Sn and ¹²¹Sb Mössbauer data and the recent x-ray diffraction investigations (25) appear to be more consistent with other descriptions (17, 31) of a 10% limit. Since the ¹¹⁹Sn Mössbauer spectra show that within this composition range three tin(IV) atoms are not replaced by two antimony(V) atoms and one tin(II) atom, it might reasonably be expected that the charge-balancing mechanism involves the replacement of two tin(IV) atoms by one antimony(V) and one antimony(III). It might also be

envisaged that the process would either involve substitution into the lattice or the occupation of interstitial octahedral sites. However, it is known that antimony(III), like tin(II), has a lone pair of electrons and rarely adopts octahedral coordination (32). In this respect it is significant that the lattice parameters of antimony-doped tin(IV) oxide are similar to those of pure tin(IV) oxide (33), and are therefore inconsistent with the accommodation of species with lone pairs of electrons within the lattice. Although the surface segregation of antimony at high temperatures (25) could in principle provide more favorable antimony(III) sites without affecting the lattice parameters, the x-ray photoelectron investigations (25) have not identified such surface species. The Mössbauer parameters of monophasic, rutile-type tin-antimony oxides containing low concentrations of antimony and calcined for long periods at temperatures exceeding 600°C do not provide evidence for the accommodation of antimony(III) within the lattice and are unable to confirm the expected reduction of antimony(V) to antimony(III).

The Mössbauer parameters must therefore be considered in terms of the formation of the mixed oxide without reduction of either antimony(V) or tin(IV). Closer examination of the antimony(V) chemical isomer shifts, especially those of materials calcined for long periods or at high temperatures, shows that they decrease relative to the value reported for Sb_2O_4 ($\delta \sim 8.7 \text{ mms}^{-1}$) (24, 26), as the antimony concentration in the tin-antimony oxides decreases. It appears that the *s* electron density at the antimony nucleus is highest when the antimony concentration is between 3 and 10%, and thereby complements the ^{119}Sn Mössbauer data which showed the accumulation of electron density over the tin-containing species as the antimony content approaches a concentration of 10%. Therefore, the formation of monophasic materials containing antimony within the tin(IV) oxide lattice is restricted to those materials with an antimony content of less than 10% when heated at temperatures exceeding 600°C for long periods. In addition, within this composition range, charge balance is maintained by the delocalization of electron density into a low-energy conduction band composed largely of 5*s* orbitals by a mechanism similar to that which has been used to account for the low ^{119}Sn Mössbauer chemical isomer shifts and conduction properties in colored cesium tin(II) bromide (19–22). Such a process conforms with the band structure (18, 34, 35) of tin(IV) oxide, which has been used (36) to account for the increasing (31) *n*-type semiconductivity of the material which reportedly reaches a maximum on addition of 3% antimony.

The sample containing 3% antimony and calcined at 1000°C for 20 days gives the most negative antimony(V) chemical isomer shift ($\delta = 8.228 \text{ mms}^{-1}$) and corresponds to the highest *s* electron density at the antimony(V) nucleus. The optimized specific activity for butadiene

formation (37) of this equilibrated rutile-type material has been linked with the maximized surface enrichment of antimony ions which occurs without the separation of free Sb_2O_4 . It is possible that the deep blue color change in these materials at 400°C which has been correlated (25) with the beginning of surface enrichment is connected with the delocalization of electrons into the conduction band and the formation of solid solutions. The catalytic activity of these tin–antimony oxides has been associated (38) with the possible formation of Sn^{4+} and Sb^{3+} active centers with acidic and basic function. It is interesting that the ESR signals from low-antimony-content tin–antimony oxides (39) may be attributable to the trapping at anion vacancies of free electrons that are created by the substitution of antimony in the tin(IV) oxide lattice. It is therefore possible that the surface reducing or basic sites may consist of trapped electrons which, as the antimony concentration increases, become delocalized into a conduction band.

The active centers in tin–antimony oxide catalysts may therefore be composed of Sn^{4+} ions and Sb^{3+} or trapped electrons. The decrease in specific catalytic activity for the oxidative reactions of butene over the catalyst containing high concentrations of antimony (38) has been used to support the assignment of Sn^{4+} as an acid center. The ^{119}Sn Mössbauer spectra confirm the retention of tin in the oxidation state of (IV). Similarly, the enhanced activity and selectivity of mixed oxides containing low acidity and high basicity, that is, where the basic sites are formed by the presence of a low concentration of antimony, also are supported by the Mössbauer spectra, which show that delocalization of electrons over the tin- and antimony-containing phases is optimized in materials of these compositions.

Tin–Molybdenum Oxides. A tin–molybdenum oxide ($\text{Sn}_{0.98}\text{Mo}_{0.02}\text{O}_2$) that also can be used for the catalytic oxidation of propene to acrolein gave a ^{119}Sn Mössbauer spectrum ($\delta = 0.03 \text{ mms}^{-1}$) confirming that the tin(IV) species is not reduced to tin(II). The result is therefore compatible with ESR investigations (40) that have described the material as containing pentavalent molybdenum ions in substitutional sites in the tin(IV) oxide lattice. The quadrupole splitting ($\Delta = 0.68 \text{ mms}^{-1}$) is comparable to that recorded for the tin–antimony oxide of analogous composition (Table I) and reflects the similar distortion of the tin(IV) oxide lattice by replacing tin atoms with different cations of similar size.

Mixed Oxides Used in Adsorption Processes. The adsorption of acetic acid (up to $4.31 \mu\text{mol m}^{-2}$) and pyridine (up to $2.69 \mu\text{mol m}^{-2}$) on oxides of formula $\text{Sn}_{1-x}\text{Sb}_x\text{O}_2$ ($x = 0.00, 0.02, 0.10, 0.75$) did not significantly alter the Mössbauer parameters of the pure materials. Therefore, despite infrared evidence for the adsorption of bases to Lewis acid sites on metal oxides (41, 42), such processes are unlikely to involve the bulk tin cations in tin(IV) oxide or mixed tin–antimony oxide catalysts

Table III. ^{119}Sn and ^{121}Sb Mössbauer Parameters of Tin–Antimony

x	Treatment	Tin	
		$\delta^b \pm 0.03$ (mms^{-1})	$\Delta \pm 0.03$ (mms^{-1})
0.20	14 d/600° sealed tube	0.15	0.75
0.20	reduced by 5.4%	0.18	0.72
0.20	reduced by 10.3%	0.18	0.69
0.20	reduced by 30.2%	0.11	0.66

^a The standard deviations are in units of the last decimal place and correspond to 95% confidence limits.

in a charge-balancing role or give any significant modification to the rutile-type lattice structures.

The ^{119}Sn Mössbauer spectra of the tin–molybdenum oxide ($\text{Sn}_{0.98}\text{Mo}_{0.02}\text{O}_2$) showed the oxide to be unaffected by the adsorption of 1.6 $\mu\text{mol m}^{-2}$ of pyridine at 400°C despite the reported reduction of tin and iron during the chemisorption of hydrocarbons on tin–molybdenum– and iron–molybdenum–oxide catalysts (43, 44, 45).

Reaction of Tin–Antimony Oxides with Hydrogen. The tin–antimony oxides in which $x = 0.20$ were reduced by the hydrogen/nitrogen gas mixtures by 4%, 10%, and 30%. The ^{119}Sn and ^{121}Sb Mössbauer parameters of the materials following such treatment are given in Table III.

The ^{119}Sn Mössbauer chemical isomer shifts are, within the limits of experimental accuracy, identical to those of the pure mixed oxide, and therefore show no evidence for the formation of tin(II) despite the reduction of the tin–antimony by as much as 30%. The decrease in quadrupole splitting that accompanies the increased reduction is also

Table IV. ^{119}Sn and ^{121}Sb Mössbauer Parameters of Tin–Antimony

x	Treatment	Tin	
		$\delta^b \pm 0.03$ (mms^{-1})	$\Delta \pm 0.03$ (mms^{-1})
0.20	14 d/600°C sealed tube	0.15	0.75
0.20	reacted with butene and oxygen	0.04	0.67
0.02	20 d/1000°C	0.05	0.66
0.02	reacted with butene and oxygen	−0.05	0.56

^a The standard deviations are in units of the last decimal place and correspond to 95% confidence limits.

Oxides (Sn_{1-x}Sb_xO₂) Following Reaction with Hydrogen^a

<i>Antimony(V)</i>		<i>Antimony(III)</i>		e^2qQ (mms^{-1})	<i>Area Ratio</i> <i>Sb(III):Sb(V)</i>
δ° (mms^{-1})	Γ	δ° (mms^{-1})	Γ (mms^{-1})		
8.440(52)	3.96(22)				
8.195(52)	3.64(20)	-4.11(40)	3.52(88)	16.2(12)	0.51(6)
8.261(56)	3.68(22)	-4.01(20)	4.37(54)	15.1(6)	1.28(6)
8.093(96)	4.00(40)	-3.20(46)	2.97(40)	6.0(12)	1.39(8)

^b δ relative to SnO₂.^c δ relative to InSb.

significant since it reflects a diminishing electric field gradient at the tin nucleus.

The ¹²¹Sb Mössbauer spectra, however, (Figure 3) clearly show that the reaction of tin-antimony oxides with hydrogen involves the reduction of antimony(V) to antimony(III).

Reaction of Tin-Antimony Oxides with Oxygen and Butene. The ¹¹⁹Sn and ¹²¹Sb Mössbauer parameters of tin-antimony oxides containing either 20 or 2% antimony following their use as catalysts for the oxidation of butene are given in Table IV.

The ¹¹⁹Sn Mössbauer chemical isomer shifts are more negative and the quadrupole splittings are smaller than the values recorded for the pure mixed oxides. Therefore, the process appears to resemble that which occurred during the reduction of the tin-antimony oxide by hydrogen and which showed quite clearly that tin(IV) was not reduced to tin(II).

The ¹²¹Sb Mössbauer spectrum of the material containing 20% antimony confirms that antimony(V) is reduced to antimony(III). The

Oxides (Sn_{1-x}Sb_xO₂) Following Reaction with Butene and Oxygen^a

<i>Antimony(V)</i>		<i>Antimony(III)</i>		e^2qQ (mms^{-1})	<i>Area Ratio</i> <i>Sb(III):Sb(V)</i>
δ° (mms^{-1})	Γ	δ° (mms^{-1})	Γ (mms^{-1})		
8.440(52)	3.96(22)				
8.577(15)	3.60(60)	-4.73(40)	3.90(40)	15.70(50)	0.38(2)
8.228(116)	3.24(44)				
8.10(70)	3.85(30)				

^b δ relative to SnO₂.^c δ relative to InSb.

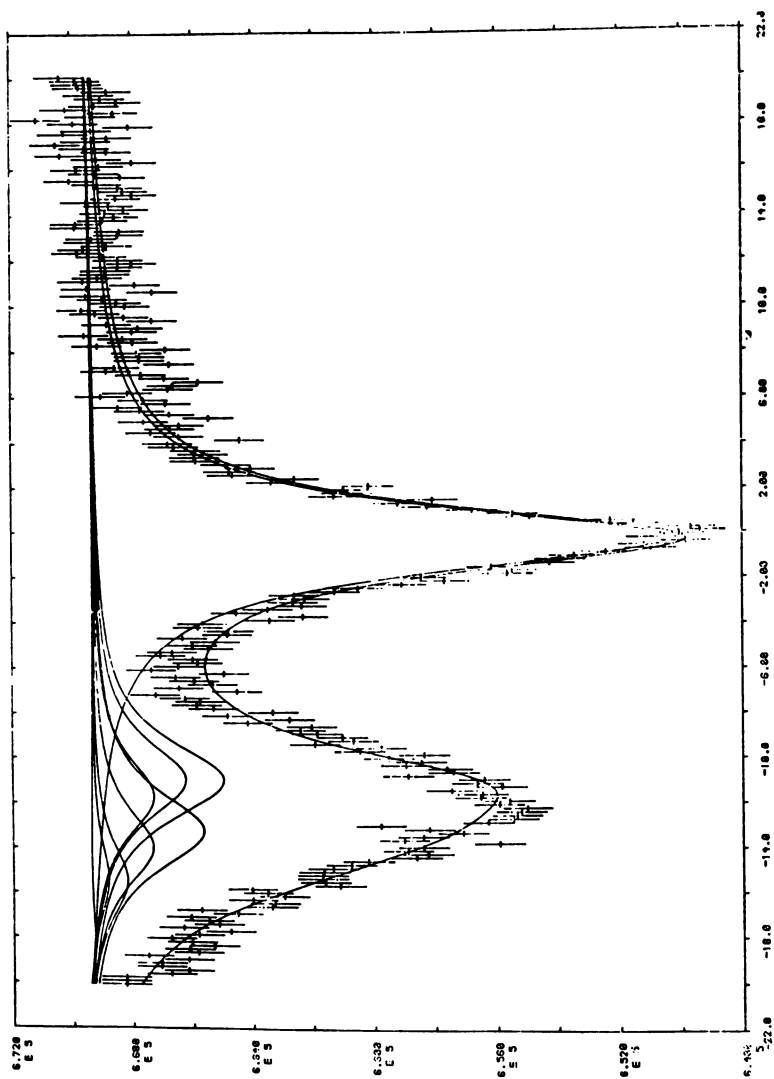


Figure 3. Antimony-121 Mössbauer spectrum of $\text{Sn}_{0.80}\text{Sb}_{0.20}\text{O}_2$ following reaction with 10% hydrogen/90% nitrogen gas mixture at 480°C

composition of this material may be described as a two-phase system in which one phase is constituted by the rutile-type tin(IV) oxide with antimony within the lattice and the second phase by an antimony oxide (25). Hence the reduction of antimony(V) to antimony(III) in this material under catalytic conditions may be associated with either the reduction of antimony in the rutile phase or the reduction of Sb_6O_{13} or Sb_2O_4 to antimony(III) oxide.

The material containing 2% antimony is quite different since it represents the single-phase material containing antimony in the tin(IV) oxide lattice. The ^{119}Sn Mössbauer parameters of this material following its use in the catalytic process are remarkably similar to those of pure tin(IV) oxide. This decrease in electron density at the tin nuclei, and the apparent recovery of the lattice structure, implies a decrease in both the lattice and valence contribution to the electric field gradient at the tin nucleus and, by analogy with the materials reacted with hydrogen, is consistent with the reduction of antimony(V) within the lattice to antimony(III). However, the ^{121}Sb Mössbauer spectra give no evidence for the formation of antimony(III), but this absence may reflect the low sensitivity of the technique to the detection of such a low concentration of the species.

The problem remains, however, as to the accommodation of any antimony(III) species if created by such a mechanism. It is interesting in this respect that antimony-doped tin(IV) oxide gives evidence (33) for the presence of twin boundaries. Since twinning is a means of slightly changing the anion to cation stoichiometry of a crystal and of providing sites with different coordination, it is possible that small concentrations of antimony(III) formed by reduction of antimony(V) could segregate to these twin boundaries and thereby enjoy more favorable sites.

The failure of Mössbauer spectroscopy to identify any reduction of tin(IV) to tin(II) and the proposed reduction of antimony(V) to antimony(III) during the catalytic reaction may be correlated with mechanisms that have been proposed for chemisorption and catalytic reactions of olefins on tin-antimony oxides (5, 27). These mechanisms have involved partial reduction of antimony(V) to antimony(III) and the formation of a π -allyl intermediate species (17, 38). A similar mechanism has been postulated for the reaction of propene over tin-molybdenum oxide catalysts (46).

Literature Cited

1. Hucknall, D. J. "Selective Oxidation of Hydrocarbons"; Academic: New York, 1974; p. 42.
2. Tricker, M. J. "Surface and Defect Properties of Solids"; Roberts, M. W.; Thomas, J. M., Eds.; Chem. Soc.: London, 1977; Vol. 6, p. 106.

3. Berry, F. J. "Advances in Inorganic Chemistry and Radiochemistry"; Emeleus, H. J.; Sharpe, A. G., Eds.; Academic: New York, 1978; Vol. 21, p. 255.
4. Skalkina, L. V.; Suzdalev, I. P.; Kolchin, I. K.; Margolis, L. Y. *Kinet. Catal.* 1969, 10, 378.
5. Suzdalev, I. P.; Firsova, A. A.; Aleksandrov, A. U.; Margolis, L. Y.; Baltrunas, D. A. *Dokl. Akad. Nauk, S.S.S.R.* 1972, 204, 408.
6. Birchall, T.; Bouchard, R. J.; Shannon, R. D. *Can. J. Chem.* 1973, 51, 2077.
7. Berry, F. J.; Maddock, A. G. *Inorg. Chim. Acta* 1978, 31, 181.
8. Bancroft, G. M.; Maddock, A. G.; Ong, W. K.; Prince, R. H.; Stone, A. J. *J. Chem. Soc (A)* 1967, 1966.
9. Player, M. A.; Woodhams, F. W. D. *J. Phys. Chem.* 1978, 11, 191.
10. Stevens, J. G.; Bowen, L. H. "Mössbauer Effect Methodology"; Plenum: New York, 1969; Vol. 5, p. 27.
11. Stevens, J. G.; Ruby, S. L. *Phys. Lett.* 1970, 32A, 91.
12. Berry, F. J.; Maddock, A. G. *Radiochim. Acta* 1977, 24, 32.
13. Baur, W. H.; Kahn, A. A. *Acta Crystallogr.* 1971, B27, 2133.
14. Stewart, D. J.; Knop, O.; Ayasse, C.; Woodhams, F. W. D. *Can. J. Chem.* 1972, 50, 690.
15. Borquet, J. P.; Chu, Y. Y.; Kistner, O. C.; Periman, M. L.; Emery, G. T. *Phys. Rev. Lett.* 1966, 17, 809.
16. Greenwood, N. N.; Perkins, P. G.; Wall, D. H. *Phys. Lett.* 1968, 28A, 339.
17. Godin, G. W.; McCain, C. C.; Porter, E. A. *Porous Struct. Catal. Transp. Processes Heterogeneous Catal., Symp.* 1968, Paper 20.
18. Wright, D. A. *Proc. Br. Ceram. Soc.* 1968, 10, 103.
19. Barrett, J.; Bird, S. R.; Donaldson, J. D.; Silver, J. *J. Chem. Soc. (A)* 1971, 3105.
20. Donaldson, J. D.; Laughlin, D.; Ross, S. D.; Silver, J. *J. Chem. Soc. (Dalton)* 1973, 1985.
21. Donaldson, J. D.; Silver, J. *Inorg. Nucl. Chem. Lett.* 1974, 10, 537.
22. Donaldson, J. D.; Silver, J.; Hadjiminolis, S.; Ross, S. D. *J. Chem. Soc. (Dalton)* 1975, 1500.
23. Wooten, J. B.; Long, G. G.; Bowen, L. H. *J. Inorg. Nucl. Chem.* 1974, 36, 2177.
24. Donaldson, J. D.; Kjekshus, A.; Nicholson, D. G.; Rakke, T. *Acta Chem. Scand.* 1975, A29, 803.
25. Cross, Y. M.; Pyke, D. R. *J. Catal.* 1979, 58, 61.
26. Long, G. G.; Stevens, J. G.; Bowen, L. H. *Inorg. Nucl. Chem. Lett.* 1969, 5, 799.
27. Roginskaya, U. E.; Dublin, D. A.; Stroeva, S. S.; Kulkova, N. V.; Gelpb-shtein, A. E. *Kinet. Katal.* 1968, 9, 1143.
28. Kustova, G. N.; Tarasova, D. V.; Olenkova, I. P.; Chumenko, N. N. *Kinet. Katal.* 1976, 17, 744.
29. Atkinson, L.; Day, P. *J. Chem. Soc. (A)* 1969, 2423.
30. Robin, M. R.; Day, P. "Advances in Inorganic Chemistry and Radiochemistry"; Emeleus, H. J.; Sharpe, A. G., Eds.; Academic: New York, 1967; Vol. 10, p. 247.
31. Wakabayashi, K.; Kamiya, Y.; Ohta, N. *Bull. Chem. Soc. Jpn.* 1968, 41, 2776.
32. Andersson, S.; Aström, A. "Solid State Chemistry"; Roth, R.; Schneider, J. S., Eds.; N.B.S. Spec. Publ. 364; N.B.S.: Washington, D.C., 1972; p. 3.
33. Pyke, D.; Reid, R.; Tilley, R. J. D. *J. Solid State Chem.* 1978, 25, 231.
34. Arai, T. *J. Phys. Soc. Jpn.* 1960, 15, 916.
35. Kohnke, E. E. *J. Phys. Chem. Solids* 1962, 23, 55.
36. Leja, E. J. *Acta Phys. Pol. A* 1970, 38, 165.

37. Herniman, H. J.; Pyke, D. R.; Reid, R. *J. Catal.* **1979**, *58*, 68.
38. McAteer, J. C. *J. Chem. Soc. Faraday Trans. 1* **1979**, *75*, 2768.
39. Berry, F. J.; McAteer, J. C., unpublished data.
40. Montgolfier, Ph.; Meriaudeau, P.; Boudeville, Y.; Che, M. *Phys. Rev. B* **1976**, *14*, 1788.
41. Thornton, E. W.; Harrison, P. G. *J. Chem. Soc., Faraday Trans. 1* **1975**, *71*, 1013.
42. Dewing, J.; Monks, G. T.; Youll, B. *J. Catal.* **1976**, *44*, 226.
43. Firsova, A. A.; Suzdalev, I. P.; Margolis, L. Y. *Russ. J. Phys. Chem.* **1974**, *48*, 1743.
44. Firsova, A. A.; Khavanskaya, N. N.; Tsyganov, A. D.; Suzdalev, I. P.; Margolis, L. Y. *Kinet. Catal.* **1971**, *12*, 708.
45. Suzdalev, I. P.; Firsova, A. A.; Margolis, L. Y. *Kinet. Catal.* **1973**, *14*, 1341.
46. Margolis, L. Y. *J. Catal.* **1971**, *21*, 93.

RECEIVED July 22, 1980.

A Mössbauer Investigation of α - Fe_2O_3 Microcrystals Supported on γ - Al_2O_3

DING YING-RU, YEN QI-JIE, HSIA YUAN-FU, JIN YONG-SHU,
and QIU JIN-HENG

Department of Chemistry, Nanking University, Nanking, China

Two samples of microcrystalline α - Fe_2O_3 supported on γ - Al_2O_3 were prepared by an impregnation method. The particle size distribution of α - Fe_2O_3 , determined by Mössbauer spectroscopy and electron microscopy depends on the preparation conditions. Under CO conversion conditions the microcrystallites of α - Fe_2O_3 can be reduced to Fe_3O_4 and nonstoichiometric ferrous oxide, and the surface reaction $\text{Fe}^{3+} \rightarrow \text{Fe}^{2+}$ is a reversible oxidation-reduction process. The interaction between α - Fe_2O_3 and γ - Al_2O_3 is not as great as that between α - Fe_2O_3 and MgO .

Supported catalysts are widely used in industry; they give the user the advantage of creating and stabilizing a large surface area (i.e. high dispersion) for the active components of the catalysts, reducing the amount of noble metal used, and improving catalytic activity, mechanical strength, and thermal and chemical stability. This type of catalyst is also valuable to the study of the surface structure and reaction mechanism of supported catalysts.

Recently, much attention has been given to the study of preparation methods and properties of supported catalysts. The results of a number of these studies (1, 2) show that an "inert support" in fact is not inert for the active components and catalytic reactions.

This chapter studies the dependence of the particle size on the preparation conditions, and the influence of the nature of the support and its particle size on the reduction of the samples through the in situ Mössbauer spectra of microcrystalline α - Fe_2O_3 supported on γ - Al_2O_3 .

Experimental

γ - Al_2O_3 , calcined at 823 K in air for 6 h with a surface area of 117 m^2/g , was used as the support material. The support was impregnated with ferric nitrate solution enriched with ^{57}Fe , and the pH value of the solution was adjusted to 1.5–2.0 with NH_4OH . After impregnation overnight, the precursor was dried at 373 K and then calcined in air at 823 K for 3 h. Thus, Sample 1 contained 3 wt % Fe_2O_3 . Sample 2 was prepared under similar conditions using the impregnation solution without NH_4^+ .

The spectrometer used is described elsewhere (3). The source was 8 mCi ^{57}Co in palladium. A 25- μm thick α -Fe foil was used as a standard to calibrate the velocity of the spectrometer. All isomer shifts were recorded with respect to α -Fe.

The in situ Mössbauer measurements at high temperature and under CO conversion conditions ($\text{H}_2\text{O}/\text{CO} = 2:1$, 623–823 K, flow rate of gas = 250 mL/h) were carried out in the quartz cell. The absorber contained 1–2 mg $^{57}\text{Fe}/\text{cm}^2$.

The Mössbauer measurements at temperatures below room temperature were carried out with the “cold finger” method.

The particle size of the microcrystallites also was determined using the electron microscopic technique.

Results and Discussion

Mössbauer Spectra at Different Temperatures. The Mössbauer spectra of two samples at different temperatures are shown in Figures 1 and 2.

From the room temperature spectra the isomer shifts of the samples were found to be 0.328 and 0.321 mm/s, respectively. As shown in Figure 1, the Mössbauer spectrum of Sample 1 exhibited only a superparamagnetic doublet, and even at 120 K no magnetic splitting was found. The quadrupole splitting value was 0.82 mm/s. Sample 2 at room temperature exhibited a magnetic splitting spectrum with a doublet superimposed on its center, and the hyperfine field calculated was 495.7 kOe. It was a little lower than the 515 kOe reported for bulk α - Fe_2O_3 (2, 4). The quadrupole splitting value was 0.77 mm/s. All of these values showed that the two samples were in the α - Fe_2O_3 state.

According to the Kündig model (5, 6), the average particle size of Sample 1 was estimated to be 5.6 nm, which is in good agreement with the electron microscopic observation.

In Figure 3 we plotted the area percent of the superparamagnetic component as a function of temperature—at 230 K it was 50%. The average particle size of Sample 2 was calculated to be 12.8 nm, according to the equation:

$$\ln(2 \times 10^{-4} \text{ K}) = \frac{KV}{kT}$$

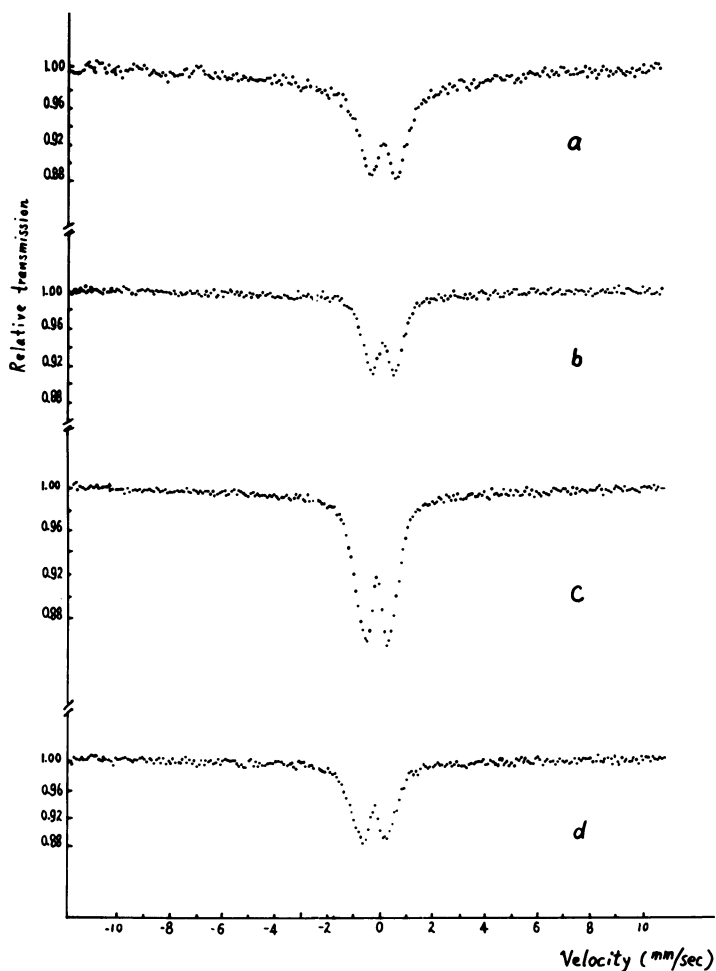


Figure 1. Mössbauer spectra of Sample 1 at different temperatures: (a) at 123 K; (b) at 284 K; (c) at 623 K; (d) at 823 K

where $K = (8.2 \pm 2.4) \times 10^3 \text{ J/m}^3$ (5, 6). While the electron microscopic observation showed that Sample 2 had a broad particle size distribution, the majority of the particles were about 7.0 nm, with some larger than 20 nm.

Mössbauer Study of the Reduction (Activation) of α -Fe₂O₃ Microcrystallites Supported on γ -Al₂O₃ Under CO Conversion Conditions. The results of the in situ Mössbauer measurements under CO conversion conditions are shown in Figures 4 and 5. A comparison of spectra under 623 K CO conversion conditions with those in air indicate that after being exposed to CO + H₂O for 30 h, the center lines of Sample 2 were

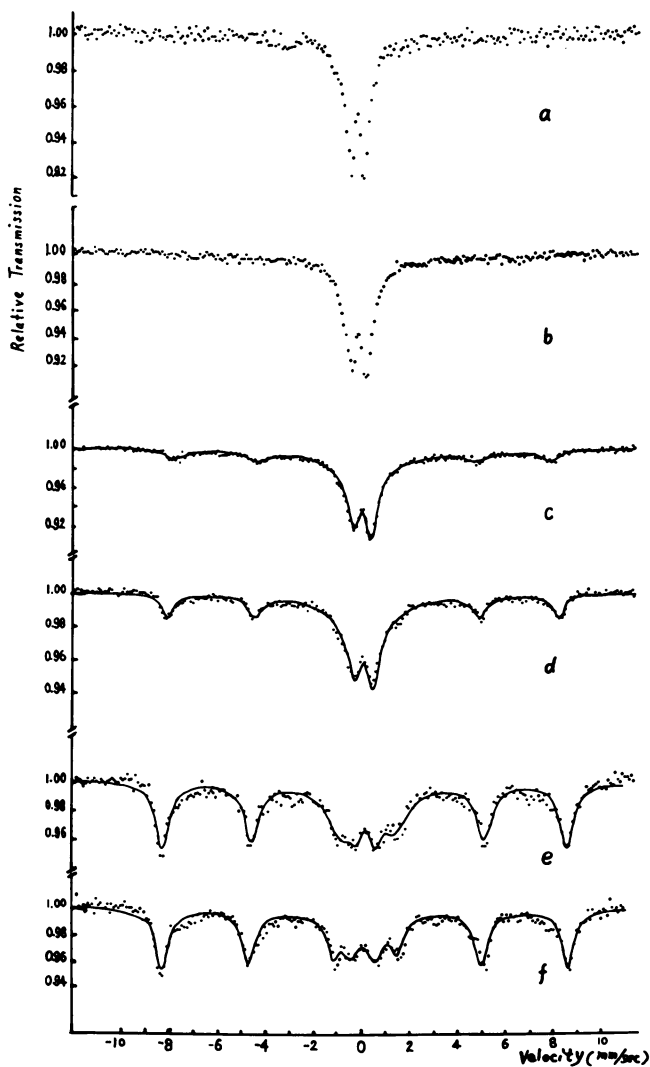


Figure 2. Mössbauer spectra of Sample 2 at different temperatures: (a) at 823 K; (b) at 623 K; (c) at 373 K; (d) at 284 K; (e) at 178 K; (f) at 121 K

broadened significantly and the quadruple splitting value increased (Figure 5a). This suggests that CO and H₂O molecules were chemisorbed on the Fe₂O₃ surface, making the environment of Fe³⁺ more asymmetric. On the other hand, the spectrum of Sample 1 did not change, probably because of the smaller particle size. Figure 4b shows that after reduction at 673 K for 10 h, a Fe²⁺ shoulder can be seen at the right side of the spectrum.

Under the CO conversion conditions at 823 K the spectra (Figures 4c and 5b) may consist of the absorption curves of Fe₃O₄ (isomer shift = 0.28 mm/s) and nonstoichiometric ferrous oxide (7, 8). After being treated for 5 h, the area percentages of Fe₃O₄ and FeO of the samples were found to be 56% and 44%, respectively, and did not change with the increasing time of treatment. When the temperature decreased to 673 K, the Fe²⁺ content decreased (Figure 4d). This suggests that the reduction of Fe³⁺ to Fe²⁺ is reversible. When the temperature decreased to 623 K, the Fe²⁺ content decreased still further (Figure 4e).

I. P. Suzdalev et al. (9) suggested that the reaction of CO with the surface of Fe₂O₃ (8-nm particles) resulted in CO₂ formation and reduction of the surface ferric ion to ferrous ion. The latter was present in a compound of the FeO type, giving two new peaks in the Mössbauer spectrum, with a quadrupole splitting value of 1.67 mm/s. The subsequent oxygen treatment of the CO-reacted sample resulted in a return of the spectrum to its original form, the FeO being oxidized back to Fe₂O₃. Our experimental results are consistent with this conclusion. As a result of the reaction of chemisorbed oxygen on the Fe₂O₃ surface, Fe²⁺ was oxidized back to Fe³⁺ at a lower temperature.

Figures 4f and 5d show that after the reduction, the Mössbauer spectra of the two samples at room temperature changed markedly. The central portion of the spectra is attributed to the presence of some superparamagnetic crystallites of ferric and ferrous oxides. The spectrum of

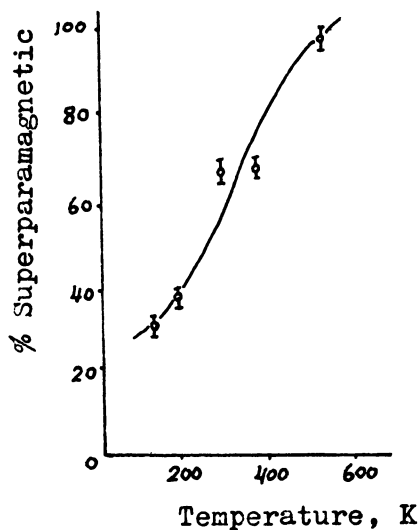


Figure 3. Temperature dependence of the superparamagnetic percentage of Sample 2

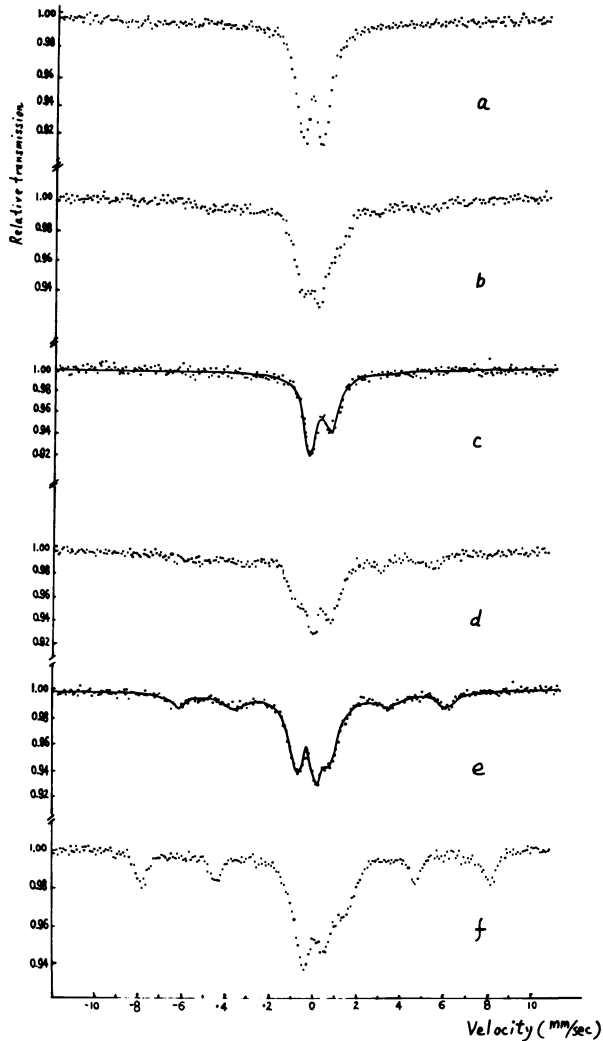


Figure 4. Mössbauer spectra of Sample 1 exposed to a $\text{CO} + \text{H}_2\text{O}$ mixture at various stages: (a) at 623 K; (b) after (a), at 673 K; (c) after (b), at 823 K; (d) after (c), at 673 K; (e) after (d), at 623 K; (f) after (e), at room temperature and exposed to CO/CO_2 mixture.

Sample 1 (Figure 4f) exhibited a magnetic splitting of Fe_3O_4 , and the hyperfine field was 490 kOe, attributable to the larger particle size of Fe_3O_4 than that of Fe_2O_3 . For Sample 2, the initial magnetic splitting spectrum of Fe_2O_3 disappeared and the trace of the large Fe_3O_4 particles appeared. The superparamagnetic lines of crystalline ferric and ferrous oxides were superimposed on both of these magnetic splitting lines.

It is clear that at first, the reduction process of microcrystalline Fe₂O₃ occurred at the surface of the larger particles, and the oxygen of Fe₂O₃ reacted with chemisorbed CO; thus, CO → CO₂, Fe³⁺ → Fe²⁺, and the Fe²⁺ component appeared. As the reduction temperature increased, some Fe₃O₄ and FeO formed. Because of the larger particle size of Fe₃O₄, the magnetic splitting spectrum appeared at room temperature.

Several authors (10, 11) have suggested that the reduction of the supported catalysts is affected by the particle size. Our study has shown that within certain particle size ranges, the reduction of the sample is affected only slightly.

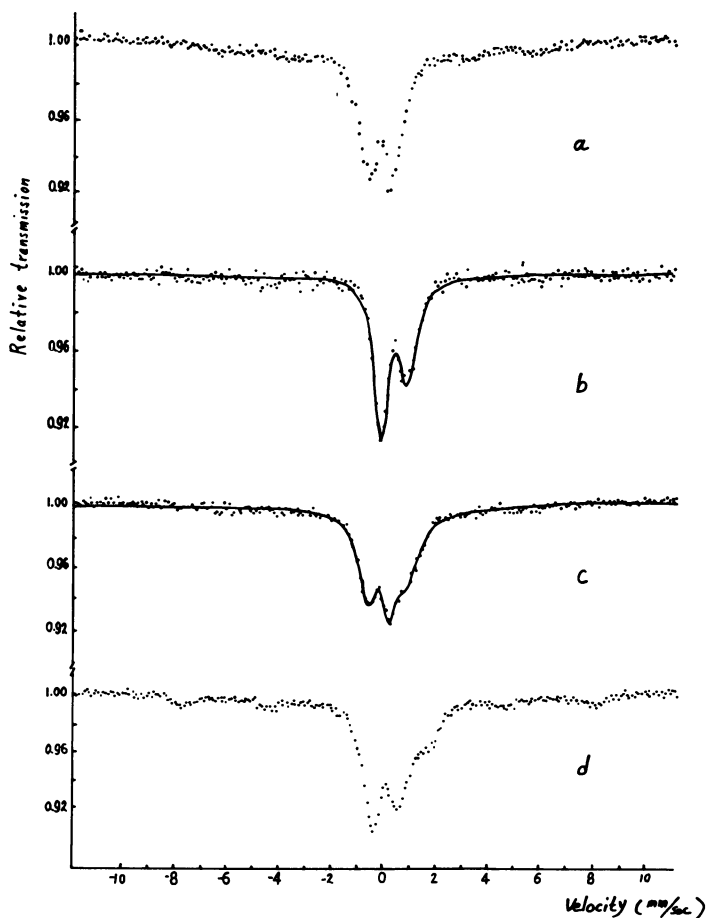


Figure 5. Mössbauer spectra of Sample 2 exposed to a CO + H₂O mixture at various stages: (a) at 623 K; (b) after (a), at 823 K; (c) after (b), at 623 K; (d) after (c), at room temperature and exposed to a CO/CO₂ mixture.

It is well known that an active component, when dispersed to a certain degree, will form an active center. Although particles of smaller sizes are more active, there is an optimum particle size range that manifests the highest activity and that depends not only on the nature of support but also on the size of reacting molecules. Further studies are needed to establish an optimum particle size range for the reduction (activation) of the α -Fe₂O₃ supported on γ -Al₂O₃ under CO conversion conditions.

Interaction of α -Fe₂O₃ with a Support and Thermal Stability of the Sample. It is generally considered that because of the similarity between Fe³⁺ and Al³⁺, there is a strong interaction between Fe₂O₃ and Al₂O₃ (12, 13). T. Yoshioko (14) studied the different types of Al₂O₃ support and suggested that the interaction of metal oxide with γ -Al₂O₃ appears to be the weakest. Our experiment showed that the reduction of Sample 2 with an average particle size greater than 10 nm was similar to that of bulk α -Fe₂O₃, which is consistent with the result of Kündig et al. (6). They suggested that the interaction of the support with Fe₂O₃ (particle size > 13.5 nm) is weak, and the reducibility is similar to that of bulk Fe₂O₃. On the other hand, for the small particles (6 nm) of Fe₂O₃, a strong interaction was not shown either. It could be reduced easily under the same CO conversion conditions. α -Fe₂O₃ microcrystallites supported on MgO (15) of the same particle size were prepared under similar conditions, but were found to be nonreducible under CO conversion conditions. From the results of these two samples it seems that the particle size and the nature of the support have an effect on the reduction of α -Fe₂O₃ microcrystallites.

After further calcination at 823 K in air for 10 h, Mössbauer spectra of the two samples just mentioned did not change as compared with the original. The interaction between α -Fe₂O₃ and γ -Al₂O₃ was weak, resulting in the limited thermal stability of the two samples.

Conclusion

The α -Fe₂O₃ microcrystallites with an average particle size of approximately 6 nm, supported on γ -Al₂O₃ were prepared by impregnating γ -Al₂O₃ with ferric nitrate solution. The pH value of the impregnation solution was adjusted to 1.5–2.0 with NH₄OH. When no NH₄⁺ ions were in the impregnation solution, a sample with a different particle size distribution was obtained.

The particle size of the α -Fe₂O₃ microcrystallites was determined by Mössbauer spectroscopy and electron microscopy. When the average particle sizes were 6 nm and greater than 10 nm under CO conversion conditions, α -Fe₂O₃ could be reduced to Fe₃O₄ and FeO, but the reduci-

bility of the two samples with different particle sizes was not the same. It was shown that Fe³⁺ → Fe²⁺ is a reversible oxidation–reduction process.

Literature Cited

1. Carbuichio, M. *J. Chem. Phys.* 1979, 70(2), 784.
2. Dumesic, J.; Topsøe, H. *Adv. Catal.* 1977, 26, 186.
3. Ying-ru, Ding; Qi-jie, Yen; Yuan-fu, Hsia; Shun-hao, Yeh; Yi, Chen; Yong-shu, Jin; Jin-heng, Qiu. *J. Phys. (Paris)* 1980, C-1–341.
4. Hobson, M. C.; Gager, H. M. *J. Catal.* 1970, 16, 254.
5. Kündig, W.; Bömmel, H.; Constabaris, G.; Lindquist, R. H. *Phys. Rev.* 1966, 142, 327.
6. Kündig, W.; Ando, K. J.; Lindquist, R. H.; Constabaris, G. *Czech. J. Phys. B* 1967, 17, 467.
7. Topsøe, H.; Dumesic, J. A.; Boudart, M. *J. Phys. (Paris)* 1974, C6–411.
8. Johnson, D. P. *Solid State Commun.* 1969, 7, 1785.
9. Suzdalev, I. P.; Shkarin, A. V.; Zhabrova, G. M. *Kinet. Katal.* 1969, 20, 218.
10. Fujimoto, K.; Boudart, M. *J. Phys. (Paris)* 1978, C2–81.
11. Gager, H. M.; Hobson, M. C. *Catal. Rev.* 1970, 11(1), 117.
12. Wertheim, G. K.; Remeika, J. P. *Phys. Lett.* 1964, 10, 14.
13. Bhide, V. G.; Date, S. K. *Phys. Rev.* 1968, 172, 345.
14. Yoshioko, T.; Koezuka, J.; Ikoma, H. *J. Catal.* 1970, 16, 264.
15. Ying-ru, Ding; Qi-jie, Yen; Yuan-fu, Hsia; Yong-shu, Jin; Jin-heng, Qui., unpublished data.

RECEIVED July 22, 1980.

CONCLUDING REMARKS

The interdisciplinary field of Mössbauer spectroscopy represents a fascinating sociological phenomenon in the physical sciences. We have here the marriage of inorganic, physical, theoretical, organometallic, and biochemists, itself a remarkable achievement, with physicists, both theorists and experimentalists, geologists and mineralogists, materials and solid state scientists, metallurgists, engineers, and biologists into a community held together by a common interest in movers, detectors, and radiochemical sources. These persons then go looking for problems—a bad thing in any kind of marriage! However, in this volume we can see how these problems (some new, some old) have been solved by applying the Mössbauer effect. The result has meant significant advances for these diverse branches of science stimulated in part, I am sure, by the symposium upon which this book is based.

When the “Natural History of the Introduction of New Physical Methods into Chemistry” comes to be written, and the Mössbauer effect will certainly have its chapter there, it will be seen that there has been a regular progression of steps that each new technique has followed in being introduced. Whether we are describing infrared, Raman, nuclear magnetic resonance, or Mössbauer spectroscopy, the history has been the same.

Any spectroscopic technique is intrinsically capable of yielding only three kinds of information:

(1) identity—on the basis that identical systems behave in an identical way; (2) purity, or the composition of a physical mixture—on the basis that physical mixing does not alter spectroscopic properties; and (3) information concerning structure, bonding, or the nature of forces between molecules.

While it seems clear that (1) and (2) provide the basis for the easiest and most straightforward analytical applications, attempts to apply techniques for these analytical purposes generally come late. This volume records reports of analyses performed by Mössbauer (known since 1959) techniques, for the first time, although more work needs to be done before the results can be put on a sound basis. For example, reliable recoil-free fraction data necessary for the cross-comparison of resonance area measurements to yield percentage compositions are largely lacking.

The Mössbauer technique, like the other spectroscopic methods developed since World War II, has followed the following sequence of steps in its evolutionary history of being introduced into chemistry:

1. Discovery that a measured parameter, δ , varies with chemical state is published by an experimental physicist; fewer than a half dozen impure compounds are examined.
2. Claim that the changes in δ correlate with an unmeasurable, derived quantity such as electronegativity, percentage of ionic character, *s*- or *p*-electron density, etc., is published by a physical chemist. The correlation is always linear, and fewer than a dozen, only slightly purer compounds are examined.
3. Disparity between the predictions of the first principles that govern the method and published results throws the field into a confusion which is not admitted. A splitting, Δ , is observed, but not adequately understood. Point-by-point data are still being taken.
4. Correlation with other measurable parameters of structure and spectroscopy is achieved, and truly useful information begins to emerge. The *x-y* recorder is brought into play to record data, and symposia are organized.
5. Commercial instrumentation is exhibited, and begins to drop in price. The technique enters general use, and its name is no longer invoked in the titles of published articles, making the literature scattered and retrieval difficult. The original practitioners decry the work of the new entrants whom they claim do not really understand the theory of the method, and they stop collecting xerographic copies of every paper published.
6. Calibrated chart paper appears. The names of the original practitioners are forgotten. The technique has arrived!

As readers of this volume will recognize, Mössbauer spectroscopy is poised on the brink of having spectra recorded on calibrated chart paper, and we await that occasion with very mixed emotions. The technical details of how that will be worked out I assign as an exercise for the representatives of the commercial instrument manufacturers.

The tremendous breadth seen in this volume is most impressive: bonding, the use of conversion electrons, analysis, applications to the environment, and biology, the use of exotic isotopes, the examination of phase transitions, relevance to catalysis, the energy problem, and academic instruction. There are extravagant claims and sobering cautionary notes. We are embarking into a very hopeful future for Mössbauer spectroscopy.

I would like to thank the commercial co-sponsors, and especially John G. Stevens, his lovely and hard-working wife, Virginia E. Stevens, and their staff at the University of North Carolina at Asheville for organizing and preparing this volume.

J. J. ZUCKERMAN

May 29, 1981

INDEX

- A**
- Absorber(s) 394
 tantalum metal 483
 zinc metal 333
- Absorber(s), Mössbauer
 background correction for 202
 granularity 197-202
 texture and spectral resolution 205-206
- Aconitase from beef-heart mitochondria, oxidized 322
- Acrolein, catalytic oxidation of
 propene to 601
 Acrolein, oxidation of propene to . 597
- Actinide organometallic compound 354
 Actinide organometallics, bonding . 359
- Al₂O₃, interaction between
 Fe₂O₃ and 616
- γ-Al₂O₃, Mössbauer investigation of
 α-Fe₂O₃ microcrystals supported on 609-617
- γ-Al₂O₃ under CO conversion conditions, reduction of α-Fe₂O₃ microcrystallites supported . 611-616
- Alkali tantalates, ¹⁸¹Ta Mössbauer studies of 481-497
- Alloys
 and archaeological materials, CEMS to study ion-implanted 101-114
 CEMS studies of iron-implanted copper 105-107
 and gold metallic compounds, isomer shifts of 43, 44f
 hydrides of binary 506
- Aluminum
 content of goethites 256, 258t
 content in hematite 258, 259t
⁵⁷Fe-implanted 92
 incorporation in iron oxides . 256-260
- American Society for Testing and Materials method(s)
 coal, comparison of Mössbauer and 240
 and the Mössbauer area method, analysis of U.S. coals by ... 189t
 of total and pyritic iron in coal, Mössbauer vs. 188-191
- American Society for Testing and Materials standard(s)
 D2492 method of coal analysis . 182
 D3177 for determining total sulfur content of coal 182
 method of sulfur determination in coal 155
- Analyzers, electrostatic electron energy 126
- Ankerite 150, 274
 Ankerite transformation during coking 279
- AnS, structure of 342
 AnTe, structure of 342
- Antimonic acid, thermal decomposition of tin(IV) hydroxide and 591-596
- Antimony
 compounds by ¹²¹Sb Mössbauer spectroscopy characterization of 361-373
 content, ¹¹⁹Tm Mössbauer parameters as a function of 596f
 -doped tin(IV) oxide 605
 oxides
 following reaction with butene and oxygen ¹¹⁹Sn and ¹²¹Sb Mössbauer parameters of tin- 602t-603t
¹²¹Sb Mössbauer investigation of 597-601
 -tin
 catalysts, active centers in . 601
 chemisorption and catalytic reactions of olefins 605
¹¹⁹Sn Mössbauer studies of catalytically active 590
 pentafluoride, oxidation of iodine with 381
- Antimony(III) 363
 complexes, ¹²¹Sb Mössbauer data for 369t
 species 367-369
 in environments 597
- Antimony(V) 363
 halide complexes, ¹²¹Sb Mössbauer data for 370t
 species 369-372
 in environments 597
- Antimony-121 Mössbauer data
 for antimony(III) complexes . 369t
 for antimony(V) halide complexes 370t
 for organoantimony(V) compounds 372t
 investigations of tin-antimony oxides 597-601
 parameters, ranges for 365t
 parameters of tin-antimony oxides (Sn_{1-x}Sb_xO₂) 593t
 transitions 362t

- Antishielding 17-20
- Archaeological artifacts by ^{57}Fe
CEMS, characterization of in-
organic solids and minerals .. 93-95
- Archaeological materials, CEMS to
study ion-implanted alloys
and 101-114
- Ash 274
and slag deposits, factors
controlling 280-282
vs. mineral matter 179
- ASTM (see American Society for
Testing and Materials)
- Atomic core wave functions 9
- Atomic orbitals, linear combination
of 9
- Attic Black Ware, Greek 111, 112f
- Attrital coals 137
- ^{197}Au (see Gold-197)
- $\text{Au}(\text{Cn})_2^-$ 47
pressure-dependent Mössbauer
measurements of 52
quadrupole splitting in 49-51
- Auger electrons 64
- AuLCl compounds, linear 52, 53f
- AuLCl compounds, nuclear quadru-
pole resonance frequencies of
chlorine in 52, 53f
- AuLPPH_3 compounds, linear 52, 53f
- Austenite 90
-Martensite carbide deter-
minations 283
spectrum for high-carbon steels . 285
- Austenitic stainless steels 284
- AuTe_2 , quadrupole splittings in .. 54
- Automatic image analysis 276
- Azotobacter vinelandii*, ferredoxin
from 310
- Azotobacter vinelandii*, nitrogenase
from 307
- B**
- Backscattering
counter for conversion electron
on x-rays 102f
- experiments, and internal
conversion 64-66
- Rutherford 546
- Barnett-Coulson ζ -expansion
technique 7
- Bases to Lewis acid sites on metal
oxides, adsorption of 601
- Battery materials, Mössbauer
studies of 523-536
- Benzene and THF solubles, con-
version of coal to 170
- Bessel functions 160
- Beta-ray spectrometer(s)
for DCEMS studies 71-77
electrostatic 75, 76f
magnetic 72, 73f
- Bimetallic catalyst systems, iron-
ruthenium 553-571
 ^{57}Fe Mössbauer parameters 562t
 ^{99}Ru Mössbauer parameters 563t
reaction scheme 570f
- Biotite 146
- Bonding
in actinide organometallics 359
of ^{237}Np organometallics and
their uranium analogues . 358-359
properties and Mössbauer param-
eters in linear gold(I) 51-57
systematics in gold compounds . 46
- σ -bonding properties of the ligands
in gold(I) 51
- Bromine-containing molecules, self-
consistent field and charge
molecular orbital calculations . 3-35
- Butene and oxygen, ^{119}Sn and ^{121}Sb
Mössbauer parameters of tin-
antimony oxides following
reaction with 602t-603t
- C**
- C_5H_5^- ligand 354
[($\text{C}_5\text{H}_5\text{N}$) $_2$] $[\text{NO}_3]^{127}\text{I}$ Mössbauer
spectrum 384f
- CaCO_3 (calcite) 150
- $\text{Cs}[\text{FIBr}]$ 387
- $\text{Cs}[\text{FICl}]$ 387
[(CH_3) $_4\text{N}][\text{BrICl}]$, ^{127}I Mössbauer
spectrum of 385, 386f
- Calcite (CaCO_3) 150
- Carbide(s)
determinations, austenite-marten-
site- 283
- Hagg 585
(Fe_5C_2) 579-588
produced by ion implantation .. 110
- Carbon-implanted iron foils, CEMS
studies 107-110
- Carbon system of steels, iron- .. 283-286
- Carbonate minerals in coal 150-153
- Carbonates and clay minerals in
coal, iron-bearing 276
- Catalyst(s)
active centers in tin-antimony
oxide 601
- catalytic conversion of coal-
derived synthesis gas to
gasoline-range hydrocarbons
and olefins using bifunc-
tional zeolite 574
- colloidal palladium 542
- ^{57}Fe Mössbauer parameters of
iron-ruthenium bimetallic . 562t
by ^{57}Fe and ^{99}Ru Mössbauer
spectroscopy, characteriza-
tion of mixed-metal 553-571
- Fischer-Tropsch 556
- Mössbauer results of various 578t-579t
- Mössbauer spectroscopic investi-
gation of oxidation 589-605

- Catalyst(s) (*continued*)
 reduction of supported 615
⁹⁹Ru Mössbauer parameters of
 iron-ruthenium bimetallic . 563*t*
 solutions used in metallization of
 plastics Mössbauer studies of
 colloidal 539-551
 spectra of oxidatively coagulated
 colloidal 544*f*
 supported 609
 used in synthesis gas conversion,
 Mössbauer and magnetic
 studies on bifunctional
 medium-ore zeolite-iron .573-588
 for synthesis gas conversion,
 zeolite-Silicalite-based 574
 systems bimetallic554-556
 iron-ruthenium553-571
 system, palladium-tin col-
 loidal542, 543*f*
- Cathode
 KFeS₂-LiKFeS₂ 535
 Li₂VS₂ 526
 materials, solid-state 525
 TaS₂-LiTaS₂533-535
- Cementite 585
 (Fe₃C)579-588
 formation of285, 286*f*
- CEMS (*see* Conversion electron
 Mössbauer spectroscopy)
- Ceramic objects, studies of glazes
 on painted111-114
- Chalcogenides
 chemical shifts for ⁶⁷Zn in 335*t*
 resonance for zinc 335
 isomer shifts for338-341
- Chalcopyrite 216
- Channeltrons 70
 detector, low-temperature CEMS
 apparatus using 71
- Char gasification 166
- Chlorine in AuLCl compounds,
 nuclear quadrupole resonance
 frequencies of52, 53*f*
- Chlorine-containing molecules, self-
 consistent field and charge
 molecular orbital calculations . 3-35
- Chlorite(s)148, 274
- Clarain 137
- Clay(s)
 and iron carbonate phases during
 coking, transformations of
 ferrous 279
 iron oxides in247-260
 minerals in coal143-150
 iron-bearing carbonates and .. 276
 minerals, ferrous 274
 mixed-layer 149
 -rich coal 274
- Clostridium pasteurianum*, nitroge-
 nase from 307
- Clusters
 [2Fe-2S] 306
- Clusters (*continued*)
 [4Fe-4S] 307
 iron-sulfur305-324
 of nitrogenase306-310
- P-Cluster of nitrogenase307-308
 stable oxidation states of the
 cofactor centers 309*f*
- CO conversion conditions, reduction
 (activation) of α-Fe₂O₃ micro-
 crystallites supported on
 γ-Al₂O₃ under611-616
- CO with the surface Fe₂O₃,
 reaction 613
- Coal(s) 274
 after various treatments, Möss-
 bauer analysis of191-194
 analysis, ASTM Standard D2492
 method 182
- ASTM
 method to determine sulfur ... 224
 method and the Mössbauer
 area method, analysis of
 U.S. 189*t*
 Standard D3177 for determin-
 ing total sulfur content .. 182
 standard method of sulfur
 determination 155
- atritral 137
- to benzene and THF solubles,
 conversion 170
- carbonate minerals150-153
 characterization and utilization,
 application of Mössbauer
 spectroscopy135-172
- chemical and Mössbauer
 analyses182-197
- chemical states of nonpyritic iron
 in brown209-218
- clay minerals143-150
- clay-rich 274
- and coal process products,
 Mössbauer spectra 226
- to coke, transformation 165
- combustion163-165
- comparison of the Mössbauer and
 ASTM methods 240
- derived synthesis gas to gasoline-
 range hydrocarbons and ole-
 fins using bifunctional zeolite
 catalysts, catalytic conversion 574
- direct combustion280-282
- forms of sulfur 182
- gasification 166
- high-sulfur low-quality 276
- intensity method to determine
 total and pyritic iron con-
 centration187-188
- iron 227
- bearing minerals140-155
 in fresh 274
 vs. sulfur abundance 276
- oxides 155
- sulfides140-143, 142*t*

- Coal(s) (*continued*)
 iron (*continued*)
 -sulfur minerals 136, 225
 liquefaction 167-172
 residues, iron sulfides 168
 lithologic components 137
 macerals 137
 mineral matter in 137
 mineralogy-pyritic sulfur
 determinations 274-276
 Mössbauer
 vs. ASTM method of total and
 pyritic 188-191
 effect study of Victorian
 brown 209-218
 spectroscopy of bed-moist vs.
 dried 211-218
f-values of iron compounds 203, 204*t*
 organic and inorganic com-
 ponents 136-140
 oxidation of strip-mine 276
 pollution from 163
 quantitative investigations . 177-206
 resonance area method to deter-
 mine total and pyritic iron
 concentration from 183-187
 by resonance intensity method,
 Mössbauer analysis 194*t*-195*t*
 by rank, classification of ... 138*t*-139*t*
 sulfate(s) 153-155
 phases 275
 survey 231
 utilization 163-172
 environmental problems related 163
 water in bed-moist 210
 Cobalt-iron in the zeolite catalyst,
 state of iron and 575
 Coke 165-166, 274
 transformation of coal 165
 Coking
 ankerite transformation during . 279
 behavior of pyrite during 278-279
 illite transformation during ... 279
 mineral transformations during 277-279
 siderite transformation during .. 279
 transformations of ferrous clay
 and iron carbonate phases
 during 279
 Colloid formation process 544
 Colloidal catalyst
 solutions used in metallization of
 plastics, Mössbauer
 studies 539-551
 spectra of oxidatively coagulated 544*f*
 system, pallidum-tin 542, 543*f*
 Combustion, coal 163-165
 Contact density, and charge trans-
 fer, ¹⁹⁷Au isomer shift 41-45
 Conversion electron Mössbauer
 spectroscopy 63-97
 advances in theoretical aspects
 and data reduction 77-84
 apparatus using a channeltron
 detector, low-temperature .. 71
 Conversion electron Mössbauer
 spectroscopy (*continued*)
 applications of ⁵⁷Fe 84-95
 applications of ¹¹⁹Sn 95-96
 characterization of inorganic
 solids and minerals and
 archaeological artifacts by
⁵⁷Fe 93-95
 characterization of steel surfaces
 by 90-91
 data for Eu₂SiO₄ 121
 depth-resolved
 depth-selective or energy-
 differential 125
 detectors, integral 68-77
 energy-differential ⁵⁷Fe 125-132
 of ¹⁵¹Eu 117-123
 instrumentation, advances 68-77
 integral 64
 ion-implantation studies 91-93
 metallurgical applications 90-91
 phase identification by 85
 resonant effect in 119
 studies
 of carbon-implanted iron
 foils 107-110
 depth-resolved 81-84
 electron spectrometer for . 126, 127*f*
 integral 78-80
 ion-implanted alloys and
 archaeological materials 101-114
 iron-implanted copper alloys 105-107
 of nitrogen-implanted iron
 foils, ⁵⁷Fe 88, 89*f*
 surface selectivity of ⁵⁷Fe 66, 67*f*
 surface selectivity and
 sensitivity of 67-68
 of ¹⁶⁹Tm 117-123
 Conversion
 electron spectra vs. gamma-ray
 transmission spectra ... 117-123
 electrons or x-rays, backscattering
 counter 102*f*
 of isomer shifts to electron counts 43-45
 x-ray Mössbauer spectroscopy
 (CXMS) 101
 K-conversion electrons 64-66
 L-conversion electrons 64
 Coordination complexes, isomer
 shifts in metallic systems 41-43
 Copper alloys, CEMS studies of
 iron-implanted 105-107
 Corrosion of iron and steels,
 aqueous oxidation 84-87
 Counter for conversion electrons or
 x-rays, backscattering 102*f*
 Cu¹²⁹I 380
 Cusachs approximations 5
 CXMS (*see* Conversion x-ray Möss-
 bauer spectroscopy)
 Cyanide complexes, ⁹⁹Ru Mössbauer
 parameters ruthenium(II) ... 559

D

- DCEM spectra of a fluorinated iron foil, ^{57}Fe 74f
- DCEMS (*see* Depth-resolved conversion electron Mössbauer spectroscopy)
- Debye-Waller factor of pyrite 157
- Debye-Waller factors of the Mössbauer source 156
- Depth-resolved conversion electron Mössbauer spectroscopy 64
- applications 95
- depth resolution by 67-68
- to measure the magnetic field near the surface of iron ... 95
- studies, beta-ray spectrometers for 71-77
- Depth resolution by DCEMS 67-68
- Depth-selective or energy-differential CEMS 125
- Desulfovibrio gigas*, ferredoxin from the sulfate-reducing bacterium 310
- Desulfovibrio gigas*, Mössbauer spectra of ferredoxin from ... 313
- Detector(s)
- gas 70
- integral 68-77
- low-temperature CEMS apparatus using a channeltron ... 71
- Deuterium isotope effect on the spin crossover behavior in $[\text{Fe}(\text{2-pic})_3]\text{Cl}_2 \cdot \text{Sol}$... 437-440
- Dichalcogenides, lithium intercalation compounds of the transition-metal layer 523-536
- Dichalcogenides, structure and properties of layer transition-metal 524-525
- Dipole moments for halogen-containing molecules 10t
- Dipyridine iodine(I) nitrate of $([\text{I}(\text{py})_2]\text{NO}_3)$ 383
- Dolomite 150, 234
- Doppler shift, contribution of zero-point motion to the second-order 337-338
- Doppler shift, second-order 492
- Durain 137
- ^{161}Dy spectroscopy 512
- ^{161}Dy isomer shifts in the hydrides of DyT_2 513
- DyT_2 , ^{161}Dy isomer shifts in the hydrides of 513
- E**
- Escherichia coli*, glutamate synthase from 322
- Electric field gradient calculations for ^{181}Ta in LiTaO_3 490-493
- contributions and orbital populations for iodine in iodine-containing molecules ... 22t-23t

Electric field gradient

(continued)

- at the halogen nucleus, quadrupole coupling constant and .14-29
- in $\text{KAu}(\text{CN})_2$ 47
- for ^{7}Li in LiNbO_3 and LiTaO_3 , point-charge calculations 495, 496f
- for ^{93}Nb in LiNbO_3 and LiTaO_3 , point-charge calculations 495, 496f
- for ^{181}Ta in LiNbO_3 and LiTaO_3 , point-charge calculations 495, 496f
- Electroless plating, and sensitization 541
- Electroless plating, steps in metalizing plastics by 541f
- Electron(s)
- Auger 64
- charge density at the Mössbauer nucleus, isomer shift 9-14
- K-conversion 64-66
- L-conversion 64
- counts, conversion of isomer shifts 43-45
- detectors 70
- energy analyzers, electrostatic .. 126
- of gold, behavior of the valence with matter, interactions of
- low-energy 82
- re-emission Mössbauer spectroscopy 292-298
- spectra, vs. gamma-ray transmission spectra, conversion .117-123
- spectrometer for CEMS studies 126, 127f
- spectrometer for ^{57}Fe Mössbauer spectroscopy 125-132
- or x-rays, backscattering counter for conversion 102f
- Electroneutrality principle, Pauling's 54
- Electronic behavior in linear gold(I) compounds 47
- industry 540
- properties of intermetallic, inorganic, and organometallic compounds, application of Mössbauer spectroscopy to study 39-59
- Electrostatic beta-ray spectrometers 75, 76f
- Electrostatic electron energy analyzers 126
- Energy analyzers, electrostatic electron . 126
- differential CEMS, depth-selective or 125
- differential ^{57}Fe CEMS ... 125-132
- Gibbs free 405
- spectroscopic 222t
- Environmental problems related to coal utilization 163
- Environments, antimony(III) species 597

- G**
- $Gd_{0.1}La_{0.9}Ni_5H_2$ 514
- Gallium-67 333
- ZnO vs. ZnO isomer shift 336
- Gamma ray transmission spectra,
conversion electron spectra
vs. 117-123
- Gas conversion, Mössbauer and
magnetic studies on bifunc-
tional medium-pore zeolite-
iron catalysts used in syn-
thesis 573-588
- Gas detectors 70
- Gasification, char 166
- Gasification, coal 166
- Gibbs free energy 405
- Gibbsite 251
- Glazes on painted ceramic objects,
studies 111-114
- Glutamate synthase from *E. coli* .. 322
- Coethite(s) 155
- aluminum content of 256, 258f
- (α -FeOOH) 247
- Gold
- behavior of the valence
electrons 39-59
- compounds, bonding systematics
in 46
- metallic compounds and alloys,
isomer shifts 43, 44f
- 6p and 5d orbitals 47
- Gold(I)
- bonding properties and Möss-
bauer parameters in linear 51-57
- complexes, isomer shifts 43, 44f
- compounds, electronic behavior
in linear 47
- and gold(III), chemical corre-
lations between 54-57
- linear compounds, quadrupole
splitting for 50
- Gold(III)
- chemical correlations between
gold(I) and 54-57
- complexes, isomer shifts 43, 44f
- compounds, quadrupole split-
tings in 54
- square-planar
compounds, quadrupole
splitting 50
- Gold-197
- isomer shifts 39-59
- contact density, and charge
transfer 41-45
- Mössbauer spectroscopy to study
electronic properties of
intermetallic, inorganic,
and organometallic com-
pounds, application of 39-59
- quadrupole splittings 39-59
- Goldanskii-Karyagin effect 341-342
- Greek Attic Black Ware 111, 112f
- Gypsum 153-154
- H**
- H_5IO_6 380
- Hagg carbide 585
- (Fe_5C_2) 579-588
- Halogen-containing
compounds, application of
molecular orbital calcula-
tions to Mössbauer
spectroscopy 3-35
- compounds, application of
molecular orbital calcula-
tions to NMR spectroscopy 3-35
- molecules, dipole moments for . 10f
- molecules, orbital energies for . 12f
- Halogen nucleus, quadrupole
coupling constant and elec-
tric field gradient 14-29
- Halloysite 250
- Hamiltonian
- Liouville 469
- matrix elements 4
- for the Mössbauer effect system 348
- parameters, spin 466-478
- Hartree-Fock
- Dirac calculations 11
- Slater calculations 11
- wave functions, atomic 7
- Hazen Magnex process 163
- He- CH_4 flow proportional
counters 68-69
- Hematite 155
- aluminum content 258, 259f
- (α - Fe_2O_3) 247
- Hexachloroantimonate(V) salts
([$R_2C:NH_2$][$SbCl_6$]) keti-
minium 373
- Hf $_2$ Fe 508
- Hf $_2$ FeH $_3$ 508
- High-spin (HS) \rightleftharpoons low-spin (LS)
transition 405-449
- HiPIP (High-potential iron pro-
tein) -type EPR signal in the
oxidized state, proteins that
exhibit 306-323
- Holoproteins 309
- Hydride(s)
- of A_2B compounds 510f
- of AB compounds 506f
- of AB_2 compounds 510f
- valence state of Europium
in some 513f
- of AB_3 compounds 514f
- of AB_5 compounds 515f
- of binary alloys 506
- binary metallic 501
- compounds of the form
- A_2BH_x 508
- ABH_x 505-508
- AB_2H_x 508-514
- AB_5H_x 514-515
- crystal structure of 512
- of DyT_2 , ^{161}Dy isomer shifts .. 513
- of FeTi 507
- Mössbauer spectrum 506, 508f

- Hydride(s) (*continued*)
 formation, thermodynamics of . 503
 ternary501, 502*t*
 Hydriding materials, setup503, 504*f*
 Hydrocarbons and olefins using
 bifunctional zeolite catalysts,
 catalytic conversion of coal-
 derived synthesis gas to
 gasoline-range 574
 Hydrogen
 -absorbing intermetallic com-
 pounds, surface 516
 absorption mechanism role of
 surface layers in515-517
 compressor 502
 in intermetallic compounds 501
 phase diagram measure-
 ments503-505
¹¹⁹Sn and ¹²¹Sb Mössbauer
 parameters of tin-antimony
 oxides following reaction
 with602*t*-603*t*
 storage materials501-518
 Bis(hydrotris(3,5-dimethyl-1-pyra-
 zolyl)borate iron(II), high-
 pressure Mössbauer effect
 study of453-461
 Hydroxide, stannic 549
 Hyperfine field calculation29-33
 Hyperfine interaction(s) 464
 energies 481
 isotropic 470
²³⁷Np 348
 Hückel calculations, iterative
 extended 4
 Hückel type equations, extended .. 4
- I**
- ¹²⁴I (*see* Iodine-127)
 [I₂]⁺ cation 381
 ([I(py)₂]NO₃), dipyrindine
 iodine(I) nitrate of 383
 Illite146, 234, 235, 274
 Mössbauer spectrum of 147*f*
 transformation during coking .. 279
 Ilmenite FeTiO₃ 272
 Indian Northern Black Polished
 Ware112*f*, 113
 Inertinite 137
 Inorganic, and organometallic
 compounds, application of
¹⁹⁷Au Mössbauer spectroscopy
 to study electronic properties
 of intermetallic39-59
 Inorganic solids and minerals and
 archaeological artifacts by
⁵⁷Fe CEMS, characterization .93-95
 Instrumentation, advances in
 CEMS68-77
 Intensity method to determine
 total and pyritic iron concen-
 tration in coal187-188
 Intercalation525-526
 Intermetallic-hydrogen com-
 pound phase diagram mea-
 surements503-505
 Intermetallic, inorganic, and
 organometallic compounds,
 application of ⁵⁹⁷Au Möss-
 bauer spectroscopy to study
 electronic properties of39-59
 Internal conversion and backscat-
 tering experiments64-66
 IO₂F₃ · SbF₅ 383
¹²⁷I Mössbauer spectrum of ... 385*f*
 Iodides, alkali 380
 Iodine 381
 anions
 correlation between the
 quadrupole coupling con-
 stants and ligand electro-
 negativity 376
 fluoro 386
¹²⁷I Mössbauer data and
 orbital occupation num-
 bers for382*t*-383*t*
 polyhalide 384-390
 with antimony pentafluoride,
 oxidation of 381
 application of ¹²⁷I Mössbauer
 spectroscopy to anion
 and cations of375-390
 -containing molecules, electric
 field gradient contributions
 and orbital populations ..22*t*-23*t*
 -containing molecules, self-
 consistent field and charge
 molecular orbital calcula-
 tions of 3-35
 and iodine ions, ¹²⁷I Mössbauer
 data for380*t*-381*t*
 ions, and ¹²⁷I Mössbauer data
 for iodine380*t*-381*t*
 parameters for N(C₂H₅)₄FeI₄,
 calculated 32*t*
 Sternheimer shielding factor ... 20*t*
 Iodine(I) nitrate of
 ([I(py)₂]NO₃), dipyrindine .. 383
 Iodine-127 376
 Mössbauer data and orbital
 occupation numbers for
 iodine anions382*t*-383*t*
 Mössbauer spectrum of
 [(C₅H₅N)₂I]NO₃ 384*f*
 Iodine-129 376
 Mössbauer measurements, ⁵⁷Fe 29-34
 Mössbauer study of the high-
 pressure phase transition
 of tellurium, ¹²⁵Te393-401
 probes in tellurium 394
 Iodine-197 Mössbauer data for
 iodine and iodine ions .380*t*-381*t*
 Iodine-197 Mössbauer spectros-
 copy to anions and cations of
 iodine application375-390

- Ion-implantation103-105
 studies, CEMS91-93
 studies by ^{57}Fe 91-93
- Ion-implanted alloys and archaeological materials, CEMS to study101-114
 carbides produced by 110
 nitrides produced by 110
 process 104f
- Ion's spin fluctuation rate, critical slowing down of Mössbauer 463-478
- Ion system, Kramers464, 471-473
- Iron
 -bearing mineral(s)
 carbonates and clay 276
 in coal140-155
 in fossil fuels by ^{57}Fe Mössbauer spectroscopy, analysis of221-242
 in fresh 274
 in petroleum source rock by ^{57}Fe Mössbauer spectroscopy, analysis of ..221-242
 vs. sulfur abundance in coal . 276
 in brown coals, chemical states of nonpyritic209-218
 -carbon system of steels ...283-286
 carbonate phases during coking, transformations of ferrous clay 279
 coal 227
 compounds, Mössbauer f -values of203, 204t
 concentration, intensity method to determine total and pyritic187-188
 concentration, resonance area method to determine total and pyritic183-187
 Mössbauer vs. ASTM method of total and pyritic ...188-191
 -cobalt in the zeolite catalyst, state of iron 575
 -containing protein, molybdenum- 305
 DCEMS to measure to magnetic field near the surface 95
 using $\text{Fe}(\text{NO}_3)_3$, Mössbauer spectrum of Silicalite impregnated with 577f
- foils
 carbon-implanted CEMS studies107-110
 ^{57}Fe CEMS study of nitrogen-implanted88, 89f
 ^{57}Fe DCEM spectra of a fluorinated 74f
 in hydrogen atmospheres, decarburization 91
 -implanted copper alloys, CEMS studies105-107
 and iron-cobalt in the zeolite catalyst, state of 575

Iron (*continued*)

- molybdenum-nitrogen system . 288
 nonpyritic 183
 and other ores, characterization and processing 266
 oxyhydroxide 276
 oxides
 aluminum incorporation ..256-260
 in clay247-260
 in coal 155
 in soil, analysis247-260
 -platinum alloys 555
 protein, high-potential 307
 -ruthenium
 alloys on silica 555
 bimetallic catalyst systems 553-571
 ^{57}Fe Mössbauer parameters 562t
 reaction scheme for 570f
 ^{99}Ru Mössbauer parameters 563t
 samples
 ^{57}Fe Mössbauer spectra ...564f, 566f, 567f
 ^{99}Ru Mössbauer spectra 565f, 568f
 x-ray powder patterns 570f
 and steels, aqueous oxidation
 corrosion84-87
 sulfates, Mössbauer parameters . 154t
 sulfide 282
 in coal140-143, 142t
 liquefaction residues 168
 -sulfur clusters305-324
 -sulfur minerals in coal136, 225
 surfaces, phosphating 87
 -titanium alloy, internally nitrided 287f
 -titanium-nitrogen system 287
 -zeolite catalysts used in synthesis gas conversion, Mössbauer and magnetic studies on bifunctional medium-pore573-588
- Iron(II) complexes formed with pyrazolylborate ligands 457
- Iron(II) phosphate octahydrate .87, 94
- Iron(II) spin crossover systems, effect of metal dilution ...408-433
- Iron(II) sulfate 231
 hydrates 226
- Iron(II) for zinc(II) in the $[\text{Fe}_x\text{Zn}_{1-x}(2\text{-pic})_3]\text{Cl}_2 \cdot \text{C}_2\text{H}_5\text{OH}$ system, effect of substituting 412
- Iron(III) carboxylates 216
- Iron-57
 CEMS
 applications84-95
 characterization of inorganic solids and minerals and archaeological artifacts .93-95
 energy-differential125-132
 study of nitrogen-implanted iron foils88, 89f
 surface selectivity66, 67f

Iron-57 (*continued*)

- DCEM spectra of a fluorinated
from foil 74*f*
and ^{129}I Mössbauer measure-
ments 29–34
-implanted aluminum 92
ion-implantation studies 91–93
Mössbauer
parameters of iron–ruthenium
bimetallic catalysts 562*t*
spectroscopy
analysis of iron-bearing
minerals in fossil
fuels 221–242
analysis of iron-bearing
minerals in petroleum
source rock 221–242
electron spectrometer ... 125–132
spectrum of iron–ruthenium
samples 564*f*
and ^{99}Ru Mössbauer spectros-
copy, characterization of
mixed-metal catalysts .. 553–571
Isomer shift(s) 528
calibration 378–380
contact density, and charge
transfer, ^{197}Au 41–45
and electron charge density at
the Mössbauer nucleus ... 9–14
to electron counts, conversion .. 43–45
of gold 43, 44*f*
of gold(I) complexes 43, 44*f*
of gold(III) complexes 43, 44*f*
of metallic compounds and
alloys 43, 44*f*
in metallic systems and coordi-
nation complexes 41–43
 ^{237}Np 348–350
for ^{99}Ru Mössbauer spectra ... 558
in tantalates, ^{181}Ta 488
for various zinc source and
absorber combinations 342*t*
Isotope effect on the spin crossover
behavior in $[\text{Fe}(2\text{-pic})_3]\text{Cl}_2$ ·
Sol, deuterium 437–440
Isotropic hyperfine interaction ... 470
- J**
- Jarosite(s) 153, 234, 235, 275
- K**
- K_2FeO_4 , critical slowing down of
spin fluctuations 476–478
 K_2FeO_4 , Mössbauer spectra .. 476, 477*f*
 $\text{KAu}(\text{CN})_2$, electric field gradients 47
 $\text{K}[\text{Au}(\text{CN})_2]$, pseudoatomic
model and interpretation of
the quadrupole splitting 45–51
Kaolinite 144, 250
Ketazine 373
Ketimines ($\text{R}_2\text{C}:\text{NH}$) 361
- Ketiminium hexachloroantimo-
nate(V) salts ($[\text{R}_3\text{C}:\text{NH}_2]\text{-}$
 $[\text{SbCl}_6]$) 373
 $\text{KFeS}_3\text{-LiKFeS}_2$ cathode 535
Kramers
ion 464
system, non-ion 471–473
Theorem 464
 KTaO_3 , ^{181}Ta Mössbauer
spectroscopy 486–489
- L**
- LaNi_5 517
Larmor period 351, 465
Laves phase materials 513
Laves phase structure 508
Lepidocrocite ($\gamma\text{-FeOOH}$) 250
Lewis acid sites on metal oxides,
adsorption of bases 601
LCAO (*see* Linear combination of
atomic orbitals)
 $\text{Li}_{0.86}\text{Fe}_{0.05}\text{Ta}_{0.95}\text{S}_2$, ^{57}Fe
Mössbauer spectra 534*f*
 $\text{LiKFeS}_2\text{-KFeS}_2$ cathode 535
 Li_xMS_2 525
 LiNbO_3 487, 488
 LiNbO_3 and LiTaO_3 , point-charge
calculation of the electric field
gradients
for ^7Li 495, 496*f*
for ^{93}Nb 495, 496*f*
for ^{181}Ta 495, 496*f*
 LiTaO_3
ferroelectric phase transition . 487–497
structure in ferroelectric and
paraelectric phase 487*f*
 ^{181}Ta Mössbauer spectros-
copy 486–489
 ^{181}Ta spectra 490, 491*f*
temperature-induced variation
of the electric quadrupole
interaction 490–493
 $\text{LiTaS}_2\text{-TaS}_2$ cathode 533–535
 Li_xTiS_2 525
 Li_xVS_2 cathode 526
Ligand
electronegativity for iodine
anions, and correlation
between the quadrupole
coupling constants 387
field theory 405–449
 ^{237}Np isomer shifts 356*t*–357*t*
Lindgren's Dirac–Fock scheme .. 48
Linear combination of atomic
orbitals 9
Liouville Hamiltonian 469
Liquefaction, coal 167–172
Lithium-intercalated MS_2 com-
pounds 525
Lithium intercalation compounds
of the transition-metal layer
dichalcogenides 523–536

- Lithium-7 in LiNbO_3 and LiTaO_3 ,
point-charge calculations of
the electric field gradients 495, 496f
Lithium-7 NMR studies 495
Lithologic components of coal ... 137
Low-spin (LS) transition,
high-spin (HS) 405-449

M

- Macerals, coal 137
Magnesium metal, Eu-doped 121
Magnesium siderite 235
Magnetic
beta-ray spectrometer 72, 73f
crossover 405-449
field, effective 471
field near the surface of iron,
DCEMS to measure 95
hyperfine fields 29-34
interaction, ^{237}Np 351
phase transitions, relaxation
effects associated with .. 463-478
studies on bifunctional medium-
pore zeolite-iron catalysts
used in synthesis gas con-
version, Mössbauer 573-588
Magnetite 155, 266
Magnetization curve, Weiss 470
Marcasite 140, 179, 211, 225
Mössbauer spectra 143f, 180f
Markoffian relaxation process ... 466
Martensite-austenite, -carbide
determinations 283
Martensite spectrum for high-
carbon steels 285
Mass absorption coefficients 78
for pyrite, Mössbauer 275
Matrix elements, Hamiltonian ... 4
Mayer's process 163
Melanterite 153-154
Metal
complexes, spin crossover in
transition 405-449
dilution in the Fe/Co/2-pic
system, effect 417, 419f, 420f
dilution studies on
[Fe_xZn_{1-x}(2-pic)₃]Cl₂ ·
C₂H₅OH 413
-mixed catalysts by ^{57}Fe and
 ^{99}Ru Mössbauer spectroscopy,
characterization .. 553-571
oxides, adsorption of bases to
Lewis acid sites 601
surfaces, improving durability .. 107
Metallic systems and coordination
complexes, isomer shifts 41-43
Metallization of plastics, Möss-
bauer studies of colloidal
catalyst solutions used 539-551
Metallizing plastics by electroless
plating, steps 541f
Metallurgical applications,
CEMS 90-91

- Methyleneaminolithium com-
pounds 373
Micas 146
Mineral(s) (in)
coal
carbonate 150-153
clay 143-150
iron-bearing 140-155
iron-sulfur 136, 225
matter 137
fossil fuels by ^{57}Fe Mössbauer
spectroscopy, analysis of
iron-bearing 221-242
matter vs. ash 179
petroleum source rock by ^{57}Fe
Mössbauer spectroscopy,
analysis of iron-bearing .. 221-242
sulfur 224
transformations during coking 277-279
Mineralogy-pyritic sulfur deter-
minations, coal 274-276
Mitochondria, oxidized aconitase
from beef-heart 322
MoFe protein 307
Molecular
core wave functions 9
orbital calculations of
bromine-containing mole-
cules, self-consistent field
and charge 3-35
of chlorine-containing mole-
cules, self-consistent field
and charge 3-35
of fluorine-containing mole-
cules, self-consistent field
and charge 3-35
of iodine-containing mole-
cules, self-consistent field
and charge 3-35
to Mössbauer spectroscopy of
halogen-containing com-
pounds, application ... 3-35
orbital, self-consistent charge .. 3-35
Molybdenum 286
and iron-containing protein ... 305
-nitrogen system, iron- 288
oxides, tin- 601
Montmorillonite(s) 148, 274
Mössbauer
absorber(s), background
correction 202
granularity 197-202
texture and spectral resolu-
tion 205-206
analysis
of coal after various
treatments 191-194
of coals by resonance intensity
method 194t-195t
problems in quantitative .. 197-206
of steels 283-299
area method, analysis of U.S.
coals, and by ASTM
methods 189t

- Mössbauer (*continued*)
 and ASTM methods for coal,
 comparison of 240
 vs. ASTM method of total and
 pyritic iron in coal188-191
 effect
 study of the spin state in
 bis(hydrotris(3,5-di-
 methyl-1-pyrazoly)
 borate iron(II), high-
 pressure453-461
 study of Victorian brown
 coal209-218
 system, Hamiltonian for 348
 in ^{67}Zn 329-344
 investigation of $\alpha\text{-Fe}_2\text{O}_3$ micro-
 crystals supported on
 $\gamma\text{-Al}_2\text{O}_3$ 609-617
 ion's spin fluctuation rate, criti-
 cal slowing down463-478
 and magnetic studies on bifunc-
 tional medium-pore zeolite-
 iron catalysts used in syn-
 thesis gas conversion .. 573-588
 mass-absorption coefficient for
 pyrite 275
 measurements of AuCN,
 pressure-dependent 52
 measurements, ^{57}Fe and ^{129}I ..29-34
 nucleus 464
 isomer shift and electron
 charge density 9-14
 parameters
 empirical relationships ... 376-377
 in linear gold(I), bonding
 properties51-57
 ranges for ^{121}Sb 365*t*
 resonance, transducer calibra-
 tion for ^{67}Zn 332-333
 scattering to examine pottery
 surface glazes111-114
 source, Debye-Waller factors .. 156
 spectra
 of coals and coal process
 products 226
 of ^{57}Fe -enriched ferredoxin
 from *A. vinelandii* 314*f*
 of ferredoxin from *D. gigas* .. 313
 spectroscopic investigations of
 oxidation catalysts589-605
 spectroscopy
 analysis of iron-bearing min-
 erals in fossil fuels by
 ^{57}Fe 221-242
 analysis of iron-bearing min-
 erals in petroleum source
 rock by ^{57}Fe 221-242
 to anions and cations of
 iodine application of
 ^{127}I 375-390
 of bed-moist vs. dried
 coal211-218
 characterization of antimony
 compounds by ^{121}Sb ..361-373
- Mössbauer (*continued*)
 spectroscopy (*continued*)
 characterization of mixed-
 metal catalysts by ^{57}Fe
 and ^{99}Ru 553-571
 to coal characterization and
 utilization, application 135-172
 conversion x-ray (CXMS) ... 101
 depth-resolved conversion
 electron 64
 electron re-emission292-298
 electron spectrometer for
 ^{57}Fe 125-132
 of halogen-containing com-
 pounds, application of
 molecular orbital calcu-
 lations 3-35
 for pyritic sulfur determina-
 tion155-163
 in the steel industry, appli-
 cations265-299
 ^{119}Sn 539-551
 to study electronic proper-
 ties of intermetallic, inor-
 ganic, and organometallic
 compounds, application .39-59
 technical problems 229
 x-ray re-emission292-298
 studies
 of the alkali tantalates,
 ^{181}Ta 481-497
 of battery materials523-536
 of catalytically active tin-anti-
 mony oxides, ^{121}Sn 590
 of colloidal catalyst solutions
 used in metallization of
 plastics539-551
f-values of iron compounds
 in coals203, 204*t*
 MS_2 compounds, lithium-inter-
 calated 525
 Mulliken population analysis 8
 Muscovite 146
- N**
- $\text{N}(\text{C}_2\text{H}_5)_4\text{FeI}_4$, tetraiodoferrate
 cluster FeI_4^- 29-34
 $\text{N}(\text{C}_2\text{H}_5)_4\text{FeI}_4$, calculated iodine
 parameters 32*t*
 $\text{Na}_3\text{H}_2\text{IO}_6$ 379
 Neptunium
 fluorides, isomer shifts 350*f*
 organometallic compounds,
 preparation 354
 oxides, isomer shifts 350*f*
 Neptunium(III) organometallics,
 isomer shifts 359*t*
 Neptunium(IV) organometallic
 from ^{237}Np Mössbauer spec-
 tra, covalency347-359
 Neptunium-237
 hyperfine interactions 348
 intermediate relaxation effects 351-352

- Neptunium-237 (*continued*)
 isomer shift 348–350
 and covalency 354–359
 for ligands 356t–357t
 magnetic interaction 351
 Mössbauer spectra, covalency
 of neptunium(IV) organo-
 metallics from 347–359
 Mössbauer spectra of NpCp₃X
 compounds 354
 organometallics and their
 uranium analogues,
 bonding 358–359
 physics 348
 quadrupole interaction 350–351
 Niobium-93 in LiNbO₃ and
 LiTaO₃, point-charge calcu-
 lations of the electric field
 gradients 495, 496f
 Niobium-93 NMR studies 495
 Nitrided steels, internally 286–292
 Nitrides produced by ion implanta-
 tion 110
 Nitrogen
 -implanted iron foils, Fe
 CEMS study 88, 89f
 system, iron–molybdenum- 288
 system, iron–titanium- 287
 Nitrogenase
 from *Azobacter vinelandii* 307
 from *Clostridium pasteurianum* 307
 clusters 306–310
 (FeMo-co) 307
 (M-centers), cofactor center 308–310
 P-cluster 307–308
 stable oxidation states of the
 cofactor centers 309f
 NMR
 spectroscopy of halogen-contain-
 ing compounds, application
 of molecular orbital calcu-
 lations 3–35
 studies, ⁷Li 495
 studies, ⁷Nb 495
 Northern Black Polished Ware,
 Indian 112f, 113
²³⁷Np (*see* Neptunium-237)
 Np(acac)₂Cl₂ · THF, Mössbauer
 spectrum 356f
 Np(acac)₂(MeCp)₂, Mössbauer
 spectrum 357f
 NpCp₄ compounds, isomer
 shifts 358t–359t
 NpCp₃BH₄, Mössbauer spectra .. 355f
 NpCp₃OCH(CH₃)₂, Mössbauer
 spectrum 355f
 Np–Cp_n-X_{4-n} compounds, Möss-
 bauer parameters 356t–357t
 Np(COT)₂ compounds, isomer
 shifts 358t–359t
 Np(MeCp)₃BH₄, Mössbauer
 spectra 355f
 Np(MeCp)₃Cl, Mössbauer
 spectrum 352f
- O**
- Oil shales, survey 235–239
 Olefins on tin–antimony oxides,
 chemisorption and catalytic
 reactions 605
 Opposed diamond anvil cell,
 schematic of 454f
 Opposed diamond anvil cell
 technique 454–456
 Orbital
 calculations to Mössbauer spec-
 troscopy of halogen-contain-
 ing compounds, application
 of molecular 3–35
 energies for halogen-containing
 molecules 12t
 populations for iodine in iodine-
 containing molecules, and
 electric field gradient con-
 tributions 22t–23t
 Ores
 characterization and processing
 of iron 266
 direct-reduction processes 268
 iron 266
 raw and beneficiated 266
 taconite 266
 Organoantimony(V) compounds,
¹²¹Sb Mössbauer data 372t
 Organometallic(s)
 bonding in actinide 359
 compound
 actinide 354
 application of ¹⁹⁷Au Möss-
 bauer spectroscopy to
 study electronic proper-
 ties of intermetallic, and
 inorganic 39–59
 preparation of neptunium .. 354
 isomer shifts of neptunium(III) 359t
 from ²³⁷Np Mössbauer spectra,
 covalency of nep-
 tunium(IV) 347–359
 Oxidation catalysts, Mössbauer
 spectroscopic investigations 589–605
 Oxidation corrosion of iron and
 steels, aqueous 84–87
 Oxide(s)
 adsorption of bases to Lewis
 acid sites on metal 601
 antimony-doped tin(IV) 605
 catalysts, active centers in
 tin–antimony 601
 chemisorption and catalytic
 reactions of olefins on
 tin–antimony 605
 in clay, iron 247–260
 in coal, iron 155
 environments, tin(IV) species . 596
 following reaction with butene
 and oxygen, ¹¹⁹Sn and ¹²¹Sb
 Mössbauer parameters of
 tin–antimony 602t–603t

Oxide(s) (*continued*)

- following reaction with hydro-
gen, ^{119}Sn and ^{121}Sb
Mössbauer parameters of
tin-antimony 602t-603t
 ^{121}Sb Mössbauer investigations
of tin-antimony 597-601
($\text{Sn}_{1-x}\text{Sb}_x\text{O}_2$), ^{121}Sb Mössbauer
parameters of tin-antimony 593t
($\text{Sn}_{1-x}\text{Sb}_x\text{O}_2$), ^{119}Sn Mössbauer
parameters of tin-antimony 592t
in steels, surface and sub-
surface 292-298
tin-molybdenum 601
 ^{119}Tm Mössbauer investigations
of tin-antimony 596-597
- Oxygen, ^{119}Sn and ^{121}Sb Möss-
bauer parameters of tin-anti-
mony oxides following reac-
tion with butene 602t-603t

P

- Palladium
catalyst, colloidal 542
-iron, alloys 555
-tin alloy formation 544
-tin colloidal catalyst
system 542, 543f
- Parameters, spin Hamiltonian .. 466-478
- Pauli paramagnet 507
- Pauling's electroneutrality principle 54
- Periodate ion 379
- Petroleum source rock by ^{57}Fe
Mössbauer spectroscopy,
analysis of iron-bearing
minerals 221-242
- Phosphating of iron surfaces 87
- Photons, x-ray 64
- Phyllosilicates (layer-lattice sili-
cates) 143
- Plastics by electroless plating,
steps in metallizing 541f
- Plastics, Mössbauer studies of col-
loidal catalyst solutions used
in metallization 539-551
- Pollution from coal 163
- Pollution, sources of SO_2 163
- Pottery surface glazes, Mössbauer
scattering to examine 111-114
- Pressure-dependent Mössbauer
measurements of AuCN 52
- Pressure-dependent Mössbauer
measurements of $[\text{Au}(\text{CN})_2]^-$ 5
- Process products, Mössbauer spec-
tra of coals and coal 226
- Propene to acrolein, oxidation 597
- catalytic 601
- Protein(s)
that exhibit an HiPIP-type
EPR signal in the oxidized
state 306-323
high-potential iron 307
with magnetic properties 323

Protein(s) (*continued*)

- MoFe 307
molybdenum- and iron-con-
taining 305
- Pyrazolylborate ligands, iron(II)
complexes formed with 457
- Pyrite 211, 225, 274
Debye-Waller factor 157
during coking, behavior 278-279
(FeS_2) 140-143
to goethite, transformation .. 276, 277f
-marcasite 232, 235
Mössbauer mass-absorption
coefficient 275
Mössbauer spectrum(a) ... 141f, 180f
portable analyzer 230
quantitative investigations ... 177-206
- Pyritic sulfur 224
(S_2^{2-}) 182
- Pyritic sulfur determinations
coal mineralogy- 274-276
comparison 162f
Mössbauer spectroscopy ... 155-163
- Pyrrhotite(s) 168, 278

Q

- Quadrupole
coupling 532
constant and electric field
gradient at the halogen
nucleus 14-29
constants and ligand electro-
negativity for iodine
anions, correlation
between 376
interaction, ^{237}Np 350-351
splitting in
 $[\text{Au}(\text{CN})_2]^-$ 49-51
 AuTe_2 54
for gold(I) linear compounds 50
gold(III) compounds 54
for gold(III) square-planar
compounds 50
 $\text{K}[\text{Au}(\text{CN})_2]$, pseudoatomic
model and interpretation 45-51
- Quartz transducer 334

R

- s-d* Rehybridization effects 42
- Relaxation
effects associated with magnetic
phase transitions 463-478
effects, ^{237}Np intermediate .. 351-352
process, Markoffian 466
rate parameters 476
- Resonance area method to deter-
mine total and pyritic iron
concentration from coal ... 183-187
- Resonance intensity method,
Mössbauer analysis of
coals 194t-195t

- Resonant effect in CEMS 119
 Rozenite 153-154
 β -RuCl₃ 563
 [Ru(NH₃)₅X]²ⁿ, ruthenium(II) pentaamines 559
 RuO₂ 558
 quadrupole-split of ruthenium dioxide 557
 Ruthenium
 complexes, chemical bonding and structure 559
 dioxide (RuO₂), quadrupole-split spectra 557
 -iron
 alloys on silica 555
 bimetallic catalyst systems 553-571
 reaction scheme 570f
 bimetallic catalysts, ⁵⁷Fe Mössbauer parameters .. 562t
 samples, x-ray powder patterns 570f
 Ruthenium(II) pentaamines ([Ru(NH₃)₅X]²ⁿ) 559
 Ruthenium-99 Mössbauer parameters of iron-ruthenium bimetallic catalysts 563t
 parameters ruthenium(II)-cyanide complexes 559
 spectra 556-560
 isomer shifts 558
 spectroscopy, and characterization of mixed-metal catalysts by ⁵⁷Fe 553-571
 Ruthenium-99, 90-KeV Mössbauer transition 556
 Ruthenocene 558
 [Ru(C₅H₅)₂], quadrupole-split spectra 557
 Rutherford backscattering 546
- S**
- S²⁻ (*see* Sulfide)
 S₂²⁻ (pyritic sulfur) 182
 Samian Ware 111, 112f
 Sands, titanium-bearing 272
 SbCl₅, interaction of R₂C:NH with 361-373
 SCC (*see* Self-consistent charge)
 SCF (*see* Self-consistent field)
 ScFe₂H_x 513
 Self-consistent
 charge molecular orbital 3-35
 field molecular orbital calculations of 3-35
 bromine-containing molecules 3-35
 chlorine-containing molecules 3-35
 fluorine-containing molecules 3-35
 iodine-containing molecules .. 3-35
 Sternheimer factors 22t
 Sensitization and electroless plating 541
 Serpentine 144
 Shaft-furnace reduction process .. 268
 Shaft-reduction furnace, schematic .270f
 Shielding 17-20
 function, Sternheimer 14, 17
 Siderite 150, 174
 transformation during coking .. 279
 Silicalite
 and comparison of zeolite ZSM-5 575t
 impregnated with iron using Fe(NO₃)₃, Mössbauer spectrum 577f
 Mössbauer spectrum of reduced pore structure of zeolite ZSM-5 -zeolite-based catalysts for synthesis gas conversion 574
 pore structure of zeolite ZSM-5 574f
 Silicates, chain 143
 Silicates, layer-lattice (phyllosilicates) 143
 Silicon-steels 293
 Sintering 267
 Slag deposits, factors controlling ash 280-282
 Slater-type orbitals 4
 Smectites 148
 Sn²⁺ 544
 SO₂ pollution, sources 163
 SO₄²⁻ (sulfate sulfur) 182
 Soil, analysis of iron oxides ... 247-260
 Sources 394
 Spectra of coals and coal process products, Mössbauer 226
 Spectra, hyperfine structure of ¹⁸¹Ta gamma-resonance ... 483-486
 Spectrometer
 for CEMS studies, electron .126, 127f
 for DCEMS studies, beta-ray ..71-77
 with a double-frequency interferometer, ⁶⁷Zn 336
 electrostatic beta-ray 75, 76f
 for ⁵⁷Fe Mössbauer spectroscopy, electron 125-132
 high-pressure Mössbauer 395
 magnetic beta-ray 72, 73f
 Spectroscopic energies 222t
 Spectroscopic evidence three-iron center in ferredoxins 311
 Spectroscopy, depth-resolved conversion electron Mössbauer .. 64
 Spectroscopy of halogen-containing compounds, application of molecular orbital calculations to NMR 3-35
 Spin
 crossover
 behavior in [Fe(2-pic)₃]Cl₂ · Sol, deuterium isotope effect 437-440
 phenomenological thermodynamic model 413-416
 in the solvates [Fe(2-pic)₃]Cl₂ · Sol (Sol=C₂H₅OH) 434-437
 structural change accompanying 441-448

Spin (<i>continued</i>)	
crossover (<i>continued</i>)	
system(s), effect of metal dilution in iron(II) . . .	408-433
system, mechanism of spin transition in a crystalline	412
in transition metal complexes	405-449
fluctuation rate, critical slowing down of Mössbauer ion's	463-478
fluctuations in K_2FeO_4 , critical slowing down	476-478
Hamiltonian parameters . . .	466-478
state	
in bis[hydrotris(3,5-dimethyl-1-pyrazolyl) borate iron(II), high-pressure Mössbauer effect study	453-461
transformation in $Fe[HB(3,5-Me_2pz)_3]_2$	454-456
transformation in $Fe[HB(pz)_3]_2$	454-456
transition	
characteristics in $[Fe_xM_{1-x}(phen)_2(NCS)_2]$	424-429
in a crystalline spin crossover system, mechanism	412
driving force and possible mechanism	408-413
$[Fe(phen)_2(NCS)_2]$, effective trigger for	446-447
of $[Fe(phen)_2(NCS)_2]$, influence of the preparation method	440-441
Stannic hydroxide	549
Steel(s)	
aqueous oxidation corrosion of iron	84-87
austenite spectrum for high-carbon	285
austenitic stainless	284
industry, applications of Mössbauer spectroscopy	265-299
internally nitrided	286-292
iron-carbon system	283-286
martensite spectrum for high-carbon	285
Mössbauer analysis	283-299
precipitation-strengthened high-strength low-alloy (HSLA)	286
silicon-	293
surface(s)	
by CEMS, characterization . . .	90-91
regions of nitrided	88
and subsurface oxides	292-298
treatments	87-90
Sternheimer	
factors	45
self-consistent	18f, 22t
functions, self-consistent	19f
shielding	
factor for iodine and halides . .	20t
functions	14, 17
Stress, measurement of surface . . .	91
Sulfate(s)	
in coal	153-155
Mössbauer parameters of iron .	154t
phases in coal	275
sulfur	224
(SO_4^{2-})	182
Sulfide iron	282
in coal	140-143, 142t
Sulfides in coal liquefaction residues, iron	168
Sulfur	
abundance in coal, iron-bearing minerals vs.	276
in coal, ASTM method to determine	224
in coals, forms	182
content of coal, ASTM Standard D3177 for determining total	182
determination(s)	
in coal, ASTM standard method	155
coal mineralogy-pyritic sulfur	274-276
comparison of pyritic	162f
Mössbauer spectroscopy for pyritic	155-163
-iron clusters	305-324
mineral(s)	224
in coal, -iron	136, 225
pyritic	224
sulfate	224
Surface(s)	
by CEMS characterization of steel	90-91
improving durability of metal .	107
selectivity of ^{57}Fe CEMS	66, 67f
selectivity and sensitivity of CEMS	67-68
stress, measurement	91
treatments of steels	87-90
Syngas	166
Synthesis gas	
conversion, Mössbauer and magnetic studies on bifunctional medium-pore zeolite-iron catalysts used in	573-588
conversion, zeolite-Silicalite-based catalysts for	574
to gasoline-range hydrocarbons and olefins bifunctional zeolite catalysts, catalytic conversion of coal-derived	574
Synthetic fuels, production	166
Szomolnokite	153-154
T	
TaC	489
Taconite ore	266
Tantalates	
crystal structure and ferroelectric properties	486

- Tantalates (*continued*)
- ¹⁸¹Ta isomer shifts 488
 - ¹⁸¹Ta Mössbauer spectra of the alkali 486*f*, 488
 - ¹⁸¹Ta Mössbauer studies of the alkali 481–497
- Tantalum
- compounds, ¹⁸¹Ta Mössbauer data 489*t*
 - dichalcogenides 489
 - metal absorbers 483
 - ¹⁸¹Ta Mössbauer spectroscopy of LiTaO₃ 486–489
- Tantalum-181
- gamma-resonance spectra, hyperfine structure 483–486
 - isomer shift in tantalates 488
 - isomer shift, temperature dependence 491
 - in LiNbO₃ and LiTaO₃, point-charge calculations of the electric field gradients .. 495, 496*f*
 - in LiTaO₃, electric field gradient calculations 490–493
 - Mössbauer data on tantalum compounds 489*t*
 - spectra of the alkali tantalates 486*f*, 488
 - spectroscopy of KTaO₃ .. 486–489
 - spectroscopy of NaTaO₃ .. 486–489
 - studies of the alkali tantalates 487–497
 - nuclear parameters of the 6.2-keV gamma resonance . 484*t*
 - quadrupole-split spectra as a computer-simulated .. 484, 485*f*
 - spectra of LiTaO₃ 490, 491*f*
- TaS₂–LiTaS₂ cathode 533–535
- TaSe₂ 489
- Tellurium
- bonding in trigonal 397
 - crystal structure of trigonal 397
 - ¹²⁹I probes 394
 - lattice structure 394
 - under pressure, structural and electronic changes 394
 - ¹²⁵Te and ¹²⁹I Mössbauer study of the high-pressure phase transition of 393–401
 - ¹²⁵Te probes in 399
- Tellurium-125 and ¹²⁹I Mössbauer study of the high-pressure phase transition of tellurium 393–401
- Tellurium-125 probes in tellurium . 399
- Tetraiodoferrate cluster FeI₄⁻ in N(C₂H₅)₄FeI₄ 29–34
- TFA (*see* trifluoroacetic acid)
- THF solubles, and conversion of coal to benzene 170
- Theorem, Kramers 464
- Thermodynamic model of spin crossover, phenomenological 413–416
- Thirring expansion 157
- Thulium-169, CEMS 117–123
- Thulium-169 8.4-keV resonance 122, 123*f*
- TiN₂ 288
- Tin
- antimony oxide(s) catalysts, active centers 601
 - chemisorption and catalytic reactions 605
 - following reaction with butene and oxygen, ¹¹⁹Sn and ¹²¹Sb Mössbauer parameters 602*t*–603*t*
 - following reaction with hydrogen, ¹¹⁹Sn and ¹²¹Sb Mössbauer parameters 602*t*–603*t*
 - ¹¹⁹Sn Mössbauer studies of catalytically active 590
 - (Sn_{1-x}Sb_xO₂), ¹²¹Sb Mössbauer parameters 593*t*
 - ¹²¹Sb Mössbauer investigations 597–601
 - (Sn_{1-x}Sb_xO₂), ¹¹⁹Sn Mössbauer parameters 592*t*
 - ¹¹⁹Tn Mössbauer investigation 596–597
 - aqueous corrosion 95–96
 - molybdenum oxides 601
 - palladium alloy formation ... 544
 - palladium colloidal catalyst system 542, 543*f*
- Tin(II) 596
- Tin(IV)
- hydroxide and antimonite acid, thermal decomposition .. 591–596
 - oxide, antimony-doped 605
 - species in oxide environments .. 596
- Tin-119 Mössbauer investigation of tin–antimony oxides 596–597
- parameters as a function of antimony content 596*f*
- parameters of tin–antimony oxides (Sn_{1-x}Sb_xO₂) ... 592*t*
- studies of catalytically active tin–antimony oxides 590
- Titanium-bearing sands 272
- Titanium–nitrogen system, iron– .. 287
- Townes–Dailey theory 46
- Transducer
- calibration for ⁶⁷Zn Mössbauer resonance 332–333
 - quartz 334
 - for use with ⁶⁷Zn 330, 331*f*
- Transition metal complexes, spin crossover ... 405–449
- dichalcogenides, structure and properties layer 524–525
- layer dichalcogenides, lithium intercalation compounds 523–536
- Transmission spectra, conversion electron spectra vs. gamma-ray 117–123

Trifluoroacetic acid	191	Zeolite	
Trigonal tellurium, bonding	397	catalysts, catalytic conversion	
Trigonal tellurium, crystal		of coal-derived synthesis	
structure	397	gas to gasoline-range hydro-	
Tris(cyclopentadienyl)uraniumIV		carbons and olefins using	
chloride	354	bifunctional	574
Troilite	171, 278	-iron catalysts used in synthesis	
		gas conversion, Mössbauer	
		and magnetic studies on bi-	
		functional medium-pore	573-588
		-Silicalite-based catalysts for	
		synthesis gas conversion ...	574
		ZSM-5	
		magnetization as a function of	
		temperature for	586f
		Mössbauer spectrum of	
		carbided	582f
		Mössbauer spectrum of	
		and Silicalite, comparison ...	575t
		and Silicalite, pore structure .	574f
		Zero-point motion to the second-	
		order Doppler shift, contri-	
		bution	337-338
		Zinc	
		chalcogenides	
		chemical shifts for ^{67}Zn in ...	335t
		isomer shifts	338-341
		resonance	335
		metal absorber	333
		metal, structure	342
		oxide	
		absorbers	334
		effect of temperature on	
		isomer shift	337-338
		isomer shift, $^{68}(\text{Ga})\text{ZnO}$ vs. .	336
		spectrum, effect of pressure on	337
		structure	342
		quadrupole	333
		interaction in zinc ...	342-343
		quadrupole structure	333
		source and absorber combina-	
		tions, isomer shifts for	
		various	342t
		and zinc oxide quadrupole	
		interaction in	342-343
		Zinc(II) in the $[\text{Fe}_2\text{Zn}_{1-x}(\text{2-pic})_3-$	
		$\text{Cl}_2 \cdot \text{C}_2\text{H}_5\text{OH}$ system, effect	
		of substituting iron(II)	412
		Zinc-67	
		general properties	329-330
		Mössbauer effect	329-344
		Mössbauer resonance, transducer	
		calibration	332-333
		spectrometer with a double-	
		frequency interferometer ..	336
		in the zinc chalcogenides,	
		chemical shifts	335t

Jacket design by Joan Wolbier.
Editing and Production by Susan Moses and V. J. DeVeaux.
Typeset by Service Composition Co., Baltimore, MD.
Printed and bound by Maple Press Co., York, PA.